Plasmonics and Nanophotonics for Advancing Radiative Cooling

Dissertation

Zur Erlangung des akademischen Grades eines

Doktors der Naturwissenschaen

Dr. rer. nat.

An der

Universität Bayreuth

Fakultät für Biologie, Chemie und Geowissenschaen

Vorgelegt von

Kishin Matsumori

geboren in Iwate, Japan

Bayreuth, 2023

This doctoral thesis was prepared at the chair of Physical Chemistry I at the University of Bayreuth from April 2019 until December 2022 and was supervised by Prof. Dr. Markus Retsch.

This is a full reprint of the thesis submitted to obtain the academic degree of Doctor of Natural Sciences (Dr. rer. nat.) and approved by the Faculty of Biology, Chemistry and Geosciences of the University of Bayreuth.

Date of submission:	17.01.2023
Acceptance by the exam commission:	25.01.2023
Date of defense:	21.06.2023

Acting dean: Prof. Dr. Benedikt Westermann

Doctoral committee:

Prof. Dr. Markus Retsch	(Reviewer)
PD Dr. Svend-Age Biehs	(Reviewer)
Prof. Dr. Mukundan Thelakkat	(Chairman)
Prof. Dr. Georg Papastavrou	

Summary

Heat always flows from a hot to a cold object, and the temperature of the hot object decreases. This is true even though those objects are spatially separated since they exchange heat by thermal radiation. Such a cooling process is known as radiative cooling, which has gained considerable attention as an eco-friendly cooling technology. An object facing the sky can carry heat to the cold outer space, and the object´s temperature passively decreases. This is because the atmospheric transparency window (ATW) locates in a wavelength range from 8 μm to 13 μm, and the blackbody radiation has an intensity peak in the ATW at ambient temperature (around 300 K). To maximize the cooling performance, the object must have absorption spectrally confined in the ATW. It is required to engineer the absorption properties of the object to obtain such selective absorption, and plasmonics and nanophotonics have been utilized as promising techniques for absorption engineering.

In this dissertation, in order to seek innovative approaches to absorption engineering for radiative cooling, I theoretically investigate plasmonic phenomena called electromagnetically induced transparency (EIT) and absorption (EIA). EIT and EIA originate from an optical interaction between two optical elements: one has a high optical loss, and another has a low optical loss. It is known that EIT and EIA can modulate and enhance the absorption of plasmonic systems. Those plasmonic phenomena have been widely investigated and utilized for various applications; however, they have not been applied to radiative cooling yet.

EIT is accompanied by mode splitting, in which a single peak absorption splits into two peaks by near-field interaction. This mode splitting of EIT may be beneficial for achieving broadband absorption since multiple absorption peaks are essential to widen the absorption bandwidth of a system. From this fact, I explore an approach to realizing selective absorption in the ATW by utilizing mode splitting. Using a finite element method (FEM) simulation, I design a semishell absorber, comprised of a dielectric SiO_2 core partially covered with an indium tin oxide (ITO) shell. The SiO_2 core supports a low-loss Mie resonance, and the ITO shell supports a high-loss localized surface plasmon (LSP). By optimizing structural parameters, the semishell absorber can possess a strong absorption only in the ATW. This broadband absorption is attributed to the fact that a mode splitting occurs in the LSP of the ITO shell. The mechanism of this mode splitting is elucidated by building quantitative models, showing that the LSP of the ITO shell strongly interacts with a magnetic dipole resonance of the SiO_2 core.

EIA can dramatically enhance the absorption of plasmonic systems. Therefore, plasmonic systems that intrinsically have weak absorption may be improved by applying EIA. This kind of absorption improvement may increase the degree of freedom for absorption engineering. However, the mechanism of EIA is still unclear, as described in previous studies interpreting EIA in different ways. To utilize EIA for radiative cooling, a thorough understanding of EIA is essential. Thus, I establish theories that greatly expand the current knowledge of EIA. My theoretical investigations suggest that there are two different EIAs. One is characterized by absorption enhancement occurring in a low-loss optical element by near-field interaction. By designing a coupled-oscillator model, I find a critical parameter to describe this EIA and reveal the condition to maximize EIA. Another EIA is attributed to absorption enhancement occurring in a high-loss optical element. When a spatial distance between optical elements is comparable to a wavelength, intermediate-field interaction occurs with phase retardation. This phase retardation can excite constructive interference between the optical elements, amplifying an optical resonance of the high-loss optical element. Using the coupled-dipole method, I formulate this phase-retarded interaction, enabling us to find an optimal spatial distance to maximize EIA by intermediate-field interaction.

In addition, this dissertation addresses another approach to further advancing radiative cooling. Even though selective absorption in the ATW is realized, the cooling performance is severely degraded under

high humidity since the atmosphere becomes opaque even in the ATW. It has been suggested that asymmetric light transmission (ALT) filters, which possess high transmission only on one-way light illumination, may be able to recover the cooling performance under high humidity. However, this approach remains controversial because thorough investigations of such ALT filters have not been given. In this dissertation, I focus on a representative ALT filter, a dielectric corner reflector (DCR), which has a one-dimensional triangular grating on one side. It has been understood that the DCR possesses ATW properties by total internal reflections (TIRs). However, the understanding of the DCR´s reflection has contained ambiguity since the effect of evanescent waves excited by TIRs has not been appropriately accounted for. Using the FEM simulation, I find that the evanescent waves can leak from the DCR, resulting in a reflection reduction. Based on this finding, I create a quantitative model, enabling us to optimize the DCR for a high-performance ALT filter.

Zusammenfassung

Wärme fließt immer von einem wärmeren Objekt in Richtung eines kälteren Objekts und die Temperatur des warmen Objekts nimmt dabei ab. Dies trifft auch dann zu, wenn die Objekte räumlich voneinander getrennt sind, da die Wärme mittels Wärmestrahlung übertragen wird. Ein solcher Kühlungsprozess wird ,,radiative cooling (Strahlungskühlung)'' genannt. Dieser Mechanismus hat als umweltfreundliche Kühlungstechnologie vermehrt an Aufmerksamkeit gewonnen. Ein Objekt, welches dem Himmel zugewandt ist, kann Wärme in das Weltall transportieren, dabei nimmt die Wärme des Objekts passiv ab. Dies ist der Fall, da das atmosphärische Fenster bei einer Wellenlänge von 8 µm bis 13 µm liegt und die Hohlraumstrahlung ihr Maximum im atmosphärischen Fenster bei Außentemperatur hat (ca. 300K). Um die Kühlungsleistung zu maximieren, muss das Absorptionsspektrum des Objektes auf das atmosphärische Fenster beschränkt sein. Um derartige selektive Absorptionseigenschaften zu erreichen, müssen diese dementsprechend konstruiert werden. Die Bereiche Plasmonik und Nanophotonik bieten vielversprechende Techniken hierzu.

In dieser Arbeit stelle ich theoretische Untersuchungen zu den plasmonischen Phänomenen der elektromagnetisch induzierter Transparenz (EIT) und Absorption (EIA) an, um innovative Herangehensweisen an den Mechanismus des radiative cooling zu finden. EIT und EIA stammen von der optischen Interaktion zweier optischer Elemente: eines besitzt eine hohe optische Dämpfung, das andere eine niedrige. Es ist bekannt, dass EIT und EIA die Absorption von optischen Systemen modulieren können. Diese plasmonischen Phänomene sind bereits oft untersucht und in verschiedenen Bereichen eingesetzt worden, haben allerdings auf dem Gebiet des radiative cooling bisher noch keine Anwendung gefunden.

Bei EIT ist das sogenannte mode-splitting zu beobachten, wobei eine einzelne Absorptionsspitze durch Nahfeld-Interaktion in zwei Spitzen geteilt wird. Dies ist gegebenenfalls hilfreich dabei, Breitbandabsorption zu erreichen, da multiple Spitzen essenziell sind, um die Bandweite der Absorption eines Systems zu erweitern. Anhand dieser Tatsache untersuche ich die Möglichkeit, auf das atmosphärische Fenster begrenzte Absorption mithilfe von mode splitting zu erreichen. Ich entwerfe einen semi-shell absorber, bestehend aus einem dielektrischen SiO2-Kern, welcher teils mit einer Indium-Zinnoxid (ITO)-Schale bedeckt ist, anhand einer Finite-Elemente-Methode (FEM)-Simulation. Der SiO2-Kern fördert eine Mie-Resonanz mit geringem Verlust, und die ITO-Schale bewirkt ein lokalisiertes Oberflächen-Plasmon (LSP) mit hohem Verlust. Indem die strukturellen Parameter optimiert werden, kann der semi-shell absorber so konstruiert werden, dass nur im atmosphärischen Fenster starke Absorption vorliegt. Diese Breitband-Absorption wird der Tatsache zugeschrieben, dass mode-splitting in dem LSP der ITO-Schale stattfindet. Der Mechanismus dieses mode-splitting wird durch die Entwicklung von quantitativen Modellen, welche die starke Interaktion des LSP der ITO-Schale mit einer magnetischen Dipol-Resonanz des SiO2-Kerns zeigen, verdeutlicht.

EIA kann die Absorptionseigenschaften von plasmonischen Systemen dramatisch erhöhen. Daher können Systeme, welche an sich schwache Absorptionseigenschaften besitzen, durch den Einsatz von EIA verbessert werden. Diese Art von Verbesserung der Absorption kann den Spielraum für die Konstruktion von Absorptionseigenschaften erhöhen. Allerdings ist der Mechanismus von EIA weiterhin unklar, wie aus Vorarbeiten, in welchen EIA unterschiedlich interpretiert wurde, ersichtlich ist. Um EIA für radiative cooling zu nutzen, ist ein umfangreiches Verständnis von EIA essenziell. Daher stelle ich Theorien auf, welche den aktuellen Wissensstand zu EIA deutlich erweitern. Meine theoretischen Untersuchungen suggerieren, dass es zwei verschiedene Arten von EIAs gibt. Eine von ihnen ist gekennzeichnet von einer Erhöhung der Absorption in einem optischen Element mit geringem Verlust durch Nahfeld-Interaktion. Anhand eines von mir entworfenen gepaarten Oszillator-Modells entdecke ich einen wesentlichen Parameter, um diese Art von EIA zu beschreiben und zeige die Bedingungen auf, unter denen EIA

maximiert werden kann. Eine weitere Art von EIA kann in einem optischen Element mit hohem Verlust zu erhöhter Absorption führen. Wenn eine räumliche Distanz zwischen optischen Elementen mit einer Wellenlänge vergleichbar ist, findet die Zwischen-Feld-Interaktion mit einer Phasenverzögerung statt. Diese Phasenverzögerung kann eine konstruktive Einflussnahme zwischen den optischen Elemente zur Folge haben und die optische Resonanz des optischen Elements mit hohen Verlust erhöhen. Anhand der gekoppelten-Dipol-Methode konzipiere ich diese phasenverzögerte Interaktion, welche uns erlaubt, die optimale räumliche Distanz zur Maximierung von EIA mittels Zwischen-Feld-Interaktion zu finden.

Zusätzlich thematisiert diese Dissertation einen weiteren Ansatz, um Fortschritte im Bereich radiative cooling zu machen. Auch, wenn selektive Absorption im atmosphärischen Fenster realisiert wird, wird die Kühlungsleistung bei hoher Luftfeuchtigkeit deutlich gemindert, da die Atmosphäre auch im atmosphärischen Fenster lichtundurchlässig wird. Vorarbeiten weisen darauf hin, dass asymmetrische Lichttransmissionsfilter (ALT), welche eine hohe Übertragungsrate alleinig bei einseitiger Belichtung besitzen, die Kühlungsleistund bei hoher Luftfeuchtigkeit verbessern können. Allerdings bleibt dieser Ansatz umstritten, da gründliche Untersuchungen dieser Art von Filter bisher ausstehend sind. In dieser Arbeit befasse ich mich mit einem repräsentativen ALT-Filter, einem dielektrischen Ecken-Reflektor (DCR), welcher ein eindimensionales dreieckiges Gitter auf einer Seite besitzt. Es wurde dargelegt, dass der DCR die Eingenschaften des atmosphärischen Fenster durch die Summe der inneren Spiegelungen besitzt (TIRs). Allerdings gibt es Unklarheiten hinsichtlich der Spiegelungen des DCR, da der Effekt der flüchtigen Wellen, welche durch die TIRs ausgelöst werden, nicht ausreichend in Betracht gezogen wurde. Mithilfe der FEM-Simulation stelle ich fest, dass die schwindenden Wellen aus dem DCR austreten können, welches in einer Abnahme der Spiegelung resultiert. Auf Grundlage dieses Ergebnisses entwerfe ich ein quantitatives Modell, welches es uns ermöglicht, den DCR zu einem Hochperformance-ALT-Filter zu optimieren.

List of publications

I wrote my thesis as a cumulative dissertation and present the results of the following publications in peer-reviewed journals:

1. **K. Matsumori**, R. Fujimura, and M. Retsch
   "Selective Broadband Absorption by Mode Splitting for Radiative Cooling"
   Opt. Express **30**(9), 14258 – 14273 (2022) https://doi.org/10.1364/OE.452912

2. **K. Matsumori**, R. Fujimura, and M. Retsch
   "Reflection Mechanism of Dielectric Corner Reflectors: The Role of the Diffraction of Evanescent Waves and the Goos-Hänchen Shift"
   ACS Omega **7**(27), 23353 – 23361 (2022) https://doi.org/10.1021/acsomega.2c01537

The thesis also includes the following manuscripts submitted to peer-reviewed journals:

3. **K. Matsumori**, R. Fujimura, and M. Retsch
   "Coupling Strength and Total Damping Govern Electromagnetically Induced Absorption in Coupled Plasmonic Systems"
   Accepted by *Adv. Photonics Res.* on March 14, 2023 https://doi.org/10.1002/adpr.202200211

4. **K. Matsumori**, R. Fujimura, and M. Retsch
   "Electromagnetically Induced Absorption Overcomes the Upper Limit of Light Absorption: DipoleDipole Coupling with Phase Retardation in Plasmonic-Dielectric Dimers"
   Accepted by *J. Phys. Chem. C* on August 15, 2023 https://doi.org/10.1021/acs.jpcc.3c03307

Abbreviations

MIR	Mid-infrared
ATW	Atmospheric transparency window
RC	Radiative cooler
MA	Metamaterial absorber
MIM	Metal-insulator-metal
SPP	Surface plasmon polariton
PSP	Propagating surface plasmon
LSP	Localized surface plasmon
ED	Electric dipole
MD	Magnetic dipole
EQ	Electric quadrupole
MQ	Magnetic quadrupole
TD	Two-dipole
FD	Four-dipole
EIT	Electromagnetically induced transparency
EIA	Electromagnetically induced absorption
ITO	Indium tin oxide
AZO	Aluminum-doped zinc oxide
FDTD	Finite-difference time-domain
RCWA	Rigorous coupled-wave analysis
FEM	Finite element method
TCMT	Temporal coupled mode theory
CDM	Coupled-dipole method
CO	Coupled-oscillator
ECO	Extended coupled-oscillator
GCO	Generalized coupled-oscillator
PPA	Plasmonic-polymer antenna
DQA	Dipolar-quadrupolar antenna
DCR	Dielectric corner reflector
GH	Goos-Hänchen

TIR	Total internal reflection
DL	Diffractional loss
SP	Stationary-phase
EF	Energy-flux

Contents

1. Preface and outline

Global warming is one of the fatal problems our society is facing in the 21st century. Compared to the average temperature in 1900, the average temperature in 2020 is 1 °C higher. The temperature rise by 2100, estimated based on the framework of the Shared Socioeconomic Pathway [1], is suggested to be 5 °C higher in case we ignore potential global environmental impacts caused by our socioeconomic development [2, 3]. In order to deal with the temperature rise, it is expected that the demand for space cooling will keep increasing in both industrial and residential building sectors. The increase in demand appears as an increase in electricity consumption since traditional cooling systems, such as air-conditioning, require a large amount of electricity. According to a report from the International Energy Agency, space cooling accounts for 16% of building sector electricity consumption in 2021. The energy demand for space cooling has risen by 4 % per year since 2000 [4]. By consuming electricity, we can maintain comfortable temperatures in buildings. However, high electricity consumption causes critical problems. According to the Statistical Review of World Energy by British Petroleum, fossil fuels, such as coal and natural gas, are dominantly used for electricity production, accounting for 60 % of global total electricity production [5]. Electricity production by fossil fuels is accompanied by a significant amount of CO_2 emission, accelerating global warming. In addition, we also have to pay attention to reserves-to-production (R/P) ratios, which measure how many years a non-renewable resource will remain if consumption rates do not change from the current statute. The report from British Petroleum says that R/P rates of coal and natural gases are about 130 years and 50 years, respectively [5]. These data indicate that the energy crisis is associated with global warming, and global warming and the energy crisis will worsen further if we keep relying on traditional cooling technologies.

Passive cooling techniques have been expected to enable breakthroughs for next-generation cooling technologies [6, 7]. Passive cooling does not emit CO_2 nor require any electrical energy input. A concept of passive cooling is mitigating the temperature rise of buildings by utilizing natural processes. The temperature of buildings is increased by heat sources inside buildings, sunlight exposure, and so on. Depending on the means to deal with these heat gains, passive cooling is classified into three groups: heat protection, heat modulation, and heat dissipation techniques. The heat protection technique is meant to reduce heat gain from sunlight. As for the heat modulation technique, the heat produced in buildings during the daytime is stored using material properties, such as thermal mass and phase change materials, and released during nighttime. These two techniques aim to minimize heat gain inside and outside buildings. In contrast, the heat dissipation technique reduces the temperature of buildings by disposing of heat to the colder environment through conduction, convection, and radiation heat transfers. Therefore, if the aim is to reduce the temperature of buildings, the heat dissipation technique must be chosen. The mentioned techniques have many sub-classifications, in case of the heat dissipation technique, it is further categorized into evaporative and radiative cooling among others.

Radiative cooling is a natural process occurring under a clear sky. In the mid-infrared (MIR) range, the atmosphere has a transparency window from 8 μm to 13 μm in wavelength. This spectral range is called the atmospheric transparency window (ATW). Conveniently, an intensity peak of the blackbody radiation at ambient temperature (≈ 300 K) locates in the ATW. Thus, thermal radiation emitted from the earth´s surface can access the massive heat sink of outer space with a temperature of 3 K. The earth´s surface is mainly heated by sunlight absorption during the daytime. The heat on earth can be disposed to outer space during the nighttime by radiative heat transfer, resulting in a temperature reduction of the earth´s surface. This temperature reduction is substantial and can for example be seen as frost on leaves in the early morning.

Until now, radiative cooling has been intensively and interdisciplinarily investigated, and many different developments have been made on radiative coolers (RCs) for practical applications [8-10]. For

example, natural radiative cooling occurs only during the nighttime, but the temperature of buildings must be decreased during the daytime. For daytime radiative cooling, reflective surfaces operating only in the visible range have been designed [11-17]. For commercialization purposes, the coloration of RCs has also been explored [18-21]. Additionally, RCs have been investigated not only for buildings but also for clothing that directly cools down the human body [22, 23]. The atmospheric temperature changes depending on the seasons, and radiative cooling is needed only during summer. To deal with this problem, self-adaptive RCs, which can be deactivated in winter, have been designed using phase change materials [24-26]. Furthermore, it has been suggested that RCs can also work to improve the energy conversion efficiency of photovoltaics and other power generation systems [27-29].

In addition to the aforementioned tremendous achievements, maximization of temperature reduction is a fundamentally crucial task. In 1975, Catalanotti et al. suggested that radiative cooling can be considerably enhanced by optimizing the absorption properties of an RC [30]. This is because the atmosphere is opaque outside of the ATW; therefore, the atmosphere also emits thermal radiation in the MIR region. If an RC has a blackbody-like absorption, net energy flows from the atmosphere to the RC when the RC´s temperature becomes lower than the ambient temperature, resulting in a heat gain of the RC. In contrast, if the RC´s absorption is spectrally confined in the ATW, a significant temperature reduction can be observed because the heat gain from atmospheric radiation is minimized. Recent theoretical works suggest that a temperature reduction of about 30 K from the ambient temperature can be achieved if the ideal absorption properties for radiative cooling are realized [31-33].

Unfortunately, such absorption cannot be found in natural materials. The optical properties of materials are determined by intrinsic features, such as electric permittivity and magnetic permeability. However, when materials are scaled down to subwavelength, they possess optical responses different from their bulk forms. In addition, their optical responses are tunable by adequately designing their geometric structure. For example, nanometer-sized materials can enhance light scattering/absorption and confine light into small volumes beyond the optical diffraction limit. These physical phenomena suggest a capability of controlling light by designing subwavelength structures. From this fact, plasmonics and nanophotonics stem as nanotechnologies for optical manipulations. By designing a system based on plasmonics and photonics, we can create materials with desired optical properties. Such artificial materials are called metamaterials.

Metamaterials have been developed for a negative refractive index [34, 35] and applied to achieve perfect absorption (100% absorptivity) [36, 37]. The first perfect metamaterial absorber (MA) was proposed by Landy et at. in 2008, to the best of my knowledge [38]. Subsequently, many researchers designed MAs based on Landy´s MA, and one of the most common design principles for perfect absorption was established. The most common design is based on a metal-insulator-metal (MIM) structure. The top metal layer is an array of plasmonic particles. This plasmonic array is separated from the bottom metal layer by the middle insulator layer. In general, metals and dielectrics have only electric responses to an incident electromagnetic wave because their magnetic permeability is one. However, in the MIM structure, electric resonances of the plasmonic particles induce current loops by interacting with the bottom metal layer, and magnetic dipoles are created in the insulator layer. The magnetic dipoles allow the MA to possess a complex relative magnetic permeability; therefore, an effective impedance of the MA can match that of free space at a certain wavelength. This impedance matching achieves zero reflectance. The incident electromagnetic wave is strongly localized in the MA and absorbed by Ohmic losses of materials, resulting in perfect absorption. By properly designing a top plasmonic array, an absorption peak can be obtained at a specific wavelength, and broadband absorption is also achievable.

As a promising means to obtain well-controlled absorption, MAs have been applied to realize high-performance RCs [39-42]. Many metamaterial RCs possess nearly ideal absorption for radiative cooling. However, metamaterial RCs have a severe drawback. Since their nano- and micro-structures are complex,

their fabrications heavily rely on top-down techniques, such as e-beam lithography. However, top-down techniques are expensive, time-consuming, and unsuitable for producing large-area devices. Since it is expected that RCs will be applied on rooftops and exterior walls of buildings, RCs are required to be scalable. As an alternative approach, various polymer-based RCs have been proposed by synthesizing suitable polymers, such as PDMS [43-45]. In this case, nano- and micro-structures are not required; therefore, scalable RCs can be obtained. However, the absorption of polymer-based RCs cannot be precisely controlled, hindering us from obtaining ideal absorption. Thus, metamaterial-based approaches are still most suitable for engineering the absorption of high-performance RCs.

For the advancement of RCs, the conventional metamaterial-based approach must be extended, and new design principles for RCs must be developed. Thus, we must discover absorption mechanisms that enable us to realize strong and broadband absorption by using simple structures. Various plasmonic and photonic phenomena can provide us with additional control in absorption engineering, such as plasmonic hybridization [46-51] and surface lattice resonances [52-55]. These can occur in simple two- or many-particle systems and can be applied to control absorption peak position and bandwidth. However, those phenomena cannot enhance and widen absorption with precise control. As an alternative, I focus attention on electromagnetically induced transparency (EIT) and absorption (EIA) [56-61]. EIT and EIA occur when a high-loss and a low-loss optical element strongly interact. EIT and EIA are known for absorption phenomena that modulate and amplify the absorption of plasmonic and photonic systems. The modulation and amplification can be achieved by controlling the strength of an interaction. Previous studies have shown that those phenomena can occur in simple systems if their structures are properly designed. Based on these facts, I expect that RCs can be advanced by utilizing EIT and EIA phenomena.

In this dissertation, I theoretically investigate EIT and EIA by utilizing numerical simulations and building quantitative models. Additionally, I explore whether these models can establish an alternative route to achieving the ideal absorption for radiative cooling. This dissertation is outlined as follows: **Chapter 2** introduces theoretical background of this dissertation. Chapter 2 provides following five contents: **Section 2.1**) the mechanism of radiative cooling, **Section 2.2**) insights into light-matter interactions on the subwavelength scale, **Section 2.3**) basic knowledge of materials for plasmonics and photonics, **Section 2.4**) the mechanism of perfect absorption and a review of MAs proposed in previous studies, **Section 2.5**) the fundamental understanding of EIT and EIA from previous studies. **Chapter 3** presents my research motivation arising from Chapter 2. This chapter also outlines my research contributions during my Ph.D., which are discussed in the following four chapters (Chapter 4 is for references of Chapters 1-3). In **Chapter 5**, I propose an EIT-based MA, which can be fabricated by using colloidal lithography. Even though the proposed MA is simple, the MA can possess strong broadband absorption confined to the ATW. In **Chapters 6 and 7**, the current understanding of EIA is considerably extended. Since the interpretations of EIA presented in the previous studies contain ambiguity, I unify them and establish a thorough understanding of EIA. I develop guidance to maximize EIA, which can be applied to various plasmonic systems. EIA can significantly improve the absorption of plasmonic systems. Thus, the findings from my work are expected to benefit future advancement in RCs. In **Chapter 8**, I address an additional important topic to further progress radiative cooling: asymmetric light transmission (ALT) filters for improving cooling performance under harsh atmospheric conditions.

2. Introduction and state-of-the-art

2.1. Fundamentals of radiative cooling

This chapter introduces the fundamental theory of radiative cooling. Radiative cooling is formulated by considering an energy balance between outgoing and incoming radiations on an RC. This energy balance is determined by the optical properties and temperatures of the RC, atmosphere, and sun. By considering the energy balance, we find two indicators evaluating cooling performance: cooling power and cooling temperature. The cooling power is the net outgoing power from the RC at a given temperature. The cooling temperature is a temperature reduction of the RC from an ambient temperature. Depending on how we utilize the RC and where the RC is placed, it is determined which indicator is more important to optimize the RC.

2.1.1. Cooling power and cooling temperature

Firstly, we overview solar irradiance, atmospheric transmission, and blackbody radiation. In Figure 2.1, solar irradiance is plotted on the left *y*-axis. Solar irradiance has a maximum at around a wavelength of 500 nm and is concentrated in a wavelength range of 0.3 – 2.5 μm. By integrating solar irradiance over the wavelength, the total power of solar irradiance is about 1000 W/m^2. The atmospheric transmittance is plotted on the right *y*-axis of Figure 2.1a. In a wavelength range of 8 – 13 μm, the atmosphere is transparent, which is called the primary ATW. There is another ATW, called the secondary ATW spanning a wavelength range of 16 – 25 μm. Compared to the primary ATW, the secondary ATW is relatively sensitive to the condition of the atmosphere, which will be discussed in detail later. The atmosphere is opaque outside of the ATWs because water vapor and CO_2 strongly absorb radiation. According to Kirchhoff's law, a good absorber can be a good emitter. Therefore, the atmosphere strongly emits thermal radiation outside of the ATWs. In addition to water vapor and CO_2, ozone possesses strong absorption in a wavelength range of 9.3 – 10 μm. Next, we consider blackbody radiation given by Planck´s law

$$I_{\mathrm{BB}}(\lambda, T) = \frac{2hc^2}{\lambda^5} \frac{1}{\exp\left(\frac{hc}{\lambda k_{\mathrm{B}} T}\right) - 1} \qquad 2.1$$

where λ is the wavelength, T is the temperature of the blackbody, h is the Planck constant, c is the speed of light, and $k_{\mathrm{B}} \approx 1.38 \times 10^{-23}$ J/K is the Boltzmann constant. I_{BB} with T = 300 K is shown on the left *y*-axis of Figure 2.1. It can be found that a radiation peak locates inside the primary ATW. Therefore, if the RC is facing the sky, the thermal radiation of the RC can pass through the atmosphere, and the heat of the RC is dissipated in the cold outer space with a temperature of 3 K.

It can be found that the RC has three different radiative heat transfer channels: sun – RC, atmosphere – RC, and space – RC. To understand those heat transfers, we must know their temperatures. The sun and space are always much hotter and colder than the RC, respectively. One question is how high the temperature of the atmosphere is. The study by Granqvist et al. can address this question [62]. They investigated the absorptivity of the atmosphere and found that the absorptivity reaches 99% at an altitude lower than about 0.5 km. This result is attributed to the fact that the atmosphere comprises several different layers, and the troposphere, which is the lowest part of the atmosphere (altitude of 0 – 10 km), contains most of the water vapor. In the troposphere, the temperature decreases with an increase in altitude at a rate of 6.5 °C/km. Therefore, these results indicate that the temperature of the atmosphere can be approximated as the ambient temperature of the earth's surface to consider radiative cooling.

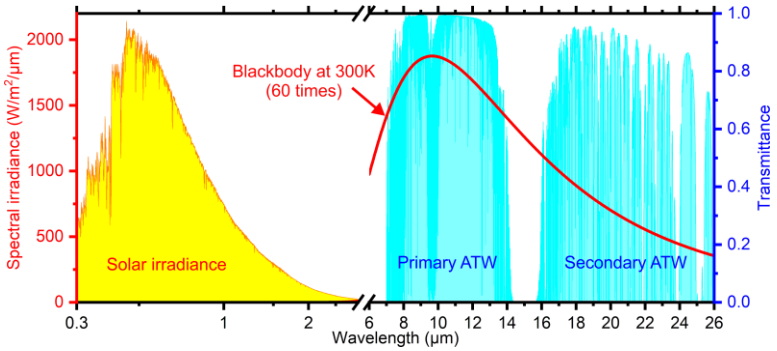

Figure 2.1. Solar irradiance, atmospheric transmittance, and blackbody radiation. The yellow shaded area shows the solar irradiance taken from Ref. [63]. The blue-shaded area is the atmospheric transmittance for precipitable water of 1 mm and air mass of 1, which was taken from Ref. [64]. The red line is the blackbody radiation calculated by Plank´s law at 300 K. The irradiance is multiplied by 60.

Based on the considerations pointed out above, radiative cooling is formulated. First, I briefly summarize the general radiative heat transfer. Let's consider that there are two infinitely large flat plates facing each other parallelly (Figure 2.2). Plate1 has an emissivity of $e_1(\lambda)$ and a temperature of T_1. Plate2 is a blackbody $e_2(\lambda) = 1$ with a temperature of T_2. These plates do not reflect incoming thermal radiation, and their emissivity is angular independent. By using Equation 2.1, a net heat flow from Plate1 to Plate2 through their thermal radiation is given as

$$q = \pi \int_0^\infty e_1(\lambda) I_{\mathrm{BB}}(\lambda, T_1) d\lambda - \pi \int_0^\infty e_1(\lambda)[e_2(\lambda) I_{\mathrm{BB}}(\lambda, T_2)] d\lambda \qquad 2.2$$

where π comes from the integration of the solid angle over the hemisphere. The first term of Equation 2.2 describes the thermal radiation that Plate1 emits, and the second term gives how much Plate1 absorbs the thermal radiation of Plate2. To simplify Equation 2.2, we assume that $e_1(\lambda)$ is independent of the wavelength; therefore, $e_1(\lambda) \rightarrow e_1$. This simplification makes q as

$$q = e_1 \sigma (T_1^4 - T_2^4) \qquad 2.3$$

where $\sigma \approx 5.67 \times 10^{-8}$ W/m^2/K^4 is the Stefan-Boltzmann constant. Equation 2.3 shows that the net energy flow is proportional to the fourth power of the temperatures, and the heat flow of Plate1 → Plate2 occurs only when $T_1 > T_2$. Figure 2.2b illustrates radiative cooling. Comparing Figure 2.2b with Figure 2.2a, it is found that the RC corresponds to Plate1, and the effects from the sun, the atmosphere, and the space correspond to Plate2. In a similar manner to Equation 2.2, the radiative heat transfer for radiative cooling can be given as

$$q_{\mathrm{rad}} = q_{\mathrm{out}} - q_{\mathrm{in}} \qquad 2.4$$

where q_{out} is outgoing thermal radiation from the RC, and q_{in} is incoming thermal radiation from the sun, atmosphere, and space. However, the space is extremely cold, so we can safely ignore the effects of the space. In general, the emissivity of the RC is angular dependent. Therefore, the emissivity of the RC must be expressed as $e_r(\lambda, \theta, \varphi)$, where θ and φ are the zenith and azimuth angles, respectively (Figure 2.2c). In addition, the emissivity of the atmosphere is also zenith angular dependent. The atmospheric transmittance $t_a(\lambda, \theta)$ can be described by considering an extinction coefficient of the atmosphere $\kappa_a(\lambda)$ and a pathlength $l(\lambda, \theta) = l(\lambda)/\cos\theta$

$$t_{\mathrm{a}}(\lambda, \theta) = \exp\left(-\frac{\kappa_a(\lambda) l(\lambda)}{\cos\theta}\right) = t_{\mathrm{a}}(\lambda)^{\frac{1}{\cos\theta}} \qquad 2.5$$

where $t_a(\lambda)$ is the atmospheric transmittance in the zenith direction. From Equation 2.5, the atmospheric emissivity is given as $e_a(\lambda, \theta) = 1 - t_a(\lambda, \theta)$. Using $e_r(\lambda, \theta, \varphi)$ and $e_a(\lambda, \theta)$, q_{out} and $q_{in} = q_{atm} + q_{sun}$ can be written as

$$q_{out} = \int \cos\theta \int_0^\infty e_r(\lambda, \theta, \varphi) I_{BB}(\lambda, T_r) d\lambda d\Omega \quad 2.6$$

$$q_{atm} = \int \cos\theta \int_0^\infty e_r(\lambda, \theta, \varphi)[e_a(\lambda, \theta) I_{BB}(\lambda, T_a)] d\lambda d\Omega \quad 2.7$$

$$q_{sun} = \cos\theta_s \int_0^\infty e_r(\lambda, \theta_s, \varphi_s) I_S(\lambda) d\lambda \quad 2.8$$

where q_{atm} and q_{sun} are the atmospheric and solar absorptions of the RC, respectively. T_r and T_a are the temperatures of the RC and the atmosphere, respectively. T_a can be considered as the ambient temperature. Ω is the solid angle. θ_s and φ_s are the incident angle of the sunlight. $I_S(\lambda)$ is spectral solar irradiance, which is shown in Figure 2.1a. In addition to those radiative heat transfer processes, conduction and convection heat transfers between the RC and the surrounding must also be considered to evaluate net cooling performance

$$q_{nonrad} = h_c(T_a - T_r) \quad 2.9$$

where h_c is the effective conduction and convection heat transfer coefficient. From Equations 2.4 and 2.9, the net cooling power at given T_r and T_a is

$$q_{cool} = q_{rad} - q_{nonrad} = q_{out} - q_{in} - q_{nonrad} = q_{out} - q_{loss} \quad 2.10$$

where q_{loss} is the net heat gain caused by external factors. T_r can keep decreasing until the entire heat exchange process reaches the equilibrium point, namely, $q_{cool} = 0$. Thus, the cooling temperature is found from $q_{cool} = 0$. From Equation 2.10, it is immediately found that q_{loss} has to be minimized to maximize the cooling power (q_{cool}) and the cooling temperature ($\Delta T_{cool} = T_a - T_r$). In this dissertation, I focus on minimizing q_{loss} by tailoring the absorption properties of the RC. Therefore, q_{nonrad} will not be paid attention to, and q_{in} will only be considered.

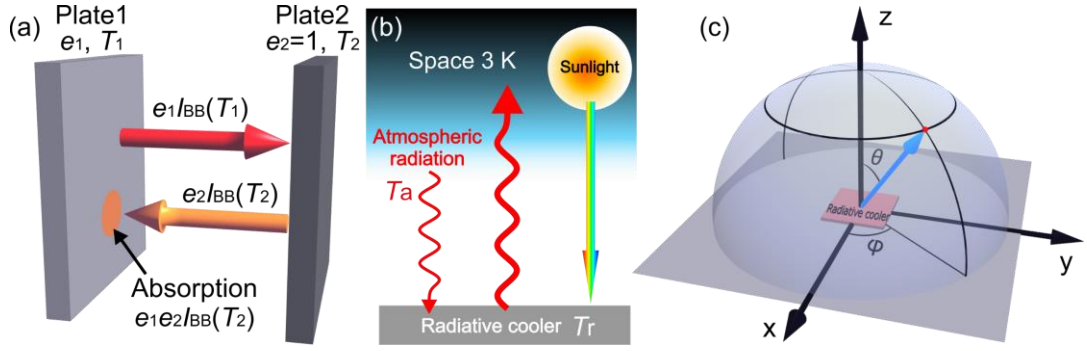

Figure 2.2. Schematic illustrations of (a) radiative heat transfer between infinitely large flat plates, (b) radiative heat transfer of radiative cooling, and (c) the spherical coordinate for calculating radiative cooling power.

2.1.2. Wavelength dependency: Selective vs. Broadband emissivity

The optimum emissivity for radiative cooling differs depending on the condition of the atmosphere. In addition, the optimum emissivity can also differ depending on which cooling performance, the cooling power or the cooling temperature, must be maximized. We first overview how conditions of the atmosphere

affect its transmittance. As mentioned in Section 2.1, atmospheric transmittance is influenced by water vapor. The water vapor content of the atmosphere is described by precipitable water (PW), which measures all amounts of water in a column perpendicular to the earth´s surface. PW is given as thickness (mm) and can be related to the relative humidity. Figure 2.3a shows how the atmospheric transmittance changes with an increase in PW. Since the atmosphere becomes more absorptive when the water vapor content is high, the transmittance in the ATWs decreases. Compared to the primary ATW, the second ATW is more sensitive to PW. This indicates that in dry areas, an RC can have access to outer space in a wider wavelength range, and radiative cooling can be intensified by utilizing the secondary ATW. However, the secondary ATW is usually closed in humid areas.

Based on the fundamental understanding of the atmospheric transmission, we quantitively consider q_{cool}. For simplicity, we now set $q_{sun} = q_{nonrad} = 0$ ($q_{sun} = 0$ corresponds to nighttime radiative cooling). This simplification allows us to reduce $q_{cool} \rightarrow q_{out} - q_{atm}$. We further simplify q_{cool} by considering that radiative cooling occurs only in the zenith direction ($\theta = 0°$) and an RC has a blackbody-like absorption ($e_r(\lambda) = 1$). Thus, q_{cool} is given as

$$q_{\mathrm{cool}}(\lambda) = q_{\mathrm{out}}(\lambda) - q_{\mathrm{atm}}(\lambda) = e_{\mathrm{r}}(\lambda)[I_{\mathrm{BB}}(\lambda, T_{\mathrm{r}}) - e_{\mathrm{a}}(\lambda) I_{\mathrm{BB}}(\lambda, T_{\mathrm{a}})] \qquad 2.11$$

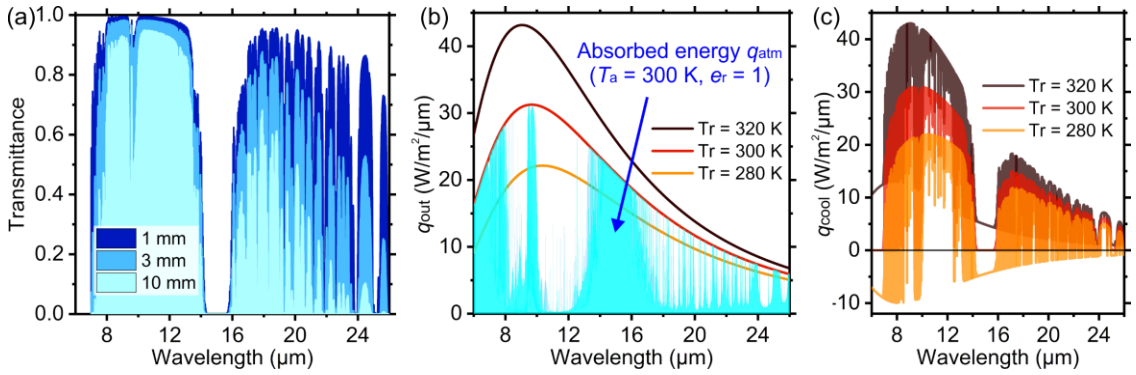

Figure 2.3. Effect of the atmosphere condition on radiative cooling. (a) The atmospheric transmittance with different PWs. The transmittances are taken from Ref. [64]. (b) The energy balance of q_{cool} (Equation 2.10) is considered with $q_{sun} = q_{nonrad} = 0$ and $\theta = 0°$. The radiative cooler is blackbody; therefore, $e_r = 1$. The solid lines are q_{out} with different T_r, and the blue shaded area is q_{atm} with $T_a = 300$ K. These quantities are given by Equation 2.11. (c) q_{cool} calculated using Figure 2.3b.

Figure 2.3b visualizes Equation 2.11 for $T_a = 300$ K with different T_r. $q_{atm}(\lambda)$ is calculated using the atmospheric transmittance with PW = 1 mm. We consider that the RC initially has $T_r = 320$ K, and its temperature decreases as $T_r = 320$ K $\rightarrow$ 300 K $\rightarrow$ 280 K by radiative cooling. When $T_r > T_a$, $q_{out}(\lambda)$ is larger than $q_{atm}(\lambda)$ in the entire MIR range. After T_r decreases and reaches $T_r = T_a$, $q_{out}(\lambda)$ becomes equal to $q_{atm}(\lambda)$ at wavelengths where the atmosphere is opaque, but q_{out} still can exceed q_{atm} in the ATWs. With a further decrease in T_r, $q_{atm}(\lambda)$ overcomes $q_{out}(\lambda)$ in the opaque areas, meaning that the RC strongly absorbs the atmospheric radiation. Figure 2.3c shows $q_{cool}(\lambda)$ calculated using Figure 2.3b. For all T_r, $q_{cool}(\lambda)$ is larger than zero in the ATWs because of $q_{atm}(\lambda) \approx 0$. In contrast, when $T_r < T_a$, $q_{cool}(\lambda)$ has negative values outside of the ATWs. From Figure 2.3c, it is found that we should consider two different situations depending on the temperature difference between the RC and the atmosphere:

A) $T_r > T_a$: $q_{cool}(\lambda)$ is positive at all wavelengths; therefore, the blackbody-like RC is optimum to maximize the cooling power. A net cooling power can be increased by increasing T_r. Even though both ATWs are closed due to a high PW, radiative cooling can still occur.

B) $T_r < T_a$: To maximize ΔT_{cool}, $q_{cool}(\lambda)$ has to remain positive at a low T_r. Therefore, an optimum RC should not have blackbody-like emissivity but must have high emissivity only in the ATWs. With such a selective emissivity, $q_{atm}(\lambda)$ is minimized, and many parts of the negative values of $q_{cool}(\lambda)$ shown in Figure 2.3c can be eliminated.

For case B, an optimum emission profile can vary depending on PW. As mentioned earlier, the secondary ATW closes with a high PW. In this case, $q_{cool}(\lambda)$ becomes negative over the secondary ATW; therefore, net cooling power cannot be positive at low T_r. To achieve a large ΔT_{cool} under a high PW, an RC must have high emissivity only in the primary ATW.

Next, we overview the influence of the emissivity profile of an RC on cooling performance by referring to previous studies. Li et al. conducted a systematic analysis of cooling performance using six different emissivity profiles (Figure 2.4a) [33]. Those emissivity profiles are omnidirectional for zenith and azimuth angles. Coolers 1-3 correspond to selective RCs, and Coolers 4-5 correspond to blackbody-like RCs. Li et al. used the atmospheric transmittance with a low PW, which possesses a fully opened secondary ATW. Figure 2.4b shows a cooling power calculated using Equation 2.10. When $T_r > T_a$, the blackbody-like RCs possess the highest cooling power, and Cooler 6´s cooling power reaches 486 W/m^2 at T_r = 340 K. The cooling powers of the blackbody-like RCs steeply decrease with a decrease in T_r. In contrast, the cooling powers of the selective RCs decrease slowly and exceed the cooling powers of the blackbody-like RCs at $T_r < T_a$. At T_r = 260 K, Cooler 2 with dual-band emissivity still has a positive cooling power of 61 W/m^2. Therefore, an RC with selective emissivity can take advantage to achieve a large ΔT_{cool}.

Hossain et al. investigated the influence of relative humidity (RH) on ΔT_{cool} [65]. In Figure 2.4, ΔT_{cool} is plotted by calculating q_{cool} = 0 with parasitic heat gains: 3 % of total solar absorption (q_{sun}) and non-radiative heat transfer (q_{nonrad}) with h_c = 2 W/m^2/K Two emissivity profiles were examined: Cooler 1 and a blackbody-like RC without any emissivity in a wavelength range of 0.3 – 2.5 μm (similar to Cooler5). For any RH, Cooler 1 is capable of having a larger ΔT_{cool} than the blackbody-like RC because Cooler 1´s q_{cool} keeps being positive at a low T_r. If we consider an RH dependency of Cooler 2, it can be found that Cooler 2 may have a lower ΔT_{cool} than Cooler 1 since the secondary ATW is sensitive to RH. This indicates that Cooler 1 is the best emissivity profile to achieve a large ΔT_{cool} under non-zero RH conditions. With increasing RH, the q_{cool} of both RCs decreases, and the difference between them becomes small. Since both primary and secondary ATWs become opaque with a high RH, the heat gain by q_{atm} increases. Therefore, the RC loses cooling abilities no matter what kind of emissivity profile it has. Dong et al. investigated RH dependency in more detail, which showed similar results to Figure 2.4c [66].

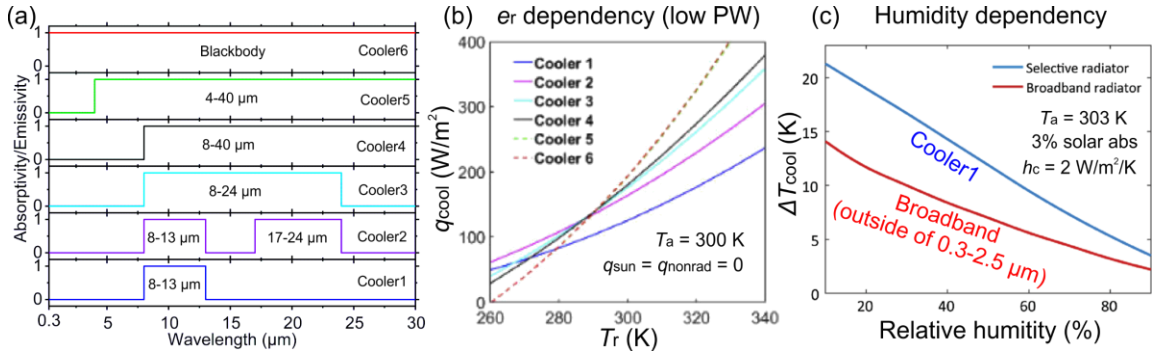

Figure 2.4. Wavelength dependency of radiative cooling. (a) Six different emission profiles for radiative cooling and (b) their cooling powers as a function of T_r. Reprinted with permission from Ref. [33] © 2020 Optical Society of America under the terms of the OSA Open Access Publishing Agreement. (c) Humidity dependency of the temperature reduction for Cooler1 and broadband cooler with a unity emissivity except for 0.3 – 2.5 μm. T_a = 30 °C is considered. T_r is obtained by taking an equilibrium state q_{cool} = 0. Reprinted with permission from Ref. [65] © 2016 The Authors. Published by WILEY‐VCH Verlag GmbH & Co. KGaA, Weinheim.

2.1.3. Dealing with high humidity

Throughout this chapter, it has been introduced that the atmosphere plays a significant role in radiative cooling, and humidity is one of the adverse factors, which severely degrades cooling performance [66, 67]. The humidity of the atmosphere keeps changing time by time and over the seasons. In addition, humidity is completely different depending on geological locations. Therefore, the high stability of cooling performance under different humidity is a fundamentally important function to make radiative cooling more practical. One approach to deal with high humidity is that an RC possesses selective emissivity only in the primary ATW because the primary ATW is relatively insensitive to humidity compared to the secondary ATW [45, 66]. However, as mentioned earlier, the transmittance of the primary ATW also decreases significantly with an increase in humidity.

As an alternative approach, it has been proposed to use an optical filter that allows the thermal radiation of an RC to pass through but forbids incoming atmospheric radiation to enter (see Figure 2.5a). Such an optical filter with asymmetric optical properties is called an asymmetric light transmission (ALT) filter. Wong et al. employed a theoretical investigation and suggested that the cooling performance of an RC can be preserved under high humidity by using an ALT filter [68]. The research in this direction has been extended theoretically and experimentally [69, 70]. However, it has been pointed out that Wong´s study did not fully consider the optical properties of their ALT filter; therefore, the feasibility of the approach based on an ALT filter is still controversial [71]. In addition, there are still uncertainties in radiative heat transfer with such an ALT filter. Let's consider a simple radiative heat transfer model shown in Figure 2.5b. In the primary ATW, an RC can be considered as a blackbody, and the atmosphere is semi-transparent ($e_a \approx 0.5$). The temperature contrast between the RC (T_r), atmosphere (T_a), and space (T_s) is $T_a > T_r >> T_s$; therefore, the thermal radiation of the space can be ignored. Thermal radiation emitted by the RC ($I_{BB}(T_r)$) is partially absorbed by the atmosphere ($e_a I_{BB}(T_r)$), and the rest of the radiation goes to space without reflection at the atmosphere ($(1 - e_a)I_{BB}(T_r)$). The atmospheric radiation goes to the RC ($e_a I_{BB}(T_a)$); however, it is not absorbed by the RC but is perfectly reflected by the ALT filter. This reflection cancels out the energy flow of the atmospheric radiation. Therefore, the RC can keep emitting thermal radiation without any heat gain from the atmospheric radiation. However, if such a heat transfer model is right, it suggests that radiative heat transfer occurs from a cool to a hot object, which violates the second law of thermodynamics. Such violation can be allowed if an ALT filter is made of non-reciprocal materials, such as magneto-optical materials [71]. However, non-reciprocal materials require control of external electric or magnetic fields for their ALT properties, which is not suitable for RCs. Thus, an ALT filter for radiative cooling must be designed based on reciprocal materials. Several ALT filters made of reciprocal materials have been proposed, but as mentioned earlier, their ALT properties have not been thoroughly investigated. Based on those considerations, it is still not clear whether such ALT filters can preserve cooling performance under high humidity [70, 72].

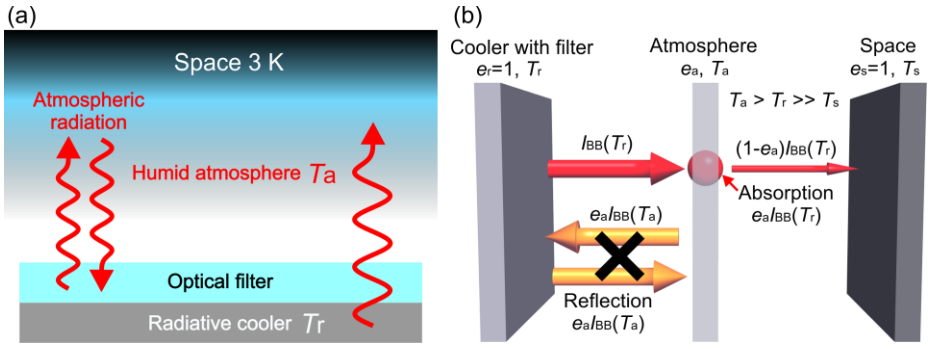

Figure 2.5. (a) Schematic illustration of radiative cooling with an optical filter reflecting the atmospheric radiation. (b) Schematic illustration of radiative heat transfer between a radiative cooler with the optical filter, semi-transparent atmosphere, and the space.

2.2. Fundamentals of light-matter interactions

According to Kirchhoff's law, emissivity is equal to absorptivity. Therefore, the absorption properties of RCs must be optimized to maximize cooling performance. By understanding light-matter interaction and designing structures on the subwavelength scale, we can control the absorption properties of materials. This chapter introduces the fundamentals of light-matter interaction for absorption engineering.

2.2.1. Electromagnetic wave propagation in dielectrics and metals

Maxwell´s equations are the foundation of classical electromagnetism, which enables us to describe many optical phenomena, even in nano- and micro-scales. To understand electromagnetic waves propagating in materials, three important quantities have to be considered in Maxwell´s equations: 1) the volume density of electric charge ρ, 2) the volume density of electric dipoles **P**, and 3) the current density **J** [73]. These quantities are macroscopically averaged over microscopic responses of atoms composing materials. Maxwell´s equations are given as

$$\nabla \cdot \mathbf{D} = \rho \tag{2.12}$$

$$\nabla \cdot \mathbf{B} = 0 \tag{2.13}$$

$$\nabla \times \mathbf{E} = -\frac{\partial \mathbf{B}}{\partial t} = -\mu_0 \frac{\partial \mathbf{H}}{\partial t} \tag{2.14}$$

$$\nabla \times \mathbf{H} = \frac{\partial \mathbf{D}}{\partial t} + \mathbf{J} = \varepsilon_0 \frac{\partial \mathbf{E}}{\partial t} + \frac{\partial \mathbf{P}}{\partial t} + \mathbf{J} \tag{2.15}$$

where ε_0 and μ_0 are the permittivity and permeability of the vacuum, respectively. **E** and **H** are the electric and magnetic field. **D** and **B** are the electric displacement and the magnetic flux density, respectively. For a general representation, those are given by a convolution of the impulse response of a material and the electromagnetic field [74, 75]. In frequency domain, the convolution produces $\mathbf{D}(\mathbf{k}, \omega) = \varepsilon_0\mathbf{E}(\mathbf{k}, \omega) + \mathbf{P}(\mathbf{k}, \omega) = \varepsilon_0\varepsilon(\mathbf{k}, \omega)\mathbf{E}(\mathbf{k}, \omega)$ and $\mathbf{B}(\mathbf{k}, \omega) = \mu_0\mu(\mathbf{k}, \omega)\mathbf{H}(\mathbf{k}, \omega)$, where **k** and ω are the wavevector and the angular frequency, respectively. $\varepsilon(\mathbf{k}, \omega)$ and $\mu(\mathbf{k}, \omega)$ are the relative permittivity and permeability describing the optical responses of a material. By considering the limit of a spacially local response ($\mathbf{k} = 0$), we can simplify the relative permittiviy and permerbility as $\varepsilon(\omega)$ and $\mu(\omega)$, respectively. In the following, those variables will be simply denoded as ε and μ. By taking curl on both sides of Equations 2.14 and 2.15, the general wave equations are given as

$$\nabla^2\mathbf{E} = \frac{1}{c^2}\frac{\partial^2\mathbf{E}}{\partial t^2} + \mu_0\left[\frac{\partial}{\partial t}\left(\frac{\partial \mathbf{P}}{\partial t}\right) + \frac{\partial \mathbf{J}}{\partial t}\right] \tag{2.16}$$

where $c = (\varepsilon_0\mu_0)^{-1/2}$ is the vacuum speed of light. $\nabla\times(\nabla\times\mathbf{E}) = \nabla(\nabla\cdot\mathbf{E}) - \nabla^2\mathbf{E}$ with $\nabla\cdot\mathbf{E} = 0$ is used to derive Equation 2.16. The last two terms on the right side of Equations 2.16 are the source terms. The term $\partial\mathbf{P}/\partial$t describes the influence of the polarization of a dielectric on light propagation. Using the relationships $\rho_P = -\nabla\cdot\mathbf{P}$ and $\nabla\cdot\mathbf{J}_P + \partial\rho_P/\partial t = 0$ (ρ_P: the polarization charge density, $\mathbf{J}_P$: the polarization current density), we get

$$\frac{\partial \mathbf{P}}{\partial t} = \mathbf{J}_P \tag{2.17}$$

The term **J** in Equation 2.16 is the conduction term describing wave propagation in a metal. Based on Ohm´s law, in a similar manner to **D**, **J** is connected to **E** by $\mathbf{J}(\mathbf{k}, \omega) = \sigma(\mathbf{k}, \omega)\mathbf{E}(\mathbf{k}, \omega)$, where $\sigma(\mathbf{k}, \omega)$ is the conductivity. For a simplicity, the conductivity will be expressed as σ in the following. From Equation 2.17, it is understood that the current density is linked to the polarization. Based on this, the bracket of the right side of Equation 2.16 can be recognized as the total current density $\mathbf{J}_{tot} = \mathbf{J} + \partial\mathbf{P}/\partial$t.

We consider light propagation in a dielectric using Equation 2.16 with $\mathbf{J} = 0$. $\mathbf{P}$ originates from the displacement of the electrons bound to the atoms. Considering that the electrons with a charge of $-e$ are displaced with a distance $\mathbf{r}$ from the center of atoms, the macroscopic electric dipole moment of such electrons can be expressed as $\mathbf{P} = -Ne\mathbf{r}$, where N is the number of electrons per unit volume. Since the displacement of the bound electrons can be approximated using a mechanical harmonic oscillator model, $\mathbf{r}$ is given by the equation of motion

$$m\frac{\partial^2 \mathbf{r}}{\partial t^2} + m\gamma\frac{\partial \mathbf{r}}{\partial t} + K\mathbf{r} = -e\mathbf{E} \tag{2.18}$$

where m is the mass of the electron, γ is the damping constant by friction, K is the spring constant between the negative electron and positive core atom, and $-e\mathbf{E}$ is the Coulomb force. The external electric field is time-harmonic $\mathbf{E}(z, t) = \mathbf{E}(z)e^{-i\omega t}$; therefore, $\mathbf{r}$ is also time-harmonic $\mathbf{r} = \mathbf{r}_0 e^{-i\omega t}$. By solving Equation 2.18, $\mathbf{P}$ is written as

$$\mathbf{P} = \varepsilon_0 \frac{\omega_\mathrm{p}^2}{\omega_0^2 - \omega^2 - i\gamma\omega}\mathbf{E} = \varepsilon_0 \chi \mathbf{E} \tag{2.19}$$

where $\omega_\mathrm{p} = (Ne^2/m\varepsilon_0)^{1/2}$ is the plasma frequency, ω_0 is the resonance frequency of the bound electron, and χ is the electric susceptibility. Using the relationship between $\mathbf{D}$ and $\mathbf{P}$, we get the relative permittivity $\varepsilon = 1 + \chi$ as

$$\varepsilon = \varepsilon' + i\varepsilon'' = \left[1 + \frac{(\omega_0^2 - \omega^2)\omega_\mathrm{p}^2}{(\omega_0^2 - \omega^2)^2 + \gamma^2\omega^2}\right] + i\frac{\gamma\omega\omega_\mathrm{p}^2}{(\omega_0^2 - \omega^2)^2 + \gamma^2\omega^2} \tag{2.20}$$

This is the Lorentz model describing the relative permittivity of dielectrics. By substituting $\varepsilon = 1 + \chi$ and $\mathbf{J} = 0$ into Equation 2.16, we get

$$\nabla^2\mathbf{E} = \frac{1}{c^2}\frac{\partial^2 \mathbf{E}}{\partial t^2} + \mu_0\frac{\partial^2 \mathbf{P}}{\partial t^2} = \frac{1}{c^2}\frac{\partial^2}{\partial t^2}\left(\mathbf{E} + \frac{1}{\varepsilon_0}\mathbf{P}\right) = \frac{1}{c^2}\varepsilon\frac{\partial^2 \mathbf{E}}{\partial t^2} = -\frac{\omega^2}{c^2}\varepsilon\mathbf{E} \tag{2.21}$$

The solution of Equation 2.21 is given in the form of $\mathbf{E}(z, t) = \mathbf{E}_0 e^{i(kz - \omega t)}$, where k is the wave number, and z is the propagation direction of the light. The wave number is a real number in free space, but it becomes a complex number in dielectrics as seen in Equation 2.20

$$k = \frac{\omega}{c}\sqrt{\varepsilon} = k_0\sqrt{\varepsilon} = k_0 n = k_0(n' + in'') = k' + ik'' \tag{2.22}$$

where $k_0 = \omega/c$ is the wave number in free space, and $n = n' + in'' = \varepsilon^{1/2}$ is the refractive index. The general form of the refractive index is given as $n = (\varepsilon\mu)^{1/2}$ if a material is magnetic as well. Using Equation 2.22, the solution of the wave equation of Equation 2.21 can be written as

$$\mathbf{E} = \mathbf{E}_0 e^{i[(k' + ik'')z - i\omega t]} = \mathbf{E}_0 e^{-k''z} e^{i(k'z - i\omega t)} \tag{2.23}$$

The term $e^{-k''z}$ describes that the amplitude of light in dielectric media exponentially attenuates with an increase in the propagation distance. Therefore, n'' is called the extinction coefficient. Figure 2.6a shows the relative permittivity and refractive index calculated using the Lorentz model. In these plots, the wavelength $\lambda = 2\pi c/\omega$ is used on the x-axis. Both the relative permittivity and refractive index have similar spectral shapes. They have high dispersion around the resonance wavelength. This kind of high dispersion is found around a resonance of a molecular vibration of a dielectric. Dielectrics are transparent at wavelengths far from the resonance wavelength. This wavelength region can usually be found in the visible and NIR regions for many dielectrics.

Next, we consider light propagation in a metal. Since the free electrons of the metal are not bound to the atoms, the motion of the free electrons cannot be described using the harmonic oscillator model. Instead, we need to consider the flow of the free electron gas, which can be done by removing the restoring force

term ($K = 0$) in Equation 2.18. Therefore, the relative permittivity of the metal can be derived by substituting $\omega_0 = 0$ into the Lorentz model

$$\varepsilon = \varepsilon' + i\varepsilon'' = 1 - \frac{\omega_p^2}{\omega^2 + i\gamma\omega} = \left[1 - \frac{\omega_p^2}{\omega^2 + \gamma^2}\right] + i\frac{\gamma\omega_p^2}{\omega(\omega^2 + \gamma^2)} \qquad 2.24$$

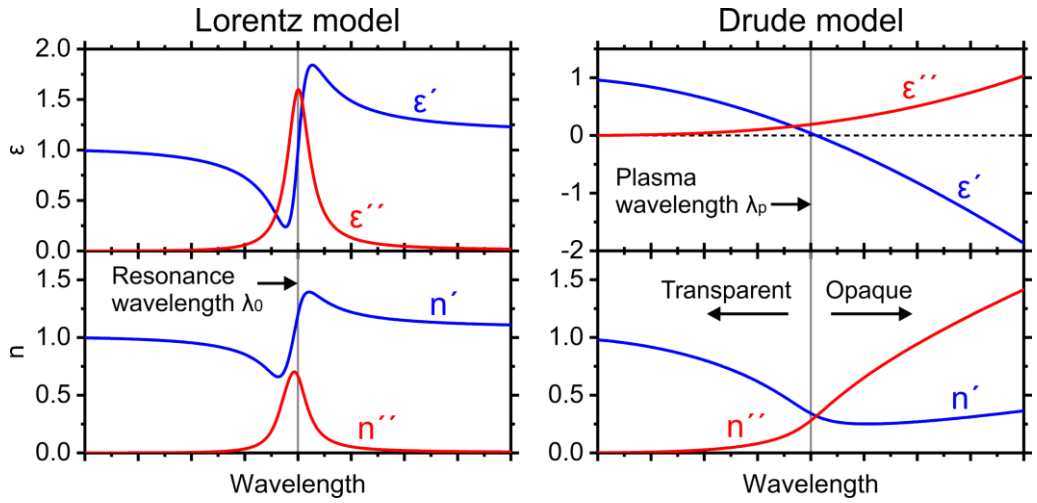

Figure 2.6. (a) The Lorentz model (Equation 2.20) and (b) the Drude model (Equation 2.24). The top panel shows the relative permittivity, and the bottom panel shows the refractive index. For the Lorentz model, $\omega_p = 0.4\omega_0$ and $\gamma = 0.1\omega_0$ are used. The gray line shows the resonance wavelength $\lambda_0 = 2\pi c/\omega_0$. For the Drude model, $\gamma = 0.1\omega_p$ is considered. The gray line shows the plasma wavelength $\lambda_p = 2\pi c/\omega_p$.

Equation 2.24 is called the Drude model. The relationships given by Equations 2.22 and 2.23 can also be applied to Equation 2.24. In a low-frequency regime $\omega << \gamma$ giving $\varepsilon' << \varepsilon''$, the refractive index of the metal is reduced to

$$n = \sqrt{\varepsilon} \approx \sqrt{\frac{i\omega_p^2}{\gamma\omega}} = (1+i)\sqrt{\frac{\omega_p^2}{2\gamma\omega}}, \qquad n_D' \approx n_D'' \qquad 2.25$$

The reciprocal of $k'' = k_0 n''$ gives the skin depth δ of the metal. As seen in Equation 2.23, the skin depth describes how far the incoming light can penetrate the metal until the amplitude of light decreases to $1/e$

$$\delta = \frac{1}{k_0 n''} = \frac{c}{\omega}\sqrt{\frac{2\gamma\omega}{\omega_p^2}} = \sqrt{\frac{2}{\omega}\left(\frac{\gamma c^2}{\omega_p^2}\right)} = \sqrt{\frac{2}{\omega}\left(\frac{\gamma}{\varepsilon_0\mu_0\omega_p^2}\right)} = \sqrt{\frac{2}{\mu_0\sigma_0\omega}} \qquad 2.26$$

where $\sigma_0 = \varepsilon_0\omega_p^2/\gamma = Ne^2/m\gamma$ is the conductivity. Figure 2.6b shows the relative permittivity and refractive index calculated by the Drude model. In contrast to the Lorentz model, the Drude model does not have drastic spectral change since the motion of electron gas is not restricted by the restoring force. For the relative permittivity, ε' becomes negative at wavelengths longer than the plasma wavelength $\lambda_p = 2\pi c/\omega_p$. This means that the free electron gas responds in the opposite direction to the electric field, forbidding light from entering a metal. Consequently, metals have a strong reflection in that wavelength region. In a wavelength range shorter than λ_p, the Drude model suggests that metal becomes transparent because n'' toward zero with a decrease in the wavelength. However, metals usually have interband transition absorptions in that short wavelength range, which the Drude model does not take into account. Even though the Drude model fails to provide a full description of the optical response of metals, the Drude model still

provides us with good agreement with experimental data at wavelengths longer than λ_p. A complete description of the optical properties of metals can be provided by combining the Drude and Lorentz models

$$\varepsilon = 1 - \frac{\omega_p^2}{\omega^2 + i\gamma\omega} + \sum_j \frac{f_j \omega_p^2}{\omega_j^2 - \omega^2 - i\gamma_j \omega} \quad 2.27$$

This model is called the Drude-Lorentz model. The optical response of free electrons is described by the Drude part, and the interband transitions are compensated by the Lorentz part. In the Lorentz part, it is taken into account that different electrons *j* are bound by different resonance frequencies ω_j and different damping rates γ_j. f_j is an oscillator strength describing how strongly bound electrons couple to the external electric field.

Before the end of this section, it has to be mentioned that the factor "1" in the Lorentz and Drude model has to be rewritten by $\varepsilon(\infty)$ to consider real materials. ε_∞ is the background permittivity at high frequency, originating from the positive background of the ion cores. In general, the background permittivity falls into a range of $1 < \varepsilon_\infty < 10$.

2.2.2. Surface waves at an interface

This section treats an electromagnetic wave propagating along an interface of two different media. This type of wave is called a surface wave. The surface wave is bound to the interface; therefore, they cannot be observed in the far-field. The interesting characteristics of the surface wave are that its wavevector is much higher than a wave propagating free space, and its electromagnetic field amplitude exponentially decreases perpendicular to the interface. Therefore, the surface wave is also called an evanescent wave. Before we detail the excitation conditions of the evanescent wave, we briefly overview the boundary conditions of electromagnetic fields at the interface [73].

We consider that two media with different relative permittivities are touching each other (see Figure 2.7). The bottom half of the space ($z < 0$) is filled with Medium1 with $\varepsilon_1(\omega)$, and the top half ($z > 0$) is filled with Medium2 with $\varepsilon_2(\omega)$. At this interface, the following four boundary conditions must be fulfilled for the normal vector of the interface **n**:

A) $\mathbf{n} \times (\mathbf{E}_2 - \mathbf{E}_1) = 0$: The tangential components of electric fields must be continuous.
B) $\mathbf{n} \times (\mathbf{H}_2 - \mathbf{H}_1) = \boldsymbol{j}_s$: The tangential components of magnetic fields must be continuous if there is no surface current $\boldsymbol{j}_s$ on the interface.
C) $\mathbf{n} \cdot (\mathbf{D}_2 - \mathbf{D}_1) = \rho_s$: The normal components of electric field displacements must be continuous if there is no surface charge ρ_s on the interface.
D) $\mathbf{n} \cdot (\mathbf{B}_2 - \mathbf{B}_1) = 0$: The normal components of magnetic flux densities must be continuous.

As understood from Maxwell´s equations, those boundary conditions are not independent of each other. For an electromagnetic wave, we have to consider another boundary condition, which satisfies the continuity of the wave at the interface. When the electromagnetic wave with a wavevector of $\mathbf{k}_1$ is incident on the interface at an incident angle of θ_1, a transmitted wave with a wavevector of $\mathbf{k}_2$ appears at a refraction angle of θ_2 (see Figure 2.7). The tangential components of the wavevectors must satisfy the following condition

$$\mathbf{k}_1 \sin\theta_1 = \mathbf{k}_2 \sin\theta_2 \quad 2.28$$

Based on the boundary conditions, we will confirm the existence of the evanescent wave at the interface by using the Helmholtz equation, which is given by Equations 2.21 [74, 75]

$$\nabla^2 \mathbf{E}(\mathbf{r}, \omega) + k_0^2 \varepsilon \mathbf{E}(\mathbf{r}, \omega) = 0 \quad 2.29$$

It is assumed that the electromagnetic wave propagates in the *x*-*z* plane, which gives the wave vector of $\mathbf{k}_j \cdot \mathbf{r} = k_{jx}x + k_{jz}z$, where the subscript $j \in 1, 2$ represents Medium1 and Medium2. Based on Equation 2.28, k_{jx}

must be the same for Medium1 and Medium2, meaning $k_x = k_{1x} = k_{2x}$. Therefore, the electromagnetic wave is written as

$$\mathbf{E}_j(\mathbf{r},\omega) = \mathbf{E}_j e^{i(k_x x + k_{jz} z - \omega t)} \tag{2.30}$$

Substituting Equation 2.30 into Equation 2.29 gives

$$\left(\frac{\partial^2}{\partial x^2} + \frac{\partial^2}{\partial z^2}\right)\mathbf{E}_j(\mathbf{r},\omega) + k_0^2 \varepsilon_j \mathbf{E}_j(\mathbf{r},\omega) = \left(-k_x^2 - k_{jz}^2 + k_0^2 \varepsilon_j\right)\mathbf{E}_j(\mathbf{r},\omega) = 0 \tag{2.31}$$

To satisfy Equation 2.31, the following relationship has to be fulfilled.

$$k_0^2 \varepsilon_j = k_x^2 + k_{jz}^2 \tag{2.32}$$

Next, we define polarization of the electromagnetic wave. TE and TM polarizations are expressed as

$$\mathbf{E}_j = \begin{pmatrix} 0 \\ E_{jy} \\ 0 \end{pmatrix}, \mathbf{H}_j = \begin{pmatrix} H_{jx} \\ 0 \\ H_{jz} \end{pmatrix} \text{ for TE}, \qquad \mathbf{E}_j = \begin{pmatrix} E_{jx} \\ 0 \\ E_{jz} \end{pmatrix}, \mathbf{H}_j = \begin{pmatrix} 0 \\ H_{jy} \\ 0 \end{pmatrix} \text{ for TM} \tag{2.33}$$

We first treat the electromagnetic wave with TE polarization. From Equation 2.14 of Maxwell´s equations, the electric and magnetic fields are written as

$$\nabla \times \mathbf{E}_j(\mathbf{r},\omega) = -\frac{\partial E_{jy}(\mathbf{r},\omega)}{\partial z}\hat{\mathbf{e}}_x + \frac{\partial E_{jy}(\mathbf{r},\omega)}{\partial x}\hat{\mathbf{e}}_z = \left(-ik_{jz}\hat{\mathbf{e}}_x + ik_x\hat{\mathbf{e}}_z\right)E_{jy}(\mathbf{r},\omega) \tag{2.34}$$

$$-\mu_0 \frac{\partial \mathbf{H}_j(\mathbf{r},\omega)}{\partial t} = i\omega\mu_0 \mathbf{H}_j(\mathbf{r},\omega) = i\omega\mu_0\left[H_{jx}(\mathbf{r},\omega)\hat{\mathbf{e}}_x + H_{jz}(\mathbf{r},\omega)\hat{\mathbf{e}}_z\right] \tag{2.35}$$

Equations 2.34 and 2.35 must be equal; therefore,

$$H_{jx}(\mathbf{r},\omega) = -\frac{k_{jz}}{\omega\mu_0}E_{jy}(\mathbf{r},\omega), \qquad H_{jz}(\mathbf{r},\omega) = \frac{k_x}{\omega\mu_0}E_{jy}(\mathbf{r},\omega) \tag{2.36}$$

The tangential components of the electric and magnetic fields must be continuous; therefore, $E_{1y} = E_{2y}$ and $H_{1x} = H_{2x}$. From Equation 2.36, we get the following relationship

$$k_{1z} - k_{2z} = 0 \tag{2.37}$$

Considering Equation 2.32, it is immediately found that this relationship cannot be satisfied, meaning that the electromagnetic wave with TE polarization cannot propagate on the interface.

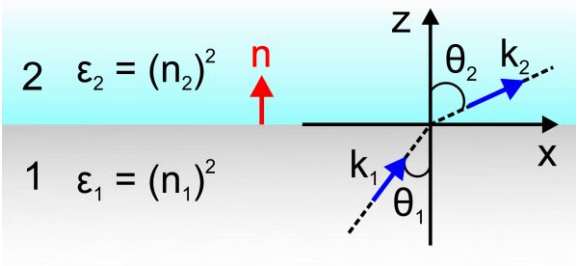

Figure 2.7 Schematic illustration of boundary conditions.

We turn our focus to TM polarization. In a similar manner to the case of TE polarization, we derive the electric and magnetic fields by using Equation 2.15 of Maxwell´s equations

$$\nabla \times \mathbf{H}_{\mathrm{j}}(\mathbf{r},\omega) = -\frac{\partial H_{\mathrm{jy}}(\mathbf{r},\omega)}{\partial z}\hat{\mathbf{e}}_{\mathrm{x}} + \frac{\partial H_{\mathrm{jy}}(\mathbf{r},\omega)}{\partial x}\hat{\mathbf{e}}_{\mathrm{z}} = \left(-ik_{\mathrm{jz}}\hat{\mathbf{e}}_{\mathrm{x}} + ik_{\mathrm{x}}\hat{\mathbf{e}}_{\mathrm{z}}\right)H_{\mathrm{jy}}(\mathbf{r},\omega) \tag{2.38}$$

$$\varepsilon_0\varepsilon_{\mathrm{j}}\frac{\partial \mathbf{E}_{\mathrm{j}}(\mathbf{r},\omega)}{\partial t} = -i\omega\varepsilon_0\varepsilon_{\mathrm{j}}\mathbf{E}_{\mathrm{j}}(\mathbf{r},\omega) = -i\omega\varepsilon_0\varepsilon_{\mathrm{j}}\left[E_{\mathrm{jx}}(\mathbf{r},\omega)\hat{\mathbf{e}}_{\mathrm{x}} + E_{\mathrm{jz}}(\mathbf{r},\omega)\hat{\mathbf{e}}_{\mathrm{z}}\right] \tag{2.39}$$

Equations 2.38 and 2.39 must be equal.

$$E_{\mathrm{jx}}(\mathbf{r},\omega) = \frac{k_{\mathrm{jz}}}{\omega\varepsilon_0\varepsilon_{\mathrm{j}}}H_{\mathrm{jy}}(\mathbf{r},\omega), \qquad E_{\mathrm{jz}}(\mathbf{r},\omega) = i\frac{k_{\mathrm{x}}}{\omega\varepsilon_0\varepsilon_{\mathrm{j}}}H_{\mathrm{jy}}(\mathbf{r},\omega) \tag{2.40}$$

Equation 2.40 must satisfy the boundary conditions of $H_{1\mathrm{y}} = H_{2\mathrm{y}}$ and $E_{1\mathrm{x}} = E_{2\mathrm{x}}$, which gives the following relationship

$$\frac{\varepsilon_1}{\varepsilon_2} = \frac{k_{1\mathrm{z}}}{k_{2\mathrm{z}}} = \frac{\sqrt{k_0^2\varepsilon_1 - k_{\mathrm{x}}^2}}{\sqrt{k_0^2\varepsilon_2 - k_{\mathrm{x}}^2}} \tag{2.41}$$

Equation 2.32 is used to derive Equation 2.41. Equation 2.41 gives the *x*- and *z*-components of the wavevector of the electromagnetic wave propagating on the interface

$$k_{\mathrm{x}} = \sqrt{\frac{\varepsilon_1\varepsilon_2}{\varepsilon_1+\varepsilon_2}}k_0 = \sqrt{\frac{\varepsilon_1\varepsilon_2}{\varepsilon_1+\varepsilon_2}}\frac{\omega}{c}, \qquad k_{\mathrm{jz}} = \frac{\varepsilon_{\mathrm{j}}}{\sqrt{\varepsilon_1+\varepsilon_2}}k_0 \tag{2.42}$$

For simplicity, it is assumed that Medium1 and Medium2 are lossless. In this case, k_{x} and k_{jz} should be real and imaginary numbers, respectively. These criteria ensure that the wave exit as an evanescent wave propagating in the *x*-direction, and its amplitude decays exponentially in the *z*-direction. Therefore, to support such an evanescent wave, the materials comprising the interface must have $\varepsilon_1\varepsilon_2 < 0$ and $\varepsilon_1 + \varepsilon_2 < 0$. These conditions can be satisfied only when either ε_1 or ε_2 is negative; thus, the interface must be a metal-dielectric interface. We consider that Medium1 is a metal and Medium2 is a dielectric (Figure 2.8a). In this situation, the evanescent wave propagating in the dielectric is bound to the surface charge of the metal. This surface charge oscillates collectively and is called a surface plasmon. The state that the surface plasmon coexists with an electromagnetic wave is called surface plasmon polaritons (SPPs). Since the SPP given by Equation 2.42 propagates, this SPP is called a propagating surface plasmon (PSP).

k_{x} given by Equation 2.42 describes the dispersion of a PSP. We now consider that the dielectric is lossless and has a constant relative permittivity, and the metal is described by the Drude model. Therefore, k_{x} is a complex function and can be rewritten as $k_{\mathrm{x}} = k_{\mathrm{x}}' + ik_{\mathrm{x}}''$. The propagation length of the PSP is found from $1/k_{\mathrm{x}}''$. If we consider a case that the metal does not possess a damping ($\gamma = 0$), corresponding to the perfect conductor, we obtain k_{x} using the Drude model as

$$k_{\mathrm{x}} = k_{\mathrm{x}}' + ik_{\mathrm{x}}'' \approx \sqrt{\frac{\varepsilon_1'\varepsilon_2}{\varepsilon_1'+\varepsilon_2}}\frac{\omega}{c} = \sqrt{\frac{\left(\omega^2-\omega_{\mathrm{p}}^2\right)\varepsilon_2}{\left(\omega^2-\omega_{\mathrm{p}}^2\right)+\omega^2\varepsilon_2}}\frac{\omega}{c} \tag{2.43}$$

Equation 2.43 diverges when its denominator becomes zero, giving the surface plasmon frequency

$$\omega_{\mathrm{sp}} = \frac{\omega_{\mathrm{p}}}{\sqrt{1+\varepsilon_2}} \tag{2.44}$$

The dispersion relation of k_{x} with $\varepsilon_2 = 1$ is shown in Figure 2.8b. For this plot, all variables of the Drude model are normalized by the plasma frequency ω_{p}. The solid red and blue lines show k_{x}' and k_{x}'' for the lossless case (Equation 2.43). k_{x}' appears in the region of $\omega > \omega_{\mathrm{p}}$; however, as described earlier, the metal

becomes transparent in that frequency range; therefore, the PSP cannot exist in that frequency region. In $\omega_p < \omega < \omega_{sp}$ (the blue shaded area of Figure 2.8b), k_x becomes purely imaginary even though the free electron damping is ignored. This situation forbids the PSP from propagating along the interface. In a frequency region lower than ω_{sp}, k_x' has another branch, which proves the existence of the PSP. As can be expected from Equation 2.43, k_x' significantly increases, and a group velocity becomes zero with approaching ω_{sp}. The same properties of k_x can be applied to the case of the metal with non-zero free electron damping. The dashed lines consider k_x' with different damping rates. In this case, k_x' does not go to infinity but is maximized when $\omega \rightarrow \omega_{sp}$. k_x' appears in the region of $\omega_p < \omega < \omega_{sp}$ by increasing γ, but k_x'' is still large in that region, prohibiting supporting the PSP. Therefore, in any value of γ, the PSP can be supported in the frequency range of $\omega < \omega_{sp}$.

PSPs cannot be excited by directly illuminating light on a metal surface since the PSP dispersion cannot match that of the light coming from free space (see the solid gray line in Figure 2.8b). To excite PSPs, various approaches have been developed. A widely-used technique is structuring a grating on a metal surface [76-79]. A reciprocal space of the grating can add a wavevector to the light propagating in free space, attributed to the diffraction of light. Therefore, the light line can move in a region where the PSP dispersion exists.

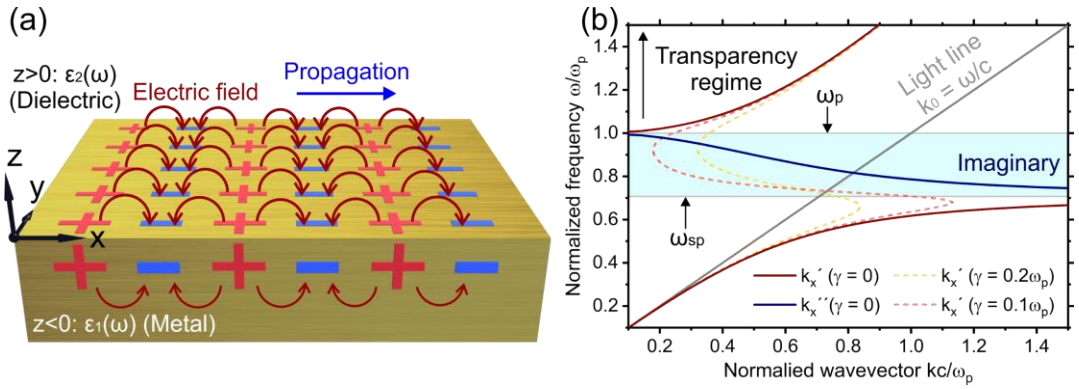

Figure 2.8. Surface plasmon polariton. (a) The image of a PSP. (b) The dispersion relation of a metal-dielectric interface k_x. The dispersion relation is calculated using Equation 2.43 with the Drude model. The solid red and blue lines are the real and imaginary parts of k_x without the free electron damping $\gamma = 0$. The dashed lines are the real part of k_x with the free electron damping. The solid grey line shows the dispersion of the electromagnetic wave in the air.

2.2.3. Optical properties of particles in the quasi-static limit

The optical properties of materials are determined by their electric permittivity and magnetic permeability. In general, those properties are intrinsic features. However, when the size of materials is comparable to or smaller than a wavelength, this subwavelength material can possess unique optical properties different from bulk materials. One of the most famous examples of this phenomenon is stained glass. The stained glass contains metallic nanoparticles. Bulk metals act like a mirror; however, metallic nanoparticles can act as light absorbers, enabling us to produce a color. This light absorption originates from localized surface plasmons (LSPs), a collective oscillation of free electrons in metallic nanoparticles.

To understand the optical properties of such subwavelength particles, their electric polarizabilities are considered. As understood from Section 3.1, the optical responses of a bound electron are characterized by its electric dipole moment. Since LSPs are also dipolar oscillations, the optical responses of subwavelength particles can be explained similarly to the polarization of the bound electron. By knowing the polarizability, we can understand the particle´s extinction, scattering, and absorption properties.

2.2.3.1. Localized surface plasmons

We consider the optical properties of a particle in the quasi-static limit. This limit is given by comparing a wavelength and particle size. When a wave propagates in the *z*-direction, the propagation is expressed by e^{ikz}. If a particle with a radius of *a* is placed in free space, how fast the wave changes over the particle is found as e^{ika}. In a limit of $ka << 1$, we get $e^{ika} \approx 1$, meaning that the wave is spatially constant over the particle. This situation corresponds to considering that the wave is an electrostatic field. From this consideration, the quasi-static limit is given as $ka << 1$ (alternatively, $2\pi a << \lambda$). In general, the electric polarizability of a spherical particle in the quasi-static limit is obtained by solving the Laplace equation $\nabla^2 \Phi = 0$ and $\mathbf{E} = -\nabla\Phi$ (Φ is the electric scalar potential) in the spherical coordinate since the electrostatic field is considered [75, 80].

Here, another approach is used to derive electric polarizability, which was introduced by Barnes [81]. It is considered that a flat plate of Medium1 with relative permittivity ε_1 is in a parallel-plate capacitor. A flat plate of Medium2 with relative permittivity ε_2 is embedded in Medium1 (see Figure 2.9a). Medium1 is dielectric, and Medium2 is dielectric or metal. The electric field of the capacitor without the media is $\mathbf{E}_0$. The net electric field in the media is $\mathbf{E}_j$ ($j \in 1, 2$). This electric field induces the polarization of the media, which is described by the polarization density of the media $\mathbf{P}_j$. This polarization density is equal to the surface charge density σ_j. $\mathbf{P}_j$ can be written using the susceptibility χ_j as $\mathbf{P}_j = \varepsilon_0\chi_j\mathbf{E}_j = \varepsilon_0(\varepsilon_j - 1)\mathbf{E}_j$. In the capacitor, Medium1 is considered a background medium, and $\mathbf{E}_1 = \mathbf{E}_0/\varepsilon_1$ (from the boundary condition $\mathbf{D}_1 - \mathbf{D}_0 = 0$) is taken as a background field. At the interfaces of the media, the net surface charge of $\sigma = \sigma_2 - \sigma_1$ is created, and this net surface charge creates the net polarization density $\mathbf{P}$ of the interface. $\mathbf{P}$ is given as

$$\mathbf{P} = \varepsilon_0\chi\mathbf{E}_2 = \varepsilon_0(\chi_2 - \chi_1)\mathbf{E}_2 = \varepsilon_0(\varepsilon_2 - \varepsilon_1)\mathbf{E}_2 \qquad 2.45$$

where χ is the net susceptibility given by the difference in the electric responses of the media. Using the electric field $\mathbf{E}_P$ induced by $\mathbf{P}$, the effective electric field $\mathbf{E}_2$ can also be written as

$$\mathbf{E}_2 = \mathbf{E}_1 + \mathbf{E}_P, \qquad \mathbf{E}_P = -\frac{\mathbf{P}}{\varepsilon_0\varepsilon_1} \qquad 2.46$$

where $\mathbf{E}_P$ is given by Gauss´s law, and its $1/\varepsilon_1$ describes that the background medium screens the surface charge. Using Equations 2.45 and 2.46, we can obtain $\mathbf{P}$ as

$$\mathbf{P} = \varepsilon_0\varepsilon_1\frac{\varepsilon_2 - \varepsilon_1}{\varepsilon_2}\mathbf{E}_1 = \varepsilon_0\varepsilon_1\epsilon\mathbf{E}_1 \qquad 2.47$$

where ϵ is the polarizability of Medium2 embedded in Medium1.

Next, we consider the polarizability of a small particle embedded in Medium1 (Figure 2.9b). Since the distribution of surface charge alters when the geometry of Medium2 changes, the electric field inside Medium2 cannot be explained by Equation 2.46. This change in the surface charge distribution can be taken into account by adding the shape factor *L* to the net polarization density $\mathbf{P}$, which gives the electric field inside the particle as

$$\mathbf{E}_2{}' = \mathbf{E}_1 + \mathbf{E}_P', \qquad \mathbf{E}_P{}' = -L\frac{\mathbf{P}}{\varepsilon_0\varepsilon_1} \qquad 2.48$$

By substituting Equation 2.48 into Equation 2.45, we get

$$\mathbf{P}' = \varepsilon_0\varepsilon_1\frac{\varepsilon_2 - \varepsilon_1}{\varepsilon_1 + L(\varepsilon_2 - \varepsilon_1)}\mathbf{E}_1 = \varepsilon_0\varepsilon_1\epsilon'\mathbf{E}_1 \qquad 2.49$$

ϵ' gives the polarizability per unit volume of the particle with a shape determined by *L*. The polarizability of the particle is given as

$$\alpha = V\epsilon' = V\frac{\varepsilon_2 - \varepsilon_1}{\varepsilon_1 + L(\varepsilon_2 - \varepsilon_1)} \tag{2.50}$$

where V is the volume of the particle. Equation 2.50 coincides with the result from the Laplace equation [75, 80]. In Equation 2.50, there is the factor of $\varepsilon_2 - \varepsilon_1$, which originates from the difference in susceptibility between the particle and its surrounding. It can be found that the polarizability diverges when its denominator becomes zero, meaning $\mathrm{Re}[\varepsilon_2] = (1 - 1/L)\varepsilon_1$. This is the condition of the optical resonance of the particle. L can be given for different shapes of ellipsoidal particles, such as a sphere, oblate, and prolate spheroid. For a prolate spheroid with $b = c$, L becomes [80]

$$L = \frac{1 - e^2}{e^2}\left[-1 + \frac{1}{2e}\ln\left(\frac{1+e}{1-e}\right)\right], \qquad e^2 = 1 - \frac{b^2}{a^2} \tag{2.51}$$

For a spherical particle, we get $L = 1/3$. Using this value, the polarizability of a spherical particle is

$$\alpha = V\frac{\varepsilon_2 - \varepsilon_1}{\varepsilon_2 + 2\varepsilon_1} \tag{2.52}$$

For Equation 2.52, the resonance condition is given as $\mathrm{Re}[\varepsilon_2] = -2\varepsilon_1$. This condition is called the Fröhlich condition and can be satisfied by a metallic particle since ε_2 is required to be a negative value. The Fröhlich condition can also be satisfied when ε_1 is negative and ε_2 is positive, meaning that Medium1 is a metal and Medium2 is a dielectric. In addition to metals, some dielectric materials, such as SiO_2, can also possess a negative permertivity in the MIR range. Therefore, a system composed of dielectrics can also fulfill the Fröhlich condition. For a simplicity, we will forcus on one of the most important cases for this dissertation, which is a metallic particle placed in a dielectric medium. By substituting $\varepsilon_1 = 1$ (Medium1 is air) and the Drude model into Equation 2.50, we get

$$\alpha = V\frac{\omega_\mathrm{p}^2}{\omega_0^2 - \omega^2 - i\gamma\omega} = \frac{\alpha_0}{\omega_0^2 - \omega^2 - i\gamma\omega}, \qquad \omega_0 = \sqrt{L}\omega_\mathrm{p} \tag{2.53}$$

where $\alpha_0 = V\omega_\mathrm{p}^2$ is the oscillator strength, and ω_0 is the resonance frequency. This resonance frequency is found for the spherical particle as $\omega_0 = \omega_\mathrm{p}/3^{1/2}$. From Equation 2.53, it is found that the polarizability can be expressed as the Lorentz oscillator model. Under the Fröhlich condition, the free electrons of metallic particles collectively oscillate. This oscillation is also an SPP but is different from a PSP. In the case of a particle, the SPP cannot propagate but is localized in a finite volume of the particle. Therefore, the SPP of the particle is called an LSP. The quasi-static electric fields inside and outside of the spherical particle can be found by solving the Laplace equation [75, 80]

$$\mathbf{E}_\mathrm{in} = \frac{3\varepsilon_1}{\varepsilon_2 + 2\varepsilon_1}\mathbf{E}_1, \qquad \mathbf{E}_\mathrm{out} = \mathbf{E}_1 + \frac{3\mathbf{n}(\mathbf{n}\cdot\mathbf{p}) - \mathbf{p}}{4\pi\varepsilon_0\varepsilon_1}\frac{1}{r^3}, \qquad \mathbf{p} = \varepsilon_0\varepsilon_1\alpha\mathbf{E}_1 \tag{2.54}$$

where $\mathbf{n}$ is the unit vector in the direction of r (Figure 2.9b). $\mathbf{p}$ is the dipole moment of the spherical particle. In general, the electric field inside of the particle is smaller than the external field. The field outside the particle comprises the contributions from the external field and a field created by the particle. The created field allows the particle to have an optical cross-section larger than its geometrical cross-section at the resonance condition, enabling the particle to couple to the external field strongly.

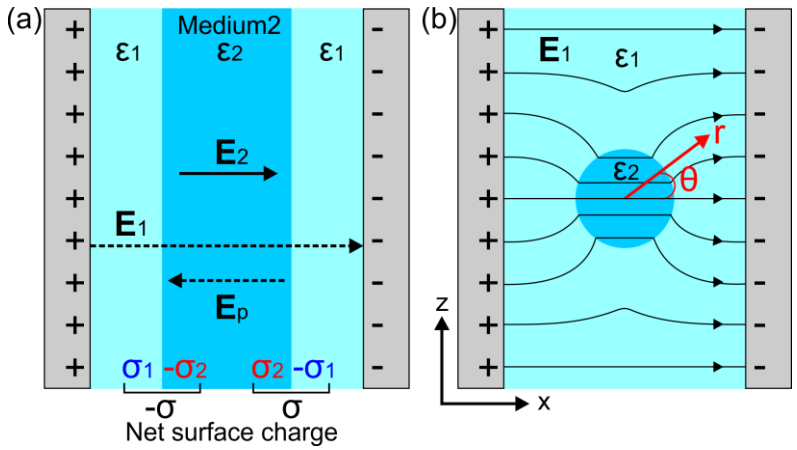

Figure 2.9. Image of an LSP. (a) A flat plate made of Medium2 is embedded in a parallel plate capacitor filled with Medium1. (c) A particle made of Medium2 is embedded in a parallel plate capacitor filled with Medium1.

The resonance condition of a particle in the quasi-static limit can also be described differently [82]. It is considered that a particle with ε_2 is in a closed system with a volume Ω. This closed system is sufficiently larger than a field created by the particle. The surrounding of the particle is a lossless dielectric with ε_1. The volumes of the surrounding and particle are Ω_1 and Ω_2, giving $\Omega = \Omega_1 + \Omega_2$. Under the quasi-static limit, $\nabla\times\mathbf{E} = 0$ and $\mathbf{E} = -\nabla\Phi$ have to be fulfilled. The stored electric field energy of the particle in the volume Ω is given as

$$\int_{\Omega} \varepsilon \boldsymbol{E}\cdot\boldsymbol{E}dV = \int_{\Omega_1} \varepsilon_1 \overline{E^2} dV + \int_{\Omega_2} \varepsilon_2 \overline{E^2} dV = 0 \qquad 2.55$$

where $\overline{E^2}$ is the time-averaged electric field in the system. By considering that the particle is comprised of one type of material, the nontrivial solution of Equation 2.55 is given as

$$-\varepsilon_2 = \frac{\int_{\Omega_1} \varepsilon_1 \overline{E^2} dV}{\int_{\Omega_2} \overline{E^2} dV} \qquad 2.56$$

The right side of Equation 2.56 is a positive value; therefore, ε_2 must be a negative value. This result shows that under the quasi-static limit, an optical resonance of the particle occurs only when the particle is made of metal, which coincides with the Fröhlich condition. Based on the Drude model, the real part of the permittivity of metal keeps decreasing with an increase in the wavelength (Figure 2.6). Therefore, an LSP can redshift by controlling the right side of Equation 2.56. Figure 2.10 summarizes Equation 2.56. Figure 2.10a considers a metallic particle embedded in media with different ε_1. The field distributions are identical for both media. However, the energy stored in the dielectric medium increases with an increase in ε_1, resulting in a redshift of the LSP. Figure 2.10b shows the electric field distribution of a core-shell particle. The core-shell particle is composed of a concentric metallic shell and a dielectric core. We consider that the outer radius of the shell is fixed, but its inner radius changes, meaning that the shell thickness changes. With decreasing the shell thickness, the volume of the metallic particle decreases, and the volume of the dielectric core increases. In addition, the electric field inside the core increases. This increases the right side of Equation 2.56. Thus, tuning the shell thickness is a promising approach to controlling an LSP. The last example is a metallic nanorod with the same length but a different radius (Figure 2.10c). The same interpretation for the core-shell can be applied to the case of the nanorod. With an increase in the radius, the volume ratio increases, and the stored energy in the surrounding dielectric medium increases. Therefore, its LSP redshifts.

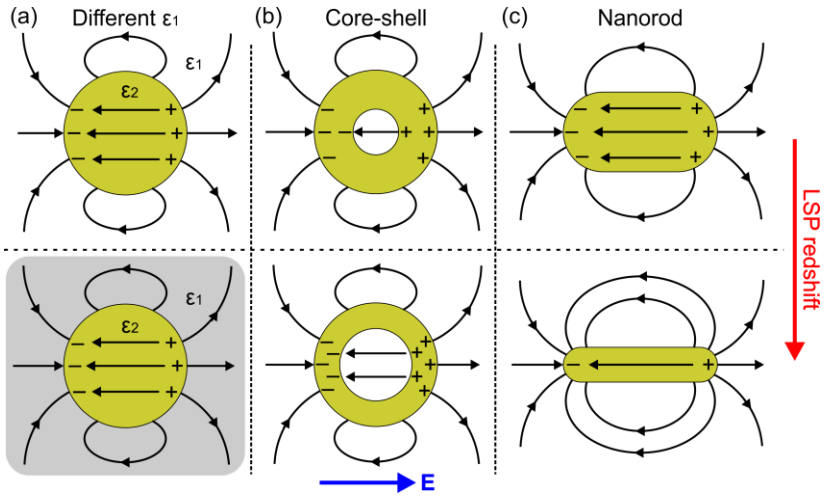

Figure 2.10. Schematic illustrations of a redshift of an LSP. Based on Equation 2.56, an LSP resonance is redshifted by (a) embedding a metallic particle in a high refractive index medium, (b) thinning the shell thicknesses of a core-shell particle, and (c) reducing the radius of a nanorod. The blue arrow shows the direction of the external field. The black arrows are the electric fields created by the particles.

From Equations 2.53 and 2.56, it is understood that an LSP is not determined by a particle´s size but is determined by the aspect ratio of the particle. However, these results are given under the quasi-static limit. If the particle size becomes large, the polarizability of the particle cannot be described by Equation 2.53. Here the size dependency of the polarizability is discussed. The polarizability in the quasi-static limit only considers the damping originating from the elastic friction of free electrons. In addition, three size-dependent damping effects have to be taken into account [83-86]:

A) When a particle is smaller than the mean free path of free electrons, the surface scattering of the free electrons increases the damping.
B) An oscillating dipole emits an electromagnetic wave. This emission recoils the free electrons, resulting in radiative damping. The radiative damping becomes strong with an increase in the number of free electrons.
C) Free electrons cannot oscillate collectively in a particle with a size comparable to the wavelength. As a result, phase retardation occurs on the oscillation. This effect is called dynamic depolarization.

Based on these three considerations, the size-dependent polarizability of a metallic particle with a radius of a is obtained. The net damping of the free electrons influenced by the surface scattering can be rewritten as

$$\gamma_{\mathrm{int}} = \gamma + A\frac{v_{\mathrm{F}}}{a} \qquad 2.57$$

where γ is the damping rate of the Drude model, v_{F} is the Fermi velocity of the free electron, and A is the scaling factor describing the surface scattering, being between 0 to 1. The last two considerations influence the external field vicinity of the particle, which is characterized as the radiation effects. The radiation effects are given as

$$E_{\mathrm{rad}} = \frac{1}{\varepsilon_0 \varepsilon_{\mathrm{m}}}\left(\frac{ik^3}{6\pi} + \frac{k^2}{2\pi a}\right)p \qquad 2.58$$

where ε_{m} is the relative permittivity of the surrounding, k is the wave number, and p is the net dipole moment. In the bracket of Equation 2.58, the first and second terms describe the radiative damping and retardation effect, respectively. Using Equations 2.54 and 2.58, the net electric dipole moment is written as

$$p = \varepsilon_0 \varepsilon_\mathrm{m} \alpha (E_0 + E_\mathrm{rad}) \tag{2.59}$$

where E_0 is the incident field. $E_0 + E_\mathrm{rad}$ describes the net external field of the particle. By substituting Equation 2.58 into Equation 2.59, the dipole moment is modified as

$$p = \varepsilon_0 \varepsilon_\mathrm{m} \frac{\alpha}{1 - \alpha \left(\frac{ik^3}{6\pi} + \frac{k^2}{2\pi a} \right)} E_0 = \varepsilon_0 \varepsilon_\mathrm{m} \alpha_\mathrm{s} E_0 \tag{2.60}$$

where α_S is the size-dependent polarizability. For more detail, α given by Equation 2.53 is substituted in Equation 2.60 (the surrounding is now air $\varepsilon_\mathrm{m} = 1$)

$$\begin{aligned} \alpha_\mathrm{s} &= \frac{\alpha_0}{(\omega_0^2 - \omega^2 - i\gamma_\mathrm{int}\omega) - \alpha_0 \left(\frac{ik^3}{6\pi} + \frac{k^2}{2\pi a} \right)} \\ &= \frac{\alpha_0}{\left[\omega_0^2 - 2\left(\frac{\omega_\mathrm{p}^2}{3} \right)(ka)^2 \right] - \omega^2 - i\left[\gamma_\mathrm{int} + \frac{2\omega_\mathrm{p}^2}{9\omega}(ka)^3 \right] \omega} \end{aligned} \tag{2.61}$$

$\alpha_0 = V\omega_\mathrm{p}^2 = (4a^3/3)\omega_\mathrm{p}^2$ is used to derive Equation 2.61. The effective resonance frequency and damping of α_S are given as

$$\omega_\mathrm{LSP} = \sqrt{1 - 2(ka)^2}\,\omega_0 \tag{2.62}$$

$$\Gamma = \gamma_\mathrm{int} + \frac{2\omega_\mathrm{p}^2}{9\omega}(ka)^3 = \gamma_\mathrm{int} + \gamma_\mathrm{rad} \tag{2.63}$$

ω_LSP and Γ involve the effects of dynamic depolarization and radiative damping, respectively. If the quasi-static limit $ka << 1$ is considered, Equation 2.61 is reduced to the size-independent polarizability. From Equation 2.62, it is understood that the resonance frequency redshifts from ω_0 with increasing the particle size. Equation 2.63 shows that the effect of radiative damping becomes significant for a large particle. By modifying the radiative damping, we get

$$\gamma_\mathrm{rad} = \alpha_0 \frac{k^3}{6\pi\omega} = V\omega_\mathrm{p}^2 \frac{1}{6\pi\omega} \frac{\omega^3}{c^3} = \frac{VNe^2}{6\pi\varepsilon_0 mc^3}\omega^2 = \tau_\mathrm{rad}\omega^2 \tag{2.64}$$

where N is the number of electrons per unit volume. τ_rad is the radiative damping coefficient given by the Abraham-Lorentz force [87]. Using Equations 2.62-2.64, the size-dependent polarizability can be modified into a simple form

$$\alpha_\mathrm{s} = \frac{\alpha_0}{\omega_\mathrm{LSP}^2 - \omega^2 - i(\gamma_\mathrm{int} + \tau_\mathrm{rad}\omega^2)\omega} \tag{2.65}$$

Figure 2.11 shows the absolute value of the size-dependent polarizability at $\omega = \omega_\mathrm{LSP}$ as a function of ka. The dashed gray line presents the size-independent polarizability given by Equation 2.53, which is constant over ka. By including the size-dependent effects, the polarizability possesses different profiles. The red solid line only considers the dynamic depolarization effect. The polarizability is the same as the dashed gray line at a small ka, but it dramatically decreases with an increase in ka. This decrease is attributed to the redshift of ω_LSP. The solid blue line takes only the radiative damping effect into account. The line profile is similar to the red line, but it decreases slowly with increasing ka. This decrease is because the radiative damping increases with an increase in ka, weakening the amplitude of the polarizability. The solid green line shows the influence of the electron surface scattering effect. The polarizability increases with an increase in ka because the electron scattering is inversely proportional to the radius of the particle. The solid black line includes all three effects. Interestingly, it possesses a maximum, meaning that there is an optimum size to amplify the polarizability.

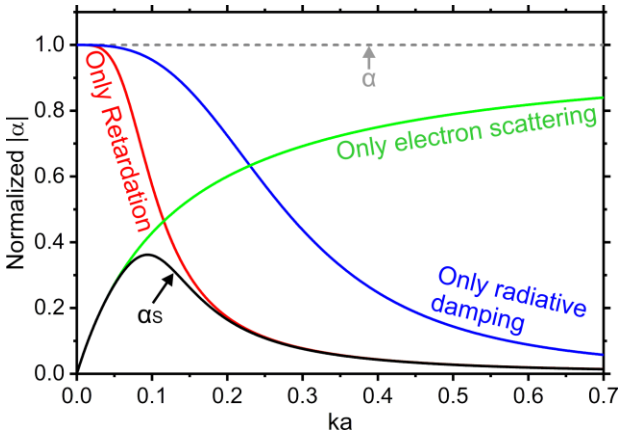

Figure 2.11. The size-dependent polarizability of a metallic spherical particle. The dashed gray line is a reference calculated using Equation 2.53. The solid green, red, and blue lines are calculated using Equation 2.65 only considering the electron surface scattering, dynamic depolarization, and radiative damping, respectively. The dashed black line considers all these three effects. For these plots, $\omega = \omega_{LSP}$, $\omega_p = 1.36 \times 10^{16}$ 1/s, $\gamma = 1.1 \times 10^{14}$ 1/s, $v_F = 1.4 \times 10^6$ m/s, and $A = 4$ are used. All plots are absolute values of the polarizability normalized by the reference.

2.2.3.2. Radiation of oscillating dipole and its extinction, scattering, and absorption

We have considered an optical response of a metallic particle under the electrostatic approximation. When we consider an external field oscillating with time-harmonic, the dipole moment of the particle also oscillates. As widely known, the oscillating dipole (oscillating charge) emits electromagnetic energy. This is the origin of light scattering. For a localized oscillating source, a charge $\rho(\mathbf{r},t)$ and a current $\mathbf{J}(\mathbf{r},t)$ are written as [87]

$$\rho(\mathbf{r},t) = \rho(\mathbf{r})e^{-i\omega t}, \qquad \mathbf{J}(\mathbf{r},t) = \mathbf{J}(\mathbf{r})e^{-i\omega t} \tag{2.66}$$

The vector potential $\mathbf{A}(\mathbf{r},t)$ is given by using the current

$$\mathbf{A}(\mathbf{r}) = \frac{\mu_0}{4\pi}\int_\Omega \mathbf{J}(\mathbf{r}')\frac{e^{ik|\mathbf{r}-\mathbf{r}'|}}{|\mathbf{r}-\mathbf{r}'|}d^3r' \tag{2.67}$$

where $\mathbf{r}$ is the position of the fields created by the source, and $\mathbf{r}'$ is the position of the source (Figure 2.12a). Since $\mathbf{B} = \nabla\times\mathbf{A}$ and $\mathbf{E} = (iZ_0/k)\nabla\times\mathbf{H}$, where Z_0 is the impedance of free space, the created electric and magnetic fields can be found from a current distribution of the source. It is assumed that the source dimension d is much smaller than a wavelength; therefore, $d << \lambda$. In addition, when $|\mathbf{r}| >> |\mathbf{r}'|$, we get $|\mathbf{r} - \mathbf{r}'| \approx R - \mathbf{n}\cdot\mathbf{r}'$ where R is the distance from the center of the source to $\mathbf{r}$, and $\mathbf{n}$ is the unit vector in the direction of R. In the far-field $d << \lambda << R$, we obtain the following series expansion of Equation 2.67 in the power of k

$$\lim_{kR\to\infty}\mathbf{A}(\mathbf{r}) = \mu_0\frac{e^{ikR}}{4\pi R}\sum_n\frac{(-ik)^n}{n!}\int_\Omega \mathbf{J}(\mathbf{r}')(\mathbf{n}\cdot\mathbf{r}')^n d^3r' \tag{2.68}$$

Equation 2.68 shows that the $\mathbf{A}$ decreases inversely proportional to R in the far-field. By keeping the first term ($n = 0$) of Equation 2.68, we can obtain the vector potential of an electric dipole moment $\mathbf{p}$

$$\mathbf{A}(\mathbf{r}) = -i\omega\mu_0\frac{e^{ikR}}{4\pi R}\int_\Omega \mathbf{r}'\rho(\mathbf{r}')d^3r' = -i\omega\mu_0\frac{e^{ikR}}{4\pi R}\mathbf{p} = -i\frac{\mu_0}{\varepsilon_0 Z_0}k\frac{e^{ikR}}{4\pi R}\mathbf{p} \tag{2.69}$$

Using $\mathbf{B} = \nabla\times\mathbf{A}$ and $\mathbf{E} = (iZ_0/k)\nabla\times\mathbf{H}$, the fields created by the electric dipole moment are given as

$$\mathbf{H}_\mathrm{e}(\mathbf{r}) = \frac{1}{\varepsilon_0 Z_0}\left(k^2 + \frac{ik}{R}\right)(\mathbf{n}\times\mathbf{p})\frac{\mathrm{e}^{ikR}}{4\pi R} = \frac{1}{\varepsilon_0 Z_0}\mathbf{G}_\mathrm{M}(\mathbf{r}-\mathbf{r}')\cdot\mathbf{p} \tag{2.70}$$

$$\mathbf{E}_\mathrm{e}(\mathbf{r}) = \frac{1}{\varepsilon_0}\left\{k^2(\mathbf{n}\times\mathbf{p})\times\mathbf{n} + \left(\frac{1}{R^2} - \frac{ik}{R}\right)[3\mathbf{n}(\mathbf{n}\cdot\mathbf{p}) - \mathbf{p}]\right\}\frac{\mathrm{e}^{ikR}}{4\pi R} = \frac{1}{\varepsilon_0}\mathbf{G}_\mathrm{E}(\mathbf{r}-\mathbf{r}')\cdot\mathbf{p} \tag{2.71}$$

where $\mathbf{G}_\mathrm{E}$ and $\mathbf{G}_\mathrm{M}$ are the dyadic Green´s functions [74]. In the near-field regime $R << \lambda$, Equations 2.70 and 2.71 are reduced to

$$\mathbf{H}_\mathrm{e}(\mathbf{r}) = \frac{ik(\mathbf{n}\times\mathbf{p})}{4\pi\varepsilon_0 Z_0 R^2}, \qquad \mathbf{E}_\mathrm{e}(\mathbf{r}) = \frac{3\mathbf{n}(\mathbf{n}\cdot\mathbf{p}) - \mathbf{p}}{4\pi\varepsilon_0 R^3} \tag{2.72}$$

This electric field coincides with Equation 2.54. The magnetic field is smaller than the electric field by a factor of kR. Thus, the electric field is predominant in the near-field. In the far-field regime $R >> \lambda$, the electric and magnetic fields are transverse and propagate like a spherical wave. This electromagnetic wave is the scattered wave of the oscillating dipole moment, which is given from Equations 2.70 and 2.71 as

$$\mathbf{H}_\mathrm{e}(\mathbf{r}) = \frac{k^2}{\varepsilon_0 Z_0}(\mathbf{n}\times\mathbf{p})\frac{\mathrm{e}^{ikR}}{4\pi R} \tag{2.73}$$

$$\mathbf{E}_\mathrm{e}(\mathbf{r}) = \frac{k^2}{\varepsilon_0}[(\mathbf{n}\times\mathbf{p})\times\mathbf{n}]\frac{\mathrm{e}^{ikR}}{4\pi R} = \frac{k^2}{\varepsilon_0}[\mathbf{p} - \mathbf{n}(\mathbf{n}\cdot\mathbf{p})]\frac{\mathrm{e}^{ikR}}{4\pi R} \tag{2.74}$$

When an electromagnetic wave strikes a small particle, part of this incident wave´s energy is scattered away by the particle´s dipole resonance, described by Equations 2.73 and 2.74. In addition, the particle absorbs part of the incident wave´s energy by the Joule heating. Those energies are considered as energy loss of the incident wave, and total energy loss by scattering and absorption is called extinction. We formulate the extinction by defining the incident wave as $\mathbf{E}_\mathrm{in}(\mathbf{r})$ and $\mathbf{H}_\mathrm{in}(\mathbf{r})$, and the scattered wave as $\mathbf{E}_\mathrm{sca}(\mathbf{r})$ and $\mathbf{H}_\mathrm{sca}(\mathbf{r})$. The incident wave is a plane wave. The total field of this system is expressed as $\mathbf{E}_\mathrm{tot}(\mathbf{r}) = \mathbf{E}_\mathrm{in}(\mathbf{r}) + \mathbf{E}_\mathrm{sca}(\mathbf{r})$ and $\mathbf{H}_\mathrm{tot}(\mathbf{r}) = \mathbf{H}_\mathrm{in}(\mathbf{r}) + \mathbf{H}_\mathrm{sca}(\mathbf{r})$. The time-averaged net energy flow $\mathbf{S}_\mathrm{tot}$ of the systems is

$$\mathbf{S}_\mathrm{tot}(\mathbf{r}) = \frac{1}{2}\mathrm{Re}[\mathbf{E}_\mathrm{tot}(\mathbf{r})\times\mathbf{H}^*_\mathrm{tot}(\mathbf{r})] = \mathbf{S}_\mathrm{in}(\mathbf{r}) + \mathbf{S}_\mathrm{sca}(\mathbf{r}) + \mathbf{S}_\mathrm{ext}(\mathbf{r}) \tag{2.75}$$

$$\begin{cases} \mathbf{S}_\mathrm{in}(\mathbf{r}) = \frac{1}{2}\mathrm{Re}[\mathbf{E}_\mathrm{in}(\mathbf{r})\times\mathbf{H}^*_\mathrm{in}(\mathbf{r})] \\ \mathbf{S}_\mathrm{sca}(\mathbf{r}) = \frac{1}{2}\mathrm{Re}[\mathbf{E}_\mathrm{sca}(\mathbf{r})\times\mathbf{H}^*_\mathrm{sca}(\mathbf{r})] \\ \mathbf{S}_\mathrm{ext}(\mathbf{r}) = \frac{1}{2}\mathrm{Re}[\mathbf{E}_\mathrm{in}(\mathbf{r})\times\mathbf{H}^*_\mathrm{sca}(\mathbf{r})] + \frac{1}{2}\mathrm{Re}[\mathbf{E}_\mathrm{sca}(\mathbf{r})\times\mathbf{H}^*_\mathrm{in}(\mathbf{r})] \end{cases} \tag{2.76}$$

The net energy flow can be divided into three contributions: the incident wave, the scattered wave, and the energy originating from the interference between the incident and the scattered wave. We consider that a particle is at the origin of the Cartesian coordinate, and the particle is inside a closed surface Σ with a radius of r (Figure 2.12b). The radius is $kr >> 1$, and the surrounding of the particle is a lossless medium. The surface integration of the energy flow over Σ gives the net energy W, defined as the energy difference between outgoing and incoming waves on Σ [88]. For the total energy W_tot, if $\mathbf{S}_\mathrm{tot}$´s outgoing energy is smaller than $\mathbf{S}_\mathrm{tot}$´s incoming energy, this means that the particle absorbs the incident wave. In this case, W_tot can be considered as the absorbed energy $W_\mathrm{tot} = W_\mathrm{abs}$. The incident wave´s energy W_in becomes zero since the incoming and outgoing energy of $\mathbf{S}_\mathrm{in}$ on Σ are equal. The scattered wave´s energy W_sca is given by only the outgoing energy of $\mathbf{S}_\mathrm{sca}$ because the scattered wave is emitted from the particle. Based on these considerations, the extinction W_ext is found from $W_\mathrm{tot} = W_\mathrm{abs} = -W_\mathrm{sca} + W_\mathrm{ext}$. Thus, the extinction is a sum of the absorption and scattering of the particle. We know that the scattered wave of the particle is given by its

electric dipole moment. Therefore, by using Equations 2.70 and 2.71, we can calculate W_{ext} and W_{sca}, and we can get extinction and scattering cross-sections

$$C_{\text{ext}} = \frac{W_{\text{ext}}}{I_{\text{in}}} = -\frac{1}{I_{\text{in}}}\int_{\Sigma}\mathbf{S}_{\text{ext}}(\mathbf{r})\cdot\mathbf{n}dS = \frac{k}{\varepsilon_0\varepsilon_{\text{m}}|\mathbf{E}_{\text{in}}|^2}\text{Im}[\mathbf{p}\cdot\mathbf{E}_{\text{in}}^{*}(\mathbf{r})] = k\text{Im}[\alpha] \quad 2.77$$

$$C_{\text{sca}} = \frac{W_{\text{sca}}}{I_{\text{in}}} = \frac{1}{I_{\text{in}}}\int_{\Sigma}\mathbf{S}_{\text{sca}}(\mathbf{r})\cdot\mathbf{n}dS = \frac{k^4}{6\pi\varepsilon_0^2\varepsilon_{\text{m}}^2|\mathbf{E}_{\text{in}}|^2}|\mathbf{p}|^2 = \frac{k^4}{6\pi}|\alpha|^2 \quad 2.78$$

where $I_{in} = |\mathbf{E}_{in}|/2Z_0$ is the incident wave´s energy, and $\mathbf{n}$ is the normal unit vector of the surface Σ. $\mathbf{p} = \varepsilon_0\varepsilon_m\alpha\mathbf{E}_{in}$ is used to derive Equations 2.77 and 2.78. The absorption cross-section is given as $C_{abs} = C_{ext} - C_{sca}$.

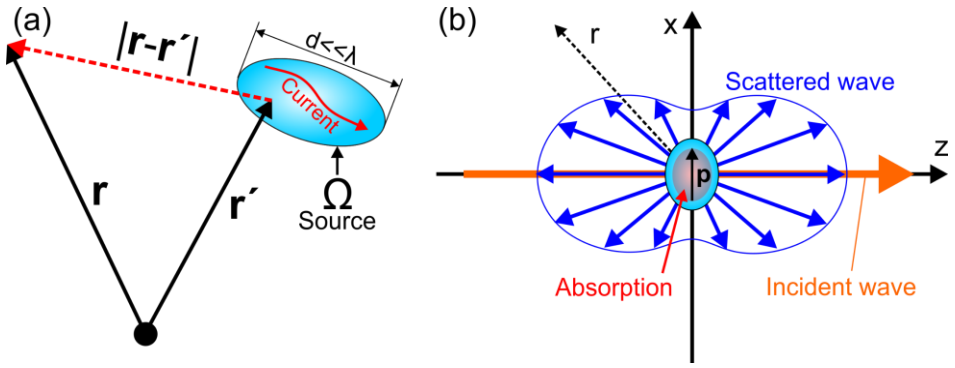

Figure 2.12. Schematic illustrations of (a) Equation 2.70 and (b) scattering and absorption of a small particle.

Using the polarizability of a metallic spherical particle (Equation 2.65), the extinction, scattering, and absorption cross-sections are given as

$$C_{\text{ext}} = (\gamma_{\text{int}}\omega^2 + \tau_{\text{rad}}\omega^4)\frac{\alpha_0/c}{(\omega_{\text{LSP}}^2 - \omega^2)^2 + (\gamma_{\text{int}} + \tau_{\text{rad}}\omega^2)^2\omega^2} \quad 2.79$$

$$C_{\text{sca}} = \tau_{\text{rad}}\omega^4\frac{\alpha_0/c}{(\omega_{\text{LSP}}^2 - \omega^2)^2 + (\gamma_{\text{int}} + \tau_{\text{rad}}\omega^2)^2\omega^2} \quad 2.80$$

$$C_{\text{abs}} = \gamma_{\text{int}}\omega^2\frac{\alpha_0/c}{(\omega_{\text{LSP}}^2 - \omega^2)^2 + (\gamma_{\text{int}} + \tau_{\text{rad}}\omega^2)^2\omega^2} \quad 2.81$$

Even though different shapes of particles are examined, their polarizability can be approximated by the Lorentz model; therefore, Equations 2.79-2.81 can be applied to describe the optical properties of a particle with an arbitrary shape. One might notice that the extinction becomes equal to the absorption if the size-independent polarizability ($\tau_{rad} = 0$) is used. This can be valid when the particle is tiny. Using Equations 2.80 and 2.81, the condition to maximize the particle´s absorption can be found. At the resonance condition $\omega = \omega_{LSP}$, the scattering and absorption cross-sections are given as

$$C_{\text{sca}} = \frac{\alpha_0}{c}\frac{{\tau_{\text{rad}}\omega_{\text{LSP}}}^2}{(\gamma_{\text{int}} + \tau_{\text{rad}}\omega_{\text{LSP}}^2)^2}, \qquad C_{\text{abs}} = \frac{\alpha_0}{c}\frac{\gamma_{\text{int}}}{(\gamma_{\text{int}} + \tau_{\text{rad}}\omega_{\text{LSP}}^2)^2} \quad 2.82$$

By dividing the numerator and denominator by the square of the radiative damping $(\tau_{rad}{\omega_{LSP}}^2)^2$, Equation 2.82 can be simplified as

$$C_{\text{sca}} = A\frac{1}{(1+\sigma)^2}, \qquad C_{\text{abs}} = A\frac{\sigma}{(1+\sigma)^2}, \qquad A = \frac{\alpha_0}{c\tau_{\text{rad}}\omega_{\text{LSP}}^2} \quad 2.83$$

where $\sigma = \gamma_{int}/(\tau_{rad}\omega_{LSP}^2)$ is the ratio of the intrinsic to radiative damping. Figure 2.13 shows Equation 2.83 as a function of σ. In this plot, it is considered that γ_{int} is nearly constant, and the radiative damping increases with an increase in the particle size. The scattering keeps decreasing with increasing σ. Meanwhile, the absorption is maximized at $\sigma = 1$. At this point, C_{abs} is equal to C_{sca}. The condition of $C_{sca} = C_{abs}$ ($\sigma = 1$) is called critical coupling [89-91]. From the critical coupling condition, it is understood that there is an optimum particle size to maximize C_{abs} since the radiative damping is a function of the volume of the particle (Equation 2.64). When $\sigma > 1$, C_{abs} becomes larger than C_{sca} because $C_{abs} = \sigma C_{sca}$. The scattering cross-section is maximized when $\sigma = 0$, meaning that the radiative damping dominates the total damping of the particle. Under this condition, the scattering cross-section becomes identical to the extinction cross-section, and the extinction cross-section is also maximized. Comparing C_{abs} to C_{sca}, it is found that the maximum absorption is equal to 1/4 of the maximum scattering. From Equation 2.83, the scattering and absorption cross-sections are also proportional to the following factor

$$A = \left(\frac{V\omega_p^2}{c}\right)\left(\frac{6\pi c^3}{V\omega_p^2}\frac{1}{{\omega_{LSP}}^2}\right) = 6\pi\left(\frac{c}{\omega_{LSP}}\right)^2 = \frac{3}{2\pi}{\lambda_{LSP}}^2 \qquad 2.84$$

Equation 2.64 was used to derive Equation 2.84. Using this factor, we understand that the maximum scattering and absorption cross-sections can be $C_{sca(max)} = 3\lambda_{LSP}^2/(2\pi)$ and $C_{abs(max)} = C_{sca(max)}/4 = 3\lambda_{LSP}^2/(8\pi)$, respectively [89-91]. Those are the ultimate maximum values for the scattering and absorption cross-sections of a particle with electric dipole resonance.

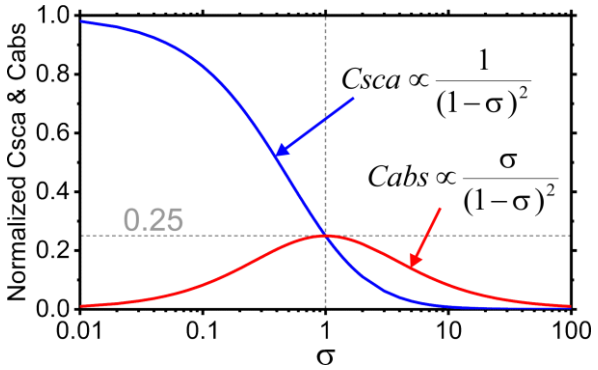

Figure 2.13. Plot of Equation 2.83 as a function of σ. C_{sca} and C_{abs} are normalized by A.

2.2.3.3. Mechanistic description of localized surface plasmons

In the previous sections, the optical responses of a metallic particle under the quasi-static limit have been discussed. However, the underlying physics of its LSP may not be understood straightforwardly. To provide an intuitive picture of the LSP, we consider a mechanical system. It was shown that the polarizability of the metallic particle resembles the Lorentz model. This indicates that the LSP can be explained by designing a harmonic oscillator (HO) model (Figure 2.14a). The HO model comprises an object with a mass of m. The object is connected to a spring with a spring constant of k. The damping rate of the HO model is γ. In addition, it is considered that the object feels a recoil force proportional to a rate of τ and jerk (jerk is a rate of acceleration). This recoil force corresponds to the radiation reaction force acting on an oscillating charge (radiative damping). The external force working on the object is time-harmonic, meaning $f(t) = fe^{-i\omega t}$. Therefore, the displacement of the object from its equilibrium position is also time-harmonic, giving $x(t) = xe^{-i\omega t}$. The equation of motion of the HO model can be expressed as [92]

$$m\frac{d^2x(t)}{dt^2} + m\gamma\frac{dx(t)}{dt} + kx(t) = f(t) + m\tau\frac{d^3x(t)}{dt^3} \qquad 2.85$$

By solving Equation 2.85 and normalizing by m, we get

$$x(t) = \frac{F(t)}{\omega_{\text{res}}^2 - \omega^2 - i(\gamma + \tau\omega^2)\omega} \tag{2.86}$$

where $\omega_{\text{res}} = (k/m)^{1/2}$ is the resonance frequency, and $F(\text{t}) = Fe^{-i\omega t} = (f/m)e^{-i\omega t}$ is the normalized external force. For example, if the object with a volume V has a charge of $Q = VNq$, where N is the number of electrons per unit volume, and q is the charge of electron, and if the object feels an external electric field of $E(t) = Ee^{-i\omega t}$, the external force per mass can be given by the Coulomb force per mass $F(\text{t}) = (Q/m)E(t)$. In this system, the mass of the object may be approximiatly expressed as $m = VNm_{\text{e}}$, where m_{e} is the mass of electron. Based on this, Equation 2.86 is rewritten as

$$x(t) = \frac{Q/m}{\omega_{\text{res}}^2 - \omega^2 - i(\gamma + \tau\omega^2)\omega} E(t) = \varepsilon_0 \frac{\omega_{\text{p}}^2}{\omega_{\text{res}}^2 - \omega^2 - i(\gamma + \tau\omega^2)\omega} \frac{E(t)}{Nq} \tag{2.87}$$

where $\omega_{\text{p}} = (Nq^2/\varepsilon_0 m_{\text{e}})^{1/2}$ is the plasma frequency. By multiplying Equation 2.87 by Q, we get $Qx(t) = \varepsilon_0 \alpha E(t)$, coinciding with the electric dipole moment given by the size-dependent polarizability (Equation 2.65). Therefore, it has been proved that Equation 2.87 is an appropriate mechanical model to describe LSPs. In the HO model, the optical extinction described by Equation 2.77 can be considered as the work done by the incident field. The time-average power per mass is given as

$$P_{\text{ext}} = \left\langle \text{Re}\left[F^*(t) \times \frac{\text{d}x(t)}{\text{d}t} \right] \right\rangle = (\gamma\omega^2 + \tau\omega^4) \frac{F^2/2}{(\omega_0^2 - \omega^2)^2 + (\gamma\omega + \tau\omega^3)^2} \tag{2.88}$$

P_{ext} is in a similar form to the extinction cross-section C_{ext} shown in Equation 2.79. By comparing P_{ext} with C_{ext}, the scattering P_{sca} and absorption P_{abs} of the HO model are found in the following forms

$$P_{\text{sca}} = \tau\omega^4 \frac{F^2/2}{(\omega_0^2 - \omega^2)^2 + (\gamma\omega + \tau\omega^3)^2} \tag{2.89}$$

$$P_{\text{abs}} = \gamma\omega^2 \frac{F^2/2}{(\omega_0^2 - \omega^2)^2 + (\gamma\omega + \tau\omega^3)^2} \tag{2.90}$$

Kats et al. examined the validity of the HO model by comparing it to a numerical simulation based on the finite-difference time-domain (FDTD) method [92]. They used an Au antenna on a Si substrate (Figure 2.14b) and calculated scattering and absorption cross-sections of the antenna. They demonstrated that the HO model fits well with the FDTD simulation. They also examined the near-field of the antenna at a point shown as a red mark in Figure 2.14b. In the HO model, the near-field intensity can be described by $|\mathbf{E}|^2 \propto |x(t)|^2$ since the near-field of an LSP is proportional to the amplitude of an electric dipole moment (Equation 2.72). Kats´s analysis indicated that 60 % of the conduction electrons of the Au antenna couple to the external wave and contribute to the LSP resonance. Based on the results from Kats et al., it is proved that the HO model can describe the LSP resonance quantitatively.

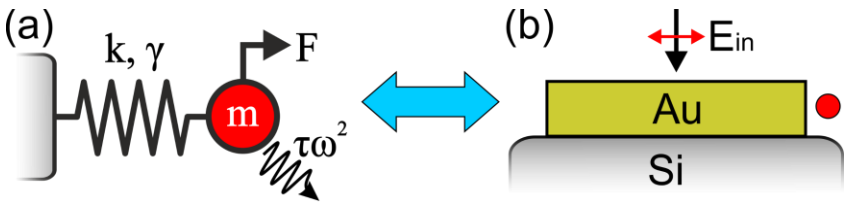

Figure 2.14. (a) The HO model. (b) Schematic illustration of the Au antenna from Ref. [92]. Ref. [92] proved that the optical properties of the Au antenna can be described by using the HO model.

2.2.4. Optical properties of particles beyond the quasi-static limit

We have focused on an optical resonance of a particle under the quasi-static limit. In this case, it is required that the particle´s real part of permittivity must be a negative value to support an LSP. However, when the particle size is beyond the quasi-static limit, this constraint is removed, and dielectric particles can also possess optical resonances. In general, the optical resonance of a metallic particle is dominated by an electric dipole moment. On the other hand, a dielectric particle can possess strong higher-order mode resonances by increasing its size.

We first understand the difference between metallic and dielectric particles by considering their stored electromagnetic energies [93]. In general, an optical resonance of a small particle can be approximated by an optical resonator, such as the Fabry-Perot resonator. We consider that the optical resonator with a characteristic size of a has relative permittivity ε. Therefore, its refractive index is $n = (\varepsilon)^{1/2}$. The surrounding of the optical resonator is a lossless dielectric. At its resonance condition, the electric energy $U_E = \varepsilon_0 \varepsilon E^2/2$ of the optical resonator is transformed into the magnetic energy $U_H = \mu_0 H^2/2$ with $\pi/2$ phase shift in time (Figure 2.15). This energy transformation occurs back and forth and satisfies energy conservation. However, the energy conservation will not be satisfied if the optical resonator becomes smaller than $\lambda/2n$, which is the optical diffraction limit. Under the quasi-static limit, the magnetic field is not time-variant, and the magnetic energy becomes negligibly small, resulting in $\nabla \times \mathbf{E} = 0$ and $U_E >> U_H$ (Equation 2.72). Therefore, a self-sustained oscillation cannot be supported in the optical resonator. This description indicates that dielectric particles must be larger than $\lambda/2n$ to support their optical resonance, and they cannot confine the electromagnetic wave beyond the diffraction limit. On the other hand, metallic particles possess large kinetic energy U_K originating from the motion of free electrons. Thus, the energy conservation can be satisfied by $U_E = U_H + U_K$ even under the quasi-static limit, enabling us to enhance near-field confinement beyond the diffraction limit.

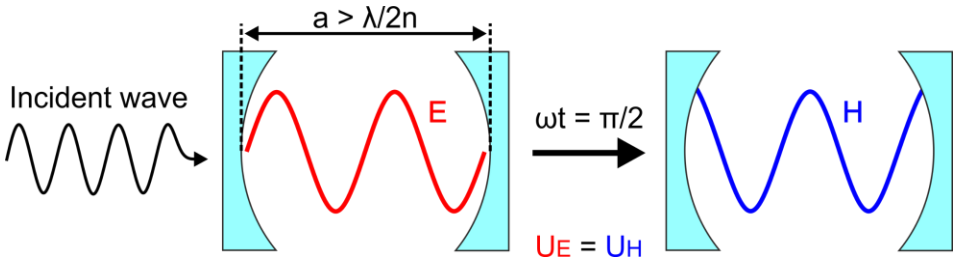

Figure 2.15. Schematic illustration of a dielectric optical resonator at its resonance condition.

2.2.4.1. Mie theory

In 1908, Gustav Mie formulated the exact solution of the wave equation expanded in the spherical coordinate [80]. This exact solution is named the Mie theory. The Mie theory is not confined to specific materials and particle sizes. One restriction of Mie theory is that it can only treat spherical particles (Note: for a particle with an arbitrary shape, the Cartesian multitude expansion can be used [94, 95]). Since the derivation procedure of Mie theory requires considerable mathematical operations [80], I only show important results from Mie theory. Figure 2.16a shows a spherical particle and an incident plane wave. The incident wave with x-polarization propagates along the z-direction. The electric field amplitude of the incident wave is E_0. The spherical particle with a radius R is homogeneous and has a refractive index of N_1. The surrounding of the particle is a lossless medium with a refractive index of N, and the wave number in the medium is $k = 2\pi N/\lambda$. The electric and magnetic fields of the particle´s scattered wave are divided into two components along the azimuth and zenith directions (see Figure 2.16b)

$$\begin{cases} E_{S\theta} = \dfrac{\cos\phi}{\rho}\sum_{n=1}^{\infty} i^n \dfrac{2n+1}{n(n+1)} E_0(ia_n\xi_n{}'(\rho)\tau_n - b_n\xi_n(\rho)\pi_n) \\ H_{S\theta} = \dfrac{N}{Z_0}\dfrac{\sin\phi}{\rho}\sum_{n=1}^{\infty} i^n \dfrac{2n+1}{n(n+1)} E_0(ib_n\xi_n{}'(\rho)\tau_n - a_n\xi_n(\rho)\pi_n) \\ E_{S\phi} = \dfrac{\sin\phi}{\rho}\sum_{n=1}^{\infty} i^n \dfrac{2n+1}{n(n+1)} E_0(b_n\xi_n(\rho)\tau_n - ia_n\xi_n{}'(\rho)\pi_n) \\ H_{S\phi} = \dfrac{N}{Z_0}\dfrac{\cos\phi}{\rho}\sum_{n=1}^{\infty} i^n \dfrac{2n+1}{n(n+1)} E_0(ib_n\xi_n{}'(\rho)\pi_n - a_n\xi_n(\rho)\tau_n) \end{cases} \quad 2.91$$

where $\rho = kr$, $m = N_1/N$, and x is the size parameter given by $x = kR$. ξ_n is the Riccati-Bessel function. $\pi_n = P_n^1(\cos\theta)/\sin\theta$, $\tau_n = dP_n^1(\cos\theta)/d\theta$ and $P_n^1(\cos\theta)$ is the associated Legendre function of the first kind. a_n and b_n are known as the Mie or scattering coefficients for electric and magnetic modes, respectively

$$a_n = \frac{m\psi_n(mx)\psi_n{}'(x) - \psi_n(x)\psi_n{}'(mx)}{m\psi_n(mx)\xi_n{}'(x) - \xi_n(x)\psi_n{}'(mx)} \quad 2.92$$

$$b_n = \frac{\psi_n(mx)\psi_n{}'(x) - m\psi_n(x)\psi_n{}'(mx)}{\psi_n(mx)\xi_n{}'(x) - m\xi_n(x)\psi_n{}'(mx)} \quad 2.93$$

where ψ_n is the Riccati-Bessel function. n gives the order of the resonance mode. For example, n = 1 and 2 give dipole and quadrupolar modes, respectively. By using Equation 2.91, the extinction and scattering cross-sections are obtained similarly to Equations 2.75-2.78

$$C_{\text{ext}} = \frac{2\pi}{k^2}\sum_{n=1}^{\infty}(2n+1)\text{Re}[a_n + b_n] \quad 2.94$$

$$C_{\text{sca}} = \frac{2\pi}{k^2}\sum_{n=1}^{\infty}(2n+1)(|a_n|^2 + |b_n|^2) \quad 2.95$$

The absorption cross-section is given as $C_{\text{abs}} = C_{\text{ext}} - C_{\text{sca}}$. I only showed results for homogeneous spherical particles, but it is possible to obtain solutions for concentric core-shell particles [80]. The expressions of the scattered fields and optical cross-sections for core-shell particles are the same, but the Mie coefficients differ.

In Figure 2.13, it was discussed that there are conditions to maximize the absorption and scattering of an electric dipole resonance (a_1), which are found as $C_{\text{abs},a1} = C_{\text{sca},a1}$ for absorption and $C_{\text{abs},a1} = 0$ for scattering. These conditions are the same for electric and magnetic higher-order modes. The universal values of the maximum absorption and scattering cross-sections are given as $C_{\text{abs},an} = C_{\text{abs},bn} = (2n + 1)\lambda_0^2/8\pi$ and $C_{\text{sca},an} = C_{\text{sca},bn} = (2n + 1)\lambda_0^2/2\pi$ for a single resonance mode with n-th order (subscripts an and bn indicate the resonance mode and order given in Equations 2.94 and 2.95) [96-99]. λ_0 is a resonance wavelength of a resonance mode.

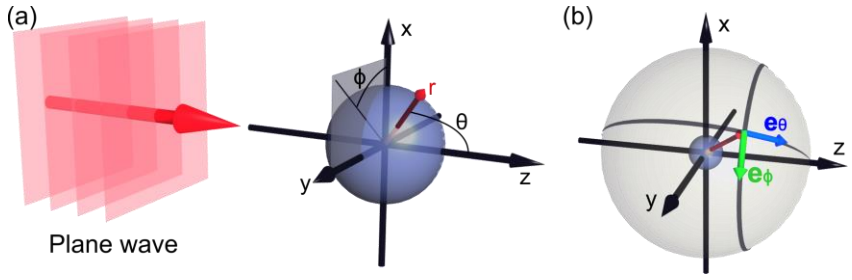

Figure 2.16. Image of Mie theory. (a) The orientation of the incident wave and the particle in the Cartesian coordinate. (b) The azimuth- and zenith-components of the electric and magnetic fields.

2.2.4.2. Magnetic dipole moment and electric/magnetic polarizabilities

The dipole resonances are the lowest energy resonances and are crucial for optical engineering. From the Mie theory, it is found that a particle can possess electric and magnetic dipole resonances. In Section 2.2.3.2, we have discussed the optical properties of an electric dipole moment by considering its vector potential. To gain an insight into a magnetic dipole resonance, we again consider the series expansion of Equation 2.68. For the electric dipole moment, we only use the first term of the series expansion. We can obtain magnetic dipole, electric quadrupole, and magnetic quadrupole moments from the second, third, and fourth terms. The second term of the vector potential expansion is given as [87]

$$\mathbf{A}(\mathbf{r}) = \mu_0 \frac{\mathrm{e}^{ikR}}{4\pi R}\left(\frac{1}{R} - ik\right)\int_{\Omega} \mathbf{J}(\mathbf{r}')(\mathbf{n}\cdot\mathbf{r}')d^3r' \qquad 2.96$$

After many mathematical operations, Equation 2.96 is given as a function of a magnetic dipole moment

$$\mathbf{A}(\mathbf{r}) = \frac{\mathrm{e}^{ikR}}{4\pi R}\left(ik - \frac{1}{R}\right)(\mathbf{n}\times\mathbf{m}), \qquad \mathbf{m} = \frac{1}{2}\int_{\Omega} \mathbf{r}\times\mathbf{J}d^3r = \chi\mathbf{H}_{\mathrm{in}} \qquad 2.97$$

where $\mathbf{m}$ is the magnetic dipole moment, and χ is the magnetic polarizability. In a similar manner to the electric polarizability, the magnetic polarizability can also be approximated by using the Lorentz model [100, 101]. The magnetic dipole moment is induced when there is a loop of current or electric field displacement, which can be understood from the Biot–Savart law. In metallic particles, such a current loop can be induced by eddy currents. However, the magnetic dipole resonance of metallic particles is much weaker than their electric dipole resonance originating from a plasmon resonance [102-104]. Meanwhile, dielectric particles can support a strong magnetic dipole resonance by anti-parallel electric displacement currents (Figure 2.17a). Generally, this magnetic dipole resonance is observed at around a wavelength satisfying $\lambda \approx 2RN_1$ [80, 105, 106]. The magnetic dipole is electrically induced but strongly couples with the magnetic field of the incident wave. Using Equation 2.97, the magnetic and electric fields created by the magnetic dipole moment are given as

$$\mathbf{H}_{\mathrm{m}}(\mathbf{r}) = \left\{k^2(\mathbf{n}\times\mathbf{m})\times\mathbf{n} + \left(\frac{1}{R^2} - \frac{ik}{R}\right)[3\mathbf{n}(\mathbf{n}\cdot\mathbf{m}) - \mathbf{m}]\right\}\frac{\mathrm{e}^{ikR}}{4\pi R} = \mathbf{G}_{\mathrm{E}}(\mathbf{r}-\mathbf{r}')\cdot\mathbf{m} \qquad 2.98$$

$$\mathbf{E}_{\mathrm{m}}(\mathbf{r}) = -Z_0\left(k^2 + \frac{ik}{R}\right)(\mathbf{n}\times\mathbf{m})\frac{\mathrm{e}^{ikR}}{4\pi R} = -Z_0\mathbf{G}_{\mathrm{M}}(\mathbf{r}-\mathbf{r}')\cdot\mathbf{m} \qquad 2.99$$

Comparing Equations 2.70-2.71 and Equations 2.98-2.99, one might find that the fields of the magnetic dipole moment can be linked to those of the electric dipole moment by $\mathbf{p} \leftrightarrow \mathbf{m}$, $\mathbf{E}_{\mathrm{e}} \leftrightarrow \mathbf{H}_{\mathrm{m}}$, and $\mathbf{H}_{\mathrm{e}} \leftrightarrow -\mathbf{E}_{\mathrm{m}}$ (Figure 2.17b). In a similar manner to the electric dipole moment, the extinction and scattering cross-sections of the magnetic dipole moment can be obtained as

$$C_{\mathrm{ext}} = \frac{\mu_0 k}{\varepsilon_0\varepsilon_{\mathrm{m}}|\mathbf{E}_{\mathrm{in}}|^2}\mathrm{Im}[\mathbf{m}\cdot\mathbf{H}_{\mathrm{in}}^*(\mathbf{r})] = \frac{k}{\varepsilon_{\mathrm{m}}}\mathrm{Im}[\chi] \qquad 2.100$$

$$C_{\mathrm{sca}} = \frac{\mu_0 k^4}{6\pi\varepsilon_0\varepsilon_{\mathrm{m}}|\mathbf{E}_{\mathrm{in}}|^2}|\mathbf{m}|^2 = \frac{k^4}{6\pi\varepsilon_{\mathrm{m}}}|\chi|^2 \qquad 2.101$$

The scattering and absorption cross-sections of the magnetic dipole moment have the same properties as those of the electric dipole moment (Equations 2.77 and 2.78). The same can be applied to higher-order modes [96-99].

By comparing the optical cross-sections from the Mie theory to those from the vector potential expansion, we can express the electric and magnetic polarizabilities of spherical particles using the Mie coefficients. For the electric dipole moment, the Mie theory gives $C_{\mathrm{ext}} = 6\pi\mathrm{Re}[a_1]/k^2$. This must be equal to Equation 2.77; therefore, we get $6\pi\mathrm{Re}[a_1]/k^2 = k\mathrm{Im}[\alpha]$. The same thing is applied to the magnetic dipole moment. From this comparison, we find the electric and magnetic polarizabilities as [107]

$$\alpha = i\frac{6\pi}{k^3}a_1, \qquad \chi = i\frac{6\pi}{k^3}b_1 \tag{2.102}$$

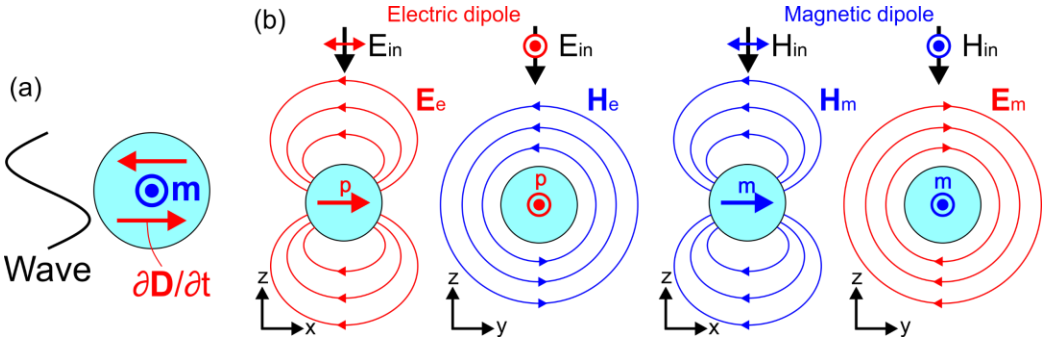

Figure 2.17. The optical properties of a dielectric particle. (a) Schematic illustration of a magnetic dipole resonance. (b) Schematic illustrations of electromagnetic fields created by electric and magnetic dipole moments.

2.2.4.3. Optical properties of dielectric particles

Using the Mie theory, we will understand the optical properties of a dielectric spherical particle. The particle has a radius of R and a refractive index of N_1. The surrounding is air. Figure 2.18 shows the scattering efficiencies $Q_{sca} = C_{sca}/\pi R^2$. The scattering spectra are plotted as a function of the wavelength normalized by the particle´s diameter. For $N_1 = 1.6$, the spectra for the modes up to $n = 2$ are shown (Figure 2.18a). The dielectric particle possesses not only an electric dipole resonance but also magnetic dipole and quadrupole resonances. The different order modes spectrally overlap, especially in a range of $\lambda/2R \leq 2$. In this range, dielectric particles possess strong forward scattering. By increasing N_1 to 3.5, the scattering bandwidths become narrow (Figure 2.18b). This is because the incident wave can be confined efficiently in a high refractive index medium, resulting in a small radiative damping of the dielectric particle. Similar to $N_1 = 1.6$, the different order modes overlap when $\lambda/2R \leq 2$.

As mentioned earlier, the absorption of any order modes is maximized when $C_{abs} = C_{sca}$ is satisfied [96-99]. For metallic particles, this condition can be satisfied just by tuning their particle size since its radiative damping is size-dependent. However, this cannot be applied to dielectric particles. This is because resonance peaks of the dielectric particles just blueshift or redshift by decreasing or increasing R, respectively. Therefore, the intrinsic damping must be controlled to maximize the absorption of the dielectric particles. However, controlling the intrinsic damping is not straightforward since it is linked to the material´s properties.

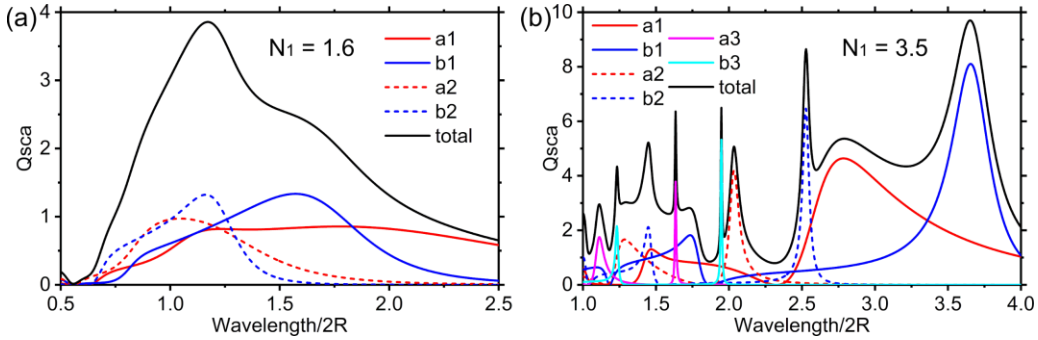

Figure 2.18. The scattering efficiency of a dielectric spherical particle with (a) $N_1 = 1.6$ and (b) $N_1 = 3.5$.

One attractive scattering property of dielectric particles is that the scattering direction can be controlled by combining different order modes. We first consider a combination of an electric and a magnetic dipole moment. In a dielectric particle, those dipole moments orthogonally oscillate (Figure 2.19a). In this situation, if the dipole moments have the same resonance frequency, their scattered waves interfere constructively in the forward direction and destructively in the backward direction. This means that the particle can have the scattered wave only in the forward direction. The complete cancellation of the scattered wave in the backward direction occurs when the scattered field amplitude of the electric and magnetic dipole moments are equal, meaning $a_1 = b_1$. This is called the Kerker effect [106, 108-110]. The Kerker effect-like scattering can also be obtained by combining other order modes. The middle of Figure 2.19b shows radial plots of scattering intensities of different modes [110]. The electric dipole (ED), magnetic dipole (MD), electric quadrupole (EQ), and magnetic quadrupole (MQ) have symmetric scattering patterns in the azimuth and zenith angles. Therefore, they scatter the incident wave in all directions. For the forward direction, the electric fields of all resonant modes point in the same direction (the red arrows in Figure 2.19b). However, depending on combinations of the modes, their electric fields point in the opposite direction for the backward direction (for example, ED and EQ). This indicates that the unidirectional forward scattering can be obtained by properly combining different modes (the top and bottom orange circles of Figure 2.19b). By combining all modes and achieving $a_1 = a_2 = b_1 = b_2$, the unidirectionality of the scattering is improved.

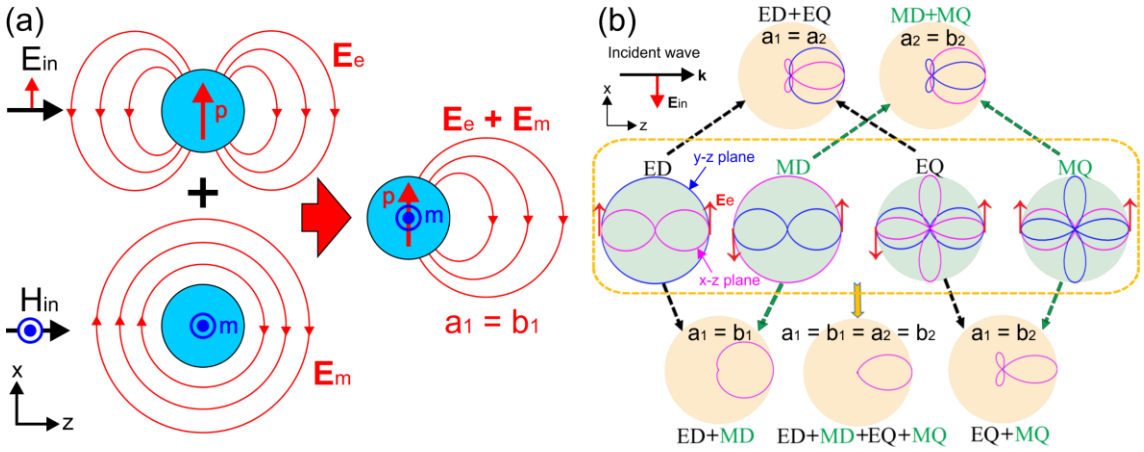

Figure 2.19. Scattering properties of dielectric particles. (a) Schematic illustration of the Kerker effect. (b) The radial plots of the scattering intensities of individual resonance modes (middle) and the resonance modes combined with other modes (top and bottom). The red arrows show the direction of the scattered wave´s electric fields. The magenta and blue lines are the scattering intensities in the x-z and y-z plains. Reprinted with permission from Ref. [110] © 2018 Optical Society of America under the terms of the OSA Open Access Publishing Agreement.

2.3. Materials for plasmonics and photonics

The optical properties of materials play an essential role in controlling the optical resonances of particles. This section will briefly discuss representative materials for plasmonics and photonics. Metals and dielectrics are considered plasmonic and photonic materials, respectively. However, with proper chemical composition controls, metal oxides can act as both plasmonic and nanophotonic materials in specific wavelength ranges. On the other hand, in the MIR range, some dielectrics can act like plasmonic materials with extremely low intrinsic damping. Based on those understanding of materials, various plasmonic and photonic structures have been designed for radiative cooling and other applications.

2.3.1. Metals and transparent conducting oxides

The characteristic of metals is that the real part of permittivity Re[ε] has negative values. A wavelength range where Re[ε] becomes negative can be found from a wavelength satisfying Re[ε] = 0. Such a wavelength is sometimes called the crossover wavelength. From the Drude model, the crossover wavelength may be given as $\lambda_C \propto 1/(\omega_p^2/\varepsilon_\infty - \gamma^2)^{1/2}$. A good metal is considered as it has low intrinsic damping. In this case, the crossover wavelength is dominated by the plasma frequency; therefore, $\lambda_C \approx \lambda_p \propto 1/\omega_p = (m\varepsilon_0/Ne^2)^{1/2}$. This shows that free electron concentration determines the crossover wavelength. Au and Ag have been recognized as representative plasmonic materials because of their low intrinsic damping. Rakic et al. investigated the optical properties of 11 metals, including Au and Ag [111]. Their result shows that Au and Ag have high free electron concentrations in the order of 10^{23} cm^{-3}, and their plasma frequencies are almost the same as $\omega_p \approx 1.37 \times 10^{16}$ rad/s ($\lambda_p \approx 0.137$ μm). The intrinsic damping rates are $\gamma \approx 8.05 \times 10^{13}$ rad/s for Au and $\gamma \approx 7.29 \times 10^{13}$ rad/s for Ag (Figure 2.20a). The drawback of these metals is that they have interband transitions in part of the visible range. For example, the interband transitions of Au are found at wavelengths shorter than about 400 nm. Ag´s interband transitions occur in a wavelength range shorter than about 350 nm. Thus, Au and Ag cannot act as plasmonic materials in part of the visible range even though their crossover wavelengths appear in the UV range.

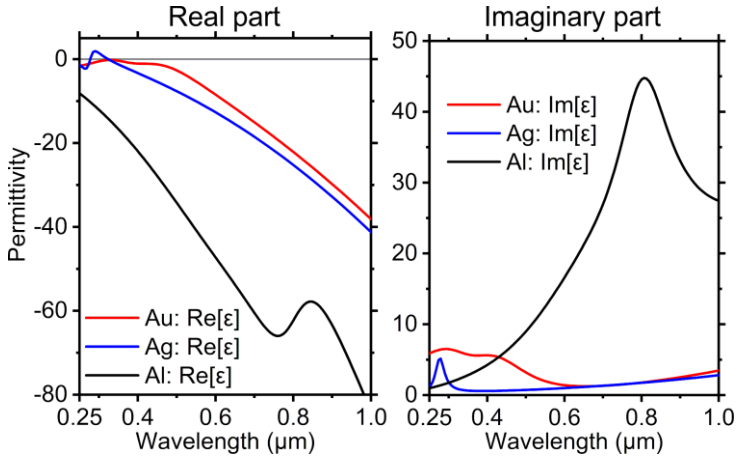

Figure 2.20. Plasmonic materials in the visible range. The real and imaginary parts of permittivities of Au, Ag, and Al. The data are taken from Ref. [111].

Despite the good optical properties of noble metals, another drawback is that noble metals are expensive, which is not suitable for producing scalable devices. To solve the problems regarding cost, Al has been used as an alternative plasmonic material. Al is abundant on the earth and has good optical properties. Rakic et al. also investigated Al, and they found that Al has $\omega_p \approx 2.28 \times 10^{16}$ rad/s ($\lambda_p \approx 0.083$

μm) and $\gamma \approx 7.14 \times 10^{13}$ rad/s. Therefore, Al can be operated as a plasmonic material in a broader wavelength range than Au and Ag (Figure 2.20). Al also has an interband transition at around 800 nm but is weaker than Au and Ag. Another cost-effective plasmonic material is Titanium nitride (TiN) [112-114]. It is known that the optical properties of TiN are very similar to Au. One attractive property of TiN is its high thermal stability. For example, the melting point of Au is about 1000 °C. Even though TiN has similar optical properties to Au, TiN´s melting point is about 3000 °C.

The metals mentioned above are known for plasmonic materials in the visible range. This is because their crossover wavelengths are in the visible range and the Fröhlich condition is usually satisfied at around crossover wavelengths. Theoretically, a plasmonic particle made of metal can excite an LSP at any wavelength by properly designing its shape. For example, based on Equation 2.56, an LSP of a core-shell particle can be induced in the IR range by making an extremely thin metal shell. However, thinning the shell increases the surface scattering of free electrons, leading to large optical damping and attenuating the LSP. Therefore, it is required to find alternative materials for plasmonics in the IR range.

Some metal oxides are known as semiconductors. Those are sometimes called transparent conducting oxides (TCOs) since they act like a dielectric in the visible range and behave like a metal in the IR range [115-117]. The conductivity of most TCOs is attributed to free electrons, meaning that TOCs are n-type semiconductors. TCOs have low free carrier concentrations in the order of 10^{18}-10^{22} cm^{-3}; therefore, their plasma frequencies stay in the IR range. Indium oxide (In_2O_3) and zinc oxide (ZnO) are representative TCOs that can be highly doped and chemically stable. Their free carriers originate from oxygen vacancies in their lattices, providing two electrons per oxygen vacancy. The free carrier concentrations can be even higher by making Sn-doped In_2O_3 (ITO) and Al-doped ZnO (AZO). The origin of free carriers in metals and the TCOs are different, but the optical properties of the TCOs can be well described by the Drude-Lorentz model (Figure 2.21a) [118, 119]. The plasma frequencies of the TCOs are roughly ten times higher than their intrinsic damping; therefore, the crossover wavelengths of the TCOs appear close to their plasma wavelength. In contrast to the metals, the optical properties of the TCOs are significantly influenced by synthetic processes and deposition methods, providing additional control in the crossover wavelength [120-122]. One of the easiest ways to control the crossover wavelength may be post-deposition annealing. For example, it has been reported that the crossover wavelength of ITO can be moved from the near-IR to mid-IR by heating an ITO film in an oxygen-rich environment [122]. In this process, oxygen vacancies in ITO are occupied, reducing the free carrier density. Figure 2.21b shows the extinction spectra of nanoparticles made of different TCOs [117]. Even though the shape of particles is not designed, they can induce LSPs in a broad wavelength range. Therefore, combining TCOs and structural design provides us with additional control in LSPs.

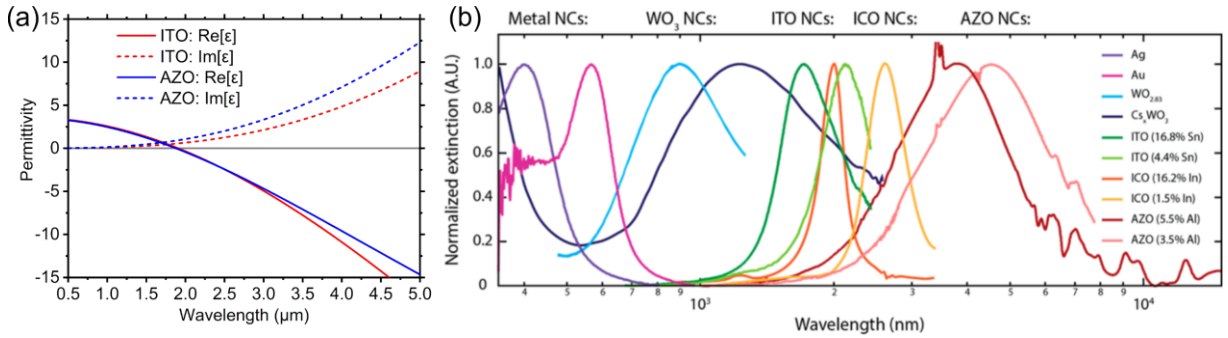

Figure 2.21. Plasmonic materials in the IR range. (a) The permittivity spectra of ITO and AZO given by the Drude model. For ITO, the fitting values are given by Ref. [118]. For AZO, the Drude model was fitted to an experimental value from Ref. [119]. (b) The extinction spectra of nanocrystals (NCs) made of different plasmonic materials. Reprinted with permission from Ref. [117] © 2014, American Chemical Society.

2.3.2. Dielectrics

In contrast to metals and TCOs, the optical properties of dielectrics are usually characterized using the refractive index. In the visible range, some polymers are transparent and have a nearly constant refractive index, such as Polystyrene (PS, $n \approx 1.6$), Poly(methyl methacrylate) (PMMA, $n \approx 1.5$), and Polydimethylsiloxane (PDMS, $n \approx 1.4$) [123] (Figure 2.22a). The refractive index of PS is relatively high among polymers [124]. SiO_2 is an abundant ceramic on the earth, and it has $n \approx 1.5$ [125], which is similar to the refractive indices of polymers. Other ceramics, such as TiO_2, SiC, and Si_3N_4 possesses a high refractive index of about 2.5. A higher refractive index can be accessible from Si and Ge in the IR range. The refractive indices of those semiconductors reach about 4. Their refractive indices are also high in the visible range, but intrinsic absorption is also strong; therefore, those semiconductors are considered IR dielectric materials. Extremely high refractive indices are obtained by other IR dielectric materials, such as PbTe ($n \approx 5.6$) [126]. To my knowledge, the highest refractive index may be obtained from Bi_2Te_3 ($n \approx 7$) [127]. The refractive indices of those IR dielectric materials are nearly constant over the near- and mid-IR ranges.

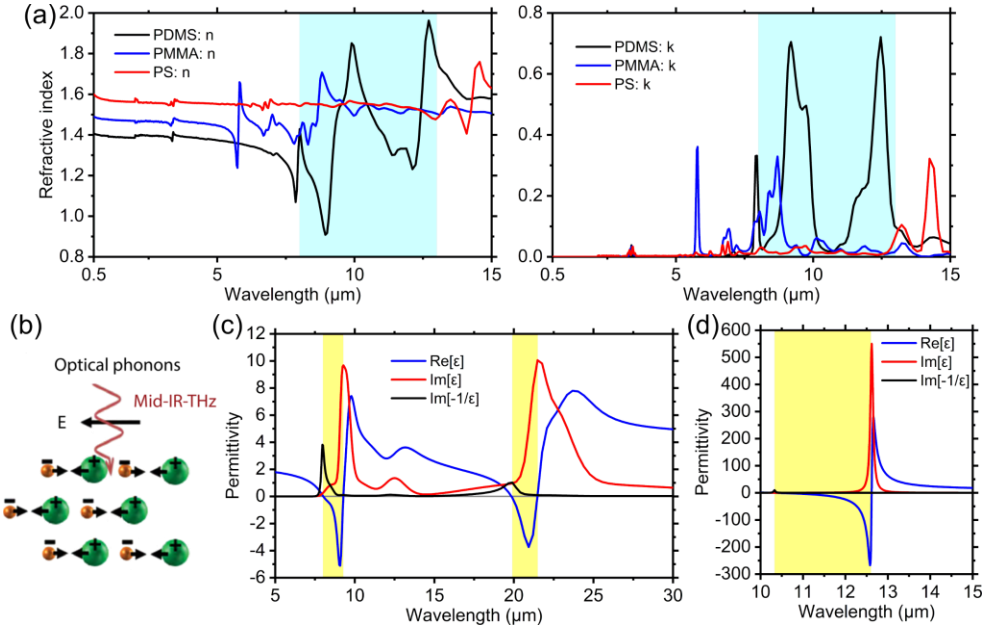

Figure 2.22. Photonic materials. (a) The refractive indices and extinction coefficients of PS, PMMA, and PDMS. The data were taken from Ref. [123, 128]. The blue-shaded areas indicate the primary ATW. (b) Schematic of optical phonons. Reprinted with permission from Ref. [129] Copyright CC BY-NC-ND 3.0. (c) The permittivity of SiO_2. The data are taken from Ref. [130]. (d) The permittivity of SiC. The data are taken from Ref. [131]. For (c) and (d), the yellow-shaded areas show the Reststrahlen bands.

In the mid-IR range, the polymers have high dispersions and strong intrinsic absorption by molecular vibrations [128] (Figure 2.22a). Some ceramics also have high dispersion and strong absorption. Those ceramics have two different types of optical phonon modes: the transverse optical (TO) and longitudinal optical (LO) modes, in which phonon oscillation is transverse and parallel to the wavevector of the incident wave, respectively [129, 132]. Figure 2.22b presents an image of the TO mode. The TO mode can be excited directly by the incident wave, resulting in strong absorption. This absorption can be found in the imaginary part of permittivity Im[ε]. However, the LO mode is invisible in Im[ε]. To find the LO mode, the energy loss function Im[$-1/\varepsilon$] is considered [133, 134]. Between those two modes, the real part of permittivity Re[ε] becomes negative, and the ceramics can act like a metal, resulting in strong reflection. This wavelength

range is called the Reststrahlen band [129, 132]. For example, SiO_2 has two Reststrahlen bands in 8 – 9.28 μm and 19.9 – 21.5 μm [130] (Figure 2.22c). SiC possesses a wide Reststrahlen band in 10.33 – 12.6 μm [131] (Figure 2.22d). Since the negative Re[ε] can satisfy the Fröhlich condition, ceramic particles can excite optical resonance resembling an LSP. This resonance is called surface phonon polaritons (SPhPs). SPhPs are excited at a wavelength close to the LO mode. SPhPs cannot confine electromagnetic fields like plasmon resonance since SPhPs do not contain any free electrons [93]. Instead, the ceramics have extremely low intrinsic damping on the order of $\gamma \approx 10^{12}$ rad/s, roughly 10^2 smaller than the noble metals. Therefore, the bandwidth of SPhPs is narrow.

2.4. Conventional metamaterial absorbers

The terms *plasmonics* and *nanophotonics* have stemmed from the fact that optical properties of materials can be controlled by designing nano- and micro-structures based on the knowledge introduced in Section 2.2. Engineered materials can possess unique and optimal optical properties for specific applications. Therefore, those engineered materials are usually called *metamaterials*. In this chapter, I will introduce the fundamental design principles of metamaterials for electromagnetic wave absorbers. In addition, I will point out the disadvantage of those absorbers for radiative cooling.

Electromagnetic wave absorbers can be categorized into two types. One is a perfect absorber, where an absorber has ≈ 100% absorptivity (perfect absorption) at a specific wavelength. Second is a broadband absorber, whose absorption has a high intensity over a wide wavelength range. For radiative cooling, an RC has to be perfect and broadband absorber simultaneously. In addition, precise control in absorption bandwidth is required since absorption should occur only in the primary ATW to maximize the temperature reduction.

2.4.1. Mechanism of perfect absorption

Firstly, we will overview the mechanism of perfect absorption. We imagine subwavelength particles are placed periodically on a two-dimensional lattice in the *x*- and *y*-directions (Figure 2.23a is the side view of the array). The particles are identical and only possess electric dipole resonances. The periodicity of the array is smaller than the wavelength; thus, there is no diffraction effect. The incident wave normally strikes on the array. In this case, the transmission and reflection of the array can be described based on the scattering properties of the electric dipole moment. As understood from the previous chapter, the scattered wave of the electric dipole moment is symmetric in the forward and backward directions. In the array, the particles act like Huygens sources and create a scattered plane wave of the array, which is also symmetric in the forward and backward directions. The scattered wave of the array in the backward direction corresponds to the reflected wave of the array. On the other hand, the transmitted wave of the array is a superposition of the incident wave and the scattered wave in the forward direction. Based on these considerations, if the reflection and transmission coefficients of the array are given as r_p and t_p, respectively, r_p is solely determined by the scattered wave, and t_p can be expressed as $1 + r_\mathrm{p}$, where 1 indicates the incident wave. The absorptivity of the array is given as [91, 135]

$$A = 1 - \left|r_\mathrm{p}\right|^2 - \left|t_\mathrm{p}\right|^2 = 1 - \left|r_\mathrm{p}\right|^2 - \left|1 + r_\mathrm{p}\right|^2 \qquad 2.103$$

Since the electric dipole moment is complex, the reflection coefficient may be given as $r_\mathrm{p} = r_\mathrm{p}' + ir_\mathrm{p}''$. Using the complex reflection coefficient, a condition to maximize the array´s absorption is found as $r_\mathrm{p} = -1/2$ and $t_\mathrm{p} = 1/2$. Under this condition, the array´s absorption can reach $A = 1/2$. This is the ultimate absorption limit of the array. Under this condition, the reflectance and transmittance become $|r_\mathrm{p}|^2 = |t_\mathrm{p}|^2 = 1/4$.

By considering the energy balance in a unit cell of the array, it is found that there is an optimum periodicity to achieve maximum absorption. If the array is the square lattice and the periodicity in the *x*- and *y*-directions is Λ, the power of the incident wave in the unit cell is $P_\mathrm{in} = \Lambda^2 I_0$, where $I_0 = |E_\mathrm{in}|^2/2Z_0$ is the power density of the incident wave. When the absorption of the array is maximized, half of the incident wave´s power must be absorbed by the array; therefore, the absorbed power in the unit cell is $P_\mathrm{abs} = P_\mathrm{in}/2 = \Lambda^2 I_0/2$. From this equation, we get an absorption cross-section of the particle in the unit cell: $C_\mathrm{abs} = P_\mathrm{abs}/I_0 = \Lambda^2/2$. For the maximum absorption of the array, the absorption of the particle must also be maximized; therefore, the critical coupling $C_\mathrm{abs} = C_\mathrm{sca}$ must be satisfied. The total power that the particle can extract from the incident wave is given as the extinction cross-section $C_\mathrm{ext} = 2C_\mathrm{abs} = \Lambda^2$. Thus, the optimum periodicity is found as $\Lambda = C_\mathrm{ext}^{1/2}$. For example, if lateral interactions between particles can be ignored [100], the absorption and scattering cross-sections of the particle may be found as $C_\mathrm{abs} = C_\mathrm{sca} = 3\lambda_0^2/8\pi$. The extinction becomes $C_\mathrm{ext} = 3\lambda_0^2/4\pi$, yielding the optimum periodicity as $\Lambda = (3/4\pi)^{1/2}\lambda_0$.

To achieve $A = 1$, we must include magnetic dipole moments in the array (Figure 2.23b). The array of magnetic dipole moments behaves similarly to the case of the array of electric dipole moments. When the electric and magnetic dipole moments coexist in the array, their scattered waves interfere destructively in the backward direction and constructively in the forward direction. Therefore, this electric-magnetic array´s reflection and transmission coefficients may be given as $r = r_p - r_m$ and $t = 1 + r_p + r_m$, respectively (r_m is the reflection coefficient of the array only with magnetic dipole moments). Therefore, the absorptivity is given as [91, 135]

$$A = 1 - \left|r_p - r_m\right|^2 - \left|1 + r_p + r_m\right|^2 \qquad 2.104$$

When $r_p = r_m = -1/2$ occurs, perfect absorption $A = 1$ can be achieved. This condition for the perfect absorption coincides with the Kerker condition for the forward scattering; therefore, the array has no reflection. In the forward direction, the scattered wave of the array has the same amplitude as the incident wave, but the scattered wave is π phase shifted from the incident field. Consequently, the incident and scattered waves are canceled out, resulting in no transmission. The perfect absorption found from Equation 2.104 may be understood by considering the Poynting theorem. In an electromagnetic wave, half of its energy is stored as electric energy, and the other half is stored as magnetic energy. An electric dipole moment can efficiently couple only to the incident wave´s electric field; therefore, the array composed of electric dipole moments can absorb only half of the incident wave´s energy. On the other hand, if an array contains electric and magnetic dipole moments, the array can fully couple with the incident wave, enabling us to obtain perfect absorption.

We again consider the absorption of the particle in the unit cell of the array to find an optimum periodicity. The array now has $A = 1$ so that the absorbed power in the unit cell is $P_{abs} = P_{in} = \Lambda^2 I_0$, which gives the absorption cross-section of the particle in the unit cell as $C_{abs} = \Lambda^2$. Under the Kerker condition, the amplitudes of the electric and magnetic dipole moments must be equal. Therefore, they have the same absorption cross-section of $C_{abs,p} = C_{abs,m} = \Lambda^2/2$, where the subscripts p and m indicate the electric and magnetic dipole moments, respectively. In contrast to the case of the array supporting only electric dipole moments, the electric-magnetic array does not possess a scattering cross-section under the resonance condition. Therefore, the total energy that the unit cell extracts from the incident field is solely determined by the absorption of the particle. When the particle has both electric and magnetic dipole moments, its maximum absorption is given as $C_{abs} = C_{abs,p} + C_{abs,m} = 2\times(3\lambda_0^2/8\pi)$, and we may find an optimum periodicity of the array from $\Lambda^2 = C_{abs} = 3\lambda_0^2/4\pi$.

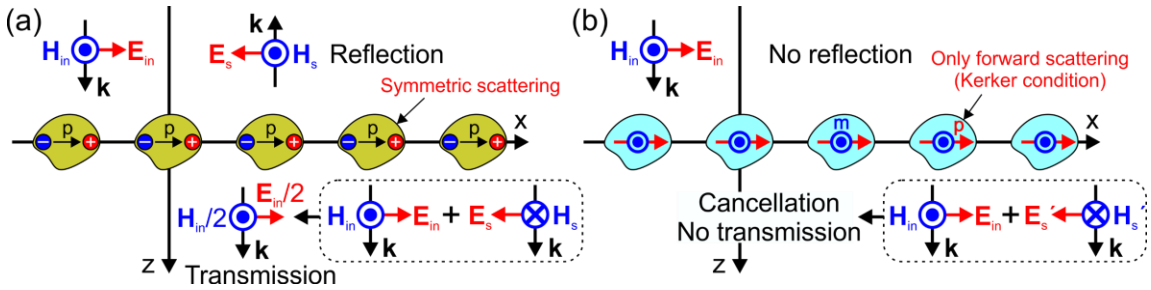

Figure 2.23. (a) Schematic of the periodic array supporting only electric dipole moments. (b) Schematic of the periodic array supporting both electric and magnetic dipole moments.

Based on the understanding made above, it is found that perfect absorption is attainable by designing particles supporting electric and magnetic dipole moments [101, 136, 137]. These particles must simultaneously satisfy the Kerker condition and the critical coupling condition. For example, Ag@n-Si core-shell particles can satisfy these conditions. It was theoretically demonstrated that an array composed of the

Ag@n-Si core-shell particles achieves perfect absorption in the visible range [136]. In addition, a SiO_2 microsphere can satisfy the generalized Kerker condition, and an array composed of the SiO_2 microspheres can possess perfect absorption in the MIR range [138]. However, it is still challenging to precisely control the absorption peak position and absorption bandwidth of such array systems. Therefore, a different approach has been widely used to obtain perfect absorption, which will be introduced in the following section.

2.4.2. Perfect absorbers

From the previous section, it is understood that a system must support electric and magnetic dipole moments for perfect absorption. A practical implementation of perfect absorption is designing a system that plasmonic particles are placed over a metal back-reflector with a lossless dielectric spacer (Figure 2.24a). The plasmonic particles are arranged periodically and possess an electric dipole moment. When the distance between the plasmonic array and the back-reflector is sufficiently small, an image electric dipole is created in the back-reflector, and a loop of displacement current is created. This current loop generates a strong magnetic dipole moment in the spacer, usually called a magnetic plasmon resonance (MPR) [139-142]. The MPR strongly confines the incident magnetic field in the spacer. The amplitude of the magnetic dipole moment can be controlled by tuning the thickness of the spacer: a thinner spacer makes a stronger magnetic dipole [143-147].

In such a metal-insulator-metal (MIM) structure, transmission is blocked by the back-reflector so that there are only reflection and absorption. Therefore, for perfect absorption, reflection must be eliminated. The reflection of the MIM structure is comprised of a wave reflected by the back-reflector and a scattered wave created by the MIM structure [147]. The magnetic dipole moments in the MIM structure point in an opposite direction to that of the electric-magnetic array introduced earlier. In this case, the Kerker effect of the MIM structure may be considered as that scattering occurs only in the backward direction. This means that the scattered wave can destructively interfere with the wave reflected by the back-reflector. Therefore, it is possible to eliminate the reflection. In a similar manner to the electric-magnetic array, the MIM structure can possess perfect absorption when the critical coupling condition of the plasmonic particle is satisfied. Electromagnetic wave absorbers designed based on such absorption mechanisms are called metamaterial absorbers (MAs) [36, 37].

Perfect absorption of a MA can be interpreted by considering its effective medium [148]. Since electric and magnetic dipoles coexist, optical responses of the MA are described by an effective permittivity $\varepsilon_{\text{eff}}(\omega)$ and effective permeability $\mu_{\text{eff}}(\omega)$ (Figure 2.24a). The impedance of the effective medium is given by $Z_{\text{eff}} = (\mu_{\text{eff}}(\omega)/\varepsilon_{\text{eff}}(\omega))^{1/2}$. To eliminate reflection of the effective medium, the impedance matching $\varepsilon_{\text{eff}}(\omega) = \mu_{\text{eff}}(\omega)$ has to be fulfilled. The impedance Z_{eff} can be retrieved by using the temporal coupled mode theory (TCMT) [147]. The MA has no transmission because of its back-reflector so the MA can be approximated as a resonator with a single input and output. The TCMT for this resonator can be written as (Figure 2.24b) [149]

$$\frac{\mathrm{d}a}{\mathrm{d}t} = i\omega_0 a - (\gamma_{\text{int}} + \gamma_{\text{rad}})a + \kappa s_+, \qquad s_- = -s_+ + \kappa a, \qquad \kappa = \sqrt{2\gamma_{\text{rad}}} \tag{2.105}$$

where a is the mode amplitude of the resonator, ω_0 is the resonance angular frequency of the electric and magnetic dipole, γ_{int} and γ_{rad} are intrinsic and radiative damping, s_+ and s_- are the powers of incoming and outgoing waves, and κ is coupling rate to the incident wave. The reflection coefficient of this system is given as

$$r = \frac{s_-}{s_+} = -1 + \frac{\kappa^2}{i(\omega - \omega_0) + (\gamma_{\text{int}} + \gamma_{\text{rad}})} = \frac{Z_{\text{eff}} - 1}{Z_{\text{eff}} + 1} \tag{2.106}$$

Using Equation 2.106, the impedance of the MA is expressed as

$$Z_{\text{eff}} = \frac{1+r}{1-r} = \frac{\gamma_{\text{rad}}}{i(\omega-\omega_0)+\gamma_{\text{int}}} \qquad 2.107$$

At the resonance condition $\omega = \omega_0$, the impedance matching $Z_{\text{eff}} = 1$ is satisfied by $\gamma_{\text{int}} = \gamma_{\text{rad}}$, which corresponds to the critical coupling condition of a single particle. The absorptivity of the MA under the resonance condition may be described as

$$A = 1 - |r|^2 = 1 - \left|\frac{\gamma_{\text{int}} - \gamma_{\text{rad}}}{\gamma_{\text{int}} + \gamma_{\text{rad}}}\right|^2 = 1 - \left|\frac{\sigma - 1}{\sigma + 1}\right|^2, \qquad \sigma = \frac{\gamma_{\text{int}}}{\gamma_{\text{rad}}} \qquad 2.108$$

Figure 2.24c presents Equation 2.108 as a function of $\gamma_{\text{int}}/\gamma_{\text{rad}}$. Surprisingly, it shows that high absorptivity can be obtained even though the critical coupling condition is not fully satisfied. For absorptivity over 80 %, $\gamma_{\text{int}}/\gamma_{\text{rad}}$ must be in a range of $0.38 < \gamma_{\text{int}}/\gamma_{\text{rad}} < 2.6$, which promises a high fabrication tolerance of MAs to achieve strong absorption. From Equation 2.108 and findings from the electric-magnetic array, we can find the following three criteria to achieve perfect absorption:

A) The electric and magnetic dipole moments must have the same resonance frequency.
B) The thickness of the spacer must be optimized to satisfy the Kerker condition.
C) The array of plasmonic particles must be designed to satisfy the critical coupling condition.

The first criterion is automatically fulfilled in the MA since the displacement current loop is associated with the oscillation of the electric dipoles. The second and third criteria have to be simultaneously achieved because both determine the radiative damping of the MA.

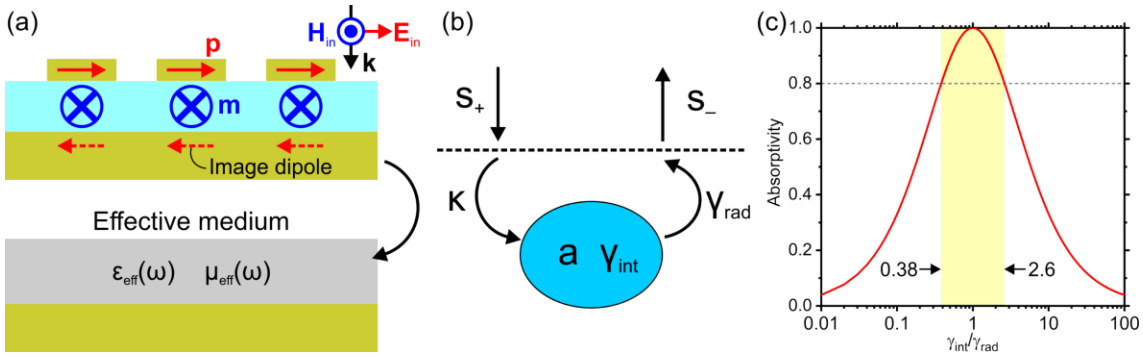

Figure 2.24. Perfect absorption by a MA. (a) Schematic illustrations of a MA under its resonance condition and its effective medium. (b) Schematic illustration of the TCMT for a single input resonator. (c) The plot of Equation 2.108 as a function of $\gamma_{\text{int}}/\gamma_{\text{rad}}$.

In the following, several examples of MAs will be introduced. Figure 2.25a shows a MA proposed by Landy et at. in 2008 [38]. A unit cell of the MA is composed of a Cu split ring resonator (SRR) stacked above a Cu strip. The width of the SRR is 4 mm. Figure 2.25a also shows its absorption spectra. The solid red line is a spectrum calculated using the FDTD simulation. The blue line is the experimental spectrum, and the dashed gray line is a Gaussian fitting to the experimental spectrum. The numerical result is in good agreement with the experimental one. The MA has a strong absorption at around 26 mm in wavelength. The drawback of the MA is that multiple layers of the structure shown in Figure 2.25a are required to achieve perfect absorption, which complicates fabrication procedures.

Figure 2.25b shows a MA composed of a crossbar resonator (CBR) [150]. The length and width of the CBR are 1.7 μm and 0.4 μm, respectively. The CBRs are placed with a periodicity of 2 μm, and Au is used for the CBR and a back-reflector. The thickness of a spacer is 0.185 μm, which is thin enough to induce

image electric dipoles in the back-reflector. The absorption obtained using the CST Microwave Studio agrees with the experimental data. In contrast to the MA made of the SRR, the MA based on CBR does not require multiple layers to achieve strong absorption.

The common disadvantages of those MAs are that they require a top-down process, such as electron beam lithography, to make a top plasmonic array. To overcome this limitation, Walter et al. incorporated colloidal lithography in their fabrication processes [151]. Dao et al. adapted Walter´s fabrication technique and produced a MA over an area with several square centimeters [152] (Figure 2.25c). Dao´s fabrication procedure was the following: First, Al-Al_2O_3-Al film was prepared. Next, a closed-pack polystyrene colloidal monolayer was produced on the film. Then, the reactive ion etching (RIE) technique was used to reduce the size of the colloidal particles. For the final step, the PS-masked Al layer was milled to form Al nano-disks. The diameter of the Al nano-disk can be controlled, and the authors achieved diameters in a range of 0.7 – 3.3 μm. The Al-based MA possesses nearly perfect absorption in the mid-IR range. With an increase in the diameter of the Al nano-disk, the absorption peak (reflection dip) moves from 2.85 μm to 8.65 μm in wavelength. Dao et al. also conducted a numerical investigation using the RCWA technique. Their numerical results reproduced the experimental ones.

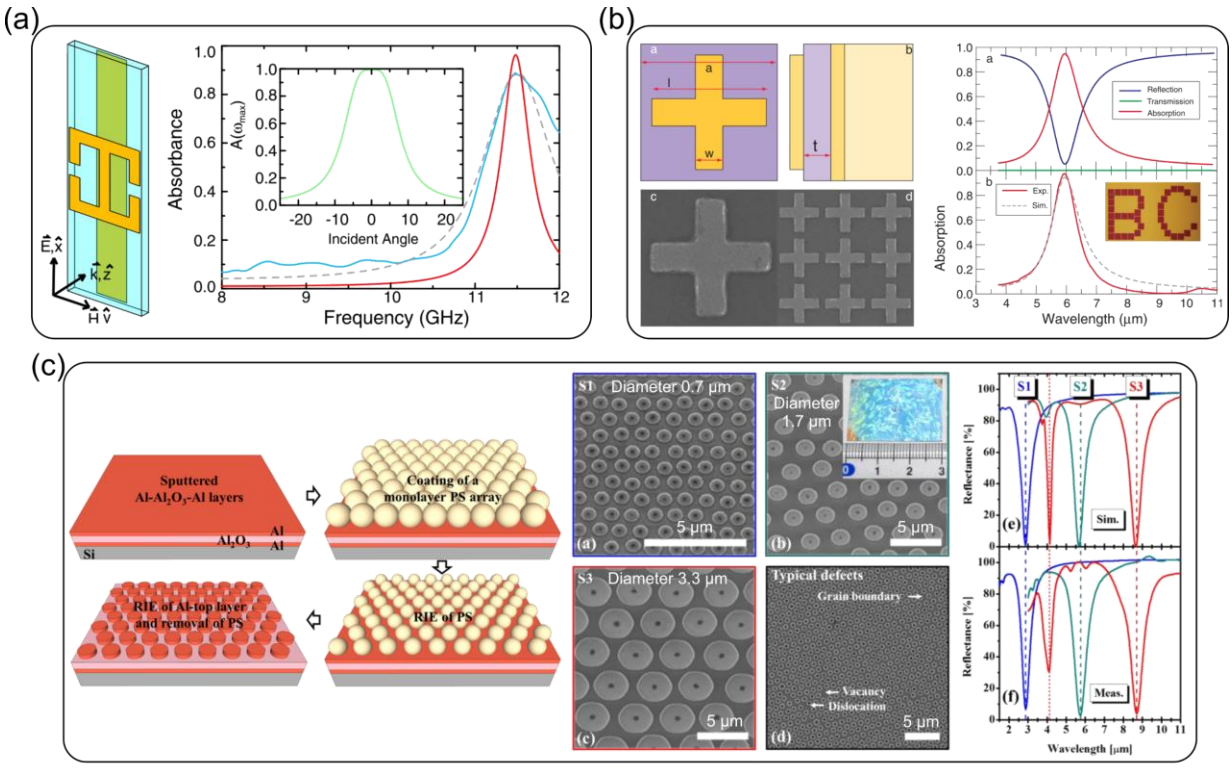

Figure 2.25. Examples of MAs. (a) The SRR-based MA. Reprinted with permission from Ref. [38] ©2008 American Physical Society. (b) The CRR-based MA. Reprinted with permission from Ref. [150] ©2010 American Physical Society. (c) The Al-based MA. Reprinted with permission from Ref. [152] © 2015, American Chemical Society.

So far, we have considered periodic arrays for MAs. Since periodic arrays can provide the same spacing for all particles, the particles can absorb the same amount of incoming light on the entire area of the MAs, which is essential for perfect absorption. However, this periodicity may degrade the absorption of the MAs at a high incident angle because of diffraction effects. We consider a MA with a one-dimensional periodic array composed of metal strips to describe the diffraction effects. The periodicity provides an extra wavevector on the surface. If an incident wave with TM polarization strikes on the MA at an incident angle

of θ, a PSP is excited if $\beta = k\sin\theta + mg$ is satisfied. β is the propagation constant of a metal-dielectric interface, m is diffraction mode, and $g = 2\pi/\Lambda$ is a reciprocal lattice vector [76-79]. In general, the periodicities of MAs are much smaller than the incident wavelength; therefore, PSPs are not excited for a small θ. However, for a diffraction mode of $m = -1$, PSPs can redshift with an increase in θ, resulting in simultaneous excitation of PSPs and LSPs of the array. They interact with each other destructively, degrading the absorption properties of MAs at a high θ [79]. If the incident wave has TE polarization, a different scenario of diffraction effects may be considered. PSPs are not excited by TE polarization. Instead, diffraction modes occur by collective interference of scattered waves of particles of the array. This diffraction phenomenon is known as surface lattice resonances (SLRs) [153]. SLRs have a variety of applications, but it is an undesirable effect on MAs. An incident angle dependency of SLRs is found from the Rayleigh anomaly $\omega/c = k\sin\theta + mg$.

For radiative cooling, absorptivity must be insensitive in a wide incident angle range [154]. Therefore, those diffraction effects must be avoided. Making disordered arrays is one of the most promising approaches to dealing with diffraction effects. Tittl et al. fabricated randomly distributed Au nano-disks on top of an MgF_2-Au layer by using colloidal lithography [155] (Figure 2.26a). The diameter of the Au nano-disk was 160 nm. Tittl et al. measured the reflectance of this MA and confirmed that a reflection dip (absorption peak) does not shift with an increase in the incident angle. They attributed this incident angle independency to the MA´s impedance nearly perfectly matched to that of free space.

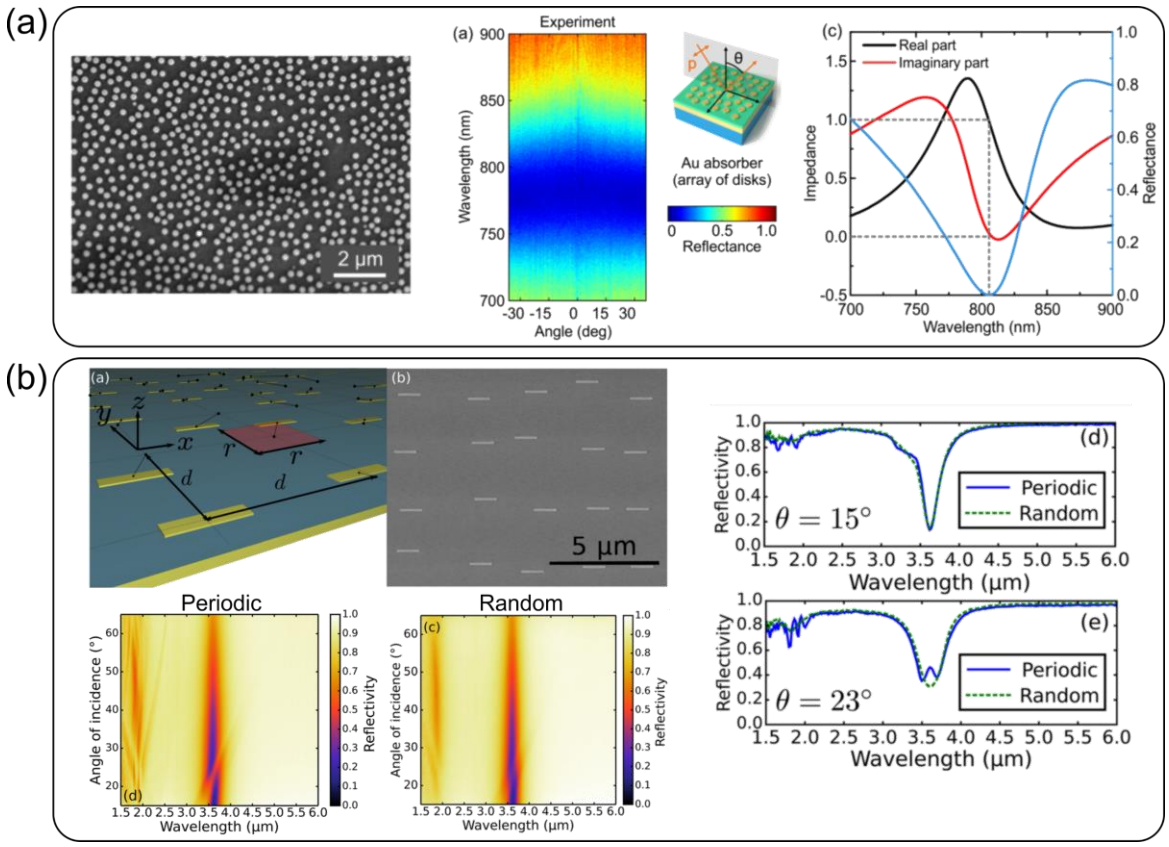

Figure 2.26. The MAs with discorded arrays. (a) The Au nano-disks fabricated using colloidal lithography. Reprinted with permission from Ref. [155] © 2014, American Chemical Society. (b) The Au rectangular resonators fabricated using electron beam lithography. Reprinted with permission from Ref. [156], rights managed by AIP Publishing.

Chevalier et al. conducted a systematic analysis for a disordered MA [156] (Figure 2.26b). They fabricated Au rectangular resonators on top of a SiO_2-Au layer by using an electron beam lithography. They first determined a center-to-center distance between the rectangular resonators as d = 2.6 μm and introduced a random distribution with r = 1.2 μm from the center. The color maps of reflection spectra were obtained using an FTIR spectrometer for the MAs with periodic and random arrays. For both MAs, a pronounced reflection dip can be confirmed at a wavelength of 3.6 μm. However, the periodic system shows splitting in reflection dip due to a distractive interaction between the LSP and the diffraction effect. The diffraction effect redshifts with an increase in the incident angle, and the splitting disappears at a high incident angle. In contrast, the random system has a very weak diffraction effect. To eliminate the diffraction effect, Chevalier et. al. suggested that r must be increased to 2.2 μm. The reflection spectra from the color maps were directly compared. It was confirmed that the reflection of the periodic and random MAs are almost the same except for the diffraction effect on the periodic MA.

2.4.3. Broadband absorbers

There are two approaches to widening the absorption bandwidth of MAs. One is mixing different plasmonic particles on a MA´s array to obtain multiple absorption peaks at different wavelengths [157-161]. The absorption spectra of the plasmonic particles must spectrally overlap to obtain broadband absorption. This multi-particle approach enables us to control absorption bandwidth precisely (Figure 2.27a), but MA´s structure becomes significantly complicated. Another approach is using a metal with high intrinsic damping [162]. This approach does not require a complicated structure, and absorption bandwidth can be widened just by using a high-loss metal for an array. However, the sharp edge of the absorption band cannot be achieved. Since the absorption of MAs must be confined into the primary ATW for high cooling performance, the lossy-metal approach is not appropriate. Therefore, we will focus on the multi-particle approach in the following. First, we have to understand the limitation of the multi-particle approach. Wang et al. theoretically investigated a MA composed of tungsten square resonators with different widths [157]. By increasing the number of square resonators in a unit cell, the absorption bandwidth can be widened; however, the absorption decreases simultaneously. As shown earlier, the periodicity of an array must be optimized based on an absorption cross-section of an isolated particle for perfect absorption. However, the multi-particle array requires a large unit cell (Figure 2.27a). Therefore, the absorption cross-section of each square resonator cannot cover the entire unit cell, resulting in weak absorption. The same result can be confirmed in the study of Cheng et al. [158]. They experimentally investigated the absorption properties of a MA composed of six different Ag nano-disks. Their MA has a wide absorption bandwidth of 2 μm, but its absorption is weak in an entire wavelength range. By reducing the number of nano-disks, the absorption can be recovered, but as expected, the absorption bandwidth decreases.

From the multi-particle approach, we can find that a particle must have broadband absorption to achieve *perfect broadband absorption*. By doing so, we do not need to increase the number of different resonators. One representative approach to increasing the absorption bandwidth of a particle is utilizing rainbow trapping, which is known as an optical phenomenon that slows down wave propagation and stores the wave´s energy in an optical system [163-165]. Rainbow trapping has been studied for waveguides comprised of, for example, metal-insulator-metal and insulator-metal-metal systems. An incident wave can be stopped at a certain position in the waveguides, and the stop can occur spectrally successively over a wide wavelength range. However, the conditions for rainbow trapping require constraints on materials. This limitation can be overcome by hyperbolic metamaterials possessing anisotropic electric permittivity. Figure 2.27b shows an anisotropic MA composed of 20 Au-Ge layers (Au: 15 nm, Ge: 35 nm) [166]. The top and bottom widths of this sawtooth-shaped resonator are 150 nm and 600 nm, respectively. A numerical simulation based on the RCWA method showed that the MA possesses nearly perfect absorption over a wavelength range of 3 – 5 μm, which cannot be achieved using the multi-particle approach. The magnetic field distribution maps illustrate that the incident wave is trapped in the sawtooth-shaped resonator and the position of the stored magnetic field changes depending on the wavelength. This is because rainbow trapping is determined by a dispersion relation of propagation constant for the resonator´s surface, and the dispersion

relation depends on the width of the resonator. The energy of the incident wave is localized in the resonator for long enough time to be completely dissipated, resulting in strong absorption. This broadband absorption by rainbow trapping has been confirmed experimentally [167]. Figure 2.27c shows the absorption spectra of three different samples: Sample1 is a MA comprised of Ag strips, and Sample2 and Sample3 are anisotropic MAs with Ag-SiO_2 layers. The top and bottom widths (W_s, W_l) of the sawtooth-shaped resonators are (500 nm, 950 nm) and (480 nm, 1.14 μm) for Sample2 and Sample3, respectively. By making sawtooth-shaped resonators and increasing the number of Ag-SiO_2 layers, the absorption bandwidth is dramatically improved without decreasing the absorption intensity.

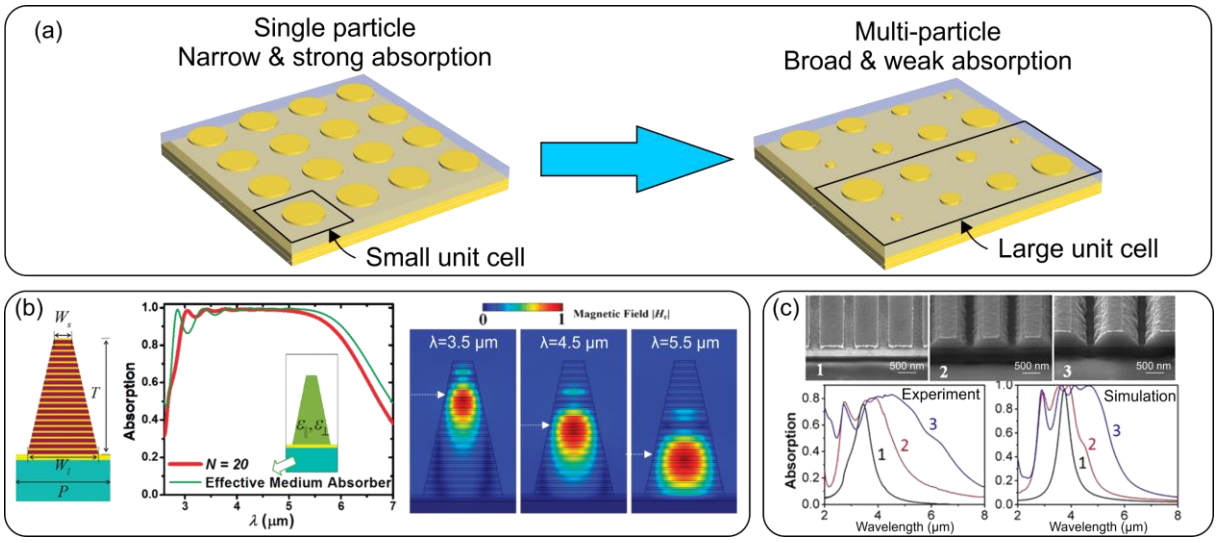

Figure 2.27. Broadband MAs. (a) Schematic illustration of the multi-particle approach. (b and c) The anisotropic metamaterial absorbers. Reprinted with permission from (b) Ref. [166] © 2012, American Chemical Society and (c) Ref. [167] Copyright CC BY-NC-ND 3.0.

2.4.4. Metamaterial absorbers for radiative cooling

MAs have been applied to radiative cooling [39-41]. Figure 2.28a presents a MA comprised of a rectangular resonator with two metal-insulator layers [40]. Those layers are made of the same metal, but the insulator parts are made of dielectrics with different refractive indices. For the top layer, a dielectric with a lower refractive index is used; therefore, the absorption peak of the top metal-insulator layer appears at a short wavelength. On the other hand, the bottom metal-insulator layer is composed of a high refractive index dielectric, resulting in an absorption peak at a long wavelength. By combining the double-layer resonators with different sizes, broadband absorption over the primary ATW can be realized. In 2015, Hossain et al. proposed an anisotropic MA, which is one of the most well-known systems in the radiative cooling community [39] (Figure 2.28b). The anisotropic MA is based on a conical resonator made of seven Al-Ge layers. The optimized anisotropic MA possesses an average absorptivity of 90 % in the primary ATW. Since the resonator is highly symmetric, its absorptivity is independent of the polarization of the incident wave.

Those MAs possess nearly ideal absorptivity for radiative cooling. However, their structures are complex and require top-down fabrication processes, hindering radiative cooling from practical uses. In addition, another drawback is that they heavily rely on a back-reflector to achieve strong absorption. Since the back-reflector loose flexibility of RCs, it makes it challenging to apply RCs on curved surfaces.

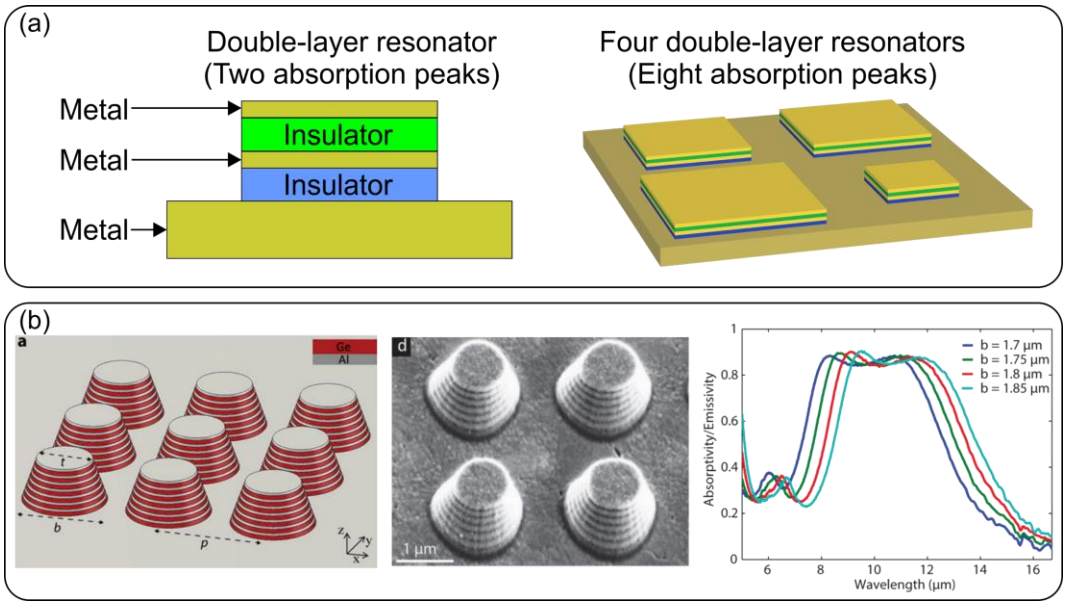

Figure 2.28. MAs for radiative cooling. (a) The multi-resonator approach from Ref. [40]. (b) The anisotropic metamaterial approach. Reprinted with permission from Ref. [39] © 2015 WILEY‐VCH Verlag GmbH & Co. KGaA, Weinheim.

2.5. Absorption engineering by bright-dark oscillator systems

As introduced in Section 2.4, MAs can provide well-controlled absorption for radiative; however, they require complex structures. Therefore, in addition to the conventional approaches, it is beneficial to figure out different means to engineer absorption for advancing radiative cooling. To increase the degree of freedom for absorption engineering, we may consider electromagnetic field interaction between two different optical elements.

In Section 2.2, it was introduced that an optical resonance can be described based on a mechanical harmonic oscillator model. When we consider that such optical resonances interact through their near-field, such coupling phenomena can be interpreted using a coupled-oscillator (CO) model. The CO model comprises two harmonic oscillators connected with a spring (Figure 2.29a). The CO model has been widely used to investigate various coupling phenomena occurring in plasmonic and photonic systems, and representative ones are electromagnetically induced transparency (EIT) and absorption (EIA). EIT and EIA can be observed if oscillators strongly interact, and one oscillator has a larger damping than another. The oscillator with a large damping rate can couple with an incident wave in a wide wavelength range. Thus, this oscillator is considered a bright oscillator. On the other hand, another oscillator with a low damping does not couple or couples with the incident wave but at a specific wavelength. Such an oscillator is considered a dark oscillator. EIT is known as a special case of Fano resonance. As a consequence of EIT, an optical resonance of the bright oscillator splits into two modes, and a transparency window is created at a resonance of the dark oscillator (Figure 2.29b). EIA is known as a counterpart of EIT: EIA dramatically enhances light absorption at a resonance of the dark oscillator (Figure 2.29c).

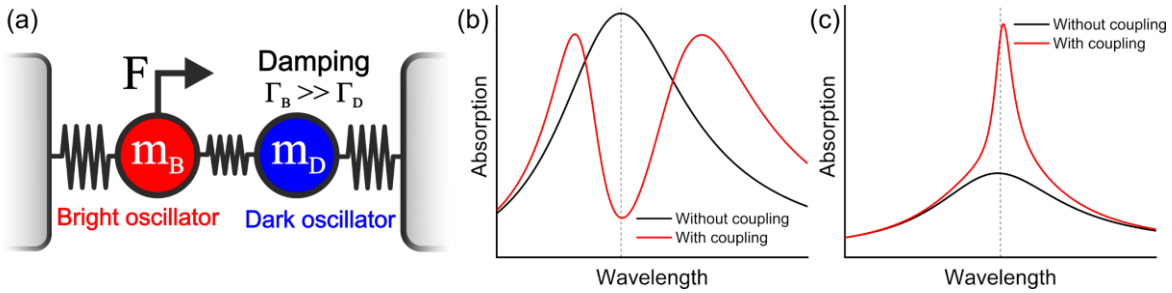

Figure 2.29. (a) Schematic of the CO model describing bright-dark coupled systems. (b – c) Images of (b) EIT and (c) EIA. The solid black and red lines are absorption spectra of the CO model without and with coupling between bright and dark oscillators. The dashed gray lines show a resonance wavelength of the dark oscillator.

2.5.1. Electromagnetically induced transparency

Fano resonance was theoretically established by Ugo Fano in 1961 to describe autoionization in atoms [168]. Fano resonance is observed as an asymmetric line shape in an optical spectrum. This asymmetric line shape is attributed to quantum interference between a continuum and a discrete state excited from a ground state. Since the physical backgrounds of quantum interference and general wave interference are similar, Fano-like resonances can be induced in plasmonic systems [169-171]. The Fano theory is based on the quantum mechanical approach. It cannot fully consider Fano-like resonances of the coupled-plasmonic systems, such as Lorentzian-like oscillation of the bright oscillator. The Fano theory has been modified to overcome this limitation using the electromagnetic theory or the CO model [172-174]. Based on the study of Gallinet et al. [175], the modified Fano theory is given as

$$\sigma_t(\omega) = \sigma_s(\omega)\sigma_a(\omega), \qquad \sigma_s(\omega) = \frac{a^2}{\left(\frac{\omega^2 - \omega_s^2}{2W_s\omega_s}\right)^2 + 1}, \qquad \sigma_a(\omega) = \frac{\left(\frac{\omega^2 - \omega_a^2}{2W_a\omega_a} + q\right)^2 + b}{\left(\frac{\omega^2 - \omega_a^2}{2W_a\omega_a}\right)^2 + 1} \qquad 2.109$$

where σ_t is the resonance strength of an entire system, σ_s describes a bright mode´s Lorentzian line shape, and σ_a introduces an asymmetric line shape by interference between a bright and a dark mode. W_n and ω_n (n $\in$ s, a) are the spectral half-width and the central frequency, respectively (Equation 2.109 considers $W_n << \omega_n$). In σ_s, a gives an amplitude of the resonance. In σ_a, q is the asymmetric parameter, which is constant and can take positive and negative values. b is the modulation damping parameter, originating from the damping of the dark mode. The parameters of σ_a are related to the dark mode´s resonance frequency ω_d and damping γ_d. Equation 2.109 is summarized in Figure 2.30a and b. Figure 2.30a only considers σ_a, corresponding to the Fano theory. When $q \neq 0$, the spectra show asymmetric line shapes. With an increase in γ_d, b reduces a spectral dip for $q = 0$ and $q \neq 0$. Figure 2.30b shows the modified Fano theory given by σ_t. Since the effect of σ_s is included, all spectra have Lorentzian line shape in their background.

Figure 2.30c presents a representative coupled plasmonic system exhibiting Fano resonance. This system comprises a dipolar antenna combined with a quadrupolar antenna in a planar configuration. When an incident wave is polarized along the long axis of the dipolar antenna, the dipolar antenna can strongly couple to the incident wave. The quadrupolar antenna is excited only through near-field coupling to the dipolar antenna. The dipolar antenna has a large radiative damping. In contrast, the quadrupolar antenna has a small radiative damping by its nature of anti-phase resonance of two dipolar bars. Based on these considerations, the dipolar and quadrupolar antennas correspond to the bright and dark oscillators, respectively. The dashed black line of Figure 2.30c shows the numerically obtained reflectance of an array composed of this coupled plasmonic element. σ_t is fitted to the numerical result (the solid red line). It can be understood that σ_t reproduces the numerical result, meaning that σ_t is an appropriate model to describe the asymmetric line shape of the coupled plasmonic system. The extracted σ_a is also shown in Figure 2.30c.

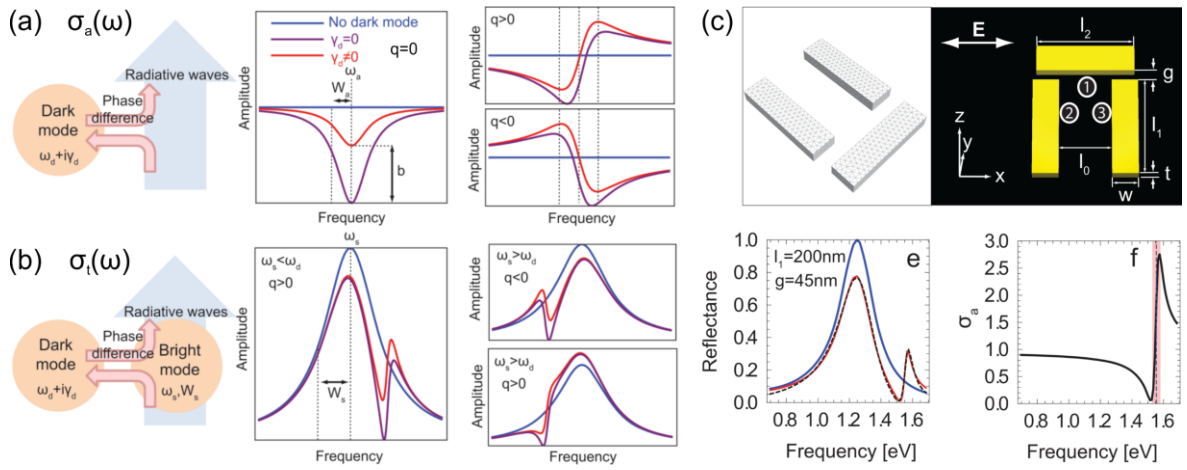

Figure 2.30. Fano resonance. (a) Schematic illustrations of the Fano theory established by Ugo Fano and the parameter dependencies of σ_a. (b) Schematic of the modified Fano theory and the parameter dependencies of σ_t. (c) An example of coupled plasmonic systems exhibiting Fano resonance. Reprinted with permission from Ref. [175] © 2011, American Chemical Society.

Having understood Fano resonance, we consider EIT. EIT also originates from quantum interference in atomic systems and has been investigated using Λ-type three-level atomic systems [176]. As mentioned earlier, EIT is a special case of Fano resonance, and EIT is defined as $q \approx 0$ ($\omega_s \approx \omega_d$) [177]. For intuitive

insight into EIT, we use the CO model shown in Figure 2.29a. The equations of motion for the bright and dark oscillators are given as [176]

$$\frac{\mathrm{d}^2 x_\mathrm{B}}{\mathrm{d}t^2} + \Gamma_\mathrm{B}\frac{\mathrm{d}x_\mathrm{B}}{\mathrm{d}t} + \omega_\mathrm{B}^2 x_\mathrm{B} - \kappa^2 x_\mathrm{D} = F(t) \qquad 2.110$$

$$\frac{\mathrm{d}^2 x_\mathrm{D}}{\mathrm{d}t^2} + \Gamma_\mathrm{D}\frac{\mathrm{d}x_\mathrm{D}}{\mathrm{d}t} + \omega_\mathrm{D}^2 x_\mathrm{D} - \kappa^2 x_\mathrm{B} = 0 \qquad 2.111$$

where x_i (i ∈ B, D) is the displacement, ω_i is the resonance frequency, and Γ_i is the damping rate. κ is the coupling rate describing the near-field coupling between a bright and a dark oscillator in a coupled plasmonic system. Since the resonance frequencies need to be $\omega_\mathrm{B} \approx \omega_\mathrm{D}$ for EIT, we consider that $\omega_\mathrm{B} = \omega_\mathrm{D} = \omega_0$. The external force per mass $F(t) = F_0 e^{-i\omega t}$ is time-harmonic, and the displacement is also time-harmonic: $x_\mathrm{i} = c_\mathrm{i} e^{-i\omega t}$. The self-consistent forms of Equations 2.110 and 2.111 are

$$x_\mathrm{B} = \frac{\omega_\mathrm{D}^2 - \omega^2 - i\Gamma_\mathrm{D}\omega}{(\omega_\mathrm{B}^2 - \omega^2 - i\Gamma_\mathrm{B}\omega)(\omega_\mathrm{D}^2 - \omega^2 - i\Gamma_\mathrm{D}\omega) - \kappa^4} F(t) \qquad 2.112$$

$$x_\mathrm{D} = \frac{\kappa^2}{(\omega_\mathrm{B}^2 - \omega^2 - i\Gamma_\mathrm{B}\omega)(\omega_\mathrm{D}^2 - \omega^2 - i\Gamma_\mathrm{D}\omega) - \kappa^4} F(t) \qquad 2.113$$

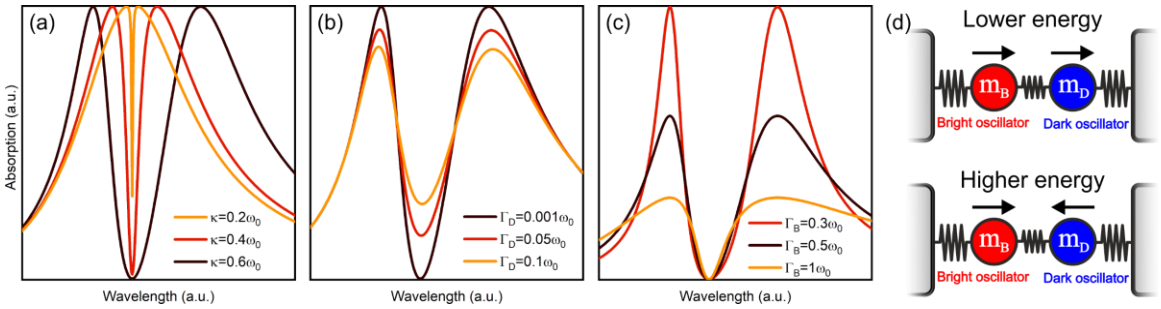

Figure 2.31. (a-c) Absorption spectra calculated using Equation 2.114. All dark-red lines are the same absorption spectrum. (a) κ dependency ($\Gamma_\mathrm{B} = 0.5\omega_0$ and $\Gamma_\mathrm{D} = 0.001\omega_0$). (b) Γ_D dependency ($\Gamma_\mathrm{B} = 0.5\omega_0$ and $\kappa = 0.6\omega_0$). (c) Γ_B dependency ($\Gamma_\mathrm{D} = 0.001\omega_0$ and $\kappa = 0.6\omega_0$). (d) Schematic illustrations of oscillations at lower energy and higher energy absorption peaks.

Since the external force works only on the bright oscillator, the power dissipation per mass of the entire system is given as

$$P(\omega) = \left\langle \mathrm{Re}\left[F^*(t) \times \frac{dx_\mathrm{B}}{dt}\right]\right\rangle = \Gamma_\mathrm{B}\omega^2|x_\mathrm{B}|^2 + \Gamma_\mathrm{D}\omega^2|x_\mathrm{D}|^2 \qquad 2.114$$

Equation 2.114 can describe many optical properties of coupled plasmonic systems, such as reflection, transmission, and absorption. Since we are interested in absorption engineering, we consider Equation 2.114 as the absorption of a coupled plasmonic system. Figure 2.31 shows a systematic analysis of Equation 2.114. In the systematic analysis, all parameters are normalized by the resonance frequency. In Figure 2.31a, the κ dependency is presented for $\Gamma_\mathrm{B} = 0.5\omega_0$ and $\Gamma_\mathrm{D} = 0.001\omega_0$. By increasing in κ, two absorption peaks are created, and the separation of those peaks becomes large. This phenomenon is called mode splitting. By mode splitting, an absorption dip appears at the resonance wavelength. The dip becomes deeper for a large κ, resulting in a transparency window. Since EIT is a consequence of creating a transparency window, it is understood that κ must be sufficiently large to induce EIT. Figure 2.31b shows Γ_D dependency for $\Gamma_\mathrm{B} = 0.5\omega_0$ and $\kappa = 0.6\omega_0$. In contrast to the κ dependency, Γ_D does not influence mode splitting. With an increase in Γ_D, the absorption peak amplitudes decrease, and the absorption dip becomes less intense. Figure 2.31c

describes Γ_B dependency for $\Gamma_D = 0.001\omega_0$ and $\kappa = 0.6\omega_0$. Γ_B influences mode splitting, but it is less intense compared to κ dependency. Γ_B dramatically changes the absorption peak amplitudes; however, the absorption dip is not affected by an increase in Γ_B. The systematic analysis shows that the three parameters (Γ_B, Γ_D, κ) interplay and determine the EIT properties of coupled plasmonic systems. The origin of two absorption peaks can be understood from Figure 2.31d. The bright and dark oscillators resonate in phase for the lower energy peak. On the other hand, those oscillators resonate anti-phase for the higher energy peak.

For more insight into mode splitting, we observe the displacement x_i. Figure 2.32a shows real and imaginary parts of x_i. For the bright oscillator, we can find two Lorentzian-like dispersions in wavelength ranges of $\lambda > \lambda_0$ and $\lambda < \lambda_0$, where λ_0 is the resonance wavelength. At $\lambda = \lambda_0$, the slope of Re[x_B] is negative, and Im[x_B] is zero. Therefore, EIT can give a large group index $n_g = n + \omega dn/d\omega$ at the resonance. This phenomenon leads to slow group velocity; therefore, EIT has been investigated for slow light applications [56, 178]. The dark oscillator´s displacement also has two Lorentzian-like dispersions in $\lambda > \lambda_0$ and $\lambda < \lambda_0$. However, the Lorentzian-like dispersion in $\lambda < \lambda_0$ has an opposite sign compared to a normal Lorentzian-like dispersion. This suggests that anti-phase resonance occurs between the bright and dark oscillators in $\lambda < \lambda_0$. The phases are calculated by $\varphi_i = \arg(x_i)$ and plotted in Figure 2.32b. φ_B is positive in the entire wavelength range. Contrary, φ_D is equal to φ_B in $\lambda > \lambda_0$ and becomes negative in $\lambda < \lambda_0$. At around $\lambda = \lambda_0$, both φ_B and φ_D abruptly change. By having a closer look at this abrupt change, we can find that φ_B crosses $\pi/2$, and φ_D changes from π to $-\pi$ at $\lambda = \lambda_0$. Figure 2.32b shows a phase difference of $\varphi_B - \varphi_D$. In $\lambda > \lambda_0$ and $\lambda < \lambda_0$, the phase difference is zero and π¸respectively. This result proves that the lower energy resonance is in-phase oscillation and the higher energy resonance is anti-phase, as shown in Figure 2.31d. The abrupt change occurs at around $\lambda = \lambda_0$, and it is found that the phase difference is $-\pi/2$.

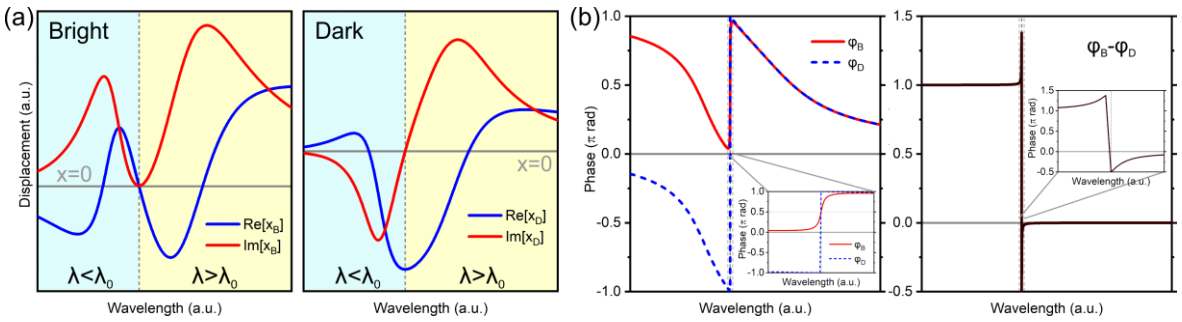

Figure 2.32. The displacements and phases of the CO model with $\Gamma_B = 0.5\omega_0$, $\Gamma_D = 0.001\omega_0$, and $\kappa = 0.6\omega_0$. (a) The real and imaginary parts of the displacement of the oscillators are presented as red and blue solid lines, respectively. The vertical dashed gray line shows the resonance wavelength. (b) The phases of the bright and dark oscillators and the phase difference between them are shown. The insets zoom around the resonance wavelength.

Based on the understanding of EIT, we will see some examples of EIT in coupled plasmonic systems. We first confirm the validity of the CO model by checking the study by Na Liu et al. [57] (Figure 2.33a). Their coupled plasmonic system comprises a dipolar antenna *vertically* placed over a quadrupolar antenna, slightly different from the one shown in Figure 2.30c. Figure 2.33a also shows the optical properties of the dipolar-quadrupolar antenna (DQA) with different displacements of *s*. The coupling strength is maximized when the dipolar antenna is placed close to the tip of the quadrupolar antenna. Therefore, its mode splitting becomes stronger with an increase in *s*, creating a transparency window. Na Liu et al. designed a CO model to describe the underlying physics of EIT. Their CO model was well fitted to the experimental absorption spectral, meaning the CO model is a proper mechanical model to investigate EIT properties of coupled plasmonic systems.

Pin Wu et al. proposed a coupled plasmonic system composed of three split ring resonators (SRRs): one vertical SRR (VSRR) and two horizontal SRRs (HSRRs) [58] (Figure 2.33b). An incident wave is polarized along the VSRR so that the VSRR can couple to the incident wave. An LSP of the VSRR creates a current loop, inducing a magnetic dipole resonance. The HSRRs are resonated only by coupling with fields created by the VSRR. Thus, the VSRR and HSRRs correspond to the bright and dark oscillators, respectively. The coupling between the VSRR and HSRRs occurs based on Lenz´s law, and the current loops are created in the HSRRs to eliminate the magnetic field of the VSRR. For strong coupling, the magnetic field of the VSRR has to pass through the center of the HSRRs. Therefore, the coupling becomes stronger when a lateral displacement D is large. The absorption profile of the SRR-based system change depending on D, and an EIT-like spectrum can be observed for a large D. To describe the mechanism of EIT, Pin Wu et al. designed a quantitative model based on an RLC circuit approach. Their RLC model well reproduced the numerical results. The magnetic field distribution maps show that the magnetic fields of the HSRRs become stronger with increasing D, proving the existence of a coupling phenomenon based on Lenz´s law. Their magnetic field analysis explained that there is $\pi/2$ phase difference in the resonances of the VSRR and HSRRs, coinciding with the analysis made in Figure 2.32b.

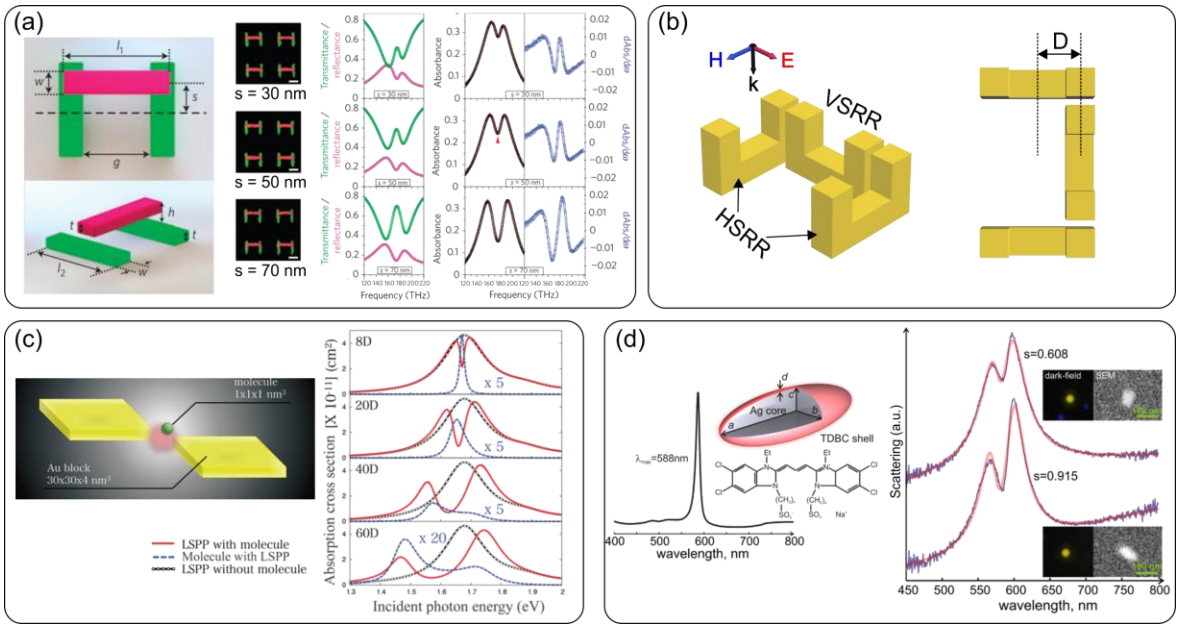

Figure 2.33. (a) The optical properties of the DQA with different lateral displacements. The absorption spectra are calculated by $A = 1 - R - T$, where R and T are reflectance and transmittance. Reprinted with permission from Ref. [57] © 2009, Nature Publishing Group. (b) The SRR-based plasmonic system with different lateral displacements Ref. [58]. (c) The absorption properties of the plasmonic composite system composed of the Au block dimer and the single molecule. The dashed red solid and blue lines are for the dimer and molecule in the composite system, respectively. The absorption spectra of the molecule are amplified from the original values. The solid black lines are reference absorption spectra of the dimer without the molecule. Reprinted with permission from Ref. [179] © 2015, American Chemical Society. (d) The scattering properties of the Ag nano-spheroid with the molecular shell made of J-aggregate. The blue and pink solid lines are scattering spectra from measurements and a CO model fitting, respectively. Reprinted with permission from Ref. [180] © 2013, The Author(s) CC BY 3.0.

In addition to fully plasmonic systems, plasmonic composite systems also can induce EIT [181]. For example, Murata et al. numerically investigated a mode splitting phenomenon of a plasmonic dimer coupling with a single molecule [179] (Figure 2.33c). The plasmonic dimer is composed of two Au blocks. The single molecule possesses a dipolar resonance and is resonated only through near-field coupling to an

LSP of the Au blocks. The single molecule is placed between the blocks, where the near-field is the strongest. To investigate the coupling strength dependency, the strength of the dipole resonance of the molecule is increased from 8 to 60 Debye. With an increase in the coupling strength, the mode splitting is intensified, and a transparency window is created in the same way as the other plasmonic systems. Murata et al. mentioned that the near-field coupling significantly enhances the molecule's absorption since the electromagnetic energy is concentrated on the molecule at the transparency window. This result indicates that the mode splitting phenomenon can enhance the absorption of a dark oscillator. With further increase in the coupling strength, the molecule's absorption also split into two peaks, resulting in a strong coupling phenomenon, such as Rabi splitting.

An EIT-like spectral profile has been observed in plasmonic composite systems not only theoretically but also experimentally. Zengin et al. experimentally investigated a mode splitting phenomenon of an Ag nano-spheroid covered with a molecular shell made of J-aggregate [180] (Figure 2.33d). Measured scattering spectra of different sizes of the Ag nano-spheroid (solid blue lines) show mode splitting, which is attributed to a strong near-field interaction between an LSP and a molecular vibration of J-aggregate. For an insight into the mode splitting, Zengin et al. compared the experimental results with their CO model (solid pink lines). The CO model reproduced the experimental data well, proving that the CO model is an appropriate qualitative model to describe the mode splitting of plasmonic composite systems.

2.5.2. Electromagnetically induced absorption

EIA is first observed by Akulshin et al. in a two-level atomic system [182, 183]. Akulshin et al. suggested that EIA is a result of quantum constructive interference. EIA has been investigated using coupled plasmonic systems. However, in contrast to EIT, there is no unified interpretation of the mechanism of EIA. I will introduce three different interpretations of EIA in the following.

The first interpretation is that EIA is induced by a phase-retarded coupling. Using a DQA shown in Figure 2.34a, Taubert et al. experimentally and theoretically investigated EIA [59, 184]. The DQA has a vertical distance of d_z = 100 nm. With increasing a lateral displacement S of the dipolar antenna, the absorption of the DQA is enhanced at around a wavelength of 2 μm (150 THz), and its spectral shape becomes an EIA-like profile. Taubert et al. explained that the coupling has near- and far-field effects because of a relatively large spatial distance between the dipolar and quadrupolar antenna. These effects cause phase retardation in coupling. This phase-retarded coupling allows constructive interaction in the DQA. Therefore, an LSP of the DQA is amplified, resulting in EIA. To elucidate EIA by constructive coupling, Taubert et al. proposed an extended CO model by modifying Equations 2.110 and 2.111

$$\frac{\mathrm{d}^2 x_\mathrm{B}(t)}{\mathrm{d}t^2} + \Gamma_\mathrm{B}\frac{\mathrm{d}x_\mathrm{B}(t)}{\mathrm{d}t} + \omega_\mathrm{B}^2 x_\mathrm{B}(t) - \kappa^2 e^{i\phi} x_\mathrm{D}(t) = F(t) \tag{2.115}$$

$$\frac{\mathrm{d}^2 x_\mathrm{D}(t)}{\mathrm{d}t^2} + \Gamma_\mathrm{D}\frac{\mathrm{d}x_\mathrm{D}(t)}{\mathrm{d}t} + \omega_\mathrm{D}^2 x_\mathrm{D}(t) - \kappa^2 e^{i\phi} x_\mathrm{B}(t) = 0 \tag{2.116}$$

where, $F(t) = F_0 e^{-i\omega t}$ is the external force per mass, and $x_\mathrm{i}(t) = c_\mathrm{i} e^{-i\omega t}$ is the displacement. φ describes the phase retardation in the coupling. The self-consistent forms of Equations 2.115 and 2.116 are

$$x_\mathrm{B}(t) = \frac{\omega_\mathrm{D}^2 - \omega^2 - i\Gamma_\mathrm{D}\omega}{(\omega_\mathrm{B}^2 - \omega^2 - i\Gamma_\mathrm{B}\omega)(\omega_\mathrm{D}^2 - \omega^2 - i\Gamma_\mathrm{D}\omega) - \kappa^4 e^{i2\varphi}} F(t) \tag{2.117}$$

$$x_\mathrm{D}(t) = \frac{\kappa^2 e^{i\phi}}{(\omega_\mathrm{B}^2 - \omega^2 - i\Gamma_\mathrm{B}\omega)(\omega_\mathrm{D}^2 - \omega^2 - i\Gamma_\mathrm{D}\omega) - \kappa^4 e^{i2\varphi}} F(t) \tag{2.118}$$

The dissipated power of the extended CO model can be obtained similarly to Equation 2.114. Taubert et al. employed a systematic study of the dissipated power. For this study, some approximations were made based on $\omega \approx \omega_B \approx \omega_D$. Their study indicates that EIT-like spectral profiles are observed when $\varphi < \pi/4$, and the EIT-like feature becomes the most pronounced at $\varphi = 0$. EIA-like spectral profiles are also confirmed in a phase range of $\varphi > \pi/4$, and the strongest sharp absorption peak appears at $\varphi = \pi/2$. These results can be easily understood from Equation 2.117. At the resonance $\omega_0 = \omega_B = \omega_D$, the power dissipation per mass of the extended CO model is given as

$$P(\omega) \propto \frac{1}{(-\Gamma_B \Gamma_D \omega_0^2 - \kappa^4 \cos 2\varphi)^2 + (\kappa^4 \sin 2\varphi)^2} \qquad 2.119$$

Equation 2.119 is minimized and maximized when $\varphi = 0$ and $\varphi = \pi/2$, respectively. Therefore, it is understood that $\varphi = 0$ and $\varphi = \pi/2$ correspond to destructive and constructive coupling, respectively. The signature of EIT-like and EIA-like spectral profiles become pronounced by increasing the coupling strength. With a further increase in the coupling strength, the power dissipation becomes negative, which is not the case for coupled plasmonic systems [184].

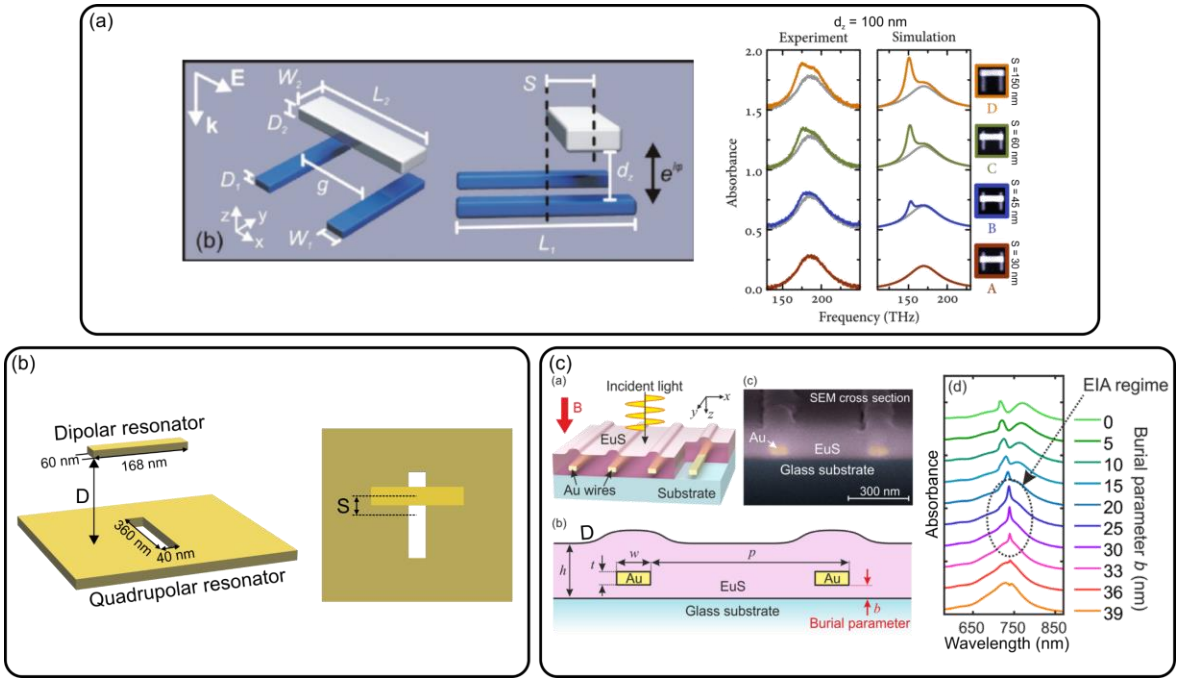

Figure 2.34. EIA by the phase-retarded coupling. (a) The dipolar-quadrupolar antenna with a large vertical displacement between the dipolar and quadrupolar antennas. Reprinted with permission from Ref. [59] © 2012, American Chemical Society. (b) The MA based on EIA from Ref. [185] (d) The plasmonic system composed of a grating of Au wires embedded in the EuS film. Reprinted with permission from Ref. [186], CC BY 4.0.

The interpretation of EIA proposed by Taubert et at. has been applied to design plasmonic systems for various applications. For example, Jinna He et al. proposed a MA whose strong absorption is attributed to EIA [185] (Figure 2.34b). Their structure is similar to the DQA, but their dark oscillator is a metal film with a long slot, which is designed based on Babinet's principle. The long slot possesses magnetic quadrupolar resonance. When a lateral displacement S is increased with a fixed vertical displacement D = 175 nm, an

EIA-like absorption peak appears at around a wavelength of 705 nm. D dependency for a fixed S = 70 nm shows that the absorption spectra change from EIA-like to EIT-like spectral profiles with a decrease in D. Phase retardation was investigated based on Equations 2.115-2.118. The results showed that the phase changes from 0 to $\pi/2$ with an increase in D; therefore, Jinna He et al. concluded that their perfect absorption is attributed to EIA by phase-retarded coupling.

Floess et al. designed a plasmonic waveguide system composed of Au wire-grating embedded in a EuS film for a large Faraday rotation [186] (Figure 2.34c). Their system exhibit EIA by an interaction between an LSP of the Au wires and a waveguide mode of the EuS film. The interaction involves phase retardation, which can be controlled by changing the Burial parameter b. The plasmonic waveguide possesses an EIT-like absorption profile for a small b, but it turns into an EIA-like absorption profile at a certain b. This spectral change is similar to the cases of the systems mentioned above.

Taubert´s interpretation of EIA has been utilized to describe the EIA of different plasmonic systems; however, it still contains ambiguity. Taubert et. al. also investigated the time-dependent electric field around the dipolar and quadrupolar antennas at the resonance and measured a phase difference between their oscillations [59, 184]. This electric field analysis suggested an $\pi/2$ phase difference, which coincides with a criterion for constructive coupling. However, as indicated by the CO model (Figure 2.32b) and the study by Pin Wu et al. (Figure 2.33b), the resonances of the bright and dark oscillators intrinsically have $\pi/2$ phase difference because of their damping. Therefore, the phase difference that Taubert et al. observed may not be a distance-dependent phase retardation. In addition, Ming-li Wan et al. investigated the EIA of a plasmonic system similar to Figure 2.34b. They demonstrated EIA with a vertical distance that is small enough to suppress the retardation effects. This result suggests that phase-retarded coupling may not be required to induce EIA [187].

When examining plasmonic-polymer composite systems, we arrive at a different interpretation of EIA [60, 188]. Adato et al. explained that a critical parameter to induce EIA is a ratio of the intrinsic damping γ_{int} to the radiative damping γ_{rad} in a plasmonic component of a composite system [60]. Their analysis was based on the TCMT introduced in Equation 2.105. A plasmonic particle can be approximated as an optical cavity with a single input and output port. Thus, the absorption of the plasmonic component may be given by Equation 2.106 (Figure 2.35a). Adato et al. suggested that there are two regimes of $\gamma_{int}/\gamma_{rad}$: an over-coupled regime for $\gamma_{int}/\gamma_{rad} < 1$ and an under-coupled regime for $\gamma_{int}/\gamma_{rad} > 1$. When the plasmonic component is combined with a polymer component, the intrinsic damping of the entire system becomes a sum of intrinsic dampings of the plasmonic and polymer components. Therefore, the entire system has a larger $\gamma_{int}/\gamma_{rad}$ than the isolated plasmonic component. Suppose the plasmonic component has sufficiently small $\gamma_{int}/\gamma_{rad}$ in the over-coupled region (red mark in Figure 2.35a). In that case, the absorption of the entire system can be enhanced at the resonance of the polymer component (red arrow in Figure 2.35a), resulting in EIA. In contrast, if the plasmonic component has $\gamma_{int}/\gamma_{rad} \geq 1$ (green and blue marks in Figure 2.35a), the absorption of the entire system becomes weaker than the initial state (green and blue arrows in Figure 2.35a). Therefore, the absorption of the entire system shows an EIT-like spectral profile.

Based on the findings in Figure 2.35a, Adato et al. demonstrated EIA by using two different composite systems. One system is an Ag nano-spheroid covered with a polymer shell. It was assumed that a molecular vibration of the polymer shell is tunable so that the molecular vibration occurs at the resonance frequency of an LSP of the Ag nano-spheroid. In Figure 2.35b, the Ag nano-spheroids with three different lengths are considered: a = 90 nm for $\gamma_{int}/\gamma_{rad} < 1$, a = 60 nm for $\gamma_{int}/\gamma_{rad} \approx 1$, and a = 30 nm for $\gamma_{int}/\gamma_{rad} > 1$. The bottom panel of Figure 2.35b presents the absorption spectra of those spheroids with the shell (solid lines) and without the shell (dashed line). Depending on a, the absorption spectra of the spheroids have different spectral profiles. When a = 90 nm, the absorption is enhanced by adding the shell and has an EIA-like spectral profile. In contrast, the spheroids with a = 60 nm and 30 nm possess an absorption dip at the

resonance of the molecular vibration. These spectral changes coincide with the findings in Figure 2.35a. Another system that Adato et al. investigated was a MA covered with a thin polymer film that has a molecular vibration at 1686 cm^{-1} (6 μm in wavelength). The size of a dipolar antenna on top of the MA was determined so that its LSP has the same resonance frequency as the polymer film. As discussed in Chapter 2.4, radiative damping of a MIM structure can be controlled by changing a gap size (thickness of an insulator layer). Based on this, the MAs with four different gaps are considered: gap = 400 nm for $\gamma_{int}/\gamma_{rad} < 1$, gap = 280 nm and 200 nm for $\gamma_{int}/\gamma_{rad} \approx 1$, and gap = 80 nm for $\gamma_{int}/\gamma_{rad} > 1$ (the middle panel of Figure 2.35c). In the bottom panel of Figure 2.35c, it is found that those three cases fall into the same result as the case of the Ag nano-spheroid. The absorption of the MA with gap = 400 nm is dramatically enhanced by the plasmon-molecular coupling and has an EIA-like spectral profile. The MA with a gap smaller than 280 nm has an EIT like-spectral profile. This is because the absorption decreases at the resonance of the polymer shell.

As shown in Figure 2.35, plasmonic-polymer composite systems can exhibit EIA-like properties only when $\gamma_{int}/\gamma_{rad} < 1$. However, it has not been described exactly how $\gamma_{int}/\gamma_{rad}$ influences absorption enhancement. As discussed in Figure 2.33c, Murata et al. suggested that the absorption of a polymer component can be dramatically enhanced by near-field coupling to an LSP. However, Adato´s work did not reveal whether EIA is attributed to absorption enhancement in the plasmonic or polymer component. This ambiguity must be cleared for designing new types of EIA-based plasmonic systems.

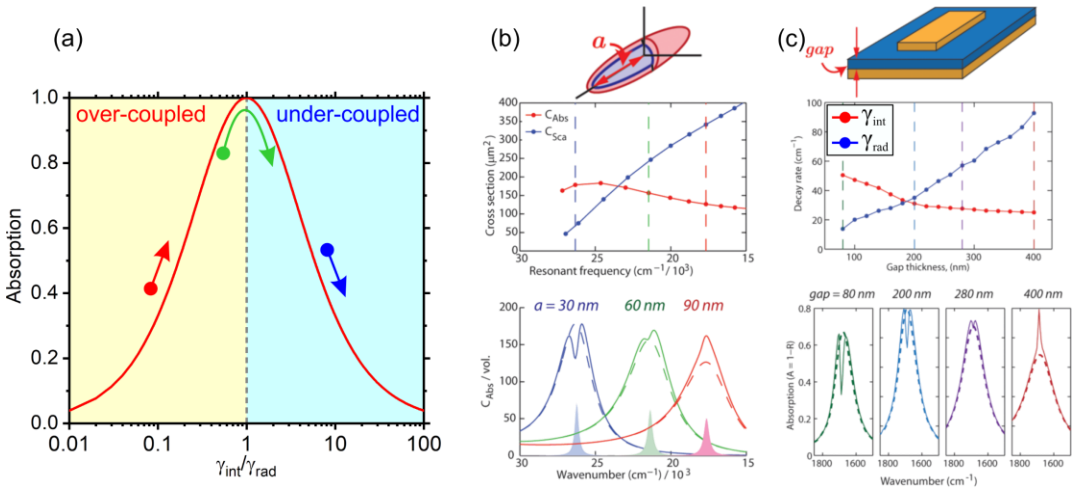

Figure 2.35. EIA of plasmonic-polymer composite systems. (a) Absorption of a single port cavity calculated by the TCMT. The yellow and cyan-shaded areas indicate the over- and under-coupled regimes. (b) The Ag-spheroid covered with a polymer shell with tunable molecular vibration. (c) The MA covered with a polymer thin film. Reprinted with permission from Ref. [60] © 2013, American Chemical Society.

In addition to the interpretations mentioned above, Tassin et al. suggested that intrinsic damping and coupling strength are key parameters to induce EIA in coupled-plasmonic systems [61]. Their analysis considered a two-dimensional array composed of coupled-plasmonic elements. In this case, the electromagnetic responses of such an array can be averaged by an electric current sheet with an effective surface conductivity. This surface conductivity can be approximately described using the CO model given by Equations 2.112 and 2.113. Using the effective surface conductivity, reflectance and transmittance of the array can be calculated. Figure 2.36a shows a systematic analysis of the array´s absorption for three parameters: the bright oscillator´s damping Γ_B, the dark oscillator´s damping Γ_D, and coupling strength κ. In this analysis, it was considered that the bright and dark oscillates have the same resonance frequency, and all three parameters (Γ_B, Γ_D, κ) are normalized by the resonance frequency. The analysis suggested that

the dark oscillator´s damping must be moderately large, and the coupling strength must be moderately small to induce EIA.

Tassin et al. experimentally reproduced the systematic analysis by using a copper cut wire as the bright oscillator and two copper closed-ring resonators as the dark oscillator (Figure 2.36b). In this system, the coupling strength can be increased by increasing the lateral displacement of the cut wire *d*. With decreasing *d*, the mode splitting becomes smaller, and the sharp absorption peak appears over a broad background spectrum. This experimental result corresponds to the case of the right column of Figure 2.36a. Similar experimental results have been observed in different plasmonic systems [189].

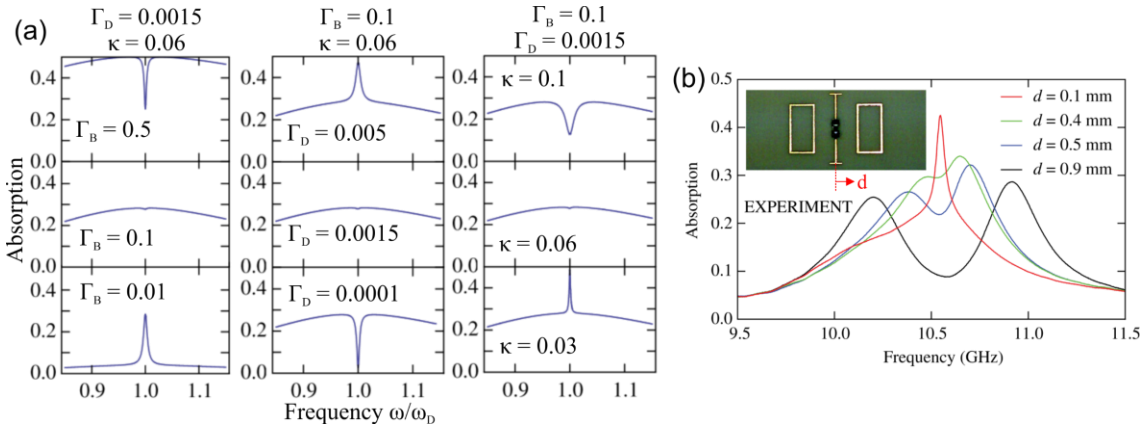

Figure 2.36. EIA originating from a weak coupling. (a) Systematic analysis of absorption properties of an array composed of coupled-plasmonic elements. (b) The absorption spectra of the plasmonic-coupled system composed of the cupper cut wire and the copper closed-ring resonators. Reprinted with permission from Ref. [61] © 2012 American Physical Society.

In summary, in this chapter, I described the fundamental mechanism of radiative cooling. Also, I discussed the essential fundamentals of optical engineering for maximizing the temperature reduction of RCs. Having understood radiative cooling and optical engineering, I introduced several examples of RCs based on plasmonic/nanophotonic absorbers. They are capable of achieving the optimal absorption properties for radiative cooling. However, I pointed out their significant drawback: they are not suitable for producing a scalable RC since they require complex nano- and micro-structures. I suggested that EIT and EIA may contribute to realizing a scalable RC, and I provided the mechanistic descriptions of EIT and EIA. Based on the findings from this chapter, I conducted various theoretical investigations to advance radiative cooling, summarized in the following chapter.

3. Overview of contributions

This chapter outlines my research contributions that will be discussed in the following chapters (Figure 3.1). During my Ph.D., my main research aim was to discover innovative approaches for absorption engineering in order to advance radiative cooling. As shown in Section 2.5, EIT and EIA have great potential to provide us with additional controllable variables in absorption engineering. From this fact, I followed the idea that by utilizing EIT and EIA, one may be able to pave a way to develop RCs possessing scalability and well-controlled absorption simultaneously. To assess the feasibility of this approach, a deep understanding of EIT and EIA is essential. Through the extensive research introduced in Section 2.5.1, the mechanism of EIT has been uncovered. In Chapter 5, I will seek a new approach to achieve selective broadband absorption by utilizing EIT based on the established knowledge. In contrast to EIT, as discussed in Section 2.5.2, the interpretations of EIA still contain ambiguities in its underlying physics. It is crucial to establish a thorough understanding of EIA for developing EIA-based RCs. In Chapters 6 and 7, I will focus on fundamental investigations to elucidate the mechanism of EIA, which I expect to benefit future advancements in radiative cooling.

Aside from the main research focus, in Chapter 8, I will discuss an additional topic to further advance radiative cooling. In Section 2.1.3, I introduced that the cooling performance of RCs is degraded under high humidity since the atmosphere becomes absorptive even in the primary ATW. In order to solve this problem, it has been suggested that an ALT filter may be capable of recovering cooling performance. Various ALT filters have been proposed for radiative cooling [72]; however, a thorough understanding of those ALT filters has not been given. Therefore, I investigate the optical properties of a dielectric corner reflector (DCR), which is widely known as a conventional ALT filter. I greatly extend the current knowledge of the DCR and expect that it will be a crucial foundation for future investigating radiative cooling for high humidity.

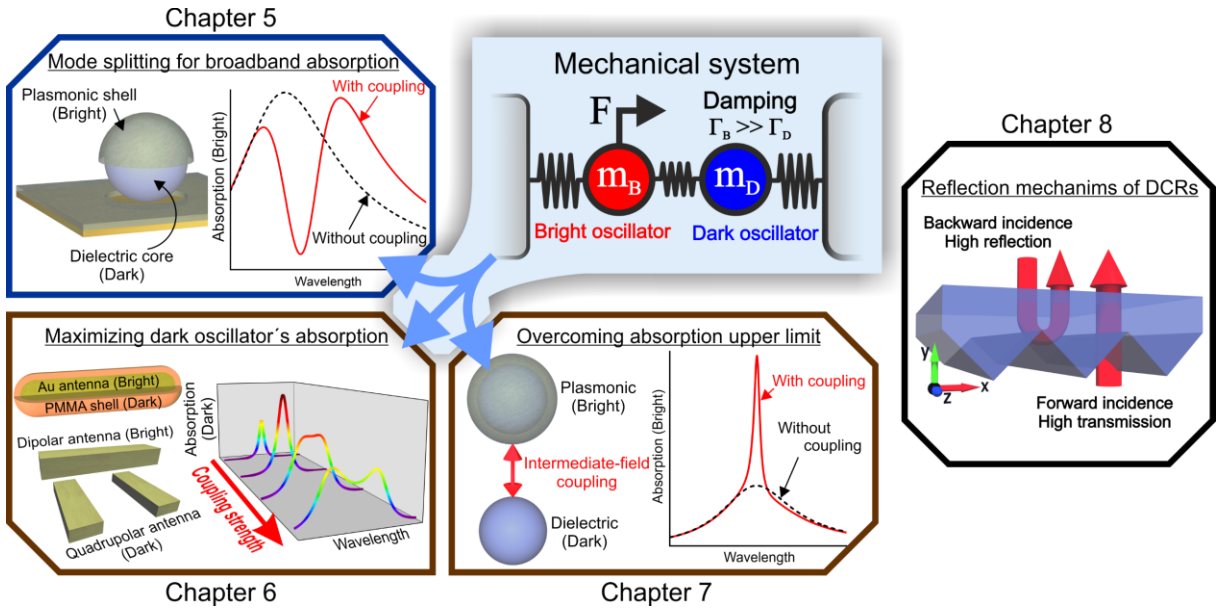

Figure 3.1. Graphical overview of my research contributions.

3.1. Synopsis

In Chapter 5, I investigate an EIT-based MA. A semishell is a plasmonic nanostructure composed of a dielectric core partially covered by a plasmonic shell. The semishell can be fabricated using colloidal lithography. Therefore, by designing an MA with the semishell, we can produce scalable devices. An LSP of the semishell can be easily tuned by changing sphere size and shell thickness, enabling us to obtain the absorption peak at a certain wavelength. A drawback of the semishell is that it does not possess broadband absorption since the semishell is a dipole resonator. To widen the absorption bandwidth of the semishell, we may be able to use near-field interaction between the LSP of the shell and a Mie resonance of the core. The core is generally made of low refractive index dielectrics, such as SiO_2. Therefore, the core does not act as an optical resonator. However, as seen in Chapter 2.3, SiO_2 has high dispersion in the MIR range, allowing the core to support a Mie resonance with low damping. Therefore, a strong interaction between the LSP and Mie resonance can be expected to induce a strong mode splitting. This mode splitting may enable us to increase the absorption bandwidth of the semishell without requiring additional complex structural design.

Based on this idea, I designed a semishell absorber composed of an ITO shell and a SiO_2 core (Figure 3.2a). The absorption properties of the semishell absorber were numerically investigated using COMSOL multiphysics, which is a commercial software based on the finite element method (FEM) [190, 191]. The proposed structure is simple and possesses strong broadband absorption. In Figure 3.2b, the solid black line shows an absorption spectrum of the semishell absorber whose structural parameters have been optimized for radiative cooling. Its high absorptivity is confined to the primary ATW. The average absorptivity in the primary ATW is 87%. This high average absorptivity cannot be obtained if the SiO_2 core is absent (the gray dashed line of Figure 3.2b). Figure 3.2c shows the absorption spectra of each component of the absorber. It is understood that the ITO shell possesses two pronounced peaks by mode splitting, resulting in broadband absorption. This mode splitting is attributed to an interaction between an LSP of the ITO shell and a magnetic dipole Mie resonance of the SiO_2 core. For more insight into the mode splitting phenomenon, I employed quantitative analysis using a CO model and the coupled dipole method (CDM). The CDM is a numerical method that can describe dipole-dipole interactions based on scattered fields given by Equations 2.70-2.71 for electric dipole moments and Equations 2.98-2.99 for magnetic dipole moments. The quantitative analysis not only develops a deeper understanding of mode splitting but also introduces significant findings regarding EIA, which suggests that a dipole-dipole interaction may induce EIA by phase-retarded coupling.

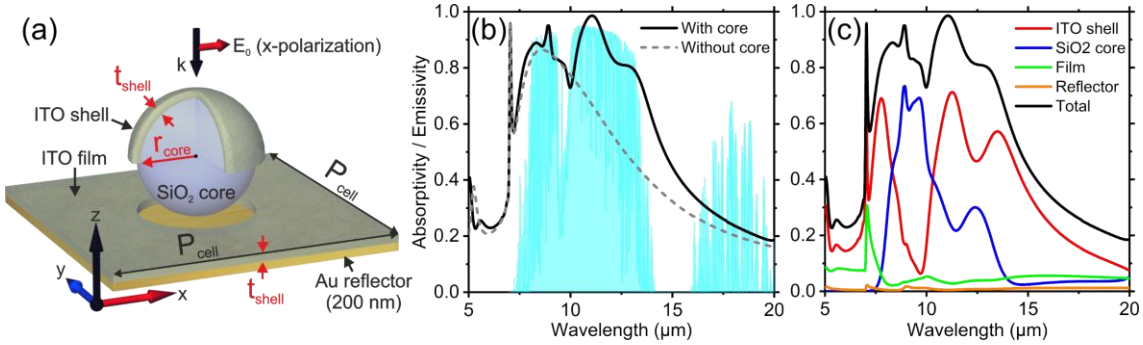

Figure 3.2. Overview of Chapter 5. (a) Schematic of the semishell absorber. (b) The absorption spectra of the semishell absorber with and without the SiO_2 core. (c) The absorption spectra of each component of the semishell absorber.

In Chapter 6, I established a unified interpretation of EIA occurring in coupled-plasmonic systems introduced in Chapter 2.5. This chapter builds a foundation for further investigating the EIA of a dipole-dipole system discussed in Chapter 8. I used two coupled-plasmonic systems well-known for EIA: a

plasmonic-polymer antenna (PPA) and a fully plasmonic dipole-quadrupolar antenna (DQA) (Figure 3.3a). In the PPA, the near-field of a plasmonic antenna strongly interacts with the molecular vibration of a polymer shell. According to Adato´s work, EIA is observed when the radiative damping γ_{rad} of the plasmonic antenna significantly overcomes its intrinsic damping γ_{int} (Figure 2.35). However, the EIA of the DQA is explained differently. Taubert described that the dipolar and quadrupolar antennas are spatially separated so that the coupling between the antennas involves phase retardation. This phase retardation makes the coupling constructive, resulting in EIA (Figure 2.34).

To elucidate the mechanism of EIA of those coupled-plasmonic systems, I built an extended CO (ECO) model that can consider all intrinsic and radiative damping channels in those systems. This consideration was based on the interpretations of EIA introduced in Figure 2.35 and Figure 2.36. Using the FEM simulation and the ECO model, I investigated the optical properties of the PPA and DQA. The ECO model well reproduced the results from the FEM simulation, proving that the ECO model is an appropriate quantitative model to investigate those systems. It was found that for both systems, EIA is attributed to an absorption enhancement occurring in the dark oscillator. This absorption enhancement was understood as the following: the dark oscillator interacts with the bright oscillator through the near-field, and the dark oscillator strongly absorbs the energy transferred from the bright oscillator. Using the ECO, I formulated a critical parameter Φ to maximize the absorption of the dark oscillator. Φ is a ratio of coupling strength to total damping of the entire system. The maximum absorption of the dark oscillator is given by $\Phi = 1$. $\Phi = 1$ means that the amount of energy transferred between the oscillators takes balance with the amount of energy dissipated in the entire system. This coupling state can be considered a critical coupling state.

A systematic analysis was employed by calculating optical spectra using the ECO model for a deeper insight into the mechanism of EIA. Figure 3.3b presents the bright oscillator´s extinction and the dark oscillator´s absorption as functions of the wavelength and Φ. In this analysis, it was considered that the dark oscillator does not possess radiative damping, and the bright and dark oscillators have the same resonance wavelength. With an increase in Φ, the bright oscillator´s extinction splits into two peaks, and the mode splitting becomes strong. The bright oscillator´s absorption also has the same trend in the spectral change. Meanwhile, the dark oscillator´s absorption is enhanced by increasing Φ to 1, and the absorption starts decreasing when Φ exceeds 1. The dark oscillator´s absorption also shows mode splitting for a large Φ. From Figure 3.3b, it was understood that the bright oscillator´s absorption always has an EIT-like spectral profile, but the dark oscillator´s absorption can possess a pronounced peak when $\Phi \approx 1$.

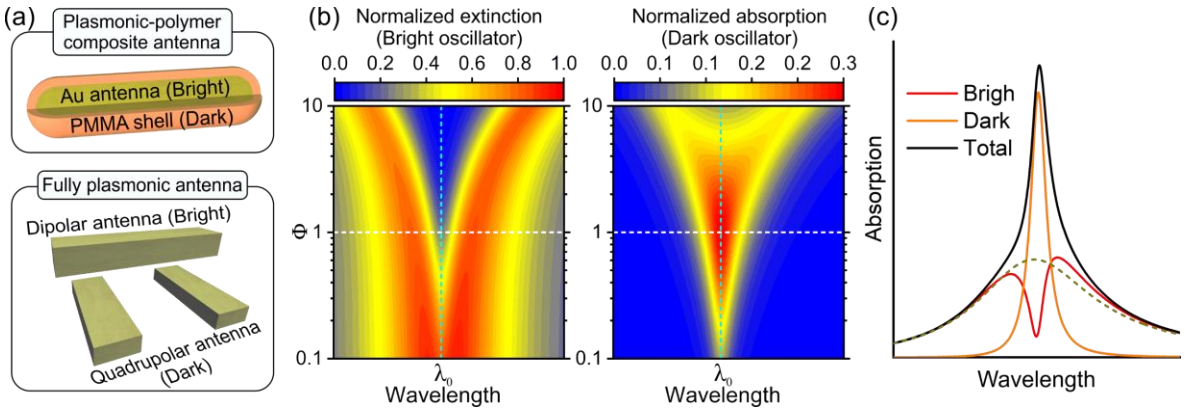

Figure 3.3. Overview of Chapter 6. (a) Schematics of the two coupled plasmonic systems well-known for EIA. (b) The color maps of the normalized extinction of the bright oscillator and the normalized absorption of the dark oscillator. These color maps are calculated using the ECO model. (c) Schematic image of EIA of coupled plasmonic systems.

From the discussion above, it is found that EIA is attributed to maximizing the dark oscillator´s absorption by satisfying $\Phi = 1$. However, an EIA-like spectral profile in the total absorption of the entire system cannot be observed just by satisfying $\Phi = 1$. In addition, the absorption of the bright oscillator must be sufficiently smaller than that of the dark oscillator (Figure 3.3c). This situation can occur only when the bright oscillator has sufficiently large $\gamma_{rad}/\gamma_{int}$. However, $\Phi = 1$ does not depend on $\gamma_{rad}/\gamma_{int}$ of the bright oscillator. Therefore, if EIA of the coupled plasmonic systems is recognized as the EIA-like spectral profile shown in Figure 3.3c, $\gamma_{rad}/\gamma_{int}$ of the bright oscillator is a critical parameter to achieve EIA. On the other hand, if EIA is considered the maximum absorption of the dark oscillator, EIA is solely determined by $\Phi = 1$. This interpretation of EIA is applied not only to the PPA and DQA but also to other coupled plasmonic systems. Throughout Chapter 6, an effect of phase-retarded coupling is not found for the DQA, contradicting the studies introduced in Figure 2.34a.

In Chapter 7, I focused on EIA originating from phase-retarded coupling. As mentioned in Section 2.5.2, the EIA of atomic systems is attributed to constructive quantum interference. However, EIA that we have observed in the coupled plasmonic systems is related to destructive interference, which can be understood from the bright oscillator´s absorption involving mode splitting. Therefore, it is found that the coupled plasmonic systems are not suitable systems to achieve constructive interference. However, the findings from Chapter 8 suggests that a dipole-dipole interaction may realize phase-retarded coupling, which may result in constructive interference.

Therefore, for this investigation, I considered a system where a plasmonic particle interacts with a dielectric particle through their scattered field. In general, a plasmonic particle has higher damping than a dielectric particle, and both particles can strongly couple with an incident wave. Thus, the plasmonic and dielectric particles can correspond to a bright and a dark oscillator, respectively. Suppose those particles are on the subwavelength scale. In this case, their optical resonances can be approximated by electric or magnetic dipole moments, which allowed me to use the CDM to analyze the optical properties of such a system. In this plasmonic-dielectric dimer system, it is considered that the dielectric particle does not have intrinsic damping. Thus, the dielectric particle acts only as a scattering particle. In this case, if constructive interference occurs, EIA is expected to appear as a result of absorption enhancement in the plasmonic particle.

Firstly, I formulated the phase-retarded coupling using the CDM. Based on this formulation, I designed an ECO model to provide an intuitive picture of the phase-retarded coupling. These quantitative analyses predict that three forces originating from the incident and scattered waves work on the plasmonic particle. Those forces have different phases that can be controlled by changing an interparticle distance. Thus, the forces can constructively work on the plasmonic particle when the interparticle distance is optimized. Consequently, the amplitude of the plasmonic particle´s dipolar resonance is dramatically enhanced, resulting in EIA.

To demonstrate EIA by the phase-retarded coupling, I designed a plasmonic-dielectric dimer composed of a plasmonic core-shell particle and a dielectric sphere (Figure 3.4a). Figure 3.4b shows the optical properties of those particles without coupling. The plasmonic core-shell particle has a broad absorption spectrum due to its LSP, and the dielectric sphere has a narrow scattering spectrum due to its dipolar magnetic Mie resonance. They have resonance peaks at almost the same wavelength. Using the FEM simulation, the absorption properties of the plasmonic-dielectric dimer are numerically characterized. Figure 3.4c presents the absorption spectra of the dimer with different interparticle distances d (Note that since the dielectric sphere is lossless, the absorption spectra are dominated by the absorption of the plasmonic core-shell particle). The dashed gray line is a reference absorption spectrum of the isolated plasmonic core-shell particle, taken from Figure 3.4b. The vertical blue line indicates the resonance wavelength of the dielectric particle. It is found that the absorption has an EIT-like spectral profile for small and large d, but it is significantly enhanced at $d \approx 2$ μm. This absorption enhancement is attributed to EIA by the phase-retarded coupling and is considerably stronger than the EIA by near-field coupling observed in Chapter 6.

An optimum d to maximize the EIA can be easily found using a d-dependent function P_{pm}. P_{pm} is derived from the CDM and describes the degree of absorption enhancement at the resonance. $P_{pm} = 1$ means that there is no absorption enhancement. $P_{pm} > 1$ indicates that constructive interference occurs, resulting in an EIA-like spectral profile. Meanwhile, the absorption spectrum possesses an EIT-like spectral profile when $P_{pm} < 1$. P_{pm} shown in Figure 3.4d shows that the absorption of the plasmonic core-shell particle has an EIA-like feature when d is intermediately large. This prediction coincides with the spectral changes observed in Figure 3.4c. P_{pm} is maximized at around $d = 2$ μm, and the plasmonic core-shell particle also has maximum absorption at $d \approx 2$ μm, proving the robustness of P_{pm}. P_{pm} is a versatile function that can be applied to different dipole-dipole systems and dimer orientations. Thus, P_{pm} possesses the potential to provide us with an additional degree of freedom to enhance the absorption of plasmonic systems.

In summary, in Chapters 6 and 7, I theoretically investigated EIA using various plasmonic and photonic structures and revealed that there are two different types of EIA. One originates from the fact that near-field coupling between bright and dark oscillators enhances the absorption of the dark oscillator. Another is attributed to the fact that the absorption of a bright oscillator is strengthened by constructive interference occurring in intermediate-field coupling. I elucidated the conditions to maximize those EIAs, benefiting the optimization of EIA-based systems. I expect that these fundamental understandings of EIA can provide us with new approaches for enhancing and controlling the absorption properties of RCs to maximize cooling performance.

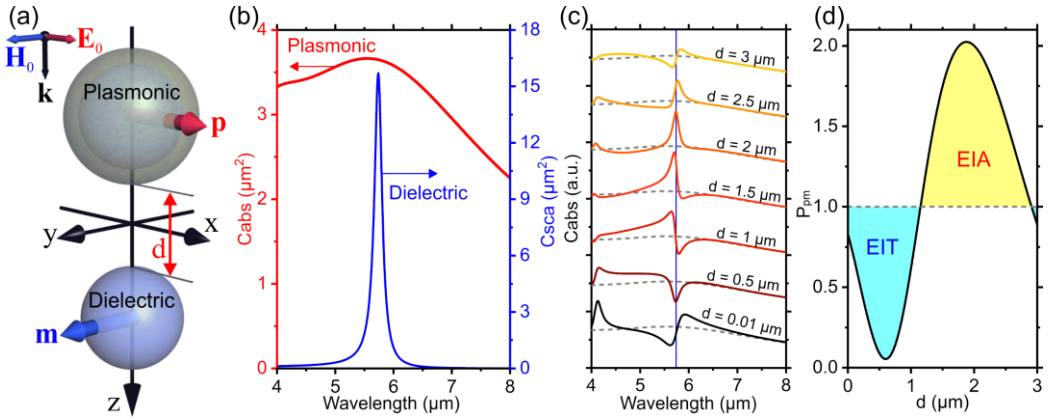

Figure 3.4. Overview of Chapter 7. (a) Schematic of the plasmonic-dielectric dimer. (b) The absorption spectrum of the isolated plasmonic core-shell (red line) and the scattering spectrum of the isolated dielectric sphere. (c) d-dependency of the plasmonic core-shell´s absorption. (d) P_{pm} as a function of d.

Chapter 8 contributes to an additional topic regarding ALT filters for radiative cooling and discusses the reflection mechanism of a DCR (Figure 3.5a). The DCR is a conventional photonic structure composed of a one-dimensional grating with a triangular structure. The triangular structure is sufficiently larger than the wavelengths of an incident light; therefore, total internal reflections (TIRs) occur in the triangular structure only for the backward incidence, resulting in the ALT properties of the DCR. Many different ALT filters have been proposed for various applications. However, I considered that the DCR can be one of the most suitable ALT films for radiative cooling because other ALT filters are based on nonreciprocal materials or composed of complex structures. These aspects are problematic for the production of a scalable ALT filters. In contrast, the structure of the DCR is relatively simple, and the DCR does not require nonreciprocal materials for ALT.

In order to figure out the feasibility of the DCR recovering cooling performance under high humidity, it is crucial to understand the optical properties of the DCR. In general, the optical properties of the DCR are described based on geometrical optics. However, geometrical optics is not sufficient since the TIRs

create evanescent waves on the surfaces of the triangular structure. These evanescent waves propagate on the surfaces for a certain distance, which is determined by the Goos-Hänchen (GH) shift. Thus, energies carried by the evanescent waves can leak from the DCR when the evanescent waves strike the downward corner of the triangular structure because of wave diffraction. This diffraction of the evanescent waves is expected to weaken the reflection of the DCR for the backward incidence.

For a better understanding of the effects of the diffraction, I built a quantitative model based on the GH shift. This model is called the diffraction loss (DL) model and considers that the amount of the evanescent wave´s energy leaking from the triangular structure is proportional to the GH shift. Figure 3.5b shows reflection spectra for the backward incidence calculated by the FEM simulation (solid line) and the DL model (dashed line). The *x*-axis of the plot is the wavelength λ_0 normalized by the side length of the triangular structure *L*. The DL model is in good agreement with the FEM simulation, proving that the DL model is an appropriate model to investigate the reflection properties of the DCR. Since the GH shift is proportional to the wavelength, the reflectance linearly decreases with an increase in the wavelength. To prove that the reflection reduction is attributed to the diffraction of the evanescent waves, electric field distribution maps are shown in Figure 3.5c. These maps consider DCRs with different base angles. For the base angle of 45°, the incident wave is confined in the triangular structure, resulting in high reflectance. In contrast, by decreasing the base angle, it is found that a significant amount of the incident wave´s energy leaks from the triangular structure by the diffraction of the evanescent waves. This is because the GH shift becomes larger when the incident angle is close to the critical angle. These fundamental understandings of the DCR enable us to optimize the structural parameters and maximize the ALT properties.

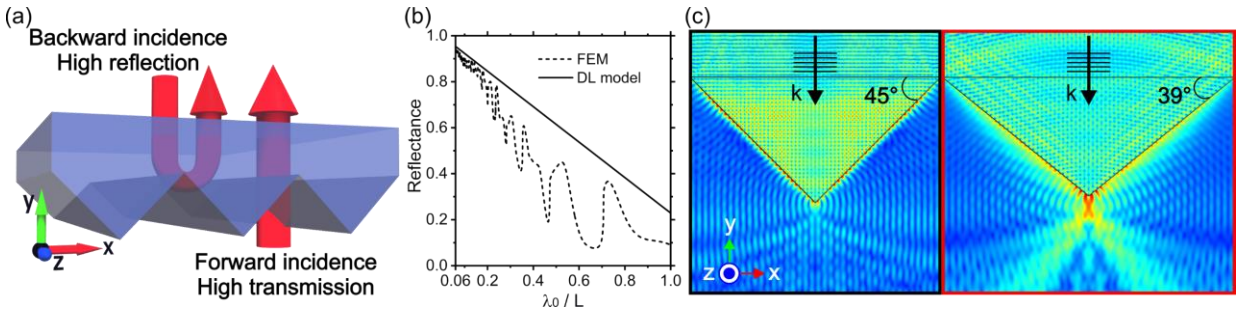

Figure 3.5. Overview of Chapter 8. (a) Schematic of the DCR. (b) Reflection spectra of the DCR for the backward incidence. The solid and dashed lines are calculated using the FEM simulation and the DL model. (c) Color maps of the electric field distribution of DCRs with different base angles.

3.2. Individual contributions to publications and manuscripts

Chapter 5. Selective broadband absorption by mode splitting for radiative cooling

Authors: **Kishin Matsumori**, Ryushi Fujimura, and Markus Retsch

Status: Published in *Optics Express* **30**(9), 14258 – 14273 (2022)

Author contributions: I conceptualized the work, performed the numerical simulation, formulated the theory, prepared the figures, and wrote the manuscript. Prof. Fujimura checked the validity of the formulated theory and corrected the manuscript. Prof. Retsch supervised the work and corrected the manuscript. Prof. Fujimura and Prof. Retsch were involved in scientific discussions.

Chapter 6. Coupling strength and total damping govern electromagnetically induced absorption in coupled plasmonic systems

Authors: **Kishin Matsumori**, Ryushi Fujimura, and Markus Retsch

Status: Accepted by *Adv. Photonics Res.*

Author contributions: I conceptualized the work, performed the numerical simulation, formulated the theory, prepared the figures, and wrote the manuscript. Prof. Fujimura checked the validity of the formulated theory and corrected the manuscript. Prof. Retsch supervised the work and corrected the manuscript. Prof. Fujimura and Prof. Retsch were involved in scientific discussions.

Chapter 7. Overcoming the upper limit for light absorption by electromagnetically induced absorption: dipole-dipole coupling with phase retardation in plasmonic-dielectric dimers

Authors: **Kishin Matsumori**, Ryushi Fujimura, and Markus Retsch

Status: Accepted by *J. Phys. Chem. C*

Author contributions: I conceptualized the work, performed the numerical simulation, formulated the theory, prepared the figures, and wrote the manuscript. Prof. Fujimura checked the validity of the formulated theory and corrected the manuscript. Prof. Retsch supervised the work and corrected the manuscript. Prof. Fujimura and Prof. Retsch were involved in scientific discussions.

Chapter 8. Reflection Mechanism of Dielectric Corner Reflectors: The Role of the Diffraction of Evanescent Waves and the Goos-Hänchen Shift

Authors: **Kishin Matsumori**, Ryushi Fujimura, and Markus Retsch

Status: Published in *ACS Omega* **7**(27), 23353 – 23361 (2022)

Author contributions: I conceptualized the work, performed the numerical simulation, formulated the theory, prepared the figures, and wrote the manuscript. Prof. Fujimura checked the validity of the formulated theory and corrected the manuscript. Prof. Retsch supervised the work and corrected the manuscript. Prof. Fujimura and Prof. Retsch were involved in scientific discussions.

4. References of Chapters 1-3

1. B. C. O'Neill, E. Kriegler, K. L. Ebi, E. Kemp-Benedict, K. Riahi, D. S. Rothman, B. J. van Ruijven, D. P. van Vuuren, J. Birkmann, K. Kok, M. Levy, and W. Solecki, "The roads ahead: Narratives for shared socioeconomic pathways describing world futures in the 21st century," Glob. Environ. Change. **42**, 169-180 (2017).

2. J. Tollefson, "How hot will Earth get by 2100?," Nature **580**(7804), 443-445 (2020).

3. M. R. Allen, O. P. Dube, W. Solecki, F. Aragón-Durand, W. Cramer, S. Humphreys, M. Kainuma, J. Kala, N. Mahowald, Y. Mulugetta, R. Perez, M. Wairiu, and K. Zickfeld, "2018: Framing and Context. In: Global Warming of 1.5°C. An IPCC Special Report on the impacts of global warming of 1.5°C above pre-industrial levels and related global greenhouse gas emission pathways, in the context of strengthening the global response to the threat of climate change, sustainable development, and efforts to eradicate povert," (2022).

4. "IEA (2022), Space Cooling, IEA, Paris" (2022), retrieved https://www.iea.org/reports/space-cooling.

5. Z. F. Huang and X. L. Ruan, "Nanoparticle embedded double-layer coating for daytime radiative cooling," Int. J. Heat Mass Transf. **104**, 890-896 (2017).

6. K. M. Al-Obaidi, M. Ismail, and A. M. Abdul Rahman, "Passive cooling techniques through reflective and radiative roofs in tropical houses in Southeast Asia: A literature review," Front. Archit. Res. **3**(3), 283-297 (2014).

7. Y.-l. Song, K. S. Darani, A. I. Khdair, G. Abu-Rumman, and R. Kalbasi, "A review on conventional passive cooling methods applicable to arid and warm climates considering economic cost and efficiency analysis in resource-based cities," Energy Reports **7**, 2784-2820 (2021).

8. B. Zhao, M. Hu, X. Ao, N. Chen, and G. Pei, "Radiative cooling: A review of fundamentals, materials, applications, and prospects," Appl. Energy **236**, 489-513 (2019).

9. J. Liu, J. Zhang, H. Tang, Z. Zhou, D. Zhang, L. Ye, and D. Zhao, "Recent advances in the development of radiative sky cooling inspired from solar thermal harvesting," Nano Energy **81**, 105611 (2021).

10. S. Fan and W. Li, "Photonics and thermodynamics concepts in radiative cooling," Nat. Photonics **16**(3), 182-190 (2022).

11. A. Leroy, B. Bhatia, C. C. Kelsall, A. Castillejo-Cuberos, H. M. Di Capua, L. Zhao, L. Zhang, A. M. Guzman, and E. N. Wang, "High-performance subambient radiative cooling enabled by optically selective and thermally insulating polyethylene aerogel," Sci. Adv. **5**(10), eaat9480 (2019).

12. T. Suichi, A. Ishikawa, T. Tanaka, Y. Hayashi, and K. Tsuruta, "Whitish daytime radiative cooling using diffuse reflection of non-resonant silica nanoshells," Sci. Rep. **10**(1), 6486 (2020).

13. H. Zhong, P. Zhang, Y. Li, X. Yang, Y. Zhao, and Z. Wang, "Highly Solar-Reflective Structures for Daytime Radiative Cooling under High Humidity," ACS Appl. Mater. Interfaces **12**(46), 51409-51417 (2020).

14. X. Li, J. Peoples, Z. Huang, Z. Zhao, J. Qiu, and X. Ruan, "Full Daytime Sub-ambient Radiative Cooling in Commercial-like Paints with High Figure of Merit," Cell Reports Physical Science **1**(10), 100221 (2020).

15. S. Atiganyanun, J. B. Plumley, S. J. Han, K. Hsu, J. Cytrynbaum, T. L. Peng, S. M. Han, and S. E. Han, "Effective Radiative Cooling by Paint-Format Microsphere-Based Photonic Random Media," ACS Photonics **5**(4), 1181-1187 (2018).

16. D. Li, X. Liu, W. Li, Z. Lin, B. Zhu, Z. Li, J. Li, B. Li, S. Fan, J. Xie, and J. Zhu, "Scalable and hierarchically designed polymer film as a selective thermal emitter for high-performance all-day radiative cooling," Nat. Nanotechnol. **16**(2), 153-158 (2021).

17. H. Ma, L. Wang, S. Dou, H. Zhao, M. Huang, Z. Xu, X. Zhang, X. Xu, A. Zhang, H. Yue, G. Ali, C. Zhang, W. Zhou, Y. Li, Y. Zhan, and C. Huang, "Flexible Daytime Radiative Cooling Enhanced by Enabling Three-Phase Composites with Scattering Interfaces between Silica Microspheres and Hierarchical Porous Coatings," ACS Appl. Mater. Interfaces **13**(16), 19282-19290 (2021).

18. W. Li, Y. Shi, Z. Chen, and S. Fan, "Photonic thermal management of coloured objects," Nat. Commun. **9**(1), 4240 (2018).

19. R. A. Yalçın, E. Blandre, K. Joulain, and J. Drévillon, "Colored Radiative Cooling Coatings with Nanoparticles," ACS Photonics **7**(5), 1312-1322 (2020).

20. H. H. Kim, E. Im, and S. Lee, "Colloidal Photonic Assemblies for Colorful Radiative Cooling," Langmuir **36**(23), 6589-6596 (2020).

21. J. W. Cho, E. J. Lee, and S. K. Kim, "Full-Color Solar-Heat-Resistant Films Based on Nanometer Optical Coatings," Nano Lett. **22**(1), 380-388 (2022).

22. L. Cai, A. Y. Song, W. Li, P. C. Hsu, D. Lin, P. B. Catrysse, Y. Liu, Y. Peng, J. Chen, H. Wang, J. Xu, A. Yang, S. Fan, and Y. Cui, "Spectrally Selective Nanocomposite Textile for Outdoor Personal Cooling," Adv. Mater. **30**(35), e1802152 (2018).

23. S. Zeng, S. Pian, M. Su, Z. Wang, M. Wu, X. Liu, M. Chen, Y. Xiang, J. Wu, M. Zhang, Q. Cen, Y. Tang, X. Zhou, Z. Huang, R. Wang, A. Tunuhe, X. Sun, Z. Xia, M. Tian, M. Chen, X. Ma, L. Yang, J. Zhou, H. Zhou, Q. Yang, X. Li, Y. Ma, and G. Tao, "Hierarchical-morphology metafabric for scalable passive daytime radiative cooling," Science **373**(6555), 692-696 (2021).

24. M. Ono, K. Chen, W. Li, and S. Fan, "Self-adaptive radiative cooling based on phase change materials," Opt. Express **26**(18), A777-A787 (2018).

25. M. Ono, M. Takata, M. Shirata, T. Yoshihiro, T. Tani, M. Naya, and T. Saiki, "Self-adaptive control of infrared emissivity in a solution-processed plasmonic structure," Opt. Express **29**(22), 36048-36060 (2021).

26. S. Wang, T. Jiang, Y. Meng, R. Yang, G. Tan, and Y. Long, "Scalable thermochromic smart windows with passive radiative cooling regulation," Science **374**(6574), 1501-1504 (2021).

27. W. Li, Y. Shi, K. Chen, L. Zhu, and S. Fan, "A Comprehensive Photonic Approach for Solar Cell Cooling," ACS Photonics **4**(4), 774-782 (2017).

28. L. Fan, W. Li, W. Jin, M. Orenstein, and S. Fan, "Maximal nighttime electrical power generation via optimal radiative cooling," Opt. Express **28**(17), 25460-25470 (2020).

29. A. P. Raman, W. Li, and S. Fan, "Generating Light from Darkness," Joule **3**(11), 2679-2686 (2019).

30. S. Catalanotti, V. Cuomo, G. Piro, D. Ruggi, V. Silvestrini, and G. Troise, "The radiative cooling of selective surfaces," Solar Energy **17**(2), 83-89 (1975).

31. E. Rephaeli, A. Raman, and S. Fan, "Ultrabroadband photonic structures to achieve high-performance daytime radiative cooling," Nano Lett. **13**(4), 1457-1461 (2013).

32. Y. Shi, W. Li, A. Raman, and S. Fan, "Optimization of Multilayer Optical Films with a Memetic Algorithm and Mixed Integer Programming," ACS Photonics **5**(3), 684-691 (2017).

33. Y. Li, L. Li, L. Guo, and B. An, "Systematical analysis of ideal absorptivity for passive radiative cooling," Opt. Mater. Express **10**(8), 1767-1767 (2020).

34. A. Alù, A. Salandrino, and N. Engheta, "Negative effective permeability and left-handed materials at optical frequencies," Opt. Express **14**(4), 1557-1567 (2006).

35. A. Poddubny, I. Iorsh, P. Belov, and Y. Kivshar, "Hyperbolic metamaterials," Nat. Photonics **7**(12), 948-957 (2013).

36. C. M. Watts, X. Liu, and W. J. Padilla, "Metamaterial electromagnetic wave absorbers," Adv. Mater. **24**(23), OP98-120, OP181 (2012).

37. Y. Cui, Y. He, Y. Jin, F. Ding, L. Yang, Y. Ye, S. Zhong, Y. Lin, and S. He, "Plasmonic and metamaterial structures as electromagnetic absorbers," Laser Photonics Rev. **8**(4), 495-520 (2014).

38. N. I. Landy, S. Sajuyigbe, J. J. Mock, D. R. Smith, and W. J. Padilla, "Perfect metamaterial absorber," Phys. Rev. Lett. **100**(20), 207402 (2008).

39. M. M. Hossain, B. Jia, and M. Gu, "A Metamaterial Emitter for Highly Efficient Radiative Cooling," Adv. Opt. Mater. **3**(8), 1047-1051 (2015).

40. R. Feng, J. Qiu, L. Liu, W. Ding, and L. Chen, "Parallel LC circuit model for multi-band absorption and preliminary design of radiative cooling," Opt. Express **22 Suppl 7**, A1713-1724 (2014).

41. J. W. Cho, S. J. Park, S. J. Park, Y. B. Kim, Y. J. Moon, and S. K. Kim, "Cooling Metals via Gap Plasmon Resonance," Nano Lett. **21**(9), 3974-3980 (2021).

42. A. Kong, B. Cai, P. Shi, and X. C. Yuan, "Ultra-broadband all-dielectric metamaterial thermal emitter for passive radiative cooling," Opt. Express **27**(21), 30102-30115 (2019).

43. L. Zhou, H. Song, J. Liang, M. Singer, M. Zhou, E. Stegenburgs, N. Zhang, C. Xu, T. Ng, Z. Yu, B. Ooi, and Q. Gan, "A polydimethylsiloxane-coated metal structure for all-day radiative cooling," Nat. Sustain. **2**(8), 718-724 (2019).

44. U. Banik, A. Agrawal, H. Meddeb, O. Sergeev, N. Reininghaus, M. Gotz-Kohler, K. Gehrke, J. Stuhrenberg, M. Vehse, M. Sznajder, and C. Agert, "Efficient Thin Polymer Coating as a Selective Thermal Emitter for Passive Daytime Radiative Cooling," ACS Appl. Mater. Interfaces **13**(20), 24130-24137 (2021).

45. C. Lin, Y. Li, C. Chi, Y. S. Kwon, J. Huang, Z. Wu, J. Zheng, G. Liu, C. Y. Tso, C. Y. H. Chao, and B. Huang, "A Solution-Processed Inorganic Emitter with High Spectral Selectivity for Efficient Subambient Radiative Cooling in Hot Humid Climates," Adv. Mater. **34**(12), e2109350 (2022).

46. E. Prodan and P. Nordlander, "Plasmon hybridization in spherical nanoparticles," J. Chem. Phys. **120**(11), 5444-5454 (2004).

47. P. Nordlander and E. Prodan, "Plasmon Hybridization in Nanoparticles near Metallic Surfaces," Nano Lett. **4**(11), 2209-2213 (2004).

48. B. Kanté, S. N. Burokur, A. Sellier, A. de Lustrac, and J. M. Lourtioz, "Controlling plasmon hybridization for negative refraction metamaterials," Phys. Rev. B **79**(7), 075121 (2009).

49. H. Liu, D. A. Genov, D. M. Wu, Y. M. Liu, Z. W. Liu, C. Sun, S. N. Zhu, and X. Zhang, "Magnetic plasmon hybridization and optical activity at optical frequencies in metallic nanostructures," Phys. Rev. B **76**(7), 073101 (2007).

50. U. Zywietz, M. K. Schmidt, A. B. Evlyukhin, C. Reinhardt, J. Aizpurua, and B. N. Chichkov, "Electromagnetic Resonances of Silicon Nanoparticle Dimers in the Visible," ACS Photonics **2**(7), 913-920 (2015).

51. C. Tabor, D. Van Haute, and M. A. El-Sayed, "Effect of orientation on plasmonic coupling between gold nanorods," ACS Nano **3**(11), 3670-3678 (2009).

52. S. Zou, N. Janel, and G. C. Schatz, "Silver nanoparticle array structures that produce remarkably narrow plasmon lineshapes," J. Chem. Phys. **120**(23), 10871-10875 (2004).

53. B. Auguie and W. L. Barnes, "Collective resonances in gold nanoparticle arrays," Phys. Rev. Lett. **101**(14), 143902 (2008).

54. B. Auguié, X. M. Bendaña, W. L. Barnes, and F. J. García de Abajo, "Diffractive arrays of gold nanoparticles near an interface: Critical role of the substrate," Phys. Rev. B **82**(15)(2010).

55. P. Offermans, M. C. Schaafsma, S. R. Rodriguez, Y. Zhang, M. Crego-Calama, S. H. Brongersma, and J. Gomez Rivas, "Universal scaling of the figure of merit of plasmonic sensors," ACS Nano **5**(6), 5151-5157 (2011).

56. S. Zhang, D. A. Genov, Y. Wang, M. Liu, and X. Zhang, "Plasmon-induced transparency in metamaterials," Phys. Rev. Lett. **101**(4), 047401 (2008).

57. N. Liu, L. Langguth, T. Weiss, J. Kastel, M. Fleischhauer, T. Pfau, and H. Giessen, "Plasmonic analogue of electromagnetically induced transparency at the Drude damping limit," Nat. Mater. **8**(9), 758-762 (2009).

58. P. C. Wu, W. T. Chen, K.-Y. Yang, C. T. Hsiao, G. Sun, A. Q. Liu, N. I. Zheludev, and D. P. Tsai, "Magnetic plasmon induced transparency in three-dimensional metamolecules," Nanophotonics **1**(2), 131-138 (2012).

59. R. Taubert, M. Hentschel, J. Kastel, and H. Giessen, "Classical analog of electromagnetically induced absorption in plasmonics," Nano Lett. **12**(3), 1367−1371 (2012).

60. R. Adato, A. Artar, S. Erramilli, and H. Altug, "Engineered absorption enhancement and induced transparency in coupled molecular and plasmonic resonator systems," Nano Lett. **13**(6), 2584-2591 (2013).

61. P. Tassin, L. Zhang, R. Zhao, A. Jain, T. Koschny, and C. M. Soukoulis, "Electromagnetically induced transparency and absorption in metamaterials: the radiating two-oscillator model and its experimental confirmation," Phys. Rev. Lett. **109**(18), 187401 (2012).

62. C. G. Granqvist and A. Hjortsberg, "Radiative cooling to low temperatures: General considerations and application to selectively emitting SiO films," J. Appl. Phys. **52**(6), 4205-4220 (1981).

63. J. Marae-Djouda, R. Caputo, N. Mahi, G. Leveque, A. Akjouj, P. M. Adam, and T. Maurer, "Angular plasmon response of gold nanoparticles arrays: approaching the Rayleigh limit," Nanophotonics **6**(1), 279-288 (2017).

64. W. Li, S. Buddhiraju, and S. Fan, "Thermodynamic limits for simultaneous energy harvesting from the hot sun and cold outer space," Light Sci. Appl. **9**, 68 (2020).

65. M. M. Hossain and M. Gu, "Radiative Cooling: Principles, Progress, and Potentials," Adv. Sci. **3**(7), 1500360 (2016).

66. M. Dong, N. Chen, X. Zhao, S. Fan, and Z. Chen, "Nighttime radiative cooling in hot and humid climates," Opt. Express **27**(22), 31587-31598 (2019).

67. C. Y. Tso, K. C. Chan, and C. Y. H. Chao, "A field investigation of passive radiative cooling under Hong Kong's climate," Renewable Energy **106**, 52-61 (2017).

68. R. Y. M. Wong, C. Y. Tso, C. Y. H. Chao, B. Huang, and M. P. Wan, "Ultra-broadband asymmetric transmission metallic gratings for subtropical passive daytime radiative cooling," Solar Energy Materials and Solar Cells **186**, 330-339 (2018).

69. M. Wei, W. Wu, D. Li, H. Xu, Y. Lu, and W. Song, "Universal strategy for all-weather and all-terrain radiative cooling with non-reciprocal mid-infrared windows," Solar Energy **207**, 471-478 (2020).

70. K. C. S. Ly, X. Liu, X. Song, C. Xiao, P. Wang, H. Zhou, and T. Fan, "A Dual‐Mode Infrared Asymmetric Photonic Structure for All‐Season Passive Radiative Cooling and Heating," Adv. Funct. Mater. **32**(31), 2203789 (2022).

71. X. Wu and C. Wang, "The application of asymmetric transmission in daytime radiative cooling cannot increase the cooling power," Solar Energy Materials and Solar Cells **215**, 110662 (2020).

72. G. Ulpiani, G. Ranzi, J. Feng, and M. Santamouris, "Expanding the applicability of daytime radiative cooling: Technological developments and limitations," Energy and Buildings **243**(110990), 110990 (2021).

73. G. R. Fowles, *Introduction to modern optics*, Second ed. (Dover, New York, 1975).

74. L. Novotny and B. Hecht, *Principles of nano-optics* (Cambridge University Press, 2006).

75. S. A. Maier, *Plasmonics: fundamentals and applications* (Springer Science & Business Media, 2007).

76. T. Tanemura, K. C. Balram, D. S. Ly-Gagnon, P. Wahl, J. S. White, M. L. Brongersma, and D. A. Miller, "Multiple-wavelength focusing of surface plasmons with a nonperiodic nanoslit coupler," Nano Lett. **11**(7), 2693-2698 (2011).

77. L. Huang, X. Chen, B. Bai, Q. Tan, G. Jin, T. Zentgraf, and S. Zhang, "Helicity dependent directional surface plasmon polariton excitation using a metasurface with interfacial phase discontinuity," Light Sci. Appl. **2**(3), e70-e70 (2013).

78. M. Seo, J. Lee, and M. Lee, "Grating-coupled surface plasmon resonance on bulk stainless steel," Opt. Express **25**(22), 26939-26949 (2017).

79. W. Ren, Y. Dai, H. Cai, H. Ding, N. Pan, and X. Wang, "Tailoring the coupling between localized and propagating surface plasmons: realizing Fano-like interference and high-performance sensor," Opt. Express **21**(8), 10251-10258 (2013).

80. C. F. Bohren and D. R. Huffman, *Absorption and scattering of light by small particles* (John Wiley & Sons, 2008).

81. W. L. Barnes, "Particle plasmons: Why shape matters," Am. J. Phys. **8**(23), 10871-10875 (2016).

82. F. Wang and Y. R. Shen, "General properties of local plasmons in metal nanostructures," Phys. Rev. Lett. **97**(20), 206806 (2006).

83. G. C. Schatz, "Theoretical Studies of Surface Enhanced Raman Scattering," Acc Chem Res **17**(10)(1984).

84. A. Moroz, "Depolarization field of spheroidal particles," J. Opt. Soc. Am. B **26**(3), 517-527 (2009).

85. C. Deeb, X. Zhou, J. Plain, G. P. Wiederrecht, R. Bachelot, M. Russell, and P. K. Jain, "Size Dependence of the Plasmonic Near-Field Measured via Single-Nanoparticle Photoimaging," J. Phys. Chem. C **117**(20), 10669-10676 (2013).

86. M. Januar, B. Liu, J.-C. Cheng, K. Hatanaka, H. Misawa, H.-H. Hsiao, and K.-C. Liu, "Role of Depolarization Factors in the Evolution of a Dipolar Plasmonic Spectral Line in the Far- and Near-Field Regimes," J. Phys. Chem. C **124**(5), 3250-3259 (2020).

87. J. D. Jackson, *Classical electrodynamics* (Wiley, New York, 1962).

88. M. J. Berg, C. M. Sorensen, and A. Chakrabarti, "Extinction and the optical theorem. Part I. Single particles," J. Opt. Soc. Am. A Opt. Image. Sci. Vis. **25**(7), 1504-1513 (2008).

89. S. Tretyakov, "Maximizing Absorption and Scattering by Dipole Particles," Plasmonics **9**(4), 935-944 (2014).

90. V. Grigoriev, N. Bonod, J. Wenger, and B. Stout, "Optimizing Nanoparticle Designs for Ideal Absorption of Light," ACS Photonics **2**(2), 263-270 (2015).

91. R. Alaee, M. Albooyeh, and C. Rockstuhl, "Theory of metasurface based perfect absorbers," J. Phys. D: Appl. Phys. **50**(50), 503002 (2017).

92. M. A. Kats, N. Yu, P. Genevet, Z. Gaburro, and F. Capasso, "Effect of radiation damping on the spectral response of plasmonic components," Opt. Express **19**(22), 21748-21753 (2011).

93. J. B. Khurgin, "How to deal with the loss in plasmonics and metamaterials," Nat. Nanotechnol. **10**(1), 2-6 (2015).

94. E. E. Radescu and G. Vaman, "Exact calculation of the angular momentum loss, recoil force, and radiation intensity for an arbitrary source in terms of electric, magnetic, and toroid multipoles," Phys. Rev. E Stat. Nonlin. Soft Matter. Phys. **65**(4 Pt 2B), 046609 (2002).

95. C. G. Gray, G. Karl, and V. A. Novikov, "Magnetic multipolar contact fields: The anapole and related moments," Am. J. Phys. **78**(9), 936-948 (2010).

96. Z. Ruan and S. Fan, "Design of subwavelength superscattering nanospheres," Appl. Phys. Lett. **98**(4), 043101 (2011).

97. N. Mohammadi Estakhri and A. Alù, "Minimum-scattering superabsorbers," Phys. Rev. B **89**(12), 121416 (2014).

98. R. Fleury, J. Soric, and A. Alù, "Physical bounds on absorption and scattering for cloaked sensors," Phys. Rev. B **89**(4)(2014).

99. A. Rahimzadegan, R. Alaee, I. Fernandez-Corbaton, and C. Rockstuhl, "Fundamental limits of optical force and torque," Phys. Rev. B **95**(3), 035106 (2017).

100. M. Albooyeh, D. Morits, and S. A. Tretyakov, "Effective electric and magnetic properties of metasurfaces in transition from crystalline to amorphous state," Phys. Rev. B **85**(20), 205110 (2012).

101. V. S. Asadchy, I. A. Faniayeu, Y. Ra'di, S. A. Khakhomov, I. V. Semchenko, and S. A. Tretyakov, "Broadband Reflectionless Metasheets: Frequency-Selective Transmission and Perfect Absorption," Phys. Rev. X **5**(3), 031005 (2015).

102. P. M. Tomchuk and N. I. Grigorchuk, "Shape and size effects on the energy absorption by small metallic particles," Phys. Rev. B **73**(15)(2006).

103. A. Asenjo-Garcia, A. Manjavacas, V. Myroshnychenko, and F. J. Garcia de Abajo, "Magnetic polarization in the optical absorption of metallic nanoparticles," Opt. Express **20**(27), 28142-28152 (2012).

104. T. J. Liu, R. Y. Xu, P. Yu, Z. M. Wang, and J. Takahara, "Multipole and multimode engineering in Mie resonance-based metastructures," Nanophotonics **9**(5), 1115-1137 (2020).

105. J. van de Groep and A. Polman, "Designing dielectric resonators on substrates: combining magnetic and electric resonances," Opt. Express **21**(22), 26285-26302 (2013).

106. S. Kruk and Y. Kivshar, "Functional Meta-Optics and Nanophotonics Governed by Mie Resonances," ACS Photonics **4**(11), 2638-2649 (2017).

107. W. T. Doyle, "Optical properties of a suspension of metal spheres," Phys. Rev. B Condens. Matter. **39**(14), 9852-9858 (1989).

108. W. Liu, A. E. Miroshnichenko, D. N. Neshev, and Y. S. Kivshar, "Broadband unidirectional scattering by magneto-electric core-shell nanoparticles," ACS Nano **6**(6), 5489-5497 (2012).

109. W. Liu, J. Zhang, B. Lei, H. Ma, W. Xie, and H. Hu, "Ultra-directional forward scattering by individual core-shell nanoparticles," Opt. Express **22**(13), 16178-16187 (2014).

110. W. Liu and Y. S. Kivshar, "Generalized Kerker effects in nanophotonics and meta-optics [Invited]," Opt. Express **26**(10), 13085-13105 (2018).

111. A. D. Rakic, A. B. Djurisic, J. M. Elazar, and M. L. Majewski, "Optical properties of metallic films for vertical-cavity optoelectronic devices," Appl. Opt. **37**(22), 5271-5283 (1998).

112. U. Guler, J. C. Ndukaife, G. V. Naik, A. G. Nnanna, A. V. Kildishev, V. M. Shalaev, and A. Boltasseva, "Local heating with lithographically fabricated plasmonic titanium nitride nanoparticles," Nano Lett. **13**(12), 6078-6083 (2013).

113. U. Guler, V. M. Shalaev, and A. Boltasseva, "Nanoparticle plasmonics: going practical with transition metal nitrides," Materials Today **18**(4), 227-237 (2015).

114. U. Guler, A. Boltasseva, and V. M. Shalaev, "Refractory plasmonics," Science **344**(6181), 263-264 (2014).

115. G. V. Naik, V. M. Shalaev, and A. Boltasseva, "Alternative Plasmonic Materials: Beyond Gold and Silver," Adv. Mater. **25**(24), 3264-3294 (2013).

116. A. Agrawal, R. W. Johns, and D. J. Milliron, "Control of Localized Surface Plasmon Resonances in Metal Oxide Nanocrystals," Annu. Rev. Mater. Res. **47**(1), 1-31 (2017).

117. S. D. Lounis, E. L. Runnerstrom, A. Llordes, and D. J. Milliron, "Defect Chemistry and Plasmon Physics of Colloidal Metal Oxide Nanocrystals," J. Phys. Chem. Lett. **5**(9), 1564-1574 (2014).

118. S. Laux, N. Kaiser, A. Zöller, R. Götzelmann, H. Lauth, and H. Bernitzki, "Room-temperature deposition of indium tin oxide thin films with plasma ion-assisted evaporation," Thin Solid Films **335**(1-2), 1-5 (1998).

119. E. Shkondin, O. Takayama, M. E. A. Panah, P. Liu, P. V. Larsen, M. D. Mar, F. Jensen, and A. V. Lavrinenko, "Large-scale high aspect ratio Al-doped ZnO nanopillars arrays as anisotropic metamaterials," Opt. Mater. Express **7**(5), 1606-1627 (2017).

120. I. Del Villar, C. R. Zamarreño, M. Hernaez, P. Sanchez, F. J. Arregui, and I. R. Matias, "Generation of Surface Plasmon Resonance and Lossy Mode Resonance by thermal treatment of ITO thin-films," Opt. Laser Technol. **69**, 1-7 (2015).

121. J. W. Cleary, E. M. Smith, K. D. Leedy, G. Grzybowski, and J. Guo, "Optical and electrical properties of ultra-thin indium tin oxide nanofilms on silicon for infrared photonics," Opt. Mater. Express **8**(5), 1231-1245 (2018).

122. Y. Wang, A. C. Overvig, S. Shrestha, R. Zhang, R. Wang, N. Yu, and L. Dal Negro, "Tunability of indium tin oxide materials for mid-infrared plasmonics applications," Opt. Mater. Express **7**(8), 2727-2739 (2017).

123. X. Zhang, J. Qiu, X. Li, J. Zhao, and L. Liu, "Complex refractive indices measurements of polymers in visible and near-infrared bands," Appl. Opt. **59**(8), 2337-2344 (2020).

124. T. Higashihara and M. Ueda, "Recent Progress in High Refractive Index Polymers," Macromolecules **48**(7), 1915-1929 (2015).

125. I. H. Malitson, "Interspecimen Comparison of the Refractive Index of Fused Silica," J. Opt. Soc. Am. **55**(10), 1205-1209 (1965).

126. F. Weiting and Y. Yixun, "Temperature effects on the refractive index of lead telluride and zinc selenide," Infrared Physics **30**(4), 371-373 (1990).

127. H. N. S. Krishnamoorthy, G. Adamo, J. Yin, V. Savinov, N. I. Zheludev, and C. Soci, "Infrared dielectric metamaterials from high refractive index chalcogenides," Nat. Commun. **11**(1), 1692 (2020).

128. X. Zhang, J. Qiu, J. Zhao, X. Li, and L. Liu, "Complex refractive indices measurements of polymers in infrared bands," Journal of Quantitative Spectroscopy and Radiative Transfer **252**, 107063 (2020).

129. J. D. Caldwell, L. Lindsay, V. Giannini, I. Vurgaftman, T. L. Reinecke, S. A. Maier, and O. J. Glembocki, "Low-loss, infrared and terahertz nanophotonics using surface phonon polaritons," Nanophotonics **4**(1)(2015).

130. S. Popova, T. Tolstykh, and V. Vorobev, "Optical characteristics of amorphous quartz in the 1400-200 cm^{-1} region," Optics and Spectroscopy **33**, 444-445 (1972).

131. J. Le Gall, M. Olivier, and J. J. Greffet, "Experimental and theoretical study of reflection and coherent thermal emissionby a SiC grating supporting a surface-phonon polariton," Phys. Rev. B **55**(15), 10105-10114 (1997).

132. Y. Zhong, S. D. Malagari, T. Hamilton, and D. Wasserman, "Review of mid-infrared plasmonic materials," Journal of Nanophotonics **9**(1)(2015).

133. Y. Kayaba and T. Kikkawa, "Quantitative Determination of Complex Dielectric Function of Amorphous Silicon Dioxide on Silicon Substrate from Transmission Spectrum," Jpn. J. Appl. Phys. **48**(12)(2009).

134. C. Huck, J. Vogt, T. Neuman, T. Nagao, R. Hillenbrand, J. Aizpurua, A. Pucci, and F. Neubrech, "Strong coupling between phonon-polaritons and plasmonic nanorods," Opt. Express **24**(22), 25528-25539 (2016).

135. K. Do-Hoon and D. M. Pozar, "Optimal Characteristics of an Arbitrary Receive Antenna," IEEE Trans. Antennas Propag. **57**(12), 3720-3727 (2009).

136. Y. Ra'di, V. S. Asadchy, S. U. Kosulnikov, M. M. Omelyanovich, D. Morits, A. V. Osipov, C. R. Simovski, and S. A. Tretyakov, "Full Light Absorption in Single Arrays of Spherical Nanoparticles," ACS Photonics **2**(5), 653-660 (2015).

137. J. Tian, H. Luo, Q. Li, X. Pei, K. Du, and M. Qiu, "Near-Infrared Super-Absorbing All-Dielectric Metasurface Based on Single-Layer Germanium Nanostructures," Laser Photonics Rev. **12**(9), 1800076 (2018).

138. R. Dezert, P. Richetti, and A. Baron, "Complete multipolar description of reflection and transmission across a metasurface for perfect absorption of light," Opt. Express **27**(19), 26317-26330 (2019).

139. S. Linden, C. Enkrich, M. Wegener, J. Zhou, T. Koschny, and C. M. Soukoulis, "Magnetic Response of Metamaterials at 100 Terahertz," Science **306**, 1351-1353 (2004).

140. N. Liu, L. Fu, S. Kaiser, H. Schweizer, and H. Giessen, "Plasmonic Building Blocks for Magnetic Molecules in Three-Dimensional Optical Metamaterials," Adv. Mater. **20**(20), 3859-3865 (2008).

141. M. Cortie and M. Ford, "A plasmon-induced current loop in gold semi-shells," Nanotechnology **18**(23), 235704 (2007).

142. N. Liu, S. Mukherjee, K. Bao, L. V. Brown, J. Dorfmuller, P. Nordlander, and N. J. Halas, "Magnetic plasmon formation and propagation in artificial aromatic molecules," Nano Lett. **12**(1), 364−369 (2012).

143. A. Christ, T. Zentgraf, S. G. Tikhodeev, N. A. Gippius, J. Kuhl, and H. Giessen, "Controlling the interaction between localized and delocalized surface plasmon modes: Experiment and numerical calculations," Phys. Rev. B **74**(15), 155435 (2006).

144. B. J. Lee, L. P. Wang, and Z. M. Zhang, "Coherent thermal emission by excitation of magnetic polaritons between periodic strips and a metallic film," Opt. Express **16**(15), 11328-11336 (2008).

145. A. Christ, G. Leveque, O. J. Martin, T. Zentgraf, J. Kuhl, C. Bauer, H. Giessen, and S. G. Tikhodeev, "Near-field-induced tunability of surface plasmon polaritons in composite metallic nanostructures," J. Microsc. **229**(Pt 2), 344-353 (2008).

146. J. M. Hao, L. Zhou, and M. Qiu, "Nearly total absorption of light and heat generation by plasmonic metamaterials," Phys. Rev. B **83**(16), 165107 (2011).

147. C. Wu, B. Neuner, G. Shvets, J. John, A. Milder, B. Zollars, and S. Savoy, "Large-area wide-angle spectrally selective plasmonic absorber," Phys. Rev. B **84**(7), 075102 (2011).

148. C. Koechlin, P. Bouchon, F. Pardo, J. L. Pelouard, and R. Haidar, "Analytical description of subwavelength plasmonic MIM resonators and of their combination," Opt. Express **21**(6), 7025-7032 (2013).

149. H. A. Haus, *Waves and fields in optoelectronics* (Prentice-Hall, Inc., USA, 1984).

150. X. Liu, T. Starr, A. F. Starr, and W. J. Padilla, "Infrared spatial and frequency selective metamaterial with near-unity absorbance," Phys. Rev. Lett. **104**(20), 207403 (2010).

151. R. Walter, A. Tittl, A. Berrier, F. Sterl, T. Weiss, and H. Giessen, "Large-Area Low-Cost Tunable Plasmonic Perfect Absorber in the Near Infrared by Colloidal Etching Lithography," Adv. Opt. Mater. **3**(3), 398-403 (2015).

152. T. D. Dao, K. Chen, S. Ishii, A. Ohi, T. Nabatame, M. Kitajima, and T. Nagao, "Infrared Perfect Absorbers Fabricated by Colloidal Mask Etching of Al–Al2O3–Al Trilayers," ACS Photonics **2**(7), 964-970 (2015).

153. R. Guo, T. K. Hakala, and P. Törmä, "Geometry dependence of surface lattice resonances in plasmonic nanoparticle arrays," Phys. Rev. B **95**(15), 155423 (2017).

154. S. Jeon and J. Shin, "Directional radiation for optimal radiative cooling," Opt. Express **29**(6), 8376-8386 (2021).

155. A. Tittl, M. G. Harats, R. Walter, X. Yin, M. Schaferling, N. Liu, R. Rapaport, and H. Giessen, "Quantitative angle-resolved small-spot reflectance measurements on plasmonic perfect absorbers: impedance matching and disorder effects," ACS Nano **8**(10), 10885–10892 (2014).

156. P. Chevalier, P. Bouchon, J. Jaeck, D. Lauwick, N. Bardou, A. Kattnig, F. Pardo, and R. Haïdar, "Absorbing metasurface created by diffractionless disordered arrays of nanoantennas," Appl. Phys. Lett. **107**(25)(2015).

157. H. Wang and L. Wang, "Perfect selective metamaterial solar absorbers," Opt. Express **21 Suppl 6**, A1078-1093 (2013).

158. C. W. Cheng, M. N. Abbas, C. W. Chiu, K. T. Lai, M. H. Shih, and Y. C. Chang, "Wide-angle polarization independent infrared broadband absorbers based on metallic multi-sized disk arrays," Opt. Express **20**(9), 10376-10381 (2012).

159. K. Aydin, V. E. Ferry, R. M. Briggs, and H. A. Atwater, "Broadband polarization-independent resonant light absorption using ultrathin plasmonic super absorbers," Nat. Commun. **2**, 517 (2011).

160. A. K. Azad, W. J. Kort-Kamp, M. Sykora, N. R. Weisse-Bernstein, T. S. Luk, A. J. Taylor, D. A. Dalvit, and H. T. Chen, "Metasurface Broadband Solar Absorber," Sci. Rep. **6**, 20347 (2016).

161. Z. Liu, X. Liu, S. Huang, P. Pan, J. Chen, G. Liu, and G. Gu, "Automatically acquired broadband plasmonic-metamaterial black absorber during the metallic film-formation," ACS Appl. Mater. Interfaces **7**(8), 4962-4968 (2015).

162. F. Ding, J. Dai, Y. Chen, J. Zhu, Y. Jin, and S. I. Bozhevolnyi, "Broadband near-infrared metamaterial absorbers utilizing highly lossy metals," Sci. Rep. **6**, 39445 (2016).

163. T. Jiang, J. Zhao, and Y. Feng, "Stopping light by an air waveguide with anisotropic metamaterial cladding," Opt. Express **17**(1), 170-177 (2009).

164. M. S. Jang and H. Atwater, "Plasmonic rainbow trapping structures for light localization and spectrum splitting," Phys. Rev. Lett. **107**(20), 207401 (2011).

165. H. Hu, D. Ji, X. Zeng, K. Liu, and Q. Gan, "Rainbow trapping in hyperbolic metamaterial waveguide," Sci. Rep. **3**, 1249 (2013).

166. Y. Cui, K. H. Fung, J. Xu, H. Ma, Y. Jin, S. He, and N. X. Fang, "Ultrabroadband light absorption by a sawtooth anisotropic metamaterial slab," Nano Lett. **12**(3), 1443−1447 (2012).

167. D. Ji, H. Song, X. Zeng, H. Hu, K. Liu, N. Zhang, and Q. Gan, "Broadband absorption engineering of hyperbolic metafilm patterns," Sci. Rep. **4**, 4498 (2014).

168. U. Fano, "Effects of Configuration Interaction on Intensities and Phase Shifts," Phys. Rev. **124**(6), 1866-& (1961).

169. A. Christ, Y. Ekinci, H. H. Solak, N. A. Gippius, S. G. Tikhodeev, and O. J. F. Martin, "Controlling the Fano interference in a plasmonic lattice," Phys. Rev. B **76**(20), 201405(R) (2007).

170. J. B. Lassiter, H. Sobhani, M. W. Knight, W. S. Mielczarek, P. Nordlander, and N. J. Halas, "Designing and deconstructing the Fano lineshape in plasmonic nanoclusters," Nano Lett. **12**(2), 1058-1062 (2012).

171. F. Shafiei, F. Monticone, K. Q. Le, X. X. Liu, T. Hartsfield, A. Alu, and X. Li, "A subwavelength plasmonic metamolecule exhibiting magnetic-based optical Fano resonance," Nat. Nanotechnol. **8**(2), 95-99 (2013).

172. B. Gallinet and O. J. F. Martin, "Ab initio theory of Fano resonances in plasmonic nanostructures and metamaterials," Phys. Rev. B **83**(23), 235427 (2011).

173. V. Giannini, Y. Francescato, H. Amrania, C. C. Phillips, and S. A. Maier, "Fano resonances in nanoscale plasmonic systems: a parameter-free modeling approach," Nano Lett. **11**(7), 2835-2840 (2011).

174. Y. S. Joe, A. M. Satanin, and C. S. Kim, "Classical analogy of Fano resonances," Physica Scripta **74**(2), 259-266 (2006).

175. B. Gallinet and O. J. Martin, "Influence of electromagnetic interactions on the line shape of plasmonic Fano resonances," ACS Nano **5**(11), 8999-9008 (2011).

176. C. L. Garrido Alzar, M. A. G. Martinez, and P. Nussenzveig, "Classical analog of electromagnetically induced transparency," Am. J. Phys. **70**(1), 37-41 (2002).

177. M. F. Limonov, M. V. Rybin, A. N. Poddubny, and Y. S. Kivshar, "Fano resonances in photonics," Nat. Photonics **11**(9), 543-554 (2017).

178. P. Tassin, L. Zhang, T. Koschny, E. N. Economou, and C. M. Soukoulis, "Low-loss metamaterials based on classical electromagnetically induced transparency," Phys. Rev. Lett. **102**(5), 053901 (2009).

179. N. Murata, R. Hata, and H. Ishihara, "Crossover between Energy Transparency Resonance and Rabi Splitting in Antenna–Molecule Coupled Systems," J. Phys. Chem. C **119**(45), 25493-25498 (2015).

180. G. Zengin, G. Johansson, P. Johansson, T. J. Antosiewicz, M. Kall, and T. Shegai, "Approaching the strong coupling limit in single plasmonic nanorods interacting with J-aggregates," Sci. Rep. **3**, 3074 (2013).

181. Z. J. Yang, T. J. Antosiewicz, and T. Shegai, "Role of material loss and mode volume of plasmonic nanocavities for strong plasmon-exciton interactions," Opt. Express **24**(18), 20373-20381 (2016).

182. A. M. Akulshin, S. Barreiro, and A. Lezama, "Electromagnetically induced absorption and transparency due to resonant two-field excitation of quasidegenerate levels in Rb vapor," Phys. Rev. A **57**(4), 2996-3002 (1998).

183. A. Lezama, S. Barreiro, and A. M. Akulshin, "Electromagnetically induced absorption," Phys. Rev. A **59**(6), 4732-4735 (1999).

184. R. Taubert, M. Hentschel, and H. Giessen, "Plasmonic analog of electromagnetically induced absorption: simulations, experiments, and coupled oscillator analysis," J. Opt. Soc. Am. B **30**(12), 3123-3134 (2013).

185. J. He, P. Ding, J. Wang, C. Fan, and E. Liang, "Ultra-narrow band perfect absorbers based on plasmonic analog of electromagnetically induced absorption," Opt. Express **23**(5), 6083-6091 (2015).

186. D. Floess, M. Hentschel, T. Weiss, H.-U. Habermeier, J. Jiao, S. G. Tikhodeev, and H. Giessen, "Plasmonic Analog of Electromagnetically Induced Absorption Leads to Giant Thin Film Faraday Rotation of 14°," Phys. Rev. X **7**(2), 021048 (2017).

187. M.-l. Wan, J.-n. He, Y.-l. Song, and F.-q. Zhou, "Electromagnetically induced transparency and absorption in plasmonic metasurfaces based on near-field coupling," Phys. Lett. A **379**(30-31), 1791-1795 (2015).

188. T. Neuman, C. Huck, J. Vogt, F. Neubrech, R. Hillenbrand, J. Aizpurua, and A. Pucci, "Importance of Plasmonic Scattering for an Optimal Enhancement of Vibrational Absorption in SEIRA with Linear Metallic Antennas," J. Phys. Chem. C **119**(47), 26652-26662 (2015).

189. F. Zhang, X. Huang, W. Cai, R. Yang, Q. Fu, Y. Fan, Y. Hu, K. Qiu, W. Zhang, C. Li, and Q. Li, "EIA metamaterials based on hybrid metal/dielectric structures with dark-mode-enhanced absorption," Opt. Express **28**(12), 17481-17489 (2020).

190. K. X. Lin, L. K. Chao, H. H. Lee, R. Xin, S. Liu, T. C. Ho, B. L. Huang, K. M. Yu, and C. Y. Tso, "Potential building energy savings by passive strategies combining daytime radiative coolers and thermochromic smart windows," Case Stud. Therm. Eng. **28**(2021).

191. K. Sankaran, "Are you using the right tools in computational electromagnetics?," Engineering Reports **1**(3), e12041 (2019).

5. Selective broadband absorption by mode splitting for radiative cooling

Kishin Matsumori[1,*], Ryushi Fujimura[2], and Markus Retsch[1]

[1] Department of Chemistry, Physical Chemistry I, University of Bayreuth, 95447 Bayreuth, Germany

[2] Graduate School of Regional Development and Creativity, Utsunomiya University, 321-8585 Utsunomiya, Japan

Published in *Optics Express* **30**(9), 14258 – 14273 (2022)

Abstract: A plasmonic-photonic structure based on colloidal lithography was designed for a scalable radiative cooling system and its absorption properties were theoretically investigated. The structure comprises a SiO_2 core, which is on top of an Au reflector and partially covered by an indium tin oxide (ITO) shell. This simple and scalable structure possesses a strong selective absorption in the primary atmospheric transparency window (8–13 μm). The strong selective absorption is attributed to a mode splitting of the localized surface plasmon (LSP) of the ITO shell. To understand the mechanisms of the mode splitting, a quantitative analysis was conducted using a coupled-oscillator model and a coupled-dipole method. The analysis revealed that the mode splitting is induced by a strong coupling between the LSP of the ITO shell and a magnetic dipole Mie resonance of the SiO_2 core.

5.1. Introduction

Daytime radiative cooling is an optics-based technology that can decrease the temperature of an object below the ambient temperature without requiring any energy input [1]. This radiative cooling technology works by completely reflecting/scattering incoming sunlight to minimize heat absorption and emitting thermal radiation in the mid-infrared (MIR) range. In the MIR range, there are two atmospheric transparency windows (ATW); the primary ATW (8 – 13 μm) and the secondary ATW (16 – 28 μm). Therefore, the optical properties of the involved materials should have a strong emissivity in those wavelength ranges for a considerable cooling performance. There are two indicators to characterize the cooling performance of such a system [1, 2]. One is cooling power, which is the net radiative heat ejection at a certain temperature of the system. A high cooling power can be achieved, if the materials demonstrated a black body emissivity in the MIR range [3–6]. Another indicator is the temperature reduction, which is determined by the difference between the ambient temperature and the temperature of the system at an equilibrium state. At this equilibrium state the energy of radiative heat loss of the system equals the heat load by external sources, such as the thermal radiation of the atmosphere. For a higher temperature reduction, more precise optical engineering is required since the system should have strong selective emissivity only in the primary ATW.

Optical tailoring for radiative cooling can be realized by plasmonic absorbers, which have been extensively investigated because of their variety of energy applications, such as energy harvesting [7] and solar thermophotovoltaics [8–10]. One of the most representative plasmonic absorbers is a metal-insulator-metal (MIM) structure whose top metal layer is structured [11–16]. A strong absorption is induced by localized surface plasmons (LSPs) of the top structure, therefore, a selective broadband absorption can be obtained by mixing different size and shape of structures [8–10, 17, 18]. However, if a diversity of the

structure is increased for a wider absorption bandwidth, a density of each structure decreases, resulting in reduced absorption at all wavelengths [9, 17, 18]. An alternative approach is designing a multilayered structure [19–21]. A nearly perfect absorption can be obtained in the primary ATW because a single structure has a selective broadband absorption [21]. Broadband absorbers based on 2D photonics structures have also been designed for radiate cooling, and they showed a selective absorption only in the ATWs by phonon-polariton resonances [22–24]. Those plasmonic and photonic structures have almost ideal optical properties for radiative cooling, however, their fabrication heavily relies on top-down processes. Therefore, they are expensive and mostly not suited to produce a large-area radiative cooling system.

Difficulties in the fabrication for a scalable device can be overcome by different approaches. One is by mixing plasmonic or photonic particles in a polymer matrix [2, 25–27]. This composite film has a selective absorption in the ATWs by either broadband LSP or superposition of different order modes of Mie resonances, depending on which type of particle was used. Another approach is synthesizing polymer films so that they have intrinsic selective absorption by their molecular vibrations [28, 29]. Those two approaches do not require any complicated structures and all fabrication processes are based on bottom-up techniques, paving the way to a scalable radiative cooling system. However, these systems typically have an additional strong absorption outside or a significant absorption dip inside the primary ATW.

For a finer control of the absorption bandwidth, one of the best strategies is still designing a plasmonic or photonic structure such that a single structural motif exhibits the required strong absorption in a specific wavelength range, like multilayered structures do [21]. Therefore, in this contribution, we outline a way to satisfy a high control of absorption bandwidth and a scalable sample processing at the same time. A semishell structure [30–33] composed of a dielectric core and a metal shell is known as a plasmonic nanostructure, which can be fabricated by large-area processes using colloidal lithography [34] and metal deposition. A semishell structure has been utilized for broadband absorbers. MIM structures whose top is composed of a semishell structure possess a broadband absorption in the visible to near-infrared regions [35, 36]. A close-packed monolayer of a semishell structure combined with a metal reflector strongly absorbs radiation in a wavelength range from 3 to 6 μm [37]. These structures demonstrated a broadband absorption; however, their absorption bandwidth is not selective.

To realize a selective absorption by a semishell-based absorber, a structure has to be designed by a different approach. In the wavelength regions shorter than the primary ATW, many dielectrics have nearly constant low refractive index. In this case, the optical properties of the core are not important, and the core can be used just as a support of the metal shell. However, in the primary ATW, some dielectrics have a high dispersion, which enable the core to support both electric and magnetic Mie resonances. When the LSP of the metal shell interacts with the Mie resonance of the dielectric core at their resonance condition, the interaction may cause a mode splitting that can be seen in strong coupling, such as electromagnetic induced transparency [38–42] and Rabi splitting [43–46]. This mode splitting has the potential to give additional control on the absorption bandwidth and enable us to realize a selective absorption in the primary ATW. Based on these ideas, we discuss our theoretical investigation to design a plasmonic-photonic semishell structure combined with an Au reflector for radiative cooling applications. Indium tin oxide (ITO) and SiO_2 were chosen for the shell and core, respectively. ITO is known as an alternative plasmonic material, which works in the IR range [47, 48]. SiO_2 has a high dispersion in the primary ATW, which guarantees the excitement of Mie resonances [26]. We discuss the absorption properties of our ITO@SiO_2 semishell absorber based on Mie theory and the finite element method (FEM). To understand the absorption mechanisms in detail, we provide a quantitative analysis based on a coupled-oscillator (CO) model and the coupled-dipole method (CDM).

5.2. Optical properties of the SiO_2 core

We first investigated the optical properties of the SiO_2 core using Mie theory to determine a suitable size range for the ITO@SiO_2 semishell absorber. The extinction (C_{ext}), scattering (C_{sca}), and absorption (C_{abs}) cross-sections can be calculated as [49]

$$C_{\text{ext},n} = \frac{2\pi}{k^2}(2n+1)\text{Re}[a_n + b_n]$$

$$C_{\text{sca},n} = \frac{2\pi}{k^2}(2n+1)(|a_n|^2 + |b_n|^2)$$

$$C_{\text{abs},n} = C_{\text{ext},n} - C_{\text{sca},n}$$

where k is the angular wavenumber, a_n and b_n are Mie coefficients for n-th order of electric and magnetic modes, respectively. n = 1 and 2 correspond to dipole and quadrupole resonance, respectively. Extinction (Q_{ext}), scattering (Q_{sca}), and absorption (Q_{abs}) efficiency are cross-sections normalized by the geometrical cross-section of the core.

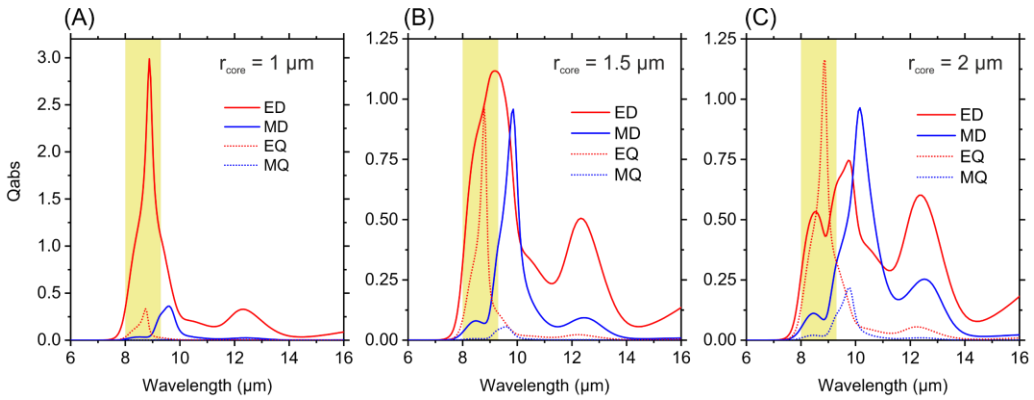

Figure 5.1. Absorption efficiency of the SiO2 sphere with a radius of (A) 1 μm, (B) 1.5 μm, and (C) 2 μm. The red and blue solid curves are the electric and magnetic dipole modes, respectively. The red and blue dashed curves are the electric and magnetic quadrupole modes, respectively.

Figure 5.1 shows the absorption efficiency of the electric dipole (ED), magnetic dipole (MD), electric quadrupole (EQ), and magnetic quadrupole (MQ) for the radius of 1 μm, 1.5 μm, and 2 μm. The yellow shaded area indicates the Reststrahlen band of SiO_2, which is the wavelength range of 8 – 9.3 μm [50]. In this band, the SiO_2 core supports a localized surface phonon polariton (LSPhP) [51]. ED and EQ for smaller radius have an absorption peak at a wavelength that satisfies the Fröhlich condition. Their absorption bandwidth is extremely narrow because of low loss of LSPhP. With increase in radius, both ED and EQ redshift and become broader because of an increase in radiative damping (see Section 5.7.1, Supporting Information) and an optical resonance induced outside of the Reststrahlen band. Magnetic modes cannot be excited inside the Reststrahlen band, therefore, the absorption peaks of MD and MQ are always outside of this band. Magnetic modes are excited when the dimension of the core is comparable to a wavelength inside the core so that magnetic modes redshift with increasing radius [52]. All modes of the Mie resonance have an absorption at a wavelength of around 12.5 μm, which is attributed to an intrinsic absorption of the transverse optical (TO) mode vibration of the Si-O bond [50]. The absorption at this wavelength increases with an increasing radius because the Mie resonances redshift and enhance electromagnetic fields inside the

SiO_2 core. Further increase of the radius makes quadrupole modes stronger and enables the core to support higher order modes. This results in a wider absorption bandwidth (see Section 5.7.1, Supporting Information) and should be avoided for a selective absorption in the primary ATW. In addition, higher order modes cause additional interactions with LSP of the ITO shell, which might degrade a selective absorption of the ITO@SiO_2 semishell absorber. Therefore, the core size should be small enough such that dipole modes dominate the total absorption of the SiO_2 core.

In the Reststrahlen band, the SiO_2 core acts like a metallic particle, meaning that the LSP of the inner surface of the ITO shell cannot be induced. Therefore, the LSP can interact only with the magnetic modes of the SiO_2 core. The SiO_2 core with 1 – 2 μm radius has its MD at around 10 μm, close to the middle of the primary ATW. This guarantees that an interaction between the LSP and MD inside the primary ATW. From these results, the proper size of the SiO_2 sphere is estimated to be 1 – 2 μm in radius.

5.3. ITO@SiO_2 semishell absorber

5.3.1. Design of the ITO@SiO_2 semishell absorber and FEM simulation

The simulation model of the ITO@SiO_2 semishell absorber is shown in Figure 5.2A. The ITO shell with thickness t_{shell} is on top of a SiO_2 core with radius r_{core}. The SiO_2 core is immobilized on a thin layer of Au. The Au layer not only reflects incoming radiation but also increases the absorption of the ITO@SiO_2 semishell structure. The ITO shell can be produced by ITO deposition on an SiO_2 nanoparticle adsorbed on an Au surface based on colloidal lithography. Therefore, we also take a perforated ITO film with thickness of t_{shell} on top of the Au reflector into account. The LSP of the perforated ITO film is not induced because of the electric conduction between the ITO film and the Au reflector. The thickness of the Au reflector is fixed as 200 nm, which is thick enough compared to the skin depth in the MIR range. The unit cell of the model has the periodicity P_{cell}.

We investigate the optical properties of the ITO@SiO_2 semishell absorber using COMSOL multiphysics, which is a commercial software package based on the finite element method (FEM). It is known that the exact optical properties of ITO depend on the deposition method [53–55]. For our investigation, the refractive index of ITO was obtained using Drude´s model with parameters in Ref. [53]. Refractive indices of SiO_2 and Au were obtained from Ref. [56, 57] and Ref. [58], respectively. The surrounding of the structure is air. According to Kirchhoff´s law, emissivity is equal to absorptivity, therefore, absorptivity of the structure was calculated to evaluate the thermal emission properties. The electromagnetic plane wave propagates along – *z* direction with *x* polarization. The amplitude of the electric field of the incident wave is E_0 = 1 V/m. The Bloch-Floquet periodic boundary conditions were applied in *x* and *y* direction. Perfectly matched layers are applied on the top and bottom of the simulation model (in the *z*-axis). The absorptivity $A(\lambda)$ was calculated by taking a volume integral of dissipated energy density over the structure and dividing the dissipated energy by the energy of the incident wave per area of the unit cell. This method gives the same result as another method, which calculates absorptivity by obtaining reflectance and transmittance of the structure (see Section 5.7.3, Supporting Information). For the evaluation, the average absorption in a wavelength range from λ_1 to λ_2 was calculated by $A_{\mathrm{ave}} = \frac{1}{\lambda_2 - \lambda_1} \int_{\lambda_1}^{\lambda_2} A(\lambda) \mathrm{d}\lambda$.

5.3.2. Absorption properties of the ITO@SiO_2 semishell absorber

We, next, turn our focus to the core-semishell structure and outline the relevance of r_{core} and t_{shell} on the absorptivity. For all calculations, P_{cell} is fixed as 7 μm. This periodicity was determined based on two

considerations: 1) The distance between the semishell structures needs to be large enough to weaken near-field interactions, which would lead to a broadening of the absorption bandwidth [11]. 2) However, P_{cell} should not be close to and exceed 8 μm (the shortest wavelength of the primary ATW). This is because the lattice resonance originated from the periodicity can interact with the LSP and the Mie resonances [59, 60], and the interaction degrades the absorption properties of the ITO@SiO_2 semishell absorber. Therefore, we selected 7 μm as the optimum P_{cell} even though the near-field interactions between the semishell structures are not negligible with this periodicity (see Section 5.7.2, Supporting Information). For r_{core} dependence (see Figure 5.2B), t_{shell} was fixed at 200 nm. The absorption bandwidth increases with an increase in r_{core} because larger SiO_2 core can support higher order modes of Mie resonance. The bandwidth is also broadened by the decrease of face-to-face distance between semishells, resulting in stronger lateral near-field interactions. In addition, the absorption of the semishell redshifts with increasing r_{core} so that the absorption increases especially in the longer wavelength range. For t_{shell} dependence (see Figure 5.2C), r_{core} was fixed at 1.4 μm. t_{shell} changes the spectral shape inside the primary ATW, but the absorption bandwidth does not change a lot for different values of t_{shell}. It is known that the absorption peak of the semishell can be controlled in a wider wavelength range by changing the radius, and in a narrower wavelength range by changing the thickness of the metal shell. Therefore, from r_{core} and t_{shell} dependences, we can find that r_{core} can be used to adjust the absorption bandwidth, and further optimizations for the selective absorption can be made by tuning t_{shell}.

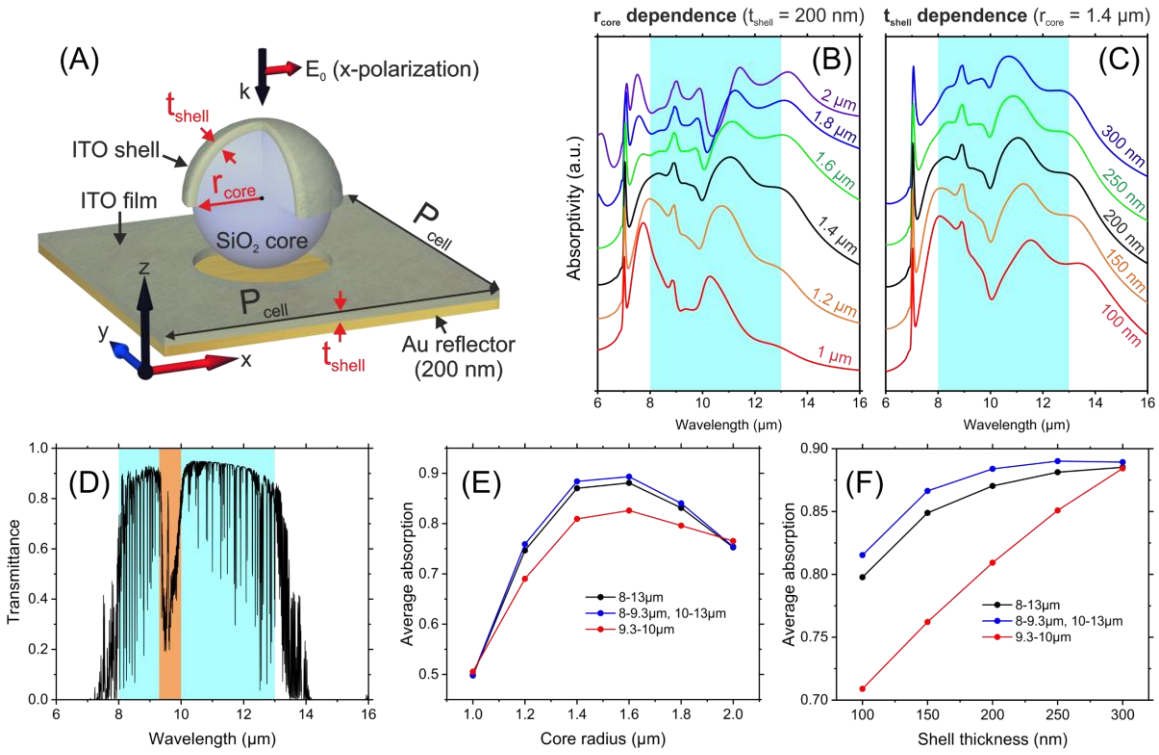

Figure 5.2. (A) A schematic illustration of the ITO@SiO_2 semishell structure. (B) r_{core} and (C) t_{shell} dependence of the absorptivity of the ITO@SiO_2 semishell structure. The blue shaded area indicates the primary ATW. (D) Transmittance of the atmosphere [61]. The blue and orange shaded areas indicate the actual primary ATW (8 – 9.3 μm and 10 – 13 μm) and the Ozone absorption band (9.3 – 10 μm), respectively. (E-F) Average absorption for Figures 5.2B and C. The black, blue, and red lines are average absorption in the primary ATW, the actual primary ATW, and the Ozone absorption band, respectively.

The average absorption was calculated for the spectra shown in Figures 5.2B and C at different wavelength ranges; the primary ATW (8 – 13 μm), Ozone absorption band (9.3 – 10 μm) [24], and the actual primary ATW (8 – 9.3 μm and 10 – 13 μm) (see Figure 5.2D). Figure 5.2E shows the average absorption for r_{core} dependence. The absorption is maximized for all wavelength ranges when r_{core} is around 1.4 – 1.6μm. The averaged absorption for r_{core} =1.4 μm and 1.6 μm in the primary ATW is 87% and 88%, respectively. This result shows that r_{core} = 1.6 μm has the highest average absorption, however, the full-width at half-maximum (FWHM) for r_{core} = 1.4 μm and 1.6 μm is about 7.7 μm and 9.4 μm, respectively. This indicates that the structure with r_{core} = 1.4 μm has a better selective absorption. Therefore, the best r_{core} is at about 1.4 μm. For t_{shell} dependence (see Figure 5.2F), FWHM is about 7.7 μm for all t_{shell}. The average absorption in the primary ATW increases with increase in t_{shell}, however, this doesn´t mean that a thicker t_{shell} has better absorption properties. With increase in t_{shell}, the absorption in the Ozone absorption range increases, which decreases the cooling power. In the actual primary ATW, the averaged absorption is maximized when t_{shell} is about 250 nm, and the value is 89%. When we check for t_{shell} = 200 nm, the average absorption is 88% in the actual primary ATW, which is 1% lower than that for t_{shell} = 250 nm. However, t_{shell} = 200 nm can have a lower absorption in the Ozone absorption range. Also, the ITO film has an intrinsic absorption and thinner ITO film absorbs less electromagnetic waves outside of the primary ATW (see Section 5.7.2, Supporting Information). Therefore, by considering all of those aspects, we decided on 200 nm as the best shell thickness.

To understand the absorption properties of the ITO@SiO_2 semishell absorber, the absorption of each component (ITO shell, SiO_2 core, perforated ITO film, Au reflector) was calculated for the structure with r_{core} = 1.4 μm and t_{shell} = 200 nm (see Figure 5.3A). We find that the total absorption is dominated by the ITO shell and the SiO_2 core absorption. The absorption of the ITO shell has three peaks (at 7.78 μm, 11.27 μm, and 13.5 μm) which are separated from each other. The absorption of the SiO_2 core has three peaks; two of them are close to each other (8.93 μm and 9.67 μm) and one of them (12.4 μm) is apart from those two peaks. A sharp peak at 7 μm is attributed to the lattice resonance. In Figure 5.3B, the absorption spectra of the structure with only SiO_2 core or only ITO shell are shown. Comparing to Figure 5.3A, those spectra are narrower and weaker than the total absorption of the ITO@SiO_2 semishell absorber. Therefore, it is found that a selective broadband absorption cannot be obtained from either only the ITO shell or from only the SiO_2 core. The SiO_2 core with and without the ITO shell has a similar absorption. However, the ITO shell has multiple peaks when it is combined with the SiO_2 core. The absorption of the ITO shell is split into two peaks and has a dip at the center of the absorption spectrum of the SiO_2 core. This indicates that the interaction between the LSP of the ITO shell and the Mie resonance of the SiO_2 core induce a mode splitting in the LSP. When we compare the absorption of the ITO@SiO_2 semishell absorber and the absorption of the SiO_2 core calculated using Mie theory, we find that the absorption dip of the ITO shell appears at around the absorption peak of the MD of the SiO_2 core (see Section 5.7.3, Supporting Information). This suggests that the mode splitting occurs because the LSP of the ITO shell interacts with the MD of the SiO_2 core. To support this statement further, we checked the absorption spectra in Figure 5.2B in detail. With increase in the core size, the absorption dip of the ITO shell redshifts. This may be because the MD of the SiO_2 core redshifts (see Section 5.7.2, Supporting Information). Even if the shell thickness changes, the dip does not shift because the MD does not shift (see Section 5.7.2, Supporting Information). The ITO shell has one more peak at 13.5 μm. This is also attributed to the mode splitting but not to the interaction between LSP and Mie resonance. This is because of the interaction between the LSP and the TO mode of SiO_2 [62].

The absorption mechanism of the proposed structure was investigated further by focusing on the four highest absorption peaks indicated by arrows in Figure 5.3A. For these resonances, we show the electric and magnetic field distribution color maps (see Figure 5.3C). Color maps were taken in the *x*-*z* plane at the center of the semishell. White arrows in electric maps represent electric field vectors. At 7.78 μm and 11.27 μm, there are electric field hot spots at the edge of the ITO shell and the magnetic field is enhanced inside

the shell. This is a characteristic field enhancement of the semishell [32, 33]. The LSP interacts with an image dipole created in the Au reflector, which enhances the electromagnetic field confinement [12]. At 8.93 μm, where the SiO_2 core has a sharp absorption peak, the electric field is not enhanced at the edge of the ITO shell, but it is strongly confined at the bottom of the SiO_2 core. The magnetic field is also confined there. Mie theory shows that the SiO_2 core has an ED and EQ at 8.93 μm (Section 5.7.3, Supporting Information), therefore, the absorption peak at 8.93 μm is attributed to the mixture of ED and EQ. Mie theory also shows that the second peak of the SiO_2 core at 9.67 μm is attributed to the mixture of ED and MD. Since the second peak is closer to the absorption peak of the MD than that of ED, the contribution of the MD is larger (Section 5.7.3, Supporting Information). At this wavelength, the magnetic field is strongly enhanced inside the SiO_2 core. There is a rotation of the electric field, and the magnetic field is enhanced at the center of the rotation by the MD of the SiO_2 core. The MD also interacts with an image dipole in the Au reflector, and the interaction widens the absorption bandwidth of the MD [63, 64]. The electric field at the edge of the ITO shell becomes weaker because of the interaction between the LSP of the ITO shell and the MD of the SiO_2 core. Therefore, the absorption dip appears in the absorption of the ITO shell at around 9.67 μm. One might think that an interaction between the LSP of the ITO shell and the ED of the SiO_2 core also contributes to the mode splitting. However, as mentioned earlier, the absorption of the ED is inside the Reststrahlen band of SiO_2, meaning that the LSP and the ED cannot interact with each other. Therefore, we can consider that the mode splitting is attributed to the interaction between the LSP of the shell and the MD of the core.

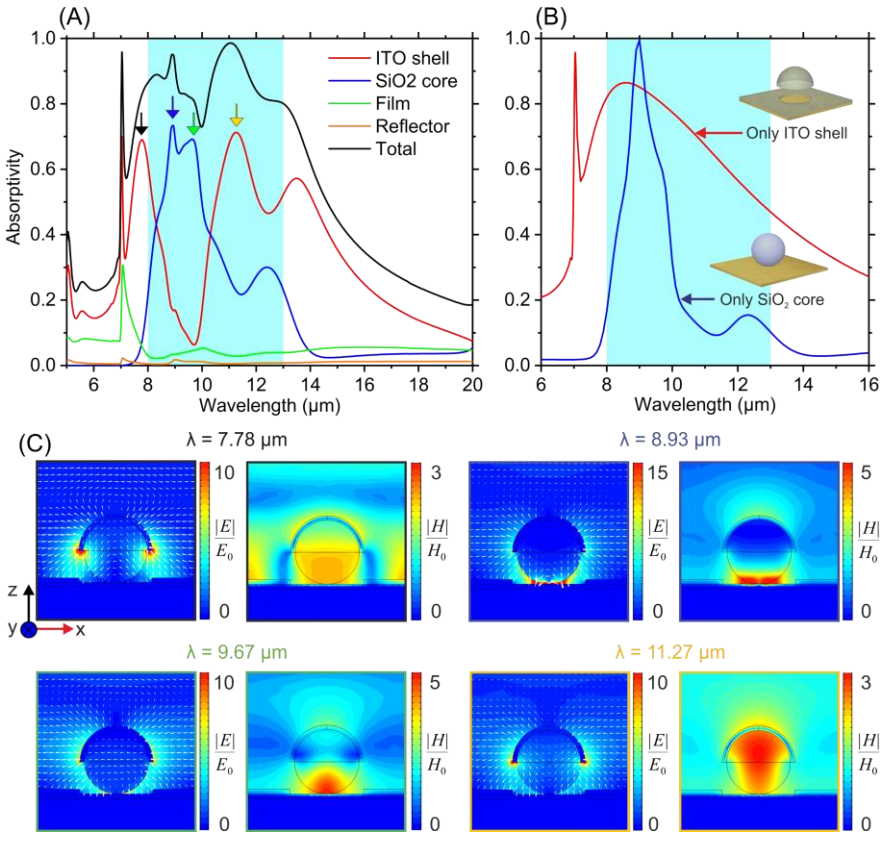

Figure 5.3. (A) Absorption spectra of each component of the ITO@SiO_2 semishell structure. The red, blue, green, and orange curves are for the ITO shell, SiO_2 core, perforated ITO film, and Au reflector, respectively. The black curve is the total absorption of the structure. (B) Color maps of electric and magnetic field distribution at wavelength indicated by arrows in Figure 5.3A. Absolute value of fields is normalized by amplitude of incident wave. The white arrows are electric field vectors.

5.4. Mode splitting mechanism

5.4.1. Coupled-oscillator model

We rationalize the mode splitting phenomena using a coupled-oscillator (CO) model, which is frequently used for a phenomenological analysis of plasmonic and photonic systems [39–41]. First, the CO model is built to describe the interaction between the LSP of ITO shell and the MD of the SiO_2 core (see Figure 5.4A). The LSP is considered as the bright oscillator with a higher damping rate and the MD is considered as the dark oscillator with a lower damping rate since the absorption bandwidth of the ITO shell is much wider than that of the MD. The equations of motion can be written as

$$\begin{aligned} \frac{\mathrm{d}^2 x_{\alpha 1}}{\mathrm{d}t^2} + \gamma_1 \frac{\mathrm{d}x_{\alpha 1}}{\mathrm{d}t} + \omega_1^2 x_{\alpha 1} - \kappa_{12}^2 x_{\alpha 2} &= F_1(t) \\ \frac{\mathrm{d}^2 x_{\alpha 2}}{\mathrm{d}t^2} + \gamma_2 \frac{\mathrm{d}x_{\alpha 2}}{\mathrm{d}t} + \omega_2^2 x_{\alpha 2} - \kappa_{12}^2 x_{\alpha 1} &= F_2(t) \end{aligned} \qquad 5.1$$

where x_n is the displacement of mass objects, γ_n is the damping rate, ω_n is the resonance angular frequency determined by the spring constant, and κ_{1n} is the coupling strength. $F_n(t)$ is the external force per mass, which works on the oscillators. $F_n(t)$ is time harmonic and expressed as $F_n(t) = F_n \exp(-i\omega t)$. Therefore, displacements are also time harmonic and can be expressed as $x_n = c_n \exp(-i\omega t)$. From Equation 5.1, x_n is written as

$$\begin{aligned} x_{\alpha 1} &= \frac{\Omega_2 F_1 + \kappa_{12}^2 F_2}{\Omega_1 \Omega_2 - \kappa_{12}^4} \exp(-i\omega t) = c_{\alpha 1} \exp(-i\omega t) \\ x_{\alpha 2} &= \frac{\Omega_1 F_2 + \kappa_{12}^2 F_1}{\Omega_1 \Omega_2 - \kappa_{12}^4} \exp(-i\omega t) = c_{\alpha 2} \exp(-i\omega t) \end{aligned} \qquad 5.2$$

where $\Omega_n = \omega_n^2 - \omega^2 - i\gamma_n \omega$. Using Equation 5.2, the time averaged dissipated power per mass of the whole system is

$$P(\omega) = \left\langle \mathrm{Re}\left[F_1^*(t) \times \frac{\mathrm{d}x_1}{\mathrm{d}t}\right]\right\rangle + \left\langle \mathrm{Re}\left[F_2^*(t) \times \frac{\mathrm{d}x_2}{\mathrm{d}t}\right]\right\rangle \qquad 5.3$$

Equation 5.3 can be divided into two terms using the absolute value of the amplitude of each oscillator (see Section 5.7.4, Supporting Information)

$$P_\alpha(\omega) = \frac{1}{2}\gamma_1 \omega^2 |c_{\alpha 1}|^2 + \frac{1}{2}\gamma_2 \omega^2 |c_{\alpha 2}|^2 = A_{\alpha 1}(\omega) + A_{\alpha 2}(\omega) \qquad 5.4$$

In Equation 5.4, the first term corresponds to an absorption of the bright oscillator (the LSP of the ITO shell) and the second term is an absorption of the dark oscillator (the MD of the SiO_2 core). In addition, the interaction between the LSP and the TO mode of SiO_2 induces the mode splitting at around 12 μm, which has to be considered as well to describe the absorption spectrum of the ITO shell. In this case, one more dark oscillator should be added (see Figure 5.4B). The external force does not work on the third oscillator because the TO mode weakly couples to the incident field. The equations of motion for the three-oscillator CO model are

$$\frac{\mathrm{d}^2 x_{\beta 1}}{\mathrm{d}t^2} + \gamma_1 \frac{dx_{\beta 1}}{dt} + \omega_1^2 x_{\beta 1} - \kappa_{12}^2 x_{\beta 2} - \kappa_{13}^2 x_{\beta 3} = F_1(t)$$
$$\frac{d^2 x_{\beta 2}}{dt^2} + \gamma_2 \frac{dx_{\beta 2}}{dt} + \omega_2^2 x_{\beta 2} - \kappa_{12}^2 x_{\beta 1} = F_2(t) \qquad 5.5$$
$$\frac{d^2 x_{\beta 3}}{dt^2} + \gamma_3 \frac{dx_{\beta 3}}{dt} + \omega_3^2 x_{\beta 3} - \kappa_{13}^2 x_{\beta 1} = 0$$

The oscillation state of each oscillator in Equation 5.5 can be expressed by the following equations

$$x_{\beta 1} = \frac{\Omega_2 \Omega_3 F_1 + \kappa_{12}^2 \Omega_3 F_2}{\Omega_1 \Omega_2 \Omega_3 - \kappa_{12}^4 \Omega_3 - \kappa_{13}^4 \Omega_2} \exp(-i\omega t) = c_{\beta 1} \exp(-i\omega t)$$
$$x_{\beta 2} = \frac{(\Omega_1 \Omega_3 - \kappa_{13}^4) F_2 + \kappa_{12}^2 \Omega_3 F_1}{\Omega_1 \Omega_2 \Omega_3 - \kappa_{12}^4 \Omega_3 - \kappa_{13}^4 \Omega_2} \exp(-i\omega t) = c_{\beta 2} \exp(-i\omega t) \qquad 5.6$$
$$x_{\beta 3} = \frac{\kappa_{13}^2 (\Omega_2 F_1 + \kappa_{12}^2 F_2)}{\Omega_1 \Omega_2 \Omega_3 - \kappa_{12}^4 \Omega_3 - \kappa_{13}^4 \Omega_2} \exp(-i\omega t) = c_{\beta 3} \exp(-i\omega t)$$

From Equations 5.3 and 5.6, the total dissipated power of the system illustrated in Figure 5.4B is

$$P_\beta(\omega) = \frac{1}{2}\gamma_1 \omega^2 |c_{\beta 1}|^2 + \frac{1}{2}\gamma_2 \omega^2 |c_{\beta 2}|^2 + \frac{1}{2}\gamma_3 \omega^2 |c_{\beta 3}|^2 = A_{\beta 1}(\omega) + A_{\beta 2}(\omega) + A_{\beta 3}(\omega) \qquad 5.7$$

where the third term describes the absorption of the TO mode of SiO_2. First, the dissipated power of a single harmonic oscillator model was fitted to the absorption of the ITO shell in Figure 5.3B to extract parameters for the bright oscillator (see Section 5.7.4, Supporting Information). From the fitting, the resonance angular frequency and the damping rate are $\omega_1 = 2.15 \times 10^{14}$ rad/s and $\gamma_1 = 1.5 \times 10^{14}$ rad/s. Next, $A_{\beta 1}(\omega)$ in Equation 5.7 was fitted to the absorption of the ITO shell in Figure 5.3A. The fitting resulted in $\omega_2 = 1.93 \times 10^{14}$ rad/s, $\gamma_2 = 1.4 \times 10^{13}$ rad/s, $\kappa_{12} = 1.16 \times 10^{14}$ rad/s for the MD and $\omega_3 = 1.51 \times 10^{14}$ rad/s, $\gamma_3 = 1.7 \times 10^{13}$ rad/s, $\kappa_{13} = 6.6 \times 10^{13}$ rad/s for the TO mode. In Figure 5.4C, $A_{\beta 1}(\omega)$, $A_{\beta 2}(\omega)$ and $A_{\beta 3}(\omega)$ are shown. Even if the interactions occurring in the ITO@SiO_2 semishell absorber are complex, $A_{\beta 1}(\omega)$ shows good agreement with the absorption spectrum of the ITO shell. The coupling state can be categorized roughly into a strong or weak coupling regime by comparing the total damping rate of the system $(\gamma_1\gamma_n)^{1/2}$ and the coupling strength κ_{1n} [44]. In general, the interaction is considered as a strong coupling when $\kappa_{1n} >> (\gamma_1\gamma_n)^{1/2}$ because the energy transfer rate between two oscillators can be quicker than their energy dissipation rates. The total damping rate of the LSP-MD is $(\gamma_1\gamma_2)^{1/2} = 4.58 \times 10^{13}$ rad/s, and that of the LSP-TO mode is $(\gamma_1\gamma_3)^{1/2} = 5.05 \times 10^{13}$ rad/s. For those interactions, the coupling strengths are larger than the total damping rates. However, the values obtained in our case are comparable, which may be considered as an intermediately strong coupling. In this coupling regime, absorption enhancement takes place in the dark oscillators because the transferred energy is concentrated into the dark oscillators [42–44]. This absorption enhancement can be observed by comparing the absorption of the SiO_2 core with and without the ITO shell at around 10 – 11 μm (see Section 5.7.4, Supporting Information).

It is obvious that the mode splitting by the interaction between the LSP and the MD improves absorption in the primary ATW. To understand how the interaction between the LSP and the TO mode contribute to the absorption of the ITO@SiO_2 semishell absorber, $A_{\beta 1}(\omega)$ is compared with $A_{\alpha 1}(\omega)$ in Equation 5.4, which is calculated using ω_2, γ_2, and κ_{12} from the fitting. $A_{\beta 1}(\omega)$ has a similar spectral shape to $A_{\alpha 1}(\omega)$ in the shorter wavelength range. In the longer wavelength range, $A_{\beta 1}(\omega)$ is weaker inside and is

larger outside of the primary ATW than $A_{\alpha 1}(\omega)$. This comparison indicates that the mode splitting by the TO mode weakens the cooling performance, which cannot be eliminated because the TO mode is the intrinsic Si-O bond vibration of SiO_2. Overall, an undesired broadening of the absorption occurs outside of the primary ATW by the TO mode, however, absorption inside the primary ATW is improved significantly by the interaction between the LSP and the MD. The absorption of the MD is not strong enough to compensate the absorption dip of the ITO shell. However, there are strong absorptions of ED and EQ of SiO_2 core in between two absorption peaks of the ITO shell, which results in a strong broadband absorption in the primary ATW.

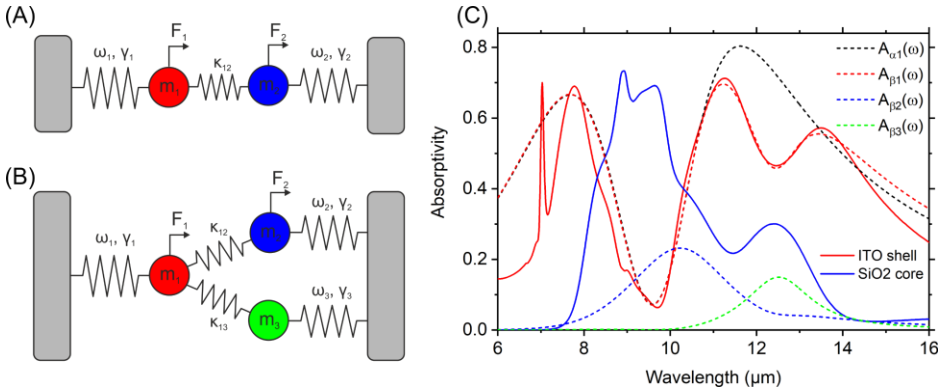

Figure 5.4. (A) Two-oscillator CO model describing the interaction between the LSP of the ITO shell and the MD of the SiO_2 core. (B) Three-oscillator CO model where one additional oscillator is added to the two-oscillator CO model to account for the interaction between the LSP of the ITO shell and the TO mode of SiO_2. (C) The CO model is fitted to the absorption of the ITO shell. The red and blue solid curves are absorption spectra of the ITO shell and the SiO_2 core in Figure 5.3A, respectively. The black dashed curve is absorption calculated from Equation 5.4 and the red, blue, green dashed curves are absorption calculated from Equation 5.7.

5.4.2. Coupled-dipole method

The mechanisms of the interaction between LSP and a molecular vibration have been extensively investigated not only theoretically but also experimentally, and it is known that the interaction can be described by the CO model [41]. To gain a deeper insight into the mechanism of the LSP-MD interaction, further quantitative analysis was employed using the coupled-dipole method (CDM). The CDM is one of the methods that can describe interactions between electric and magnetic dipoles. In our case, the electric dipole is LSP. Later, this CDM will be compared with the CO model shown in Fig. 4(A). General treatments of the CDM can be found elsewhere [60, 63, 65]. Here, we treat only one ED and one MD [66]. The schematic of the CDM model for the ED of the ITO shell and the MD of the SiO_2 core is shown in Figure 5.5A. The distance between two dipoles is D. The positions of each dipole are $\mathbf{r}_1$ = (0, 0, -D/2) for ED and $\mathbf{r}_2$ = (0, 0, D/2) for MD. The incident wave propagates along +z direction with x polarization. The electric and magnetic fields are expressed as $\mathbf{E}_{\text{in}} = E_0\hat{\mathbf{e}}_{\text{x}}\exp(\text{i}\mathbf{k}\cdot\mathbf{r})$and $\mathbf{H}_{\text{in}} = H_0\hat{\mathbf{e}}_{\text{y}}\exp(\text{i}\mathbf{k}\cdot\mathbf{r})$, where $\hat{\mathbf{e}}$ is the unit vector in Cartesian coordinate system and $\mathbf{k}$ is the wavevector. Here, the dipole moments are expressed as

$$\mathbf{p}_1 = \varepsilon_0\alpha_1\mathbf{E}_{\text{tot}}(\mathbf{r}_1) \qquad 5.8$$

$$\mathbf{m}_2 = \chi_2\mathbf{H}_{\text{tot}}(\mathbf{r}_2) \qquad 5.9$$

where ε_0 is the vacuum permittivity, and α_1 and χ_2 are the electric polarizability of LSP and the magnetic polarizability of MD, respectively. $\mathbf{E}_{tot}$ and $\mathbf{H}_{tot}$ are total electric and magnetic fields, which are the sum of the incident field and scattered field from other dipoles. The scattered electric field at $\mathbf{r}_1$ created by $\mathbf{m}_2$ and the scattered magnetic field at $\mathbf{r}_2$ created by $\mathbf{p}_1$ are

$$\mathbf{E}_{\mathrm{s}}(\mathbf{r}_1) = -Z_0\mathbf{G}_{\mathrm{M}}(\mathbf{r}_1 - \mathbf{r}_2)\cdot\mathbf{m}_2 \tag{5.10}$$

$$\mathbf{H}_{\mathrm{s}}(\mathbf{r}_2) = \frac{1}{\varepsilon_0 Z_0}\mathbf{G}_{\mathrm{M}}(\mathbf{r}_2 - \mathbf{r}_1)\cdot\mathbf{p}_1 \tag{5.11}$$

where Z_0 is the impedance of free space. $\mathbf{G}_{\mathrm{M}}$ is the dyad Green´s function which is written using $\mathbf{r}_1 - \mathbf{r}_2 = -D\hat{\mathbf{e}}_{\mathrm{z}}$, $\mathbf{r}_2 - \mathbf{r}_1 = D\hat{\mathbf{e}}_{\mathrm{z}}$, and

$$\mathbf{G}_{\mathrm{M}}(\mathbf{r}_1 - \mathbf{r}_2)\cdot\mathbf{n} = -\mathbf{G}_{\mathrm{M}}(\mathbf{r}_2 - \mathbf{r}_1)\cdot\mathbf{n} = (-\hat{\mathbf{e}}_{\mathrm{z}}\times\mathbf{n})C(D) \tag{5.12}$$

where $\mathbf{n}$ is an arbitrary vector. $C(D)$ is written as

$$\begin{aligned} C(D) &= \frac{\exp(ikD)}{4\pi D}\left(k^2 + \frac{ik}{D}\right) = \frac{\exp(ikD)}{4\pi D}\sqrt{k^4 + \frac{k^2}{D^2}}\exp\left[i\tan^{-1}\left(\frac{1}{kD}\right)\right] \\ &= i|C|\exp\{i[kD - \tan^{-1}(kD)]\} = i|C|\exp(i\varphi) \end{aligned} \tag{5.13}$$

where φ is the phase difference. From Equations 5.10-5.11, Equations 5.8-5.9 can be written as

$$\mathbf{p}_1 = \varepsilon_0\alpha_1[\mathbf{E}_{\mathrm{in}}(\mathbf{r}_1) + \mathbf{E}_{\mathrm{s}}(\mathbf{r}_1)] = \varepsilon_0\alpha_1\mathbf{E}_{\mathrm{in}}(\mathbf{r}_1) - \varepsilon_0\alpha_1 Z_0\mathbf{G}_{\mathrm{M}}(\mathbf{r}_1 - \mathbf{r}_2)\cdot\mathbf{m}_2 \tag{5.14}$$

$$\mathbf{m}_2 = \chi_2[\mathbf{H}_{\mathrm{in}}(\mathbf{r}_2) + \mathbf{H}_{\mathrm{s}}(\mathbf{r}_2)] = \chi_2\mathbf{H}_{\mathrm{in}}(\mathbf{r}_2) + \frac{1}{\varepsilon_0 Z_0}\chi_2\mathbf{G}_{\mathrm{M}}(\mathbf{r}_2 - \mathbf{r}_1)\cdot\mathbf{p}_1 \tag{5.15}$$

From Equations 5.14-5.15, a self-consistent form of $\mathbf{p}_1$ and $\mathbf{m}_2$ are (see Section 5.7.5, Supporting Information)

$$\mathbf{p}_1 = p_{1\mathrm{x}}\hat{\mathbf{e}}_{\mathrm{x}} = \varepsilon_0\frac{\alpha_1\exp\left(-i\frac{kD}{2}\right) - \alpha_1\chi_2 C(D)\exp\left(i\frac{kD}{2}\right)}{1 + \alpha_1\chi_2 C^2(D)}E_0\hat{\mathbf{e}}_{\mathrm{x}} \tag{5.16}$$

$$\mathbf{m}_2 = m_{2\mathrm{y}}\hat{\mathbf{e}}_{\mathrm{y}} = \frac{\chi_2\exp\left(i\frac{kD}{2}\right) + \alpha_1\chi_2 C(D)\exp\left(-i\frac{kD}{2}\right)}{1 + \alpha_1\chi_2 C^2(D)}H_0\hat{\mathbf{e}}_{\mathrm{y}} \tag{5.17}$$

$Z_0H_0 = E_0$ was used to derive Equations 5.16-5.17. To understand the excitation state of those dipole moments, α_1 and χ_2 are considered by approximation using the Lorentzian oscillator

$$\alpha_1 = \frac{F_{\mathrm{p}}}{\omega_{\mathrm{p}}^2 - \omega^2 - i\gamma_{\mathrm{p}}\omega} = \frac{F_{\mathrm{p}}}{\Omega_{\mathrm{p}}} \tag{5.18}$$

$$\chi_2 = \frac{F_m}{\omega_{\mathrm{m}}^2 - \omega^2 - i\gamma_{\mathrm{m}}\omega} = \frac{F_{\mathrm{m}}}{\Omega_{\mathrm{m}}} \tag{5.19}$$

where F_{p} and F_{m} are oscillator strength, ω_{p} and ω_{m} are resonance frequencies, and γ_{p} and γ_{m} are damping rates for ED and MD, respectively. Note that the size of the ITO shell and the SiO_2 core are not in the quasi-static limit ($kr_{\mathrm{core}} << 1$). In this case, radiative damping and retardation effect have to be taken into account in the damping rate of Equations 5.18-5.19 [83, 85]. However, we are only interested in phenomenological analysis, therefore, those effects were ignored. Substituting Equations 5.18-5.19 into Equations 5.16-5.17 and using the other form for $C(D)$, we obtain the electric and magnetic dipole moments as

$$p_{1x} = \varepsilon_0 \frac{\Omega_m F_p \exp\left(-i\frac{kD}{2}\right) - iF_p F_m |C| \exp(i\varphi) \exp\left(i\frac{kD}{2}\right)}{\Omega_p \Omega_m - F_p F_m |C|^2 \exp(i2\varphi)} E_0 \quad 5.20$$

$$m_{2y} = \frac{\Omega_p F_m \exp\left(i\frac{kD}{2}\right) + iF_p F_m |C| \exp(i\phi) \exp\left(-i\frac{kD}{2}\right)}{\Omega_p \Omega_m - F_p F_m |C|^2 \exp(i2\varphi)} H_0 \quad 5.21$$

It should be mentioned that Equations 5.20-5.21 from the CDM cannot explain everything about the LSP-MD interaction occurring in the ITO@SiO_2 semishell because the ITO shell is touching the SiO_2 core. In this situation, their dipoles are extremely close to each other, which the CDM cannot take into account because $|C|$ diverges at $D \rightarrow 0$. Therefore, the near-field should be carefully investigated. However, the CDM model is still useful to estimate the excitation states of interacting dipoles. Equations 5.20 and 5.21 resemble Equation 5.2 derived from the CO model. Comparing those equations, we find that the coupling strength squared κ_{12}^2 is proportional to $|C|\exp(i\varphi)$, indicating that there is a phase retardation in the coupling. This phase retardation can be found in the CO model, which describes electromagnetically induced absorption (EIA) of a plasmonic system: a dipolar antenna is vertically stacked over a quadrupolar antenna [69, 70]. Ref. [69] shows that the interaction can be destructive and show the mode splitting when the phase is 0°. On the other hand, the interaction can be constructive when the phase is 90°, resulting in EIA. In the LSP-MD interaction, D is required to be relatively large to satisfy φ = 90° (Figure 5.5B). However, the coupling strength is approximately inversely proportional to D so that it is expected to be difficult to excite a strong EIA by the LSP-MD interaction because the coupling becomes weak when φ = 90°. Since our interest is in the mode splitting by the LSP-MD interaction, it is out of scope of this paper to discuss EIA further. However, it is worth to mention that the LSP-MD interaction may be capable of exciting the EIA-like phenomena if the coupling strength could be maintained strong enough at large D.

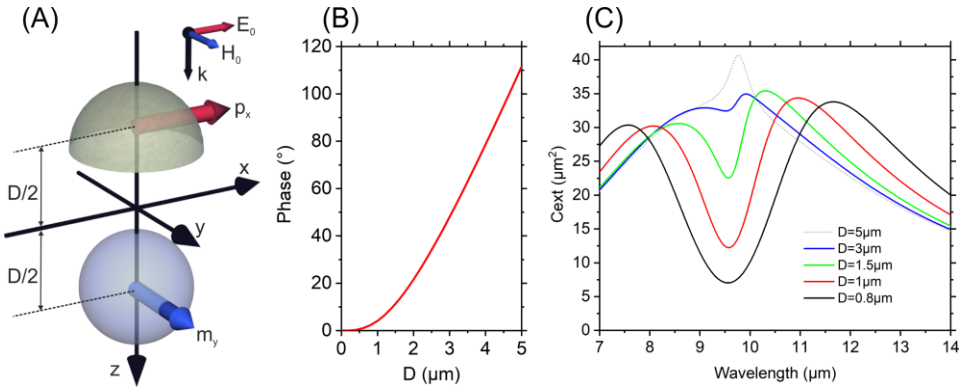

Figure 5.5. (A) A schematic illustration of the CDM for the interaction between the LSP of the ITO shell and the MD of the SiO_2 core. (B) The phase φ calculated using Equation 5.13. (C) Extinction spectra of interacting ED and MD.

To see whether the interaction between ED and MD shows mode splitting, the extinction cross-section of the system shown in Figure 5.5A was calculated following the equation [60, 65]

$$C_{ext} = \frac{k}{\varepsilon_0 |E_0|^2} \mathrm{Im}[\mathbf{E}_{in}^*(\mathbf{r}_1) \cdot \mathbf{p}_1 + \mu_0 \mathbf{H}_{in}^*(\mathbf{r}_2) \cdot \mathbf{m}_2] \quad 5.22$$

where μ_0 is the vacuum permeability and the asterisk denotes the complex conjugate. For the calculation of Equation 5.22, Equations 5.16 and 5.17 were used for $\mathbf{p}_1$ and $\mathbf{m}_2$, and Equations 5.18 and 5.19 were used

for the electric and magnetic polarizabilities in Equations 5.16 and 5.17 (see Section 5.7.6, Supporting Information). In Figure 5.5C, the extinction spectra calculated using Equation 5.22 are shown for different *D*. When $D = 5$ μm, there is almost no interaction between the ED and the MD. The sharp extinction peak of the MD of the SiO_2 sphere appears on the broad extinction of the ED of the ITO shell because the extinction is the superposition of contributions from ED and MD. With decrease in *D*, the extinction spectra start splitting and the splitting becomes larger. This is attributed to the fact that the interaction becomes stronger because the coupling strength is approximately inversely proportional to *D*. From Figure 5.5B, when *D* is smaller than 1 μm, there is almost no phase difference (less than about 4°). In the case of the ITO@SiO_2 semishell, the distance between ED and MD is expected to be smaller than 1μm. Therefore, we can recognize that the interaction is in a strong coupling state without the phase difference, which coincides the CO model shown in Figure 5.4A.

5.5. Conclusion

The absorption properties of an ITO@SiO_2 semishell absorber were investigated using Mie theory and FEM for radiative cooling. We demonstrated that this simple plasmonic-photonic composite structure can possess a selective absorption by optimizing the thickness of the ITO shell and the radius of the SiO_2 core. The optimized structure has an average absorption of 87 % in the primary ATW. When either the shell or the core is absent in the structure, this selective broadband absorption cannot be obtained. By investigating the absorption of each component of the proposed structure, we found that the absorption of the shell splits into two peaks and the absorption dip of the shell appears at the wavelength where the MD is excited in the SiO_2 core. Therefore, we attributed the mode splitting to the interaction between the LSP of the shell and the MD of the core. To understand the mode splitting mechanisms, the interaction was quantitatively investigated using a CO model and the CDM. The quantitative analyses proved that the strong interaction between LSP and MD can cause the mode splitting in the LSP of the shell. In addition to this finding, these quantitative models suggested two following things. Firstly, the absorption of the MD may be enhanced by the LSP-MD interaction because the transferred energy is concentrated on the MD. Secondly, the LSP-MD interaction may be possible to induce an EIA-like phenomena by controlling the distance between the electric and magnetic dipole moments. Further investigation is necessary to completely prove them, however, those fundamental understandings of how LSP interacts with MD provide an approach to design a new type of plasmonic and photonic structures not only for radiative cooling systems but also other applications such as chemical sensors.

For high cooling performance, incident angle insensitivity of the absorption is required. However, in this paper, a periodic structure was considered, and the periodicity is close to the primary ATW. In this case, the lattice resonance redshifts with an increase in the incident angle, which result in a degradation of absorption properties (see Section 5.7.7, Supporting Information). This undesired lattice resonance can be eliminated by randomly distributing semishells on the reflector [14, 15]. The strong selective absorption is attributed to the absorption properties of a single particle of the semishell. Therefore, it is expected that the absorption properties shown in this paper will be preserved for the structure with random distribution of the semishells [14, 15]. The proposed structure can be fabricated by relatively simple processes using colloidal lithography and ITO deposition, and the colloidal lithography can produce random distribution of particles on a large area [16, 36]. Therefore, we expect that it is possible to produce a scalable radiative cooling system with the proposed structure.

We must mention a drawback of the proposed structure for *daytime* radiative cooling. In the visible to near-infrared regions, the proposed structure may have a strong absorption because of the intrinsic ITO film and Au reflector absorption properties (see Section 5.7.8, Supporting Information). Therefore, we expect

that the radiative cooling ability of the proposed structure is attenuated under sunlight exposure. To overcome this problem, improvements in the proposed structure are required by replacing the ITO film, by using a different material for the reflector, or by combining our structure with a solar reflector/scatter [71, 72].

Funding

European Research Council (ERC) under the European Union´s Horizon 2020 research and innovation program (grant agreement no. 714968)

5.6. References

1. B. Zhao, M. Hu, X. Ao, N. Chen, and G. Pei, "Radiative cooling: A review of fundamentals, materials, applications, and prospects," Applied Energy **236**, 489-513 (2019).
2. Z. Huang, and X. Ruan, "Nanoparticle embedded double-layer coating for daytime radiative cooling," International Journal of Heat and Mass Transfer **104**, 890-896 (2017).
3. L. Zhu, A. P. Raman, and S. Fan, "Radiative cooling of solar absorbers using a visibly transparent photonic crystal thermal blackbody," PNAS **112**(40), 12282-12287 (2015).
4. J.-l. Kou, Z. Jurado, Z. Chen, S. Fan, and A. J. Minnich, "Daytime Radiative Cooling Using Near-Black Infrared Emitters," ACS Photonics **4**(3), 626-630 (2017).
5. S. Atiganyanun, J. B. Plumley, S. J. Han, K. Hsu, J. Cytrynbaum, T. L. Peng, S. M. Han, and S. E. Han, "Effective Radiative Cooling by Paint-Format Microsphere-Based Photonic Random Media," ACS Photonics **5**(4), 1181-1187 (2018).
6. S. Zeng, S. Pian, M. Su, Z. Wang, M. Wu, X. Liu, M. Chen, Y. Xiang, J. Wu, M. Zhang, Q. Cen, Y. Tang, X. Zhou, Z. Huang, R. Wang, A. Tunuhe, X. Sun, Z. Xia, M. Tian, M. Chen, X. Ma, L. Yang, J. Zhou, H. Zhou, Q. Yang, X. Li, Y. Ma, and G. Tao, "Hierarchical-morphology metafabric for scalable passive daytime radiative cooling," Science **373**(6555), 692-696 (2021).
7. H. Chalabi, D. Schoen, and M. L. Brongersma, "Hot-electron photodetection with a plasmonic nanostripe antenna," Nano Lett. **14**(3), 1374-1380 (2014).
8. A. K. Azad, W. J. Kort-Kamp, M. Sykora, N. R. Weisse-Bernstein, T. S. Luk, A. J. Taylor, D. A. Dalvit, and H. T. Chen, "Metasurface Broadband Solar Absorber," Sci. Rep. **6**, 20347 (2016).
9. H. Wang, and L. Wang, "Perfect selective metamaterial solar absorbers," Opt. Express **21**(6), A1078-1093 (2013).
10. X. Liu, T. Tyler, T. Starr, A. F. Starr, N. M. Jokerst, and W. J. Padilla, "Taming the blackbody with infrared metamaterials as selective thermal emitters," Phys. Rev. Lett. **107**(4), 045901 (2011).
11. S. D. Rezaei, J. Ho, R. J. H. Ng, S. Ramakrishna, and J. K. W. Yang, "On the correlation of absorption cross-section with plasmonic color generation," Opt. Express **25**(22), 27652-27664 (2017).
12. C. Wu, B. Neuner, G. Shvets, J. John, A. Milder, B. Zollars, and S. Savoy, "Large-area wide-angle spectrally selective plasmonic absorber," Phys. Rev. B **84**(7), 075102 (2011).
13. J. M. Hao, L. Zhou, and M. Qiu, "Nearly total absorption of light and heat generation by plasmonic metamaterials," Phys. Rev. B **83**(16), 165107 (2011).

14. A. Tittl, M. G. Harats, R. Walter, X. Yin, M. Schaferling, N. Liu, R. Rapaport, and H. Giessen, "Quantitative angle-resolved small-spot reflectance measurements on plasmonic perfect absorbers: impedance matching and disorder effects," ACS Nano **8**(10), 10885-10892 (2014).

15. P. Chevalier, P. Bouchon, J. Jaeck, D. Lauwick, N. Bardou, A. Kattnig, F. Pardo, and R. Haïdar, "Absorbing metasurface created by diffractionless disordered arrays of nanoantennas," Appl. Phys. Lett. **107**(25), 251108 (2015).

16. R. Walter, A. Tittl, A. Berrier, F. Sterl, T. Weiss, and H. Giessen, "Large-Area Low-Cost Tunable Plasmonic Perfect Absorber in the Near Infrared by Colloidal Etching Lithography," Adv. Optical Mater. **3**(3), 398-403 (2015).

17. C.-W. Cheng, "Wide-angle polarization independent infrared broadband absorbers based on metallic multisized disk arrays," Opt. Express **20**(9), 10376-10381 (2012).

18. N. W. Pech-May, L. Tobias, and M. Retsch, "Design of Multimodal Absorption in the Mid-IR: A Metal Dielectric Metal Approach," ACS Appl. Mater. Interfaces **13**(1), 1921-1929 (2021).

19. Y. Cui, K. H. Fung, J. Xu, H. Ma, Y. Jin, S. He, and N. X. Fang, "Ultrabroadband light absorption by a sawtooth anisotropic metamaterial slab," Nano Lett. **12** (3), 1443-1447 (2012).

20. D. Ji, H. Song, X. Zeng, H. Hu, K. Liu, N. Zhang, and Q. Gan, "Broadband absorption engineering of hyperbolic metafilm patterns," Sci. Rep. **4**, 4498 (2014).

21. M. M. Hossain, B. Jia, and M. Gu, "A Metamaterial Emitter for Highly Efficient Radiative Cooling," Adv. Optical Mater. **3**(8), 1047-1051 (2015).

22. E. Rephaeli, A. Raman, and S. Fan, "Ultrabroadband photonic structures to achieve high-performance daytime radiative cooling," Nano Lett. **13**(4), 1457-1461 (2013).

23. A. P. Raman, M. A. Anoma, L. Zhu, E. Rephaeli, and S. Fan, "Passive radiative cooling below ambient air temperature under direct sunlight," Nature **515**(7528), 540-544 (2014).

24. Y. Shi, W. Li, A. Raman, and S. Fan, "Optimization of Multilayer Optical Films with a Memetic Algorithm and Mixed Integer Programming," ACS Photonics **5**(3), 684-691 (2017).

25. A. R. Gentle, and G. B. Smith, "Radiative heat pumping from the Earth using surface phonon resonant nanoparticles," Nano Lett. **10**(2), 373-379 (2010).

26. Y. Zhai, Y. Ma, S. N. David, D. Zhao, R. Lou, G. Tan, R. Yang, and X. Yin, "Scalable-manufactured randomized glass-polymer hybrid metamaterial for daytime radiative cooling," Science **355**(6329), 1062-1066 (2017).

27. R. Zhu, D. Hu, Z. Chen, X. Xu, Y. Zou, L. Wang, and Y. Gu, "Plasmon-Enhanced Infrared Emission Approaching the Theoretical Limit of Radiative Cooling Ability," Nano Lett. **20**(10), 6974-6980 (2020).

28. A. Srinivasan, B. Czapla, J. Mayo, and A. Narayanaswamy, "Infrared dielectric function of polydimethylsiloxane and selective emission behavior," Appl. Phys. Lett. **109**(6), 061905 (2016).

29. U. Banik, A. Agrawal, H. Meddeb, O. Sergeev, N. Reininghaus, M. Gotz-Kohler, K. Gehrke, J. Stuhrenberg, M. Vehse, M. Sznajder, and C. Agert, "Efficient Thin Polymer Coating as a Selective Thermal Emitter for Passive Daytime Radiative Cooling," ACS Appl. Mater. Interfaces **13**(20), 24130-24137 (2021).

30. A. I. Maaroof, M. B. Cortie, N. Harris, and L. Wieczorek, "Mie and Bragg plasmons in subwavelength silver semi-shells," Small **4**(12), 2292-2299 (2008).

31. M. Frederiksen, V. E. Bochenkov, M. B. Cortie, and D. S. Sutherland, "Plasmon Hybridization and Field Confinement in Multilayer Metal–Dielectric Nanocups," J. Phys. Chem. C **117**(30), 15782-15789 (2013).

32. M. Cortie, and M. Ford, "A plasmon-induced current loop in gold semi-shells," Nanotechnology **18**(23), 235704 (2007).

33. N. A. Mirin, and N. J. Halas, "Light-Bending Nanoparticles," Nano Lett. **9**(3), 1255-1259 (2009).

34. N. Vogel, M. Retsch, C. A. Fustin, A. Del Campo, and U. Jonas, "Advances in colloidal assembly: the design of structure and hierarchy in two and three dimensions," Chem. Rev. **115**(13), 6265-6311 (2015).

35. K. Takatori, T. Okamoto, and K. Ishibashi, "Surface-plasmon-induced ultra-broadband light absorber operating in the visible to infrared range," Opt. Express **26**(2), 1342-1350 (2018).

36. K. Matsumori, and R. Fujimura, "Broadband light absorption of an Al semishell-MIM nanostrucure in the UV to near-infrared regions," Opt. Lett. **43**(12), 2981-2984 (2018).

37. W. Yu, Y. Lu, X. Chen, H. Xu, J. Shao, X. Chen, Y. Sun, J. Hao, and N. Dai, "Large – Area, Broadband, Wide – Angle Plasmonic Metasurface Absorber for Midwavelength Infrared Atmospheric Transparency Window," Adv. Optical Mater. **7**(20), 1900841 (2019).

38. P. C. Wu, W. T. Chen, K.-Y. Yang, C. T. Hsiao, G. Sun, A. Q. Liu, N. I. Zheludev, and D. P. Tsai, "Magnetic plasmon induced transparency in three-dimensional metamolecules," Nanophotonics **1**(2), 131-138 (2012).

39. N. Liu, L. Langguth, T. Weiss, J. Kastel, M. Fleischhauer, T. Pfau, and H. Giessen, "Plasmonic analogue of electromagnetically induced transparency at the Drude damping limit," Nat. Mater. **8**(9), 758-762 (2009).

40. R. Yahiaoui, J. A. Burrow, S. M. Mekonen, A. Sarangan, J. Mathews, I. Agha, and T. A. Searles, "Electromagnetically induced transparency control in terahertz metasurfaces based on bright-bright mode coupling," Phys. Rev. B **97**(15), 155403 (2018).

41. V. Krivenkov, S. Goncharov, I. Nabiev, and Y. P. Rakovich, "Induced Transparency in Plasmon-Exciton Nanostructures for Sensing Applications," Laser Photonics Rev. **13**(1), 1800176 (2019).

42. B. Gallinet, T. Siegfried, H. Sigg, P. Nordlander, and O. J. Martin, "Plasmonic radiance: probing structure at the Angstrom scale with visible light," Nano Lett. **13**(2), 497-503 (2013).

43. N. Murata, R. Hata, and H. Ishihara, "Crossover between Energy Transparency Resonance and Rabi Splitting in Antenna–Molecule Coupled Systems," J. Phys. Chem. C **119**(45), 25493-25498 (2015).

44. T. J. Antosiewicz, S. P. Apell, and T. Shegai, "Plasmon–Exciton Interactions in a Core–Shell Geometry: From Enhanced Absorption to Strong Coupling," ACS Photonics **1**(5), 454-463 (2014).

45. J. A. Faucheaux, J. Fu, and P. K. Jain, "Unified Theoretical Framework for Realizing Diverse Regimes of Strong Coupling between Plasmons and Electronic Transitions," J. Phys. Chem. C **118**(5), 2710-2717 (2014).

46. A. E. Schlather, N. Large, A. S. Urban, P. Nordlander, and N. J. Halas, "Near-field mediated plexcitonic coupling and giant Rabi splitting in individual metallic dimers," Nano Lett. **13**(7), 3281-3286 (2013).

47. S. Shrestha, Y. Wang, A. C. Overvig, M. Lu, A. Stein, L. Dal Negro, and N. F. Yu, "Indium Tin Oxide Broadband Metasurface Absorber," ACS Photonics **5**(9), 3526-3533 (2018).

48. M. Abb, Y. Wang, N. Papasimakis, C. H. de Groot, and O. L. Muskens, "Surface-enhanced infrared spectroscopy using metal oxide plasmonic antenna arrays," Nano Lett. **14**(1), 346-352 (2014).

49. C. F. Bohren, and D. R. Huffman, *Absorption and scattering of light by small particles* (John Wiley & Sons, 2008).

50. Y. Kayaba, and T. Kikkawa, "Quantitative Determination of Complex Dielectric Function of Amorphous Silicon Dioxide on Silicon Substrate from Transmission Spectrum," Jpn. J. Appl. Phys. **48**(12), 121406 (2009).

51. J. D. Caldwell, L. Lindsay, V. Giannini, I. Vurgaftman, T. L. Reinecke, S. A. Maier, and O. J. Glembocki, "Low-loss, infrared and terahertz nanophotonics using surface phonon polaritons," Nanophotonics **4**(1), 44–68 (2015).

52. J. van de Groep, and A. Polman, "Designing dielectric resonators on substrates: combining magnetic and electric resonances," Opt. Express **21**(22), 26285-26302 (2013).

53. S. Laux, N. Kaiser, A. Zöller, R. Götzelmann, H. Lauth, and H. Bernitzki, "Room-temperature deposition of indium tin oxide thin films with plasma ion-assisted evaporation," Thin Solid. Films **335**(1-2), 1-5 (1998).

54. J. W. Cleary, E. M. Smith, K. D. Leedy, G. Grzybowski, and J. Guo, "Optical and electrical properties of ultra-thin indium tin oxide nanofilms on silicon for infrared photonics," Opt. Mater. Express **8**(5), 1231-1245 (2018).

55. J. Lian, D. Zhang, R. Hong, P. Qiu, T. Lv, and D. Zhang, "Defect-Induced Tunable Permittivity of Epsilon-Near-Zero in Indium Tin Oxide Thin Films," Nanomaterials **8**(11), 922 (2018).

56. I. H. Malitson, "Interspecimen Comparison of the Refractive Index of Fused Silica," J. Opt. Soc. Am. **55**(10), 1205-1209 (1965).

57. S. Popova, T. Tolstykh, and V. Vorobev, "Optical characteristics of amorphous quartz in the 1400-200 cm^{-1} region," Optics and Spectroscopy **33**, 444-445 (1972).

58. H. J. Hagemann, W. Gudat, and C. Kunz, "Optical constants from the far infrared to the x-ray region: Mg, Al, Cu, Ag, Au, Bi, C, and Al_2O_3," J. Opt. Soc. Am. **65**(6), 742-744 (1975).

59. B. Auguie, and W. L. Barnes, "Collective resonances in gold nanoparticle arrays," Phys. Rev. Lett. **101**(14), 143902 (2008).

60. A. B. Evlyukhin, C. Reinhardt, A. Seidel, B. S. Luk'yanchuk, and B. N. Chichkov, "Optical response features of Si-nanoparticle arrays," Phys. Rev. B **82**(4), 045404 (2010).

61. "IR Transmission Spectra," https://www.gemini.edu/observing/telescopes-and-sites/sites#Transmission.

62. J. Li, R. Gan, Q. Guo, H. Liu, J. Xu, and F. Yi, "Tailoring optical responses of infrared plasmonic metamaterial absorbers by optical phonons," Opt. Express **26** (13), 16769-16781 (2018).

63. A. E. Miroshnichenko, A. B. Evlyukhin, Y. S. Kivshar, and B. N. Chichkov, "Substrate-Induced Resonant Magnetoelectric Effects for Dielectric Nanoparticles," ACS Photonics **2**(10), 1423–1428 (2015).

64. I. Sinev, I. Iorsh, A. Bogdanov, D. Permyakov, F. Komissarenko, I. Mukhin, A. Samusev, V. Valuckas, A. I. Kuznetsov, B. S. Luk'yanchuk, A. E. Miroshnichenko, and Y. S. Kivshar, "Polarization control over electric and magnetic dipole resonances of dielectric nanoparticles on metallic films," Laser Photonics Rev. **10**(5), 799-806 (2016).

65. O. Merchiers, F. Moreno, F. González, and J. M. Saiz, "Light scattering by an ensemble of interacting dipolar particles with both electric and magnetic polarizabilities," Phys. Rev. A **76**(4), 043834 (2007).

66. S. N. Sheikholeslami, A. García-Etxarri, and J. A. Dionne, "Controlling the Interplay of Electric and Magnetic Modes via Fano-like Plasmon Resonances," Nano Lett. **11**(9), 3927–3934 (2011).

67. G. C. Schatz, "Theoretical Studies of Surface Enhanced Raman Scattering," Acc. Chem. Res. **17**(10), 370–376 (1984).

68. C. Deeb, X. Zhou, J. Plain, G. P. Wiederrecht, R. Bachelot, M. Russell, and P. K. Jain, "Size Dependence of the Plasmonic Near-Field Measured via Single-Nanoparticle Photoimaging," J. Phys. Chem. C **117**(20), 10669-10676 (2013).

69. R. Taubert, M. Hentschel, and H. Giessen, "Plasmonic analog of electromagnetically induced absorption: simulations, experiments, and coupled oscillator analysis," J. Opt. Soc. Am. B **30**(12), 3123-3134 (2013).

70. R. Taubert, M. Hentschel, J. Kastel, and H. Giessen, "Classical analog of electromagnetically induced absorption in plasmonics," Nano Lett. **12**(3), 1367-1371 (2012).

71. N. W. Pech-May, and M. Retsch, "Tunable daytime passive radiative cooling based on a broadband angle selective low-pass filter," Nanoscale Adv. **2** (1), 249-255 (2020).

72. A. Leroy, B. Bhatia, C. C. Kelsall, A. Castillejo-Cuberos, H. M. Di Capua, L. Zhao, L. Zhang, A. M. Guzman, and E. N. Wang, "High-performance subambient radiative cooling enabled by optically selective and thermally insulating polyethylene aerogel," Sci Adv **5** (10), eaat9480 (2019).

5.7. Supporting information

5.7.1. Optical properties of the SiO_2 core

Scattering efficiency spectra of the SiO_2 core with a radius of 1 – 2 μm are shown in Figures 5.6A-C. The scattering properties of the SiO_2 core are similar to the absorption properties discussed in the main text. The scattering become stronger with an increasing radius. The scattering of the magnetic modes is weaker than the absorption.

Absorption efficiency for up to third-order mode is shown in Figures 5.6D-F. Higher than third order is negligibly small for core radius of up to 2 μm. With increasing the radius, the absorption of the first-order mode redshift and the second and third-order modes become stronger at the shorter wavelengths. Further increase in radius cause redshift of lower order modes and make higher-order modes stronger at the shorter wavelengths. A superposition of absorption of those multiple order modes results in broadening the absorption bandwidth.

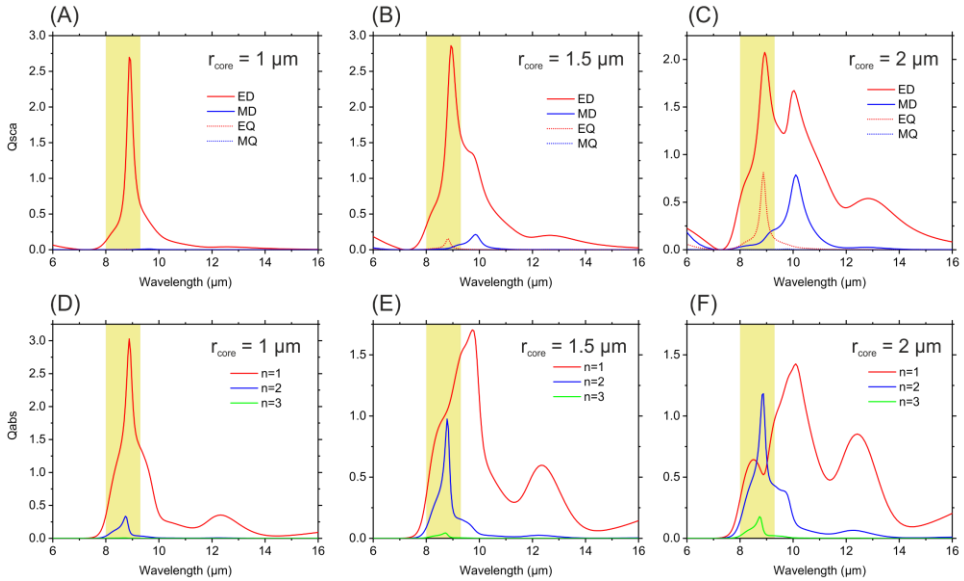

Figure 5.6. Scattering efficiency of the SiO_2 core with (A) 1 μm, (B) 1.5 μm, and (C) 2 μm in radius. The red and blue solid curves are for ED and MD, and the red and blue dashed curves are for EQ and MQ, respectively. Absorption efficiency of the SiO_2 core with (D) 1 μm, (E) 1.5 μm, and (F) 2 μm in radius. The red, blue, and green curves are for the total absorption (electric mode + magnetic mode) of the first, second, and third-order modes, respectively. The yellow shaded area indicates the Reststrahlen band of SiO_2.

5.7.2. P_{cell}, r_{core}, and t_{shell} dependence of the ITO@SiO_2 semishell absorber

Figure 5.7A shows P_{cell} dependence of the absorption of the ITO@SiO_2 semishell absorber with r_{core} = 1.4 μm and t_{shell} = 200 nm. When P_{cell} is small, lateral near field interactions between semishells are strong, which weaken the absorption. With an increase in P_{cell}, the absorption becomes stronger and maximizes at around P_{cell} = 7 μm. When P_{cell} increases further, the lattice resonance redshifts into the primary ATW. The lattice resonance destructively interacts with the LSP of the ITO shell and the Mie resonances of the SiO_2 core, therefore, the absorption properties are degraded. According to Ref. [1, 2], interactions between plasmonic particles can be ignored when the face-to-face distance is larger than approximately 2.5 times the particle diameter. The value "2.5" was found for gold nanoparticles. Our structure is composed of ITO, so the value may change. However, it can still be a good indicator to estimate the near-field interactions occurring in our system. In our case, the particle diameter is 2 × (r_{core} + t_{shell}) = 3.2 μm. Therefore, the distance required to attenuate interactions is 8 μm. In the periodic structure, the face-to-face distance is calculated as P_{cell} – 3.2 μm. This indicates that interactions are attenuated when P_{cell} is larger than 11.2 μm. However, as explained earlier, the absorption properties of the proposed structure are degraded when P_{cell} is larger than 7 μm. Therefore, P_{cell} = 7 μm can be an optimum periodicity of the proposed structure even though the near-field interactions exist.

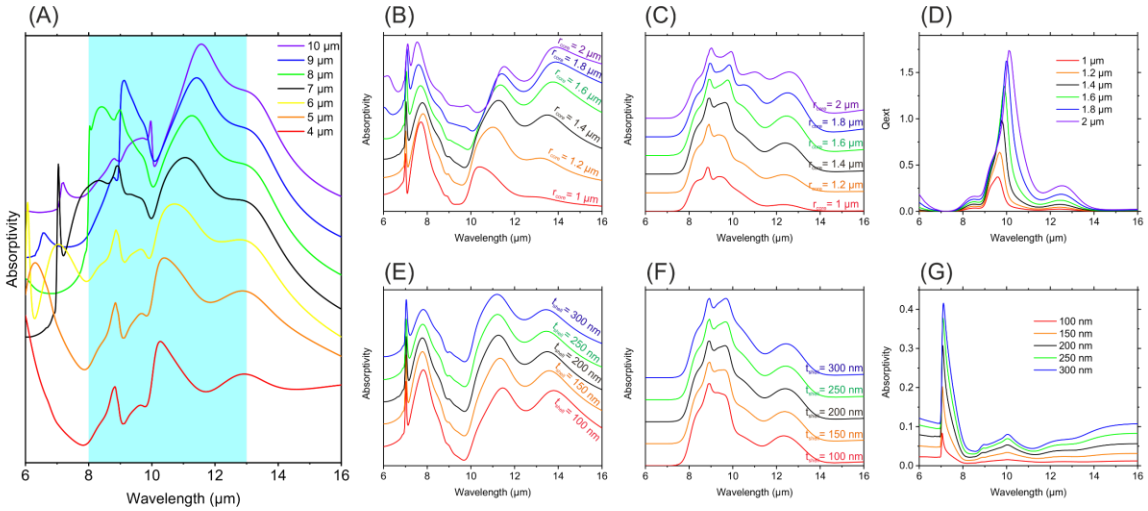

Figure 5.7. (A) P_{cell} dependence of the absorption of the ITO@SiO_2 semishell absorber. r_{core} and t_{shell} are fixed as 1.4 μm and 200 nm, respectively. The blue shaded area indicates the primary ATW. Absorption spectra of (B) the ITO shell and (C) the SiO_2 core for r_{core} dependence in Figure 5.2B. (D) Extinction efficiency of the MD of the SiO_2 core calculated by Mie theory for different radii. Absorption spectra of (E) the ITO shell, (F) the SiO_2 core, and (G) the perforated ITO film for t_{core} dependence in Figure 5.2B.

Figure 5.7B and C show absorption of the ITO shell and the SiO_2 core for r_{core} dependence in Figure 5.2B. The absorption of the shell becomes broader with an increase in r_{core}. This is because of the redshift of the absorption and stronger lateral near-field interactions between the semishells. The absorption of the SiO_2 core also becomes broader because of the excitation of the multiple order modes of the Mie resonance.

Figure 5.7D shows the extinction efficiency of the MD of the SiO_2 core calculated by Mie theory. With the increase in the radius, the absorption peak redshifts. Comparting Figure 5.7B and D, we can find that the absorption dip of the ITO shell appears at the wavelength where the MD has an absorption peak. This

may prove that the mode splitting is caused by the interaction between the LSP of the ITO shell and the MD of the SiO_2 core.

Figure 5.7E and F shows the absorption of the shell and the core for t_{shell} dependence in Figure 5.2C. There is no considerable difference in the spectral shape of the ITO shell for different t_{shell}, but the intensity of each absorption peaks changes. The absorption of the SiO_2 core does not change a lot. The absorption dip of the ITO shell does not shift with an increase in t_{shell} because the MD of the SiO_2 core does not shift. The absorption of the perforated ITO film is shown in Figure 5.7G. The absorption increases with an increase in t_{shell}. This is because of the intrinsic absorption and thick skin depth of ITO [3]. The thicker film absorbs more electromagnetic waves outside the primary ATW, therefore, t_{shell} should not be thick for the selective absorption.

5.7.3. Absorption properties of the optimized ITO@SiO_2 semishell absorber

The absorptivity calculated by integrating the dissipated power density over the ITO@SiO_2 semishell absorber is compared to the absorptivity calculated by the scattering parameter, which is commonly used [4] (see Figure 5.8A). In the scattering parameter, reflectance R and transmittance T were calculated, and absorptivity A was obtained by $A = 1 - R - T$. The ITO@SiO_2 semishell absorber has the Au reflector so that $T = 0$. The absorption spectra calculated by those methods are in good agreement with each other.

In Figure 5.8B, the absorption of the core with 1.4 μm in radius was calculated by Mie theory. The absorption peaks of ED, MD and EQ are 8.98 μm, 8.78 μm, and 9.79 μm, respectively. The contribution of MQ is negligible. This is compared with the absorption spectra of the ITO shell and the SiO_2 core in Figure 5.3A. The absorption dip of the ITO shell appears around the absorption peak of the MD of the SiO_2 core. The total absorption of the SiO_2 core calculated using Mie theory has two absorption peaks at 8.78 μm and 9.62 μm. Those absorption peaks are not solely determined by one of the resonance modes. For example, the first peak appears when the absorption of ED + EQ is maximized. The first peak locates at the absorption peak of the EQ because the absorption peaks of the ED and the EQ are close to each other. In a similar manner, the second peak is attributed to the maximum absorption of ED + MD. The second peak appears in between the peaks of the ED and MD, but is closer to the peak of the MD. This can also be seen in Figure 5.6E.

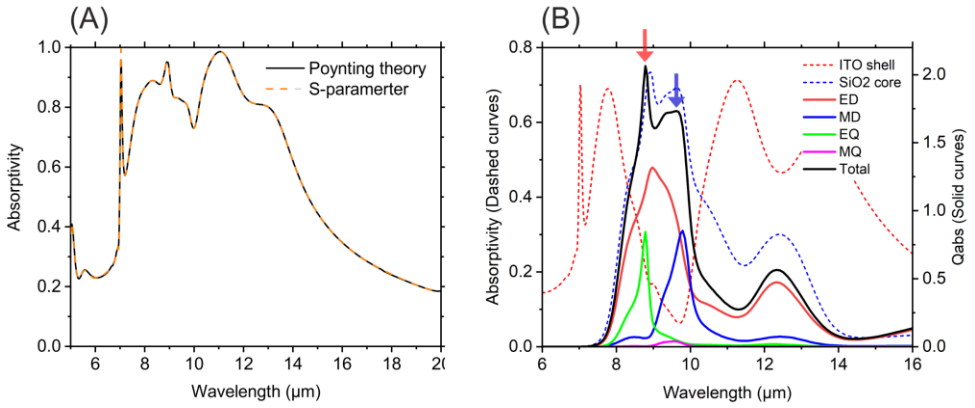

Figure 5.8. (A) Comparison between two different calculation methods for absorption. The black solid curve was calculated by taking the volume integral of the dissipated power density. The orange dashed curve was calculated by $A = 1 - R$. (B) Absorption of the SiO_2 core with 1.4 μm in radius was calculated by Mie theory. The red, blue, green, magenta, and black solid curves are for ED, MD, EQ, MQ and the total absorption, respectively. The red and blue dashed curves are for the ITO shell and the SiO_2 core in Figure 5.3A, respectively.

5.7.4. Coupled-oscillator model

From Equation 5.2, the amplitude of the oscillator´s displacement in the two-oscillator CO model in Figure 5.4A is

$$c_{\alpha 1} = \frac{(\omega_2^2 - \omega^2 - i\gamma_2\omega)F_1 + \kappa_{12}^2 F_2}{(\omega_1^2 - \omega^2 - i\gamma_1\omega)(\omega_2^2 - \omega^2 - i\gamma_2\omega) - \kappa_{12}^4} \tag{5.23}$$

$$c_{\alpha 2} = \frac{(\omega_1^2 - \omega^2 - i\gamma_1\omega)F_1 + \kappa_{12}^2 F_2}{(\omega_1^2 - \omega^2 - i\gamma_1\omega)(\omega_2^2 - \omega^2 - i\gamma_2\omega) - \kappa_{12}^4} \tag{5.24}$$

The absolute square of Equation 5.23 is

$$\begin{aligned} |c_{\alpha 1}|^2 &= \frac{[(\omega_2^2 - \omega^2)^2 + \gamma_2^2\omega^2]F_1^2}{B} + \frac{\kappa_{12}^4 F_2^2}{B} + \frac{2(\omega_2^2 - \omega^2)\kappa_{12}^2 F_1 F_2}{B} \\ &= |\widetilde{c_{\alpha 11}}|^2 + |\widetilde{c_{\alpha 12}}|^2 + \frac{2(\omega_2^2 - \omega^2)\kappa_{12}^2 F_1 F_2}{B} \end{aligned} \tag{5.25}$$

where B is

$$B = [(\omega_1^2 - \omega^2)(\omega_2^2 - \omega^2) - \gamma_1\gamma_2\omega^2 - \kappa_{12}^4]^2 + [\gamma_1\omega(\omega_2^2 - \omega^2) + \gamma_2\omega(\omega_1^2 - \omega^2)]^2$$

In a similar manner, the absolute square of Equation 5.24 is

$$\begin{aligned} |c_{\alpha 2}|^2 &= \frac{[(\omega_1^2 - \omega^2)^2 + \gamma_1^2\omega^2]F_2^2}{B} + \frac{\kappa_{12}^4 F_1^2}{B} + \frac{2(\omega_1^2 - \omega^2)\kappa_{12}^2 F_1 F_2}{B} \\ &= |\widetilde{c_{\alpha 22}}|^2 + |\widetilde{c_{\alpha 21}}|^2 + \frac{2(\omega_1^2 - \omega^2)\kappa_{12}^2 F_1 F_2}{B} \end{aligned} \tag{5.26}$$

The time averaged dissipated power by the external force $F_1(t)$ is

$$\begin{aligned} P_1(\omega) &= \left\langle \mathrm{Re}\left[F_1^*(t) \times \frac{\mathrm{d}x_1}{\mathrm{d}t}\right]\right\rangle \\ &= \frac{1}{2}\left\{\gamma_1\omega^2 \frac{\left[(\omega_2^2 - \omega^2)^2 + \gamma_2^2\omega^2\right]F_1^2}{B} + \gamma_2\omega^2 \frac{\kappa_{12}^4 F_1^2}{B} + \frac{\omega^2\kappa_{12}^2[\gamma_1(\omega_2^2 - \omega^2) + \gamma_2(\omega_1^2 - \omega^2)]F_1 F_2}{B}\right\} \\ &= \frac{1}{2}\left\{\gamma_1\omega^2|\widetilde{c_{\alpha 11}}|^2 + \gamma_2\omega^2|\widetilde{c_{\alpha 21}}|^2 + \frac{\omega^2\kappa_{12}^2[\gamma_1(\omega_2^2 - \omega^2) + \gamma_2(\omega_1^2 - \omega^2)]F_1 F_2}{B}\right\} \end{aligned} \tag{5.27}$$

In a similar manner, the time averaged dissipated power by the external force $F_2(t)$ is

$$\begin{aligned} P_2(\omega) &= \left\langle \mathrm{Re}\left[F_2^*(t) \times \frac{\mathrm{d}x_2}{\mathrm{d}t}\right]\right\rangle \\ &= \frac{1}{2}\left\{\gamma_2\omega^2 \frac{\left[(\omega_1^2 - \omega^2)^2 + \gamma_1^2\omega^2\right]F_2^2}{B} + \gamma_1\omega^2 \frac{\kappa_{12}^4 F_2^2}{B} + \frac{\omega^2\kappa_{12}^2[\gamma_1(\omega_2^2 - \omega^2) + \gamma_2(\omega_1^2 - \omega^2)]F_1 F_2}{B}\right\} \\ &= \frac{1}{2}\left\{\gamma_2\omega^2|\widetilde{c_{\alpha 22}}|^2 + \gamma_1\omega^2|\widetilde{c_{\alpha 12}}|^2 + \frac{\omega^2\kappa_{12}^2[\gamma_1(\omega_2^2 - \omega^2) + \gamma_2(\omega_1^2 - \omega^2)]F_1 F_2}{B}\right\} \end{aligned} \tag{5.28}$$

The time average dissipated power of the whole system is obtained from the summation of Equations 5.27 and 5.28 and can be written using Equations 5.25 and 5.26. This results in Equation 5.4. Similarly, Equation 5.7 can also be obtained.

For the fitting of the dissipated power of the CO model $A_{\beta 1}(\omega)$ to the absorption of the ITO shell in Figure 5.3A, the damping rate and the resonance angular frequency of the bright oscillator were obtained by using the single harmonic oscillator (SHO) without any couplings. The dissipated power of the SHO model is

$$P_0(\omega) = \frac{1}{2}\gamma_0\omega^2 \frac{F_0^2}{(\omega_0^2 - \omega^2)^2 + \gamma_0^2\omega^2} \quad 5.29$$

Equation 5.29 was fitted to the absorption of only ITO shell in Figure 5.3B. Note that the absorption in Figure 5.3B is not pure absorption of the shell, but it includes absorption of the ITO film and the Au reflector. To ignore the influence of the film and the reflector, the fitting was made using pure absorption of the ITO shell (see Figure 5.9A). There is a discrepancy because Equation 5.29 cannot consider near-field interactions between ITO shells, which cause blueshift of the absorption peak of the shell. Therefore, if the peak position is perfectly fitted, the bandwidth becomes broader than the FEM simulation. However, if the bandwidth is fitted, the peak position is redshifted from the FEM simulation. The peak position is fitted in our case, so the bandwidth is broader, especially in the shorter wavelength range.

In Figure 5.9B, the absorption spectrum of the SiO_2 core with the ITO shell is compared to that without the ITO shell. The absorption peak at around 9 μm decreases when the shell is present. This is because the absorption of the EQ of the core decreases. The SiO_2 core with the ITO shell has a higher absorption at around 11 μm comparing to the SiO_2 core without the shell. This can be understood from the CO model. The blue dashed curve is the absorption of the MD of the SiO_2 core, which is taken from Figure 5.9C in the main text. The cyan dashed curve is the absorption of the MD without the interaction with the LSP of the ITO shell. The cyan dashed curve is calculated by Equation 5.29 using the same fitting parameters used for the blue dashed curve ($\omega_0 = \omega_2 = 1.93 \times 10^{14}$ rad/s, $\gamma_0 = \gamma_2 = 1.4 \times 10^{13}$ rad/s, $F_0 = F_2$). Comparing those two curves, we find that the absorption of the MD is enhanced by the interaction between the MD and the LSP.

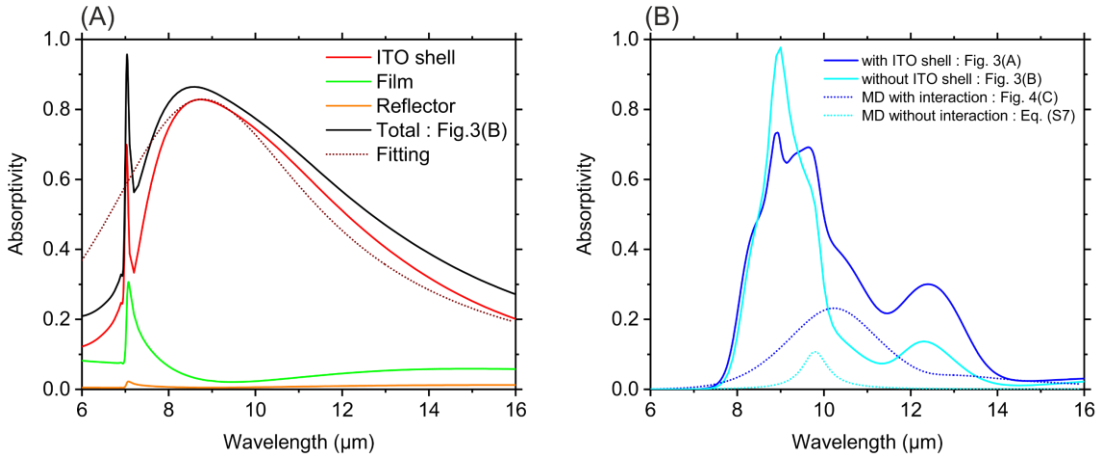

Figure 5.9. (A) Absorption spectra of each component of the ITO semishell structure (without the SiO_2 core). The red, green, orange curves are for the ITO shell, perforated ITO film, and the Au reflector, respectively. The black curve is for the total absorption of the structure, which is shown in Figure 5.3B. The red dashed curve is Equation 5.29, which is fitted to the absorption spectrum of the ITO shell. (B) The blue and cyan solid curves are absorption spectra of the SiO_2 core with and without the ITO shell, respectively. Those are taken from Figures 5.3A and B. The blue and cyan dashed curve is the absorption spectrum of the MD of the SiO_2 core with and without interaction between the MD and the LSP of the ITO shell, respectively.

5.7.5. Coupled-dipole method

The electric and magnetic dipole moments are unknown, therefore,

$$\mathbf{p}_1 = p_{1x}\hat{\mathbf{e}}_x + p_{1y}\hat{\mathbf{e}}_y + p_{1z}\hat{\mathbf{e}}_z \quad 5.30$$

$$\mathbf{m}_2 = m_{2x}\hat{\mathbf{e}}_x + m_{2y}\hat{\mathbf{e}}_y + m_{2z}\hat{\mathbf{e}}_z \tag{5.31}$$

From Equation 5.12,

$$\begin{cases} \mathbf{G}_M(\mathbf{r}_1 - \mathbf{r}_2)\cdot\hat{\mathbf{e}}_x = (-\hat{\mathbf{e}}_z \times \hat{\mathbf{e}}_x)C(D) = -\hat{\mathbf{e}}_y C(D) \\ \mathbf{G}_M(\mathbf{r}_1 - \mathbf{r}_2)\cdot\hat{\mathbf{e}}_y = (-\hat{\mathbf{e}}_z \times \hat{\mathbf{e}}_y)C(D) = \hat{\mathbf{e}}_x C(D) \\ \mathbf{G}_M(\mathbf{r}_1 - \mathbf{r}_2)\cdot\hat{\mathbf{e}}_z = (-\hat{\mathbf{e}}_z \times \hat{\mathbf{e}}_z)C(D) = 0 \end{cases} \tag{5.32}$$

$$\begin{cases} \mathbf{G}_M(\mathbf{r}_2 - \mathbf{r}_1)\cdot\hat{\mathbf{e}}_x = (\hat{\mathbf{e}}_z \times \hat{\mathbf{e}}_x)C(D) = \hat{\mathbf{e}}_y C(D) \\ \mathbf{G}_M(\mathbf{r}_2 - \mathbf{r}_1)\cdot\hat{\mathbf{e}}_y = (\hat{\mathbf{e}}_z \times \hat{\mathbf{e}}_y)C(D) = -\hat{\mathbf{e}}_x C(D) \\ \mathbf{G}_M(\mathbf{r}_2 - \mathbf{r}_1)\cdot\hat{\mathbf{e}}_z = (\hat{\mathbf{e}}_z \times \hat{\mathbf{e}}_z)C(D) = 0 \end{cases} \tag{5.33}$$

Using Equation 5.30-5.33, the scattered field of Eq. 5.10 and 5.11 can be written using

$$\mathbf{G}_M(\mathbf{r}_1 - \mathbf{r}_2)\cdot\left(m_{2x}\hat{\mathbf{e}}_x + m_{2y}\hat{\mathbf{e}}_y + m_{2z}\hat{\mathbf{e}}_z\right) = m_{2y}C(D)\hat{\mathbf{e}}_x - m_{2x}C(D)\hat{\mathbf{e}}_y \tag{5.34}$$

$$\mathbf{G}_M(\mathbf{r}_2 - \mathbf{r}_1)\cdot\left(p_{1x}\hat{\mathbf{e}}_x + p_{1y}\hat{\mathbf{e}}_y + p_{1z}\hat{\mathbf{e}}_z\right) = -p_{1y}C(D)\hat{\mathbf{e}}_x + p_{1x}C(D)\hat{\mathbf{e}}_y \tag{5.35}$$

Substituting Equation 5.34 and 5.35 into Equations 5.14 and 5.15, respectively, the electric and magnetic dipole moments are

$$\mathbf{p}_1 = \varepsilon_0\alpha_1 E_0 \exp\left(-i\frac{kD}{2}\right)\hat{\mathbf{e}}_x - \varepsilon_0\alpha_1 Z_0\left[m_{2y}C(D)\hat{\mathbf{e}}_x - m_{2x}C(D)\hat{\mathbf{e}}_y\right] \tag{5.36}$$

$$\mathbf{m}_2 = \chi_2 H_0 \exp\left(i\frac{kD}{2}\right)\hat{\mathbf{e}}_y + \frac{\chi_2}{\varepsilon_0 Z_0}\left[-p_{1y}C(D)\hat{\mathbf{e}}_x + p_{1x}C(D)\hat{\mathbf{e}}_y\right] \tag{5.37}$$

From Equations 5.36 and 5.37, vector components of the electric and magnetic dipole moments are

$$\begin{cases} p_{1x} = \varepsilon_0\alpha_1\left[E_0 \exp\left(-i\frac{kD}{2}\right) - Z_0 m_{2y}C(D)\right] \\ p_{1y} = \varepsilon_0\alpha_1 Z_0 m_{2x}C(D) = 0 \end{cases} \tag{5.38}$$

$$\begin{cases} m_{2x} = -\frac{\chi_2}{\varepsilon_0 Z_0}p_{1y}C(D) = 0 \\ m_{2y} = \chi_2\left[H_0 \exp\left(i\frac{kD}{2}\right) + \frac{1}{\varepsilon_0 Z_0}p_{1x}C(D)\right] \end{cases} \tag{5.39}$$

The self-consistent form of Equations 5.16 and 5.17 can be obtained from Equations 5.38 and 5.39.

5.7.6. Electric polarizability of the LSP and magnetic polarizability of the MD

Figure 5.10A shows extinction cross-sections of the ITO shell and SiO_2 core. The extinction cross-section of the ITO shell was calculated using the FEM simulation. This calculation was made using a simulation model that considers only one ITO shell in the air without any other structures (the SiO_2 core, ITO film, and Au reflector are absent). The inner radius and shell thickness were 1.4 μm and 200 nm, respectively. The extinction cross-section of the MD of the SiO_2 core with a radius of 1.4 μm was obtained using Mie theory. The electric polarizability of the LSP of the ITO shell (Equation 5.18) and the magnetic polarizability of the MD of the SiO_2 core (Equation 5.19) were obtained by fitting following equations [5]

$$C_{\text{ext}} = k\text{Im}[\alpha_1] \tag{5.40}$$

$$C_{\text{ext}} = k\text{Im}[\chi_2] \quad 5.41$$

From the fitting, the resonance angular frequency and the damping rate are $\omega_p = 2.03 \times 10^{14}$ rad/s and $\gamma_p = 1.5 \times 10^{14}$ rad/s for the LSP and $\omega_m = 1.93 \times 10^{14}$ rad/s and $\gamma_m = 1.1 \times 10^{13}$ rad/s for the MD. Those values were substituted into Equation 5.18 and 5.19, and we calculated Equation 5.22 by using Equations 5.16 and 5.17. Equations 5.40 and 5.41 are shown in Figure 5.10A. Equation 5.41 is in good agreement with the extinction spectrum of the MD of the SiO_2 core. Equation 5.40 also fits well to the extinction spectrum of the ITO shell, but there are some differences between them. This is because radiative damping and a retardation effect were not considered in Equation 5.18 [6, 7]. The magnetic polarizability of the SiO_2 core can also be obtained using Mie coefficient [5]

$$\chi_2 = \frac{6\pi i}{k^3} b_1 \quad 5.42$$

Figure 5.10B shows Equation 5.19 and Equation 5.42. Equation 5.19 is in good agreement with Equation 5.42.

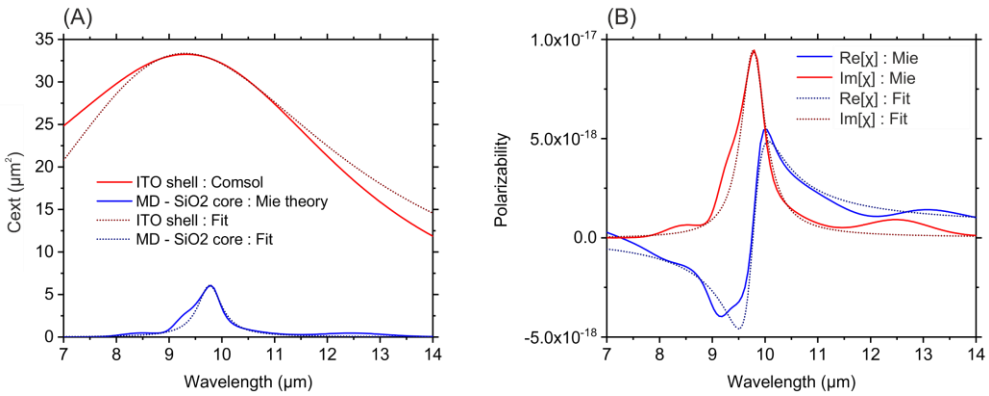

Figure 5.10. (A) The red and blue solid curves are extinction cross-sections of the ITO shell calculated by FEM simulation and the SiO_2 core calculated by Mie theory, respectively. The red and blue dashed curves are extinction calculated by Equations 5.40 and 5.41, respectively. (B) The blue and red solid curves are real and imaginary parts of the magnetic polarizability of the SiO_2 core calculated by Equation 5.42. The red and blue dashed curves are those calculated using Equation 5.19 in the main text and using fitting values of $\omega_m = 1.93 \times 10^{14}$ rad/s and $\gamma_m = 1.1 \times 10^{13}$ rad/s.

5.7.7. Incident angle dependence of the periodic structure

Figure 5.11A shows incident angle dependence of the optimized ITO@SiO_2 semishell absorber for both TE (the electric field is along the y-direction) and TM polarizations (the magnetic field is along the y-direction). With an increase in the incident angle, the absorption of the absorber is dramatically degraded for both polarizations. This is because the lattice resonance redshift with an increase in the incident angle, and the lattice resonance destructively interact with the LSP of the ITO shell and the Mie resonances of the SiO2 core. A similar effect can be observed for P_{cell} dependence shown in Figure 5.7A.

To prove the redshift of the lattice resonance, *x* component of the wavevector of the incident wave diffracted by the grating is considered

$$k_{\mathrm{diff}} = k_{\mathrm{in_x}} + k_{\mathrm{g}} = \frac{\omega}{c}\sin\theta_{\mathrm{in}} + m\frac{2\pi}{P_{\mathrm{cell}}} \qquad 5.43$$

where ω is the angular frequency, c is the speed of light in free space, θ_{in} is the incident angle and m = ± 1, ± 2, ± 3… is the diffraction order. For TE polarization, the grating coupling occurs when k_{diff} matches to the light line $k_{\mathrm{x}} = \omega/c$ [8]. For TM polarization, the dispersion relation of the interface between air and the ITO film should be considered. The dispersion of the interface can be calculated as [9, 10]

$$k_{\mathrm{SPP}} = \frac{\omega}{c}\sqrt{\frac{\varepsilon_{\mathrm{air}}\varepsilon_{\mathrm{ITO}}}{\varepsilon_{\mathrm{air}} + \varepsilon_{\mathrm{ITO}}}} \qquad 5.44$$

where $\varepsilon_{\mathrm{air}}$ and $\varepsilon_{\mathrm{ITO}}$ are the permittivities of air and ITO, respectively. The propagating surface plasmon is induced when $k_{\mathrm{diff}} = k_{\mathrm{SPP}}$. In MIR, k_{SPP} is close to the light line; therefore, $k_{\mathrm{SPP}} \approx k_{\mathrm{x}}$. Figure 5.11B shows k_{diff} for different θ_{in} and m. $k_{\mathrm{diff}} \approx k_{\mathrm{x}} \approx k_{\mathrm{SPP}}$ occurs for the diffraction order of $m = -1$ at around the primary ATW and redshifts with an increase in θ_{in}.

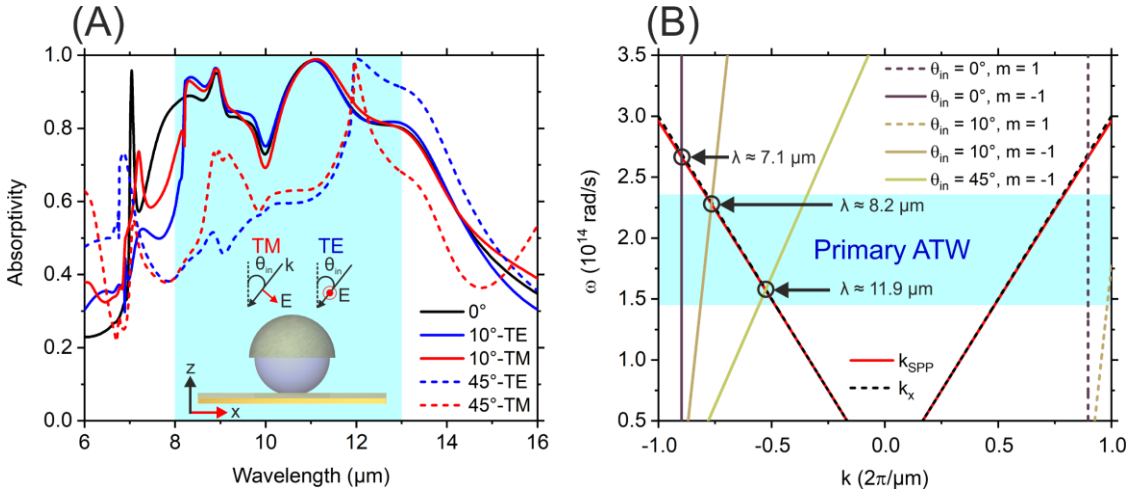

Figure 5.11. (A) The absorption spectra of the optimized ITO@SiO_2 semishell absorber for different incident angles. The black solid curve is for θ_{in} = 0°. The red and blue solid curves are for θ_{in} = 10° with TM and TE polarizations, respectively. The red and blue dashed curves are for θ_{in} = 45° with TM and TE polarizations, respectively. (B) k_{diff} for different θ_{in} and m. k_{diff} is calculated using Equation 5.43. The black dashed lines are the light line k_{x}. The red solid curves are k_{SPP} calculated by Equation 5.44.

5.7.8. Absorption properties in the visible and near-infrared regions

The absorption of the ITO film on the Au reflector (ITO@Au film) was calculated using the transfer-matrix method to estimate the absorption of the optimized ITO@SiO2 semishell absorber in the visible and near-infrared regions. The thicknesses of the ITO film and the Au reflector are 200 nm. Since ITO possesses intrinsic absorption and Au absorbs light by the interband transitions in a wavelength region shorter than about 0.5 μm, the ITO@Au film possesses strong absorption in the visible and near-infrared regions. Therefore, it is expected that the proposed structure strongly absorbs solar radiation. To understand the exact absorption properties of the proposed structure in the visible and near-infrared regions, Mie scattering of the SiO_2 microsphere has to be considered.

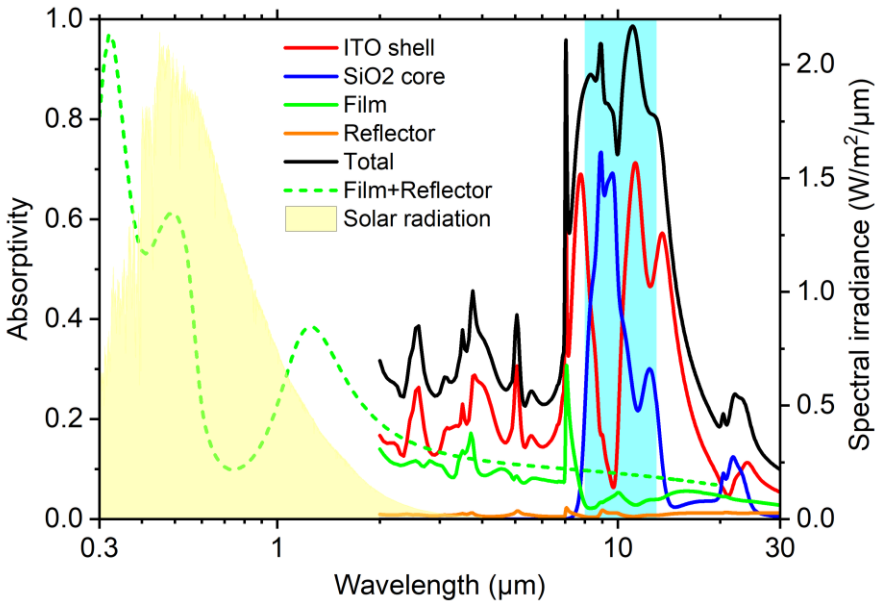

Figure 5.12. Absorption properties of the optimized ITO@SiO_2 semishell absorber in the wavelength range over the visible to mid-infrared regions. The red, blue, green, and orange solid curves are for the ITO shell, SiO_2 core, perforated ITO film, and Au reflector, respectively. The black curve is the total absorption of the structure. Those solid curves are taken from Figure 5.3A. The green dashed curve is the absorption of the ITO@Au film calculated using the transfer-matrix method. The yellow shaded area is the solar radiation taken from [11].

5.7.9. References

1. K.-H. Su, Q.-H. Wei, X. Zhang, J. J. Mock, D. R. Smith, and S. Schultz, "Interparticle Coupling Effects on Plasmon Resonances of Nanogold Particles," Nano Lett. **3**(8), 1087−1090 (2003).

2. P. K. Jain, W. Huang, and M. A. El-Sayed, "On the Universal Scaling Behavior of the Distance Decay of Plasmon Coupling in Metal Nanoparticle Pairs: A Plasmon Ruler Equation," Nano Lett. **7** (7), 2080-2088 (2007)

3. J. B. Khurgin, "Replacing noble metals with alternative materials in plasmonics and metamaterials: how good an idea?," Philos. Trans. R. Soc. A **375**(2090), 20160068 (2017).

4. J. M. Hao, L. Zhou, and M. Qiu, "Nearly total absorption of light and heat generation by plasmonic metamaterials," Phys. Rev. B **83**(16), 165107 (2011).

5. A. E. Miroshnichenko, A. B. Evlyukhin, Y. S. Kivshar, and B. N. Chichkov, "Substrate-Induced Resonant Magnetoelectric Effects for Dielectric Nanoparticles," ACS Photonics **2**(10), 1423−1428 (2015).

6. G. C. Schatz, "Theoretical Studies of Surface Enhanced Raman Scattering," Acc. Chem. Res. **17**(10), 370–376 (1984).

7. C. Deeb, X. Zhou, J. Plain, G. P. Wiederrecht, R. Bachelot, M. Russell, and P. K. Jain, "Size Dependence of the Plasmonic Near-Field Measured via Single-Nanoparticle Photoimaging," J. Phys. Chem. C **117**(20), 10669-10676 (2013).

8. R. Guo, T. K. Hakala, and P. Törmä, "Geometry dependence of surface lattice resonances in plasmonic nanoparticle arrays," Phys. Rev. B **95**(15), 155423 (2017).

9. G. K. P. Ramanandan, G. Ramakrishnan, N. Kumar, A. J. L. Adam, and P. C. M. Planken, "Emission of terahertz pulses from nanostructured metal surfaces," J. Phys. D: Appl. Phys. **47**(37), 374003 (2014).

10. M. Seo, J. Lee, and M. Lee, "Grating-coupled surface plasmon resonance on bulk stainless steel," Opt. Express **25** (22), 26939-26949 (2017).

11. "Solar Irradiance Spectrum," https://www.nrel.gov/grid/solar-resource/spectra-am1.5.html

6. Coupling strength and total damping govern electromagnetically induced absorption in coupled plasmonic systems

Kishin Matsumori[1,*], Ryushi Fujimura[2], and Markus Retsch[1]

[1] Department of Chemistry, Physical Chemistry I, University of Bayreuth, 95447 Bayreuth, Germany

[2] Graduate School of Regional Development and Creativity, Utsunomiya University, 321-8585 Utsunomiya, Japan

Accepted by *Adv. Photonics Res.*

Abstract: Electromagnetically induced absorption (EIA) is an optical phenomenon that enhances light absorption of plasmonic systems. Depending on the plasmonic system under investigation the decisive role of intrinsic vs. radiative damping and phase retardation have been pointed out to control the EIA. Here, we provide a unified interpretation and unravel the mechanism of EIA for plasmonic-dielectric composites and all-plasmonic dipolar-quadrupolar antennas. In this theoretical work, the finite element method is used to elucidate how EIA is attributed to an absorption enhancement of a resonance mode excited by near-field coupling. For a fundamental understanding, a quantitative analysis is developed by designing a generalized coupled-oscillator model. A critical parameter to maximize EIA is found, which is different to previous interpretations of such coupled plasmonic systems. Namely, the ratio of coupling strength to the total damping of the entire system, controls EIA. The generalized interpretation of EIA given by this work can be applied to many plasmonic systems and is essential for designing future optical components and devices.

6.1. Introduction

Electromagnetically induced transparency (EIT) is an optical phenomenon occurring as a result of Fano interference [1-5]. EIT can be observed in coupled plasmonic systems composed of bright and dark oscillators. The bright oscillator strongly couples with the incident field but the dark oscillator indirectly couples with an incident field through a near-field coupling to the bright oscillator. This coupling occurs destructively. Thus, an absorption spectrum is split into two peaks, and a transparency window appears at the resonance of the dark oscillator [6-10]. In the transparency window, a material´s dispersion dynamically changes [9-11]. These unique optical phenomena have been applied for slow light [10-12], nonlinear optics [13], and sensing [14, 15]. Recently, mode splitting phenomenon of EIT has been utilized to obtain a broadband absorption from simpler plasmonic systems [16, 17]. The counterpart of EIT is electromagnetically induced absorption (EIA). EIA can also be observed in similar coupled plasmonic systems for EIT. In contrast to EIT, EIA significantly enhances the absorption of the systems at the resonance of the dark oscillator, and the mode splitting is not observed [8, 9, 18-20], EIA has been extensively investigated, and EIA-based plasmonic systems have been developed for perfect absorbers [20], optical modulators [21, 22], nonlinear optics [23], and Faraday rotation [24].

The mechanism of EIT is almost the same for any type of plasmonic systems; however, the mechanism of EIA is described by different interpretations depending on the coupled plasmonic systems. One interpretation is that EIA is excited by controlling a ratio of radiative to intrinsic damping of the bright oscillator [8]. This interpretation originated from the temporal coupled mode theory, which was used to describe absorption properties of composite systems comprising a plasmonic particle covered with a thin

shell with molecular vibrational mode, such as J-aggregate or poly(methyl methacrylate) (PMMA). It is known that the absorption of plasmonic systems is maximized under the condition that its radiative damping is equal to its intrinsic damping [25, 26]. When the LSP of the plasmonic particle couples with the molecular vibration, the total intrinsic damping of the composite system becomes a sum of the intrinsic damping of the LSP and the molecular vibration. Therefore, if the plasmonic particle in the composite system has an intrinsic damping smaller than the radiative damping, the total intrinsic damping of the composite system can be equal to the radiative damping at the resonance of the molecular vibration. This spectrally local increase in the intrinsic damping results in an EIA-like spectral profile. Another interpretation of EIA can be found in a fully plasmonic system: a dipolar antenna vertically stacked over a quadrupolar antenna [18, 19]. This system suggested that there is a phase retardation in the coupling due to a near- and far-fields effect, originating from a physical distance between the dipolar and the quadrupolar antennas. It was described that this phase retardation can make the coupling destructive or constructive by controlling the distance, and an EIA-like spectral profile can be obtained when the coupling is constructive. Those two distinct interpretations have been utilized to explain EIA occurring in other coupled plasmonic systems [20, 24, 27]. However, it is still not clear how the ratio of the radiative to the intrinsic damping and the phase retardation in coupling enhance the absorption of those coupled plasmonic systems. In addition to those interpretations, planar plasmonic systems suggested that an absorption of a dark oscillator contributes to EIA [9, 28].

In this work, we integrate the previously established interpretations and develop a fundamental comprehension of EIA by theoretically investigating the absorption properties of the two-representative coupled plasmonic systems mentioned earlier: the plasmonic-polymer antenna (PPA) and the dipolar-quadrupolar antenna (DQA). Using the finite element method (FEM), we find that strong absorption enhancement occurs on the dark oscillator for both systems, which is attributed to the EIA-like spectral profile. To understand how the absorption of the dark oscillator is enhanced, we use a coupled-oscillator (CO) model that is composed of two mechanical harmonic oscillators coupled via a spring. The CO model has been widely used to investigate the optical properties, especially EIT and EIA properties of plasmonic systems. Depending on which system is investigated, different CO models has been developed [6, 7, 17-20, 28-34]. In general, those conventional CO models consider only either the intrinsic or radiative damping channels of a system. These CO models are useful to investigate the extinction, scattering, or absorption of the systems individually, but a full description of their optical properties cannot be given. This is because plasmonic structures always contains both intrinsic and radiative damping. Since it has been suggested that the system´s damping is an important parameter for plasmonic EIA [8, 9], a CO model must consider all damping channels of the systems to investigate plasmonic EIA. Based on this idea, we design a generalized CO (GCO) model involving all intrinsic and radiative damping channels. The radiative damping is given by the Abraham-Lorentz force, which works on charges emitting radiation [35, 36]. Throughout this work, we demonstrate that the GCO model quantitatively reproduces not only the absorption but also the scattering spectra obtained from the FEM for both plasmonic systems (PPA and DQA). From the GCO model, we can derive a condition to maximize plasmonic EIA via the absorption of the dark oscillator. Going beyond the established understanding of the role of radiative to intrinsic damping [8] and phase retardation of the coupling [18, 19], we find that EIA is solely determined by the ratio of the coupling strength to the total damping of the whole system.

6.2. Plasmonic-polymer composite structure

6.2.1. Design of the PPA and calculation method

First, we investigate the optical properties of a plasmonic-polymer composite system. Then, we elucidate how the ratio of radiative to intrinsic damping of a plasmonic structure influences the mechanism of EIA. For this investigation, we designed the PPA, composed of an Au antenna covered with a PMMA shell (Figure 6.1a). The Au antenna is a cylindrical structure with a radius of r. The tips of the antenna are spherical with a radius of r. The tip-to-tip length of the antenna is l. It is known that the ratio of scattering (C_{sca}) to absorption cross-section (C_{abs}) in the Au antenna can be controlled by tuning the aspect ratio of r/l [27, 37]. C_{sca} and C_{abs} are directly related to radiative and to intrinsic damping, respectively. Based on this, different ratios of radiative to intrinsic damping can be obtained by controlling C_{sca}/C_{abs}. The PMMA shell with a thickness of t uniformly covers the Au antenna. PMMA has been widely used to investigate interactions between a LSP and a molecular vibration because PMMA has a strong molecular vibration of C=O stretch at around a wavelength of 5.8 μm [8, 38, 39]. If an LSP of the Au antenna is induced at the same wavelength, the LSP of the Au antenna and the molecular vibration of PMMA strongly couple. Therefore, the size of the Au antenna should be determined such that LSP is induced at around 5.8 μm. The coupling strength between the LSP and the C=O stretch can be changed by changing the thickness. This is because the coupling becomes stronger if more molecules interact with the LSP [40, 41].

The optical properties of the PPA were calculated using COMSOL Multiphysics, which is a commercial software package based on the FEM. The dielectric function of Au was taken from Babar et. al. [42]. For PMMA, the Lorentz model was fitted to the dielectric function of PMMA obtained from Zhang et. al. [43]. From the fitting, the resonance angular frequency and the damping rate of the C=O stretch was $\omega_{C=O} = 3.26 \times 10^{14}$ rad/s (5.78 μm in wavelength) and $\gamma_{C=O} = 5.3 \times 10^{12}$ rad/s, respectively (see Section 6.6.1, Supporting Information). The refractive index of the surrounding of the PPA was fixed as $n_{bg} = 1.46$, which coincides with the background refractive index of PMMA. This is to prevent a shift of the LSP depending on the thickness of the PMMA shell. An incident field is polarized along the x-axis and propagates along the z-axis. A perfectly matched layer (PML) was applied to the surrounding of the calculation domain. C_{sca} was calculated by taking the surface integral of the Poynting vector of the scattered field over the integration sphere, which was defined in between the structure and the PML. C_{abs} was calculated by taking the volume integral of energy dissipation density over the structure. Extinction cross-section (C_{ext}) was calculated by $C_{sca} + C_{abs}$.

6.2.2. Absorption properties of the PPA

The optical properties of the bare Au antenna with different sizes are shown in the upper panels of Figure 6.1b. We have to mention that aspect ratios of those Au antennas are very high. Considering the enormous progress in the synthesis of highly anisotropic metallic nanoparticles, however, the investigated aspect ratios fall within a reasonable range [44-47]. The smallest Au antenna has $C_{sca}/C_{abs} < 1$, the medium one has $C_{sca}/C_{abs} \approx 1$, and the biggest one has $C_{sca}/C_{abs} > 1$. For all sizes, the Au antenna has one LSP mode at around 5.78 μm. The absorption spectra of the PPA with different shell thickness are also shown in the upper panels of Figure 6.1b. For the case of $C_{sca}/C_{abs} < 1$ and $C_{sca}/C_{abs} \approx 1$, there are two absorption peaks, and the distance between those two peaks becomes larger with increasing shell thickness. The absorption dip appears at the resonance of C=O stretch of PMMA, meaning that the LSP of the Au antenna strongly interacts with the C=O stretch. However, for the case of $C_{sca}/C_{abs} > 1$, the absorption spectra do not show mode splitting. The absorption is enhanced at the resonance of the C=O stretch, and a sharp absorption peak appears in addition to the broad absorption spectra. This spectral shape has been considered as EIA [8, 27]. The extinction and scattering spectra of the PPA can be found in Figure 6.7 of Supporting Information. In contrast to the

absorption, the extinction and scattering spectra show mode splitting no matter how large C_{sca}/C_{abs} is. The reason why extinction and scattering spectra of the PPA do not have a similar spectral shape to the absorption spectra is that the PMMA shell does not strongly scatter the incident field.

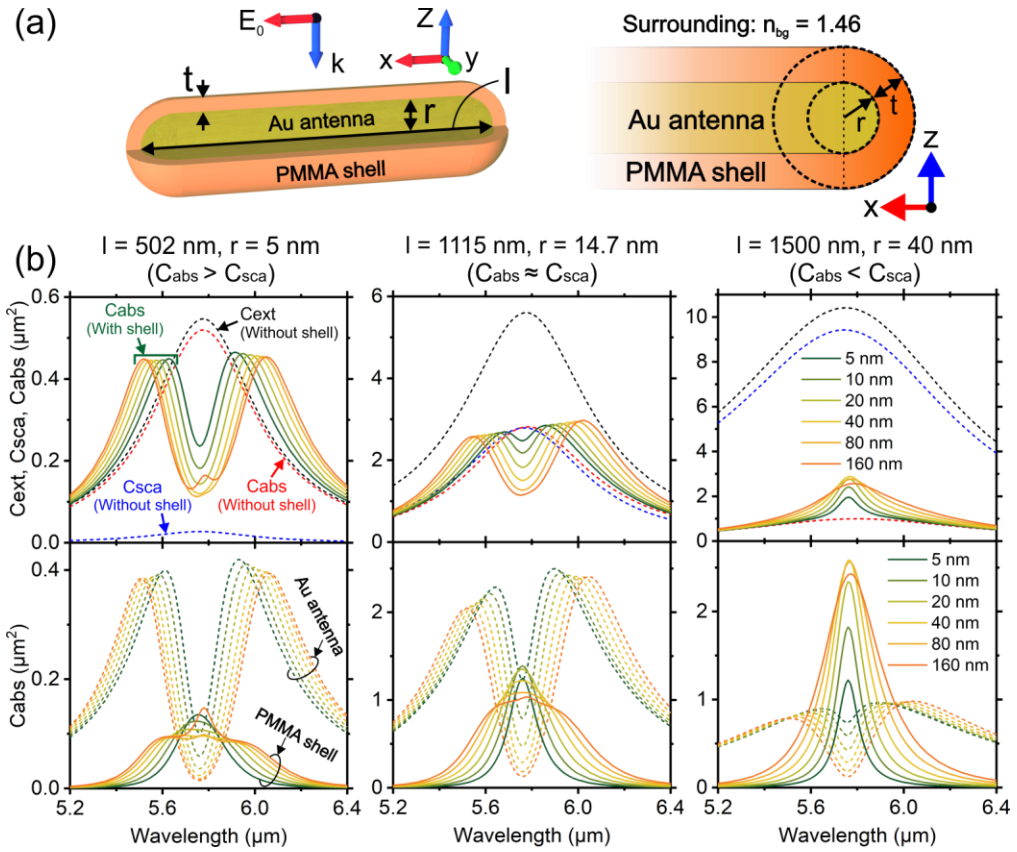

Figure 6.1. Absorption properties of the PPA with different l and r. (a) Schematic illustrations of the PPA. The refractive index of the surrounding is fixed as n_{bg} = 1.46. (b) (Upper panels) The black, blue, and red dashed lines are extinction, scattering, and absorption spectra of the Au antenna without the PMMA shell, respectively. The solid lines are absorption spectra of the PPA. (Bottom panels) The dotted and solid lines show absorption spectra of the Au antenna and the PMMA shell in the PPA, respectively.

To better understand the absorption properties of the PPA, the absorption of the PPA is divided into the absorption contribution of the Au antenna and the PMMA shell (in the lower panel of Figure 6.1b). The absorption of the Au antenna splits into two peaks for all antenna size and shell thickness. On the other hand, the PMMA shell has relatively sharp absorption spectra. In general, the C=O stretch resonance cannot be strongly coupled with the incident field so that the absorption of the PMMA shell is weak (Figure 6.8, Supporting Information). However, in the PPA, the C=O stretch couples strongly to the LSP of the Au antenna, resulting in a significant enhancement in the absorption of the PMMA shell [41, 48]. We have to note that for the smallest PPA with large t, a sharp absorption peak appears at the resonance of the C=O stretch in addition to the broad absorption spectrum (for example l = 502 nm, r = 5 nm, t = 160 nm). This sharp peak is not attributed to the coupling but is attributed to the intrinsic absorption of the C=O stretch (Figure 6.8, Supporting Information). When $C_{sca}/C_{abs} \leq 1$, the absorption of the Au antenna dominates the total absorption of the PPA. Since the mode splitting occurs on the LSP of the Au antenna by the coupling, the total absorption of the PPA shows an EIT-like spectral profile. In contrast, for the case of $C_{sca}/C_{abs} > 1$,

the absorption of the PMMA shell is stronger than that of the Au antenna, resulting in the EIA-like spectral profile of the total absorption of the PPA. These results show that C_{sca}/C_{abs} of the Au antenna is an important parameter to observe an EIA-like spectral profile, which has been demonstrated by Adato et al. [8]. In addition, our results suggests that the absorption enhancement of the PMMA shell contribute to the EIA-like spectral profile [9, 28]. Therefore, one might understand that the plasmonic EIA of the PPA is maximized when the absorption of the PMMA shell is maximized. However, for all PPA structures investigated here, we observe that the absorption of the PMMA shell increases, is maximized at a certain *t*, and becomes broader. This result indicates that there is a condition of maximum absorption of the PMMA shell, which is independent of C_{sca}/C_{abs} of the Au antenna. Since the shell thickness determines the coupling strength, the coupling strength may play a key role for the maximum absorption of the PMMA shell. In the following, we will discuss how the maximum absorption of the PMMA shell and C_{sca}/C_{abs} of the Au antenna are relevant to plasmonic EIA.

6.2.3. A generalized coupled-oscillator model

We propose a GCO model that considers all damping channels of the PPA systems, which enables us to investigate the mechanism of plasmonic EIA in this case [8, 9]. This model extends the understanding of EIA beyond the established interpretation based on intrinsic vs. radiative damping. Our GCO model consists of two harmonic oscillators. One is a bright oscillator driven by the external force. Another is a dark oscillator connected to the bright oscillator by a spring, which describes the near-field coupling of the system. Comparing the CO model and the PPA, the bright oscillator and the dark oscillator correspond to the Au antenna and the PMMA shell, respectively. The equation of motion of the CO model can be written as

$$\frac{\mathrm{d}^2 x_{\mathrm{B}\alpha}}{\mathrm{d}t^2} + \gamma_{\mathrm{B}} \frac{\mathrm{d}x_{\mathrm{B}\alpha}}{\mathrm{d}t} + \omega_{\mathrm{B}}^2 x_{\mathrm{B}\alpha} - \kappa^2 x_{\mathrm{D}\alpha} = F(t) + \tau_{\mathrm{B}} \frac{\mathrm{d}^3 x_{\mathrm{B}\alpha}}{\mathrm{d}t^3} \tag{6.1}$$

$$\frac{\mathrm{d}^2 x_{\mathrm{D}\alpha}}{\mathrm{d}t^2} + \gamma_{\mathrm{D}} \frac{\mathrm{d}x_{\mathrm{D}\alpha}}{\mathrm{d}t} + \omega_{\mathrm{D}}^2 x_{\mathrm{D}\alpha} - \kappa^2 x_{\mathrm{B}\alpha} = 0 \tag{6.2}$$

The subscripts n = B and D represent the bright and dark oscillators, respectively. The subscript α is to distinguish Equations 6.1 and 6.2 from another GCO model that will be shown later. x_n is the displacement of mass objects. γ_n is the intrinsic damping rate, ω_n is the resonance angular frequency determined by the spring constant, and κ is the coupling rate. τ_n is the radiative damping coefficient given by the Abraham-Lorentz force [35, 36], and the radiative damping rate is expressed as $\tau_n\omega^2$. The total damping of the oscillator is $\Gamma_n = \gamma_n + \tau_n\omega^2$. $F(t)$ is the external force normalized by the mass m_B, which is time-harmonic; therefore, $F(t) = F_0 e^{-i\omega t}$. The time averaged dissipated power per mass of the whole system is

$$P = \left\langle \mathrm{Re}\left[F^*(t) \times \frac{\mathrm{d}x_{\mathrm{B}}}{\mathrm{d}t} \right] \right\rangle \tag{6.3}$$

The dissipated power of the system described by Equations 6.1 and 6.2 can be written as [35]

$$\begin{aligned} P_\alpha &= \frac{1}{2}\left(\gamma_{\mathrm{B}}\omega^2 |x_{\mathrm{B}\alpha}|^2 + \tau_{\mathrm{B}}\omega^4 |x_{\mathrm{B}\alpha}|^2 + \gamma_{\mathrm{D}}\omega^2 |x_{\mathrm{D}\alpha}|^2\right) \\ &= E_{\mathrm{tot}\alpha} = A_{\mathrm{B}\alpha} + S_{\mathrm{B}\alpha} + A_{\mathrm{D}\alpha} \end{aligned} \tag{6.4}$$

The absolute square of $x_{B\alpha}$ and $x_{D\alpha}$ are

$$|x_{\mathrm{B}\alpha}|^2 = \frac{\left(\Omega_{\mathrm{D}}{}^2 + \gamma_{\mathrm{D}}{}^2\omega^2\right)F_0^2}{[\Omega_{\mathrm{B}}\Omega_{\mathrm{D}} - \Gamma_{\mathrm{B}}\gamma_{\mathrm{D}}\omega^2 - \kappa^4]^2 + \omega^2[\Gamma_{\mathrm{B}}\Omega_{\mathrm{D}} + \gamma_{\mathrm{D}}\Omega_{\mathrm{B}}]^2} \tag{6.5}$$

$$|x_{\mathrm{D}\alpha}|^2 = \frac{\kappa^4 F_0^2}{[\Omega_{\mathrm{B}}\Omega_{\mathrm{D}} - \Gamma_{\mathrm{B}}\gamma_{\mathrm{D}}\omega^2 - \kappa^4]^2 + \omega^2[\Gamma_{\mathrm{B}}\Omega_{\mathrm{D}} + \gamma_{\mathrm{D}}\Omega_{\mathrm{B}}]^2} \quad 6.6$$

where $\Omega_{\mathrm{n}} = (\omega_{\mathrm{n}}^2 - \omega^2)$. $A_{\mathrm{B}\alpha}$, $S_{\mathrm{B}\alpha}$, and $A_{\mathrm{D}\alpha}$ correspond to absorption and scattering of the bright oscillator, and absorption of the dark oscillator, respectively. $E_{\mathrm{tot}\alpha}$ is the extinction of the whole system. $E_{\mathrm{B}\alpha} = A_{\mathrm{B}\alpha} + S_{\mathrm{B}\alpha}$ and $A_{\mathrm{tot}\alpha} = A_{\mathrm{B}\alpha} + A_{\mathrm{D}\alpha}$ can be considered as the extinction of the bright oscillator and absorption of the whole system, respectively. To figure out whether the GCO model can explain the optical properties of the PPA, Equation 6.4 is fitted to optical cross-sections of the PPA calculated using the FEM simulation. Before fitting Equation 6.4, the physical constants of the GCO model has to be extracted. To extract F_0, ω_{B}, γ_{B}, and τ_{B}, a single harmonic oscillator model is fitted to optical cross-sections of the bare Au antennas (Section 6.6.2, Supporting Information), whose results are summarized in Table 6.1. ω_{D} and γ_{D} are already known from the optical properties of the C=O stretch of PMMA ($\omega_{\mathrm{D}} = \omega_{\mathrm{C=O}} = 3.26 \times 10^{14}$ rad/s and $\gamma_{\mathrm{D}} = \gamma_{\mathrm{C=O}} = 5.3 \times 10^{12}$ rad/s). Therefore, the coupling rate κ is used as a parameter to fit the GCO model to the FEM simulation. An example of the spectra calculated using the GCO model are shown in Figure 2b, and it can be confirmed that the GCO model nearly perfectly fits the spectra of the FEM simulation. The same fitting result can be obtained for all sizes of the PPA and for any t (Figure 6.10, Supporting Information). This result proves that the GCO model is an appropriate quantitative model to describe the optical properties of the PPA. Note that there is a discrepancy between the GCO model and the FEM simulation for the absorption of the PMMA shell at around the resonance of the C=O stretch. This discrepancy is attributed to the intrinsic absorption of PMMA (Figure 6.8, Supporting Information). Our GCO model only considers the coupling effect but does not take this intrinsic absorption into account.

As mentioned earlier, the absorption of the PMMA shell is strongly enhanced by the coupling between the LSP of the Au antenna and the C=O stretch of PMMA, and the absorption is maximized at a certain shell thickness. Using our GCO model, we find a condition to maximize the absorption of the PMMA shell. Considering that the absorption of the PMMA shell is enhanced at the resonance of the C=O stretch, the GCO model has to be solved at ω_{D}. From the fitting shown in Table 6.1, it is known that the resonance frequency of the LSP of the Au antenna is almost the same as that of the C=O stretch of PMMA, meaning that $\omega_{\mathrm{B}} \approx \omega_{\mathrm{D}}$. Therefore, $E_{\mathrm{B}\alpha}$ and $A_{\mathrm{D}\alpha}$ at the resonance ($\omega = \omega_0 = \omega_{\mathrm{B}} = \omega_{\mathrm{D}}$) can be written as

$$E_{\mathrm{B}\alpha}(\omega_0) = \frac{1}{\Gamma_{\mathrm{B}\alpha}} \frac{1}{(1+\Phi_\alpha)^2} \frac{F_0^2}{2} \quad 6.7$$

$$A_{\mathrm{D}\alpha}(\omega_0) = \frac{1}{\Gamma_{\mathrm{B}\alpha}} \frac{\Phi_\alpha}{(1+\Phi_\alpha)^2} \frac{F_0^2}{2} \quad 6.8$$

where $\Phi_\alpha = \kappa^4/(\Gamma_{\mathrm{B}\alpha}\gamma_{\mathrm{D}}\omega_0^2)$ and $\Gamma_{\mathrm{B}\alpha} = \gamma_{\mathrm{B}} + \tau_{\mathrm{B}}\omega_0^2$. Φ_α describes the ratio of the coupling rate to the total damping of the whole system. From Equation 6.7, it can be found that $E_{\mathrm{B}\alpha}(\omega_0)$ is maximized when there is no coupling between the bright and dark oscillators, meaning $\Phi_\alpha = 0$. Therefore, the maximum of $E_{\mathrm{B}\alpha}(\omega_0)$ can be expressed as $F_0^2/(2\Gamma_{\mathrm{B}\alpha})$. By normalizing $E_{\mathrm{B}\alpha}(\omega_0)$ and $A_{\mathrm{D}\alpha}(\omega_0)$ with $F_0^2/(2\Gamma_{\mathrm{B}\alpha})$, $E_{\mathrm{B}\alpha}(\omega_0)$ and $A_{\mathrm{D}\alpha}(\omega_0)$ can be expressed only as a function of Φ_α. In Figure 6.2c, the normalized $E_{\mathrm{B}\alpha}(\omega_0)$ and $A_{\mathrm{D}\alpha}(\omega_0)$ are shown. $E_{\mathrm{B}\alpha}(\omega_0)$ keeps decreasing with an increase in Φ_α. In contrast, $A_{\mathrm{D}\alpha}(\omega_0)$ increases with increasing Φ_α, is maximized at $\Phi_\alpha = 1$, and starts decreasing with further increase in Φ_α. Therefore, we can find that $\Phi_\alpha = 1$ is the condition for maximum absorption of the PMMA shell. We call this condition the critical coupling. The critical coupling means that energy transferred between the bright and the dark oscillators takes balance with the energy dissipated by the whole system [41, 48, 49]. From Figure 6.2c, we can find that the maximum value of the normalized $A_{\mathrm{D}\alpha}(\omega_0)$ is 0.25. This result indicates that the absorption of the PMMA shell can be maximized up to 25% of the maximum of the extinction of the Au antenna.

To calculate Φ_α for the PPA, the coupling rate of the PPA is considered. The coupling rates obtained from the fitting are shown in Figure 6.2d. The coupling rate is determined by the amplitude of the near-field created by the Au antenna. Since a smaller antenna has a lower radiative damping rate, the smaller antenna can create a stronger near-field (Figure 6.11, Supporting Information) [50], resulting in a higher coupling rate [41, 51]. In addition, as mentioned earlier, the coupling rate is influenced by the number of molecules interacting with the LSP of the Au antenna. The number of interacting molecules increase with an increase in the shell thickness of the PMMA shell. Therefore, the coupling rate is higher for thicker shell thickness. Using the values in Table 1 and the coupling rate in Figure 6.2d, Φ_α is calculated as a function of the shell thickness (Figure 6.2e). Φ_α shows similar trend as the coupling rate because all values in Φ_α except κ are constant. For the smallest, medium, and largest PPA, the critical coupling (Φ_α =1) is nearly satisfied at t = 5, 10, and 40 nm, respectively. In Figure 6.1b, we can see that the absorption of the PMMA shell is maximized at those shell thicknesses. This result demonstrates that the condition for the maximum absorption of the PMMA shell can be found from Φ_α. As described earlier, Φ_α comprises the coupling rate and the damping rate of the whole system. In consequence, C_{sca}/C_{abs} of the Au antenna, which directly correlates the ratio of radiative to intrinsic damping $q = \tau_B\omega_0^2/\gamma_B$, is not a key parameter for the maximum absorption of the PMMA shell.

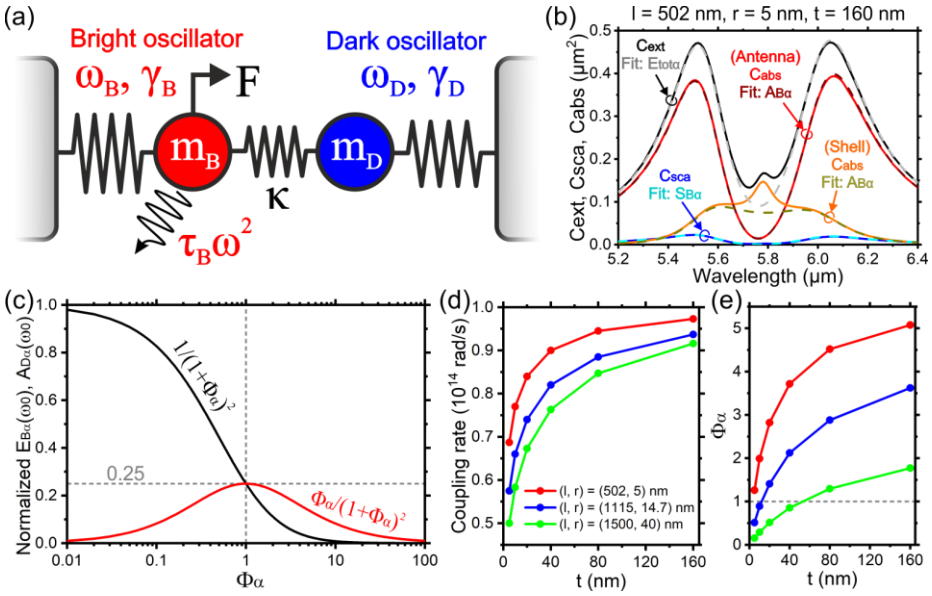

Figure 6.2. (a) Schematic illustration of the CO model. (b) Optical cross-section spectra of the PPA. The black and blue solid lines are the extinction and scattering spectra of the whole system, respectively. The red and orange solid lines are absorption spectra of the Au antenna and the PMMA shell, respectively. The dashed lines are calculated using Equation 6.4 and fitted to the solid lines. (c) $E_{B\alpha}(\omega_0)$ and $A_{D\alpha}(\omega_0)$ normalized by $F_0^2/(2\Gamma_{B\alpha})$. (d) The coupling rate and (e) Φ_α of the PPA as a function of the shell thickness t.

Table 6.1. ω_B, γ_B, and τ_B of the bare Au antennas. Those values were obtained by fitting the single harmonic oscillator model to the optical cross-sections of the bare Au antenna (see Section 6.6.2, Supporting Information).

(l, r) (nm)	ω_B (10^{14} rad/s)	γ_B (10^{13} rad/s)	$\tau_B\omega_B^2$ (10^{13} rad/s)
(502, 5)	3.26	2.95	0.16
(1115, 14.7)	3.27	1.88	1.87
(1500, 40)	3.31	0.65	6.35

We make a systematic analysis to gain an insight into the mechanism of the absorption enhancement in the PMMA shell of the PPA. $E_{B\alpha}$ and $A_{D\alpha}$ normalized by $F_0^2/(2\Gamma_{B\alpha})$ are plotted as functions of the wavelength and Φ_α (Figure 6.3a). For this plot, $\omega_0 = \omega_B = \omega_D = 3.27 \times 10^{14}$ rad/s and $\gamma_D = 5.3 \times 10^{12}$ rad/s are used. As can be seen in Equations 6.4-6.6, neither $E_{B\alpha}$ nor $A_{D\alpha}$ depend on q. Therefore, for the bright oscillator, the total damping rate is only considered by setting $\Gamma_{B\alpha} = 3.76 \times 10^{13}$ rad/s (γ_B and τ_B are arbitrary values but determined from $\gamma_B + \tau_B\omega_0^2 = 3.76 \times 10^{13}$ rad/s). κ is changed so that Φ_α can be in a range from 0.1 to 10. In Figure 6.3a, $E_{B\alpha}$ shows mode splitting which becomes stronger with an increase in Φ_α. Therefore, $E_{B\alpha}$ keeps decreasing at the resonance with an increase of Φ_α (see Figure 6.2c). For $A_{D\alpha}$, the peak becomes pronounced with an increase in Φ_α up to 1. With an increase in Φ_α beyond 1, $A_{D\alpha}$ becomes broader and weaker. This is because the mode splitting starts occurring at the resonance of the dark oscillator when $\Phi_\alpha > 1$, which describes the decrease in $A_{D\alpha}(\omega_0)$ shown in Figure 6.2c. Since the dark oscillator shows mode splitting only when the coupling is strong [48, 49, 52], the coupling can be divided into two regimes according to Φ_α: A) When $\Phi_\alpha < 1$, the coupling is in a weak coupling regime. In this regime, the energy transferred between the bright and the dark oscillators is mostly dissipated in the system. B) When $\Phi_\alpha > 1$, the coupling can be considered as the strong coupling regime because the energy is transferred between the bright and dark oscillators before the energy is dissipated by the system´s damping. By having a closer look at the absorption of the dark oscillator, we may be able to obtain more detailed information about the coupling regime (Section 6.6.3, Supporting Information). We appreciate that other groups categorize coupling regimes differently. For example, it has been suggested that the strong coupling is given by $\kappa >> (\Gamma_{B\alpha}\gamma_D)^{1/2}$ [41, 53]. As demonstrated in Figure 6.3a, Φ_α can give a clear boundary between weak and strong coupling regimes. Therefore, Φ_α may be used as an alternative indicator to find those coupling regimes.

Based on the finding from Figure 6.3a, the absorption properties of the PMMA shell shown in Figure 6.1b are considered more in detail. We demonstrate Figure 6.2e that Φ_α of the smallest PPA is larger than 1 for all t. Therefore, the absorption of the PMMA shell keeps decreasing and the absorption peak starts splitting into two peaks with an increase in t. In contrast, Φ_α of the medium and the largest PPAs cross over 1 with an increase in t. For those two PPAs, the absorption of the PMMA shell become stronger until t reaches $\Phi_\alpha = 1$, and the absorption becomes weaker and broader when Φ_α is over 1.

Having addressed the role of critical coupling in the PPA, we finally turn our focus on the influence of $q = \tau_B\omega_0^2/\gamma_B$ on the plasmonic EIA [8]. Figure 6.3b shows $E_{B\alpha}$, $S_{B\alpha}$, $A_{B\alpha}$, $A_{D\alpha}$, and $A_{tot\alpha}$ calculated at $\Phi_\alpha = 1$ in Figure 6.3a. For those spectra, q is changed so that the total damping is fixed as $\Gamma_{B\alpha} = 3.76 \times 10^{13}$ rad/s. As mentioned earlier, $E_{B\alpha}$ and $A_{D\alpha}$ are independent of q. Thus, $E_{B\alpha}$ and $A_{D\alpha}$ are almost identical for all q. All spectra in Figure 6.3b considers $\Phi_\alpha = 1$, meaning that the critical coupling is satisfied, and $A_{D\alpha}$ is maximized. With an increase in q, $S_{B\alpha}$ increases, $A_{B\alpha}$ decreases, and $A_{tot\alpha}$ changes from EIT-like (two peaks) to EIA-like profile (one pronounced peak). This spectral change of $A_{tot\alpha}$ is because two peaks of $A_{B\alpha}$ are higher than the peak of $A_{D\alpha}$ when q is small, but the peak of $A_{D\alpha}$ can be larger than those two peaks of $A_{B\alpha}$ when q is large. Therefore, we derive that q determines whether $A_{tot\alpha}$ possesses an EIT- or EIA-like spectral profiles. To observe the EIA-profile, $A_{D\alpha} > A_{B\alpha}$ has to be satisfied. This condition may be found by comparing the maximum of $A_{D\alpha}$ and the maximum of $A_{B\alpha}$ without coupling (dark yellow dashed lines in Figure 6.3b), which are $A_{D\alpha(max)} = (1/4)[F_0^2/(2\Gamma_{B\alpha})]$ and $A_{B\alpha(max)} = (\gamma_B/\Gamma_{B\alpha})[F_0^2/(2\Gamma_{B\alpha})]$. From those equations, $A_{D\alpha(max)} > A_{B\alpha(max)}$ can be obtained by $q > 3$. In general, when the absorption properties of coupled plasmonic systems are investigated, the total absorption of the system corresponding to $A_{tot\alpha}$ is considered. Thus, the plasmonic EIA has been recognized as the absorption spectral shape of $A_{tot\alpha}$ that can be seen in Figure 6.3b for $q = 4$ and 5. In this case, q plays a key role for EIA and, the condition for EIA may be found as $q > 3$. However, no matter how large q is, $A_{D\alpha}$ maximizes when the critical coupling condition is satisfied. Therefore, since EIA and the absorption of the dark oscillator are linked via Φ_α, the EIA has to be optimized based on Φ_α, not on q.

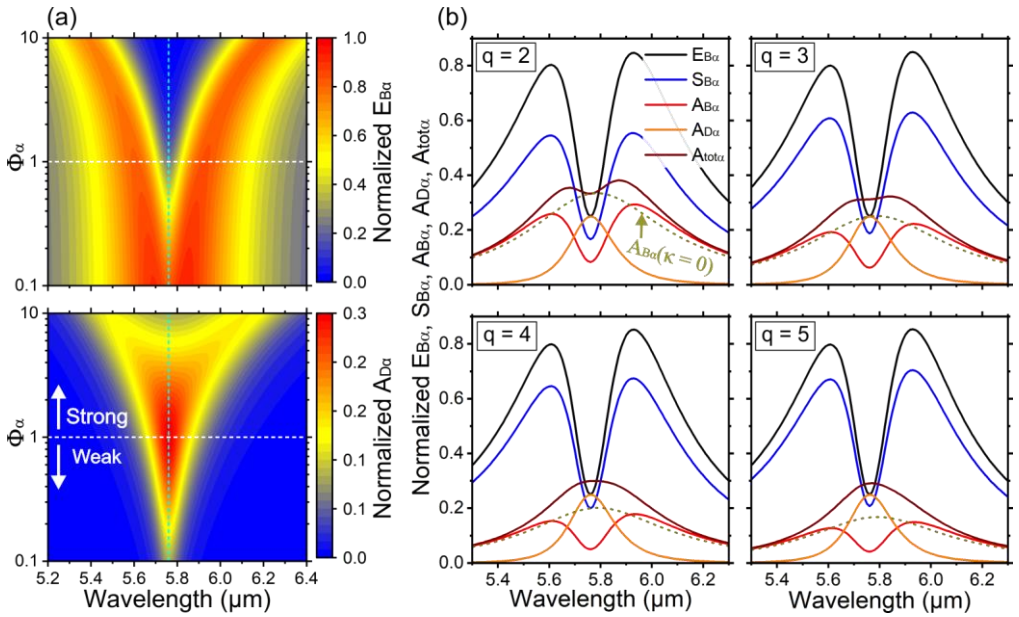

Figure 6.3. (a) Color maps of $E_{B\alpha}$ and $A_{D\alpha}$ normalized by $F_0^2/(2\Gamma_{B\alpha})$. $\omega_0 = \omega_B = \omega_D = 3.27 \times 10^{14}$ rad/s, $\Gamma_{B\alpha} = 3.76 \times 10^{13}$ rad/s, and $\gamma_D = 5.3 \times 10^{12}$ rad/s were used. q is not considered. The white dashed line indicates $\Phi_\alpha = 1$. The cyan dashed line indicates ω_0. (b) The black, blue, red, orange, and wine-red solid lines are $E_{B\alpha}$, $S_{B\alpha}$, $A_{B\alpha}$, $A_{D\alpha}$, and $A_{tot\alpha}$ normalized by $F_0^2/(2\Gamma_{B\alpha})$. Those were calculated for different $q = \tau_B\omega_0^2/\gamma_B$ and for $\Phi_\alpha = 1$ of Figure 6.3a. Since $\Gamma_{B\alpha}$ is fixed, $E_{B\alpha}$ and $A_{D\alpha}$ are nearly identical for all q. The dark-yellow dashed lines are $A_{B\alpha}$ without coupling between the bright and the dark oscillators ($\kappa = 0$).

6.3. Dipolar-quadrupolar antenna

6.3.1. Design of the DQA and calculation method

Next, we turn our focus to EIA occurring in the DQA composed of Au (Figure 6.4a). To excite EIA, the incident field should propagate along – z direction with x-polarization (parallel to the long axis of the dipolar antenna). In this configuration of the incident field, only the dipolar antenna can strongly couple with the incident field and the quadrupolar antenna interacts with the dipolar antenna through the near-field created by the dipolar antenna. In the DQA, the near-field coupling is maximized when the dipolar antenna is close to the tip of the quadrupolar antenna. As mentioned earlier, it was suggested that EIA of this fully plasmonic system is induced by the phase retardation in the coupling between the dipolar and the quadrupolar antennas. This phase retardation is attributed to the fact that there is a distance between the dipolar and the quadrupolar antennas in the z-direction [18, 19].

To elucidate the mechanism of EIA of the DQA in more detail, we investigated the absorption properties of the DQA using the FEM simulation. The size of the DQA used in our investigation is based on the works of Taubert et. al. (L_1 = 375 nm, W_1 = 60 nm, H_1 = 40 nm, L_2 = 420 nm, W_2 = 120 nm, H_2 = 60 nm, g = 220 nm, and the periodicity in the x and y directions is 700 nm) [18, 19]. The dielectric function of Au was taken from Rakic et. al. [54]. The surrounding was set as air. Since the periodic structure was considered, the Bloch-Floquet periodic boundary conditions were applied in the x and y directions. PMLs were applied on the top and bottom of the simulation model in the z-axis. Absorptance was calculated by taking a volume integral of dissipated energy density over the structures and dividing the dissipated energy by the energy of the incident wave per area of the unit cell.

6.3.2. Absorption properties of the DQA

Figure 6.4b shows absorption spectra of the dipolar antenna, quadrupolar antenna, and the DQA for different d_z. d_y is fixed as 120 nm. The absorption of the dipolar antenna shows mode splitting for all d_z. Even though the quadrupolar antenna is considered as the dark oscillator, it possesses strong absorption. This is because the LSP of the quadrupolar antenna is excited by an indirect path through near-field coupling: incident wave → dipolar oscillator → quadrupolar oscillator. During this indirect excitation process, the incident wave´s energy concentrated on the dipolar oscillator is transferred to the quadrupolar oscillator. Part of the transferred energy is absorbed by the LSP of the quadrupolar oscillator. This absorption process is the same as the PMMA shell of the PPA. In contrast to the dipolar antenna, the absorption spectral shape of the quadrupolar antenna dramatically changes with a decrease in d_z: the absorption has one sharp peak for large d_z, it is maximized at a certain d_z, and its splits into two peaks for small d_z. The absorption of the quadrupolar antenna is stronger than that of the dipolar antenna. Therefore, the total absorption of the DQA shows the EIA-like or the EIT-like spectral shapes depending on d_z. These absorption properties of the DQA are similar to those of the PPA discussed earlier.

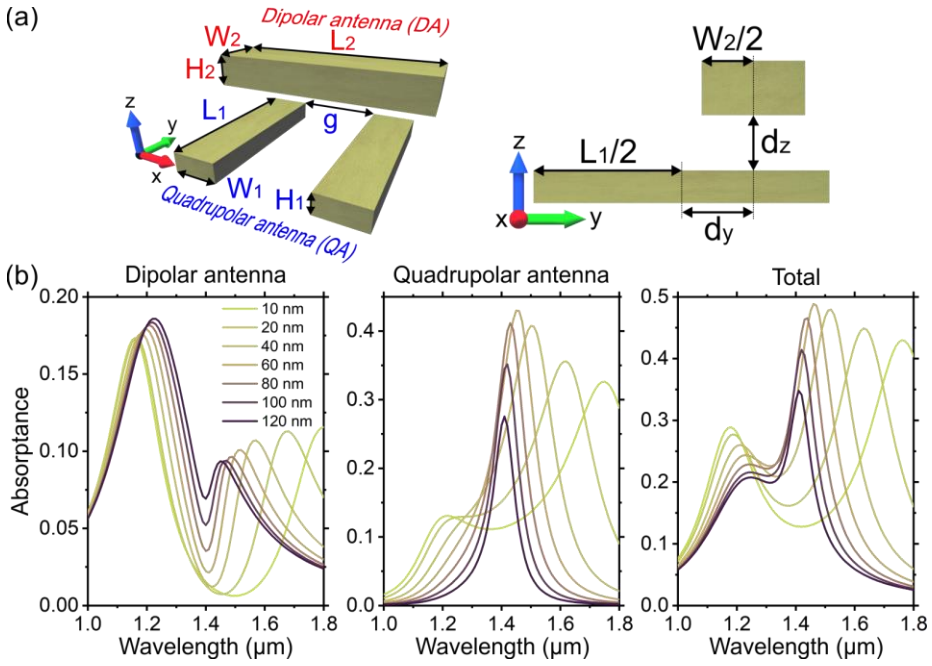

Figure 6.4. (a) Schematic illustrations of the DQA. The structural parameters are L_1 = 375 nm, W_1 = 60 nm, H_1 = 40 nm, L_2 = 420 nm, W_2 = 120 nm, H_2 = 60 nm, and g = 220 nm. The periodicity in the x- and y-directions is 700 nm. (b) Absorption spectra of the dipolar and the quadrupolar antennas in the DQA, and total absorption spectra of the DQA. d_y is fixed as 120 nm. d_z is varied in a range of 10 – 120 nm.

To gain a deeper insight into the absorption mechanism of the DQA, we again use the GCO model. In the GCO model, the dipolar and the quadrupolar antennas correspond to the bright and the dark oscillators, respectively. In general, the radiative damping of the quadrupolar antenna is ignored because it is expected that the scattering of the quadrupolar antenna is negligible [7, 49]. However, for an accurate quantitative analysis, we introduce the radiative damping of the quadrupolar antenna in the GCO model by adding τ_D on the dark oscillator. Therefore, the equations of motion of the GCO model for the DQA are

$$\frac{\mathrm{d}^2 x_{\mathrm{B}\beta}}{\mathrm{d}t^2} + \gamma_{\mathrm{B}} \frac{\mathrm{d}x_{\mathrm{B}\beta}}{\mathrm{d}t} + \omega_{\mathrm{B}}^2 x_{\mathrm{B}\beta} - \kappa^2 x_{\mathrm{D}\beta} = F(t) + \tau_{\mathrm{B}} \frac{\mathrm{d}^3 x_{\mathrm{B}\beta}}{\mathrm{d}t^3} \tag{6.9}$$

$$\frac{\mathrm{d}^2 x_{\mathrm{D}\beta}}{\mathrm{d}t^2} + \gamma_{\mathrm{D}} \frac{\mathrm{d}x_{\mathrm{D}\beta}}{\mathrm{d}t} + \omega_{\mathrm{D}}^2 x_{\mathrm{D}\beta} - \kappa^2 x_{\mathrm{B}\beta} = \tau_{\mathrm{D}} \frac{\mathrm{d}^3 x_{\mathrm{D}\beta}}{\mathrm{d}t^3} \tag{6.10}$$

The subscript β is to distinguish the GCO model of the DQA from that of the PPA. Using Equations 6.3, 6.9, and 6.10, the time-averaged dissipated power per mass of the whole system is

$$\begin{aligned} P_\beta &= \frac{1}{2}\left(\gamma_{\mathrm{B}}\omega^2\left|x_{\mathrm{B}\beta}\right|^2 + \tau_{\mathrm{B}}\omega^4\left|x_{\mathrm{B}\beta}\right|^2 + \gamma_{\mathrm{D}}\omega^2\left|x_{\mathrm{D}\beta}\right|^2 + \tau_{\mathrm{D}}\omega^4\left|x_{\mathrm{D}\beta}\right|^2\right) \\ &= E_{\mathrm{tot}\beta} = A_{\mathrm{B}\beta} + S_{\mathrm{B}\beta} + A_{\mathrm{D}\beta} + S_{\mathrm{D}\beta} \end{aligned} \tag{6.11}$$

where the absolute square of $x_{\mathrm{B}\beta}$ and $x_{\mathrm{D}\beta}$ are

$$\left|x_{\mathrm{B}\beta}\right|^2 = \frac{\left(\Omega_{\mathrm{D}}{}^2 + \Gamma_{\mathrm{D}}{}^2\omega^2\right)F_0^2}{[\Omega_{\mathrm{B}}\Omega_{\mathrm{D}} - \Gamma_{\mathrm{B}}\Gamma_{\mathrm{D}}\omega^2 - \kappa^4]^2 + \omega^2[\Gamma_{\mathrm{B}}\Omega_{\mathrm{D}} + \Gamma_{\mathrm{D}}\Omega_{\mathrm{B}}]^2} \tag{6.12}$$

$$\left|x_{\mathrm{D}\beta}\right|^2 = \frac{\kappa^4 F_0^2}{[\Omega_{\mathrm{B}}\Omega_{\mathrm{D}} - \Gamma_{\mathrm{B}}\Gamma_{\mathrm{D}}\omega^2 - \kappa^4]^2 + \omega^2[\Gamma_{\mathrm{B}}\Omega_{\mathrm{D}} + \Gamma_{\mathrm{D}}\Omega_{\mathrm{B}}]^2} \tag{6.13}$$

Compared to Equation 6.4, Equation 6.11 has an additional term $S_{\mathrm{D}\beta}$, which corresponds to the scattering of the dark oscillator. Therefore, $E_{\mathrm{D}\beta} = A_{\mathrm{D}\beta} + S_{\mathrm{D}\beta}$ and $S_{\mathrm{tot}\beta} = S_{\mathrm{B}\beta} + S_{\mathrm{D}\beta}$ can be considered as the extinction of dark oscillator and scattering of the whole system, respectively. To figure out whether the GCO model can describe the absorption properties of the DQA, $A_{\mathrm{B}\beta}$, $A_{\mathrm{D}\beta}$, and $A_{\mathrm{tot}\beta}$ were fitted to the absorption spectra of the dipolar antenna, the quadrupolar antenna, and the DQA, respectively. Before fitting the GCO model, F_0, ω_{B}, γ_{B}, and τ_{B} of the dipolar antenna without quadrupolar antenna were extracted by using the single oscillator model, resulting in $\omega_{\mathrm{B}} = 1.55 \times 10^{15}$ rad/s (1.22 μm in wavelength), $\gamma_{\mathrm{B}} = 5.23 \times 10^{13}$ rad/s, and $\tau_{\mathrm{B}}\omega_{\mathrm{B}}{}^2 = 4.47 \times 10^{14}$ rad/s (Section 6.6.4, Supporting Information). In contrast to the case of the PPA, the GCO model was fitted using all variables as fitting parameters. This fitting was made by referring the extracted F_0, ω_{B}, γ_{B}, and τ_{B}. Figure 6.5a shows examples of the fitted $A_{\mathrm{B}\beta}$, $A_{\mathrm{D}\beta}$, and $A_{\mathrm{tot}\beta}$. For all d_z, the GCO model shows good agreement not only for the total absorption of the DQA but also for the absorption of the dipolar and the quadrupolar antennas. This result proves that the GCO model is an appropriate quantitative model to describe the absorption properties of the DQA. Note that this nearly perfect fitting cannot be achieved if $\tau_{\mathrm{D}} = 0$ (Section 6.6.5, Supporting Information). From the fitting, we find that the coupling rate increases, and the resonance wavelength of the quadrupolar antenna ($\lambda_{\mathrm{D}} = 2\pi c/\omega_{\mathrm{D}}$, where c is the speed of light in vacuum) redshifts with decreasing d_z (Figure 6.5b). The resonance wavelength of the dipolar antenna also slightly redshifts in a range of 1.22 – 1.25 μm with decreasing d_z (Figure 6.13b, Supporting Information).

In a similar manner to the case of the PPA, the condition for the maximum absorption of the quadrupolar antenna is found using the CO model. Since the absorption of the quadrupolar antenna is enhanced at ω_{D} as can be seen in Figure 6.4b, Equation 6.11 should be solved at $\omega = \omega_{\mathrm{D}}$. However, for the case of the DQA, ω_{B} and ω_{D} are not aligned. Therefore, it is considered that ω_{B} is shifted from ω_{D} by an amount of δ. Using $\omega_{\mathrm{B}} = \omega_{\mathrm{D}} + \delta$, $E_{\mathrm{B}\beta}$ and $E_{\mathrm{D}\beta}$ at ω_{D} can be written as

$$E_{\mathrm{B}\beta}(\omega_{\mathrm{D}}) = \frac{1}{\Gamma_{\mathrm{B}\beta}} \frac{1}{\left(1 + \Phi_\beta\right)^2 + \Delta} \frac{F_0^2}{2} \tag{6.14}$$

$$E_{\mathrm{D}\beta}(\omega_{\mathrm{D}}) = \frac{1}{\Gamma_{\mathrm{B}\beta}} \frac{\Phi_\beta}{\left(1 + \Phi_\beta\right)^2 + \Delta} \frac{F_0^2}{2} \tag{6.15}$$

where $\Phi_\beta = \kappa^4/(\Gamma_{B\beta}\Gamma_{D\beta}\omega_D^2)$, $\Gamma_{n\beta} = \gamma_n + \tau_n\omega_D^2$, and $\Delta = \delta^2[(2\omega_D + \delta)/(\Gamma_{B\beta}\omega_D)]^2$. For $\Delta \neq 0$, the condition of maximum $E_{D\beta}(\omega_D)$ is that Φ_β becomes equal to $\Phi_{cc} = (1 + \Delta)^{1/2}$, which is the critical coupling condition when $\omega_B \neq \omega_D$. This critical coupling condition can be applied to $A_{D\beta}$ because $A_{D\beta}$ at ω_D can be written as $(\gamma_{Da}/\Gamma_{D\beta})\times E_{D\beta}(\omega_D)$. To calculate Φ_β and Φ_{cc} of the DQA, the damping rates at ω_D have to be known (Figure 6.5c). Compared to the intrinsic damping rates, the radiative damping rates dramatically change with a decrease in d_z for both the dipolar and the quadrupolar antennas, resulting in the total damping rate of the quadrupolar antenna exceeding that of the dipolar antenna at d_z = 10 nm. However, when the absorption properties of a single particle of the DQA are considered, these dramatic changes in the radiative damping rates are not observed (Section 6.6.5, Supporting Information). Since the absorption properties of the periodic structure are considered in Figure 6.4b, near-field interactions occur in lateral directions, which may influence on the radiative damping rates. Φ_β and Φ_{cc} calculated using the values in Figures 6.5b and c are shown in Figure 6.5d as a function of d_z. When d_z = 60 nm, the critical coupling $\Phi_\beta = \Phi_{cc}$ is nearly satisfied. In Figure 6.4b, it can be found that the absorption of the quadrupolar antenna is maximized at d_z = 60 nm. Therefore, these findings prove that Φ_β and Φ_{cc} can be indicators to achieve the maximum absorption of the quadrupolar antenna. Furthermore, from Φ_β and Φ_{cc}, we can understand the coupling regime of the DQA. In the case of the PPA, the coupling is classified into the weak or the strong coupling regimes by checking whether Φ_α is smaller or larger than 1. However, for the case of DQA, Φ_β has to be compared with Φ_{cc}. The absorption of the quadrupolar antenna shown in Figure 6.4b has a sharp peak for $\Phi_\beta < \Phi_{cc}$, but it shows mode splitting for $\Phi_\beta > \Phi_{cc}$. Therefore, we can consider that $\Phi_\beta < \Phi_{cc}$ gives the weak coupling regime and $\Phi_\beta > \Phi_{cc}$ gives the strong coupling regime. Since the GCO models used for the PPA and the DQA are almost the same, it is intuitively understood that the absorption properties of the DQA are nearly identical to those of the PPA.

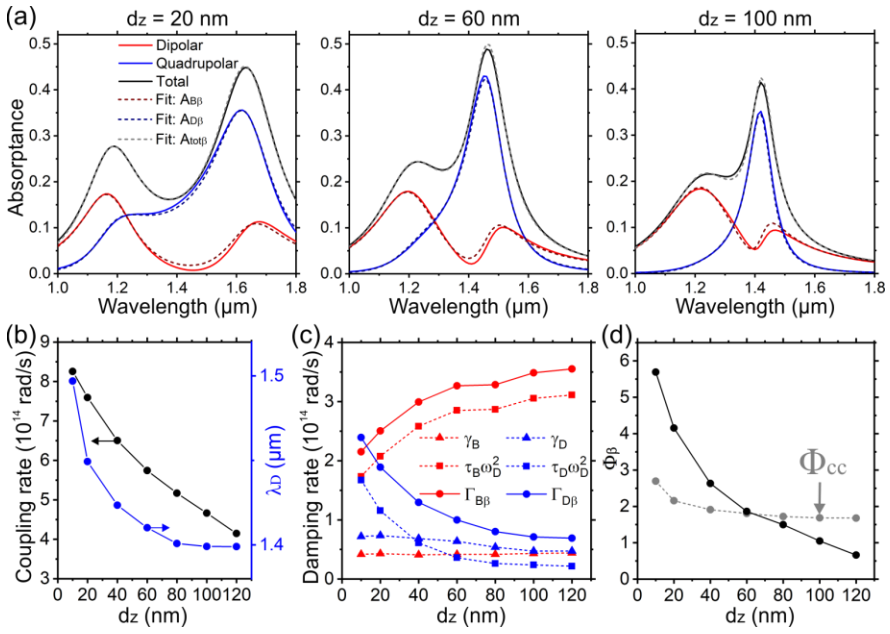

Figure 6.5. (a) $A_{B\beta}$, $A_{D\beta}$, and $A_{tot\beta}$ fitted to the absorption spectra of the dipolar antenna, the quadrupolar antenna, and the DQA, respectively. the absorption spectra of the dipolar antenna, the quadrupolar antenna, and the DQA are taken from Figure 6.4b. $A_{B\beta}$, $A_{D\beta}$, and $A_{tot\beta}$ were calculated using Equation 6.11. (b) The black and blue marks are fitting values of the coupling rate and the resonance wavelength of the quadrupolar antenna, respectively. (c) The red and blue marks are fitting values of damping rates of the dipolar and the quadrupolar antennas, respectively. The triangle, square, and circle marks are intrinsic, radiative, and total damping rates, respectively. The total damping rates were calculated by $\Gamma_{n\beta} = \gamma_n + \tau_n\omega_D^2$. (d) The black and gray marks show Φ_β and Φ_{cc}, respectively. Those were calculated using values in (b) and (c).

The d_y dependence of the absorption properties of the DQA was also investigated in a similar manner to the d_z dependency (Section 6.6.6, Supporting Information). $A_{B\beta}$, $A_{D\beta}$, and $A_{tot\beta}$ in Equation 6.11 are also in good agreement with the FEM simulation for d_y dependency. Comparing the coupling rate for d_y and d_z dependencies, it was found that two different sets of (d_y, d_z) can have a similar coupling rate. The DQA with those sets of (d_y, d_z) has almost the same absorption spectra. Therefore, we conclude that the absorption properties of the DQA are determined by the coupling rate, which can be controlled by changing the position of the dipolar antenna in the *y*-*z* plane.

If the distance between the dipolar and quadrupolar antennas is comparable to the wavelength, their coupling occurs through their far-field. In this case, the coupling may contain distance-dependent retardation effects, which has been suggested by our previous work based on the coupled-dipole method [17]. In case the gap distance of the DQA is much smaller than the wavelength (e.g., [18, 19]) we expect that the near-field coupling of the oscillators occurs in-phase. This indicates that retardation effects play a subordinate role in near-field coupled systems. Considering the facts discussed above, we conclude that the EIA in the DQA is not attributed to the phase retardation, but its EIA originates from the absorption enhancement in the quadrupolar antenna. Note that our results just indicate that a phase-retarded coupling may not be an appropriate interpretation to explain the absorption properties of the DQA, but EIA by a phase-retarded coupling may be observed in other plasmonic systems (Section 6.6.7, Supporting Information) [17, 24].

6.4. Conclusion

We theoretically investigated the absorption properties of the PPA and the DQA, which are widely known for plasmonic EIA. We find that in those coupled plasmonic systems, the absorption of the bright oscillator always splits into two peaks, and the absorption of the dark oscillator is enhanced at the resonance of the dark oscillator by near-field coupling. To gain a deeper understanding of the absorption enhancement in the dark oscillator, we introduced a GCO model including radiative damping originated from the Abraham-Lorentz force. We demonstrated that our GCO model can quantitatively describe the absorption properties of those systems. Using the GCO model, we found two essential parameters to maximize the absorption of the dark oscillator. One is the degree of coupling Φ. Φ is determined solely by the ratio between the coupling rate and the total damping rate of the whole system. Another parameter is the critical coupling state Φ_{cc}, which is equal to 1 when the resonances of the bright and the dark oscillators are aligned. When Φ is equal to Φ_{cc}, the critical coupling occurs, resulting in a maximum absorption of the dark oscillator. Our GCO model predicted that the absorption of the dark oscillator can be enhanced up to 25% of the maximum extinction of the bright oscillator without coupling.

Maximizing the absorption of the dark resonator, however, is not sufficient to observe EIA-like spectra. In addition, the bright oscillator should have a radiative damping sufficiently larger than its intrinsic one so that the absorption of the bright oscillator can be smaller than that of the dark oscillator. By doing this, the sharp absorption peak of the dark oscillator can be visible in a total absorption spectrum of a whole system, resulting in an EIA-like spectral profile. Notably, the absorption of the dark oscillator is independent of the ratio between intrinsic and radiative damping of the bright oscillator. Therefore, if plasmonic EIA is dominated by the maximization of the dark oscillator´s absorption, plasmonic EIA is determined just by Φ and Φ_{cc}. This interpretation of plasmonic EIA can be applied to many plasmonic systems similar to the PPA and the DQA.

Using our GCO model, we developed a new interpretation of plasmonic EIA, which is essential to advance EIA-based plasmonic systems. In addition, our GCO model may be able to provide details about Rabi splitting and energy transfer, which play a crucial role in plasmon-exciton coupled systems [41, 55, 56] and surface-enhanced infrared absorption spectroscopies [57]. Therefore, we expect that this work can

be beneficial for a wide range of applications and may outline an approach to develop a new type of plasmonic system.

Funding

This project has received funding from the European Research Council (ERC) under the European Union's Horizon 2020 research and innovation program (grant agreement no. 714968).

6.5. References

1. B. Gallinet, and O. J. F. Martin, "Ab initio theory of Fano resonances in plasmonic nanostructures and metamaterials," Phys. Rev. B **83** (23), 235427 (2011).
2. B. Gallinet, and O. J. Martin, "Influence of electromagnetic interactions on the line shape of plasmonic Fano resonances," ACS Nano **5** (11), 8999-9008 (2011).
3. B. Peng, S. K. Ozdemir, W. Chen, F. Nori, and L. Yang, "What is and what is not electromagnetically induced transparency in whispering-gallery microcavities," Nat. Commun. **5**, 5082 (2014).
4. M. F. Limonov, M. V. Rybin, A. N. Poddubny, and Y. S. Kivshar, "Fano resonances in photonics," Nat. Photonics **11** (9), 543-554 (2017).
5. J. A. Faucheaux, J. Fu, and P. K. Jain, "Unified Theoretical Framework for Realizing Diverse Regimes of Strong Coupling between Plasmons and Electronic Transitions," J. Phys. Chem. C **118** (5), 2710-2717 (2014).
6. C. L. Garrido Alzar, M. A. G. Martinez, and P. Nussenzveig, "Classical analog of electromagnetically induced transparency," Am. J. Phys. **70** (1), 37-41 (2002).
7. N. Liu, L. Langguth, T. Weiss, J. Kastel, M. Fleischhauer, T. Pfau, and H. Giessen, "Plasmonic analogue of electromagnetically induced transparency at the Drude damping limit," Nat. Mater. **8** (9), 758-762 (2009).
8. R. Adato, A. Artar, S. Erramilli, and H. Altug, "Engineered absorption enhancement and induced transparency in coupled molecular and plasmonic resonator systems," Nano Lett. **13** (6), 2584−2591 (2013).
9. P. Tassin, L. Zhang, R. Zhao, A. Jain, T. Koschny, and C. M. Soukoulis, "Electromagnetically induced transparency and absorption in metamaterials: the radiating two-oscillator model and its experimental confirmation," Phys. Rev. Lett. **109** (18), 187401 (2012).
10. P. Tassin, L. Zhang, T. Koschny, E. N. Economou, and C. M. Soukoulis, "Low-loss metamaterials based on classical electromagnetically induced transparency," Phys. Rev. Lett. **102** (5), 053901 (2009).
11. S. Zhang, D. A. Genov, Y. Wang, M. Liu, and X. Zhang, "Plasmon-induced transparency in metamaterials," Phys. Rev. Lett. **101** (4), 047401 (2008).
12. C. Ma, Y. Zhang, Y. Zhang, S. Bao, J. Jin, M. Li, D. Li, Y. Liu, and Y. Xu, "All-optical tunable slow-light based on an analogue of electromagnetically induced transparency in a hybrid metamaterial," Nanoscale Adv. **3** (19), 5636-5641 (2021).

13. B. Metzger, T. Schumacher, M. Hentschel, M. Lippitz, and H. Giessen, "Third Harmonic Mechanism in Complex Plasmonic Fano Structures," ACS Photonics **1** (6), 471-476 (2014).

14. N. Liu, T. Weiss, M. Mesch, L. Langguth, U. Eigenthaler, M. Hirscher, C. Sonnichsen, and H. Giessen, "Planar metamaterial analogue of electromagnetically induced transparency for plasmonic sensing," Nano Lett. **10** (4), 1103-1107 (2010).

15. J. B. Lassiter, H. Sobhani, J. A. Fan, J. Kundu, F. Capasso, P. Nordlander, and N. J. Halas, "Fano resonances in plasmonic nanoclusters: geometrical and chemical tunability," Nano Lett. **10** (8), 3184-3189 (2010).

16. J. Li, R. Gan, Q. Guo, H. Liu, J. Xu, and F. Yi, "Tailoring optical responses of infrared plasmonic metamaterial absorbers by optical phonons," Opt. Express **26** (13), 16769-16781 (2018).

17. K. Matsumori, R. Fujimura, and M. Retsch, "Selective broadband absorption by mode splitting for radiative cooling," Opt. Express **30** (9), 14258-14273 (2022).

18. R. Taubert, M. Hentschel, J. Kastel, and H. Giessen, "Classical analog of electromagnetically induced absorption in plasmonics," Nano Lett. **12** (3), 1367−1371 (2012).

19. R. Taubert, M. Hentschel, and H. Giessen, "Plasmonic analog of electromagnetically induced absorption: simulations, experiments, and coupled oscillator analysis," J. Opt. Soc. Am. B **30** (12), 3123-3134 (2013).

20. J. He, P. Ding, J. Wang, C. Fan, and E. Liang, "Ultra-narrow band perfect absorbers based on plasmonic analog of electromagnetically induced absorption," Opt. Express **23** (5), 6083-6091 (2015).

21. T. Zhang, J. Dai, Y. Dai, Y. Fan, X. Han, J. Li, F. Yin, Y. Zhou, and K. Xu, "Dynamically tunable plasmon induced absorption in graphene-assisted metallodielectric grating," Opt. Express **25** (21), 26221-26233 (2017).

22. W. Xiong, W. Wang, F. Ling, W. Yu, and J. Yao, "Modulation of terahertz electromagnetically induced absorption analogue in a hybrid metamaterial/graphene structure," AIP Advances **9** (11), 115314 (2019).

23. J. Krauth, T. Schumacher, J. Defrance, B. Metzger, M. Lippitz, T. Weiss, H. Giessen, and M. Hentschel, "Nonlinear Spectroscopy on the Plasmonic Analog of Electromagnetically Induced Absorption: Revealing Minute Structural Asymmetries," ACS Photonics **6** (11), 2850-2859 (2019).

24. D. Floess, M. Hentschel, T. Weiss, H.-U. Habermeier, J. Jiao, S. G. Tikhodeev, and H. Giessen, "Plasmonic Analog of Electromagnetically Induced Absorption Leads to Giant Thin Film Faraday Rotation of 14°," Phys. Rev. X **7** (2), 021048 (2017).

25. C. Wu, B. Neuner, G. Shvets, J. John, A. Milder, B. Zollars, and S. Savoy, "Large-area wide-angle spectrally selective plasmonic absorber," Phys. Rev. B **84** (7), 075102 (2011).

26. S. Tretyakov, "Maximizing Absorption and Scattering by Dipole Particles," Plasmonics **9** (4), 935-944 (2014).

27. T. Neuman, C. Huck, J. Vogt, F. Neubrech, R. Hillenbrand, J. Aizpurua, and A. Pucci, "Importance of Plasmonic Scattering for an Optimal Enhancement of Vibrational Absorption in SEIRA with Linear Metallic Antennas," J. Phys. Chem. C **119** (47), 26652-26662 (2015).

28. F. Zhang, X. Huang, W. Cai, R. Yang, Q. Fu, Y. Fan, Y. Hu, K. Qiu, W. Zhang, C. Li, and Q. Li, "EIA metamaterials based on hybrid metal/dielectric structures with dark-mode-enhanced absorption," Opt. Express **28** (12), 17481-17489 (2020).

29. X. Zhang, N. Xu, K. Qu, Z. Tian, R. Singh, J. Han, G. S. Agarwal, and W. Zhang, "Electromagnetically induced absorption in a three-resonator metasurface system," Sci. Rep. **5**, 10737 (2015).

30. X. Hu, S. Yuan, A. Armghan, Y. Liu, Z. Jiao, H. Lv, C. Zeng, Y. Huang, Q. Huang, Y. Wang, and J. Xia, "Plasmon induced transparency and absorption in bright–bright mode coupling metamaterials: a radiating two-oscillator model analysis," Journal of Physics D: Applied Physics **50** (2), 025301 (2017).

31. R. Yahiaoui, J. A. Burrow, S. M. Mekonen, A. Sarangan, J. Mathews, I. Agha, and T. A. Searles, "Electromagnetically induced transparency control in terahertz metasurfaces based on bright-bright mode coupling," Phys. Rev. B **97** (15), 155403 (2018).

32. S. Lee, and Q. H. Park, "Dynamic coupling of plasmonic resonators," Sci. Rep. **6**, 21989 (2016).

33. A. Lovera, B. Gallinet, P. Nordlander, and O. J. F. Martin, "Mechanisms of Fano Resonances in Coupled Plasmonic Systems," ACS Nano **7** (5), 4527–4536 (2013).

34. A. Gandman, R. T. Mackin, B. Cohn, I. V. Rubtsov, and L. Chuntonov, "Radiative Enhancement of Linear and Third-Order Vibrational Excitations by an Array of Infrared Plasmonic Antennas," ACS Nano **12** (5), 4521-4528 (2018).

35. M. A. Kats, N. Yu, P. Genevet, Z. Gaburro, and F. Capasso, "Effect of radiation damping on the spectral response of plasmonic components," Opt. Express **19** (22), 21748-21753 (2011).

36. Z. Pan, and J. Guo, "Enhanced optical absorption and electric field resonance in diabolo metal bar optical antennas," Opt. Express **21** (26), 32491-32500 (2013).

37. K. S. Lee, and M. A. El-Sayed, "Dependence of the enhanced optical scattering efficiency relative to that of absorption for gold metal nanorods on aspect ratio, size, end-cap shape, and medium refractive index," J. Phys. Chem. B **109** (43), 20331-20338 (2005).

38. K. Chen, R. Adato, and H. Altug, "Dual-band perfect absorber for multispectral plasmon-enhanced infrared spectroscopy," ACS Nano **6** (9), 7998-8006 (2012).

39. B. Cohn, K. Das, A. Basu, and L. Chuntonov, "Infrared Open Cavities for Strong Vibrational Coupling," J. Phys. Chem. Lett. **12** (29), 7060-7066 (2021).

40. H. Chen, L. Shao, K. C. Woo, J. Wang, and H.-Q. Lin, "Plasmonic–Molecular Resonance Coupling: Plasmonic Splitting versus Energy Transfer," J. Phys. Chem. C **116** (26), 14088-14095 (2012).

41. T. J. Antosiewicz, S. P. Apell, and T. Shegai, "Plasmon–Exciton Interactions in a Core–Shell Geometry: From Enhanced Absorption to Strong Coupling," ACS Photonics **1** (5), 454-463 (2014).

42. S. Babar, and J. H. Weaver, "Optical constants of Cu, Ag, and Au revisited," Appl. Opt. **54** (3), 477-481 (2015).

43. X. Zhang, J. Qiu, J. Zhao, X. Li, and L. Liu, "Complex refractive indices measurements of polymers in infrared bands," Journal of Quantitative Spectroscopy and Radiative Transfer **252**, 107063 (2020).

44. H. Luo, Z. Kang, Y. Gao, H. Peng, J. Li, G. Qin, and Y. Liu, "Large aspect ratio gold nanorods (LAR-GNRs) for mid-infrared pulse generation with a tunable wavelength near 3 mum," Opt. Express **27** (4), 4886-4896 (2019).

45. N. Li, H. Yin, X. Zhuo, B. Yang, X.-M. Zhu, and J. Wang, "Infrared-Responsive Colloidal Silver Nanorods for Surface-Enhanced Infrared Absorption," Adv. Opt. Mater. **6** (17), 1800436 (2018).

46. M. Mayer, L. Scarabelli, K. March, T. Altantzis, M. Tebbe, M. Kociak, S. Bals, F. J. Garcia de Abajo, A. Fery, and L. M. Liz-Marzan, "Controlled Living Nanowire Growth: Precise Control over the Morphology and Optical Properties of AgAuAg Bimetallic Nanowires," Nano Lett. **15** (8), 5427-5437 (2015).

47. D. Huo, M. J. Kim, Z. Lyu, Y. Shi, B. J. Wiley, and Y. Xia, "One-Dimensional Metal Nanostructures: From Colloidal Syntheses to Applications," Chem. Rev. **119** (15), 8972-9073 (2019).

48. N. Murata, R. Hata, and H. Ishihara, "Crossover between Energy Transparency Resonance and Rabi Splitting in Antenna–Molecule Coupled Systems," J. Phys. Chem. C **119** (45), 25493-25498 (2015).

49. B. Gallinet, T. Siegfried, H. Sigg, P. Nordlander, and O. J. Martin, "Plasmonic radiance: probing structure at the Angstrom scale with visible light," Nano Lett. **13** (2), 497-503 (2013).

50. C. Deeb, X. Zhou, J. Plain, G. P. Wiederrecht, R. Bachelot, M. Russell, and P. K. Jain, "Size Dependence of the Plasmonic Near-Field Measured via Single-Nanoparticle Photoimaging," J. Phys. Chem. C **117** (20), 10669-10676 (2013).

51. F. Stete, P. Schoßau, M. Bargheer, and W. Koopman, "Size-Dependent Coupling of Hybrid Core–Shell Nanorods: Toward Single-Emitter Strong-Coupling," J. Phys. Chem. C **122** (31), 17976-17982 (2018).

52. F. Stete, W. Koopman, and M. Bargheer, "Signatures of Strong Coupling on Nanoparticles: Revealing Absorption Anticrossing by Tuning the Dielectric Environment," ACS Photonics **4** (7), 1669-1676 (2017).

53. G. Zengin, G. Johansson, P. Johansson, T. J. Antosiewicz, M. Kall, and T. Shegai, "Approaching the strong coupling limit in single plasmonic nanorods interacting with J-aggregates," Sci. Rep. **3**, 3074 (2013).

54. A. D. Rakic, A. B. Djurisic, J. M. Elazar, and M. L. Majewski, "Optical properties of metallic films for vertical-cavity optoelectronic devices," Appl. Opt. **37** (22), 5271-5283 (1998).

55. A. E. Schlather, N. Large, A. S. Urban, P. Nordlander, and N. J. Halas, "Near-field mediated plexcitonic coupling and giant Rabi splitting in individual metallic dimers," Nano Lett. **13** (7), 3281−3286 (2013).

56. G. P. Wiederrecht, G. A. Wurtz, and J. Hranisavljevic, "Coherent Coupling of Molecular Excitons to Electronic Polarizations of Noble Metal Nanoparticles," Nano Lett. **4** (11), 2121-2125 (2004).

57. F. Neubrech, C. Huck, K. Weber, A. Pucci, and H. Giessen, "Surface-Enhanced Infrared Spectroscopy Using Resonant Nanoantennas," Chem. Rev. **117** (7), 5110-5145 (2017).

6.6. Supporting Information

6.6.1. Optical properties of PMMA

The permittivity of PMMA taken from Zhang et al. [1]. is shown in Figure 6.6a. The strong molecular vibration of the C=O stretch can be found at around 6 μm. Figure 6.6b shows the permittivity of PMMA at around the C=O stretch. Since the spectral resolution is not high enough and we have to extract the resonance frequency and damping rate of the C=O stretch, the Lorentz model was fitted to the permittivity. The Lorentz model is

$$\varepsilon_{\mathrm{C=O}} = \varepsilon_{\mathrm{bg}} + \frac{f\omega_{\mathrm{C=O}}^2}{\omega_{\mathrm{C=O}}^2 - \omega^2 - i\gamma_{\mathrm{C=O}}\omega} \tag{6.16}$$

where $\varepsilon_{\mathrm{bg}}$ is the dielectric constant at high frequency, f is the oscillator strength, $\omega_{\mathrm{C=O}}$ is the resonant frequency, and $\gamma_{\mathrm{C=O}}$ is the intrinsic damping rate.

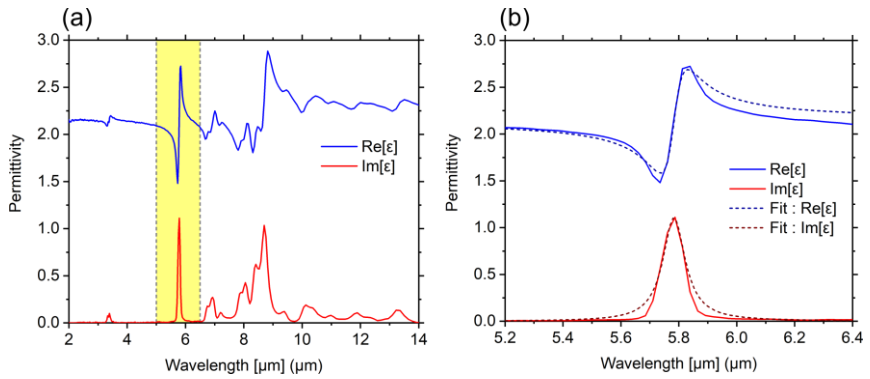

Figure 6.6. (a) The permittivity of PMMA in the infrared range. The blue and red solid lines are the real and imaginary parts of the permittivity, respectively. (a) The permittivity of PMMA at around the C=O stretch. The blue and red dashed lines are the real and the imaginary parts of the permittivity calculated using Equation 6.16, respectively.

6.6.2. Optical properties of the PPA

Figure 6.7 shows the extinction and scattering properties of the PPA. The extinction and scattering spectra show mode splitting for all *t*. Figure 6.8 shows the absorption properties of the PMMA shell with and without the Au antenna. The inside of the bare PMMA shell is filled with the material with the refractive index of 1.46, which is the same as the refractive index of the surrounding. The absorption of the bare PMMA shell increase with an increase in *t*. This intrinsic absorption appears in the absorption of the PMMA shell of the PPA.

Before fitting Equation 6.4 to the optical cross-sections of the PPA, F_0, ω_{B}, γ_{B}, and τ_{B} were extracted by fitting a single oscillator model (SO) model to the optical cross-sections of the bare Au antenna. The SO model can be written as

$$\frac{\mathrm{d}^2x_0}{\mathrm{d}t^2} + \gamma_{\mathrm{B}}\frac{\mathrm{d}x_0}{\mathrm{d}t} + \omega_{\mathrm{B}}^2 x_{\mathrm{B0}} = F(t) + \tau_{\mathrm{B}}\frac{\mathrm{d}^3x_0}{\mathrm{d}t^3} \tag{6.17}$$

The time-averaged dissipated power of the SO model can be obtained using Equation 6.3

$$P_0 = \frac{1}{2}(\gamma_B \omega^2 |x_0|^2 + \tau_B \omega^4 |x_0|^2) = E_0 = A_0 + S_0 \qquad 6.18$$

where the absolute square of x_0 is

$$|x_0|^2 = \frac{F_0^2}{(\omega_B^2 - \omega^2)^2 + (\gamma_B + \tau_B \omega^2)\omega^2}$$

In Equation 6.18, E_0, A_0, and S_0 correspond to extinction, absorption, and scattering, respectively. In Figure 6.9 the SO model fitted to the optical cross-sections of the bare Au antenna is shown. For all sizes of the Au antenna, the SO model shows nearly perfect agreement with the spectra obtained from the FEM simulation.

Figure 6.10 shows the optical cross-section spectra calculated using the FEM simulation and the CO model for two different sizes of the PPA. The CO model is in good agreement with the FEM simulation for any combination of the structural parameters.

Figure 6.11 shows the electromagnetic field distribution maps of the smallest, medium, and largest bare Au antennas. Those maps are taken at the wavelength of 5.78 μm. With decrease in the size of the Au antenna, the electric field around the antenna become stronger. This results in stronger coupling in the PPA for smaller Au antenna.

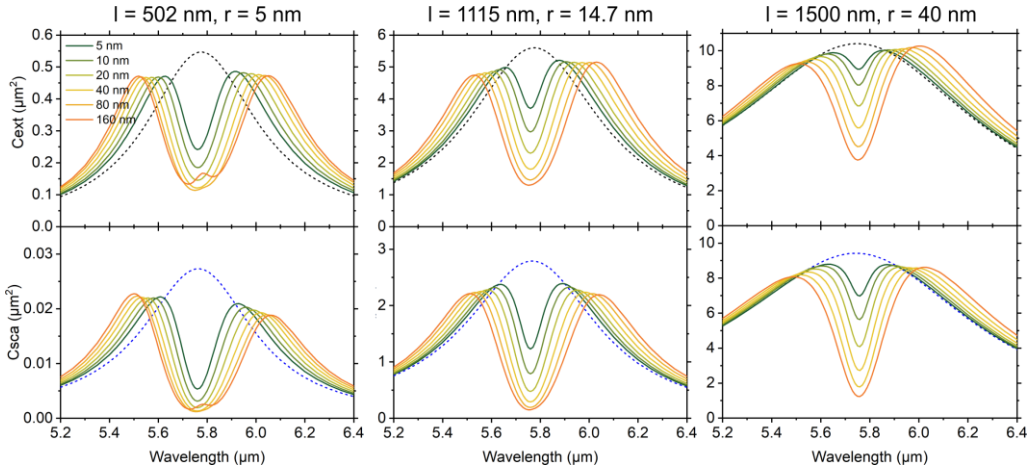

Figure 6.7. The black and blue solid lines are extinction and scattering spectra of the bare Au antenna, respectively. The dashed lines are extinction and scattering spectra of the PPA with different *t*.

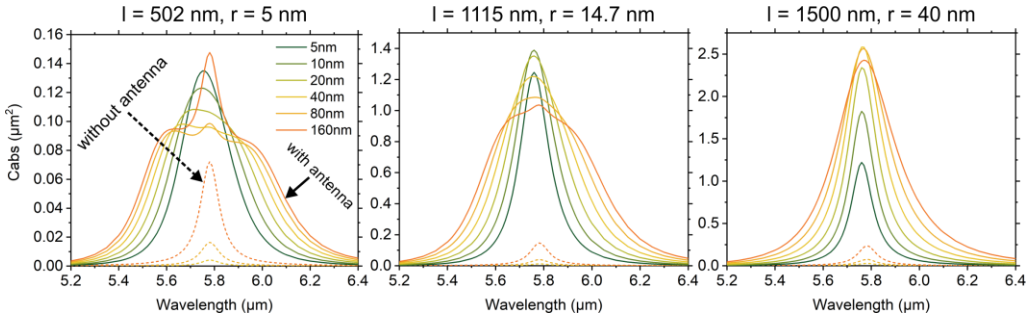

Figure 6.8. The solid lines are absorption spectra of the PMMA shell of the PPA. The dashed lines are absorption spectra of the bare PMMA shell. The inside of the bare PMMA shell is filled with the same material as the surrounding.

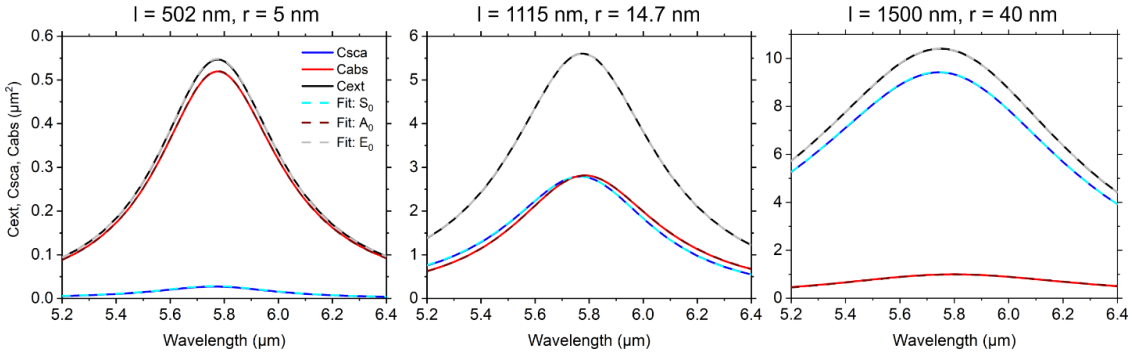

Figure 6.9. The blue, red, and black solid lines are scattering, absorption, and extinction spectra of the bare Au antenna calculated using the FEM simulation. The cyan, wine-red, and gray dashed lines are scattering, absorption, and extinction spectra calculated using Equation 6.18.

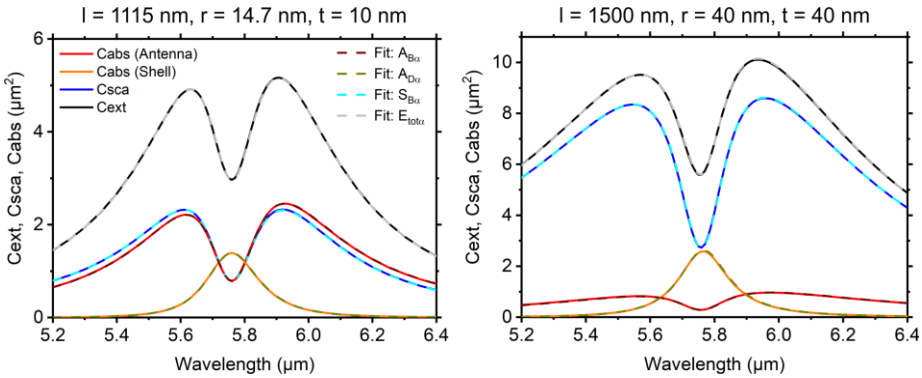

Figure 6.10. Optical cross-section spectra of the PPAs. The black and blue solid lines are the extinction and scattering spectra of the whole system, respectively. The red and orange solid lines are absorption spectra of the Au antenna and the PMMA shell, respectively. The dashed lines are calculated using Equation 6.4 and fitted to the solid lines.

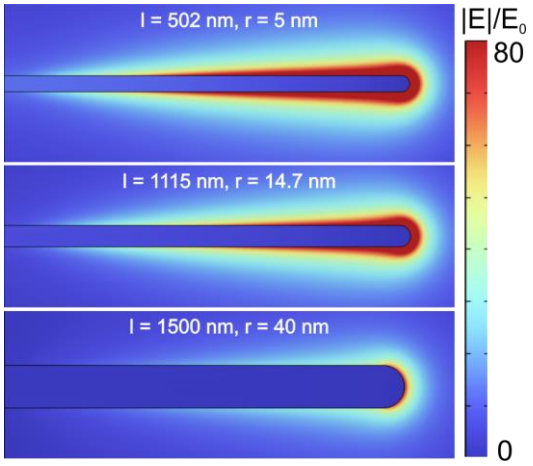

Figure 6.11. Normalized absolute electric field distribution maps of the bare Au antennas at the wavelength of 5.78 μm.

6.6.3. Weak, intermediate, and strong coupling regimes

In this work, we classified the coupling regime just by comparing whether Φ_α is larger than 1 or not. However, in other studies, such as energy transfer [2, 3] or exciton-plasmon coupling,[4-6] the strong coupling is considered as that the coupling rate is high enough so that the absorption of the dark oscillator splits into two peaks [7]. To provide deeper insight into the coupling regime for those studies, we find how large Φ_α should be to induce mode splitting in the dark oscillator. Figure 6.12 shows the color maps taken from Figure 6.3a. From the systematical analysis made in Figure 6.12, it can be found that the absorption of the dark oscillator starts by weakly splitting into two peaks when Φ_α becomes larger than about 3.5. Therefore, the CO model suggests that the coupling can be classified in the weak ($\Phi_\alpha < 1$), intermediate ($1 < \Phi_\alpha < 3.5$), and strong coupling regimes ($3.5 < \Phi_\alpha$).

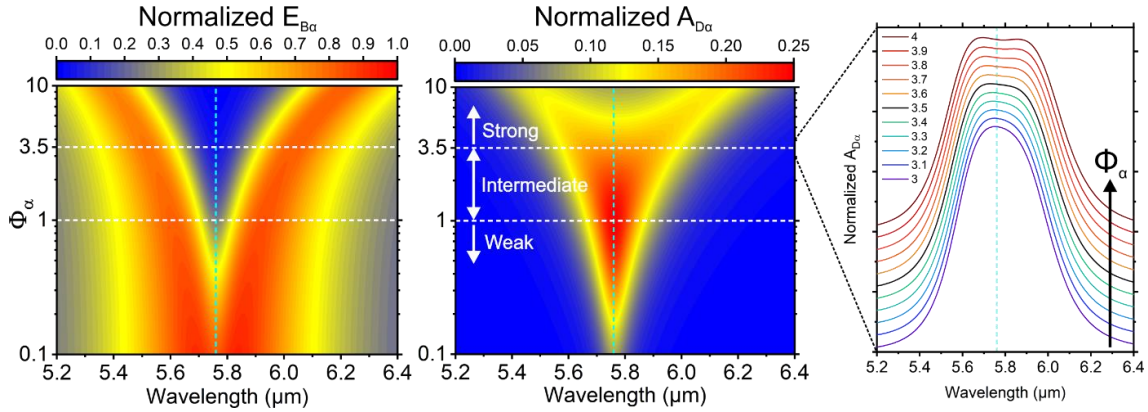

Figure 6.12. The color maps taken from Figure 6.3a and the spectra of the normalized $A_{D\alpha}$ at around $\Phi_\alpha = 3.5$.

6.6.4. Optical properties of the DQA

Equation 6.11 was fitted to the absorption spectra of the DQA by extracting F_0, ω_B, γ_B, and τ_B. Those values were obtained by fitting the SO model to the absorption spectrum of the dipolar antenna without the quadrupolar antenna. Figure 6.13a shows the SO model fitted to the absorption of the dipolar antenna obtained from the FEM simulation. The SO model shows good agreement with the FEM simulation.

Figure 6.13b shows the resonance wavelength of the dipolar and quadrupolar antennas of the DQA. Those values were obtained from the fitting. With a decrease in d_z, their resonance wavelengths redshift. In Figure 6.5c, the radiative damping rates of the dipolar and the quadrupolar antennas are plotted. Their radiative damping rates change depending on d_z. These changes are not attributed only to the resonance wavelength but also to the radiative damping coefficient. The radiative damping coefficients of the dipolar and the quadrupolar antennas are shown in Figure 6.13c. τ_B keeps decreasing with a decrease in d_z. In contrast, τ_D exponentially increases with a decrease in d_z.

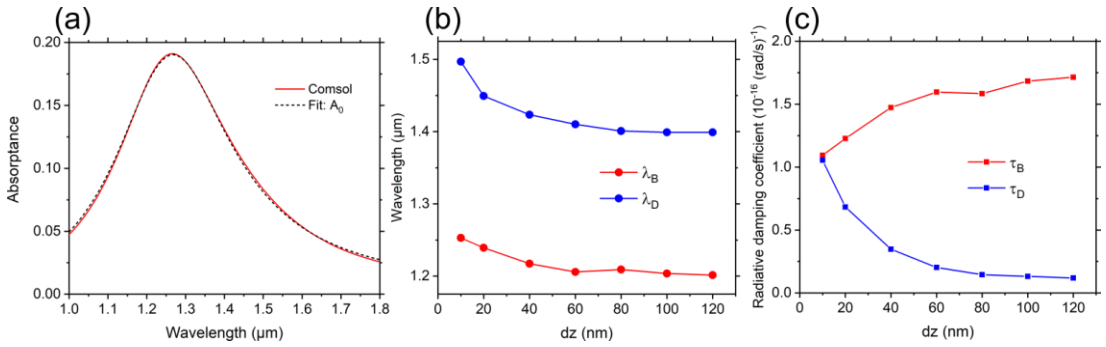

Figure 6.13. (a) The red solid line is the absorption spectrum of the dipolar antenna without the quadrupolar antenna calculated using the FEM simulation. The black dashed line is the spectrum calculated using Equation 6.18. (b) The fitting values of the resonance wavelength of the dipolar and the quadrupolar antennas of the DQA. The red and blue marks are for the dipolar and the quadrupolar antennas, respectively. (c) The red and blue marks are the fitting values of the radiative damping coefficients of the dipolar and the quadrupolar antennas, respectively.

6.6.5. Optical properties of a single particle of the DQA

In the main text, the absorption properties of the DQA in the periodic system are considered. To understand the optical properties of the DQA in more detail, a single particle of the DQA was modeled and its optical cross-sections were calculated using the FEM simulation. The size and shape of the single particle of the DQA are the same as the one shown in Figure 6.4a. The calculation method is the same as that for the PPA. Figure 6.14 shows the absorption spectra of the DQA. As with the spectra of the periodic model shown in Figure 6.4b, the absorption of the dipolar antenna shows mode splitting for all d_z. The absorption of the quadrupolar antenna is enhanced and starts splitting with an increase in d_z. The total absorption of the DQA shows a similar trend to the quadrupolar antenna.

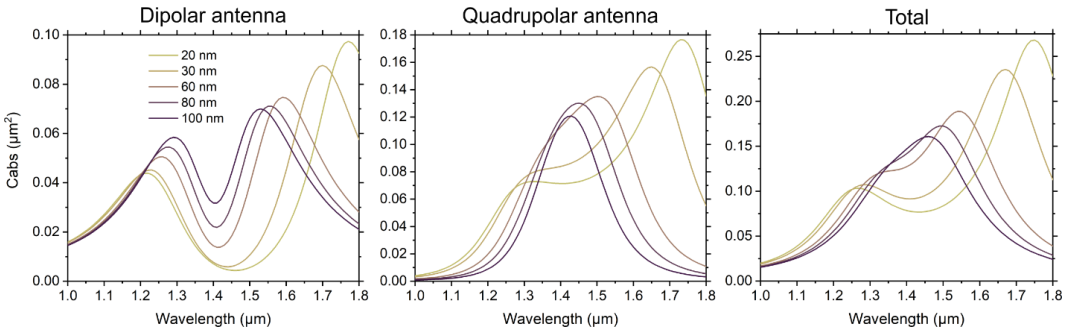

Figure 6.14. Absorption spectra of the dipolar and the quadrupolar antennas of the single particle of the DQA, and total absorption spectra of the single particle of the DQA. d_y is fixed as 120 nm. d_z is varied in a range of 20 – 100 nm.

Figure 6.15 shows extinction, scattering, and absorption cross-sections of the dipolar antenna without the quadrupolar antenna. The scattering is stronger compared to the absorption. To extract the intrinsic and radiative damping of the dipolar antenna, the SO model was fitted to the spectra obtained from the FEM simulation. The fitting resulted in $\omega_B = 1.4 \times 10^{15}$ rad/s (1.35 μm in wavelength), $\gamma_B = 4.5 \times 10^{13}$ rad/s, and $\tau_B\omega_B^2 = 4.05 \times 10^{14}$ rad/s. Based on those obtained values, the CO model described by Equation 6.11 was fitted to the extinction, scattering, and absorption spectra of the DQA (Figure 6.16). The CO model shows good agreement with the FEM simulation not only for the absorption but also the extinction and scattering,

which proves the CO model is an appropriate model to describe the overall optical properties of the DQA. Using the CO model, the total scattering of the DQA can be divided into contributions from the dipolar and the quadrupolar antennas. The scattering spectra show a similar spectral shape to the absorption spectra.

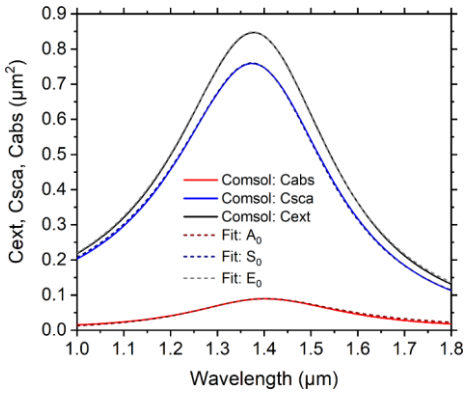

Figure 6.15. The optical properties of the single particle of dipolar antenna. The red, blue, and black solid lines are absorption, scattering, and extinction spectra calculated using the FEM simulation, respectively. The wine-red, navy, and grey dashed lines are absorption, scattering, and extinction spectra calculated using Equation 6.18, respectively.

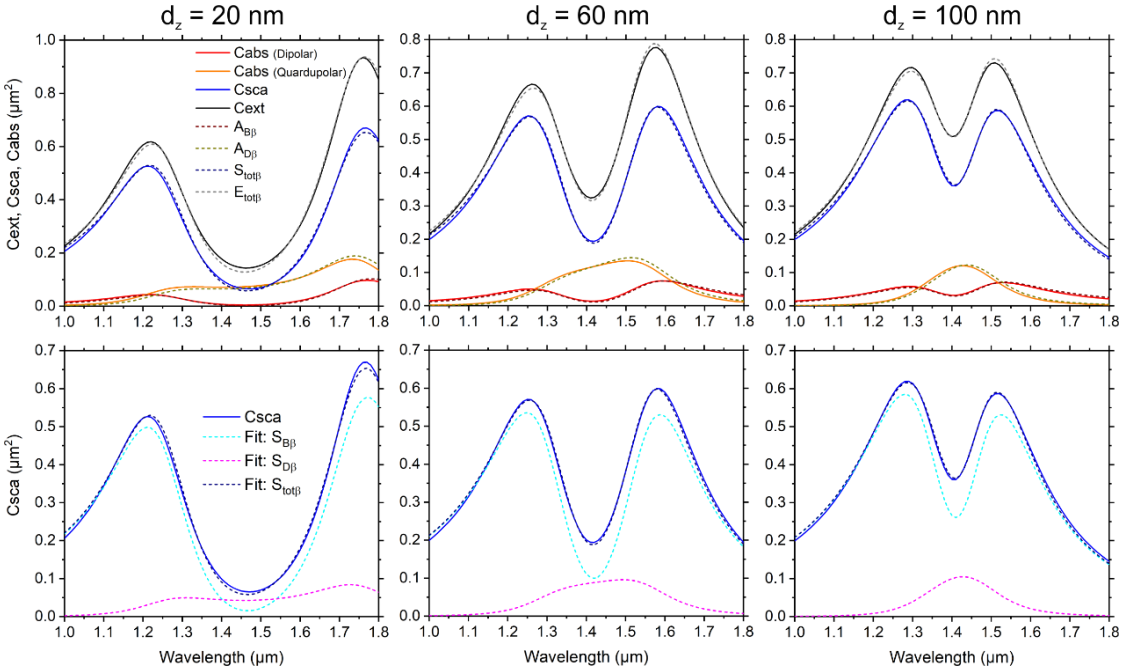

Figure 6.16. The solid lines are optical cross-sections obtained using the FEM simulation, which are taken from Figure 6.14. The dashed lines are calculated using Equation 6.11. (Top panel) $A_{B\beta}$, $A_{D\beta}$, $A_{tot\beta}$, and $E_{tot\beta}$ fitted to the absorption of the dipolar antenna, the absorption of the quadrupolar antenna, the total scattering of the DQA, and total extinction of the DQA, respectively. (Bottom panel) The blue solid and dashed lines are taken from the top panel. The cyan and magenta dashed lines are scattering spectra of the dipolar and quadrupolar antennas obtained from the CO model (Equation 6.11).

The fitting values are summarized in Figures 6.17a-d. The resonance wavelengths and the coupling rates show a similar trend to those of the periodic model shown in Figure 6.13b. However, in contrast to the periodic model, the damping rates of the single model do not dramatically change with varying d_z. The radiative damping rates of the dipolar and the quadrupolar antennas slightly increase with an increase in d_z. This increase is mainly attributed to the blueshift of the resonances, not to an increase in the radiative damping coefficients. The radiative damping coefficients are almost constant for all d_z. This result indicates that the dramatic change in the damping rates of the periodic model originates from lateral near-field interactions occurring between the DQA particles.

Φ_β and Φ_{cc} are shown in Figure 6.17e. Φ_{cc} is almost constant because the damping rates do not change significantly depending on d_z. When d_z = 80 nm, the critical coupling is nearly satisfied ($\Phi_\beta = \Phi_{cc}$). The absorption of the quadrupolar antenna (Figure 6.14) shows mode splitting for d_z with $\Phi_\beta > \Phi_{cc}$. The difference between the periodic and the single particle models is that the quadrupolar antenna of the single particle model does not have a maximum absorption at the critical coupling, but its absorption keeps increasing with an increase in Φ_β. This may be because the quadrupolar antenna can also make strong near-field through the coupling with the dipolar antenna, which is not the case for the PPA. It requires more investigations to fully understand this absorption increase, which is out of the scope of this study.

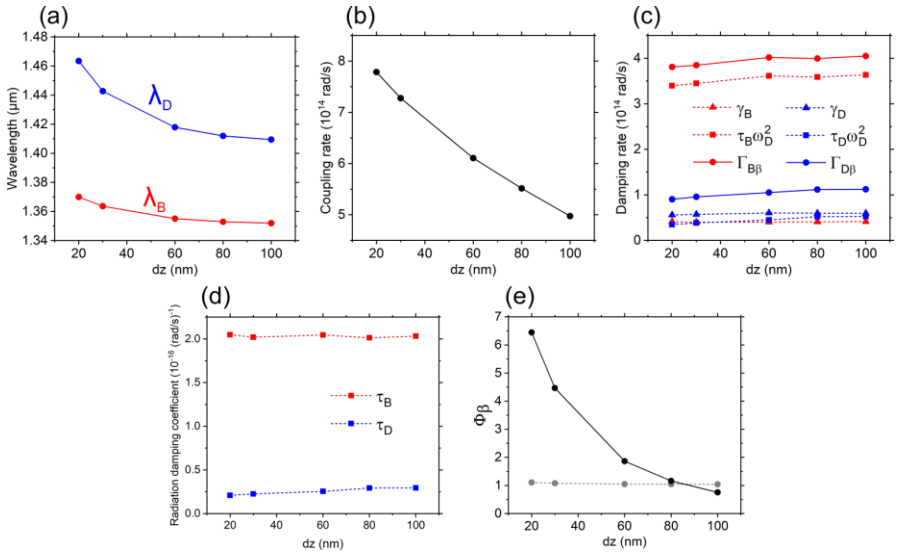

Figure 6.17. The fitting values of (a) the resonance wavelength, (b) the coupling rate, (c) the intrinsic, radiative, and total damping rates, and (d) the radiative damping coefficient. (e) The black and gray marks show Φ_β and Φ_{cc} as a function of d_z, respectively.

The DQA with vertically placed antennas and with in-plane antennas have been widely used to investigate near-field coupling in plasmonic systems. In general, it was considered that the radiative damping of the quadrupolar antenna can be ignored in those studies. However, we included the radiative damping of the quadrupolar antenna in our CO model because the CO model without its radiative damping cannot explain the optical properties of the DQA properly. To prove this, Figure 6.18 shows the optical cross-sections calculated using the CO model without the radiative damping of the quadrupolar antenna (Equation 6.4). When $E_{tot\alpha}$ is used to fit the total extinction of the DQA, $A_{D\alpha}$ and $S_{B\alpha}$ do not show good agreement with the FEM simulation (Figure 6.18a). When $A_{D\alpha}$ is tried to fit the absorption of the quadrupolar antenna, $A_{B\alpha}$, $S_{B\alpha}$, and $E_{tot\alpha}$ do not fit to the spectra obtained from the FEM simulation (Figure 6.18b).

Therefore, to describe the optical properties of the DQA, the radiative damping of the quadrupolar antenna must be taken into account.

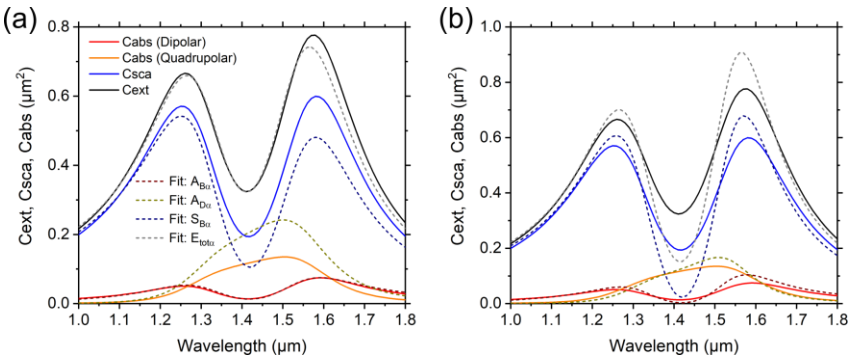

Figure 6.18. Extinction, scattering, and absorption spectra of the DQA with d_y = 60 nm and d_z =120 nm. The solid and dashed lines are calculated using the FEM simulation and the CO model (Equation 6.4), respectively. (a) The fitting parameters are $\omega_B = 1.4 \times 10^{15}$ rad/s, $\gamma_B = 4.4 \times 10^{13}$ rad/s, and $\tau_B\omega_B^2 = 3.9 \times 10^{14}$ rad/s, $\omega_D = 1.33 \times 10^{15}$ rad/s, $\gamma_B = 1.06 \times 10^{14}$ rad/s, and $\kappa = 6 \times 10^{14}$ rad/s. (b) The fitting parameters are $\omega_B = 1.4 \times 10^{15}$ rad/s, $\gamma_B = 4.4 \times 10^{13}$ rad/s, and $\tau_B\omega_B^2 = 3.9 \times 10^{14}$ rad/s, $\omega_D = 1.33 \times 10^{15}$ rad/s, $\gamma_B = 4 \times 10^{13}$ rad/s, and $\kappa = 6.1 \times 10^{14}$ rad/s.

6.6.6. d_y dependency of the DQA

Here, we again turn our focus to the absorption properties of the DQA with the periodic model. Figure 6.19 shows the absorption properties of the DQA with different d_y. d_z is fixed as 60 nm. With an increase in d_y, the absorption of the dipolar antenna shows stronger mode splitting, and the absorption of the quadrupolar antenna becomes stronger. The total absorption of the DQA shows the EIA-like spectral profile for all d_y.

Figure 6.20 shows absorption spectra calculated using the CO model described by Equation 6.11 in the main text. The CO model is in good agreement with the FEM simulation for any d_y, which is the same as the d_z dependency shown in Figure 6.5a. The fitting values used for the fitting made in Figure 6.20 are shown in Figure 6.21. In contrast to the d_z dependency, the resonance wavelength of the dipolar antenna slightly blueshifts with an increase in d_y (Figure 6.21a). The coupling rate keeps increasing with an increase in d_y because the near-field coupling is maximized when the tips of the dipolar and quadrupolar antennas are close to each other (Figure 6.21b). With an increase in the coupling rate, the radiative damping rate of the dipolar antenna decreases, and that of the quadrupolar antenna increases, which is a similar trend to the d_z dependency (Figure 6.21c). This change in the radiative damping rates is not attributed only to the shift in the resonance wavelengths but also to the change in the radiative damping coefficients (Figure 6.21d). From the fitting values, Φ_β and Φ_{cc} are calculated (Figure 6.21e). Φ_β exceeds Φ_{cc} only for d_y = 120 nm, but the difference between them is small. Therefore, mode splitting cannot be observed in the absorption of the quadrupolar antenna for all d_y (Figure 6.19).

The coupling rates for the d_y and d_z dependencies are plotted in Figure 6.22a. By comparing those two plots, we can find that the different sets of (d_y, d_z) can have a similar coupling rate. For example, in the case of Figure 6.22a, the DQAs with (d_y, d_z) = (120 nm, 100 nm) and (60 nm, 60 nm) have a coupling rate of about 4.6×10^{14} rad/s. The comparison of the absorption spectra of those DQAs is shown in Figure 6.22b. They have almost the same absorption spectra, therefore, we can understand that the absorption properties of the DQA are determined by the coupling rate that can be controlled by changing the position of the dipolar antenna in the *y*-*z* plane.

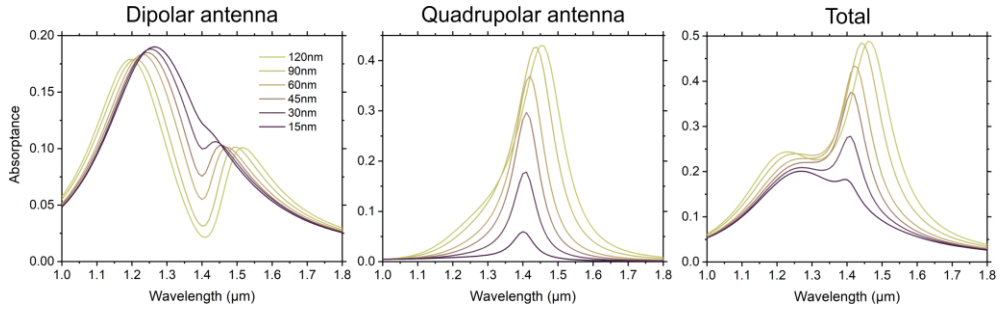

Figure 6.19. Absorption spectra of the dipolar antenna, the quadrupolar antenna, and the DQA. d_y changes in a range of 15 – 120 nm. d_z is fixed as 60 nm.

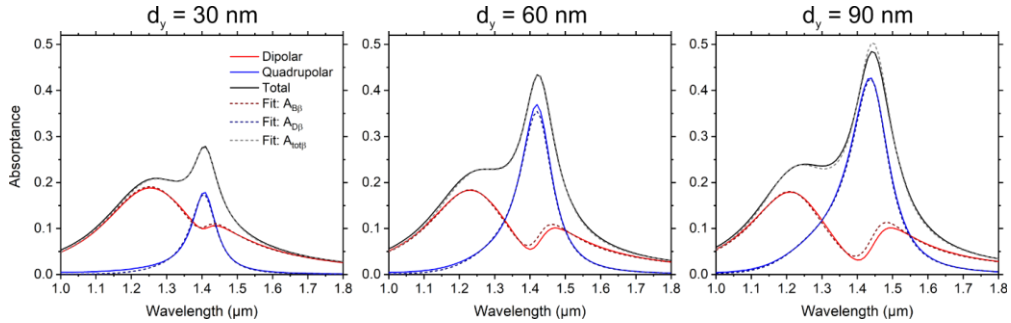

Figure 6.20. The solid and dashed lines are absorption spectra calculated using the FEM simulation and the CO model (Equation 6.11), respectively. The solid lines are taken from Figure 6.19.

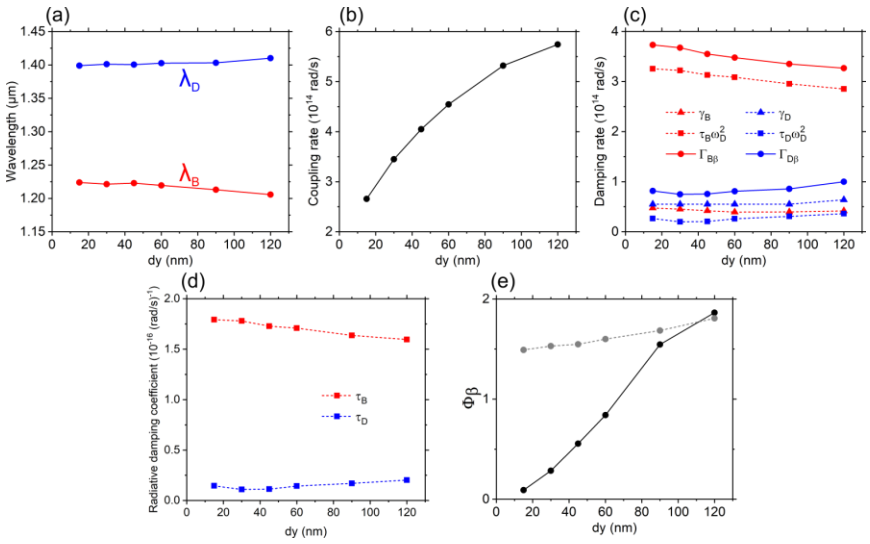

Figure 6.21. The fitting values of (a) the resonance wavelength, (b) the coupling rate, (c) the intrinsic, radiative, and total damping rates, and (d) the radiative damping coefficient. (e) The black and gray marks show Φ_β and Φ_{cc} as a function of d_y, respectively.

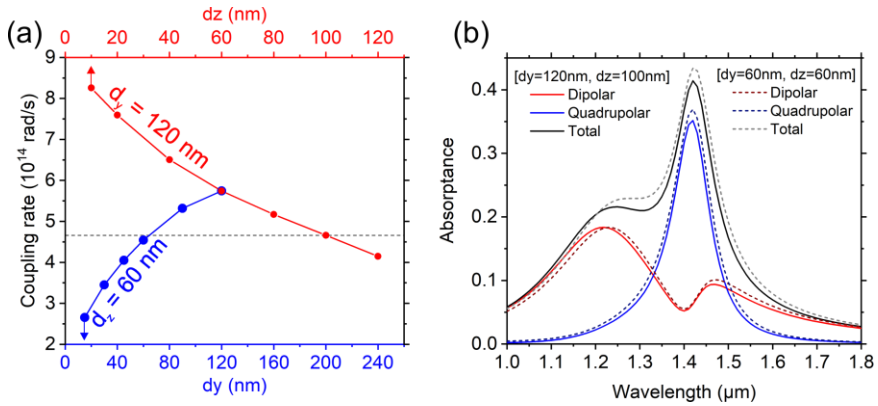

Figure 6.22. (a) The red and blue marks are the coupling rates for the d_y and d_z dependencies, respectively. Those plots are taken from Figure S16b and Figure 5a in the main text. (b) The solid and dashed lines are absorption spectra of the DQAs with (d_y, d_z) = (120 nm, 100 nm) and (60 nm, 60 nm), respectively.

6.6.7. Interactions between a LSP and a waveguide mode

Floess et al. have observed a large Faraday rotation in a thin plasmonic system composed of a grating of Au wires embedded in a EuS film (Figure 6.23a) [8]. In this system, the authors described that EIA can be induced by phase retarded interaction between a LSP of the Au wires and a waveguide mode occurring in the EuS film. The phase retardation can be controlled by changing the distance between the Au wires and the glass substrate.

Here, the absorption properties of the grating system are briefly discussed using the FEM simulation. All structural parameters and materials of the system are based on Floess et al. [8]. The authors explained that the EIA is not attributed to the magneto-optic response of EuS. Therefore, in this investigation, the diagonal elements of permittivity of EuS is only considered. Figure 6.23b shows the total absorption of the system with different *g*. When *g* is around 30 nm, the absorption is dramatically enhanced at the resonance of the waveguide mode. Figure 6.23c shows the absorption spectra of each component of the system. In contrast to the PPA and DQA, the absorption of the plasmonic wire is enhanced, which cannot be described by our GCO model.

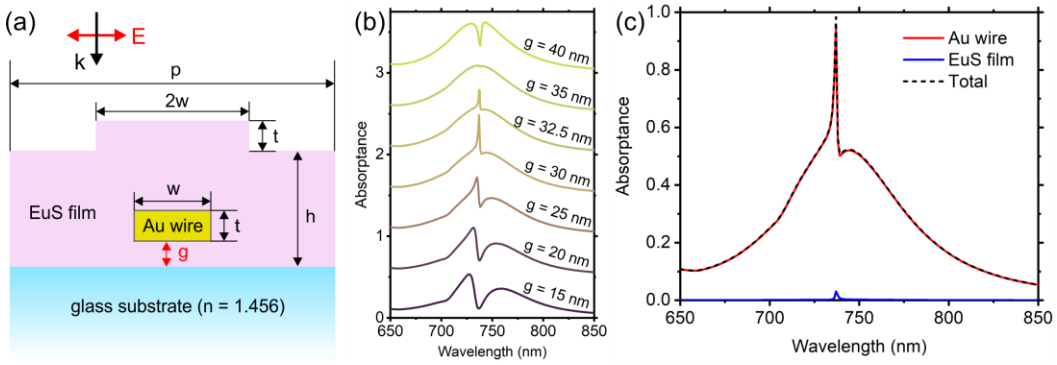

Figure 6.23. (a) Schematic illustration of the Au wire deposited in the EuS film. p = 490 nm, t = 33 nm, w = 85 nm, and h = 139 nm. (b) The absorption spectra of the grating system with different g. (c) The red and blue solid lines are the absorption spectra of the Au wire and the EuS film, respectively. The black dashed line is total absorption of the system.

6.6.8. References

1. X. Zhang, J. Qiu, J. Zhao, X. Li, and L. Liu, "Complex refractive indices measurements of polymers in infrared bands," Journal of Quantitative Spectroscopy and Radiative Transfer **252**, 107063 (2020).

2. N. Murata, R. Hata, and H. Ishihara, "Crossover between Energy Transparency Resonance and Rabi Splitting in Antenna–Molecule Coupled Systems," J. Phys. Chem. C **119** (45), 25493-25498 (2015).

3. H. Chen, L. Shao, K. C. Woo, J. Wang, and H.-Q. Lin, "Plasmonic–Molecular Resonance Coupling: Plasmonic Splitting versus Energy Transfer," J. Phys. Chem. C **116** (26), 14088-14095 (2012).

4. T. J. Antosiewicz, S. P. Apell, and T. Shegai, "Plasmon–Exciton Interactions in a Core–Shell Geometry: From Enhanced Absorption to Strong Coupling," ACS Photonics **1** (5), 454-463 (2014).

5. A. E. Schlather, N. Large, A. S. Urban, P. Nordlander, and N. J. Halas, "Near-field mediated plexcitonic coupling and giant Rabi splitting in individual metallic dimers," Nano Lett. **13** (7), 3281−3286 (2013).

6. G. P. Wiederrecht, G. A. Wurtz, and J. Hranisavljevic, "Coherent Coupling of Molecular Excitons to Electronic Polarizations of Noble Metal Nanoparticles," Nano Lett. **4** (11), 2121-2125 (2004).

7. R. Houdré, "Early stages of continuous wave experiments on cavity-polaritons," physica status solidi (b) **242** (11), 2167-2196 (2005).

8. D. Floess, M. Hentschel, T. Weiss, H.-U. Habermeier, J. Jiao, S. G. Tikhodeev, and H. Giessen, "Plasmonic Analog of Electromagnetically Induced Absorption Leads to Giant Thin Film Faraday Rotation of 14°," Phys. Rev. X **7** (2), 021048 (2017).

7. Overcoming the upper limit for light absorption by electromagnetically induced absorption: dipole-dipole coupling with phase retardation in plasmonic-dielectric dimers

Kishin Matsumori[1,*], Ryushi Fujimura[2], and Markus Retsch[1]

[1] Department of Chemistry, Physical Chemistry I, University of Bayreuth, 95447 Bayreuth, Germany

[2] Graduate School of Regional Development and Creativity, Utsunomiya University, 321-8585 Utsunomiya, Japan

Accepted by *J. Phys. Chem. C*

Abstract: Electromagnetically induced absorption (EIA) by a phase-retarded coupling is theoretically investigated using a dimer composed of a plasmonic and a dielectric particle. This phase-retarded coupling originates from the particles interacting with each other through their scattered intermediate fields (in between near and far fields). Our analysis based on the coupled-dipole method and an extended coupled-oscillator model indicates that EIA by the phase-retarded coupling occurs due to constructive interference in the scattered fields of the particles. By employing the finite element method, we demonstrate that the absorption of the plasmonic particle is dramatically enhanced by tuning the interparticle distance and achieving constructive interference. In contrast to EIA by near-field coupling, which has been intensively researched using coupled plasmonic systems, EIA by a phase-retarded coupling enables us to strengthen the absorption of plasmonic systems more significantly. This significant absorption enhancement can be beneficial to advancing various applications, such as energy harvesting and radiative cooling.

7.1. Introduction

Light absorption is of fundamental importance for various applications. The field of plasmonics has attracted considerable attention since localized surface plasmons (LSPs) can confine electromagnetic fields beyond the optical diffraction limit and enhance light absorption. Strong light absorption is induced at the resonance of the LSPs, which can be controlled by designing the composition, shape and size of a plasmonic structure. Given the high tunability of the LSPs, plasmonic structures have been designed in different wavelength ranges to advance emerging applications such as energy harvesting [1], solar-thermophotovoltaics [2, 3], radiative cooling [4], sensing [5-7], IR camouflage [8], and optical heating [9-11]. To enhance light absorption of materials, different absorption mechanisms have been utilized, such as impedance matching [12-15], Kerker effect [16-18], and rainbow trapping [19-21].

In addition to those optical phenomena, electromagnetically induced absorption (EIA) can be a potential approach to strengthening the absorption of plasmonic systems. EIA was first observed in atomic systems as substantial absorption enhancement of the system by constructive quantum interference [22, 23]. In contrast, destructive quantum interference results in electromagnetically induced transparency (EIT), which creates a transparency window in absorption spectra [24]. Since interference phenomena in quantum and classical systems are analogous, EIA-like effects have been realized in plasmonic systems. One of the most commonly used plasmonic system for EIA is a coupled system composed of bright and dark oscillators [25-29]. The bright oscillator possesses a high total (Ohmic + radiative) damping and can be excited by the external incident wave. On the other hand, the dark oscillator exhibits a low total damping and is excited

only by coupling to the electromagnetic near-field of the bright oscillator. EIA has been extensively investigated and applied to perfect light absorbers [30], optical modulators [31, 32], and nonlinear effects [33]. However, mechanistic interpretations of EIA have contained ambiguity so far.

In our previous work, we developed the unified interpretation of EIA by investigating the absorption properties of coupled plasmonic systems known for EIA: plasmonic-polymer composite and dipolar-quadrupolar antennas [34]. We concluded that their EIA is attributed to the absorption enhancement of the dark oscillator by near-field coupling, enabling the total absorption of the entire system to possess an EIA-like spectral profile (see Figure 7.1a). However, the absorption of the bright oscillator always has an EIT-like profile, meaning that the near-field coupling occurs in phase with the resonances of the bright and dark oscillators. This coupling process is equivalent to destructive interference and contradicts EIA observed in the atomic systems. Moreover, we found that EIA can enhance the dark oscillator´s absorption up to 1/4 of the maximum extinction of the isolated bright oscillator (without coupling to the dark oscillator). This finding indicates that the total absorption of the entire system cannot exceed the upper absorption bound of the isolated bright oscillator, which is given by $C_{abs} = 3\lambda_0^2/8\pi$ for a dipolar antenna (C_{abs} is the absorption cross-section, and λ_0 is the resonance wavelength) [35-38].

Mimicking EIA of the atomic systems in plasmonic systems and searching for means to overcome $C_{abs} = 3\lambda_0^2/8\pi$ by constructive interference is of great interest not only for the applications mentioned earlier but also for the physics of plasmonics [39-42]. One of the approaches to achieving constructive interference in plasmonic systems may be utilizing a phase-retarded coupling. The phase-retarded coupling has been investigated by using, for example, waveguides [43, 44] and dimers made of two scattering particles [45-52]. In the case of the dimers, interactions between particles can be characterized by two dipole moments, and the phase-retarded coupling occurs by far-field interactions. It has been observed that scattering and absorption of the dimers are strengthened and weakened by controlling their interparticle distance, which may correspond to constructive and destructive interference, respectively [49-51]. However, a rigorous understanding of the phase-retarded coupling has not been given. Also, EIA-like effects have not yet been confirmed in the dimers.

In this work, we theoretically investigate EIA excited by the phase-retarded coupling using a dimer consisting of plasmonic and dielectric particles. A LSP of the plasmonic particle and a Mie resonance of the dielectric particle exhibit dipolar resonances with high and low damping, respectively. Considering this damping contrast and that both dipolar resonances can be excited directly by the incident wave, the plasmonic and the dielectric particles are characterized as bright and quasi-dark oscillators, respectively. With an optimal interparticle distance of this dimer, we demonstrate that constructive scattered field interference excites EIA, enhancing the absorption of the plasmonic particle beyond $C_{abs} = 3\lambda_0^2/8\pi$ at a resonance condition (see Figure 7.1b). To the best of our knowledge, this type of EIA has been observed only in the interactions between a LSP and a waveguide mode [34, 53].

This paper is organized as follows. To interpret the phase-retarded coupling, we first discuss the scattering properties of isolated plasmonic and dielectric particles by considering their dipole moments. Next, we investigate a dipole-dipole coupling of the dimer using the coupled-dipole method (CDM). To give an intuitive picture of the coupling, an extended coupled-oscillator (ECO) model is designed. The ECO model suggests that three forces are working on each particle with different phases, and those phases can be controlled by changing the interparticle distance of the dimer. Consequently, the interparticle distance determines whether the coupling in the dimer becomes constructive or destructive interferences, resulting in EIA or EIT, respectively. These effects of the phase-retarded coupling on the absorption properties of the dimer are demonstrated by performing the finite element method (FEM) simulation. Finally, we present how an intrinsic loss (non-zero extinction coefficient) of the dielectric particle influences the EIA properties of the dimer.

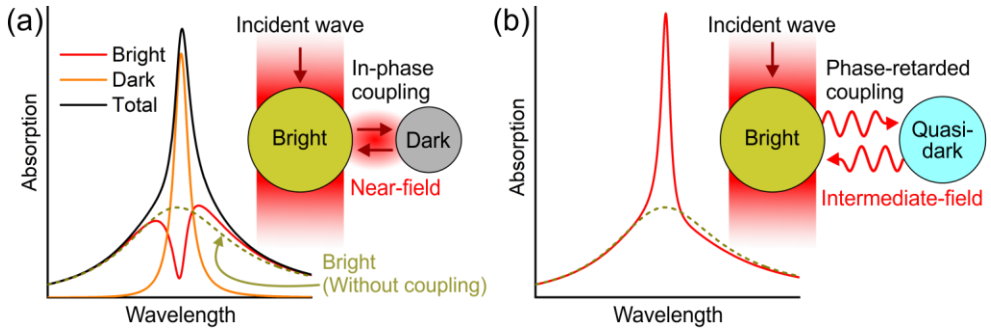

Figure 7.1. Schematic illustrations of plasmonic EIA excited by (a) in-phase and (b) phase-retarded coupling.

7.2. Scattered fields of electric and magnetic dipole moments

Plasmonic and dielectric particles with subwavelength scales can be approximated as a dipolar antenna. The optical properties of the dipolar antenna are described by its electric dipole (ED) moment $\mathbf{p}_j$ and magnetic dipole (MD) moment $\mathbf{m}_j$. The ED and MD moments at $\mathbf{r}_j$ in free space are [54]

$$\mathbf{p}_j = \varepsilon_0 \alpha_j \mathbf{E}_{in}(\mathbf{r}_j) \tag{7.1}$$

$$\mathbf{m}_j = \chi_j \mathbf{H}_{in}(\mathbf{r}_j) \tag{7.2}$$

where ε_0 is the electric permittivity in a vacuum, α_j is the electric polarizability, and χ_j is the magnetic polarizability. $\mathbf{E}_{in}(\mathbf{r}_j) = \mathbf{E}_0 e^{i\mathbf{k}\cdot\mathbf{r}_j}$ and $\mathbf{H}_{in}(\mathbf{r}_j) = \mathbf{H}_0 e^{i\mathbf{k}\cdot\mathbf{r}_j}$ are the incident electric and magnetic fields, respectively. $\mathbf{k}$ is the wave vector ($|\mathbf{k}| = 2\pi/\lambda_0$). Scattered electric and magnetic fields at $\mathbf{r}_i$ created by the ED moment are expressed as

$$\mathbf{E}_{spj}(\mathbf{r}_i) = \frac{1}{\varepsilon_0}\mathbf{G}_E(\mathbf{r}_i - \mathbf{r}_j)\cdot\mathbf{p}_j \tag{7.3}$$

$$\mathbf{H}_{spj}(\mathbf{r}_i) = \frac{1}{\varepsilon_0 Z_0}\mathbf{G}_M(\mathbf{r}_i - \mathbf{r}_j)\cdot\mathbf{p}_j \tag{7.4}$$

Similarly, scattered fields of the MD moment are

$$\mathbf{E}_{smj}(\mathbf{r}_i) = -Z_0\mathbf{G}_M(\mathbf{r}_i - \mathbf{r}_j)\cdot\mathbf{m}_j \tag{7.5}$$

$$\mathbf{H}_{smj}(\mathbf{r}_i) = \mathbf{G}_E(\mathbf{r}_i - \mathbf{r}_j)\cdot\mathbf{m}_j \tag{7.6}$$

where Z_0 is the vacuum impedance. $\mathbf{G}_E$ and $\mathbf{G}_M$ are the dyadic Green´s functions, which are expressed using $\mathbf{r}_i - \mathbf{r}_j = D\mathbf{u}_r$ (D and $\mathbf{u}_r$ are the distance and the unit vector of $\mathbf{r}_i - \mathbf{r}_j$, respectively)

$$\mathbf{G}_E(\mathbf{r}_i - \mathbf{r}_j)\cdot\mathbf{u} = g_A\mathbf{u} + g_B(\mathbf{u}_r\cdot\mathbf{u})\mathbf{u}_r \tag{7.7}$$

$$\mathbf{G}_M(\mathbf{r}_i - \mathbf{r}_j)\cdot\mathbf{u} = g_C(\mathbf{u}_r\times\mathbf{u}) \tag{7.8}$$

where $\mathbf{u}$ is the arbitrary unit vector. Equations 7.7 and 7.8 have the relationship of $\mathbf{G}_E(\mathbf{r}_i - \mathbf{r}_j) = \mathbf{G}_E(\mathbf{r}_j - \mathbf{r}_i)$ and $\mathbf{G}_M(\mathbf{r}_i - \mathbf{r}_j) = -\mathbf{G}_M(\mathbf{r}_j - \mathbf{r}_i)$, respectively. The terms g_A, g_B, and g_C in Equations 7.7 and 7.8 are

$$g_{\mathrm{A}} = \frac{e^{ikD}}{4\pi D}\left(k^2 + \frac{ik}{D} - \frac{1}{D^2}\right) \tag{7.9}$$

$$g_{\mathrm{B}} = \frac{e^{ikD}}{4\pi D}\left(-k^2 - \frac{3ik}{D} + \frac{3}{D^2}\right) \tag{7.10}$$

$$g_{\mathrm{C}} = \frac{e^{ikD}}{4\pi D}\left(k^2 + \frac{ik}{D}\right) \tag{7.11}$$

Equations 7.9-7.11 describe the amplitude and phase of the scattered fields. The scattered field of dipole moments can be categorized into three regions by comparing D with λ_0: the near (static) field for $D << \lambda_0$, the intermediate (induction) field for $D \approx \lambda_0$, and the far (radiation) field for $D >> \lambda_0$ (see Figure 7.2a). Considering Maxwell´s equations and the wave equation, each field has a time derivation in different orders: 0-th, 1-th, and 2nd order derivation for the static, induction, and radiation fields, respectively. We consider the time-harmonic system; therefore, by setting the static field as a reference, the induction and radiation fields are π/2, and π phase shifted, respectively. Equations 7.9-7.11 can be modified as

$$g_{\mathrm{A}} = \frac{1}{4\pi D}\sqrt{\left(k^2 - \frac{1}{D^2}\right)^2 + \left(\frac{k}{D}\right)^2}\; e^{i\left[kD + \arg\left(k^2 + \frac{ik}{D} - \frac{1}{D^2}\right)\right]} = |g_{\mathrm{A}}|e^{i\phi_{\mathrm{A}}} \tag{7.12}$$

$$g_{\mathrm{B}} = \frac{1}{4\pi D}\sqrt{\left(-k^2 + \frac{3}{D^2}\right)^2 + \left(\frac{3k}{D}\right)^2}\; e^{i\left[kD + \arg\left(-k^2 - \frac{3ik}{D} + \frac{3}{D^2}\right)\right]} = |g_{\mathrm{B}}|e^{i\phi_{\mathrm{B}}} \tag{7.13}$$

$$g_{\mathrm{C}} = \frac{1}{4\pi D}\sqrt{k^4 + \left(\frac{k}{D}\right)^2}\; e^{i\left[kD + \arg\left(k^2 + \frac{ik}{D}\right)\right]} = |g_{\mathrm{C}}|e^{i\phi_{\mathrm{C}}} \tag{7.14}$$

where $|g_{\mathrm{A}}|$, $|g_{\mathrm{B}}|$, and $|g_{\mathrm{C}}|$ are the scattered field amplitude, and arg() is the argument of a complex function. Note that the CDM cannot express the near field property since the scattered field amplitudes diverge with $D \rightarrow 0$. The net phases denoted as ϕ_{A}, ϕ_{B}, and ϕ_{C} can be divided into two terms

$$\phi_{\mathrm{A}} = kD + \arg\left(k^2 + \frac{ik}{D} - \frac{1}{D^2}\right) = kD + \phi_{\mathrm{a}} \tag{7.15}$$

$$\phi_{\mathrm{B}} = kD + \arg\left(-k^2 - \frac{3ik}{D} + \frac{3}{D^2}\right) = kD + \phi_{\mathrm{b}} \tag{7.16}$$

$$\phi_{\mathrm{C}} = kD + \arg\left(k^2 + \frac{ik}{D}\right) = kD + \phi_{\mathrm{c}} \tag{7.17}$$

In Equations 7.15-7.17, kD can be considered a background phase. ϕ_{a}, ϕ_{b}, and ϕ_{c} express influences from the near and intermediate fields. Equations 7.15-7.17 are shown in Figure 7.2b. The contributions from the near and intermediate fields are substantial at a small D. This contribution decreases and becomes negligible for a large D; therefore, the net phases are dominated by kD in the far field. From Equations 7.15-7.17, we can understand that the scattered fields have different phases depending on the direction and distance from the dipole moments.

We consider two dipole moments interacting with each other in the different fields defined in Figure 7.2a. For a near-field interaction occurring through the hot spots, the interaction is expected to occur in phase with the oscillations of the dipole moments. This type of interaction has been extensively researched since an electromagnetic field can be strongly confined between the dipoles [55-60]. When the distance

between the dipole moments is in a region of $D > \lambda_0$, a far-field interaction has to be considered. In that far-field case, each dipole moment is oscillated by the scattered field of another dipole moment with phase delay determined by Equations 7.15-7.17. This phase-retarded coupling may provide additional control for light-matter interactions and allow achieving EIA. In the far field, the phase can be controlled in a wide range by tuning D. However, Equations 7.12-7.14 indicate that the scattered field amplitudes are weakened with an increase in D. Since a strong interaction requires a strong electromagnetic field, it is challenging to achieve a strong interaction in the far field. However, the intermediate field can possess moderately strong field amplitude and phase control simultaneously. By considering these advantages of the intermediate field, we will outline how the phase-retarded coupling results in EIA.

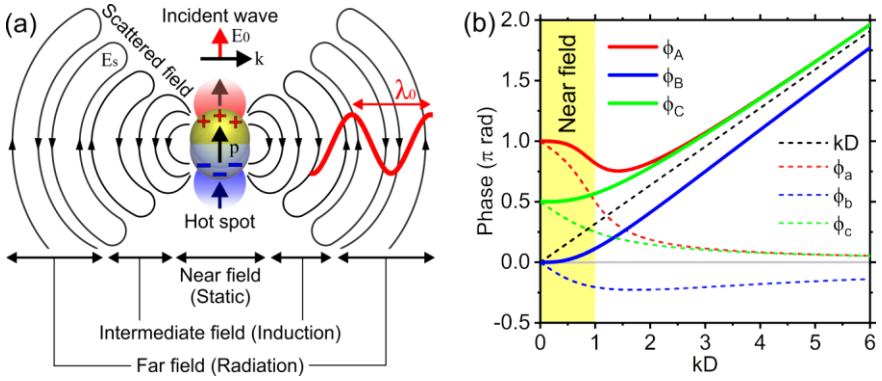

Figure 7.2. (a) Schematic illustration of a scattered electric field created by a plasmonic particle. The scattered field can be categorized into three fields: the near field ($D << \lambda_0$), the intermediate field ($D \approx \lambda_0$), and the far field ($D >> \lambda_0$). There is no clear boundary between those fields, and the illustration just gives an intuitive picture of those boundaries. (b) The phases given by Equations 7.15-7.17 are plotted as a function of kD. The red, blue, and green solid lines are the net phases of ϕ_A, ϕ_B, and ϕ_C, respectively. The red, blue, and green dashed lines are ϕ_a, ϕ_b, and ϕ_c, respectively. The yellow shaded area indicates the near field determined by $kD < 1$. Since $kD = 2\pi D/\lambda_0 \approx 6D/\lambda_0$ and the intermediate field is $D \approx \lambda_0$, the plot is for the near and intermediate fields.

7.3. Phase-retarded coupling

The phase-retarded coupling is investigated by considering that a plasmonic particle interacts with a dielectric particle. In general, any particles possess ED and MD moments; therefore, a four-dipole (FD) model has to be considered for a complete analysis of the optical properties of a dimer (Figure 7.3a). However, a plasmonic particle has a strong ED moment by a localized surface plasmon (LSP) and its MD moment is negligibly weak. A dielectric particle possesses both ED and MD moments by Mie resonances. ED and MD of a dielectric particle with a low refractive index usually spectrally overlap each other. With a high refractive index, a dielectric particle can resolve its ED and MD. Therefore, a dimer composed of plasmonic and high index dielectric particles allows us to reduce the FD model to two-dipole (TD) models (see Figure 7.3b) [59].

Using the TD models and the CDM [58, 59, 61, 62], we observe how excitation states of the LSP and Mie resonances change by the intermediate-field coupling. The incident wave propagates along the z-direction with $\mathbf{E}_{\text{in}}(\mathbf{r}_j) = E_0\hat{\mathbf{e}}_x e^{i\mathbf{k}\cdot\mathbf{r}_j}$ and $\mathbf{H}_{\text{in}}(\mathbf{r}_j) = H_0\hat{\mathbf{e}}_y e^{i\mathbf{k}\cdot\mathbf{r}_j}$, where $\hat{\mathbf{e}}$ is the unit vector in the Cartesian coordinate system. The plasmonic and dielectric particles locate at $\mathbf{r}_1 = (0, 0, -D/2)$ and $\mathbf{r}_2 = (0, 0, D/2)$, respectively. Under this condition, we first consider a $\mathbf{p}_1$-$\mathbf{m}_2$ coupling of the dimer based on our previous work [63]. The ED of the plasmonic particle $\mathbf{p}_{\text{pm1}}$ and the MD of the dielectric particle $\mathbf{m}_{\text{pm2}}$ are given using Equations 7.1-7.6

$$\mathbf{p}_{\mathrm{pm1}} = \varepsilon_0 \alpha_1 [\mathbf{E}_{\mathrm{in}}(\mathbf{r_1}) + \mathbf{E}_{\mathrm{sm2}}(\mathbf{r}_1)] = \varepsilon_0 \alpha_1 \left[E_0 \hat{\mathbf{e}}_{\mathrm{x}} e^{-i\frac{kD}{2}} - Z_0 \mathbf{G}_{\mathrm{M}}(\mathbf{r}_1 - \mathbf{r}_2) \cdot \mathbf{m}_{\mathrm{pm2}} \right] \quad 7.18$$

$$\mathbf{m}_{\mathrm{pm2}} = \chi_2 \left[\mathbf{H}_{\mathrm{in}}(\mathbf{r_2}) + \mathbf{H}_{\mathrm{sp1}}(\mathbf{r}_2) \right] = \chi_2 \left[H_0 \hat{\mathbf{e}}_{\mathrm{y}} e^{i\frac{kD}{2}} + \frac{1}{\varepsilon_0 Z_0} \mathbf{G}_{\mathrm{M}}(\mathbf{r}_2 - \mathbf{r}_1) \cdot \mathbf{p}_{\mathrm{pm1}} \right] \quad 7.19$$

For spherical particles, the electric and magnetic polarizabilities can be given as $\alpha = (6\pi i/k^3)a_1$ and $\chi = (6\pi i/k^3)b_1$, where a_1 and b_1 are Mie coefficients for first-order electric and magnetic modes, respectively [61, 64]. These polarizabilities may be approximated using the Lorentz oscillator [37]

$$\alpha_{\mathrm{j}} = \frac{f_{\mathrm{pj}}}{\omega_{\mathrm{pj}}^2 - \omega^2 - i\Gamma_{\mathrm{pj}}\omega} = \frac{f_{\mathrm{pj}}}{\Omega_{\mathrm{pj}}} \quad 7.20$$

$$\chi_{\mathrm{j}} = \frac{f_{\mathrm{mj}}}{\omega_{\mathrm{mj}}^2 - \omega^2 - i\Gamma_{\mathrm{mj}}\omega} = \frac{f_{\mathrm{mj}}}{\Omega_{\mathrm{mj}}} \quad 7.21$$

where f_{pj} and f_{mj} are the oscillator strength, ω_{pj} and ω_{mj} are the angular resonance frequency, and Γ_{pj} and Γ_{mj} are the damping rate. ω is the angular frequency in free space. Using Equations 7.18-7.21, self-consistent forms of $\mathbf{p}_{\mathrm{pm1}}$ and $\mathbf{m}_{\mathrm{pm2}}$ are (Section 7.10.1, Supporting Information)

$$\mathbf{p}_{\mathrm{pm1}} = p_{\mathrm{pm1x}} \hat{\mathbf{e}}_{\mathrm{x}} = \frac{\Omega_{\mathrm{p1}}\Omega_{\mathrm{m2}} - \Omega_{\mathrm{p1}} f_{\mathrm{m2}} |g_{\mathrm{C}}| e^{i(\phi_{\mathrm{C}} + kD)}}{\Omega_{\mathrm{p1}}\Omega_{\mathrm{m2}} + f_{\mathrm{p1}} f_{\mathrm{m2}} |g_{\mathrm{C}}|^2 e^{i2\phi_{\mathrm{C}}}} \mathbf{p}_1 \quad 7.22$$

$$\mathbf{m}_{\mathrm{pm2}} = m_{\mathrm{pm2y}} \hat{\mathbf{e}}_{\mathrm{y}} = \frac{\Omega_{\mathrm{p1}}\Omega_{\mathrm{m2}} + \Omega_{\mathrm{m2}} f_{\mathrm{p1}} |g_{\mathrm{C}}| e^{i(\phi_{\mathrm{C}} - kD)}}{\Omega_{\mathrm{p1}}\Omega_{\mathrm{m2}} + f_{\mathrm{p1}} f_{\mathrm{m2}} |g_{\mathrm{C}}|^2 e^{i2\phi_{\mathrm{C}}}} \mathbf{m}_2 \quad 7.23$$

where $\mathbf{p}_1$ and $\mathbf{m}_2$ are the ED moment of an isolated plasmonic particle and the MD moment of an isolated dielectric particle, respectively (see Equations 7.1 and 7.2). Equations 7.22 and 7.23 show that the dipole moments of the dimer result from the dipole moments of isolated particles modulated by interactions through their scattered field. In a similar manner to the $\mathbf{p}_1$-$\mathbf{m}_2$ coupling, we investigate a $\mathbf{p}_1$-$\mathbf{p}_2$ coupling by considering that the dielectric particle only has the ED at the resonance of the LSP of the plasmonic particle. In this case, the ED of the plasmonic particle $\mathbf{p}_{\mathrm{pp1}}$ and the ED of the dielectric particle $\mathbf{p}_{\mathrm{pp2}}$ can be expressed as (Section 7.10.1, Supporting Information)

$$\mathbf{p}_{\mathrm{pp1}} = p_{\mathrm{pp1x}} \hat{\mathbf{e}}_{\mathrm{x}} = \frac{\Omega_{\mathrm{p1}}\Omega_{\mathrm{p2}} + \Omega_{\mathrm{p1}} f_{\mathrm{p2}} |g_{\mathrm{A}}| e^{i(\phi_{\mathrm{A}} + kD)}}{\Omega_{\mathrm{p1}}\Omega_{\mathrm{p2}} - f_{\mathrm{p1}} f_{\mathrm{p2}} |g_{\mathrm{A}}|^2 e^{i2\phi_{\mathrm{A}}}} \mathbf{p}_1 \quad 7.24$$

$$\mathbf{p}_{\mathrm{pp2}} = p_{\mathrm{pp2x}} \hat{\mathbf{e}}_{\mathrm{x}} = \frac{\Omega_{\mathrm{p1}}\Omega_{\mathrm{p2}} + \Omega_{\mathrm{p2}} f_{\mathrm{p1}} |g_{\mathrm{A}}| e^{i(\phi_{\mathrm{A}} - kD)}}{\Omega_{\mathrm{p1}}\Omega_{\mathrm{p2}} - f_{\mathrm{p1}} f_{\mathrm{p2}} |g_{\mathrm{A}}|^2 e^{i2\phi_{\mathrm{A}}}} \mathbf{p}_2 \quad 7.25$$

In Equations 7.22-7.25, we can find that those interacting dipole moments contain the phase terms originating from the scattered fields. These results suggest that the dipole moments can be controlled by phase retardation, and the amplitude of the dipole moments can be enhanced if the dipole moments can couple constructively.

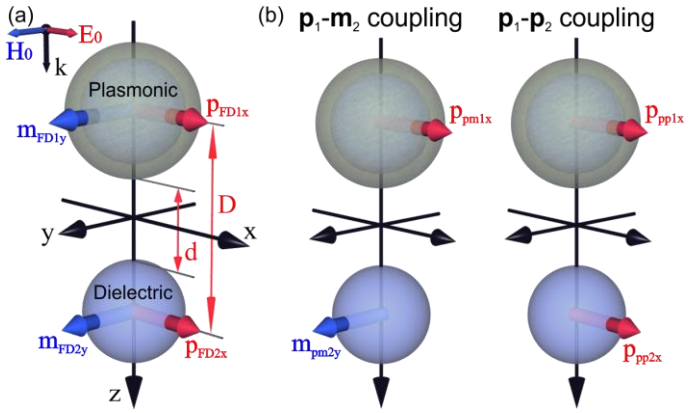

Figure 7.3. Schematic illustrations of the dimer composed of plasmonic and dielectric particles. (a) The FD model considers all dipole moments of the dimer. (b) TD models involve only two dipole moments.

We provide an intuitive understanding of the phase-retarded coupling by designing an ECO model. Our ECO model shown in Figure 7.4a comprises two mechanical harmonic oscillators: Oscillator1 and Oscillator2 correspond to the plasmonic and dielectric particles in Figure 7.3a, respectively. Therefore, Oscillator1 has a higher damping rate than Oscillator2, meaning $\Gamma_1 > \Gamma_2$. Those oscillators have angular resonant frequency ω_j. $F_1(t)e^{-i\delta/2}$ and $F_2(t)e^{i\delta/2}$ are the external forces per mass working on Oscillator1 and Oscillator2, respectively. Those forces include the phase term determined by δ to consider that the LSP of the plasmonic particle and the Mie resonance of the dielectric particle are oscillated with different phases by the incident wave. This is because the dimer axis of Figure 7.3a is parallel to the propagation direction of the incident field. The external forces are time-harmonic; therefore, $F_j(t) = f_j F_0(t)$ where $F_0(t) = F_0 e^{-i\omega t}$. F_0 is the amplitude of the external force, and f_j describes the coupling rate of the oscillator to the external force. f_j is normalized by the mass of the oscillator m_j. f_j corresponds to the oscillator strength of the polarizabilities given by Equations 7.20 and 7.21. Next, we consider the coupling between Oscillator1 and Oscillator2. From the CDM, we know that the LSP of the plasmonic particle couples with the Mie resonance of the dielectric sphere through their scattered fields. We translate this coupling process into our ECO model. The scattered field amplitude is represented as $|g|$ in the ECO model. Each oscillator couples to the scattered field of another oscillator with the coupling rate of f_j. Therefore, the coupling strength of each oscillator is given by $f_j|g|$. As explained earlier, the scattered field involves the phase delay ϕ, resulting in a phase-retarded coupling of $f_j|g|e^{i\phi}$. Therefore, the equations of motion are written as

$$\frac{d^2x_1}{dt^2} + \Gamma_1 \frac{dx_1}{dt} + \omega_1^2 x_1 - f_1|g|e^{i\phi}x_2 = f_1 F_0(t) e^{-\frac{i\delta}{2}} \tag{7.26}$$

$$\frac{d^2x_2}{dt^2} + \Gamma_2 \frac{dx_2}{dt} + \omega_2^2 x_2 - f_2|g|e^{i\phi}x_1 = f_2 F_0(t) e^{\frac{i\delta}{2}} \tag{7.27}$$

In our previous work, we demonstrated that the damping of plasmonic systems needs to be distinguished into intrinsic and radiative damping to fully characterize their optical properties [34]. However, in this work, we are interested in the phenomenological analysis to understand the oscillation state of the plasmonic-dielectric dimer. Therefore, for simplicity, we only consider the total damping (intrinsic + radiative) of the particles. A modification of Equations 7.26 and 7.27 gives

$$x_1 = \frac{1}{\Omega_1}\left[f_1 F_0(t) e^{-\frac{i\delta}{2}} + f_1|g|e^{i\phi}x_2\right] \tag{7.28}$$

$$x_2 = \frac{1}{\Omega_2}\left[f_2 F_0(t) e^{\frac{i\delta}{2}} + f_2 |g| e^{i\phi} x_1\right] \tag{7.29}$$

where $\Omega_j = \omega_j^2 - \omega^2 - i\Gamma_j\omega$. In Equation 7.28, the first term is the direct influence of the external force on Oscillator1 (see Figure 7.4b). The second term means that the oscillation of Oscillator2 works on Oscillator1 through the phase-retarded coupling. The same interpretation can be applied to Equation 7.29. Substituting Equation 7.29 into Equation 7.28 gives

$$x_1 = \frac{1}{\Omega_1}\left\{f_1 F_0(t) e^{-\frac{i\delta}{2}} + \frac{1}{\Omega_2}\left[f_1 f_2 |g| F_0(t) e^{i\left(\phi+\frac{\delta}{2}\right)} + f_1 f_2 |g|^2 e^{i2\phi} x_1\right]\right\} \tag{7.30}$$

The second term of Equation 7.30 describes the effect of the external force $F_2(t)e^{i\delta/2}$ working on Oscillator1 (see Figure 7.4c). The third term shows a round-trip coupling process of $x_1 \rightarrow x_2 \rightarrow x_1$ (see Figure 7.4d), which is described in two steps: A) the oscillation of Oscillator1 works on Oscillator2 through the coupling of $f_2|g|e^{i\phi}$. B) This coupling oscillates Oscillator2, and the oscillation of Oscillator2 works back on Oscillator1 through the coupling of $f_1|g|e^{i\phi}$. Therefore, the round-trip coupling involves a total phase delay of 2ϕ [49]. A self-consistent form of Equation 7.30 is

$$x_1 = \frac{\Omega_1\Omega_2 + \Omega_1 f_2 |g| e^{i(\phi+\delta)}}{\Omega_1\Omega_2 - f_1 f_2 |g|^2 e^{i2\phi}}\left[\frac{f_1}{\Omega_1} F_0(t) e^{-\frac{i\delta}{2}}\right] \tag{7.31}$$

Equation 7.31 coincides with $\mathbf{p}_{pp1}$ given by Equation 7.24. The $\mathbf{p}_1$-$\mathbf{m}_2$ coupling can also be described by the same coupling processes shown in Figure 7.4. Considering the coupling processes described in Figure 7.4, it can be found that three forces are working on Oscillator1, and those forces have different phases. Therefore, if those phases allow the forces to work on Oscillator1 constructively, the displacement amplitude of Oscillator1 can be enhanced. From the CDM, the phase of the coupling is a function of the interparticle distance D, meaning that the coupling may occur constructively by controlling D. By comparing the ECO model and the CDM, we can find that the coupling strength in the CDM is expressed by a combination of the oscillator strength of the polarizabilities (f_{pj} and f_{mj}), and the scattered field amplitudes ($|g_A|$ and $|g_C|$). As can be seen in Equations 7.12 and 7.14, the scattered field amplitudes dramatically decrease with an increase in D even in the intermediate field. Therefore, f_{pj} and f_{mj} must be sufficiently large to achieve strong coupling between distant particles.

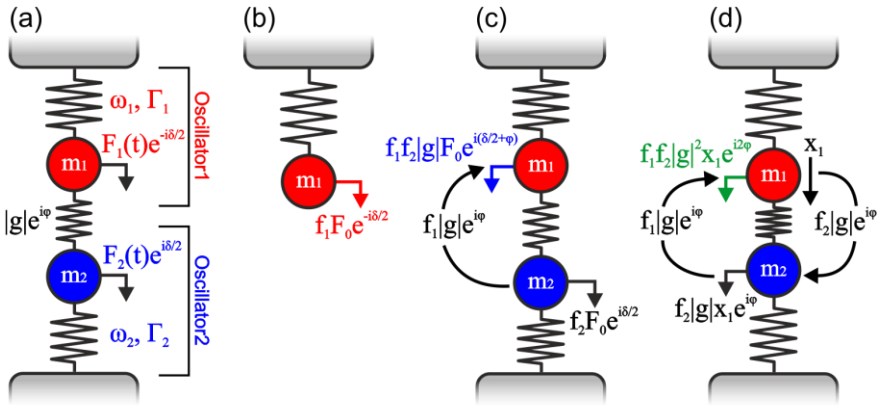

Figure 7.4. (a) Schematic illustration of the ECO model. (b – d) Schematic illustrations of (b) the first, (c) second, and (d) third term of Equation 7.30.

7.4. Constructive and destructive interference in the dimer

We figure out a condition of EIA originating from the phase-retarded coupling. As explained in the introduction, there are two types of EIA: EIA induced by near-field or phase-retarded coupling. EIA by a near-field coupling is dominated by the absorption enhancement in the dark oscillator. In contrast, for EIA by a phase-retarded coupling, it is expected that an absorption enhancement occurs in the bright oscillator. In the plasmonic-dielectric dimer, the plasmonic particle corresponds to the bright oscillator. Therefore, the dimer may possess an EIA-like spectral profile even though the dielectric particle, which corresponds to the quasi-dark oscillator, has no absorption. Based on this, to simplify our investigation, we consider that the dielectric particle is lossless (no intrinsic damping), and the plasmonic particle solely determines the absorption properties of the dimer. The optical properties of the plasmonic particle are dominated by the ED of the LSP. Extinction, scattering, and absorption cross-sections of the ED are given as (Section 7.10.2, Supporting Information) [62]

$$C_{\mathrm{extEDj}} = \frac{k}{\varepsilon_0 |\mathbf{E}_0|^2} \mathrm{Im}\left[\mathbf{p}_{\mathrm{nj}} \cdot \mathbf{E}_{\mathrm{in}}^*(\mathbf{r}_{\mathrm{j}})\right] \tag{7.32}$$

$$C_{\mathrm{scaEDj}} = \frac{k}{\varepsilon_0 |\mathbf{E}_0|^2} \mathrm{Im}\left[\left(\frac{ik^3}{6\pi\varepsilon_0} + \frac{1}{\varepsilon_0 \alpha_{\mathrm{j}}}\right) |\mathbf{p}_{\mathrm{nj}}|^2 - \mathbf{p}_{\mathrm{nj}}^* \cdot \mathbf{E}_{\mathrm{in}}(\mathbf{r}_{\mathrm{j}})\right] \tag{7.33}$$

$$C_{\mathrm{absEDj}} = C_{\mathrm{extEDj}} - C_{\mathrm{scaEDj}} = \frac{k}{\varepsilon_0 |\mathbf{E}_0|^2} \mathrm{Im}\left[-\left(\frac{ik^3}{6\pi\varepsilon_0} + \frac{1}{\varepsilon_0 \alpha_{\mathrm{j}}}\right)\right] |\mathbf{p}_{\mathrm{nj}}|^2 \tag{7.34}$$

The subscript n represents n ∈ (pm, pp). In Equations 7.32-7.34, an isotropic electric polarizability is considered. From Equation 7.34, the absorption of the plasmonic particle is proportional to the absolute square of its ED moment. When the resonances of the particles of the dimer are aligned, meaning that $\omega_{\mathrm{p1}} = \omega_{\mathrm{m2}}$ for the $\mathbf{p}_1$-$\mathbf{m}_2$ coupling and $\omega_{\mathrm{p1}} = \omega_{\mathrm{p2}}$ for the $\mathbf{p}_1$-$\mathbf{p}_2$ coupling, $|\mathbf{p}_{\mathrm{n1}}|^2$ is given as ($\omega_{\mathrm{p1}} = \omega_{\mathrm{m2}} = \omega_{\mathrm{p2}} = \omega_0$) (Section 7.10.3, Supporting Information)

$$|\mathbf{p}_{\mathrm{pm1}}|^2 = \frac{1 + \Phi_{\mathrm{pm2}}^2 + 2\Phi_{\mathrm{pm2}} \sin(\phi_{\mathrm{C}} + kD)}{1 + \Phi_{\mathrm{pm}}^2 + 2\Phi_{\mathrm{pm}} \cos(2\phi_{\mathrm{C}} + \pi)} |\mathbf{p}_1|^2 = P_{\mathrm{pm}} |\mathbf{p}_1|^2 \tag{7.35}$$

$$|\mathbf{p}_{\mathrm{pp1}}|^2 = \frac{1 + \Phi_{\mathrm{pp2}}^2 + 2\Phi_{\mathrm{pp2}} \sin(-\phi_{\mathrm{A}} - kD)}{1 + \Phi_{\mathrm{pp}}^2 + 2\Phi_{\mathrm{pp}} \cos(2\phi_{\mathrm{A}})} |\mathbf{p}_1|^2 = P_{\mathrm{pp}} |\mathbf{p}_1|^2 \tag{7.36}$$

where

$$\Phi_{\mathrm{pm}} = \frac{f_{\mathrm{p1}} f_{\mathrm{m2}} |g_{\mathrm{C}}|^2}{\Gamma_{\mathrm{p1}} \Gamma_{\mathrm{m2}} \omega_0^2} = \frac{f_{\mathrm{p1}} |g_{\mathrm{C}}|}{\Gamma_{\mathrm{p1}} \omega_0} \frac{f_{\mathrm{m2}} |g_{\mathrm{C}}|}{\Gamma_{\mathrm{m2}} \omega_0} = \Phi_{\mathrm{pm1}} \Phi_{\mathrm{pm2}} \tag{7.37}$$

$$\Phi_{\mathrm{pp}} = \frac{f_{\mathrm{p1}} f_{\mathrm{p2}} |g_{\mathrm{A}}|^2}{\Gamma_{\mathrm{p1}} \Gamma_{\mathrm{p2}} \omega_0^2} = \frac{f_{\mathrm{p1}} |g_{\mathrm{A}}|}{\Gamma_{\mathrm{p1}} \omega_0} \frac{f_{\mathrm{p2}} |g_{\mathrm{A}}|}{\Gamma_{\mathrm{p2}} \omega_0} = \Phi_{\mathrm{pp1}} \Phi_{\mathrm{pp2}} \tag{7.38}$$

Φ_{n} is the ratio of the coupling strength to the total damping of the dimer. These ratios describe how strongly the particles couple with each other [34]. Φ_{nj} is the ratios of the coupling strength to the damping of each particle. When there is no coupling ($\Phi_{\mathrm{nj}} = 0$), Equation 7.35 and 7.36 coincide with $|\mathbf{p}_1|^2$. The sine and cosine functions of Equations 7.35 and 7.36 describe the influence of phase retardation in the coupling. Depending on those functions, it is determined whether $|\mathbf{p}_{\mathrm{n1}}|^2$ can be amplified. Therefore, we can understand that the function P_{n} (in Equations 7.35 and 7.36) describes the phase-retarded coupling, and EIA is induced when $P_{\mathrm{n}} > 1$.

For a fundamental understanding of P_n, we employ a systematic analysis using a simplified form of P_n

$$P = \frac{1 + \Phi_2^2 + 2\Phi_2 \sin\theta_S}{1 + \Phi^2 + 2\Phi\cos\theta_C}, \qquad \Phi = \Phi_1\Phi_2 \tag{7.39}$$

where θ_S and θ_C are angles for the sine and cosine functions, respectively. Φ and Φ_j are dimensionless and unitless values. Comparing P and P_n, it is understood that Φ and Φ_j correspond to Φ_n and Φ_{nj}, respectively. P is the most amplified when $\sin\theta_S = 1$ and $\cos\theta_C = -1$ occur simultaneously. This is a condition for EIA excited by complete constructive interference. We first consider how Φ_1 and Φ_2 influence on P under complete constructive interference. In Figure 7.5a, we can find that P is significantly enhanced at $\Phi = 1$. This is because P diverges at $\Phi = 1$. Considering Equations 7.37 and 7.38, $\Phi = 1$ means that the damping of the entire system takes balance with the energy transferred between two dipole moments. This situation can be recognized as a critical coupling. When a set of (Φ_1, Φ_2) makes Φ larger or smaller than 1, P decreases no matter which is larger Φ_1 or Φ_2. Next, we investigate the influences of (θ_C, θ_S) on P. Figure 7.5b shows P as functions of θ_S and θ_C. (Φ_1, Φ_2) = (0.5, 2) is used for this color map. As expected from Equation 7.39, P increases for (θ_C, θ_S) → (π, π/2) and decreases for (θ_C, θ_S) → (0 or 2 π, 3π/2). It is found that $P > 1$ can be obtained even though complete constructive interference is not achieved. Therefore, partially constructive interference ((θ_C, θ_S) ≠ (π, π/2) but $P > 1$) can also contribute to EIA. The grey shaded areas of Figure 7.5b indicate $P < 1$, meaning that the coupling is destructive and EIA cannot be observed. The same properties of P shown in Figure 7.5b can be applied to P with different (Φ_1, Φ_2). However, if Φ becomes larger or smaller than 1, the area of $P < 1$ increases, and the overall intensity of P decreases (Section 7.10.4, Supporting Information).

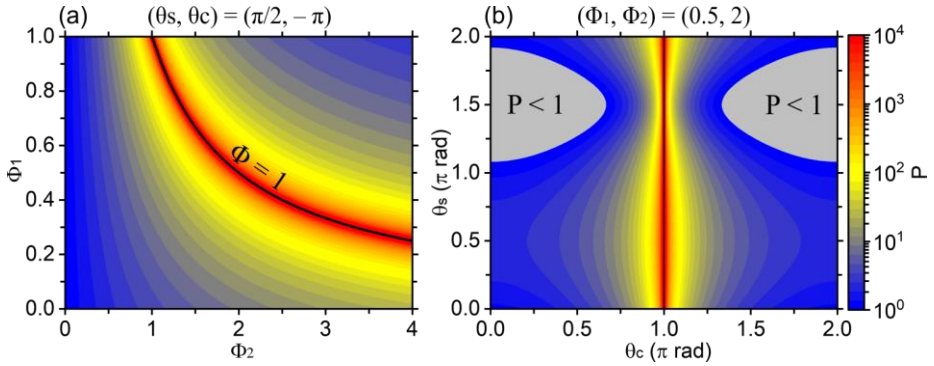

Figure 7.5. (a) The color map of Equation 7.39 as functions of Φ_1 and Φ_2. (θ_C, θ_S) = (π, π/2) is used. (b) the color map of Equation 7.39 as functions of θ_C and θ_S. (Φ_1, Φ_2) = (0.5, 2) is used.

Our systematic analysis using P suggests that $\Phi = 1$ and complete constructive interference must occur simultaneously to maximize EIA. However, Hugonin et. al. have indicated that upper bounds for absorption of any dimers may be determined independently of their material properties [51]. Therefore, this extreme condition may not be achieved since Φ is connected to material properties. Our analysis also suggests that the condition for EIA is not confined to the extreme condition and demonstrates that EIA may be induced under partially constructive interference.

Since satisfying the extreme condition is not straightforward, we focus on partially constructive interference in this work. From Equations 7.35 and 7.36, (Φ_1, Φ_2) is determined by the polarizabilities of the particles and the scattered field amplitude. (θ_C, θ_S) is solely determined by the phase of the scattered fields. If the design and materials of the particles are determined, the polarizabilities are immediately given.

In this case, P can be expressed as a function only of D. Therefore, we may be able to find an optimal D for EIA just by calculating P and finding its maximum.

7.5. Design and optical properties of the dimer

Plasmonic and dielectric particles of the dimer are designed to theoretically demonstrate EIA as discussed earlier. We use a concentric core-shell geometry for the plasmonic particle (see Figure 7.6a). The plasmonic core-shell particle consists of a dielectric core with radius r_{CS} being fully covered with a plasmonic shell with a thickness of t_{CS}. The core-shell structure has been widely used in plasmonics, and it is known that its LSP can be controlled by tuning the aspect ratio of the outer to inner radii. In addition, its scattering and absorption properties can also be controlled by changing the aspect ratio [35, 38, 39, 65]. For a dielectric particle, a sphere with a radius of r_S is used. Compared to the LSP, a Mie resonance of a dielectric sphere is relatively easily controlled by tuning r_S since the Mie resonance is not confined by the Fröhlich condition [66].

Next, proper materials for the plasmonic core-shell particle and the dielectric sphere have to be chosen. We first consider the material for the dielectric sphere. To realize the $\mathbf{p}_1$-$\mathbf{m}_2$ and $\mathbf{p}_1$-$\mathbf{p}_2$ coupling, a refractive index of the dielectric sphere has to be sufficiently large to spectrally separate its ED and MD resonances. Silicon, which has been intensively used for nanophotonics [67], possesses a high refractive index of about 3.5 [68], but the ED and MD resonances are close to each other with a refractive index of this value. A refractive index higher than that of silicon can be accessible from infrared (IR) dielectric materials, such as PbTe [69] and Bi_2Te_3 [70]. Based on those considerations, a complex refractive index of the dielectric sphere $N_S = n_S + i\kappa_S$ has to be determined. We chose $n_S = 5.6$ by referring to the refractive index of PbTe. As mentioned earlier, we simplify the system by considering a lossless dielectric sphere, meaning $\kappa_S = 0$; therefore, $N_S = n_S$ (later, we will consider the case of $\kappa_S \neq 0$). Since the material we consider for the dielectric sphere is for the IR region, materials of the plasmonic core-shell particle also have to be for that wavelength range. Metal oxides, such as AZO, are representative plasmonic materials in the IR region [68]. Therefore, we use an AZO shell for the plasmonic core-shell particle. We assume that the dielectric core has a constant refractive index of $N_{CS} = 1.55$, which can be obtained by polymers, such as PS [71].

The absorption properties of the isolated plasmonic core-shell particle are shown in Figure 7.6b. The absorption of the ED, MD, electric quadrupole (EQ), and magnetic quadruple (MQ) are calculated using Mie theory [64]. The refractive index of AZO is taken from Ref. [68]. r_{CS} and t_{CS} are determined so that the ED absorption is roughly maximized by satisfying $C_{abs} \approx C_{sca}$ (Section 7.10.5, Supporting Information) [36]. This is because we are interested in observing that EIA enhances the absorption of the plasmonic core-shell particle beyond the upper absorption limit of an isolated particle $C_{abs} = 3\lambda_0^2/8\pi$. The absorption of the plasmonic core-shell particle is dominated by the ED. The MD has a nearly constant absorption over the wavelength range. The EQ and MQ contribute to the total absorption at short wavelengths.

Scattering spectra of the dielectric spheres with different radii are shown in Figure 7.6c and 7.6d. As mentioned earlier, since the dielectric spheres are lossless, they do not possess any absorption. For both spheres, ED and MD resonances are well resolved. The dielectric spheres with $r_S = 500$ nm and 690 nm have the MD and ED at the absorption peak of the plasmonic core-shell particle, respectively. Therefore, the $\mathbf{p}_1$-$\mathbf{m}_2$ and $\mathbf{p}_1$-$\mathbf{p}_2$ coupling can be investigated using the plasmonic core-shell particle and those dielectric spheres. The dielectric sphere with $r_S = 690$ nm possesses a strong MQ resonance right next to the ED resonance. This MQ resonance may disturb observing the $\mathbf{p}_1$-$\mathbf{p}_2$ coupling.

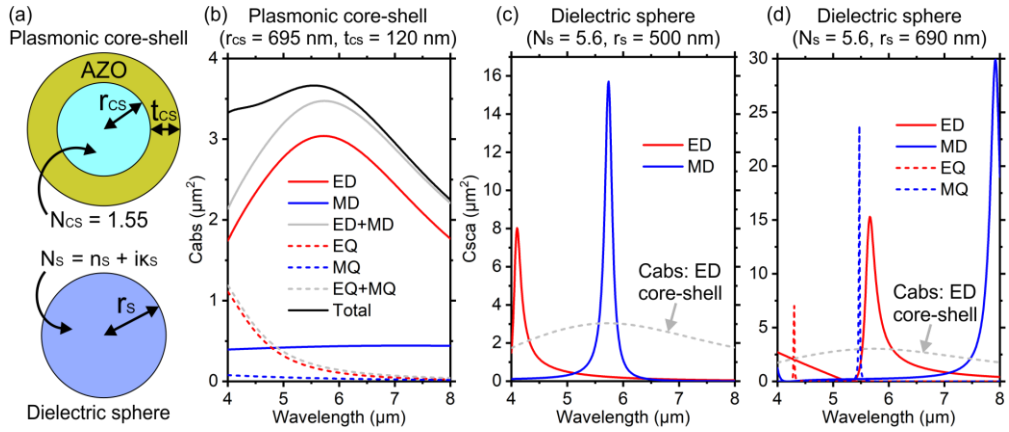

Figure 7.6. (a) Schematic illustrations of the plasmonic core-shell particle and dielectric sphere. The core-shell particle is composed of the AZO shell and the dielectric inner core with the refractive index of N_{CS} = 1.55. The shell thickness and inner core radius are t_{CS} and r_{CS}, respectively. The dielectric sphere with the radius of r_S has the complex refractive index of $N_S = n_S + i\kappa_S$. (b) The absorption properties of the plasmonic core-shell particle are shown. The red, blue, and grey solid lines are for the ED, MD, and total absorption of the dipolar resonances, respectively. The red, blue, and grey dashed lines are for the EQ, MQ, and total absorption of the quadrupolar resonances. (c and d) The scattering properties of the dielectric spheres with r_S = 500 nm and 690 nm. The red and blue solid lines are for the ED and MD, respectively. The red and blue dashed lines are for the EQ and MQ, respectively. The grey dashed line is the absorption spectrum of the ED of the plasmonic core-shell particle, which is taken from Figure 7.6b.

7.6. Calculation method of optical properties of the dimer

C_{abs} and C_{sca} (scattering cross-section) were obtained using COMSOL Multiphysics, which is a commercial software package based on the FEM. The orientations of the dimer and the incident plane wave are shown in Figure 7.3a. The plasmonic core-shell particle and dielectric sphere designed in Figure 7.6 were used. The surrounding of the dimer was air, and a perfectly matched layer (PML) was applied around the calculation domain. C_{abs} was calculated by taking the volume integral of energy dissipation density over the dimer. C_{sca} was calculated by taking the surface integral of the Poynting vector of the scattered field over the integration sphere, which was defined between the dimer and the PML.

The optical cross-sections of the dimer were also calculated using the CDM. So far, we have only discussed interactions between two dipole moments. This can be valid for phenomenological analysis. However, as seen in Figure 7.6b-d, there are small contributions from other dipole moments of the plasmonic core-shell particle and dielectric sphere (for example, the MD of the plasmonic core-shell particle), which must be considered for a complete analysis. Therefore, we calculated the optical properties of the dimer by using the FD model shown in Figure 7.3a (Sections 7.10.1 and 7.10.2, Supporting Information). In this calculation, the polarizabilities were not approximated by the Lorentz functions, but those given by Mie coefficients for accurate analysis. The CDM cannot consider quadrupole moments, but the plasmonic core-shell particle has an EQ and MQ in a short wavelength range. Therefore, the contributions from the quadrupole moments were taken into account in the total absorption of the dimer by adding EQ + MQ of the plasmonic core-shell particle, which is given by Mie theory (Figure 7.13, Supporting Information).

7.7. EIA properties of the dimer

The absorption properties of the dimer are presented in Figure 7.7. We first focus on the $\mathbf{p}_1$-$\mathbf{m}_2$ coupling shown in the top panel of Figure 7.7. The dielectric sphere with r_S = 500 nm is used in the dimer. Figure

7.7a shows absorption spectra of the dimer with different face-to-face distances *d*, which are obtained using the FEM. Since the dielectric sphere is lossless, the absorption properties of the dimer are dominated by the plasmonic core-shell particle. The grey dashed lines are the reference spectra given by the total absorption of the isolated plasmonic core-shell particle (from Figure 7.6b). When *d* is small, the absorption spectra have an absorption dip at around the MD resonance of the dielectric sphere (the blue vertical line of Figure 7.7a). This spectral profile can be recognized as EIT. In contrast, the absorption is strongly enhanced with increasing *d*, and a sharp absorption peak appears at the MD resonance of the dielectric sphere when *d* is around 2 μm. This absorption enhancement is attributed to EIA. With a further increase in *d*, the absorption spectra again show the EIT-like spectral profile.

In Figure 7.7b, the absorption of the dimer with $d = 2$ μm is calculated using the CDM. The black solid line is the total absorption of the plasmonic core-shell particle. The orange dashed line is the absorption taken from Figure 7.7a. Comparing the black solid and orange dashed lines, we find that the CDM is in good agreement with the FEM simulation, which proves that the CDM is a proper method to investigate the absorption properties of the dimer. This agreement can be confirmed for different *d* and the scattering properties of the dimer (Section 7.10.6, Supporting Information). The red and blue solid lines are the ED and MD absorptions of the plasmonic core-shell particle, respectively. It can be found that the ED absorption possesses a pronounced peak over a broad absorption, characterizing EIA by the phase retarded coupling. Interestingly, this absorption enhancement enables the plasmonic core-shell particle to exceed the upper absorption limit of $C_{abs} = 3\lambda_0^2/8\pi \approx 3.9$ μm^2 at $\lambda_0 \approx 5.7$ μm, which cannot be achieved by EIA induced by near-field coupling [34].

We investigate the EIA of the dimer using P_{pm} (Equation 7.35). P_{pm} contains $\sin(\phi_C + kD)$ and $\cos(2\phi_C + \pi)$, which are functions of *D*. *D* is the center-to-center distance of the dimer; therefore, $D = d + (r_{CS} + t_{CS}) + r_S$. Figure 7.7c shows $\sin(\phi_C + kD)$ and $\cos(2\phi_C + \pi)$ as a function of *d*. It can be found that complete constructive interference cannot be achieved by the $\mathbf{p}_1$-$\mathbf{m}_2$ coupling. To better understand the EIA of the dimer, P_{pm} has to be calculated using the variables of the polarizabilities. The variables can be extracted by fitting the Lorentz functions to the polarizabilities given by Mie coefficients (Section 7.10.5, Supporting Information). The fitting results are summarized in Table 7.1. In Figure 7.7d, P_{pm} with $\omega_0 = \omega_{m2}$ is plotted using these extracted values and the sine and cosine functions in Figure 7.7c. Depending on *d*, P_{pm} can be smaller or larger than 1. When $P_{pm} < 1$ (blue shaded area of Figure 7.7d), the absorption of the plasmonic core-shell particle is decreased by destructive interference, resulting in the EIT-like spectral profile. In contrast, $P_{pm} > 1$ (yellow shaded area of Figure 7.7d) means that constructive interference enhances the absorption of the plasmonic core-shell particle, enabling us to observe the EIA-like spectral profile. P_{pm} is maximized at around $d = 2$ μm, which can be the optimum *d* for EIA. These results from P_{pm} coincide with the FEM simulation shown in Figure 7.7a, proving that P_{pm} is an applicable function for investigating the EIA of the dimer. At $d = 2$ μm, the scattered field amplitude is $|g_C| = 2.98 \times 10^{16}$ m^{-3}, which gives (Φ_{pm1}, Φ_{pm2}, Φ_{pm}) = (0.17, 0.43, 0.07). Φ_{pm} is much smaller than 1, suggesting that the critical coupling cannot be achieved in this $\mathbf{p}_1$-$\mathbf{m}_2$ coupling.

We turn our focus to the $\mathbf{p}_1$-$\mathbf{p}_2$ coupling shown in the bottom panel of Figure 7.7. In this case, the dielectric sphere with $r_S = 690$ nm is used. Figure 7.7e shows *d* dependency of the absorption of the dimer. There are sharp absorption dips and peaks at around the wavelengths of 4.2 μm and 5.5 μm, which are attributed to the influence of the EQ and MQ of the dielectric sphere, respectively (see Figure 7.6d). At around the ED resonance of the dielectric sphere (the red vertical line of Figure 7.7e), we can see that the absorption spectra change from EIA → EIT → EIA-like profile with an increase in *d*. The dimer system with $d = 0.01$ μm has the strongest absorption, which is examined using the CDM in Figure 7.7f. The CDM (black solid line) and the FEM simulation (orange dashed line) are in good agreement, but the discrepancy between them is slightly larger than that for the $\mathbf{p}_1$-$\mathbf{m}_2$ coupling. This is because the CDM cannot take the

influence of the EQ and MQ of the dielectric sphere into account. Furthermore, the discrepancy originates from the fact that the CDM cannot fully describe the near-field effect. d = 0.01 μm means that the particles of the dimer are nearly touching each other. In this situation, the near-field effect may be expected to dominate the $\mathbf{p}_1$-$\mathbf{p}_2$ coupling. However, considering the orientations of the dimer and the incident wave, the electromagnetic hot spots of the particles weakly influence on the $\mathbf{p}_1$-$\mathbf{p}_2$ coupling. This is because the hot spots are concentrated in the x-direction so that the ED moments of the particles cannot directly interact with each other. Therefore, there is a near-field effect in the $\mathbf{p}_1$-$\mathbf{p}_2$ coupling, but the intermediate-field effect dominates the $\mathbf{p}_1$-$\mathbf{p}_2$ coupling. Figure 7.7f shows that the ED absorption of the plasmonic core-shell particle is strongly enhanced by the $\mathbf{p}_1$-$\mathbf{p}_2$ coupling. Compared to the case of the $\mathbf{p}_1$-$\mathbf{m}_2$ coupling, the absorption enhancement for the $\mathbf{p}_1$-$\mathbf{p}_2$ coupling is more significant. To understand this absorption enhancement, we use P_{pp} (Equation 7.36). Figure 7.7g shows $\sin(-\phi_A - kD)$ and $\cos(2\phi_A)$ of P_{pp}, indicating that complete constructive interference cannot be achieved by the $\mathbf{p}_1$-$\mathbf{p}_2$ coupling. Using Figure 7.7g and the extracted electric polarizability of the dielectric sphere (see Table 7.1), P_{pp} is calculated at $\omega_0 = \omega_{p2}$ and plotted in Figure 7h. P_{pp} suggests that the $\mathbf{p}_1$-$\mathbf{p}_2$ coupling becomes constructive → destructive → constructive with an increase in d, which coincide with the spectral change shown in Figure 7.7e. From the agreement between the results in Figures 7.7e and h, we can find that the optimum d for EIA is 0.01 μm. d = 0.01 μm gives the scattered field amplitude $|g_A| = 5.69 \times 10^{16}$ m^{-3}. Using this value, we get (Φ_{pp1}, Φ_{pp2}, Φ_{pp}) = (0.31, 0.77, 0.24). This Φ_{pp} is larger than $\Phi_{pm} = 0.07$, resulting in stronger EIA for the $\mathbf{p}_1$-$\mathbf{p}_2$ coupling than for the $\mathbf{p}_1$-$\mathbf{m}_2$ coupling.

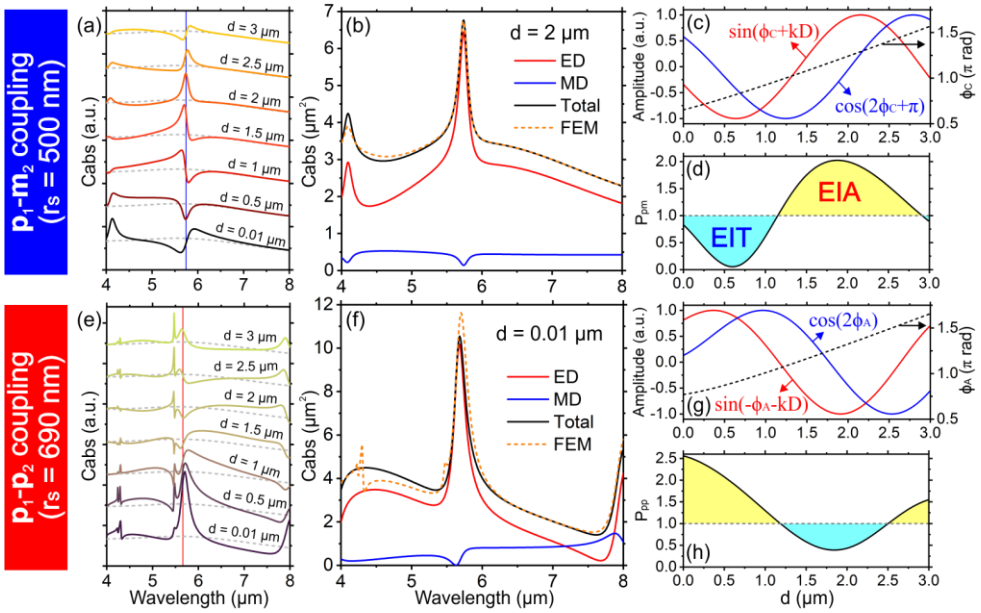

Figure 7.7. (Top panel) $\mathbf{p}_1$-$\mathbf{m}_2$ coupling of the dimer composed of the dielectric sphere with r_S = 500 nm. (Bottom panel) $\mathbf{p}_1$-$\mathbf{p}_2$ coupling of the dimer composed of the dielectric sphere with r_S = 690 nm. (a and e) d dependencies of the absorption of the dimer. d is the face-to-face distance between the particles. The absorption spectra are calculated using the FEM simulation. The grey dashed lines are the reference spectra given by the total absorption of the isolated plasmonic core-shell particle (Figure 7.6b). The blue and red solid vertical lines show the resonance wavelength of the MD and ED of the dielectric spheres, respectively. (b and f) The solid lines are the absorption spectra of the dimer, which are calculated using the CDM. The red and blue solid lines are for the ED and MD of the plasmonic core-shell particle. The black line is the total absorption of the plasmonic core-shell particle (Figure 7.13, Supporting Information). The orange dashed lines are taken from Figures 7.7a and 7e. (c and g) The sine and cosine functions of P_{pm} (Equation 7.35) and P_{pp} (Equation 7.36) are plotted as a function of d on the left vertical axis. The phases of φ_C and φ_A are shown as the black dashed line on the right vertical axis. (d and h) P_{pm} and P_{pp} are calculated at $\omega_0 = \omega_{m2} = 3.29 \times 10^{14}$ rad/s and $\omega_0 = \omega_{p2} = 3.33 \times 10^{14}$ rad/s, respectively.

Here we briefly summarize the finding from Figure 7.7. The dimer involves the phase-retarded coupling, and its EIA is attributed to partially constructive interference. An optimum d for EIA can be found relatively easily by calculating P_{pm} and P_{pp} for the $\mathbf{p}_1$-$\mathbf{m}_2$ and $\mathbf{p}_1$-$\mathbf{p}_2$ coupling, respectively. It must be mentioned that the dimer possesses different absorption properties if the positions of the plasmonic core-shell particle and dielectric sphere are swapped. By doing this, an EIA-like spectral profile cannot be observed in the absorption of the plasmonic core-shell particle (Section 7.10.7, Supporting Information). We have only discussed the absorption properties of the dimer oriented parallel to the propagation direction of the incident wave. In Sections 7.10.8 and 7.10.9, Supporting Information, we investigate the absorption properties of the dimer oriented perpendicular to the propagation direction of the incident wave. Our investigation reveals that EIA can be excited in the dimer with different orientations. Furthermore, we also investigate the n_S dependency of the absorption properties of the dimer (Section 7.10.10, Supporting Information). Even though n_S is smaller than 5.6, EIA can be observed.

Table 7.1. The oscillator strengths, resonance frequencies, and damping rates of the polarizabilities. (These values are obtained by fitting the Lorentz oscillator to the polarizabilities given by Mie coefficients. The details can be found in Section 7.10.4, Supporting Information.)

Lorentz oscillator	Core-shell particle Electric polarizability	Sphere (r_S = 500 nm) Magnetic polarizability	Sphere (r_S = 690 nm) Electric polarizability
$f_{pj\ or\ mj}$ [$m^3 \cdot (rad/s)^2$]	4.35×10^{11}	4.3×10^{10}	7.83×10^{10}
$\omega_{pj\ or\ mj}$ [rad/s]	3.31×10^{14}	3.29×10^{14}	3.33×10^{14}
$\Gamma_{pj\ or\ mj}$ [rad/s]	2.38×10^{14}	9.11×10^{12}	1.72×10^{13}

For an insight into constructive and destructive interference of the dimer, we observe electric field distribution maps obtained using the FEM simulation. Figure 7.8a is a reference electric field map of the isolated plasmonic core-shell particle at its ED resonance (λ_0 = 5.72 μm). Figure 7.8b shows the $\mathbf{p}_1$-$\mathbf{m}_2$ coupling of the dimer. From Figure 7.7d, it is known that the absorption of the plasmonic core-shell particle in the dimer with d = 0.5 μm and 2 μm possesses the EIT- and EIA-like spectral profile, respectively. The field maps of Figure 7.8b are taken at around the absorption dip (λ_0 = 5.73 μm) for d = 0.5 μm and the absorption peak (λ_0 = 5.74 μm) for d = 2 μm. The electric field around the plasmonic core-shell particle is much stronger for d = 2 μm than for d = 0.5 μm. In general, it might be expected that the electric field enhancement is stronger for the dimer with a smaller d because the electric fields of each particle are strong at a point close to the particles, and strong near-field coupling can occur if the particles are close to each other. However, as explained earlier, the coupling involves phase retardation, which can make the coupling destructive or constructive depending on d. Therefore, the electric field of the plasmonic core-shell particle can be strengthened even though d is large. This field enhancement occurs through the scattered intermediate field without relying on the electric field hot spots. In Figure 7.8c, the field maps for the $\mathbf{p}_1$-$\mathbf{p}_2$ coupling are presented. The dimers with d = 0.01 μm, 2 μm, and 3 μm are considered for those field maps. Those interparticle distances are chosen based on the findings in Figures 7.7e and h: with increasing d, the absorption of the plasmonic core-shell particle changes EIA → EIT → EIA-like profile. Therefore, the electric field around the plasmonic core-shell particle is weak for d = 2 μm (at λ_0 = 5.67 μm), and it becomes strong for d = 0.01 μm (at λ_0 = 5.7 μm) and d = 3 μm (at λ_0 = 5.64 μm). The dimer with d = 0.01 μm possesses the strongest electric field of the plasmonic core-shell particle because constructive interference occurs with a small d, meaning that the coupling is significantly strong.

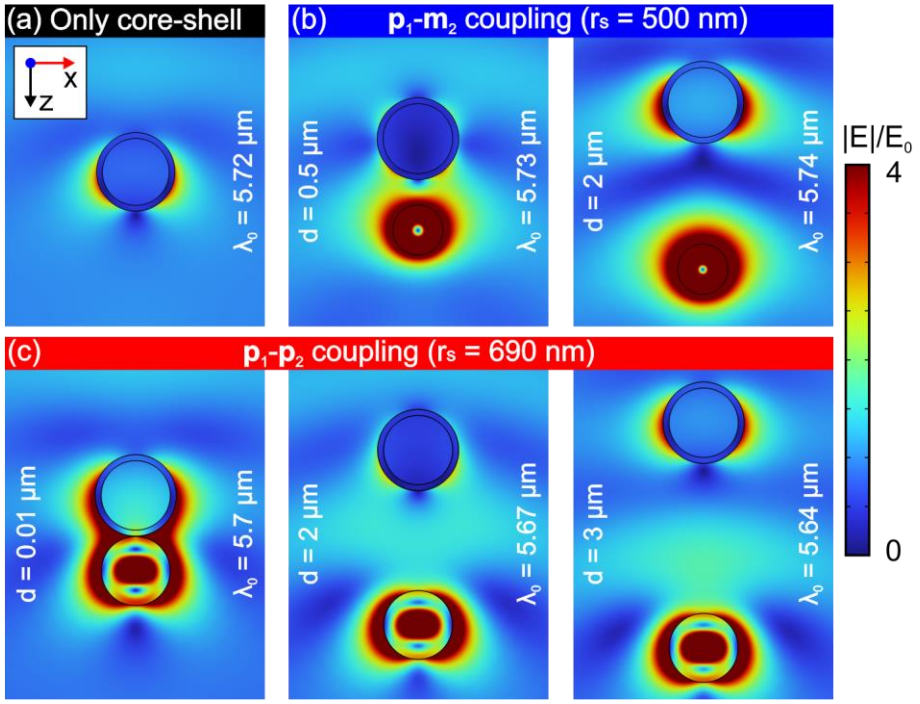

Figure 7.8. The absolute value of the electric fields are normalized by the electric field amplitude of the incident wave. (a) The field map for the isolated plasmonic core-shell particle at its ED resonance. (b) The field maps of the dimer with r_S = 500 nm. d = 0.5 μm and 2 μm are chosen to observe the destructive and constructive coupling, respectively. (c) The field maps of the dimer with r_S = 690 nm. d = 0.01 μm, 2 μm, and 3 μm are used to show the transition of constructive → destructive → constructive interference.

We have considered a dimer with a lossless dielectric sphere. However, real dielectric materials are usually not lossless. Here, we investigate the influences of an intrinsic loss κ_S of the dielectric sphere on the EIA properties of the dimer. For this investigation, a $\mathbf{p}_1$-$\mathbf{m}_2$ coupling is considered, and the dimer with r_S = 500 nm and d = 2 μm is used. Figure 7.9a shows how the absorption properties of an isolated dielectric sphere with r_S = 500 nm and n_S = 5.6 change with an increase in κ_S. Those spectra are calculated using Mie theory. The absorption becomes pronounced with increasing κ_S up to about 0.1. With a further increase in κ_S, the absorption decreases and becomes broad.

Suppose there is no coupling effect in the dimer. In this case, the total absorption of the dimer is given by a superposition of the absorptions of the isolated plasmonic core-shell particle and dielectric sphere. The dielectric sphere with a moderately high κ_S possesses a strong absorption. Therefore, the total absorption of the dimer with the lossy dielectric sphere can be strong even though EIA does not exist. In other words, the total absorption of the dimer can be improved further if EIA of the plasmonic core-shell particle coincides with the strong absorption of the dielectric sphere. To figure out whether the phase-retarded coupling can positively affect the absorption properties of the dimer with $\kappa_S \neq 0$, the total absorption spectra of the dimer without and with coupling are plotted in Figures 7.9b and 7.9c as functions of κ_S and λ. The absorption of the dimer without coupling is given by a sum of the absorptions of the isolated plasmonic core-shell particle and dielectric sphere in Figure 7.9a. The absorption of the dimer with coupling is calculated using the CDM. Comparing Figures 7.9c to 7.9b, the absorption properties with-coupling are similar to those without-coupling. A strong absorption peak is found around the MD resonance of the dielectric sphere. This pronounced peak is broadened with an increase in κ_S.

In Figure 7.9d, the maxima of the absorption spectra in Figures 7.9b and 7.9c are plotted as a function of κ_S. The maximum absorption for with-coupling is higher than without-coupling for any κ_S. The peak of the maximum absorption for with-coupling appears at $\kappa_S \approx 0.052$. Figure 7.9e shows the absorption spectra of the dimer with $\kappa_S = 0.052$. Those spectra are calculated using Mie theory and the CDM for without- and with-coupling, respectively. The absorption spectra of the plasmonic core-shell particle and dielectric sphere are separately obtained by taking their ED + MD (the EQ + MQ is considered only for the plasmonic core-shell particle). The results from the CDM are in good agreement with the FEM simulation even though the lossy dielectric sphere is considered (Figure 7.25, Supporting Information). For with-coupling (the CDM), the absorption spectral profile of the plasmonic core-shell particle is similar to what we observed in Figure 7.7b, which is the case of $\kappa_S = 0$. This result indicates that the EIA properties of the plasmonic core-shell particle discussed earlier are preserved even though $\kappa_S \neq 0$. The absorption of the dielectric sphere is slightly enhanced by the coupling. But its spectral shape is almost the same as the spectrum from Mie theory, meaning that the absorption properties of the dielectric sphere are not significantly influenced by the phase-retarded coupling. From the results in Figure 7.9e, it is understood that the dimer with coupling can possess EIA of the plasmonic core-shell particle and the strong absorption of the dielectric sphere simultaneously. When the plasmonic core-shell particle does not couple with the dielectric sphere, EIA obviously has no contribution to the total absorption of the dimer. Thus, the phase-retarded coupling can have a positive effect on improving the total absorption of the dimers with any κ_S.

Comparing with- and without-coupling in Figure 7.9d, their peaks locate at different κ_S. The peak for without-coupling appears at $\kappa_S = 0.082$. When there is no coupling effect between the plasmonic core-shell particle and dielectric sphere, the maximum absorption of the dimer is determined by the absorption of the dielectric sphere. The absorption of an isolated particle is maximized when $C_{abs} \approx C_{sca}$ is satisfied. For the dielectric sphere with $n_S = 5.6$ and $r_S = 500$ nm, this condition is satisfied with $\kappa_S \approx 0.082$ (Figure 7.26, Supporting Information). Therefore, the peak for without-coupling appears at $\kappa_S \approx 0.082$. However, as mentioned earlier, the peak for with-coupling is found at $\kappa_S = 0.052$. When the plasmonic core-shell particle couples with the dielectric sphere, the maximum absorption of the dimer is determined not only by the absorption of the dielectric sphere but also by EIA of the plasmonic core-shell particle. From Figure 7.7, it is known that EIA occurs on the ED of the plasmonic core-shell particle. Figure 7.9f shows how the ED absorption of the plasmonic core-shell particle changes depending on κ_S. Those spectra are calculated using the CDM, and the dimer with $d = 2$ μm is considered. With an increase in κ_S, EIA becomes weak, which can be described using Φ_{pm}. For the dimer investigated in Figure 7.9, f_{p1}, Γ_{p1}, ω_0, and $|g_C|$ are constant. f_{m2} is also nearly constant for different κ_S, but only Γ_{m2} increases with increasing κ_S because κ_S directly connects to the intrinsic damping of the dielectric sphere (Section 7.10.10, Supporting Information). Therefore, Φ_{pm} decreases with increasing κ_S, resulting in weak coupling. In consequence, EIA of the plasmonic core-shell particle attenuates. Based on understanding how EIA is weakened by κ_S, we can find why the peaks for with- and without-coupling in Figure 7.9d appear at different κ_S. The absorption of the dielectric sphere increases with increasing κ_S up to 0.082; however, the EIA of the plasmonic core-shell particle keeps decreasing with increasing κ_S. Therefore, the peak for with-coupling locates at κ_S slightly lower than that for without-coupling.

In summary, constructive interference can occur between the plasmonic core-shell particle and the dielectric sphere even though the dielectric sphere contains $\kappa_S \neq 0$. This constructive interference can enhance the total absorption of the dimer with any κ_S. As seen in Figure 7.9d, κ_S is an essential parameter to maximize the total absorption of the dimer. Since κ_S is determined by material properties, controlling κ_S is not straightforward. But if it is possible to control κ_S, an optimal κ_S may be found at around κ_S satisfying the critical coupling ($C_{abs} \approx C_{sca}$) of the isolated dielectric sphere. However, an increase in κ_S weakens the coupling effect because κ_S increases the damping of the entire system, resulting in weak EIA. Therefore, if

it is required to maximize the absorption of the plasmonic core-shell particle, the dielectric sphere must be lossless.

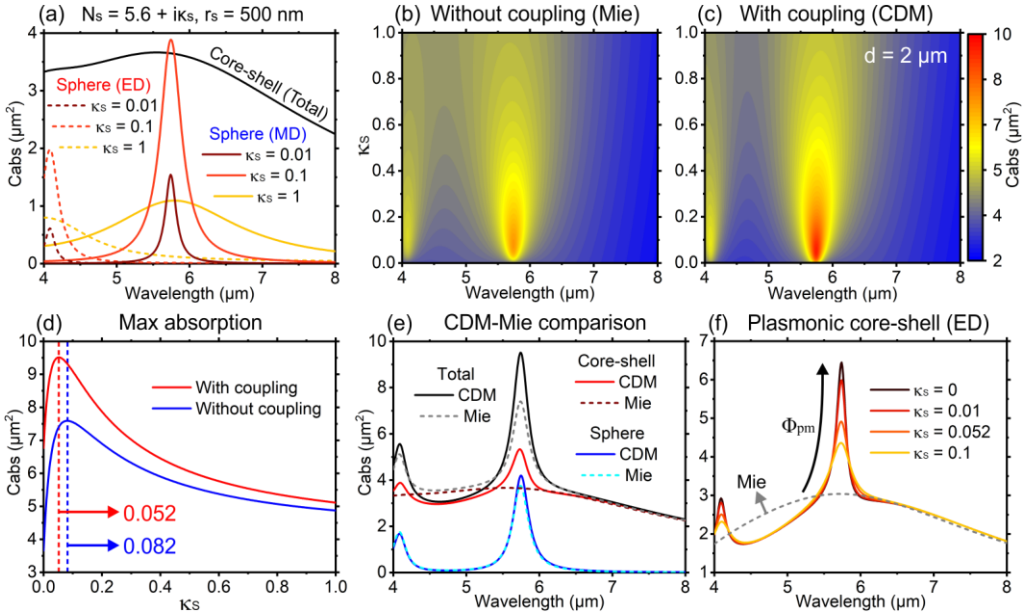

Figure 7.9. (a) Absorption properties of the dielectric sphere with $N_S = 5.6 + i\kappa_S$ and $r_S = 500$ nm. The solid and dashed lines are for the MD and ED, respectively. The black solid line is the total absorption of the plasmonic core-shell particle, taken from Figure 7.6b. (b and c) The color maps of the total absorption of the dimer with $r_S = 500$ nm and $d = 2$ μm are calculated using Mie theory and CDM for without- and with-coupling, respectively. (d) The maximum absorptions of Figures 7.9b and c are plotted as a function of κ_S. (e) The absorption properties of the plasmonic core-shell particle and the dielectric sphere with $\kappa_S = 0.052$ in the dimer with $d = 2$ μm. The solid and dashed lines are calculated using the CDM and Mie theory, respectively. (f) The influence of κ_S on the ED absorption of the plasmonic core-shell particle.

7.8. Conclusion

We investigated the mechanism of a phase-retarded coupling between plasmonic and dielectric particles. We formulated the phase-retarded coupling using the CDM, enabling us to find optimum interparticle distances of the dimer to achieve EIA for $\mathbf{p}_1$-$\mathbf{m}_2$ and $\mathbf{p}_1$-$\mathbf{p}_2$ couplings (P_{pm}: Equation 7.35 and P_{pp}: Equation 7.36). This formulation also suggests that EIA can be strengthened by balancing the coupling strength and the total damping of the dimer (Φ_{pm}: Equation 7.37 and Φ_{pp}: Equation 7.38). To demonstrate EIA by the phase-retarded coupling, we obtained the absorption spectra of the dimer using the FEM simulation. Its absorption spectra were also calculated using the CDM. The CDM agreed with the FEM simulation for any interparticle distances. Our numerical analysis suggested that EIA by the phase-retarded coupling allows the plasmonic particle to overcome the upper absorption bound of an isolated particle. EIA excited by the near-field coupling in coupled plasmonic systems cannot achieve this significant absorption enhancement. EIA properties of the dimer can be preserved even though the dielectric particle contains a lossy material; however, EIA becomes weak with an increase in the dielectric particle´s extinction coefficient. In this work, we only presented a dimer composed of two spherical particles. However, our interpretation of EIA can be applied to many systems consisting of two dipolar optical elements, providing a route to engineer the optical properties of heterostructured materials.

Funding

This project has received funding from the European Research Council (ERC) under the European Union's Horizon 2020 research and innovation program (grant agreement no. 714968).

7.9. References

1. W. Li, and J. G. Valentine, "Harvesting the loss: surface plasmon-based hot electron photodetection," Nanophotonics **6** (1), 177-191 (2017).
2. X. Liu, T. Tyler, T. Starr, A. F. Starr, N. M. Jokerst, and W. J. Padilla, "Taming the blackbody with infrared metamaterials as selective thermal emitters," Phys. Rev. Lett. **107** (4), 045901 (2011).
3. A. K. Azad, W. J. Kort-Kamp, M. Sykora, N. R. Weisse-Bernstein, T. S. Luk, A. J. Taylor, D. A. Dalvit, and H. T. Chen, "Metasurface Broadband Solar Absorber," Sci. Rep. **6** (20347 (2016).
4. M. M. Hossain, and M. Gu, "Radiative Cooling: Principles, Progress, and Potentials," Adv. Sci. **3** (7), 1500360 (2016).
5. N. Liu, M. Mesch, T. Weiss, M. Hentschel, and H. Giessen, "Infrared perfect absorber and its application as plasmonic sensor," Nano Lett. **10** (7), 2342-2348 (2010).
6. K. Chen, R. Adato, and H. Altug, "Dual-band perfect absorber for multispectral plasmon-enhanced infrared spectroscopy," ACS Nano **6** (9), 7998-8006 (2012).
7. H. Takei, N. Bessho, A. Ishii, T. Okamoto, A. Beyer, H. Vieker, and A. Golzhauser, "Enhanced infrared LSPR sensitivity of cap-shaped gold nanoparticles coupled to a metallic film," Langmuir **30** (8), 2297-2305 (2014).
8. N. Lee, T. Kim, J. S. Lim, I. Chang, and H. H. Cho, "Metamaterial-Selective Emitter for Maximizing Infrared Camouflage Performance with Energy Dissipation," ACS Appl Mater Interfaces **11** (23), 21250-21257 (2019).
9. G. Baffou, R. Quidant, and C. Girard, "Heat generation in plasmonic nanostructures: Influence of morphology," Appl. Phys. Lett. **94** (15) (2009).
10. G. Baffou, R. Quidant, and F. J. Garcia de Abajo, "Nanoscale control of optical heating in complex plasmonic systems," ACS Nano **4** (2), 709-716 (2010).
11. K. Metwally, S. Mensah, and G. Baffou, "Isosbestic Thermoplasmonic Nanostructures," ACS Photonics **4** (6), 1544-1551 (2017).
12. N. I. Landy, S. Sajuyigbe, J. J. Mock, D. R. Smith, and W. J. Padilla, "Perfect metamaterial absorber," Phys. Rev. Lett. **100** (20), 207402 (2008).
13. C. Wu, B. Neuner, G. Shvets, J. John, A. Milder, B. Zollars, and S. Savoy, "Large-area wide-angle spectrally selective plasmonic absorber," Phys. Rev. B **84** (7), 075102 (2011).
14. J. M. Hao, L. Zhou, and M. Qiu, "Nearly total absorption of light and heat generation by plasmonic metamaterials," Phys. Rev. B **83** (16), 165107 (2011).
15. A. Tittl, M. G. Harats, R. Walter, X. Yin, M. Schaferling, N. Liu, R. Rapaport, and H. Giessen, "Quantitative angle-resolved small-spot reflectance measurements on plasmonic perfect absorbers: impedance matching and disorder effects," ACS Nano **8** (10), 10885-10892 (2014).

16. K. Do-Hoon, and D. M. Pozar, "Optimal Characteristics of an Arbitrary Receive Antenna," IEEE Trans. Antennas Propag. **57** (12), 3720-3727 (2009).

17. Y. Ra'di, V. S. Asadchy, S. U. Kosulnikov, M. M. Omelyanovich, D. Morits, A. V. Osipov, C. R. Simovski, and S. A. Tretyakov, "Full Light Absorption in Single Arrays of Spherical Nanoparticles," ACS Photonics **2** (5), 653-660 (2015).

18. R. Dezert, P. Richetti, and A. Baron, "Complete multipolar description of reflection and transmission across a metasurface for perfect absorption of light," Opt. Express **27** (19), 26317-26330 (2019).

19. M. S. Jang, and H. Atwater, "Plasmonic rainbow trapping structures for light localization and spectrum splitting," Phys. Rev. Lett. **107** (20), 207401 (2011).

20. Y. Cui, K. H. Fung, J. Xu, H. Ma, Y. Jin, S. He, and N. X. Fang, "Ultrabroadband light absorption by a sawtooth anisotropic metamaterial slab," Nano Lett. **12** (3), 1443-1447 (2012).

21. D. Ji, H. Song, X. Zeng, H. Hu, K. Liu, N. Zhang, and Q. Gan, "Broadband absorption engineering of hyperbolic metafilm patterns," Sci. Rep. **4** (4498 (2014).

22. A. M. Akulshin, S. Barreiro, and A. Lezama, "Electromagnetically induced absorption and transparency due to resonant two-field excitation of quasidegenerate levels in Rb vapor," Phys. Rev. A **57** (4), 2996-3002 (1998).

23. A. Lezama, S. Barreiro, and A. M. Akulshin, "Electromagnetically induced absorption," Phys. Rev. A **59** (6), 4732-4735 (1999).

24. C. L. Garrido Alzar, M. A. G. Martinez, and P. Nussenzveig, "Classical analog of electromagnetically induced transparency," Am. J. Phys. **70** (1), 37-41 (2002).

25. R. Taubert, M. Hentschel, J. Kastel, and H. Giessen, "Classical analog of electromagnetically induced absorption in plasmonics," Nano Lett. **12** (3), 1367−1371 (2012).

26. R. Taubert, M. Hentschel, and H. Giessen, "Plasmonic analog of electromagnetically induced absorption: simulations, experiments, and coupled oscillator analysis," J. Opt. Soc. Am. B **30** (12), 3123-3134 (2013).

27. P. Tassin, L. Zhang, R. Zhao, A. Jain, T. Koschny, and C. M. Soukoulis, "Electromagnetically induced transparency and absorption in metamaterials: the radiating two-oscillator model and its experimental confirmation," Phys. Rev. Lett. **109** (18), 187401 (2012).

28. M.-l. Wan, J.-n. He, Y.-l. Song, and F.-q. Zhou, "Electromagnetically induced transparency and absorption in plasmonic metasurfaces based on near-field coupling," Phys. Lett. A **379** (30-31), 1791-1795 (2015).

29. F. Zhang, X. Huang, W. Cai, R. Yang, Q. Fu, Y. Fan, Y. Hu, K. Qiu, W. Zhang, C. Li, and Q. Li, "EIA metamaterials based on hybrid metal/dielectric structures with dark-mode-enhanced absorption," Opt. Express **28** (12), 17481-17489 (2020).

30. J. He, P. Ding, J. Wang, C. Fan, and E. Liang, "Ultra-narrow band perfect absorbers based on plasmonic analog of electromagnetically induced absorption," Opt. Express **23** (5), 6083-6091 (2015).

31. W. Xiong, W. Wang, F. Ling, W. Yu, and J. Yao, "Modulation of terahertz electromagnetically induced absorption analogue in a hybrid metamaterial/graphene structure," AIP Advances **9** (11), 115314 (2019).

32. T. Zhang, J. Dai, Y. Dai, Y. Fan, X. Han, J. Li, F. Yin, Y. Zhou, and K. Xu, "Dynamically tunable plasmon induced absorption in graphene-assisted metallodielectric grating," Opt. Express **25** (21), 26221-26233 (2017).

33. J. Krauth, T. Schumacher, J. Defrance, B. Metzger, M. Lippitz, T. Weiss, H. Giessen, and M. Hentschel, "Nonlinear Spectroscopy on the Plasmonic Analog of Electromagnetically Induced Absorption: Revealing Minute Structural Asymmetries," ACS Photonics **6** (11), 2850-2859 (2019).

34. K. Matsumori, R. Fujimura, and M. Retsch, "Coupling Strength and Total Damping Govern Electromagnetically Induced Absorption in Coupled Plasmonic Systems," Submitted to Adv. Photonics Res. (2022).

35. R. Fleury, J. Soric, and A. Alù, "Physical bounds on absorption and scattering for cloaked sensors," Phys. Rev. B **89** (4) (2014).

36. S. Tretyakov, "Maximizing Absorption and Scattering by Dipole Particles," Plasmonics **9** (4), 935-944 (2014).

37. R. Alaee, M. Albooyeh, and C. Rockstuhl, "Theory of metasurface based perfect absorbers," J. Phys. D: Appl. Phys. **50** (50), 503002 (2017).

38. V. Grigoriev, N. Bonod, J. Wenger, and B. Stout, "Optimizing Nanoparticle Designs for Ideal Absorption of Light," ACS Photonics **2** (2), 263-270 (2015).

39. E. Prodan, and P. Nordlander, "Plasmon hybridization in spherical nanoparticles," J. Chem. Phys. **120** (11), 5444-5454 (2004).

40. P. Nordlander, and E. Prodan, "Plasmon Hybridization in Nanoparticles near Metallic Surfaces," Nano Lett. **4** (11), 2209-2213 (2004).

41. S. Baur, S. Sanders, and A. Manjavacas, "Hybridization of Lattice Resonances," ACS Nano **12** (2), 1618-1629 (2018).

42. N. Liu, S. Mukherjee, K. Bao, L. V. Brown, J. Dorfmuller, P. Nordlander, and N. J. Halas, "Magnetic plasmon formation and propagation in artificial aromatic molecules," Nano Lett. **12** (1), 364-369 (2012).

43. R. D. Kekatpure, E. S. Barnard, W. Cai, and M. L. Brongersma, "Phase-coupled plasmon-induced transparency," Phys. Rev. Lett. **104** (24), 243902 (2010).

44. H. Lu, X. Liu, D. Mao, and G. Wang, "Plasmonic nanosensor based on Fano resonance in waveguide-coupled resonators," Opt. Lett. **37** (18), 3780-3782 (2012).

45. C. Dahmen, B. Schmidt, and G. von Plessen, "Radiation damping in metal nanoparticle pairs," Nano Lett. **7** (2), 318-322 (2007).

46. R. Taubert, R. Ameling, T. Weiss, A. Christ, and H. Giessen, "From near-field to far-field coupling in the third dimension: retarded interaction of particle plasmons," Nano Lett. **11** (10), 4421-4424 (2011).

47. W. Tan, Y. Sun, Z.-G. Wang, and H. Chen, "Manipulating electromagnetic responses of metal wires at the deep subwavelength scale via both near- and far-field couplings," Appl. Phys. Lett. **104** (9) (2014).

48. J. Zhong, and C. Huang, "Crowding effects of nanoparticles on energy absorption in solar absorption coatings," J. Appl. Phys. **125** (3) (2019).

49. B. Rolly, B. Stout, and N. Bonod, "Metallic dimers: When bonding transverse modes shine light," Phys. Rev. B **84** (12) (2011).

50. L. X. Ma, and C. C. Wang, "Isosbestic light absorption by metallic dimers: effect of interparticle electromagnetic coupling," Appl. Opt. **59** (4), 1028-1036 (2020).

51. J.-P. Hugonin, M. Besbes, and P. Ben-Abdallah, "Fundamental limits for light absorption and scattering induced by cooperative electromagnetic interactions," Phys. Rev. B **91** (18) (2015).

52. D. Markovich, K. Baryshnikova, A. Shalin, A. Samusev, A. Krasnok, P. Belov, and P. Ginzburg, "Enhancement of artificial magnetism via resonant bianisotropy," Sci. Rep. **6** (22546 (2016).

53. D. Floess, M. Hentschel, T. Weiss, H.-U. Habermeier, J. Jiao, S. G. Tikhodeev, and H. Giessen, "Plasmonic Analog of Electromagnetically Induced Absorption Leads to Giant Thin Film Faraday Rotation of 14°," Phys. Rev. X **7** (2), 021048 (2017).

54. J. D. Jackson, *Classical electrodynamics* (Wiley, 1962).

55. A. E. Schlather, N. Large, A. S. Urban, P. Nordlander, and N. J. Halas, "Near-field mediated plexcitonic coupling and giant Rabi splitting in individual metallic dimers," Nano Lett. **13** (7), 3281−3286 (2013).

56. Y. Huang, L. Ma, M. Hou, J. Li, Z. Xie, and Z. Zhang, "Hybridized plasmon modes and near-field enhancement of metallic nanoparticle-dimer on a mirror," Sci. Rep. **6** (30011 (2016).

57. Z. J. Yang, T. J. Antosiewicz, and T. Shegai, "Role of material loss and mode volume of plasmonic nanocavities for strong plasmon-exciton interactions," Opt. Express **24** (18), 20373-20381 (2016).

58. P. Albella, M. A. Poyli, M. K. Schmidt, S. A. Maier, F. Moreno, J. J. Sáenz, and J. Aizpurua, "Low-Loss Electric and Magnetic Field-Enhanced Spectroscopy with Subwavelength Silicon Dimers," J. Phys. Chem. C **117** (26), 13573-13584 (2013).

59. S. Sun, M. Li, Q. Du, C. E. Png, and P. Bai, "Metal–Dielectric Hybrid Dimer Nanoantenna: Coupling between Surface Plasmons and Dielectric Resonances for Fluorescence Enhancement," J. Phys. Chem. C **121** (23), 12871-12884 (2017).

60. R. M. Bakker, D. Permyakov, Y. F. Yu, D. Markovich, R. Paniagua-Dominguez, L. Gonzaga, A. Samusev, Y. Kivshar, B. Luk'yanchuk, and A. I. Kuznetsov, "Magnetic and electric hotspots with silicon nanodimers," Nano Lett. **15** (3), 2137-2142 (2015).

61. G. W. Mulholland, C. F. Bohren, and K. A. Fuller, "Light Scattering by Agglomerates: Coupled Electric and Magnetic Dipole Method," Langmuir **10** (1994).

62. O. Merchiers, F. Moreno, F. González, and J. M. Saiz, "Light scattering by an ensemble of interacting dipolar particles with both electric and magnetic polarizabilities," Phys. Rev. A **76** (4) (2007).

63. K. Matsumori, R. Fujimura, and M. Retsch, "Selective broadband absorption by mode splitting for radiative cooling," Opt. Express **30** (9), 14258-14273 (2022).

64. C. F. Bohren, and D. R. Huffman, *Absorption and scattering of light by small particles* (John Wiley & Sons, 2008).

65. C. Zhang, B.-Q. Chen, Z.-Y. Li, Y. Xia, and Y.-G. Chen, "Surface Plasmon Resonance in Bimetallic Core–Shell Nanoparticles," J. Phys. Chem. C **119** (29), 16836-16845 (2015).

66. J. van de Groep, and A. Polman, "Designing dielectric resonators on substrates: combining magnetic and electric resonances," Opt. Express **21** (22), 26285-26302 (2013).

67. I. Staude, and J. Schilling, "Metamaterial-inspired silicon nanophotonics," Nat. Photonics **11** (5), 274-284 (2017).

68. E. Shkondin, O. Takayama, M. E. A. Panah, P. Liu, P. V. Larsen, M. D. Mar, F. Jensen, and A. V. Lavrinenko, "Large-scale high aspect ratio Al-doped ZnO nanopillars arrays as anisotropic metamaterials," Opt. Mater. Express **7** (5), 1606-1627 (2017).

69. F. Weiting, and Y. Yixun, "Temperature effects on the refractive index of lead telluride and zinc selenide," Infrared Physics **30** (4), 371-373 (1990).

70. H. N. S. Krishnamoorthy, G. Adamo, J. Yin, V. Savinov, N. I. Zheludev, and C. Soci, "Infrared dielectric metamaterials from high refractive index chalcogenides," Nat. Commun. **11** (1), 1692 (2020).

71. X. Zhang, J. Qiu, J. Zhao, X. Li, and L. Liu, "Complex refractive indices measurements of polymers in infrared bands," Journal of Quantitative Spectroscopy and Radiative Transfer **252** (107063 (2020).

7.10. Supporting Information

7.10.1. Coupled-dipole method (CDM) for the dimer parallel to the incident wave propagation

We first consider the FD model composed of two ED moments and two MD moments (see Figure 7.3a). Then, we reduce it to the TD models to investigate $\mathbf{p}_1$-$\mathbf{m}_2$ and $\mathbf{p}_1$-$\mathbf{p}_2$ couplings. For the FD model, ED and MD moments can be written as [1-4]

$$\begin{aligned}\mathbf{p}_{\mathrm{FDj}} &= \varepsilon_0\alpha_{\mathrm{j}}\left[\mathbf{E}_{\mathrm{in}}(\mathbf{r}_{\mathrm{j}}) + \mathbf{E}_{\mathrm{spi}}(\mathbf{r}_{\mathrm{j}}) + \mathbf{E}_{\mathrm{smi}}(\mathbf{r}_{\mathrm{j}})\right] \\ &= \varepsilon_0\alpha_{\mathrm{j}}\left[\mathbf{E}_{\mathrm{in}}(\mathbf{r}_{\mathrm{j}}) + \frac{1}{\varepsilon_0}\mathbf{G}_{\mathrm{E}}(\mathbf{r}_{\mathrm{j}} - \mathbf{r}_{\mathrm{i}})\cdot\mathbf{p}_{\mathrm{FDi}} - Z_0\mathbf{G}_{\mathrm{M}}(\mathbf{r}_{\mathrm{j}} - \mathbf{r}_{\mathrm{i}})\cdot\mathbf{m}_{\mathrm{FDi}}\right]\end{aligned} \tag{7.40}$$

$$\begin{aligned}\mathbf{m}_{\mathrm{FDj}} &= \chi_{\mathrm{j}}\left[\mathbf{H}_{\mathrm{in}}(\mathbf{r}_{\mathrm{j}}) + \mathbf{H}_{\mathrm{spi}}(\mathbf{r}_{\mathrm{j}}) + \mathbf{H}_{\mathrm{smi}}(\mathbf{r}_{\mathrm{j}})\right] \\ &= \chi_{\mathrm{j}}\left[\mathbf{H}_{\mathrm{in}}(\mathbf{r}_{\mathrm{j}}) + \frac{1}{\varepsilon_0 Z_0}\mathbf{G}_{\mathrm{M}}(\mathbf{r}_{\mathrm{j}} - \mathbf{r}_{\mathrm{i}})\cdot\mathbf{p}_{\mathrm{FDi}} + \mathbf{G}_{\mathrm{E}}(\mathbf{r}_{\mathrm{j}} - \mathbf{r}_{\mathrm{i}})\cdot\mathbf{m}_{\mathrm{FDi}}\right]\end{aligned} \tag{7.41}$$

The subscripts i and j are 1 or 2 ($\mathrm{i} \neq \mathrm{j}$). $\mathbf{p}_{\mathrm{FDi}}$ and $\mathbf{m}_{\mathrm{FDi}}$ are unknown

$$\mathbf{p}_{\mathrm{FDi}} = p_{\mathrm{FDix}}\hat{\mathbf{e}}_{\mathrm{x}} + p_{\mathrm{FDiy}}\hat{\mathbf{e}}_{\mathrm{y}} + p_{\mathrm{FDiz}}\hat{\mathbf{e}}_{\mathrm{z}} \tag{7.42}$$

$$\mathbf{m}_{\mathrm{FDi}} = m_{\mathrm{FDix}}\hat{\mathbf{e}}_{\mathrm{x}} + m_{\mathrm{FDiy}}\hat{\mathbf{e}}_{\mathrm{y}} + m_{\mathrm{FDiz}}\hat{\mathbf{e}}_{\mathrm{z}} \tag{7.43}$$

Using the unit vector of $\mathbf{r}_1 - \mathbf{r}_2$, which is $\mathbf{u}_{\mathrm{r}} = -\mathbf{e}_{\mathrm{z}}$, Equations 7.7 and 7.8 become

$$\begin{cases}\mathbf{G}_{\mathrm{E}}(\mathbf{r}_1 - \mathbf{r}_2)\cdot\hat{\mathbf{e}}_{\mathrm{x}} = g_{\mathrm{A}}\hat{\mathbf{e}}_{\mathrm{x}} \\ \mathbf{G}_{\mathrm{E}}(\mathbf{r}_1 - \mathbf{r}_2)\cdot\hat{\mathbf{e}}_{\mathrm{y}} = g_{\mathrm{A}}\hat{\mathbf{e}}_{\mathrm{y}} \\ \mathbf{G}_{\mathrm{E}}(\mathbf{r}_1 - \mathbf{r}_2)\cdot\hat{\mathbf{e}}_{\mathrm{z}} = (g_{\mathrm{A}} + g_{\mathrm{B}})\hat{\mathbf{e}}_{\mathrm{z}} = g_{\mathrm{AB}}\hat{\mathbf{e}}_{\mathrm{z}}\end{cases} \tag{7.44}$$

$$\begin{cases}\mathbf{G}_{\mathrm{M}}(\mathbf{r}_1 - \mathbf{r}_2)\cdot\hat{\mathbf{e}}_{\mathrm{x}} = -g_{\mathrm{c}}\hat{\mathbf{e}}_{\mathrm{y}} \\ \mathbf{G}_{\mathrm{M}}(\mathbf{r}_1 - \mathbf{r}_2)\cdot\hat{\mathbf{e}}_{\mathrm{y}} = g_{\mathrm{c}}\hat{\mathbf{e}}_{\mathrm{x}} \\ \mathbf{G}_{\mathrm{M}}(\mathbf{r}_1 - \mathbf{r}_2)\cdot\hat{\mathbf{e}}_{\mathrm{z}} = 0\end{cases} \tag{7.45}$$

Equations 7.44 and 7.45 have the relationship of $\mathbf{G}_{\mathrm{E}}(\mathbf{r}_1 - \mathbf{r}_2) = \mathbf{G}_{\mathrm{E}}(\mathbf{r}_2 - \mathbf{r}_1)$ and $\mathbf{G}_{\mathrm{M}}(\mathbf{r}_1 - \mathbf{r}_2) = -\mathbf{G}_{\mathrm{M}}(\mathbf{r}_2 - \mathbf{r}_1)$, respectively. Using Equations 7.40-7.45, the dipole moments of the FD model are given as

$$\mathbf{p}_{\mathrm{FD1}}=\begin{cases} p_{\mathrm{FD1x}}=\varepsilon_0\alpha_1\left[E_0e^{-i\frac{kD}{2}}+\dfrac{1}{\varepsilon_0}g_{\mathrm{A}}p_{\mathrm{FD2x}}-Z_0g_{\mathrm{C}}m_{\mathrm{FD2y}}\right] \\ p_{\mathrm{FD1y}}=\varepsilon_0\alpha_1\left[\dfrac{1}{\varepsilon_0}g_{\mathrm{A}}p_{\mathrm{FD2y}}+Z_0g_{\mathrm{C}}m_{FD2\mathrm{x}}\right] \\ p_{\mathrm{FD1z}}=\varepsilon_0\alpha_1g_{\mathrm{AB}}p_{\mathrm{FD2z}} \end{cases} \tag{7.46}$$

$$\mathbf{m}_{\mathrm{FD1}}=\begin{cases} m_{\mathrm{FD1x}}=\chi_1\left[\dfrac{1}{\varepsilon_0Z_0}g_{\mathrm{C}}p_{\mathrm{FD2y}}+g_{\mathrm{A}}m_{\mathrm{FD2x}}\right] \\ m_{\mathrm{FD1y}}=\chi_1\left[H_0e^{-i\frac{kD}{2}}-\dfrac{1}{\varepsilon_0Z_0}g_{\mathrm{C}}p_{\mathrm{FD2x}}+g_{\mathrm{A}}m_{\mathrm{FD2}y}\right] \\ m_{\mathrm{FD1z}}=\chi_1g_{\mathrm{AB}}m_{\mathrm{FD2z}} \end{cases} \tag{7.47}$$

$$\mathbf{p}_{\mathrm{FD2}}=\begin{cases} p_{\mathrm{FD2x}}=\varepsilon_0\alpha_2\left[E_0e^{i\frac{kD}{2}}+\dfrac{1}{\varepsilon_0}g_{\mathrm{A}}p_{\mathrm{FD1x}}+Z_0g_{\mathrm{C}}m_{\mathrm{FD1y}}\right] \\ p_{\mathrm{FD2y}}=\varepsilon_0\alpha_2\left[\dfrac{1}{\varepsilon_0}g_{\mathrm{A}}p_{\mathrm{FD1y}}-Z_0g_{\mathrm{C}}m_{\mathrm{FD1x}}\right] \\ p_{\mathrm{FD1z}}=\varepsilon_0\alpha_2g_{\mathrm{AB}}p_{\mathrm{FD1z}} \end{cases} \tag{7.48}$$

$$\mathbf{m}_{\mathrm{FD2}}=\begin{cases} m_{\mathrm{FD2x}}=\chi_2\left[-\dfrac{1}{\varepsilon_0Z_0}g_{\mathrm{C}}p_{\mathrm{FD1y}}+g_{\mathrm{A}}m_{\mathrm{FD1x}}\right] \\ m_{\mathrm{FD2y}}=\chi_2\left[H_0e^{i\frac{kD}{2}}+\dfrac{1}{\varepsilon_0Z_0}g_{\mathrm{C}}p_{\mathrm{FD1x}}+g_{\mathrm{A}}m_{\mathrm{FD1}y}\right] \\ m_{\mathrm{FD2z}}=\chi_2g_{\mathrm{AB}}m_{\mathrm{FD1z}} \end{cases} \tag{7.49}$$

By solving Equations 7.46-7.49, we get nontrivial solutions only for p_{FD1x}, m_{FD1y}, p_{FD2x}, and m_{FD2y}. Substituting p_{FD2x} and m_{FD2y} into p_{FD1x}, we get

$$p_{\mathrm{FD1x}}=\varepsilon_0\alpha_1\frac{\left[e^{-i\frac{kD}{2}}+\alpha_2g_{\mathrm{A}}e^{i\frac{kD}{2}}-\chi_2g_{\mathrm{C}}e^{i\frac{kD}{2}}\right]E_0+Z_0(\alpha_2-\chi_2)g_{\mathrm{A}}g_{\mathrm{C}}m_{\mathrm{FD1y}}}{1-\alpha_1[\alpha_2g_{\mathrm{A}}^2-\chi_2g_{\mathrm{C}}^2]} \tag{7.50}$$

Similarly, m_{FD1y}, p_{FD2x}, and m_{FD2y} are

$$m_{\mathrm{FD1y}}=\chi_1\frac{\left[e^{-i\frac{kD}{2}}-\alpha_2g_{\mathrm{C}}e^{i\frac{kD}{2}}+\chi_2g_{\mathrm{A}}e^{i\frac{kD}{2}}\right]H_0+\frac{1}{\varepsilon_0Z_0}(\chi_2-\alpha_2)g_{\mathrm{A}}g_{\mathrm{C}}p_{\mathrm{FD1x}}}{1-\chi_1[\chi_2g_{\mathrm{A}}^2-\alpha_2g_{\mathrm{C}}^2]} \tag{7.51}$$

$$p_{\mathrm{FD2x}}=\varepsilon_0\alpha_2\frac{\left[e^{i\frac{kD}{2}}+\alpha_1g_{\mathrm{A}}e^{-i\frac{kD}{2}}+\chi_1g_{\mathrm{C}}e^{-i\frac{kD}{2}}\right]E_0+Z_0(\chi_1-\alpha_1)g_{\mathrm{A}}g_{\mathrm{C}}m_{\mathrm{FD2y}}}{1-\alpha_2[\alpha_1g_{\mathrm{A}}^2-\chi_1g_{\mathrm{C}}^2]} \tag{7.52}$$

$$m_{\mathrm{FD2y}}=\chi_2\frac{\left[e^{i\frac{kD}{2}}+\alpha_1g_{\mathrm{C}}e^{-i\frac{kD}{2}}+\chi_1g_{\mathrm{A}}e^{-i\frac{kD}{2}}\right]H_0+\frac{1}{\varepsilon_0Z_0}(\alpha_1-\chi_1)g_{\mathrm{A}}g_{\mathrm{C}}p_{\mathrm{FD2x}}}{1-\alpha_1[\alpha_2g_{\mathrm{A}}^2-\chi_2g_{\mathrm{C}}^2]} \tag{7.53}$$

We derive the TD model for the $\mathbf{p}_1$-$\mathbf{m}_2$ coupling by substituting $\chi_1 = \alpha_2 = 0$ into Equations 7.50-7.53

$$p_{\mathrm{pm1x}}=\frac{1-\chi_2g_{\mathrm{C}}e^{ikD}}{1+\alpha_1\chi_2g_{\mathrm{C}}^2}\left(\varepsilon_0\alpha_1E_0e^{-i\frac{kD}{2}}\right)=\frac{1-\chi_2|g_{\mathrm{C}}|e^{i(\phi_{\mathrm{C}}+kD)}}{1+\alpha_1\chi_2|g_{\mathrm{C}}|^2e^{i2\phi_{\mathrm{C}}}}p_1 \tag{7.54}$$

$$m_{\mathrm{pm2y}}=\frac{1+\alpha_1g_{\mathrm{C}}e^{-ikD}}{1+\alpha_1\chi_2g_{\mathrm{C}}^2}\left(\chi_2H_0e^{i\frac{kD}{2}}\right)=\frac{1+\alpha_1|g_{\mathrm{C}}|e^{i(\phi_{\mathrm{C}}-kD)}}{1+\alpha_1\chi_2|g_{\mathrm{C}}|^2e^{i2\phi_{\mathrm{C}}}}m_2 \tag{7.55}$$

Comparing Equations 7.50-7.53 and Equations 7.54-7.55, we change their subscripts FD → pm to distinguish the FD and TD models. In Equations S15-S16, p_1 and m_2 are ED and MD moments of the isolated particles, respectively. p_1 and m_2 are given by Equations 1 and 2 of the main text. Equations 7.22 and 7.23 can be given by using Equations 7.54 and 7.55, respectively. In a similar manner, the TD model for the $\mathbf{p}_1$-$\mathbf{p}_2$ coupling ($\chi_1 = \chi_2 = 0$) is give as

$$p_{\mathrm{pp1x}} = \frac{1+\alpha_2 g_{\mathrm{A}} e^{ikD}}{1-\alpha_1\alpha_2 g_{\mathrm{A}}^2}\left(\varepsilon_0\alpha_1 E_0 e^{-i\frac{kD}{2}}\right) = \frac{1+\alpha_2|g_{\mathrm{A}}|e^{i(\phi_{\mathrm{A}}+kD)}}{1-\alpha_1\alpha_2|g_{\mathrm{A}}|^2 e^{i2\phi_{\mathrm{A}}}}p_1 \tag{7.56}$$

$$p_{\mathrm{pp2x}} = \frac{1+\alpha_1 g_{\mathrm{A}} e^{-ikD}}{1-\alpha_1\alpha_2 g_{\mathrm{A}}^2}\left(\varepsilon_0\alpha_2 E_0 e^{i\frac{kD}{2}}\right) = \frac{1+\alpha_1|g_{\mathrm{A}}|e^{i(\phi_{\mathrm{A}}-kD)}}{1-\alpha_1\alpha_2|g_{\mathrm{A}}|^2 e^{i2\phi_{\mathrm{A}}}}p_2 \tag{7.57}$$

Equations 7.24 and 7.25 can be given using Equations 7.56 and 7.57, respectively.

7.10.2. Optical cross-sections of a dimer

Extinction, scattering, and absorption cross-sections of an ED are shown in the main text. Extinction, scattering, and absorption cross-sections of an MD are [4]

$$C_{\mathrm{extMDj}} = \frac{\mu_0 k}{\varepsilon_0|\mathbf{E}_0|^2}\mathrm{Im}\left[\mathbf{m}_{\mathrm{nj}}\cdot\mathbf{H}_{\mathrm{in}}^{*}(\mathbf{r}_{\mathrm{j}})\right] \tag{7.58}$$

$$C_{\mathrm{scaMDj}} = \frac{\mu_0 k}{\varepsilon_0|\mathbf{E}_0|^2}\mathrm{Im}\left[\left(\frac{ik^3}{6\pi}+\frac{1}{\chi_{\mathrm{j}}}\right)\left|\mathbf{m}_{\mathrm{nj}}\right|^2 - \mathbf{m}_{\mathrm{nj}}^{*}\cdot\mathbf{H}_{\mathrm{in}}(\mathbf{r}_{\mathrm{j}})\right] \tag{7.59}$$

$$C_{\mathrm{absMDj}} = C_{\mathrm{extEDj}} - C_{\mathrm{scaEDj}} = \frac{\mu_0 k}{\varepsilon_0|\mathbf{E}_0|^2}\mathrm{Im}\left[-\left(\frac{ik^3}{6\pi}+\frac{1}{\chi_{\mathrm{j}}}\right)\right]\left|\mathbf{m}_{\mathrm{nj}}\right|^2 \tag{7.60}$$

where μ_0 is the magnetic permeability in vacuum. The subscript n indicates pm, pp, or FD. Total optical cross-sections of a dimer are

$$C_{\mathrm{ext}} = \sum_{\mathrm{j}=1,2}\left[C_{\mathrm{extEDj}} + C_{\mathrm{extMDj}}\right] \tag{7.61}$$

$$C_{\mathrm{sca}} = \sum_{\mathrm{j}=1,2}\left[C_{\mathrm{scaEDj}} + C_{\mathrm{scaMDj}}\right] \tag{7.62}$$

$$C_{\mathrm{abs}} = \sum_{\mathrm{j}=1,2}\left[C_{\mathrm{absEDj}} + C_{\mathrm{absMDj}}\right] \tag{7.63}$$

The scattering cross-sections can alternatively be expressed as

$$C_{\mathrm{scaEDj}} = \frac{k}{\varepsilon_0|\mathbf{E}_0|^2}\mathrm{Im}\left\{\frac{ik^3}{6\pi\varepsilon_0}\left|\mathbf{p}_{\mathrm{nj}}\right|^2 + \mathbf{p}_{\mathrm{nj}}^{*}\cdot\left[\mathbf{E}_{\mathrm{spi}}(\mathbf{r}_{\mathrm{j}}) + \mathbf{E}_{\mathrm{smi}}(\mathbf{r}_{\mathrm{j}})\right]\right\} \tag{7.64}$$

$$C_{\mathrm{scaMDj}} = \frac{\mu_0 k}{\varepsilon_0|\mathbf{E}_0|^2}\mathrm{Im}\left\{\frac{ik^3}{6\pi}\left|\mathbf{m}_{\mathrm{nj}}\right|^2 + \mathbf{m}_{\mathrm{nj}}^{*}\cdot\left[\mathbf{H}_{\mathrm{spi}}(\mathbf{r}_{\mathrm{j}}) + \mathbf{H}_{\mathrm{smi}}(\mathbf{r}_{\mathrm{j}})\right]\right\} \tag{7.65}$$

By substituting Equations 7.40 and 7.41 into Equations 7.64 and 7.65, Equation 7.33 and Equation 7.59 can be obtained.

7.10.3. The absolute square of the dipole moments at the resonance

The ED moment given by Equation 22 of the main text can be written at the resonance ($\omega_{\alpha 1} = \omega_{\chi 2} = \omega_0$) as

$$\mathbf{p}_{\mathrm{pm1}} = \frac{-\Gamma_{\mathrm{p1}}\Gamma_{\mathrm{m2}}\omega_0^2 + i\left(\Gamma_{\mathrm{p1}}\omega_0\right)\left(f_{\mathrm{m2}}|g_{\mathrm{C}}|\right)e^{i(\phi_{\mathrm{C}}+kD)}}{-\Gamma_{\mathrm{p1}}\Gamma_{\mathrm{m2}}\omega_0^2 + f_{\mathrm{p1}}f_{\mathrm{m2}}|g_{\mathrm{C}}|^2 e^{i2\phi_{\mathrm{C}}}}\mathbf{p}_1 \tag{7.66}$$

The absolute square of Equation 7.66 is

$$\begin{aligned}
&\left|\mathbf{p}_{\mathrm{pm1}}\right|^2 \\
&= \frac{\left(\Gamma_{\mathrm{p1}}\Gamma_{\mathrm{m2}}\omega_0^2\right)^2 + \left(\Gamma_{\mathrm{p1}}\omega_0\right)^2\left(F_{\mathrm{m2}}|g_{\mathrm{C}}|\right)^2 - i\left(\Gamma_{\mathrm{p1}}\Gamma_{\mathrm{m2}}\omega_0^2\right)\left(\Gamma_{\mathrm{p1}}\omega_0\right)\left(f_{\mathrm{m2}}|g_{\mathrm{C}}|\right)\left(e^{i(\phi_{\mathrm{C}}+kD)} - e^{-i(\phi_{\mathrm{C}}+kD}\right.}{\left(\Gamma_{\mathrm{p1}}\Gamma_{\mathrm{m2}}\omega_0^2\right)^2 + \left(f_{\mathrm{p1}}f_{\mathrm{m2}}|g_{\mathrm{C}}|^2\right)^2 - \left(\Gamma_{\mathrm{p1}}\Gamma_{\mathrm{m2}}\omega_0^2\right)\left(f_{\mathrm{p1}}f_{\mathrm{m2}}|g_{\mathrm{C}}|^2\right)\left(e^{i2\phi_{\mathrm{C}}} + e^{-i2\phi_{\mathrm{C}}}\right)} \\
&= \frac{\left(\Gamma_{\mathrm{p1}}\Gamma_{\mathrm{m2}}\omega_0^2\right)^2 + \left(\Gamma_{\mathrm{p1}}\omega_0\right)^2\left(f_{\mathrm{m2}}|g_{\mathrm{C}}|\right)^2 + 2\left(\Gamma_{\mathrm{p1}}\Gamma_{\mathrm{m2}}\omega_0^2\right)\left(\Gamma_{\mathrm{p1}}\omega_0\right)\left(f_{\mathrm{m2}}|g_{\mathrm{C}}|\right)\sin(\phi_{\mathrm{C}} + kD)}{\left(\Gamma_{\mathrm{p1}}\Gamma_{\mathrm{m2}}\omega_0^2\right)^2 + \left(f_{\mathrm{p1}}f_{\mathrm{m2}}|g_{\mathrm{C}}|^2\right)^2 - 2\left(\Gamma_{\mathrm{p1}}\Gamma_{\mathrm{m2}}\omega_0^2\right)\left(f_{\mathrm{p1}}f_{\mathrm{m2}}|g_{\mathrm{C}}|^2\right)\cos(2\phi_{\mathrm{C}})}|\mathbf{p}_1|^2 \\
&= \frac{\left(\Gamma_{\mathrm{p1}}\Gamma_{\mathrm{m2}}\omega_0^2\right)^2 + \left(\Gamma_{\mathrm{p1}}\omega_0\right)^2\left(f_{\mathrm{m2}}|g_{\mathrm{C}}|\right)^2 + 2\left(\Gamma_{\mathrm{p1}}\Gamma_{\mathrm{m2}}\omega_0^2\right)\left(\Gamma_{\mathrm{p1}}\omega_0\right)\left(f_{\mathrm{m2}}|g_{\mathrm{C}}|\right)\sin(\phi_{\mathrm{C}} + kD)}{\left(\Gamma_{\mathrm{p1}}\Gamma_{\mathrm{m2}}\omega_0^2\right)^2 + \left(f_{\mathrm{p1}}f_{\mathrm{m2}}|g_{\mathrm{C}}|^2\right)^2 + 2\left(\Gamma_{\mathrm{p1}}\Gamma_{\mathrm{m2}}\omega_0^2\right)\left(f_{\mathrm{p1}}f_{\mathrm{m2}}|g_{\mathrm{C}}|^2\right)\cos(2\phi_{\mathrm{C}} + \pi)}|\mathbf{p}_1|^2
\end{aligned} \tag{7.67}$$

To make all signs positive, the cosine function is modified using $-\cos(\varphi) = \cos(\varphi + \pi)$. In our previous work, it was found that the coupling of coupled plasmonic systems can be characterized by a ratio of a coupling strength to a total damping of an entire system [5]. From our ECO model shown in Figure 7.4a, the coupling strength and the total damping of the dimer are given as $f_{\mathrm{p1}}f_{\mathrm{m2}}|g_{\mathrm{C}}|^2$ and $\Gamma_{\mathrm{p1}}\Gamma_{\mathrm{m2}}\omega_0^2$, respectively. Thus, the coupling of the dimer system may be explained by $f_{\mathrm{p1}}f_{\mathrm{m2}}|g_{\mathrm{C}}|^2/\Gamma_{\mathrm{p1}}\Gamma_{\mathrm{m2}}\omega_0^2$. Based on this, Equation 7.67 is modified as

$$\left|\mathbf{p}_{\mathrm{pm1}}\right|^2 = \frac{1 + \frac{\left(\Gamma_{\mathrm{p1}}\omega_0\right)^2\left(f_{\mathrm{m2}}|g_{\mathrm{C}}|\right)^2}{\left(\Gamma_{\mathrm{p1}}\Gamma_{\mathrm{m2}}\omega_0^2\right)^2} + 2\frac{\left(\Gamma_{\mathrm{p1}}\omega_0\right)\left(f_{\mathrm{m2}}|g_{\mathrm{C}}|\right)}{\Gamma_{\mathrm{p1}}\Gamma_{\mathrm{m2}}\omega_0^2}\sin(\phi_C + kD)}{1 + \frac{\left(f_{\mathrm{p1}}f_{\mathrm{m2}}|g_{\mathrm{C}}|^2\right)^2}{\left(\Gamma_{\mathrm{p1}}\Gamma_{\mathrm{m2}}\omega_0^2\right)^2} + 2\frac{f_{\mathrm{p1}}f_{\mathrm{m2}}|g_{\mathrm{C}}|^2}{\Gamma_{\mathrm{p1}}\Gamma_{\mathrm{m2}}\omega_0^2}\cos(2\phi_C + \pi)}|\mathbf{p}_1|^2 \tag{7.68}$$

Using Equation 7.37 and Equation 7.68, Equation 7.35 is given. The same procedure of Equations 7.66-7.68 is applied to obtain the absolute square of other ED moments.

7.10.4. (θ_{C}, θ_{S}) dependencies of P for different (Φ_1, Φ_2)

Figure 7.10 shows the color maps of Equation 7.39 with different (Φ_1, Φ_2). Figure 7.5b considers (Φ_1, Φ_2) that can satisfy the critical coupling $\Phi = 1$. Figure 7.10 considers (Φ_1, Φ_2) = (0.25, 1) and (1, 4) whose Φ become 0.25 and 4, respectively. Since the critical coupling cannot be satisfied with those Φ, an extremely strong P is not found at $\theta_{\mathrm{C}} = \pi$. In addition, the area of $P < 1$ increases with increasing or decreasing Φ from 1. This is because P with any (θ_{C}, θ_{S}) decreases when Φ becomes far from 1 (see Figure 7.5a). However, the properties of P as a function of (θ_{C}, θ_{S}) are almost the same for any combination of (Φ_1, Φ_2): P is maximized at (θ_{C}, θ_{S}) = (π, $\pi/2$) and minimized at (θ_{C}, θ_{S}) = (0 or 2 π, $3\pi/2$).

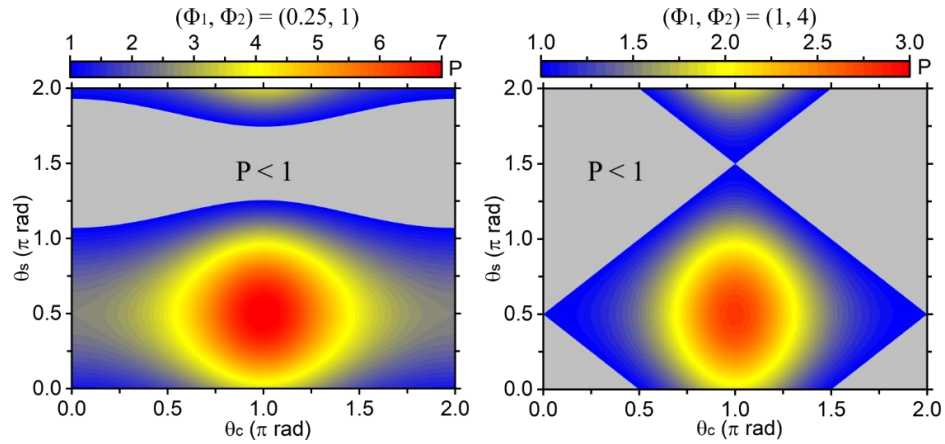

Figure 7.10. The color maps of Equation 7.39 as functions of θ_C and θ_S. (Φ_1, Φ_2) = (0.25, 1) and (1, 4) are used.

7.10.5. Optical properties of the plasmonic core-shell particle and dielectric sphere

It is known that the absorption of an isolated particle is maximized by satisfying $C_{sca} = C_{abs}$. We designed the plasmonic core-shell particle to satisfy this condition. Figure 7.11 shows scattering and absorption spectra of the plasmonic core-shell particle with r_{CS} = 695 nm and t_{CS} = 120 nm. With this design, the plasmonic core-shell particle nearly satisfies $C_{sca} = C_{abs}$ for its ED resonance at around the wavelength of 5.7 μm.

Figure 7.12 shows the electric polarizability of the plasmonic core-shell particle and the magnetic and electric polarizabilities of the dielectric sphere, which are calculated using Mie coefficients. Those values are fitted using the Lorentz oscillators given by Equations 7.20 and 7.21. The results of the fitting are summarized in Table 7.1. For all polarizabilities, the Lorentz oscillators show a good agreement with Mie coefficients.

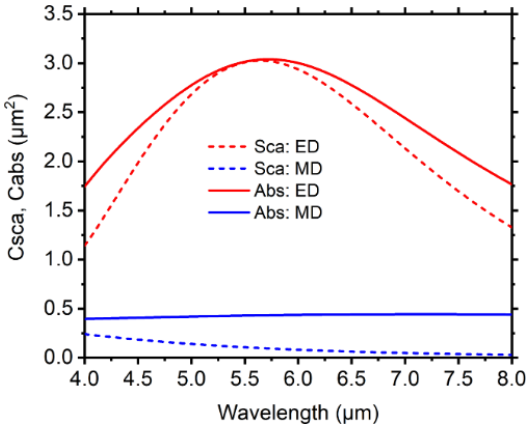

Figure 7.11. The scattering and absorption cross-sections of the plasmonic core-shell particle with r_{CS} = 695 nm and t_{CS} = 120 nm. The red and blue dashed lines are scattering cross-sections of the ED and MD, respectively. The red and blue dashed lines are absorption cross-sections of the ED and MD, respectively.

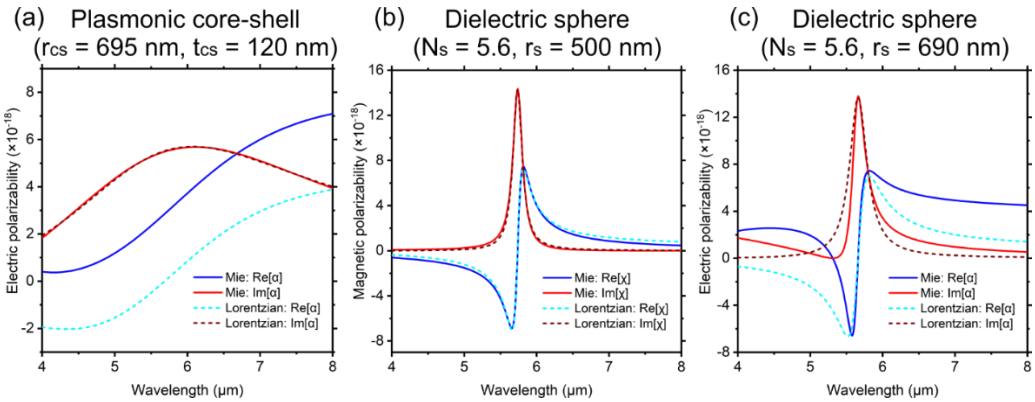

Figure 7.12. For (a-c), the blue and red solid lines are the real and imaginary parts of the polarizability given by Mie coefficient, respectively. The cyan and wine-red dashed lines are the real and imaginary parts of the polarizability given by the Lorentz oscillators (Equations 7.19 or 7.20), respectively. (a) The electric polarizability of the plasmonic core-shell particle. (b) The magnetic polarizability of the dielectric sphere with r_S = 500 nm. (c) The electric polarizability of the dielectric sphere with r_S = 690 nm.

7.10.6. Absorption and scattering properties of the dimer

The absorption spectra of the dimer with d = 2 μm and r_S = 500 nm are shown in Figure 7.13. Those spectra are calculated using the CDM. Since the dielectric sphere is lossless, its absorption is zero (the magenta and cyan solid lines). As explained in the main text, the CDM cannot consider the influence of the plasmonic core-shell particle´s EQ + MQ. Therefore, if the ED + MD of the plasmonic core-shell particle is only considered as a total absorption of the dimer, we get the grey dashed line and have a large discrepancy between the CDM and FEM simulation. To minimize this discrepancy, the green dashed line, which is the plasmonic core-shell particle´s EQ + MQ given by Mie theory, is added to the grey dashed line. This gives the total absorption of the dimer, shown as the black solid line. The black solid line is in good agreement with the FEM simulation.

The absorption spectra of the dimer with different d are shown in Figure 7.14. The CDM is in good agreement with the FEM simulation for any d. These results prove the robustness of the CDM to investigate the absorption properties of the dimer. For a small d, the discrepancy between the CDM and the FEM simulation is slightly large. This is because the CDM cannot fully consider the near-field effects, as described in the main text.

Figure 7.15 shows the scattering properties of the dimer. Since the lossless dielectric sphere is considered, the dielectric sphere does not contribute to the absorption of the dimer but contributes to the scattering of the dimer. The black solid and orange dashed lines are the total scattering of the dimer calculated using the CDM and FEM simulation, respectively. Those calculation methods are in good agreement, meaning that the CDM can properly describe the scattering properties of the dimer. Comparing Figure 7.14 with Figure 7.15, it can be found that the absorption and scattering spectral profiles of the plasmonic core-shell particle are different. This difference can be understood from Equations 7.64 and 7.65. The absorption of the dimer is determined solely by the absolute square of the dipole moments. In contrast, the scattering of the dimer is determined by the absolute square of the dipole moments and the energy exchanging terms. Comparing the equations of the extinction and Equations 7.64 and 7.65, we may understand that these energy exchanging terms are the extinction of $\mathbf{p}_j$ against the scattered fields of other dipole moments. The energy exchanging terms can be negative; therefore, some scattering spectra become negative [6].

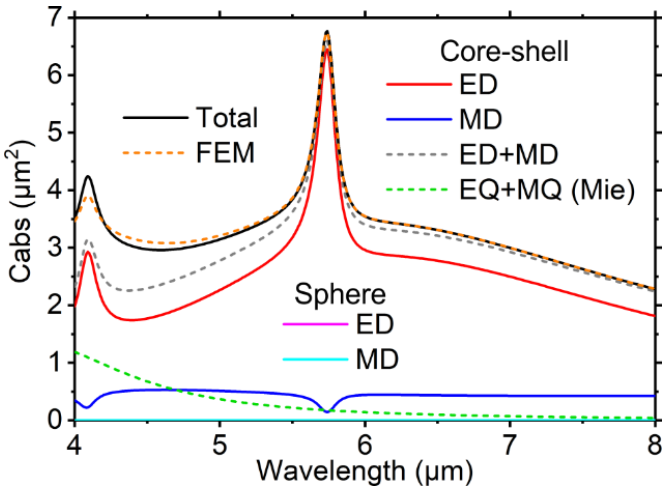

Figure 7.13. The absorption of the dimer is calculated using the CDM. The dimer with r_S = 500 nm and d = 2 μm is considered. The red and blue solid lines are the absorption spectra of the ED and MD of the plasmonic core-shell particle, respectively. The grey dashed line is the absorption of ED + MD of the plasmonic core-shell particle. The magenta and cyan solid lines are the absorption of the ED and MD of the dielectric sphere. Since the dielectric sphere is lossless, their absorptions are zero. The green dashed line is the absorption of EQ + MQ of the plasmonic core-shell particle, calculated using Mie theory. The black line is the total absorption of the dimer, given by a sum of the grey and green dashed lines. The orange dashed line is the absorption of the dimer calculated using the FEM simulation.

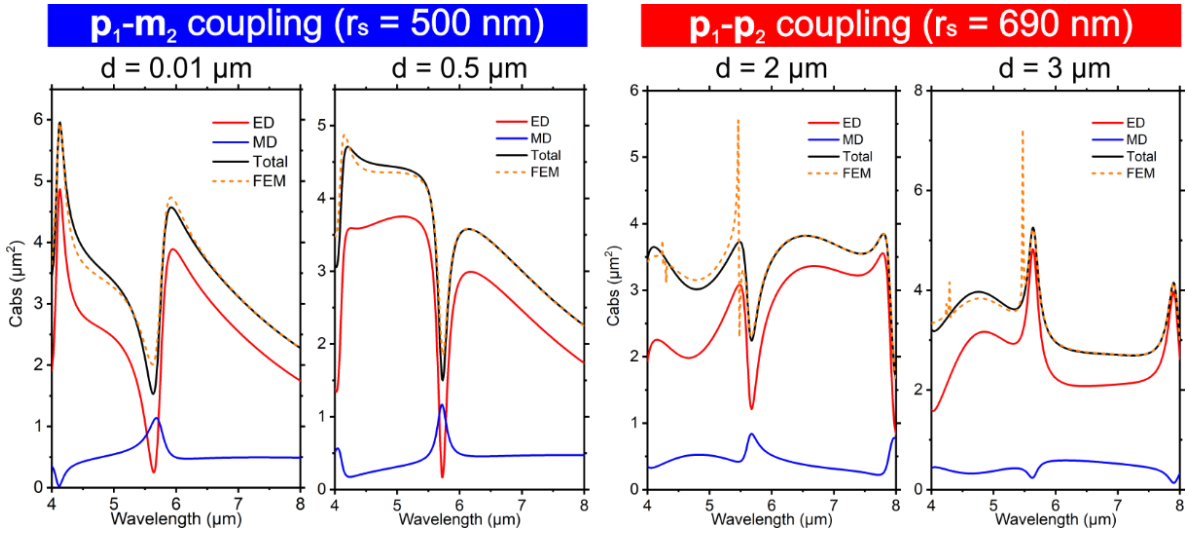

Figure 7.14. The absorption spectra of the dimer with different d. The dielectric spheres with r_S = 500 nm and 690 nm are used for the $\mathbf{p}_1$-$\mathbf{m}_2$ and $\mathbf{p}_1$-$\mathbf{p}_2$ coupling, respectively. The solid lines are calculated using the CDM. The red and blue solid lines are the ED and MD absorptions of the plasmonic core-shell particle, respectively. The black solid line is the total absorption of the plasmonic core-shell particle. The orange dashed lines are the absorption spectra obtained from the FEM simulation.

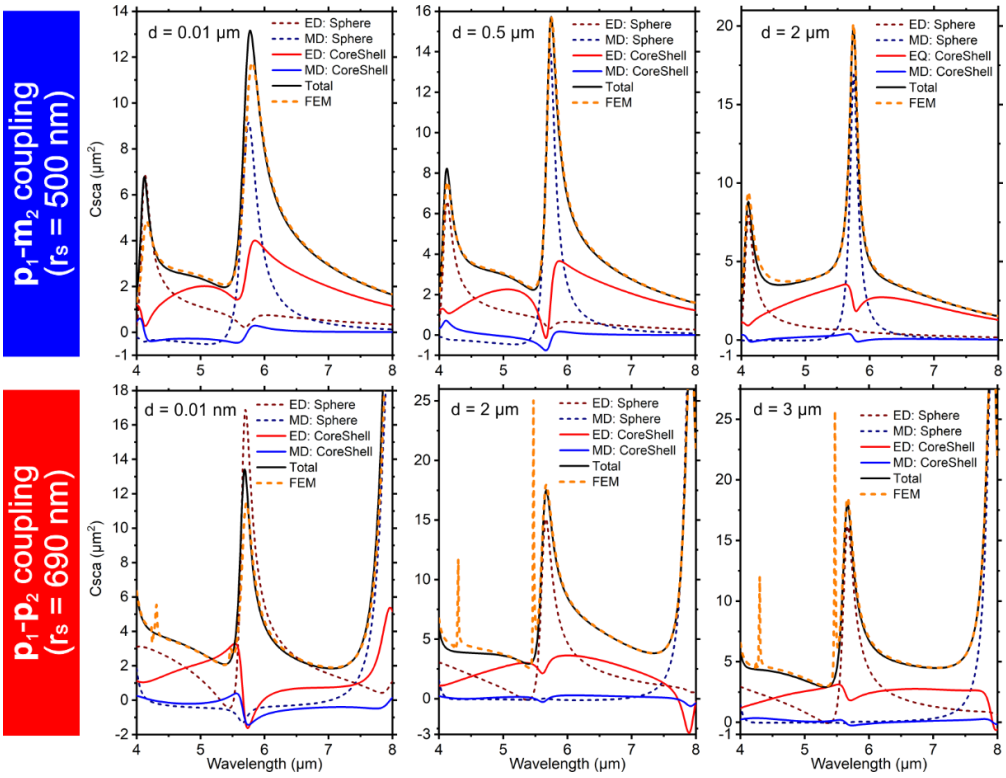

Figure 7.15. The scattering spectra of the dimer with different d and r_S. The black solid and orange dashed lines are the total scattering of the dimer, which are calculated using the CDM and FEM simulation, respectively. The red and blue solid lines are the scattering spectra of the ED and MD of the plasmonic core-shell particle, respectively. The red and blue dashed lines are the scattering spectra of the ED and MD of the dielectric sphere, respectively.

7.10.7. Absorption properties of the dimer rotated at 180° in the x-z plane

We consider that the plasmonic core-shell particle and dielectric sphere locate at $\mathbf{r}_2 = (0, 0, D/2)$ and $\mathbf{r}_1 = (0, 0, -D/2)$, respectively. Figure 7.16 shows the FD model for the dimer with this orientation. This FD model will be reduced to the TD models to investigate $\mathbf{m}_1$-$\mathbf{p}_2$ and $\mathbf{p}_1$-$\mathbf{p}_2$ coupling. For a $\mathbf{m}_1$-$\mathbf{p}_2$ coupling, the ED of the plasmonic core-shell particle $\mathbf{p}_{mp2}$ can be given using Equation 7.52 with $\mathbf{p}_{FD1} = \mathbf{m}_{FD2} = 0$ and the Lorentz oscillators shown in Equations 7.20 and 7.21

$$\mathbf{p}_{\mathrm{mp2}} = \frac{\Omega_{\mathrm{m1}}\Omega_{\mathrm{p2}} + \Omega_{\mathrm{p2}} f_{\mathrm{m1}} |g_{\mathrm{C}}| e^{i(\phi_{\mathrm{C}} - kD)}}{\Omega_{\mathrm{m1}}\Omega_{\mathrm{p2}} + f_{\mathrm{m1}} f_{\mathrm{p2}} |g_{\mathrm{C}}|^2 e^{i2\phi_{\mathrm{C}}}} \mathbf{p}_2 \qquad 7.69$$

where $\mathbf{p}_2$ is the ED moment of the isolated plasmonic core-shell particle, which is given by Equation 7.1. For a $\mathbf{p}_1$-$\mathbf{p}_2$ coupling, the ED of the plasmonic core-shell particle $\mathbf{p}_{pp2}$ can be found from Equation 7.25. Based on Section 7.10.3, the absolute square of $\mathbf{p}_{mp2}$ and $\mathbf{p}_{pp2}$ at the resonance are

$$\begin{aligned} &|\mathbf{p}_{\mathrm{mp2}}|^2 \\ &= \frac{\left(\Gamma_{\mathrm{m1}}\Gamma_{\mathrm{p2}}\omega_0^2\right)^2 + \left(\Gamma_{\mathrm{p2}}\omega_0\right)^2 (f_{\mathrm{m1}}|g_{\mathrm{C}}|)^2 + 2(\Gamma_{\mathrm{m1}}\Gamma_{\mathrm{p2}}\omega_0^2)(\Gamma_{\mathrm{p2}}\omega_0)(f_{\mathrm{m1}}|g_{\mathrm{C}}|)\sin(-\phi_{\mathrm{C}} + kD)}{\left(\Gamma_{\mathrm{m1}}\Gamma_{\mathrm{p2}}\omega_0^2\right)^2 + \left(f_{\mathrm{m1}} f_{\mathrm{p2}} |g_{\mathrm{C}}|^2\right)^2 + 2\left(\Gamma_{\mathrm{m1}}\Gamma_{\mathrm{p2}}\omega_0^2\right)\left(f_{\mathrm{m1}} f_{\mathrm{p2}} |g_{\mathrm{C}}|^2\right)\cos(2\phi_{\mathrm{C}} + \pi)} |\mathbf{p}_2|^2 \qquad 7.70 \\ &= \frac{1 + \Phi_{\mathrm{mp1}}^2 + 2\Phi_{\mathrm{mp1}}\sin(-\phi_{\mathrm{C}} + kD)}{1 + \Phi_{\mathrm{mp}}^2 + 2\Phi_{\mathrm{mp}}\cos(2\phi_{\mathrm{C}} + \pi)} |\mathbf{p}_2|^2 = P_{\mathrm{mp}}{}' |\mathbf{p}_2|^2 \end{aligned}$$

$$
\begin{aligned}
&|\mathbf{p}_{\mathrm{pp2}}|^2 \\
&= \frac{\left(\Gamma_{\mathrm{p1}}\Gamma_{\mathrm{p2}}\omega_0^2\right)^2 + \left(\Gamma_{\mathrm{p2}}\omega_0\right)^2\left(f_{\mathrm{p1}}|g_{\mathrm{A}}|\right)^2 + 2\left(\Gamma_{\mathrm{p1}}\Gamma_{\mathrm{p2}}\omega_0^2\right)\left(\Gamma_{\mathrm{p2}}\omega_0\right)\left(f_{\mathrm{p1}}|g_{\mathrm{A}}|\right)\sin(-\phi_{\mathrm{A}} + kD)}{\left(\Gamma_{\mathrm{p1}}\Gamma_{\mathrm{p2}}\omega_0^2\right)^2 + \left(f_{\mathrm{p1}}f_{\mathrm{p2}}|g_{\mathrm{A}}|^2\right)^2 + 2\left(\Gamma_{\mathrm{p1}}\Gamma_{\mathrm{p2}}\omega_0^2\right)\left(f_{\mathrm{p1}}f_{\mathrm{p2}}|g_{\mathrm{A}}|^2\right)\cos(2\phi_{\mathrm{A}})}|\mathbf{p}_2|^2 \\
&= \frac{1 + \Phi_{\mathrm{pp1}}^2 + 2\Phi_{\mathrm{pp1}}\sin(-\phi_{\mathrm{A}} + kD)}{1 + \Phi_{\mathrm{pp}}^2(g_{\mathrm{A}}) + 2\Phi_{\mathrm{pp}}(g_{\mathrm{A}})\cos(2\phi_{\mathrm{A}})}|\mathbf{p}_2|^2 = P_{\mathrm{pp}}{}'|\mathbf{p}_2|^2
\end{aligned}
\qquad 7.71
$$

In Figure 7.17, the same analysis made in Figure 7.7 is employed for the rotated dimer. Figure 7.17a shows d dependencies of the absorption of the rotated dimer. In contrast to the dimer investigated in the main text, the absorption of the rotated dimer possesses an EIT-like spectral profile for any d. In Figure 7.17b, the CDM and FEM simulation are compared, and it can be found that the CDM reproduces the spectra from the FEM simulation. For both the $\mathbf{m}_1$-$\mathbf{p}_2$ and $\mathbf{p}_1$-$\mathbf{p}_2$ coupling, the ED of the plasmonic core-shell particle possesses an absorption dip at the Mie resonance of the dielectric sphere, which is attributed to the EIT-like spectral profile.

In Figure 7.17c, the sine and cosine functions of $P_{\mathrm{pm}}{}'$ are shown. The cosine function of $P_{\mathrm{mp}}{}'$ is the same as that of P_{pm}, but their sine functions are different. The sine function of $P_{\mathrm{pm}}{}'$ is nearly constant. Using Equation 7.17, the sine function of $P_{\mathrm{pm}}{}'$ can be written as $\sin(-\phi_{\mathrm{C}} + kD) = \sin(-\phi_{\mathrm{c}})$. ϕ_{c} does not dynamically change with an increase in d (see Figure 7.2b); therefore, the sine function of $P_{\mathrm{pm}}{}'$ is nearly constant. $\sin(-\phi_{\mathrm{C}} + kD)$ is always negative, meaning that the $\mathbf{m}_1$-$\mathbf{p}_2$ coupling cannot achieve strong constructive interference. The same interpretation regarding the sine and cosine functions can be applied to the $\mathbf{p}_1$-$\mathbf{p}_2$ coupling.

Figure 7.17c also shows $P_{\mathrm{mp}}{}'$ and $P_{\mathrm{pp}}{}'$ calculated using the sine and cosine functions. For the $\mathbf{m}_1$-$\mathbf{p}_2$ coupling, $P_{\mathrm{mp}}{}'$ can be smaller and larger than 1, indicating that constructive and destructive interference occurs depending on d. On the other hand, $P_{\mathrm{pp}}{}'$ is smaller than 1 for any d; therefore, destructive interference only occurs for the $\mathbf{p}_1$-$\mathbf{p}_2$ coupling.

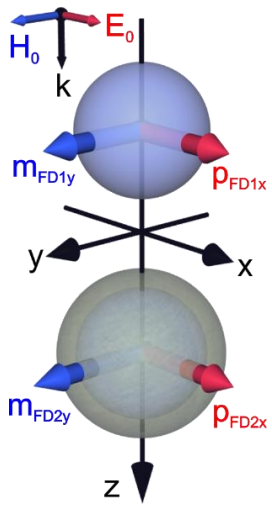

Figure 7.16. Schematic illustration of the dimer rotated at 180° in the *x*-*z* plane.

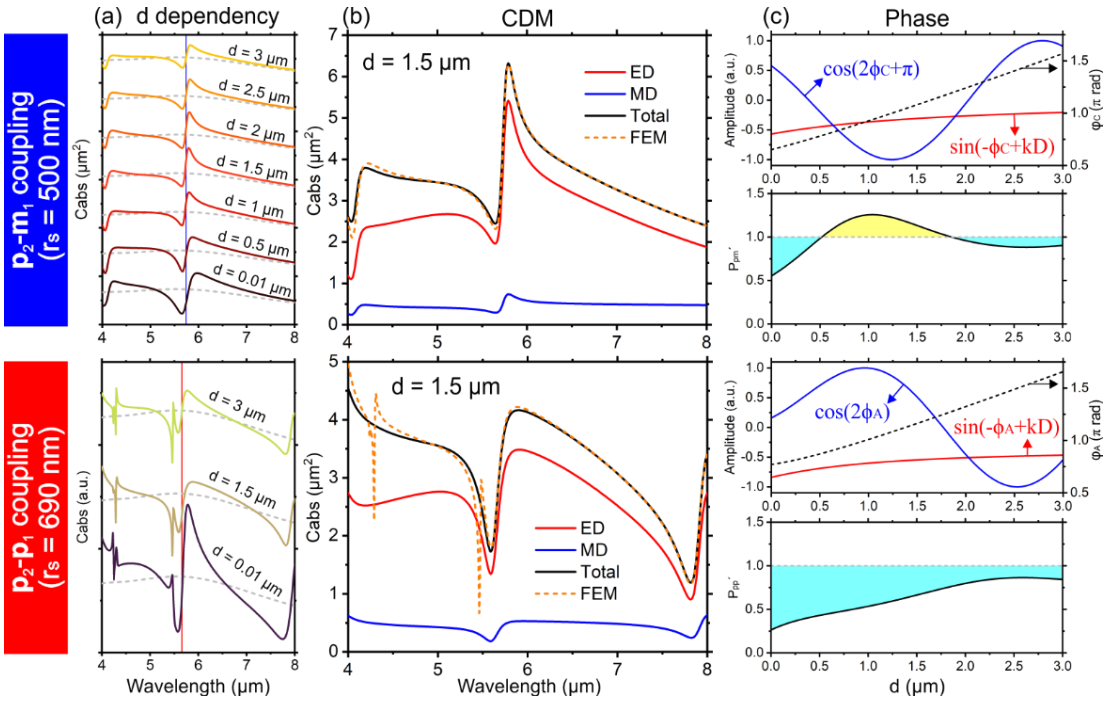

Figure 7.17. (Top panel) the $\mathbf{m}_1$-$\mathbf{p}_2$ coupling of the dimer composed of the dielectric sphere with r_S = 500 nm. (Bottom panel) the $\mathbf{p}_1$-$\mathbf{p}_2$ coupling of the dimer composed of the dielectric sphere with r_S = 690 nm. (a) *d* dependencies of the absorption of the dimer of Figure 7.16. The absorption spectra are calculated using the FEM simulation. The grey dashed lines are the reference spectra given by the total absorption of the isolated plasmonic core-shell particle. The blue and red solid vertical lines show the resonance wavelength of the MD and ED of the dielectric sphere, respectively. (b) The solid lines are the absorption spectra of the dimer, calculated using the CDM. The red and blue lines are for the ED and MD of the plasmonic core-shell particle. The black line is the total absorption of the plasmonic core-shell particle. The orange dashed lines are taken from Figure 7.17a. (c) The sine and cosine functions in $P_{pm}{}'$ (Equation 7.70) and $P_{pp}{}'$ (Equation 7.71) are plotted as a function of d on the left vertical axis. The phases of ϕ_C and ϕ_A are shown as the black dashed line on the right vertical axis. $P_{pm}{}'$ and $P_{pp}{}'$ are calculated at $\omega_0 = 3.29 \times 10^{14}$ rad/s and $\omega_0 = 3.33 \times 10^{14}$ rad/s, respectively.

7.10.8. Absorption properties of the dimer aligned parallel to the electric field of the incident wave

The orientations of the dimer and the incident wave are shown in Figure 7.18. The incident wave propagates along the *z*-direction with $\mathbf{E}_{in}(\mathbf{r}_j) = E_0\hat{\mathbf{e}}_y e^{i\mathbf{k}\cdot\mathbf{r}_j}$ and $\mathbf{H}_{in}(\mathbf{r}_j) = -H_0\hat{\mathbf{e}}_x e^{i\mathbf{k}\cdot\mathbf{r}_j}$. The plasmonic core-shell particle and dielectric sphere locate at $\mathbf{r}_1$ = (0, – *D*/2, 0) and $\mathbf{r}_2$ = (0, *D*/2, 0), respectively. Since $\mathbf{k}\cdot\mathbf{r}_j = 0$, the incident wave becomes $\mathbf{E}_{in}(\mathbf{r}_j) = E_0\hat{\mathbf{e}}_y$ and $\mathbf{H}_{in}(\mathbf{r}_j) = -H_0\hat{\mathbf{e}}_x$. The unit vector of $\mathbf{r}_1 - \mathbf{r}_2$ is $\mathbf{u}_r = -\mathbf{e}_y$. Therefore, the dyadic Green´s functions (Equations 7.7 and 7.8) are

$$\begin{cases} \mathbf{G}_E(\mathbf{r}_1 - \mathbf{r}_2)\cdot\hat{\mathbf{e}}_x = g_A\hat{\mathbf{e}}_x \\ \mathbf{G}_E(\mathbf{r}_1 - \mathbf{r}_2)\cdot\hat{\mathbf{e}}_y = g_{AB}\hat{\mathbf{e}}_y \\ \mathbf{G}_E(\mathbf{r}_1 - \mathbf{r}_2)\cdot\hat{\mathbf{e}}_z = g_A\hat{\mathbf{e}}_z \end{cases} \quad 7.72$$

$$\begin{cases} \mathbf{G}_M(\mathbf{r}_1 - \mathbf{r}_2)\cdot\hat{\mathbf{e}}_x = g_c\hat{\mathbf{e}}_z \\ \mathbf{G}_M(\mathbf{r}_1 - \mathbf{r}_2)\cdot\hat{\mathbf{e}}_y = 0 \\ \mathbf{G}_M(\mathbf{r}_1 - \mathbf{r}_2)\cdot\hat{\mathbf{e}}_z = -g_c\hat{\mathbf{e}}_x \end{cases} \quad 7.73$$

Using Equations 7.40-7.43, Equations 7.72-7.73, $\mathbf{G}_E(\mathbf{r}_1 - \mathbf{r}_2) = \mathbf{G}_E(\mathbf{r}_2 - \mathbf{r}_1)$, and $\mathbf{G}_M(\mathbf{r}_1 - \mathbf{r}_2) = -\mathbf{G}_M(\mathbf{r}_2 - \mathbf{r}_1)$, the dipole moments of the dimer of Figure 7.18 are

$$\mathbf{p}_{\mathrm{FD1}}^{\alpha}=\begin{cases}p_{\mathrm{FD1x}}^{\alpha}=\varepsilon_0\alpha_1\left[\dfrac{1}{\varepsilon_0}g_{\mathrm{A}}p_{\mathrm{FD2x}}^{\alpha}+Z_0g_{\mathrm{C}}m_{\mathrm{FD2}z}^{\alpha}\right]\\ p_{\mathrm{FD1y}}^{\alpha}=\varepsilon_0\alpha_1\left[E_0+\dfrac{1}{\varepsilon_0}g_{\mathrm{AB}}p_{\mathrm{FD2y}}^{\alpha}\right]\\ p_{\mathrm{FD1z}}^{\alpha}=\varepsilon_0\alpha_1\left[\dfrac{1}{\varepsilon_0}g_{\mathrm{A}}p_{\mathrm{FD2z}}^{\alpha}-Z_0g_{\mathrm{C}}m_{\mathrm{FD2x}}^{\alpha}\right]\end{cases} \tag{7.74}$$

$$\mathbf{m}_{\mathrm{FD1}}^{\alpha}=\begin{cases}m_{\mathrm{FD1x}}^{\alpha}=\chi_1\left[-H_0-\dfrac{1}{\varepsilon_0Z_0}g_{\mathrm{C}}p_{\mathrm{FD2z}}^{\alpha}+g_{\mathrm{A}}m_{\mathrm{FD2x}}^{\alpha}\right]\\ m_{\mathrm{FD1y}}^{\alpha}=\chi_1g_{\mathrm{AB}}(D)m_{\mathrm{FD2y}}^{\alpha}\\ m_{\mathrm{FD1z}}^{\alpha}=\chi_1\left[\dfrac{1}{\varepsilon_0Z_0}g_{\mathrm{C}}p_{\mathrm{FD2x}}^{\alpha}+g_{\mathrm{A}}m_{\mathrm{FD2z}}^{\alpha}\right]\end{cases} \tag{7.75}$$

$$\mathbf{p}_{\mathrm{FD2}}^{\alpha}=\begin{cases}p_{\mathrm{FD2x}}^{\alpha}=\varepsilon_0\alpha_2\left[\dfrac{1}{\varepsilon_0}g_{\mathrm{A}}p_{\mathrm{FD1x}}^{\alpha}-Z_0g_{\mathrm{C}}m_{\mathrm{FD1z}}^{\alpha}\right]\\ p_{\mathrm{FD2y}}^{\alpha}=\varepsilon_0\alpha_2\left[E_0+\dfrac{1}{\varepsilon_0}g_{\mathrm{AB}}p_{\mathrm{FD1y}}^{\alpha}\right]\\ p_{\mathrm{FD2z}}^{\alpha}=\varepsilon_0\alpha_2\left[\dfrac{1}{\varepsilon_0}g_{\mathrm{A}}p_{\mathrm{FD1z}}^{\alpha}+Z_0g_{\mathrm{C}}m_{\mathrm{FD1x}}^{\alpha}\right]\end{cases} \tag{7.76}$$

$$\mathbf{m}_{\mathrm{FD2}}^{\alpha}=\begin{cases}m_{\mathrm{FD2x}}^{\alpha}=\chi_2\left[-H_0+\dfrac{1}{\varepsilon_0Z_0}g_{\mathrm{C}}p_{\mathrm{FD1z}}^{\alpha}+g_{\mathrm{A}}m_{\mathrm{FD1x}}^{\alpha}\right]\\ m_{\mathrm{FD2y}}^{\alpha}=\chi_2g_{\mathrm{AB}}m_{\mathrm{FD1y}}^{\alpha}\\ m_{\mathrm{FD2z}}^{\alpha}=\chi_2\left[-\dfrac{1}{\varepsilon_0Z_0}g_{\mathrm{C}}p_{\mathrm{FD1x}}^{\alpha}+g_{\mathrm{A}}m_{\mathrm{FD1z}}^{\alpha}\right]\end{cases} \tag{7.77}$$

The superscript α is to distinguish the FD model shown in Figure 7.18 from other FD models for the dimer with different orientations. By solving Equations 7.74-7.77, we get nontrivial solutions only for $p_{\mathrm{FD1y}}^{\alpha}$, $p_{\mathrm{FD1z}}^{\alpha}$, $m_{\mathrm{FD1x}}^{\alpha}$, $p_{\mathrm{FD2y}}^{\alpha}$, $p_{\mathrm{FD2z}}^{\alpha}$, and $m_{\mathrm{FD2x}}^{\alpha}$. The self-consistent form of $p_{\mathrm{FD1y}}^{\alpha}$ and $p_{\mathrm{FD2y}}^{\alpha}$ are

$$p_{\mathrm{FD1y}}^{\alpha}=\frac{1+\alpha_2g_{\mathrm{AB}}}{1-\alpha_1\alpha_2g_{\mathrm{AB}}^2}(\varepsilon_0\alpha_1E_0)=\frac{1+\alpha_2g_{\mathrm{AB}}}{1-\alpha_1\alpha_2g_{\mathrm{AB}}^2}p_1 \tag{7.78}$$

$$p_{\mathrm{FD2y}}^{\alpha}=\frac{1+\alpha_1g_{\mathrm{AB}}}{1-\alpha_1\alpha_2g_{\mathrm{AB}}^2}(\varepsilon_0\alpha_2E_0)=\frac{1+\alpha_1g_{\mathrm{AB}}}{1-\alpha_1\alpha_2g_{\mathrm{AB}}^2}p_2 \tag{7.79}$$

where g_{AB} can be written as

$$g_{\mathrm{AB}}=\frac{e^{ikD}}{4\pi D}\left(\frac{2}{D^2}-i\frac{2k}{D}\right)=\frac{1}{4\pi D}\sqrt{\left(\frac{2}{D^2}\right)^2+\left(\frac{2k}{D}\right)^2}\;e^{i[kD+\tan^{-1}(-kD)]}=|g_{\mathrm{AB}}|e^{i\phi_{\mathrm{AB}}} \tag{7.80}$$

Substituting $p_{\mathrm{FD2z}}^{\alpha}$ and $m_{\mathrm{FD2x}}^{\alpha}$ into $p_{\mathrm{FD1z}}^{\alpha}$, we get

$$p_{\mathrm{FD1z}}^{\alpha}=\varepsilon_0\alpha_1\frac{\chi_2g_CZ_0H_0+Z_0(\alpha_2-\chi_2)g_{\mathrm{A}}g_{\mathrm{C}}m_{\mathrm{FD1x}}^{\alpha}}{1-\alpha_1[\alpha_2g_{\mathrm{A}}^2-\chi_2g_{\mathrm{C}}^2]} \tag{7.81}$$

In a similar manner, $m_{\mathrm{FD1x}}^{\alpha}$, $p_{\mathrm{FD2z}}^{\alpha}$, and $m_{\mathrm{FD2x}}^{\alpha}$ are

$$m_{\mathrm{FD1x}}^{\alpha} = \chi_1 \frac{-[1+\chi_2 g_{\mathrm{A}}]H_0 + \frac{1}{\varepsilon_0 Z_0}(\chi_2 - \alpha_2) g_{\mathrm{A}} g_{\mathrm{C}} p_{\mathrm{FD1z}}^{\alpha}}{1 - \chi_1[\chi_2 g_{\mathrm{A}}^2 - \alpha_2 g_{\mathrm{C}}^2]} \tag{7.82}$$

$$p_{\mathrm{FD2z}}^{\alpha} = \varepsilon_0 \alpha_2 \frac{-\chi_2 g_{\mathrm{C}} Z_0 H_0 + Z_0(\chi_1 - \alpha_1) g_{\mathrm{A}} g_{\mathrm{C}} m_{\mathrm{FD2x}}^{\alpha}}{1 - \alpha_2[\alpha_1 g_{\mathrm{A}}^2 - \chi_1 g_{\mathrm{C}}^2]} \tag{7.83}$$

$$m_{\mathrm{FD2x}}^{\alpha} = \chi_2 \frac{-[1+\chi_1 g_{\mathrm{A}}]H_0 + \frac{1}{\varepsilon_0 Z_0}(\alpha_1 - \chi_1) g_{\mathrm{A}} g_{\mathrm{C}} p_{\mathrm{FD2z}}^{\alpha}}{1 - \chi_2[\chi_1 g_{\mathrm{A}}^2 - \alpha_1 g_{\mathrm{C}}^2]} \tag{7.84}$$

To investigate a $\mathbf{p}_1$-$\mathbf{m}_2$ coupling, we reduce the FD model to the TD model by substituting $\chi_1 = \alpha_2 = 0$ in Equations 7.78-7.79 and Equations 7.81-7.84

$$p_{\mathrm{pm1y}}^{\alpha} = \varepsilon_0 \alpha_1 E_0 = p_1 \tag{7.85}$$

$$p_{\mathrm{pm1z}}^{\alpha} = \frac{\chi_2 g_{\mathrm{C}}}{1 + \alpha_1 \chi_2 g_{\mathrm{C}}^2}(\varepsilon_0 \alpha_1 E_0) = \frac{\chi_2 |g_{\mathrm{C}}| e^{i\phi_{\mathrm{C}}}}{1 + \alpha_1 \chi_2 |g_{\mathrm{C}}|^2 e^{i2\phi_{\mathrm{C}}}} p_1 \tag{7.86}$$

$$m_{\mathrm{pm2x}}^{\alpha} = \frac{1}{1 + \alpha_1 \chi_2 g_{\mathrm{C}}^2}(-\chi_2 H_0) = \frac{1}{1 + \alpha_1 \chi_2 |g_{\mathrm{C}}|^2 e^{i2\phi_{\mathrm{C}}}} m_2 \tag{7.87}$$

In Equations 7.85-7.87, we change their subscripts FD → pm to distinguish the FD and TD models. From Equations 7.85-7.87, it is found that the ED of the plasmonic core-shell particle has two components in the *y*- and *z*-directions. $p_{\mathrm{pm1y}}^{\alpha}$ is induced directly by the incident field, but $p_{\mathrm{pm1z}}^{\alpha}$ is indirectly induced by the scattered field of $m_{\mathrm{pm2x}}^{\alpha}$ of the dielectric sphere (see Equation 7.74). Therefore, $p_{\mathrm{pm1z}}^{\alpha}$ and $m_{\mathrm{pm2x}}^{\alpha}$ can be considered as the dark and bright oscillators, respectively. Figure 7.19a shows the absorption spectra of the dimer for the $\mathbf{p}_1$-$\mathbf{m}_2$ coupling. Those spectra are calculated using the FEM simulation. The lossless dielectric sphere is considered; therefore, the absorption of the dimer is dominated by the absorption of the plasmonic core-shell particle. The absorption spectra possess an EIA-like spectral profile for all *d*. In Figure 7.19d, the absorption of the plasmonic core-shell particle is calculated using the CDM. The absorption of the ED of the plasmonic core-shell particle can be divided into ED_y and ED_z, which originate from $p_{\mathrm{pm1y}}^{\alpha}$ and $p_{\mathrm{pm1z}}^{\alpha}$, respectively. The spectral profile of the ED_y is almost the same as that of the ED of the isolated plasmonic core-shell particle. The ED_z possesses a sharp absorption spectrum. There are no interactions between the ED_y and ED_z. Thus, the absorptions of the ED_y and ED_z can be superposed. Therefore, the total absorption of the ED possesses the sharp absorption of the ED_z over the broad absorption of the ED_y, resulting in an EIA-like spectral profile. This EIA is different from what we observed in the main text, but it corresponds to EIA originating from the excitation of the dark oscillator [7].

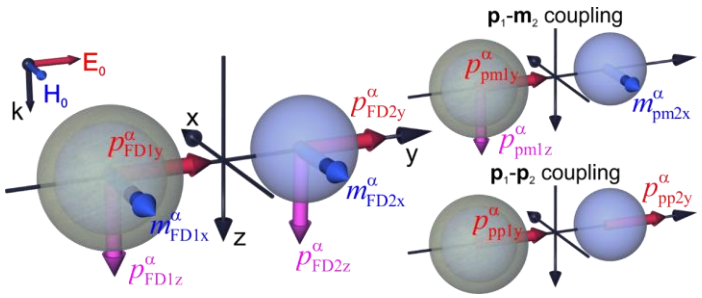

Figure 7.18. Schematic illustrations of the FD and TD models for the dimer aligned parallel to the electric field of the incident wave.

For the $\mathbf{p}_1$-$\mathbf{p}_2$ coupling ($\chi_1 = \chi_2 = 0$), the dimer with r_S = 690 nm is considered, and the dipole moments are given by Equations 7.78 and 7.79. Using the Lorentz oscillators, Equations 7.78 and 7.79 can be approximated as

$$p^{\alpha}_{\mathrm{pp1y}} = \frac{\Omega_{\mathrm{p1}}\Omega_{\mathrm{p2}} + \Omega_{\mathrm{p1}} f_{\mathrm{p2}}|g_{\mathrm{AB}}|e^{i\phi_{\mathrm{AB}}}}{\Omega_{\mathrm{p1}}\Omega_{\mathrm{p2}} - f_{\mathrm{p1}} f_{\mathrm{p2}}|g_{\mathrm{AB}}|^2 e^{i2\phi_{\mathrm{AB}}}} p_1 \tag{7.88}$$

$$p^{\alpha}_{\mathrm{pp2y}} = \frac{\Omega_{\mathrm{p1}}\Omega_{\mathrm{p2}} + \Omega_{\mathrm{p2}} f_{\mathrm{p1}}|g_{\mathrm{AB}}|e^{i\phi_{\mathrm{AB}}}}{\Omega_{\mathrm{p1}}\Omega_{\mathrm{p2}} - f_{\mathrm{p1}} f_{\mathrm{p2}}|g_{\mathrm{AB}}|^2 e^{i2\phi_{\mathrm{AB}}}} p_2 \tag{7.89}$$

The same equation can be obtained from the ECO model proposed in the main text by substituting $\delta = 0$. The absolute square of $p^{\alpha}_{\mathrm{pp1y}}$ at the resonance is (see Section 7.10.3)

$$\begin{aligned} &\left|p^{\alpha}_{\mathrm{pp1y}}\right|^2 \\ &= \frac{\left(\Gamma_{\mathrm{p1}}\Gamma_{\mathrm{p2}}\omega_0^2\right)^2 + \left(\Gamma_{\mathrm{p1}}\omega_0\right)^2\left(f_{\mathrm{p2}}|g_{\mathrm{AB}}|\right)^2 + 2\left(\Gamma_{\mathrm{p1}}\Gamma_{\mathrm{p2}}\omega_0^2\right)\left(\Gamma_{\mathrm{p1}}\omega_0\right)\left(f_{\mathrm{p2}}|g_{\mathrm{AB}}|\right)\sin(-\phi_{\mathrm{AB}})}{\left(\Gamma_{\mathrm{p1}}\Gamma_{\mathrm{p2}}\omega_0^2\right)^2 + \left(f_{\mathrm{p1}}f_{\mathrm{p2}}|g_{\mathrm{AB}}|^2\right)^2 + 2\left(\Gamma_{\mathrm{p1}}\Gamma_{\mathrm{p2}}\omega_0^2\right)\left(f_{\mathrm{p1}}f_{\mathrm{p2}}|g_{\mathrm{AB}}|^2\right)\cos(2\phi_{\mathrm{AB}})}|p_1|^2 \\ &= \frac{1 + \left(\Phi^{\alpha}_{\mathrm{pp2}}\right)^2 + 2\Phi^{\alpha}_{\mathrm{pp2}}\sin(-\phi_{\mathrm{AB}})}{1 + \left(\Phi^{\alpha}_{\mathrm{pp}}\right)^2 + 2\Phi^{\alpha}_{\mathrm{pp}}\cos(2\phi_{\mathrm{AB}})} = P^{\alpha}_{\mathrm{pp}}|p_1|^2, \qquad \Phi^{\alpha}_{\mathrm{pp}} = \frac{f_{\mathrm{p1}}|g_{\mathrm{AB}}|}{\Gamma_{\mathrm{p1}}\omega_0}\frac{f_{\mathrm{p2}}|g_{\mathrm{AB}}|}{\Gamma_{\mathrm{p2}}\omega_0} = \Phi^{\alpha}_{\mathrm{pp1}}\Phi^{\alpha}_{\mathrm{pp2}} \end{aligned} \tag{7.90}$$

In Figure 7.20, the $\mathbf{p}_1$-$\mathbf{p}_2$ coupling is investigated. Figure 7.20a shows the absorption spectra of the dimer with different *d*. The spectral profile of the absorption spectra changes from an EIT- to an EIA-like profile with an increase in *d*. For small *d*, the $\mathbf{p}_1$-$\mathbf{p}_2$ coupling of the dimer is dominated by the near-field effect because the electromagnetic hot spots are created along the *y*-direction. Figure 7.20b presents the absorption properties of the dimer with d = 3 μm, which possesses an EIA-like spectral profile. In contrast to the case of the $\mathbf{p}_1$-$\mathbf{m}_2$ coupling, the ED_y absorption of the plasmonic core-shell particle is enhanced by the phase-retarded coupling, which is attributed to EIA.

In Figure 7.19c, the sine and cosine functions of P^{α}_{pp} are plotted. We focus on the sine function of P^{α}_{pp}. Compared with $\sin(-\phi_A - kD)$ of P_{pp} of the main text, $\sin(-\phi_{AB})$ of P^{α}_{pp} slowly changes with an increase in *d*. Using Equation 7.15, we can write $-\phi_A - kD = -2kD - \phi_a$. On the other hand, the phase ϕ_{AB} is given as $\phi_{AB} = kD + \phi_{ab}$. Therefore, $\sin(-\phi_{AB})$ oscillates twice as slow as $\sin(-\phi_A - kD)$ with increasing *d*. Figure 7.20c also shows P^{α}_{pp}, indicating that the absorption of the plasmonic core-shell particle possesses an EIT-like profile in a range of d < 2.5 μm and becomes an EIA-like profile when $d \rightarrow 3$ μm. This coincides with the spectral change shown in Figure 7.20a.

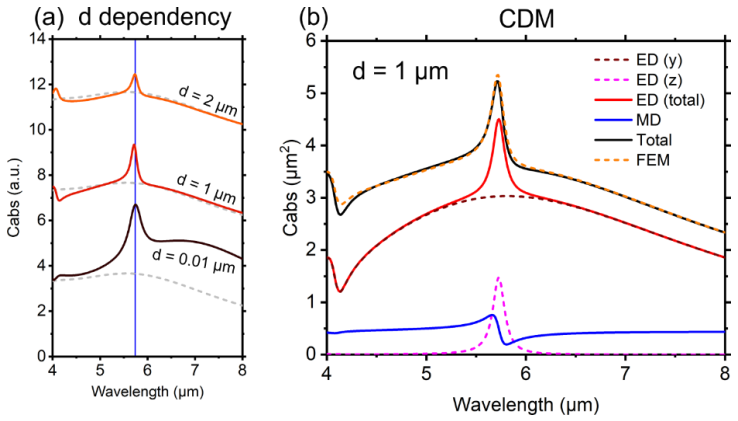

Figure 7.19. The $\mathbf{p}_1$-$\mathbf{m}_2$ coupling of the dimer composed of the dielectric sphere with r_S = 500 nm. The orientation of the dimer is shown in Figure 7.18. (a) d dependency of the absorption of the dimer. The absorption spectra are calculated using the FEM simulation. The grey dashed lines are the reference spectra given by the total absorption of the plasmonic core-shell particle. The blue solid vertical line shows the resonance wavelength of the MD of the dielectric sphere. (b) The red and blue lines are for ED and MD of the plasmonic core-shell particle. The wine-red and magenta dashed lines are the absorption of ED_y and ED_z of the plasmonic core-shell particle. The black line is the total absorption of the dimer. Those spectra are calculated using the CDM. The orange dashed line is taken from Figure 7.19a.

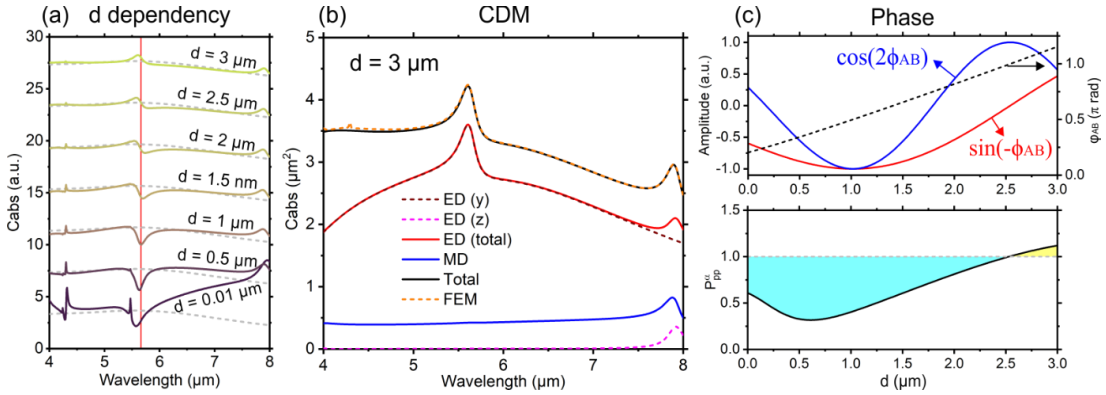

Figure 7.20. The $\mathbf{p}_1$-$\mathbf{p}_2$ coupling of the dimer composed of the dielectric sphere with r_S = 690 nm. The orientation of the dimer is shown in Figure 7.18. (a) d dependencies of the absorption of the dimer. The absorption spectra are calculated using the FEM simulation. The grey dashed lines are reference spectra given by the total absorption of the plasmonic core-shell particle. The red solid vertical line shows the resonance wavelength of the ED of the dielectric sphere. (b) The red and blue lines are for the ED and MD of the plasmonic core-shell particle. The wine-red and magenta dashed lines are the ED_y and ED_z absorptions of the plasmonic core-shell particle. The black line is the total absorption of the dimer. Those spectra are calculated using the CDM. The orange dashed line is taken from Figure 7.20a. (c) The sine and cosine functions of P_{pp}^{α} (Equation 7.86) are plotted as a function of d. On the right vertical axis, the phase of φ_{AB} is shown as the black dashed lines. P_{pp}^{α} is calculated at $\omega_0 = 3.33 \times 10^{14}$ rad/s.

7.10.9. Absorption properties of a dimer aligned parallel to the magnetic field of the incident wave

Figure 7.21 shows the orientations of the incident wave and the dimer. The incident wave propagates along the *z*-direction with $\mathbf{E}_{in}(\mathbf{r}_j) = E_0\hat{\mathbf{e}}_x e^{i\mathbf{k}\cdot\mathbf{r}_j}$ and $\mathbf{H}_{in}(\mathbf{r}_j) = H_0\hat{\mathbf{e}}_y e^{i\mathbf{k}\cdot\mathbf{r}_j}$. The plasmonic core-shell particle and the dielectric sphere locate at $\mathbf{r}_1$ = (0, – *D*/2, 0) and $\mathbf{r}_2$ = (0, *D*/2, 0), respectively. Therefore, the incident wave can be written as $\mathbf{E}_{in}(\mathbf{r}_j) = E_0\hat{\mathbf{e}}_x$ and $\mathbf{H}_{in}(\mathbf{r}_j) = H_0\hat{\mathbf{e}}_y$. We can use the same dyadic Green´s functions

given by Equations 7.72 and 7.73. In a similar manner to Section 7.10.8, the FD model shown in Figure 7.21 is given as

$$\mathbf{p}_{\mathrm{FD1}}^{\sigma}=\begin{cases}p_{\mathrm{FD1x}}^{\sigma}=\varepsilon_0\alpha_1\left[E_0+\dfrac{1}{\varepsilon_0}g_{\mathrm{A}}p_{\mathrm{FD2x}}^{\sigma}+Z_0g_{\mathrm{C}}m_{\mathrm{FD2z}}^{\sigma}\right]\\ p_{\mathrm{FD1y}}^{\sigma}=\alpha_1g_{\mathrm{AB}}p_{\mathrm{FD2y}}^{\sigma}=0\\ p_{\mathrm{FD1z}}^{\sigma}=\varepsilon_0\alpha_1\left[\dfrac{1}{\varepsilon_0}g_{\mathrm{A}}p_{\mathrm{FD2z}}^{\sigma}-Z_0g_{\mathrm{C}}m_{\mathrm{FD2x}}^{\sigma}\right]\end{cases} \tag{7.91}$$

$$\mathbf{m}_{\mathrm{FD1}}^{\sigma}=\begin{cases}m_{\mathrm{FD1x}}^{\sigma}=\chi_1\left[-\dfrac{1}{\varepsilon_0Z_0}g_{\mathrm{C}}p_{\mathrm{FD2z}}^{\sigma}+g_{\mathrm{A}}m_{\mathrm{FD2x}}^{\sigma}\right]\\ m_{\mathrm{FD1y}}^{\sigma}=\chi_1\left[H_0+g_{\mathrm{AB}}m_{\mathrm{FD2y}}^{\sigma}\right]\\ m_{\mathrm{FD1z}}^{\sigma}=\chi_1\left[\dfrac{1}{\varepsilon_0Z_0}g_{\mathrm{C}}p_{\mathrm{FD2x}}^{\sigma}+g_{\mathrm{A}}m_{\mathrm{FD2z}}^{\sigma}\right]\end{cases} \tag{7.92}$$

$$\mathbf{p}_{\mathrm{FD2}}^{\sigma}=\begin{cases}p_{\mathrm{FD2x}}^{\sigma}=\varepsilon_0\alpha_2\left[E_0+\dfrac{1}{\varepsilon_0}g_{\mathrm{A}}p_{\mathrm{FD1x}}^{\sigma}-Z_0g_{\mathrm{C}}m_{\mathrm{FD1z}}^{\sigma}\right]\\ p_{\mathrm{FD2y}}^{\sigma}=\alpha_1g_{\mathrm{AB}}p_{\mathrm{FD1y}}^{\sigma}\\ p_{\mathrm{FD2z}}^{\sigma}=\varepsilon_0\alpha_2\left[\dfrac{1}{\varepsilon_0}g_{\mathrm{A}}p_{\mathrm{FD1z}}^{\sigma}+Z_0g_{\mathrm{C}}m_{\mathrm{FD1x}}^{\sigma}\right]\end{cases} \tag{7.93}$$

$$\mathbf{m}_{\mathrm{FD2}}^{\sigma}=\begin{cases}m_{\mathrm{FD2x}}^{\sigma}=\chi_2\left[\dfrac{1}{\varepsilon_0Z_0}g_{\mathrm{C}}p_{\mathrm{FD1z}}^{\sigma}+g_{\mathrm{A}}m_{\mathrm{FD1x}}^{\sigma}\right]\\ m_{\mathrm{FD2y}}^{\sigma}=\chi_2\left[H_0+g_{\mathrm{AB}}m_{\mathrm{FD1y}}^{\sigma}\right]\\ m_{\mathrm{FD2z}}^{\sigma}=\chi_2\left[-\dfrac{1}{\varepsilon_0Z_0}g_{\mathrm{C}}p_{\mathrm{FD1x}}^{\sigma}+g_{\mathrm{A}}m_{\mathrm{FD1z}}^{\sigma}\right]\end{cases} \tag{7.94}$$

The superscript σ is to distinguish the FD model shown in Figure 7.21 from other FD models. By solving Equations 7.91-7.94, we get nontrivial solutions for $p_{\mathrm{FD1x}}^{\sigma}$, $m_{\mathrm{FD1y}}^{\sigma}$, $m_{\mathrm{FD1z}}^{\sigma}$, $p_{\mathrm{FD2x}}^{\sigma}$, $m_{\mathrm{FD2y}}^{\sigma}$, and $m_{\mathrm{FD2z}}^{\sigma}$. The self-consistent form of $m_{\mathrm{FD1y}}^{\sigma}$ and $m_{\mathrm{FD2y}}^{\sigma}$ are

$$m_{\mathrm{FD1y}}^{\sigma}=\chi_1\frac{1+\chi_2g_{\mathrm{AB}}}{1-\chi_1\chi_2g_{\mathrm{AB}}^2}H_0 \tag{7.95}$$

$$m_{\mathrm{FD2y}}^{\sigma}=\chi_2\frac{1+\chi_1g_{\mathrm{AB}}}{1-\alpha_1\chi_2g_{\mathrm{AB}}^2}H_0 \tag{7.96}$$

Substituting $p_{\mathrm{FD2x}}^{\sigma}$ and $m_{\mathrm{FD2z}}^{\sigma}$ into $p_{\mathrm{FD1x}}^{\sigma}$, we get

$$p_{\mathrm{FD1x}}^{\sigma}=\varepsilon_0\alpha_1\frac{[1+\alpha_2g_{\mathrm{A}}]E_0+Z_0(\chi_2-\alpha_2)g_{\mathrm{A}}g_{\mathrm{C}}m_{\mathrm{FD1z}}^{\sigma}}{1-\alpha_1[\alpha_2g_{\mathrm{A}}^2-\chi_2g_{\mathrm{C}}^2]} \tag{7.97}$$

In a similar manner, $m_{\mathrm{FD1z}}^{\sigma}$, $p_{\mathrm{FD2x}}^{\sigma}$, and $m_{\mathrm{FD2z}}^{\sigma}$ are

$$m_{\mathrm{FD1z}}^{\sigma}=\chi_1\frac{\alpha_2g_{\mathrm{C}}H_0+\dfrac{1}{\varepsilon_0Z_0}(\alpha_2-\chi_2)g_{\mathrm{A}}g_{\mathrm{C}}p_{\mathrm{FD1x}}^{\sigma}}{1-\chi_1[\chi_2g_{\mathrm{A}}^2-\alpha_2g_{\mathrm{C}}^2)]} \tag{7.98}$$

$$p_{\mathrm{FD2x}}^{\sigma}=\varepsilon_0\alpha_2\frac{[1+\alpha_1g_{\mathrm{A}}]E_0+Z_0(\alpha_1-\chi_1)g_{\mathrm{A}}g_{\mathrm{C}}m_{\mathrm{FD2z}}^{\sigma}}{1-\alpha_2[\alpha_1g_{\mathrm{A}}^2-\chi_1g_{\mathrm{C}}^2]} \tag{7.99}$$

$$m_{\mathrm{FD2z}}^{\sigma} = \chi_2 \frac{-\alpha_1 g_{\mathrm{C}} H_0 + \frac{1}{\varepsilon_0 Z_0}(\chi_1 - \alpha_1) g_{\mathrm{A}} g_{\mathrm{C}} p_{\mathrm{FD2x}}^{\sigma}}{1 - \chi_2[\chi_1 g_{\mathrm{A}}^2 - \alpha_1 g_{\mathrm{C}}^2]} \tag{7.100}$$

Using Equations 7.95-7.100, we derive the TD model for a $\mathbf{p}_1$-$\mathbf{m}_2$ coupling ($\chi_1 = \alpha_2 = 0$)

$$p_{\mathrm{pm1x}}^{\sigma} = \frac{1}{1 + \alpha_1 \chi_2 g_{\mathrm{C}}^2}(\varepsilon_0 \alpha_1 E_0) = \frac{1}{1 + \alpha_1 \chi_2 |g_{\mathrm{C}}|^2 e^{i2\phi_{\mathrm{C}}}} p_1 \tag{7.101}$$

$$m_{\mathrm{pm2z}}^{\sigma} = -\frac{\alpha_1 g_{\mathrm{C}}}{1 + \alpha_1 \chi_2 g_{\mathrm{C}}^2}(\chi_2 H_0) = -\frac{\alpha_1 |g_{\mathrm{C}}| e^{i\phi_{\mathrm{C}}}}{1 + \alpha_1 \chi_2 |g_{\mathrm{C}}|^2 e^{i2\phi_{\mathrm{C}}}} m_2 \tag{7.102}$$

$$m_{\mathrm{pm2y}}^{\sigma} = \chi_2 H_0 = m_2 \tag{7.103}$$

From Equations 7.102 and 7.103, the MD of the dielectric sphere has two components in the *z*- and *y*-directions. $m_{\mathrm{pm2y}}^{\sigma}$ does not interact with $p_{\mathrm{pm1x}}^{\sigma}$ and is excited directly by the incident wave. In contrast, $m_{\mathrm{pm2z}}^{\sigma}$ is excited solely by $p_{\mathrm{pm1x}}^{\sigma}$ (see Equation 7.94); therefore, the coupling between $p_{\mathrm{pm1x}}^{\sigma}$ and $m_{\mathrm{pm2z}}^{\sigma}$ can be considered based on a bright-dark oscillator interaction. Using the Lorentz oscillators, Equations 7.101 and 7.103 can be written as

$$p_{\mathrm{pm1x}}^{\sigma} = \frac{\Omega_{\mathrm{p1}} \Omega_{\mathrm{m2}}}{\Omega_{\mathrm{p1}} \Omega_{\mathrm{m2}} + f_{\mathrm{p1}} f_{\mathrm{m2}} |g_{\mathrm{C}}|^2 e^{i2\phi_{\mathrm{C}}}} p_1 \tag{7.104}$$

$$m_{\mathrm{pm2z}}^{\sigma} = -\frac{\Omega_{\mathrm{m2}} f_{\mathrm{p1}} |g_{\mathrm{C}}| e^{i\phi_{\mathrm{C}}}}{\Omega_{\mathrm{p1}} \Omega_{\mathrm{m2}} + f_{\mathrm{p1}} f_{\mathrm{m2}} |g_{\mathrm{C}}|^2 e^{i2\phi_{\mathrm{C}}}} m_2 \tag{7.105}$$

A similar equation can be obtained from the ECO model proposed in the main text by substituting $F_2(t) = 0$ and $\delta = 0$. The absolute square of $p_{\mathrm{pm1x}}^{\sigma}$ at the resonance is (see Section 7.10.3)

$$\begin{aligned} &\left|p_{\mathrm{pm1x}}^{\sigma}\right|^2 \\ &= \frac{\left(\Gamma_{\mathrm{p1}} \Gamma_{\mathrm{m2}} \omega_0^2\right)^2}{\left(\Gamma_{\mathrm{p1}} \Gamma_{\mathrm{m2}} \omega_0^2\right)^2 + \left(F_{\mathrm{p1}} F_{\mathrm{m2}} |g_{\mathrm{C}}|^2\right)^2 + 2\left(\Gamma_{\mathrm{p1}} \Gamma_{\mathrm{m2}} \omega_0^2\right)\left(f_{\mathrm{p1}} f_{\mathrm{m2}} |g_{\mathrm{C}}|^2\right) \cos(2\phi_{\mathrm{C}} + \pi)} |p_1|^2 \\ &= \frac{1}{1 + \Phi_{\mathrm{pm}}^2 + 2\Phi_{\mathrm{pm}} \cos(2\phi_{\mathrm{C}} + \pi)} = P_{\mathrm{pm}}^{\sigma} |p_1|^2 \end{aligned} \tag{7.106}$$

As seen in Equation 7.106, the phase-retarded coupling is solely determined by the cosine function of the denominator. Therefore, the condition for EIA can be found from $\cos(2\varphi_{\mathrm{C}} + \pi) = -1$. The top panel of Figure 7.22 shows the absorption properties of the dimer with $r_{\mathrm{S}} = 500$ nm. Since we have proved the applicability of the *P* function to investigate EIA, we first consider P_{pm}^{σ} to find an optimum *d* for EIA, then the absorption properties of the dimer are investigated. Figure 7.22a shows the cosine function of P_{pm}^{σ}. The cosine function becomes -1 at around $d \approx 1.25$ μm. However, P_{pm}^{σ} is not maximized at $d \approx 1.25$ μm. The maximum appears at *d* slightly smaller than 1.25 μm. This is because the scattered field amplitude $|g_{\mathrm{C}}|$ keeps decreasing with an increase in *d*; therefore, P_{pm}^{σ} also decreases. This is the reason why the maximum of P_{pm}^{σ} occurs at *d* shifted from a point where $\cos(2\varphi_{\mathrm{C}} + \pi) = -1$ is achieved. P_{pm}^{σ} indicates that the absorption of the dimer changes EIT → EIA → EIT-like spectral profile with an increase in *d*. Figure 7.22b shows the *d* dependency of the absorption properties of the dimer. Those spectra are calculated using the FEM simulation. The dimer with $d = 0.01$ μm and 2.5 μm possesses the EIT-like profile, and that with $d = 1$ μm possesses the EIA-like profile. This result coincides with what P_{pm}^{σ} predicted in Figure 7.22a. In Figure 7.22c, the

absorption properties of the dimer with d = 1 μm are presented. The ED absorption of the plasmonic core-shell particle is enhanced by the phase retarded coupling.

For a $\mathbf{p}_1$-$\mathbf{p}_2$ coupling ($\chi_1 = \chi_2 = 0$), the dimer with r_S = 690 nm is considered, and the dipole moments are given by Equations 7.97 and 7.99.

$$p_{\mathrm{pp1x}}^{\sigma} = \frac{1+\alpha_2 g_{\mathrm{A}}}{1-\alpha_1\alpha_2 g_{\mathrm{A}}^2}(\varepsilon_0\alpha_1 E_0) = \frac{1+\alpha_2|g_{\mathrm{A}}|e^{i\phi_{\mathrm{A}}}}{1-\alpha_1\alpha_2|g_{\mathrm{A}}|^2 e^{i2\phi_{\mathrm{A}}}}p_1 \tag{7.107}$$

$$p_{\mathrm{pp2x}}^{\sigma} = \frac{1+\alpha_1 g_{\mathrm{A}}}{1-\alpha_1\alpha_2 g_{\mathrm{A}}^2}(\varepsilon_0\alpha_2 E_0) = \frac{1+\alpha_1|g_{\mathrm{A}}|e^{i\phi_{\mathrm{A}}}}{1-\alpha_1\alpha_2|g_{\mathrm{A}}|^2 e^{i2\phi_{\mathrm{A}}}}p_2 \tag{7.108}$$

Using the Lorentz oscillators, Equations 7.107 and 7.108 can be written as

$$p_{\mathrm{pp1x}}^{\sigma} = \frac{\Omega_{\mathrm{p1}}\Omega_{\mathrm{p2}} + \Omega_{\mathrm{p1}} f_{\mathrm{p2}}|g_{\mathrm{A}}|e^{i\phi_{\mathrm{A}}}}{\Omega_{\mathrm{p1}}\Omega_{\mathrm{p2}} - f_{\mathrm{p1}} f_{\mathrm{p2}}|g_{\mathrm{A}}|^2 e^{i2\phi_{\mathrm{A}}}}p_1 \tag{7.109}$$

$$p_{\mathrm{pp2x}}^{\sigma} = \frac{\Omega_{\mathrm{p1}}\Omega_{\mathrm{p2}} + \Omega_{\mathrm{p2}} f_{\mathrm{p1}}|g_{\mathrm{A}}|e^{i\phi_{\mathrm{A}}}}{\Omega_{\mathrm{p1}}\Omega_{\mathrm{p2}} - f_{\mathrm{p1}} f_{\mathrm{p2}}|g_{\mathrm{A}}|^2 e^{i2\phi_{\mathrm{A}}}}p_2 \tag{7.110}$$

The same equation can be obtained from the ECO model proposed in the main text by substituting $\delta = 0$. The absolute square of p_{pp}^{σ} at the resonance is (see Section 7.10.3)

$$\begin{aligned}
&\left|p_{\mathrm{pp1x}}^{\sigma}\right|^2 \\
&= \frac{\left(\Gamma_{\mathrm{p1}}\Gamma_{\mathrm{p2}}\omega_0^2\right)^2 + \left(\Gamma_{\mathrm{p1}}\omega_0\right)^2\left(f_{\mathrm{p2}}|g_{\mathrm{A}}|\right)^2 + 2\left(\Gamma_{\mathrm{p1}}\Gamma_{\mathrm{p2}}\omega_0^2\right)\left(\Gamma_{\mathrm{p1}}\omega_0\right)\left(f_{\mathrm{p2}}|g_{\mathrm{A}}|\right)\sin(-\phi_{\mathrm{A}})}{\left(\Gamma_{\mathrm{p1}}\Gamma_{\mathrm{p2}}\omega_0^2\right)^2 + \left(f_{\mathrm{p1}}f_{\mathrm{p2}}|g_{\mathrm{A}}|^2\right)^2 + 2\left(\Gamma_{\mathrm{p1}}\Gamma_{\mathrm{p2}}\omega_0^2\right)\left(f_{\mathrm{p1}}f_{\mathrm{p2}}|g_{\mathrm{A}}|^2\right)\cos(2\phi_{\mathrm{A}})}|p_1|^2 \\
&= \frac{1+\Phi_{\mathrm{pp2}}^2 + 2\Phi_{\mathrm{pp2}}\sin(-\phi_{\mathrm{A}})}{1+\Phi_{\mathrm{pp}}^2 + 2\Phi_{\mathrm{pp}}\cos(2\phi_{\mathrm{A}})} = P_{\mathrm{pp}}^{\sigma}|p_1|^2
\end{aligned} \tag{7.111}$$

The sine and cosine functions of P_{pp}^{σ} are plotted in Figure 7.22d. It can be found that $\sin(-\varphi_{\mathrm{A}}) = 1$ and $\cos(2\varphi_{\mathrm{A}}) = -1$ can occur simultaneously at around d = 2.5 μm; therefore, complete constructive interference can be achieved. P_{pp}^{σ} is also plotted in Figure 7.22d. The maximum of P_{pp}^{σ} can be found at around d = 2.5 μm. The peak position is slightly shifted to a smaller d from 2.5 μm because of the same reason described earlier. P_{pp}^{σ} indicates that the absorption of the dimer changes from an EIT- to an EIA-like profile with an increase in d. The absorption spectra of the dimer calculated using the FEM simulation are shown in Figure 7.22e. For a small d, a dip and a sharp peak can be found at around the ED resonance of the dielectric sphere. The dip is attributed to destructive interference. The sharp peak originates from a coupling between the ED of the plasmonic core-shell particle and the MQ of the dielectric sphere. The dimer with d = 2.5 μm possesses the EIA-like profile. Figure 7.22f shows the absorption properties of the dimer with d = 2.5 μm. The ED absorption of the plasmonic core-shell particle is enhanced by complete constructive interference, resulting in the EIA-like profile.

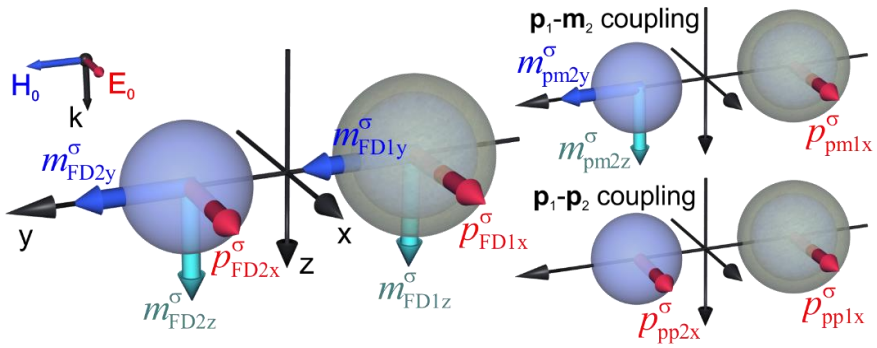

Figure 7.21. Schematic illustrations of the FD and TD models for the dimer oriented parallel to the magnetic field of the incident wave.

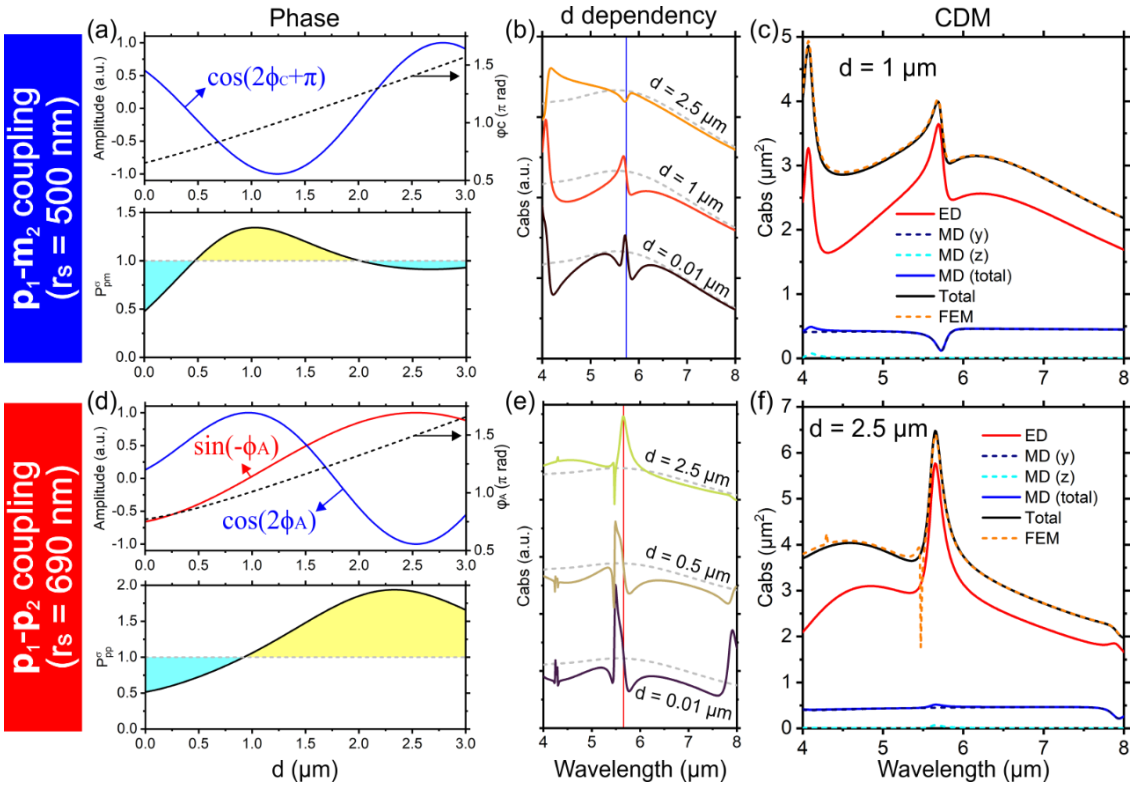

Figure 7.22. (Top panel) The $\mathbf{p}_1$-$\mathbf{m}_2$ coupling of the dimer composed of the dielectric sphere with r_S = 500 nm. (Bottom panel) The $\mathbf{p}_1$-$\mathbf{p}_2$ coupling of the dimer composed of the dielectric sphere with r_S = 690 nm. (a and d) The sine and cosine functions in P^{σ}_{pm} (Equation 7.102) and P^{σ}_{pp} (Equation 7.107) are plotted as a function of d. On the right vertical axis, the phases of ϕ_C and ϕ_A are shown as black dashed lines. P^{σ}_{pm} and P^{σ}_{pp} are calculated at $\omega_0 = 3.29 \times 10^{14}$ rad/s and $\omega_0 = 3.33 \times 10^{14}$ rad/s, respectively. (b and e) d dependencies of the absorption of the dimer of Figure 7.21. The absorption spectra are calculated using the FEM simulation. The grey dashed lines are the reference spectra given by the total absorption of the isolated plasmonic core-shell particle. The blue and red solid vertical lines show the resonance wavelength of MD and ED of the dielectric spheres, respectively. (c and f) The red and blue lines are for ED and MD of the plasmonic core-shell particle. The black line is the total absorption of the dimer. The orange dashed lines are the absorption spectra given by the FEM simulation.

7.10.10. N_S dependency of the absorption properties of the dimer

In the main text, we only investigate the dimer comprising the dielectric sphere with $N_S = n_S = 5.6$. Here we discuss how the absorption properties of the dimer change if n_S changes. For this investigation, we use the dimer shown in Figure 7.3, and a $\mathbf{p}_1$-$\mathbf{m}_2$ coupling is only considered. Figure 7.23 shows scattering properties and magnetic polarizability of the dielectric sphere with different N_S. r_S is determined so that its MD resonance occurs at around the ED resonance of the plasmonic core-shell particle. The scattering spectra and magnetic polarizability are calculated using Mie theory. As mentioned in the main text, the dimer with low n_S has ED and MD resonances close to each other. The Lorentz oscillator is fitted to the polarizability given by Mie coefficient. The fitting results are summarized in Table 7.2.

In Figure 7.24, the same analysis made in Figure 7.7 is employed using the dielectric sphere characterized in Figure 7.23. For this analysis, we only use the CDM. A pronounced EIA peak can be found even though n_S is small. However, an EIA peak becomes broad with a decrease in n_S. In addition, the MD and ED of the dielectric sphere cannot be resolved for a small n_S; therefore, the influence of the ED of the dielectric sphere cannot be ignored. For large n_S, a strong and sharp EIA peak can be observed.

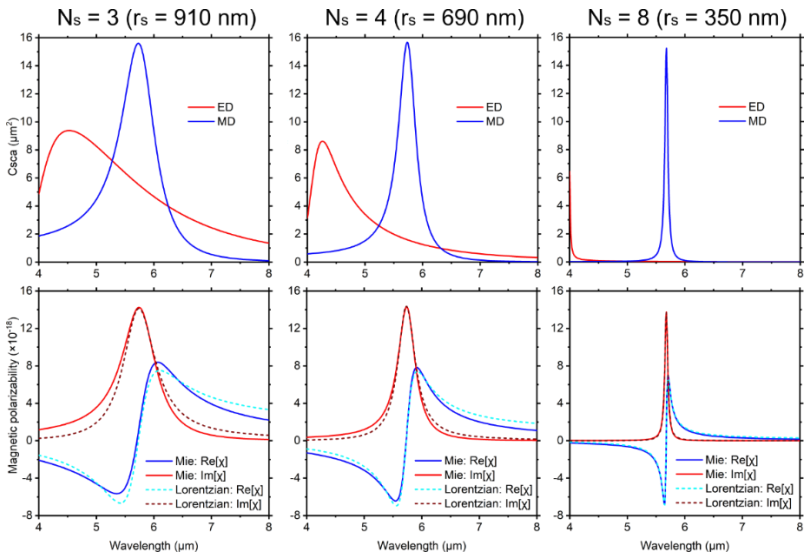

Figure 7.23. The optical properties of the dielectric sphere with different N_S and r_S. r_S is determined so that the MD resonance of the dielectric sphere occurs at the ED resonance of the plasmonic core-shell particle. The top panel shows the scattering properties, and the bottom panel shows the magnetic polarizabilities.

Table 7.2. Fitting values used in Figure 7.23

Lorentz	$N_S = 3$, $r_S = 910$ nm Magnetic polarizability	$N_S = 4$, $r_S = 690$ nm Magnetic polarizability	$N_S = 8$, $r_S = 350$ nm Magnetic polarizability
f_{m2} [$m^3 \cdot (rad/s)^2$]	1.81×10^{11}	9.89×10^{10}	1.64×10^{10}
ω_{m2} [rad/s]	3.29×10^{14}	3.29×10^{14}	3.32×10^{14}
Γ_{m2} [rad/s]	3.89×10^{13}	2.09×10^{13}	3.55×10^{12}

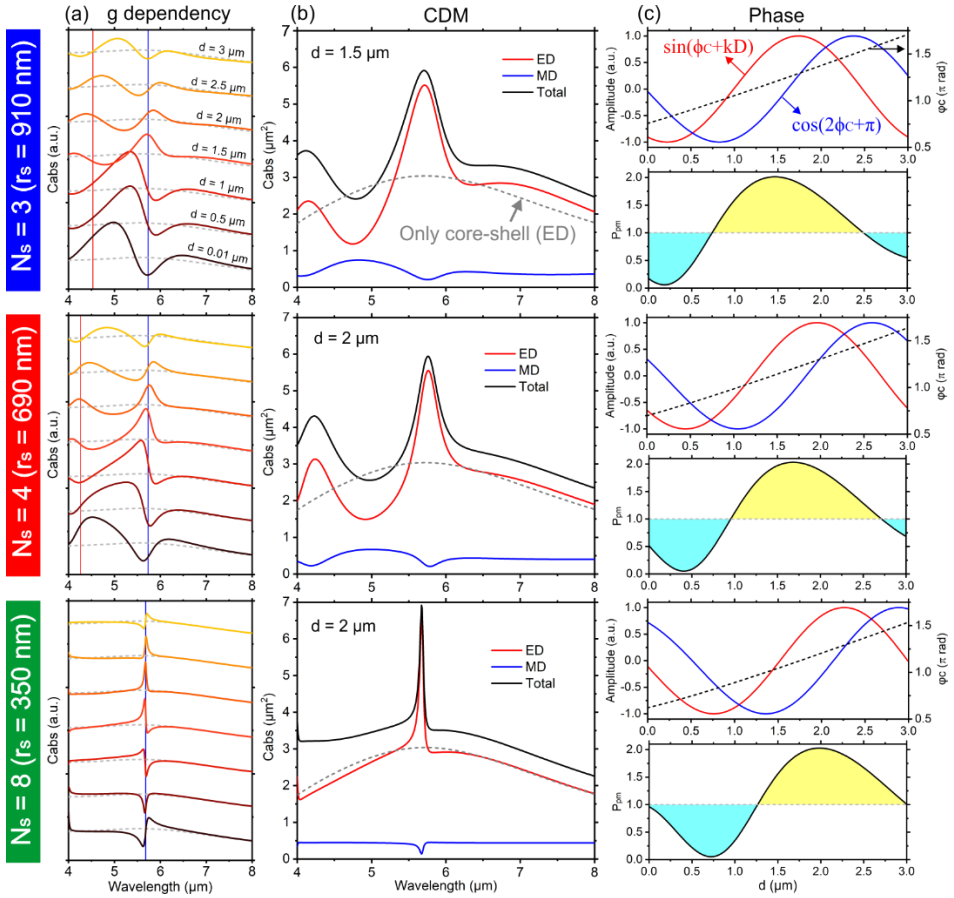

Figure 7.24. The $\mathbf{p}_1$-$\mathbf{m}_2$ coupling of the dimer composed of the dielectric sphere with (Top panel) N_S = 3, (Middle panel) N_S = 4, and (Bottom panel) N_S = 8. the dimer shown in Figure 7.3 is considered. (a) *d* dependencies of the absorption of the dimer. The absorption spectra are calculated using the CDM. The grey dashed lines are the reference spectra given by the total absorption of the isolated plasmonic core-shell particle. The blue and red solid vertical lines show the resonance wavelength of the MD and ED of the dielectric spheres, respectively. (b) The solid lines are the absorption spectra of the dimer, which are calculated using the CDM. The red, blue, and black lines are for the ED, MD, and total absorption of the plasmonic core-shell particle, respectively. (c) The sine and cosine functions of P_{pm} (Equation 7.35) are plotted as a function of d. On the right vertical axis, the phase of ϕ_C is shown as the black dashed lines. P_{pm} is calculated at the MD resonance of the dielectric sphere shown in Table 7.2.

7.10.11. κ_S dependency of the absorption properties of the dimer

Figure 7.25 shows a comparison between the CDM and the FEM simulation. The absorption spectra given by the CDM are taken from Figure 7.9e. Even though $\kappa_S \neq 0$, the CDM is in good agreement with the FEM simulation. In Figure 7.26, the optical properties of the dielectric sphere with κ_S = 0.082 are shown. C_{abs} and C_{sca} of the MD are nearly equal, meaning that the absorption of the MD is maximized. The magnetic polarizabilities of the dielectric sphere with different κ_S are shown in Figure 7.26.

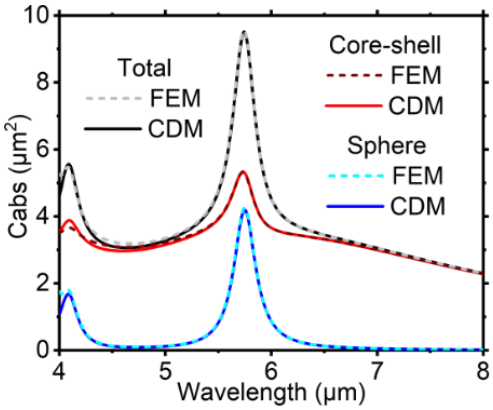

Figure 7.25. The absorption spectra of the dimer with the lossy dielectric sphere. The structural and material parameters are the same as in Figure 7.9e. The solid and dashed lines are calculated using the CDM and the FEM simulation, respectively. The total absorptions of the plasmonic core-shell particle, dielectric sphere, and the dimer are shown.

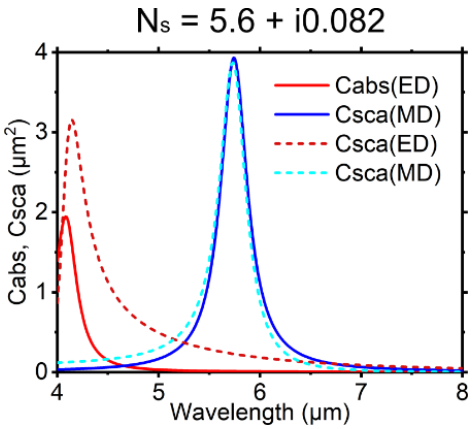

Figure 7.26. The optical properties of the dielectric sphere with N_S = 5.6 + *i*0.082 and r_S = 500 nm. The spectra are calculated using Mie theory.

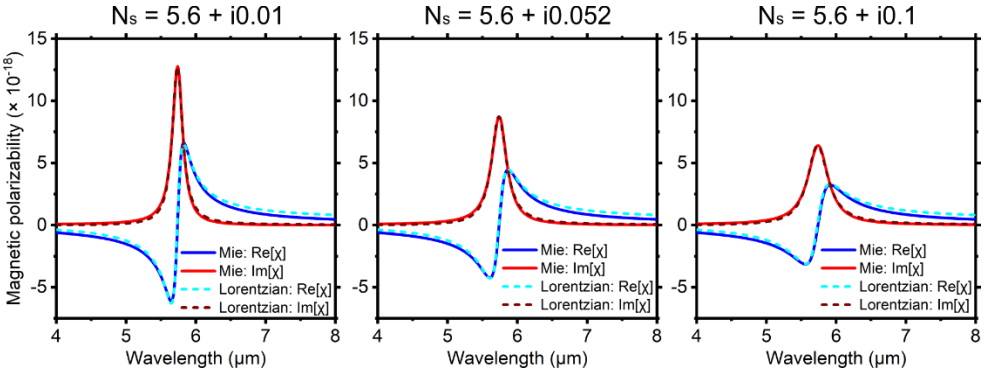

Figure 7.27. The magnetic polarizabilities of the dielectric sphere with r_S = 500 nm and different κ_S. The solid lines are calculated using Mie theory. The dashed lines are calculated using the Lorentz function with fitting values shown in Table 7.3.

Table 7.3. Fitting values used in Figure 7.27

Lorentz	$N_S = 5.6 + i0.01$ Magnetic polarizability	$N_S = 5.6 + i0.052$ Magnetic polarizability	$N_S = 5.6 + i0.1$ Magnetic polarizability
f_{m2} $[m^3 \cdot (rad/s)^2]$	4.30×10^{10}	4.30×10^{10}	4.29×10^{10}
ω_{m2} [rad/s]	3.29×10^{14}	3.29×10^{14}	3.29×10^{14}
Γ_{m2} [rad/s]	1.02×10^{13}	1.50×10^{13}	2.03×10^{13}

7.10.12. References

1. P. Albella, M. A. Poyli, M. K. Schmidt, S. A. Maier, F. Moreno, J. J. Sáenz, and J. Aizpurua, "Low-Loss Electric and Magnetic Field-Enhanced Spectroscopy with Subwavelength Silicon Dimers," J. Phys. Chem. C **117** (26), 13573-13584 (2013).

2. S. Sun, M. Li, Q. Du, C. E. Png, and P. Bai, "Metal–Dielectric Hybrid Dimer Nanoantenna: Coupling between Surface Plasmons and Dielectric Resonances for Fluorescence Enhancement," J. Phys. Chem. C **121** (23), 12871-12884 (2017).

3. G. W. Mulholland, C. F. Bohren, and K. A. Fuller, "Light Scattering by Agglomerates: Coupled Electric and Magnetic Dipole Method," Langmuir **10** ((1994).

4. O. Merchiers, F. Moreno, F. González, and J. M. Saiz, "Light scattering by an ensemble of interacting dipolar particles with both electric and magnetic polarizabilities," Phys. Rev. A **76** (4) (2007).

5. K. Matsumori, R. Fujimura, and M. Retsch, "Coupling Strength and Total Damping Govern Electromagnetically Induced Absorption in Coupled Plasmonic Systems," Submitted to Adv. Photonics Res (2022).

6. A. E. Miroshnichenko, A. B. Evlyukhin, Y. S. Kivshar, and B. N. Chichkov, "Substrate-Induced Resonant Magnetoelectric Effects for Dielectric Nanoparticles," ACS Photonics **2** ((2015).

7. F. Zhang, X. Huang, W. Cai, R. Yang, Q. Fu, Y. Fan, Y. Hu, K. Qiu, W. Zhang, C. Li, and Q. Li, "EIA metamaterials based on hybrid metal/dielectric structures with dark-mode-enhanced absorption," Opt. Express **28** (12), 17481-17489 (2020).

8. Reflection Mechanism of Dielectric Corner Reflectors: The Role of the Diffraction of Evanescent Waves and the Goos-Hänchen Shift

Kishin Matsumori[1,*], Ryushi Fujimura[2], and Markus Retsch[1]

[1] Department of Chemistry, Physical Chemistry I, University of Bayreuth, 95447 Bayreuth, Germany

[2] Graduate School of Regional Development and Creativity, Utsunomiya University, 321-8585 Utsunomiya, Japan

Published in *ACS Omega* **7**(27), 23353 – 23361 (2022)

Reproduced with permission from American Chemical Society

Abstract: Nano- and microstructures have been developed for asymmetric light transmission (ALT) filters operating in a wide wavelength range. One of the most straightforward structures with ALT properties is a dielectric corner reflector (DCR) comprising a one-dimensional grating of a triangular shape on one surface. The DCR possesses strong reflection only for one-way light illumination due to multiple total internal reflections (TIRs) inside the triangular grating. For triangular structures being much larger than the wavelength of light, the reflection properties are expected to be fully described by geometrical optics. However, geometrical optics do not account for the Goos−Hänchen (GH) shift, which is caused by the evanescent wave of the TIR. In this work, the reflection mechanism of DCRs is elucidated using the finite element method and a quantitative model built by considering the GH shift. The reduction in reflection of the DCR is dominated by diffraction of the evanescent wave at the corner of the triangular structure. Our model is based on simple mathematics and can optimize the DCR geometry for applications addressing a wide wavelength range such as radiative cooling.

8.1. Introduction

Asymmetric light transmission (ALT) is an optical phenomenon in which transmission differs for forward and backward illumination of a device. ALT has been mainly investigated for optical communications, but it may be applied to advance energy applications, such as radiative cooling. Radiative cooling can passively cool down an object below the ambient temperature by emitting thermal radiation in the mid-infrared range (MIR) to the cold outer space [1]. However, under high humidity, it is known that the cooling performance is severely degraded since the thermal emission to outer space is attenuated, and an additional heat transfer between the emitter and the atmosphere needs to be considered [2, 3]. Optical elements acting like ALT filters in the MIR range have recently been controversially discussed to counteract the cooling performance degradation under high humidity conditions. The fundamental idea of such a filter is to reflect the incoming atmospheric radiation while retaining the transmission of the outgoing thermal radiation [4, 5]. An experimental proof of the feasibility of such a filter has not been shown, and a complete theoretical analysis is also missing, especially with a full description of the mode-to-mode conversion [6, 7]. Further progress in this direction requires a thorough understanding of the optical properties of a suitable ALT filter, which, furthermore, should cover a broad wavelength range and work independently of the light polarization. Ultimately, for transitioning into a potential application, such an ALT filter needed to be simple and scalable to manufacture.

ALT can be achieved by optical non-reciprocity [8-11], planar chiral structures [12, 13], photonic crystals [14, 15], and hyperbolic metamaterials [16]. Those structures can show a high performance in ALT. However, they mainly operate only at a specific wavelength. Widening the operational wavelength of ALT has been achieved by designing grating structures [17-19]. ALT of grating structures is attributed to a difference in diffraction modes for the forward and backward illumination. In this case, the intensity of zeroth-order transmission is the same for both illuminations, limiting ALT performance. In addition, their structure requires precise control of the periodicity of the grating, which makes it challenging to produce a scalable device. A dielectric microsphere whose top is partially covered by a perfect light absorber has been proposed as an ALT structure with a more straightforward fabrication process [20]. The microsphere acts as a ball lens, which focuses the incoming light on one point. This focused light is absorbed by the perfect absorber, resulting in low transmission only for one way. The operational wavelength range of ALT can be controlled by adjusting the size of the microsphere. This ALT is not attributed to a diffraction mode at all. Therefore, the periodicity of the microspheres is not essential, providing a considerable fabrication tolerance. However, light absorption is not desirable for radiative cooling because light absorption increases the temperature of a system, which causes degradation in cooling performance.

One alternative structure for broadband ALT is a dielectric corner reflector (DCR) [5, 21]. The DCR is a film with a one-dimensional grating of a triangular structure. The DCR is composed of a relatively simple microstructure that can be made of a low-cost polymer by a mechanical stamping [22], enabling the production of large-area devices. The DCR can have high reflectance only when the light propagates into the DCR from the flat side. This is because a round-trip reflection, in which the light is reflected multiple times and its propagation direction is redirected backward, is made inside the triangular structure. The round-trip reflection is attributed to total internal reflections (TIRs) occurring at the surfaces of the triangular structure. The ALT of the DCR does not rely on either diffraction modes of the grating or light absorption. Therefore, a high-performance ALT for radiative cooling can be achieved. From a geometrical optics point of view, it is expected that the DCR can possess nearly perfect reflection in the MIR region by designing a triangular structure much larger than the wavelength. This is because the surfaces of the triangular structure can act as a reflective surface by TIR comparable to metallic surfaces. However, the reflectance of the DCR linearly decreases with an increase in the wavelength. This decrease occurs even though the triangular structure is sufficiently larger than the wavelength. Braginsky and Vyatchanin and Tarabrin suggested that evanescent waves created by TIRs could be diffracted at the downward corner of the triangular structure [23, 24]. Therefore, the reflectance can decrease even within the geometrical optics regime. This diffraction loss was theoretically estimated; however, Braginsky and Vyatchanin and Tarabrin just considered the whole field around the surface of the triangular structure but did not consider the direction of energy flux (EF) of the evanescent wave around the downward corner. In addition, their mathematical approach was too simplified compared to the diffraction of the evanescent wave created by the surface plasmon polaritons [25, 26]. Therefore, their simple analysis may lose a lot of important information describing the diffraction loss mechanisms.

In this work, the reflection mechanism of a DCR was theoretically investigated by building a quantitative model to fundamentally understand the inherent reflection reduction. We built the model by considering the following: (1) part of the incident light is shifted outside of the DCR by the Goos-Hänchen (GH) shift and (2) the energy of the incident light shifted outside is lost by diffraction of the evanescent wave. Reflection spectra of the DCR estimated using our model were in good agreement with reflection spectra obtained using the finite element method (FEM). Electric field distribution maps obtained from the FEM simulation demonstrated that the diffraction of the evanescent wave occurs at the downward corner of the triangular structure. Our model suggests that this diffraction occurs no matter how large the DCR is relative to the wavelength. Our analysis is not confined to a specific wavelength range, which enables us to

contribute to high-performance DCRs not only for radiative cooling but also for other applications requiring an ALT, such as silicon solar cells [27] and luminescent solar concentrators [28].

8.2. Goos-Hänchen shift

When the TIR reflects the light, the reflected light is laterally shifted from a point predicted by geometrical optics. This lateral shift is called the GH shift (Figure 8.1a). The amount of the shift was first formulated by Artmann [29]. He obtained the GH shift by mathematically treating the phase difference between the incident and reflected lights. His stationary-phase (SP) method gives the GH shift for TE and TM polarizations as

$$d_{\mathrm{GH(SP)}}^{\mathrm{TE}} = \frac{\lambda_0}{\pi n_1} \frac{\tan\theta}{\sqrt{\sin^2\theta - n^2}} \tag{8.1}$$

$$d_{\mathrm{GH(SP)}}^{\mathrm{TM}} = d_{\mathrm{GH(SP)}}^{\mathrm{TE}} \frac{n^2(1-n^2)}{n^4\cos^2\theta + \sin^2\theta - n^2} \tag{8.2}$$

where λ_0 is the wavelength in vacuum, θ is the incident angle, n is n_2/n_1, and n_1 and n_2 are refractive indices of an optically denser and less dense medium, respectively. Equations 8.1 and 8.2 are plotted in Figure 8.1b. After the SP method was proposed, Renard proposed an EF method [30]. This method is based on a consideration that the total EF of an evanescent wave created in an optically less dense medium (blue arrow in Figure 8.1a) must be conserved by the EF entering back into an optically denser medium (red arrow in Figure 8.1a). The EF method gives the GH shift as

$$d_{\mathrm{GH(EF)}}^{\mathrm{TE}} = \frac{\lambda_0}{\pi n_1} \frac{\sin\theta\cos\theta}{(1-n^2)\sqrt{\sin^2\theta - n^2}} \tag{8.3}$$

$$d_{\mathrm{GH(EF)}}^{\mathrm{TM}} = d_{\mathrm{GH(EF)}}^{\mathrm{TE}} \frac{n^2(1-n^2)}{n^4\cos^2\theta + \sin^2\theta - n^2} \tag{8.4}$$

Equations 8.3 and 8.4 are plotted in Figure 8.1b. It can be observed that there is a considerable discrepancy between the SP and EF methods at the incident angle far from the critical angle $\theta_c = \sin^{-1}(n_2/n_1)$. Yasumoto pointed out that this discrepancy occurs because the EF created by the interference between the incident and reflected light (yellow arrow in Figure 8.1a) is not considered in the EF method [31]. The GH shift calculated by considering both the evanescent wave and the interference coincides with the SP method [31, 32]. At the incident angle close to θ_c, the GH shift is dominated by the EF of the evanescent wave. In contrast, when the incident angle is far from θ_c, the GH shift is dominated by the EF of the interference. Based on an understanding of the GH shift, we will investigate the reflection properties of the DCR.

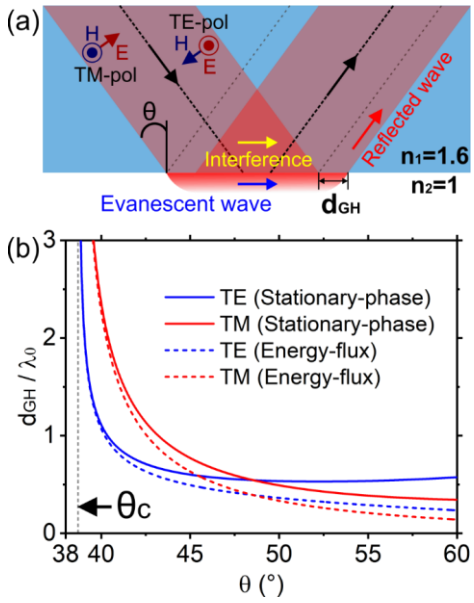

Figure 8.1. (a) Schematic illustration of the GH shift. The gray dashed lines show the reflected light path, predicted by geometrical optics. (b) GH shift calculated using the SP method and the EF method. The refractive indices of the optically denser and less dense medium are n_1 = 1.6 and n_2 = 1, respectively. The GH shift is normalized by the wavelength in vacuum.

8.3. DCRs in geometrical optics and nano-optics

8.3.1. Round-trip condition

Figure 8.2a shows a schematic of the DCR. We considered that the grating and triangular structures are infinitely large in the *x* and *z*-direction, respectively. The forward incidence is that the light illuminates on the structured side. In this case, the DCR has high transmission. For the backward incidence, in which the light illuminates on the DCR from the flat side, the DCR can have a high reflectance by the round-trip reflection. Figure 8.2b shows the cross-section of one grating period, consisting of an isosceles triangular structure with a width W and a base angle θ_b. In Figure 8.2b, two light paths inside the triangular structure are shown for backward incidence at the incident angle θ_{in}. For Path1, the light is reflected at Interface1 and goes to Interface2. Then, the light is reflected again at Interface2 and goes back to the flat side of the DCR. Path2 is in the opposite direction to Path1. We first consider the case of normal incidence, where $\theta_{in} = 0°$, to find the round-trip condition. In this case, Path1 and Path2 are now identical ($\theta_{11} = \theta_{22} = \theta_b$), meaning that only Path1 needs to be considered. The round-trip condition can be found using Snell´s law and taking into account the incident angles at each interface, which are θ_{11} and θ_{12} (Section 8.8.1, Supporting Information).

$$\theta_c < \theta_b < \frac{180° - \theta_c}{3} \qquad 8.5$$

From the round-trip condition, a refractive index of the DCR n_1 should be larger than 1.42 when the surrounding of the DCR is the air. The minimum of the condition is determined by θ_c. For our study, n_1 = 1.6 is considered, which conventional polymers, such as polystyrene, possess [33, 34]. In this case, θ_b can be in an angle range from 38.7° to 47.1° to satisfy the round-trip condition. (Figure 8.6b, Supporting Information).

When the light is incident on the DCR at an oblique angle, we have to find round-trip conditions for Path1 and Path2 separately. Figure 8.2c shows the round-trip condition for the oblique incidence. The yellow and blue shaded areas indicate the round-trip conditions for Path1 and Path2, respectively. The round-trip condition for oblique incidence can be satisfied in the area where those two areas overlap each other (Section 8.8.1, Supporting Information). When θ_b is 45°, the round-trip reflection can occur at an incident angle up to about 6° for n_1 = 1.6. In the experimental system, the refraction at the flat surface of the DCR has to be taken into account. In this case, the condition can be satisfied up to the incident angle of 10° (Figure 8.8b, Supporting Information). For simplicity, the flat surface of the DCR is ignored, and this refraction is not considered in further theoretical investigations. The propagation direction of the light after the round-trip reflection, denoted by θ_{out} in Figure 8.2b, can be found in Section 8.8.1, Supporting Information. θ_{out} is equal to θ_{in} when θ_b is 45°, meaning that the DCR can act as a retroreflector [35, 36].

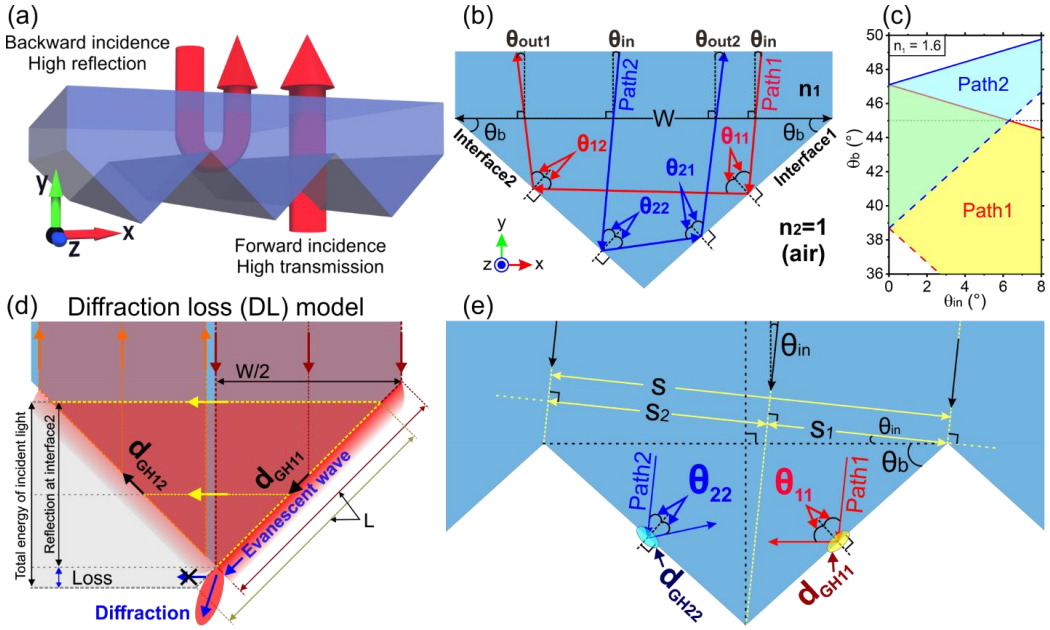

Figure 8.2. (a) Illustration of the DCR. (b) Schematic illustration of the cross-section of the DCR. The red and blue lines indicate the light paths inside the triangular structure. (c) Round-trip condition at oblique incidence for n_1 = 1.6. (d) Schematic illustration of the diffraction loss (DL) model. The red shaded area shows the light traveling along Path1 in (b). The dark red, yellow, and orange arrows indicate that the incident light strikes on Interface1, the light reflected at Interface1 and traveling to Interface2, and the light reflected at Interface2, respectively. The gray shaded area shows an imaginary path of the reflected light indicated by the yellow arrows if Interface1 was infinitely long and if there was no reflection at Interface2. (e) DL model for oblique incidence.

8.3.2. DL model

By considering the GH shift and the geometry of the triangular structure, we investigate the reflection mechanism of the DCR in detail using Figure 8.2d. First, we only consider Path1 for normal incidence and assume that the plane wave strikes only one-half of the triangular structure (red arrows in Figure 8.2d). As mentioned earlier, the incident angle at Interface1 θ_{11} is equal to θ_b when θ_{in} = 0°. The center of the reflected light is laterally shifted on Interface1 by the GH shift d_{GH11}. However, Interface1 is not infinite. Therefore, the amount of the reflected light´s energy, which is determined by the GH shift d_{GH11}, cannot completely come back into the structure (blue arrows in Figure 8.2d). According to the physical mechanism of the GH shift mentioned earlier, this energy is related to the evanescent wave propagating in the optically less dense

medium. From the research on propagating surface plasmon, it has been known that a propagating evanescent wave can be diffracted at the corner of the metal film [25, 26]. A similar diffraction scenario is expected for the DCR because the evanescent wave still has an EF at the downward corner of the triangular structure. In addition, the EF created by the interference between the incident and reflected lights is also attributed to the GH shift. This amount of energy may also be diffracted at the downward corner. The rest of the incident light reaches Interface2 (yellow arrows in Figure 8.2d) and is reflected at Interface2 by the TIR (orange arrows in Figure 8.2d). The GH shift d_{GH12} occurs at Interface2, but the EF of either the evanescent wave or the interference is not toward the downward corner. Therefore, all the energy of the light reflected at Interface2 can go back into the triangular structure. Consequently, we expect a fraction of the incident energy to be lost by the diffraction governed by d_{GH11} during one cycle of the round-trip reflection. The same process happens for Path2. From this diffraction loss (DL) model, the reflectance of the DCR can be estimated by using the ratio of d_{GH11} to the side length of the triangular structure L. The DL model gives the reflectance of the DCR for normal incidence as

$$R_{\mathrm{n}} = 1 - \frac{d_{\mathrm{GH11}}}{L} \tag{8.6}$$

For oblique incidence, a different amount of energy is lost during the round-trip reflection in Path1 and Path2 because the incident angles $\theta_{11} = \theta_{\mathrm{b}} + \theta_{\mathrm{in}}$ and $\theta_{22} = \theta_{\mathrm{b}} - \theta_{\mathrm{in}}$ are different, resulting in $d_{GH11} \neq d_{GH22}$. When light is normally incident on the DCR, the energy of the incident light on Interface1 is equal to that on Interface2. However, for oblique incidence, the energy of the incident light striking on Interface1 and Interface2 is different (Figure 8.2e). This has to be taken into account in the DL model by considering the cross-section of the incident light entering a single triangular structure. The cross-section of the incident light can be expressed as $s = W\cos\theta_{\mathrm{in}}$. The cross-section of the incident light that goes to Interface1 is $s_1 = L\cos(\theta_{\mathrm{b}} + \theta_{\mathrm{in}})$, and the rest goes to Interface2. Therefore, the reflectance of the DCR for oblique incidence can be estimated by

$$R_{\mathrm{o}} = R_{\mathrm{o1}} + R_{\mathrm{o2}} = \frac{s_1}{s}\left(1 - \frac{d_{\mathrm{GH11}}}{L}\right) + \frac{s_2}{s}\left(1 - \frac{d_{\mathrm{GH22}}}{L}\right) \tag{8.7}$$

where R_{o1} and R_{o2} are the reflectance for Path1 and Path2, respectively. Equation 8.7 coincides with Equation 8.6 when $\theta_{\mathrm{in}} = 0°$. The DL model shows that a lossless reflection cannot be obtained because the GH shift cannot be zero even if the triangular structure was sufficiently larger than the wavelength. It has to be mentioned that, for Path2, part of the light reflected at Interface2 (R_{22}) does not strike on Interface1. However, R_{22} points to the flat top surface of the DCR. Therefore, R_{22} is not lost and is counted in the total reflectance of the DCR (Section 8.8.1, Supporting Information).

8.4. Results and discussion

8.4.1. DL model with SP and EF methods

We investigate the reflection properties of the DCR for backward incidence with TM polarization using the FEM (see Section 8.6, Method). In this investigation, reflection and refraction occurring at the flat top surface of the DCR are ignored. We also used the DL model to gain insight into reflection mechanism of the DCR. Reflection spectra are plotted as a function of the normalized unit of λ_0/L.

First, we compare the DL model (Equation 8.6) with the SP method (Equation 8.2) and that with the EF method (Equation 8.4) to understand which method can properly describe the reflection of the DCR. Figure 8.3a shows the reflection spectra of the DCR with $n_1 = 1.6$ and $\theta_{\mathrm{b}} = 45°$ at the incident angle of $\theta_{\mathrm{in}} = 0°$. The dashed lines are spectra calculated by the FEM simulation. The black and red solid lines are

calculated using the DL model with the SP and EF methods, respectively. There is a difference in spectral shape between the FEM and the DL model because the FEM considers the grating effect [21], but the DL model does not. In terms of how reflectance decreases with an increase in the wavelength, it can be found that the DL model with the SP method is in good agreement with the FEM simulation. When the EF method is used in the DL model, the reflectance is slightly overestimated, indicating that the evanescent wave's energy and the energy created by the interference are lost by diffraction. From this result, we use only the SP method for further investigations.

8.4.2. λ_0/L and n_1 dependencies

The reflectance of the FEM approximately linearly decreases with an increase in the wavelength for a fixed L (Figure 8.3a). Our DL model indicates that this linear decrease in reflectance is attributed to the GH shift being proportional to the wavelength. For a fixed wavelength, the reflectance can be higher for a large L since the reflection reduction of the DCR is inversely proportional to L (Equation 8.6). We are interested in the high reflectance of the DCR; therefore, we focus on a region of λ_0/L in which the reflectance can exceed 80 %. In Figure 8.3b, the n_1 dependence of the reflection of the DCR is examined by changing n_1 in a range where the round-trip condition is satisfied. For those spectra, other parameters are fixed as $\theta_b = 45°$ and $\theta_{in} = 0°$. The DL model shows a good agreement with the FEM for all n_1. Since the GH shift is small for large n_1 and less energy is lost by the diffraction, the reflectance is higher when n_1 is larger. From the λ_0/L and n_1 dependencies, we conclude that a DCR with large L and large n_1 can possess strong reflection. However, an increase in L increases the size of the structure, which is undesirable for some applications requiring a compact system. In addition, increasing n_1 is not straightforward in experimental systems [37]. Therefore, it is required to find an optimum combination of L and n_1 to achieve a high-performance DCR.

8.4.3. θ_b dependence

Figure 8.3c shows reflection spectra calculated for different θ_b with $n_1 = 1.6$ and $\theta_{in} = 0°$. For this calculation, L is fixed, and W is changed with the change in θ_b. The GH shift decreases with an increase in the incident angle (Figure 8.1b) so that the DCR with higher θ_b can possess a higher reflectance. However, the round-trip condition can be satisfied in a smaller incident angle range for larger θ_b (Figure 8.2c); therefore, there is a trade-off between higher reflectance and the incident angle insensitivity. This trade-off can be compensated just by increasing L. When θ_b is larger, the DL model shows good agreement with the FEM. However, the DL model cannot reproduce the results from the FEM when θ_b is close to θ_c. This is because neither the SP nor the EF methods can explain the GH shift around θ_c.

8.4.4. Influence of the GH shift around θ_c

The GH shifts derived by Equations 8.1-8.4 diverge at θ_c (Figure 8.1b). However, when the incident light is a beam, such as a Gaussian beam, the GH shift has a maximum value at slightly greater than θ_c because of angular distribution in wave vector components of the incident beam. In the case of the DCR, we consider a plane wave as the incident light. In this case, diffraction occurs when the light strikes on the upward corners of the DCR (Figure 8.3d) [38]. Therefore, the incident light on the triangular structure's surfaces is no longer a plane wave. The GH shift around θ_c was formulated using the Weber function [39, 40] or modified Bessel function [41] for the Gaussian beam. Using the modified Bessel function [41], the GH shift for TE and TM polarizations is

$$d_{\mathrm{GH(CA)}}^{\mathrm{TE}} = \frac{1}{\cos\theta}\sqrt{\frac{\pi\tan\theta}{2\sqrt{2}n_1}}S\left[\frac{kw_0\sigma_0}{2\sqrt{2}}\right]\sqrt{\frac{w_0}{k}} \quad 8.8$$

$$d_{\mathrm{GH(CA)}}^{\mathrm{TM}} = \frac{d_{\mathrm{GH(CA)}}^{\mathrm{TE}}}{n_1^2\sin^2\theta - \cos^2\theta} \quad 8.9$$

where

$$\sigma_0 = \frac{1 - n_1^2\sin^2\theta}{n_1\sin 2\theta}$$

$$S[x] = e^{-x^2}\sqrt{|x|}\left[\mathrm{I}_{-\frac{1}{4}}(x^2) - \mathrm{sgn}(x)\mathrm{I}_{\frac{1}{4}}(x^2)\right]$$

w_0 is the beam waist of the Gaussian beam, k is the angular wavenumber expressed as $2\pi/\lambda_0$, and $\mathrm{I}_v(x)$ is the modified Bessel function of the first kind. Equations 8.8 and 8.9 hold in a limitation of $kw_0 >> 1$. Equations 8.8 and 8.9 are plotted in Figure 8.3e for different ratios of w_0/λ_0. Compared to the SP method, those equations have a different line shape around θ_c but coincide with the SP method at the incident angle far from θ_c. With a decrease in w_0/λ_0, the maximum of the GH shift decreases and slightly shifts to a larger θ. Since the GH shift around θ_c is influenced by the angular distribution of wave vector components, the diffraction pattern at the upward corners of the DCR has to be carefully investigated for detailed analysis. However, for our phenomenological investigation, we use Equations 8.8 and 8.9 because the GH shift at around θ_c shows a similar line shape for different angular distributions, for example, for the case of the single-slit diffraction beam [40, 41]. The beam waist determines the angular distribution of wave vector components in the Gaussian beam, so we use w_0 as a parameter that determines the diffraction pattern of the upward corners of the triangular structure.

In Figure 8.3c, the blue dashed-dotted line shows the reflection spectra estimated by the DL model using Equation 8.9 with w_0 determined by $w_0/L \approx 1.7$. In this case, the DL model shows a similar trend to the FEM. We can understand why the reflectance does not linearly decrease for $\theta_b = 39°$ by considering the wavelength dependence of plane wave diffraction at the upward corners. Diffraction is weaker for smaller wavelengths, resulting in a larger GH shift. However, diffraction becomes stronger for longer wavelengths, and the GH shift becomes smaller. Therefore, the slope of the reflection spectrum is steeper in the shorter wavelength range, but the slope becomes gradually less steep with an increase in the wavelength.

8.4.5. Oblique incidence

Considering the GH shift around θ_c, the reflection properties of the DCR at oblique incidence are investigated using the DL model in Equation 8.7. Figure 8.3f shows the reflection spectrum of the DCR with $n_1 = 1.6$ and $\theta_b = 45°$. The incident angle is $\theta_{in} = 6°$, which is the upper limit of the incident angle that can satisfy the round-trip condition (see Figure 8.2c). In this case, the incident light's energy on Interface1 and Interface2 is different, determined as $s_1/s \approx 0.45$ and $s_2/s \approx 0.55$, respectively. In addition, the incident angles at Interface1 for Path1 and at Interface2 for Path2 are different. The incident angle θ_{11} is 51° at Interface1 for Path1. θ_{11} is much larger than θ_c. Therefore, the SP method can be used for d_{GH11} in the DL model. The incident angle θ_{22} is 39° at Interface2 for Path2. θ_{22} is now close to θ_c, so d_{GH22} should be expressed using Equation 8.9. w_0 is used again as a fitting parameter. When $w_0/L \approx 1.7$, the DL model shows good agreement with the FEM. For Path1, the reflectance linearly and slowly decreases with an increase in the wavelength because the GH shift is small for the incident angle of 51° (Figure 8.1b). For Path2, the reflectance decreases nonlinearly with an increase in the wavelength because θ_{22} is close to θ_c. The

reflectance for Path1 is higher than that for Path2 even though $s_1/s < s_2/s$ because d_{GH11} is much smaller than d_{GH22}. Overall, our proposed DL model is robust for any combinations of the structural parameters of the DCR, and the DL model can consider the incident angle dependence of the DCR.

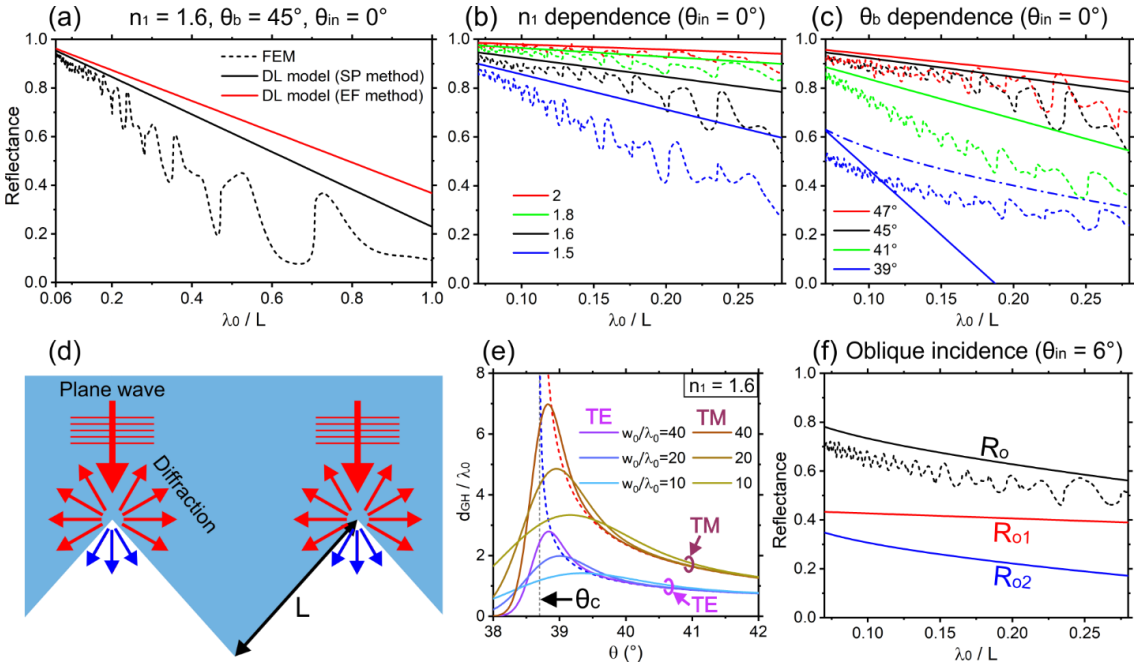

Figure 8.3. For (a – c), the dashed lines are reflection spectra calculated by the FEM simulation. The solid lines are calculated by the DL model (Equation 8.6) using the SP method (Equation 8.2). The incident light is TM polarized. Only backward incidence is considered. (a) Reflectance of the DCR with $n_1 = 1.6$ and $\theta_b = 45°$ at $\theta_{in} = 0°$. The red solid line is calculated by the DL model using the EF method. (b) n_1 dependence. θ_b and θ_{in} are 45° and 0°, respectively. The red, green, black, and blue lines are for $n_1 = 2$, 1.8, 1.6, and 1.5, respectively. (c) θ_b dependence for the DCR with $n_1 = 1.6$ and $\theta_{in} = 0°$. L is fixed and W changes according to θ_b. The red, black, green, and blue lines are for θ_b is 47°, 45°, 41°, and 39°, respectively. The blue dashed-dotted line is calculated using the DL model with Equation 8.9. w_0 is determined so that w_0/L becomes about 1.7. (d) Schematic illustration of the plane wave diffracted at the triangular structure's upward corners. (e) GH shift at around θ_c, which is given by Equations 8.8 and 8.9 for TE and TM polarizations. The blue and red dashed lines are the SP method, found in Figure 8.1b. (f) Reflection spectra for $n_1 = 1.6$, $\theta_b = 45°$, and $\theta_{in} = 6°$. The reflection spectra obtained from the DL model for Path1 (R_{o1}) and Path2 (R_{o2}) are the red and blue lines, respectively. R_{o1} and R_{o2} are calculated using Equation 8.7 with Equation 8.2 and with Equation 8.9, respectively. The black solid is the sum of the red and blue solid lines.

8.4.6. Polarization dependence and transmission for forward incidence

The same investigations are made for TE polarization (Figure 8.10, Supporting Information). The DL model also shows good agreement with the FEM for TE polarization. The DCR has the same reflection properties for TE and TM polarizations. The GH shift for TE polarization is smaller than that for TM polarization when the incident angle is smaller than about 48° (Figure 8.1b). Therefore, the reflectance is higher for TE polarization for normal incidence. For the DCR with θ_b close to θ_c, the same fitting made in Figure 8.3c was employed for TE polarization using w_0 as a fitting parameter. The fitting resulted in $w_0/L \approx 3.5$, which is significantly different from that for TM polarization. To understand the physical meaning of those values, the polarization dependence of the diffraction pattern created by upward corners of the DCR has to be investigated in detail.[38]

Compared with TE polarization, the FEM and the DL model difference is larger for TM polarization for all reflection spectra. The diffraction at the upward corner may contribute to this discrepancy. Our analysis suggested that the value of w_0 can be smaller for TM polarization, meaning that the diffraction at the upward corner is more substantial for TM polarization. If the diffraction is strong, more incident light may go outside the DCR (blue arrows in Figure 8.3d), which the DL model does not consider.

The transmission properties of the DCR for the forward incidence can be found in Figure 8.12, Supporting Information. The transmission was calculated without taking the reflection and refraction at the flat surface of the DCR into account. The transmission is > 90 % for normal and oblique incidence for TM and TE polarizations. Since the DCR has a high reflectance for backward incidence, it can act as a high-performance broadband ALT filter in a specific incident angle range.

8.4.7. Diffraction of evanescent waves

For a better insight into the reflection mechanisms of the DCR, electric field distribution maps for TM and TE polarizations were obtained using the FEM. The top row of Figure 8.4 shows the field maps of the DCR with $n_1 = 1.6$ for TM polarization at $\lambda_0/L \approx 0.07$. For the DCR with $\theta_b = 45°$ and $\theta_{in} = 0°$ (Figure 8.4a), the electric field is confined inside the DCR, which attributes to the high reflectance. The GH shift for $\theta_b = 45°$ is not large, so the diffraction of the evanescent wave at the downward corner is not significant. Figure 8.4b shows the field map of the DCR with $\theta_b = 39°$. The incident angle is 0°. Compared to $\theta_b = 45°$, the electric field at the interfaces of the triangular structure is stronger because the penetration depth of the evanescent wave is larger for the incident angle close to θ_c. Interestingly, strong electric fields in the air region lower than the downward corner can be found. These fields are attributed to the diffraction of the evanescent wave. Figure 8.4c shows the field map for the DCR with $\theta_b = 45°$ and $\theta_{in} = 6°$. In this configuration, the incident angles at Interface1 and Interface2 are 51° and 39°, respectively. At interface1, the incident angle is much higher than θ_c, resulting in a weak evanescent wave. On the other hand, the incident angle at Interface2 is close to $\theta_{c,}$ so the evanescent wave is strong. Therefore, the diffraction of evanescent waves can be observed only along Interface2. This field map confirms why the reflectance is smaller for Path2, as shown in Figure 8.3f. The bottom row of Figure 8.4 shows the field maps for TE polarization, which are similar to those for TM polarization. This is because, as mentioned earlier, the DCR has almost the same reflection properties for both polarizations. The field maps at large λ_0/L can be found in Section 8.8.2, Supporting Information. In all cases, more energy of the incident light reaches outside of the triangular structure because the reflection reduction of the DCR is proportional to λ_0/L.

We must mention the diffraction of the EF created by the interference between incident and reflected lights, which cannot be observed in the field maps. Since the contribution of the interference on the GH shift is small compared to the evanescent wave (Figure 8.1b), we conclude that the diffraction of the evanescent wave dominates the reduction in reflection of the DCR. To understand the mechanism of diffraction loss by the GH shift, a more detailed mathematical analysis is required by considering the EF of electromagnetic waves inside and outside the triangular structure [42].

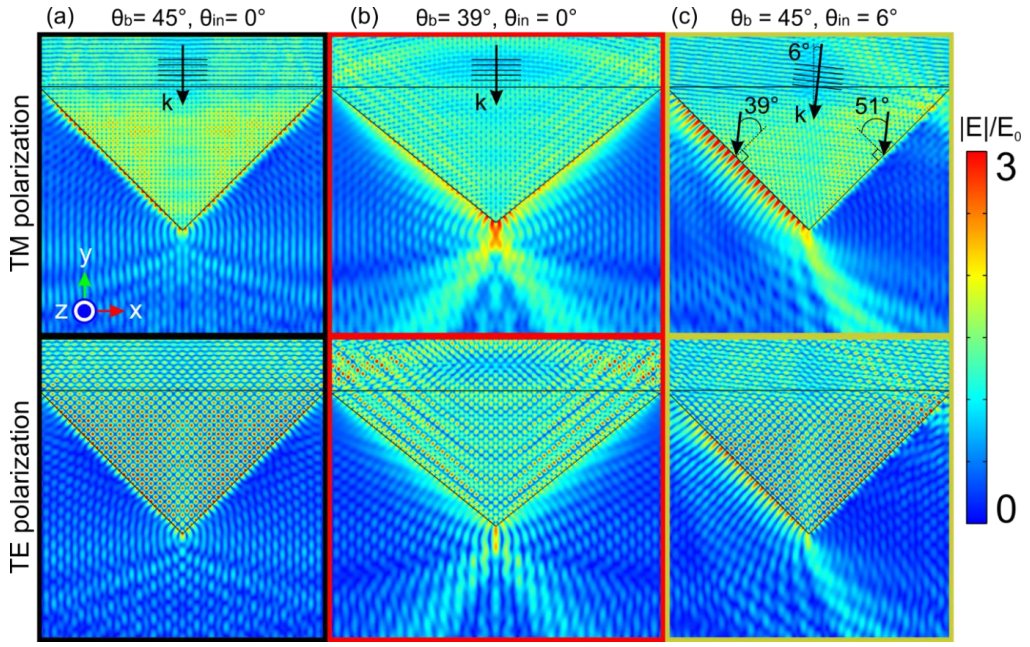

Figure 8.4. Color maps of the absolute value of electric field distribution at $\lambda_0/L \approx 0.07$ for (a) $\theta_b = 45°$ and $\theta_{in} = 0°$, (b) $\theta_b = 39°$ and $\theta_{in} = 0°$, and (c) $\theta_b = 45°$ and $\theta_{in} = 6°$. n_1 and n_2 are 1.6 and 1, respectively. The incident light is (top row) TM and (bottom row) TE polarized.

8.4.8. Optimization of the DCR

Next, we discuss how to optimize the DCR for high reflectance in a specific wavelength range using the DL model. As mentioned earlier, the reflectance of the DCR linearly decreases with increasing wavelength. Therefore, we only have to consider the reflectance at the maximum of the wavelength range λ_{max} to find an optimum size of the DCR. For example, if the DCR has to have a reflectance higher than 90% in a wavelength range shorter than λ_{max} for normal incidence and unpolarized light, we can find an optimum W of the DCR with arbitrary n_1 and θ_b using Equation 8.6

$$1 - \frac{d^{TE}_{GH(SP)}|_{\lambda_0=\lambda_{max}} + d^{TM}_{GH(SP)}|_{\lambda_0=\lambda_{max}}}{2L} \geq 0.9 \qquad 8.10$$

Since the GH shift is large at around θ_c, a DCR with $\theta_b \approx \theta_c$ cannot possess a high reflectance. Also, the expression of the GH shift around θ_c is relatively complicated. Therefore, for simplicity, θ_b close to θ_c is not considered, and only the SP method is used in Equation 8.10. From Equation 8.10, when $n_2 = 1$, W should be

$$\frac{W}{\lambda_{max}} \geq \frac{10 \sin\theta_b}{\pi\sqrt{n_1^2 \sin^2\theta_b - 1}}\left(1 + \frac{1}{n_1^2 \sin^2\theta_b - \cos^2\theta_b}\right) \qquad 8.11$$

$L = W/2\cos\theta_b$ was used to derive Equation 8.11. Figure 8.5 shows Equation 8.11 in the round-trip condition for normal incidence (Equation 8.5). The SP method diverges at θ_c, so Equation 8.11 was calculated for θ_b larger than $\theta_c + 1°$. W/λ_{max} is smaller for larger n_1 and larger θ_b because the GH shift becomes smaller. The DCR can be optimized efficiently by determining n_1 and θ_b depending on applications and finding W from Figure 8.5. For radiative cooling, high reflectance in a wide incident angle range is expected so that 45° is an optimum angle for θ_b (Figure 8.2c). For example, in the case of $n_1 = 1.6$ and $\theta_b = 45°$, W/λ_{max} is 9.7. Since many polymers have a refractive index lower than 1.6 [33, 34], it can be found that the DCR made of a

polymer is required to be $W/\lambda_{max} > 9.7$ for reflectance higher than 90%. It should be mentioned that, as can be seen in Figure 8.3, the DL model slightly overestimates the reflectance of the DCR. Therefore, the DCR has to be slightly larger than the W estimated by Equation 8.11.

Besides the structural optimization shown in Figure 8.5, a challenge for using such DCR structures as filters for radiative cooling applications is their sensitivity to the incident angle (Figure 8.2c). As outlined in Section 1, the feasibility of their ALT properties is also controversially debated until now [4-7]. Our improved understanding of the reflection mechanism of a DCR enabled us to reassess their contribution to radiative cooling. Our simplified mode-to-mode conversion analysis indicates a potential positive effect (Section 8.8.3, Supporting Information). However, it also requires further analysis to take all contributions into account.

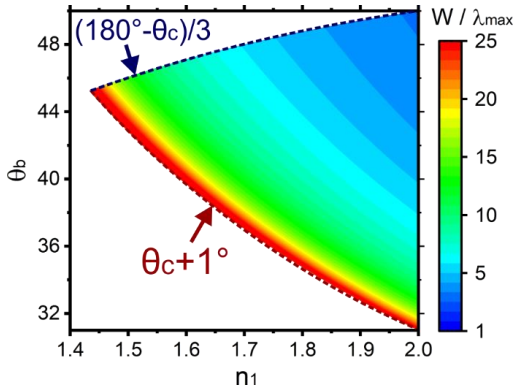

Figure 8.5. Size optimization of the DCR for reflectance higher than 90% in a wavelength range shorter than λ_{max}.

8.5. Conclusion

We have revealed the reflection mechanism of a DCR by using the DL model. From the DL model, we found that the reflectance of the DCR can be estimated just by considering the GH shift and the geometry of the triangular structure. The reflection spectra of the DCR were calculated using the FEM for different structural parameter combinations, which were compared with the spectra estimated by the DL model. Even though the DL model does not require any complicated mathematics, the DL model showed good agreement with the FEM. From the comparison, we revealed that the reflectance linearly decreases with an increase in the wavelength because the GH shift is proportional to the wavelength. We obtained the electric field distribution maps using the FEM and demonstrated that the diffraction of the evanescent wave occurs at the downward corner of the triangular structure. Since the GH shift does not become zero even though the triangular structure is significantly larger than the wavelength, this diffraction causes the intrinsic reflection reduction of the DCR.

In addition to radiative cooling, the DL model is useful to optimize the DCR efficiently for its potential applications, such as silicon solar cells [27], luminescent solar concentrators [28], non-contact temperature sensors [22], and free-space optical communications [43, 44]. Furthermore, our work may be essential to better understand light-matter interactions in other systems. For example, recently, coloration has been achieved by hemispherical dielectric microstructures [45-47]. The coloration is attributed to the round-trip reflection by TIRs and light interference occurring inside the microstructure. Geometrical optics explained this coloration mechanism. However, since TIR plays a pivotal role in this coloration mechanism, the GH

shift and the diffraction of evanescent waves may also contribute to the reflected spectrum. Therefore, we expect that our DL model provides a deeper insight into the coloration mechanism of those microstructures.

8.6. Method

FEM simulation: The optical properties of the DCR for the forward and backward incidence were investigated using COMSOL multiphysics, a commercial software package based on the FEM. The simulation model of the DCR was built in two dimensions. Figure 8.2b is a unit cell of the simulation model. The periodic boundary condition was applied to the *x*-direction to consider the infinitely long grating. The periodicity is the same as the width of the triangular structure. The film part of the DCR, which is on top of the triangular structure, was considered infinitely thick to remove noise from the Fabry-Perot resonance. The perfectly matched layers were applied on the top and bottom of the model in the *y*-direction. To obtain total reflectance and transmittance, not only zeroth-order but also all higher-order diffraction modes were taken into account. The incident light is a plane wave with either TE (the electric field is along the *z*-direction) or TM (the magnetic field is along the *z*-direction) polarization.

Funding

This project has received funding from the European Research Council (ERC) under the European Union's Horizon 2020 research and innovation program (grant agreement no. 714968).

8.7. References

1. B. Zhao, M. Hu, X. Ao, N. Chen, and G. Pei, "Radiative cooling: A review of fundamentals, materials, applications, and prospects," Appl. Energy **236**, 489-513 (2019).
2. C. Y. Tso, K. C. Chan, and C. Y. H. Chao, "A field investigation of passive radiative cooling under Hong Kong's climate," Renewable Energy **106**, 52-61 (2017).
3. M. Dong, N. Chen, X. Zhao, S. Fan, and Z. Chen, "Nighttime radiative cooling in hot and humid climates," Opt. Express **27** (22), 31587-31598 (2019).
4. R. Y. M. Wong, C. Y. Tso, C. Y. H. Chao, B. Huang, and M. P. Wan, "Ultra-broadband asymmetric transmission metallic gratings for subtropical passive daytime radiative cooling," Solar Energy Materials and Solar Cells **186**, 330-339 (2018).
5. M. Wei, W. Wu, D. Li, H. Xu, Y. Lu, and W. Song, "Universal strategy for all-weather and all-terrain radiative cooling with non-reciprocal mid-infrared windows," Solar Energy **207**, 471-478 (2020).
6. X. Wu, and C. Wang, "The application of asymmetric transmission in daytime radiative cooling cannot increase the cooling power," Solar Energy Materials and Solar Cells **215** (2020).
7. G. Ulpiani, G. Ranzi, J. Feng, and M. Santamouris, "Expanding the applicability of daytime radiative cooling: Technological developments and limitations," Energy and Buildings **243** (110990), 110990 (2021).
8. A. B. Khanikaev, S. H. Mousavi, G. Shvets, and Y. S. Kivshar, "One-way extraordinary optical transmission and nonreciprocal spoof plasmons," Phys. Rev. Lett. **105** (12), 126804 (2010).

9. M. Lawrence, D. R. Barton, 3rd, and J. A. Dionne, "Nonreciprocal Flat Optics with Silicon Metasurfaces," Nano Lett. **18** (2), 1104-1109 (2018).

10. D. Jalas, A. Petrov, M. Eich, W. Freude, S. Fan, Z. Yu, R. Baets, M. Popović, A. Melloni, J. D. Joannopoulos, M. Vanwolleghem, C. R. Doerr, and H. Renner, "What is — and what is not — an optical isolator," Nat. Photonics **7** (8), 579-582 (2013).

11. S. Fan, R. Baets, A. Petrov, Z. Yu, J. D. Joannopoulos, W. Freude, A. Melloni, M. Popovic, M. Vanwolleghem, D. Jalas, M. Eich, M. Krause, H. Renner, E. Brinkmeyer, and C. R. Doerr, "Comment on "Nonreciprocal light propagation in a silicon photonic circuit"," Science **335** (6064), 38; author reply 38 (2012).

12. A. S. Schwanecke, V. A. Fedotov, V. V. Khardikov, S. L. Prosvirnin, Y. Chen, and N. I. Zheludev, "Nanostructured metal film with asymmetric optical transmission," Nano Lett. **8** (9), 2940-2943 (2008).

13. R. Singh, E. Plum, C. Menzel, C. Rockstuhl, A. K. Azad, R. A. Cheville, F. Lederer, W. Zhang, and N. I. Zheludev, "Terahertz metamaterial with asymmetric transmission," Phys. Rev. B **80** (15), 153104 (2009).

14. C. Wang, C. Z. Zhou, and Z. Y. Li, "On-chip optical diode based on silicon photonic crystal heterojunctions," Opt. Express **19** (27), 26948-26955 (2011).

15. C. Wang, X. L. Zhong, and Z. Y. Li, "Linear and passive silicon optical isolator," Sci. Rep. **2**, 674 (2012).

16. T. Xu, and H. J. Lezec, "Visible-frequency asymmetric transmission devices incorporating a hyperbolic metamaterial," Nat. Commun. **5**, 4141 (2014).

17. B. Tang, Z. Li, Z. Liu, F. Callewaert, and K. Aydin, "Broadband asymmetric light transmission through tapered metallic gratings at visible frequencies," Sci. Rep. **6**, 39166 (2016).

18. A. Ozer, H. Kocer, and H. Kurt, "Broadband and polarization-independent asymmetric transmission of visible light through a three-dimensional trapezoidal metallic metasurface," J. Opt. Soc. Am. B **35** (9), 2111-2117 (2018).

19. R. Zhu, X. Wu, Y. Hou, G. Zheng, J. Zhu, and F. Gao, "Broadband Asymmetric Light Transmission at Metal/Dielectric Composite Grating," Sci. Rep. **8** (1), 999 (2018).

20. A. Ghobadi, S. A. Dereshgi, B. Butun, and E. Ozbay, "Ultra-broadband Asymmetric Light Transmission and Absorption Through The Use of Metal Free Multilayer Capped Dielectric Microsphere Resonator," Sci. Rep. **7** (1), 14538 (2017).

21. G. Bose, I. Vartiainen, M. Roussey, M. Kuittinen, J. Tervo, and J. Turunen, "Dielectric V-ridge gratings: transition from antireflection to retroreflection," Appl. Opt. **56** (11), 3004-3009 (2017).

22. M. W. Khalid, R. Ahmed, A. K. Yetisen, and H. Butt, "Flexible corner cube retroreflector array for temperature and strain sensing," RSC Adv. **8** (14), 7588-7598 (2018).

23. V. B. Braginsky, and S. P. Vyatchanin, "Corner reflectors and quantum-non-demolition measurements in gravitational wave antennae," Phys. Lett. A **324** (5-6), 345-360 (2004).

24. S. P. Tarabrin, "An approximate analysis of the diffraction losses in corner reflectors," Moscow University Physics Bulletin **62** (2), 81-85 (2007).

25. V. B. Zon, "Reflection, refraction, and transformation into photons of surface plasmons on a metal wedge," J. Opt. Soc. Am. B **24** (8), 1960-1967 (2007).

26. I. A. Kotelnikov, V. V. Gerasimov, and B. A. Knyazev, "Diffraction of a surface wave on a conducting rectangular wedge," Phys. Rev. A **87** (2), 023828 (2013).

27. A. Gaucher, A. Cattoni, C. Dupuis, W. Chen, R. Cariou, M. Foldyna, L. Lalouat, E. Drouard, C. Seassal, I. C. P. Roca, and S. Collin, "Ultrathin Epitaxial Silicon Solar Cells with Inverted Nanopyramid Arrays for Efficient Light Trapping," Nano Lett. **16** (9), 5358−5364 (2016).

28. V. Oliveto, and D.-A. Borca-Tasciuc, "Broadband asymmetric light transmission interfaces for luminescent solar concentrators," Nanoscale Adv. **3** (12), 3627-3633 (2021).

29. K. Artmann, "Berechnung der Seitenversetzung des totalreflektierten Strahles," Annalen der Physik **437** (1-2), 87-102 (1948).

30. R. H. Renard, "Total Reflection: A New Evaluation of the Goos–Hänchen Shift," J. Opt. Soc. Am. **54** (10), 1190-1197 (1964).

31. K. Yasumoto, and Y. Ōishi, "A new evaluation of the Goos–Hänchen shift and associated time delay," J. Appl. Phys. **54** (5), 2170-2176 (1983).

32. X. Chen, X. J. Lu, P. L. Zhao, and Q. B. Zhu, "Energy flux and Goos-Hanchen shift in frustrated total internal reflection," Opt. Lett. **37** (9), 1526-1528 (2012).

33. X. Zhang, J. Qiu, X. Li, J. Zhao, and L. Liu, "Complex refractive indices measurements of polymers in visible and near-infrared bands," Appl. Opt. **59** (8), 2337-2344 (2020).

34. X. Zhang, J. Qiu, J. Zhao, X. Li, and L. Liu, "Complex refractive indices measurements of polymers in infrared bands," Journal of Quantitative Spectroscopy and Radiative Transfer **252**, 107063 (2020).

35. A. Lundvall, F. Nikolajeff, and T. Lindstrom, "High performing micromachined retroreflector," Opt. Express **11** (20), 2459-2473 (2003).

36. A. Arbabi, E. Arbabi, Y. Horie, S. M. Kamali, and A. Faraon, "Planar metasurface retroreflector," Nat. Photonics **11** (7), 415-420 (2017).

37. T. Higashihara, and M. Ueda, "Recent Progress in High Refractive Index Polymers," Macromolecules **48** (7), 1915-1929 (2015).

38. G. Gennarelli, and G. Riccio, "Plane-wave diffraction by an obtuse-angled dielectric wedge," J. Opt. Soc. Am. A Opt. Image. Sci. Vis. **28** (4), 627-632 (2011).

39. B. R. Horowitz, and T. Tamir, "Lateral Displacement of a Light Beam at a Dielectric Interface," J. Opt. Soc. Am. **61** (5), 586-594 (1971).

40. H. M. Lai, F. C. Cheng, and W. K. Tang, "Goos–Hänchen effect around and off the critical angle," J. Opt. Soc. Am. A **3** (4), 550-557 (1986).

41. M. P. Araújo, S. De Leo, and G. G. Maia, "Closed-form expression for the Goos-Hänchen lateral displacement," Phys. Rev. A **93** (2), 023801 (2016).

42. H. M. Lai, C. W. Kwok, Y. W. Loo, and B. Y. Xu, "Energy-flux pattern in the goos-Hanchen effect," Phys. Rev. E Stat. Phys. Plasmas Fluids Relat. Interdiscip. Topics **62** (5 Pt B), 7330-7339 (2000).

43. H. Jia, H. Yin, H. Zhang, X. Wang, S. Chang, and J. Yang, "Study on the heterodyning scattering of retroreflective free-space optical communication with optical heterodyning," J. Opt. Soc. Am. A Opt. Image. Sci. Vis. **30** (11), 2286-2290 (2013).

44. G. Yang, S. You, M. Bi, B. Fan, Y. Lu, X. Zhou, J. Li, H. Geng, and T. Wang, "Wave-optics simulation of the double-pass beam propagation in modulating retro-reflector FSO systems using a corner cube reflector," Appl. Opt. **56** (26), 7474-7483 (2017).

45. A. E. Goodling, S. Nagelberg, B. Kaehr, C. H. Meredith, S. I. Cheon, A. P. Saunders, M. Kolle, and L. D. Zarzar, "Colouration by total internal reflection and interference at microscale concave interfaces," Nature **566** (7745), 523-527 (2019).

46. A. E. Goodling, S. Nagelberg, M. Kolle, and L. D. Zarzar, "Tunable and Responsive Structural Color from Polymeric Microstructured Surfaces Enabled by Interference of Totally Internally Reflected Light," ACS Materials Lett. **2** (7), 754-763 (2020).

47. K. Li, T. Li, T. Zhang, H. Li, A. Li, Z. Li, X. Lai, X. Hou, Y. Wang, L. Shi, M. Li, and Y. Song, "Facile full-color printing with a single transparent ink," Sci. Adv. **7** (39), eabh1992 (2021).

8.8. Supporting information

8.8.1. Round-trip reflection for normal and oblique incidence

First, we consider normal incidence. In this case, the paths of the incident light inside the triangular structure do not have to be distinguished, so only the path from Interface1 to Interface2 is considered. For the round-trip reflection, the total internal reflection (TIR) should occur at both interfaces (Figure 8.6a). Snell´s law at Interface1 is

$$n_1 \sin\theta_\mathrm{b} = n_2 \sin\theta_1$$

where θ_b is the angle of the triangle. For TIR, $\theta_1 > 90°$

$$\theta_\mathrm{b} > \sin^{-1}\frac{n_2}{n_1} = \theta_\mathrm{c} \qquad 8.12$$

where θ_c is the critical angle. At Interface2, again, Snell´s law is

$$n_1 \sin\theta_2 = n_2 \sin\theta_3$$

For TIR, $\theta_3 > 90°$, therefore,

$$\theta_2 = 180° - 3\theta_\mathrm{b} > \sin^{-1}\frac{n_2}{n_1} = \theta_\mathrm{c}$$

$$\theta_\mathrm{b} < \frac{180° - \theta_\mathrm{c}}{3} \qquad 8.13$$

From Equations 8.12 and 8.13, the round-trip condition is

$$\theta_c < \theta_b < \frac{180° - \theta_c}{3} \qquad 8.14$$

Equation 8.14 is plotted in Figure 8.6b. We can find that the condition is satisfied only when the refractive index n_1 is larger than 1.42. The round-trip condition can be satisfied in a wider θ_b with an increase in n_1.

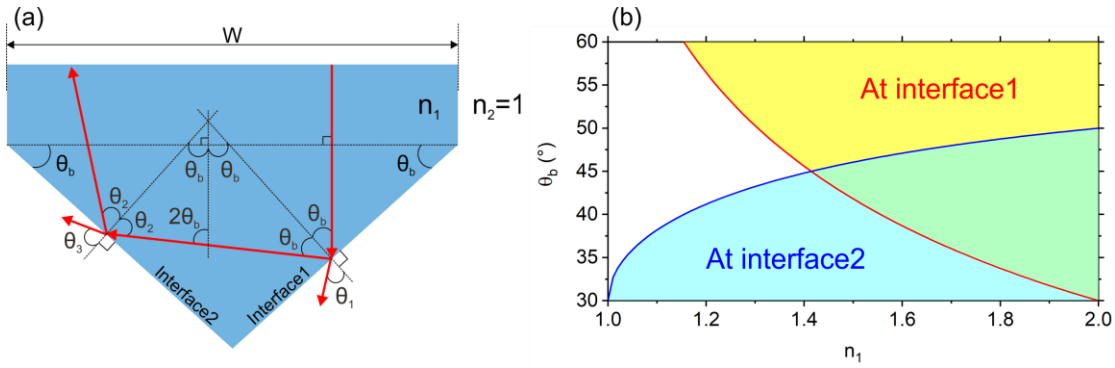

Figure 8.6. (a) Schematic illustration of the round-trip reflection for normal incidence. (b) The round-trip condition for the DCR. The yellow and blue areas indicate Equations 8.12 and 8.13, respectively. The overlapped area is Equation 8.14.

To take into account the oblique incident angle, we have to modify the round-trip condition Equation 8.14 by considering two different paths of the incident light inside the triangular structure. From Figure 8.7a, the incident angle at Interface1 is now $\theta_{11} = \theta_b + \theta_{in}$. Therefore, the round-trip condition for Path1 is

$$\theta_c - \theta_{in} < \theta_b < \frac{180° - \theta_c - \theta_{in}}{3} \qquad 8.15$$

The incident angle at Interface2 is $\theta_{22} = \theta_b - \theta_{in}$. From this, the condition for Path2 is

$$\theta_c + \theta_{in} < \theta_b < \frac{180° - \theta_c + \theta_{in}}{3} \qquad 8.16$$

To obtain the round-trip reflection for both paths, θ_b should be

$$\theta_c + \theta_{in} < \theta_b < \frac{180° - \theta_c - \theta_{in}}{3} \qquad 8.17$$

This is a round-trip condition for oblique incidence. Equations 8.15 and 8.16 are plotted in Figure 8.2c. For $n_1 = 1.6$, the round-trip condition can be satisfied up to the incident angle of 6° when θ_b is 45°. Figure 8.7b and 8.7c show the direction in which the light goes after the round-trip reflection (θ_{out} in Figure 8.7a). When θ_b is 45°, θ_{out} is exactly the same as θ_{in} for both paths. This means that the DCR with $\theta_b = 45°$ can act as a retroreflector.

For an experimental system, refraction at the flat top surface of the DCR should be considered (Figure 8.8a). The refraction angle θ_r at the flat surface is

$$\theta_r = \sin^{-1}\left(\frac{n_2}{n_1} sin\theta'_{in}\right) \qquad 8.18$$

The round-trip condition for the experimental system can be obtained just by substituting θ_r into θ_{in} in Equations 8.15, 8.16, and 8.17. Because of the refraction at the surface, the round-trip condition can be satisfied at a wider incident angle (see Figure 8.8b).

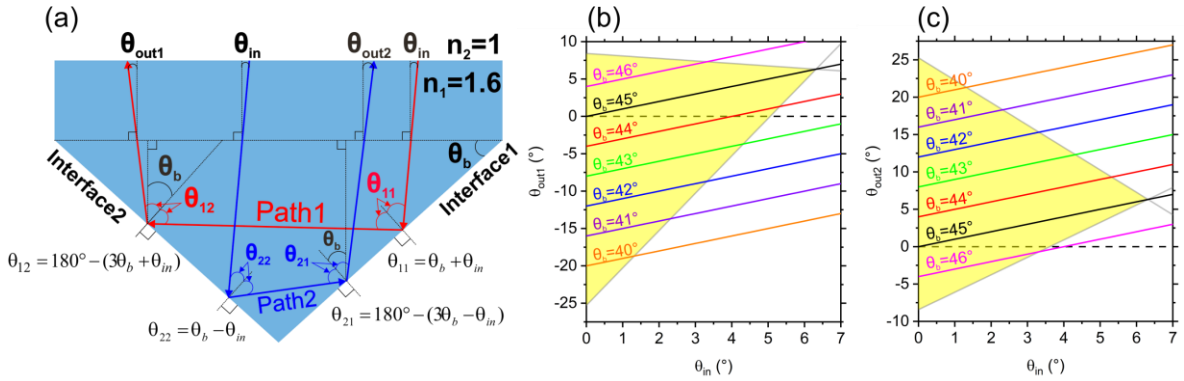

Figure 8.7. (a) Schematic illustration of the round-trip reflection for oblique incidence. (b – c) θ_{out} for Path1 and Path2. The yellow area indicates the round-trip condition.

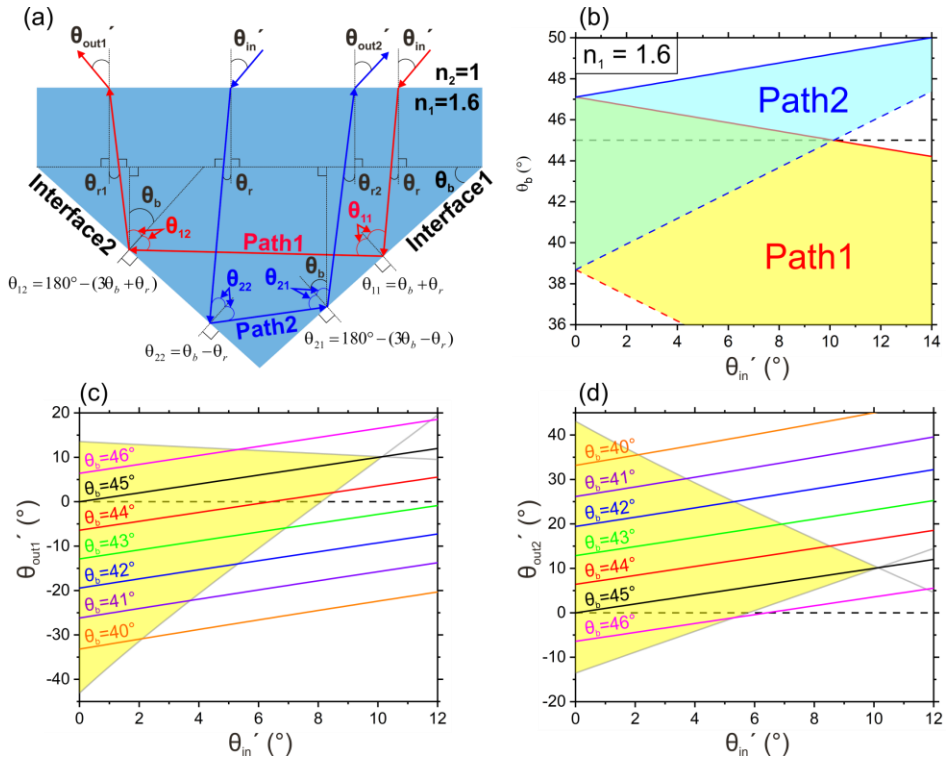

Figure 8.8. (a) Schematic illustration of the round-trip reflection for oblique incidence. The refraction at the surface of the structure is considered. (b) The round-trip condition for oblique incidence. The yellow and blue areas indicate Equations 8.15 and 8.16 with modification to take into account refraction at the film surface. (c – d) θ_{out}´ for Path1 and Path2. The yellow area indicates the round-trip condition.

For Path2, it is expected that part of the light reflected at Interface2 (R_{22}) goes to the flat surface of the DCR without striking on Interface1. Here, R_{22} will be roughly estimated based on Figure 8.2e. We only consider the incident light determined by s_2 and the situation satisfying Equation 8.17 for arbitrary n_1 (Figure 8.9a). The ratio of the energy of R_{22} to the total energy of the incident light can be found as h/H. h can be found using a right triangle defined by an angle θ_x and lengths h, x, and l. θ_x is $90° - \theta_{22} - \theta_b$. From this, h, x, and l can be written as

$$l\cos\theta_x = x \tag{8.19}$$

$$l\sin\theta_x = h \tag{8.20}$$

$$(W - x)\tan\theta_b = h \tag{8.21}$$

From Equations 8.19-8.21, h can be written as

$$h = \frac{W\tan\theta_b\tan\theta_x}{\tan\theta_b + \tan\theta_x} \tag{8.22}$$

The energy of the incident light determined by h/H goes to the flat surface of the DCR without any reflection at Interface1. The rest of the energy of the incident light, which is reflected by the round-trip reflection, is expressed as

$$f = 1 - \frac{h}{H} = 1 - \frac{2\tan\theta_x}{\tan\theta_b + \tan\theta_x} \tag{8.23}$$

Equation 8.23 is plotted in Figure 8.9b for $\theta_b = 45°$. When the flat top surface of the DCR is ignored, R_{22} goes back to the direction where the incident light is coming, meaning that R_{22} is not lost in the total reflectance of the DCR. Next, we consider the case that the thickness of the DCR is finite, and there is the flat top surface. The incident angle of R_{22} at the top surface θ_y is much greater than θ_c (Figure 8.9c). θ_y can be expressed as $\theta_y = 2\theta_{22} + \theta_{in}$. When θ_{in} is 0°, θ_y is 90°, meaning that since $\theta_b = 45°$ is now considered, all incident light reflected at Interface2 goes to Interface1. Therefore, R_{22} does not exist in this case. For θ_{in} greater than 0°, R_{22} exists and is reflected at the flat top surface of the DCR by TIR. After R_{22} is reflected, R_{22} propagates along an optical path that is like a mirror image of the blue arrows shown in Figure 8.9a. (R_{22} goes into a triangular structure next to or far from the one that we consider in Figure 8.9a, depending on how thick the top film of the DCR is. This R_{22} strikes on Interface1 of that triangular structure at an incident angle of θ_{22}. θ_{22} is greater than $\theta_{c.\ Therefore}$, R_{22} is reflected at Interface1 and goes to the flat top surface. The incident angle of the reflected R_{22} at the flat top surface is θ_{in} ($\theta_{in} << \theta_c$), resulting in that the reflected R_{22} passes through the flat top surface.)

s_1/s and s_2/s are shown in Figure 8.9b for $\theta_b = 45°$. The description of s, s_1, and s_2 can be found in the main text (see Figure 8.2e). For oblique incidence, more energy of the incident light strikes on Interface2. Therefore, s_2/s is larger than s_1/s. The difference between those increases with an increase in θ_{in}. By taking all those things into account, for both cases (with and without the flat top surface of the DCR), the net reflectance of Path2 becomes $f \times (s_2/s)$. However, R_{22} is also reflected back to the direction where the incident light is coming, meaning no reduction in reflection of the DCR by R_{22}. Therefore, we only have to consider s_1/s and s_2/s to calculate reflectance using the DL model (Equation 8.7).

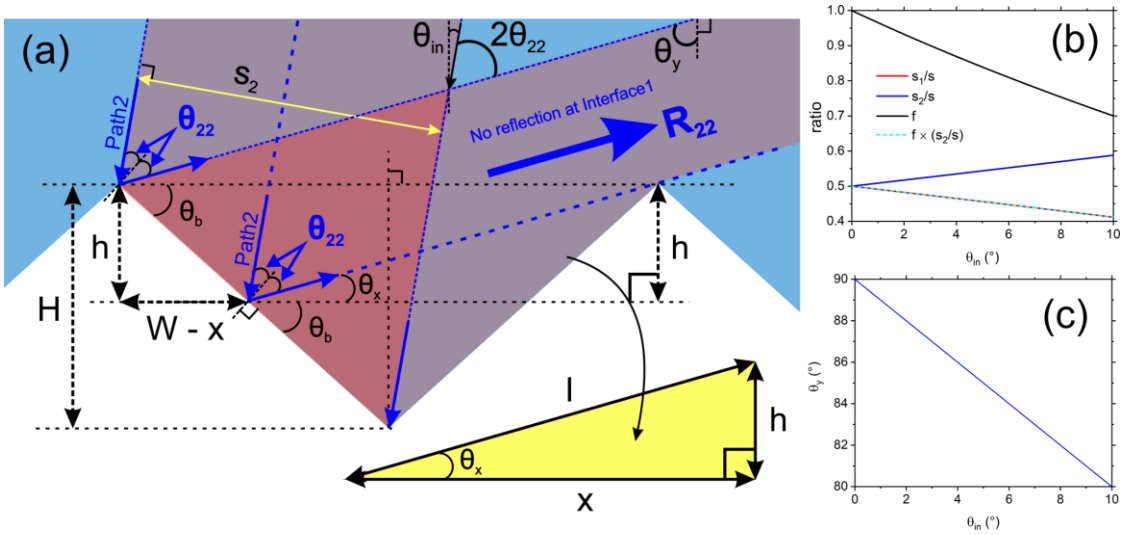

Figure 8.9. (a) Schematic illustration of the round-trip reflection of Path2. (b) The red, blue, and black lines show s_1/s, s_2/s, and f, respectively. The cyan dashed line is $f \times (s_2/s)$. (c) The incident angle θ_y. For (b) and (c), $\theta_b = 45°$ was considered.

8.8.2. Optical properties of the DCR

Figure 8.10 shows reflection spectra of the DCR for the backward incidence with TE polarization. The calculation methods for those spectra are the same for Figure 8.3. The normalized electric field maps for TM and TE polarization at $\lambda_0/L \approx 0.28$ are shown in Figure 8.11.

Figure 8.12 shows transmission spectra for the forward incidence. The infinitely thick film is considered. Therefore, there is no reflection at the flat top surface of the DCR. The DCR has high transmission not only for normal incident but also for high incident angle. This result shows that the DCR can act as an ALT filter. However, in the experimental system, the transmission severely decreases at a high incident angle because of the TIR at the flat top surface of the DCR. This strong reflection can be weakened by applying an antireflection structure on the flat surface, such as Moth´s eye [1]. Figure 8.13 shows electric field distribution maps for the forward incidence for both TM and TE polarizations at $\lambda_0/L \approx 0.07$.

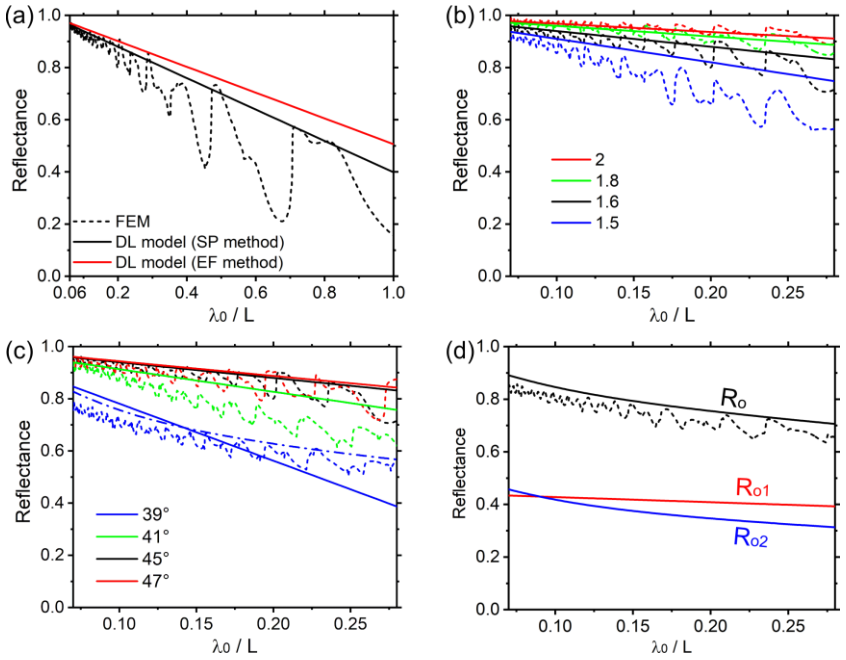

Figure 8.10. For (a – c), the dashed lines are reflection spectra calculated by the FEM for all figures. The solid lines are calculated by the DL model with the SP method. The incident light is TE polarized. The backward incidence is considered. (a) The reflectance of the DCR with n_1 = 1.6 and θ_b = 45° at θ_{in} = 0°. The red solid line is calculated by the DL model using the EF method. (b) n_1 dependence. θ_b and θ_{in} are 45° and 0°, respectively. The red, green, black, and blue lines are for n_1 = 2, 1.8, 1.6, and 1.5, respectively. (c) θ_b dependence for the DCR with n_1 = 1.6 and θ_{in} = 0°. L is fixed and W changes according to θ_b. The red, black, green, and blue lines are for θ_b is 47°, 45°, 41°, and 39°, respectively. The blue dashed-dotted line is calculated using the DL model with Equation 8.8. w_0 is determined so that w_0/L becomes about 3.5. (d) Reflection spectra for n_1 = 1.6, θ_b = 45°, and θ_{in} = 6°. The red and blue lines are calculated using the SP method and Equation 8.8, respectively.

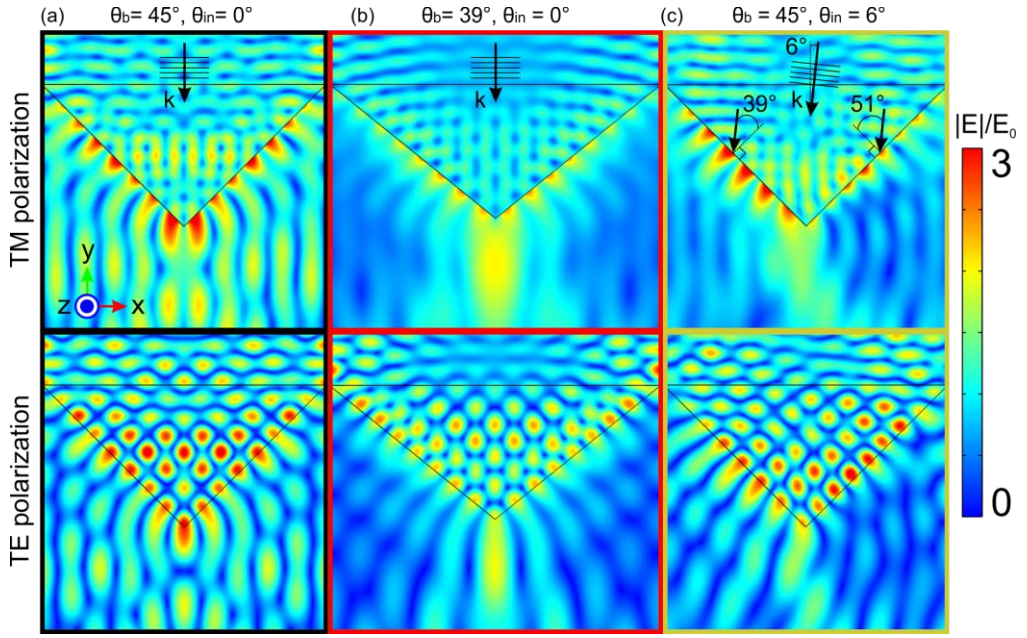

Figure 8.11. Color maps of the absolute value of electric field distribution at $\lambda_0/L \approx 0.28$. n_1 is 1.6, and the incident light is (top row) TM and (bottom row) TE polarized.

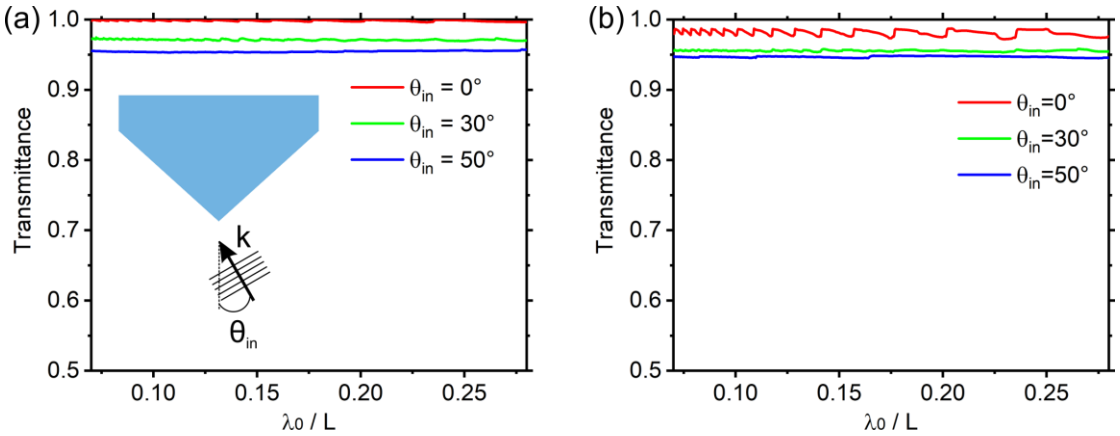

Figure 8.12. Transmission spectra of the DCR for the forward incidence with (a) TM and (b) TE polarization. The structural parameters of the DCR are n_1 = 1.6 and θ_b = 45°.

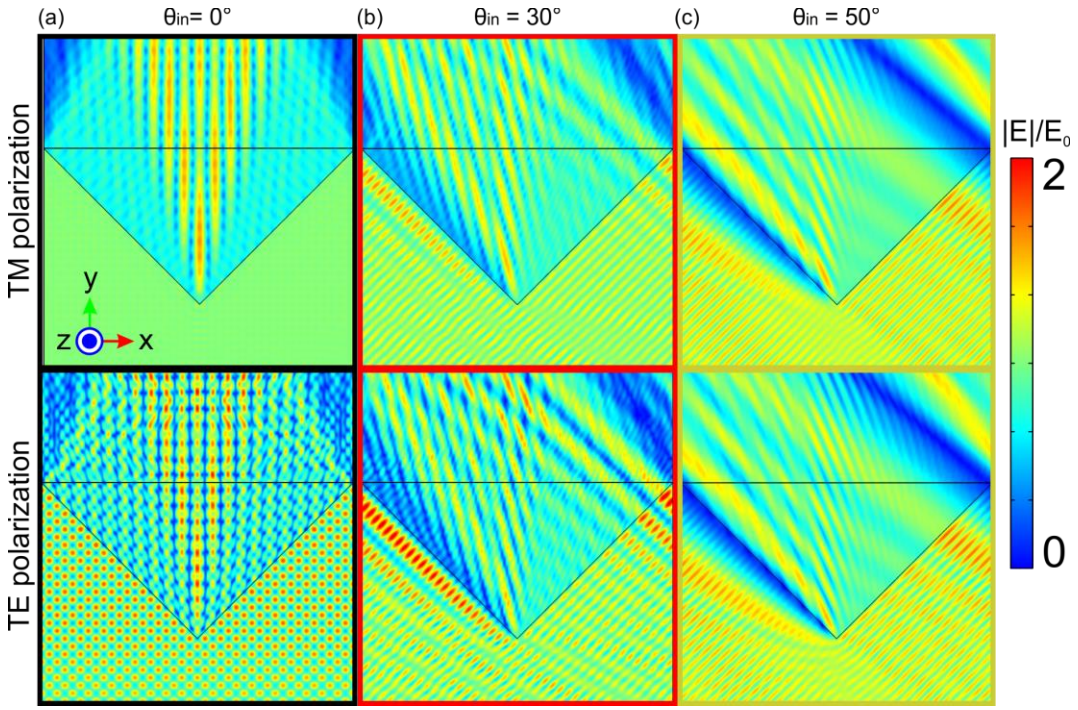

Figure 8.13. Color maps of the absolute value of electric field distribution for the forward incidence at $\lambda_0/L \approx 0.07$. n_1 = 1.6, θ_b = 45°, and the incident light is (top row) TM and (bottom row) TE polarized.

8.8.3. Mode-to-mode conversion of the DCR

Understanding the mode-to-mode conversion of the DCR is necessary to gain insight into its ALT properties [2, 3]. This is also important to examine the feasibility of the DCR for radiative cooling under high humidity condition [4, 5]. First of all, the DCR cannot act as an optical diode because a reciprocal material is considered for the DCR and mode-to-mode conversion occurs [3]. However, as can be seen in Figure 8.3, Figure 8.10 and Figure 8.12, the DCR can possess ALT properties.

When the triangular structure of the DCR is sufficiently larger than the wavelength, geometrical optics dominates the optical properties of the DCR. Therefore, we investigate the mode-to-mode conversion of the DCR from the point of view of geometrical optics. Figure 8.14 shows some possible optical pathways of the incident light inside the DCR for the forward incidence. Reflection and refraction occurring in the DCR are considered only. The flat top surface is ignored in this analysis. The DCR has $\theta_b = 45°$ and $n_1 = 1.6$. The incident angle is θ_{inF}. s, s_1, and s_2 are defined in Figure 8.2e in the main text. In Figure 8.14, R and T indicate reflected and transmitted light, respectively. When $\theta_{inF} > 45°$, the incident light strikes only on Interface1. From this, we consider two situations: $\theta_{inF} < 45°$ (Figure 8.14a) and $\theta_{inF} > 45°$ (Figure 8.14b). Similarly, optical pathways inside the DCR for the backward incidence are considered in Figure 8.15.

The reflection and refraction angles in Figures 8.14 and 8.15 are summarized in Tables 8.1 and 8.2, and Figure 8.16. For example, some reflection angles, θ_{F5}, and $\theta_{F3''}$, exceed the critical angle for all incident angles, so the transmitted light for those pathways does not exist. For backward incidence with $\theta_{inB} < 45°$, there is a range of θ_{inB} in which only two reflections occur (yellow shaded area in Figure 8.16). This angle range is the round-trip condition (Equation 8.17). For $\theta_{inB} > 45°$, there is also a range of θ_{inB} in which reflection can occur only once (cyan shaded area in Figure 8.16).

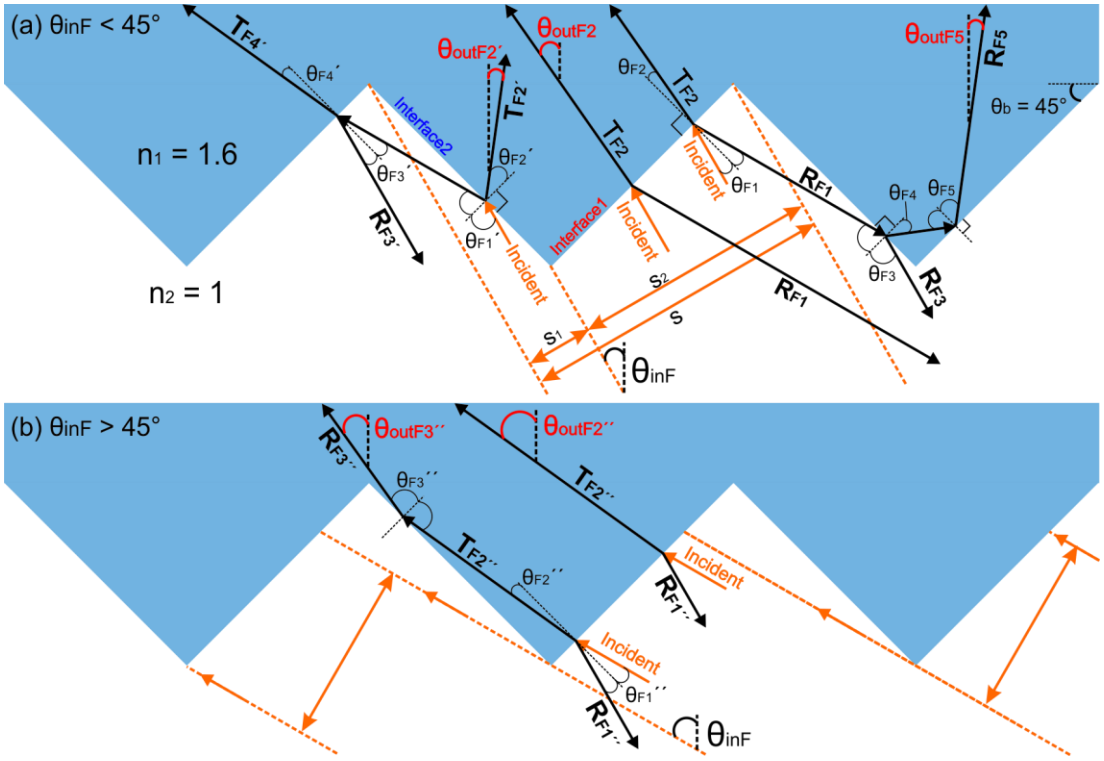

Figure 8.14. Optical pathways of the incident light after multiple refractions and reflections inside the DCR. The DCR has $\theta_b = 45°$ and $n_1 = 1.6$. The forward incidence with (a) $\theta_{inF} < 45°$ and (b) $\theta_{inF} > 45°$ are considered.

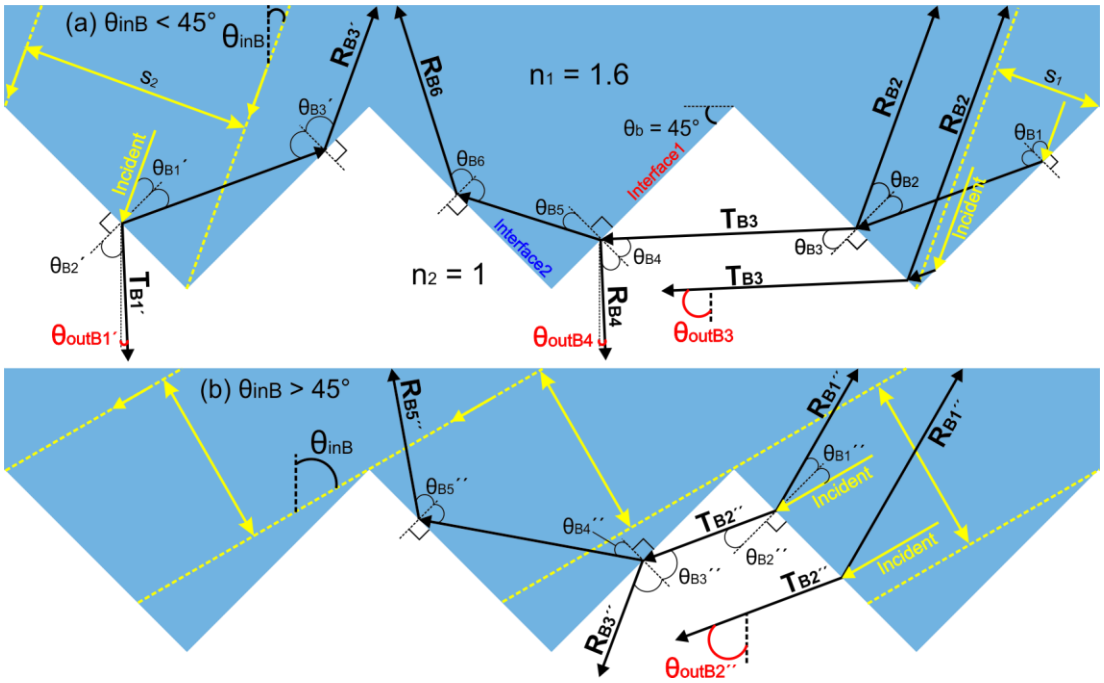

Figure 8.15. Optical pathways of the incident light after multiple refractions and reflections inside the DCR. The DCR has $\theta_b = 45°$ and $n_1 = 1.6$. The backward incidence with (a) $\theta_{inB} < 45°$ and (b) $\theta_{inB} > 45°$ are considered.

Table 8.1. The reflection and refraction angles in Figure 8.14

$\theta_{F1} = (90° - \theta_b) - \theta_{inF}$	$\theta_{F1'} = (90° - \theta_b) + \theta_{inF}$	$\theta_{F1''} = \theta_{inF} - \theta_b$
$\theta_{F2} = \sin^{-1}\left(\frac{n_2}{n_1}\sin\theta_{F1}\right)$	$\theta_{F2'} = \sin^{-1}\left(\frac{n_2}{n_1}\sin\theta_{F1'}\right)$	$\theta_{F2''} = \sin^{-1}\left(\frac{n_2}{n_1}\sin\theta_{F1''}\right)$
$\theta_{F3} = 180° - 2\theta_b - \theta_{F1}$	$\theta_{F3'} = \theta_{F3} = 180° - 2\theta_b - \theta_{F1'}$	$\theta_{F3''} = 180° - 2\theta_b - \theta_{F2''}$
$\theta_{F4} = \sin^{-1}\left(\frac{n_2}{n_1}\sin\theta_{F3}\right)$	$\theta_{F4'} = \sin^{-1}\left(\frac{n_2}{n_1}\sin\theta_{F3'}\right)$	
$\theta_{F5} = 180° - 2\theta_b - \theta_{F4}$		

Table 8.2. The reflection and refraction angles in Figure 8.15

$\theta_{B1} = \theta_b + \theta_{inB}$	$\theta_{B1'} = \theta_b - \theta_{inB}$	$\theta_{B1''} = \theta_{inB} - \theta_b$
$\theta_{B2} = 180° - (3\theta_b + \theta_{inB})$	$\theta_{B2'} = \sin^{-1}\left(\frac{n_1}{n_2}\sin\theta_{B1'}\right)$	$\theta_{B2''} = \sin^{-1}\left(\frac{n_1}{n_2}\sin\theta_{B1''}\right)$
$\theta_{B3} = \sin^{-1}\left(\frac{n_1}{n_2}\sin\theta_{B2}\right)$	$\theta_{B3'} = 180° - (3\theta_b - \theta_{inB})$	$\theta_{B3''} = 180° - 2\theta_b - \theta_{B2''}$
$\theta_{B4} = 180° - 2\theta_b - \theta_{B3}$		$\theta_{B4''} = \sin^{-1}\left(\frac{n_2}{n_1}\sin\theta_{B3''}\right)$
$\theta_{B5} = \sin^{-1}\left(\frac{n_2}{n_1}\sin\theta_{B4}\right)$		$\theta_{B5''} = 180° - 2\theta_b - \theta_{B4''}$
$\theta_{B6} = 180° - 2\theta_b - \theta_{B5}$		

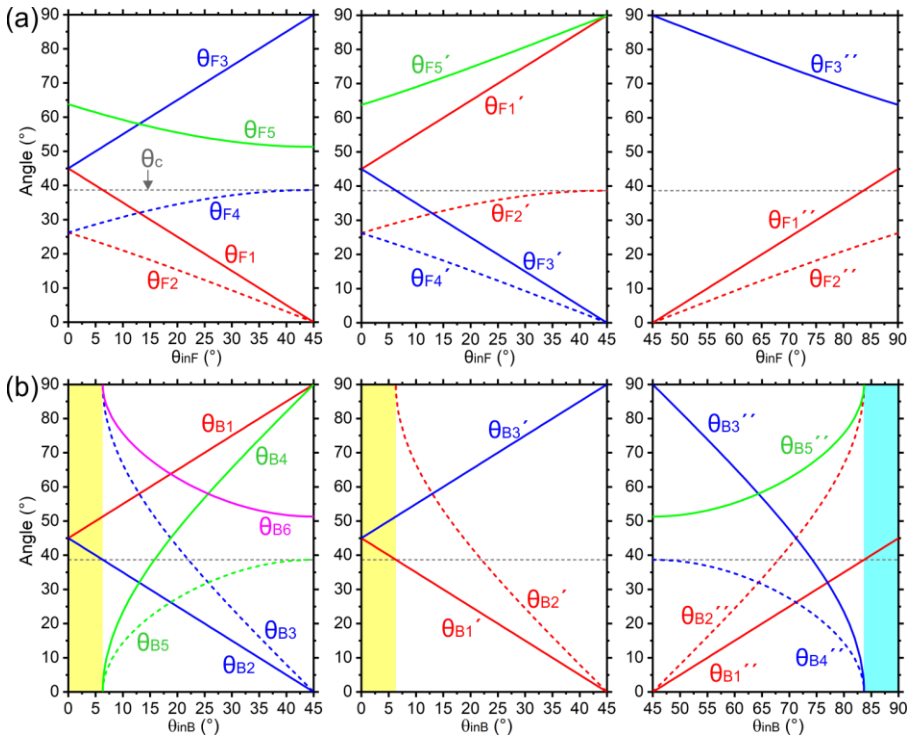

Figure 8.16. The reflection and refraction angles shown in (a) Figure 8.14 and (b) Figure 8.15. The grey dashed line indicates the critical angle. The yellow shaded areas show the round-trip condition. The cyan shaded area indicates the angle range in which only one TIR occurs.

Based on the reflection and refraction angles in Figure 8.16, we roughly examine the mode-to-mode conversion of the DCR. For an optical system composed of a reciprocal material, the same modes must exist for forward and backward incidence. We may be able to find those modes by observing two different angles for both incidences. One is input angles, which are the incident angles denoted as θ_{inF} and θ_{inB}. Another is output angles defined by a propagation direction of the light after experiencing multiple reflections and refractions in the DCR. The output angles are denoted as θ_{outF} and θ_{outB} for the forward and backward incidence, respectively (Figures 8.14 and 8.15). If there are the same modes for both incidences, sets of (θ_{outF}, θ_{inF}) = (θ_{inB}, θ_{outB}) can be found.

We first focus on the input and output angles that can be close to the round-trip condition (± 6° for θ_b = 45° and n_1 = 1.6. This can be found from Equation 8.17 and Figure 8.2c). For the forward incidence with θ_{inF} < 45°, the lights T_{F2}, R_{F5}, and $T_{F2'}$ can have small θ_{outF} (Figure 8.14). For the backward incidence with θ_{inB} < 45°, R_{B4} and $T_{B1'}$ can have small θ_{outB} (Figure 8.15). In Figure 8.17, the output angles of those lights are plotted as a function of the input angles. Since the optical phenomena occurring in the DCR are mirror symmetry for the positive and negative input angles, the absolute value of the input and output angles are considered. In Figure 8.17a, it can be found that the output angles for the forward incidence can exist for all input angles in the range of θ_{inF} < 45°. In contrast, the DCR does not have any output angles for backward incidence in a specific range of θ_{inB}. This angle range corresponds to the round-trip condition. (θ_{outF}, θ_{inF}) = (θ_{inB}, θ_{outB}) can be found outside of the round-trip condition. We next turn our focus to the input and output angles far from the round-trip condition. The lights $T_{F2''}$ and $R_{F3''}$ for the forward incidence have θ_{inF} > 45° (Figure 8.14). Considering the optical pathways and the input and output angles, we can find that the modes of $T_{B2''}$ and T_{B3} for the backward incidence correspond to the modes of $T_{F2''}$ and $R_{F3''}$, respectively (Figure 8.17b).

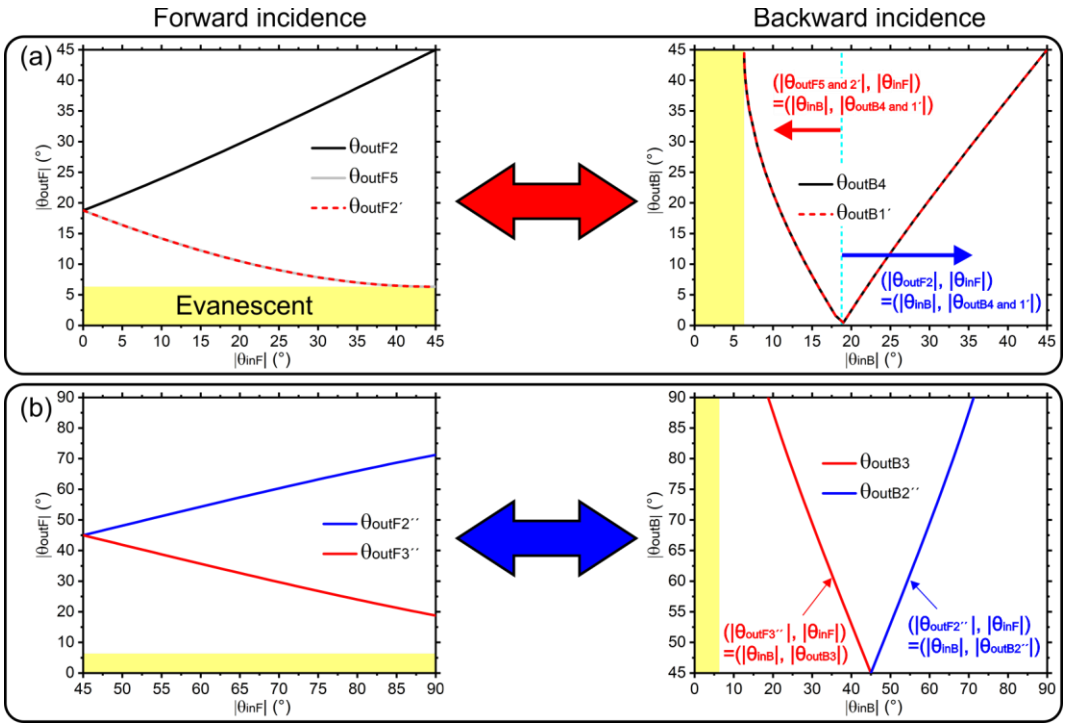

Figure 8.17. The input angles and output angles for the forward and backward incidence in the angle ranges (a) close to and (b) far from the round-trip condition. The round-trip condition is indicated by the yellow shaded areas.

From Figure 8.17, we find that there are output angles for any input angles for the forward incidence, but the output angle cannot be found in the round-trip condition for the backward incidence. Our analysis still does not consider some optical pathways (Figures 8.14 and 8.15). Those missing pathways may result in the input and output angles in high angle ranges but not in the round-trip condition. Therefore, this result indicates that all incident light can pass through the DCR for the forward incidence, but the DCR blocks the light for the backward incidence in the round-trip condition. In general, it may be expected that the mode-to-mode conversion occurs from ray to ray by reflection and refraction for the structure much larger than the wavelength. However, in the round-trip condition, all incident light is converted into evanescent modes for the backward incidence. To observe the transmitted light in the round-trip condition for the forward incidence, the incident light has to be converted to evanescent modes once. Then, the evanescent waves are decoupled at the interface of the triangular structure, such as a fluctuated total internal reflection.

Having the findings of the mode-to-mode conversion, we assess the possibility that the DCR can improve radiative cooling under high humidity. If the DCR is placed above the thermal emitter, a part of the incoming atmospheric radiation is converted into an evanescent wave. In this case, we must consider the near-field radiative heat transfer (NRHT) [6, 7]. NRHT can occur in a smaller gap size than a thermal wavelength. If the distance between the DCR and thermal emitter is sufficiently larger than the penetration depth of the evanescent wave, radiative heat transfer from the atmosphere to the thermal emitter can be forbidden. Therefore, the heat gain from atmospheric radiation may be decreased by using the DCR without hindering the transmission of outgoing thermal radiation from the thermal emitter (Figure 8.17). Since the humid atmosphere is semi-transparent, part of the outgoing thermal radiation is absorbed by the atmosphere, and the rest can reach the cold outer space.

Our simplified mode-to-mode conversion analysis indicates the DCR may have the potential to restore the cooling performance under high humidity. However, in our analysis made here, some optical pathways, the diffraction modes of the grating, the diffraction of evanescent waves (DL model), the flat top surface of the DCR, and light absorption of the DCR are not considered. Further investigations have to take all those into account to evaluate the feasibility of the DCR for radiative cooling under high humidity [8].

8.8.4. References

1. M. Kraus, Z. Diao, K. Weishaupt, J. P. Spatz, K. Taschner, H. Bartzsch, R. Schmittgens, and R. Brunner, "Combined 'moth-eye' structured and graded index-layer anti-reflecting coating for high index glasses," Opt. Express **27** (24), 34655-34664 (2019).

2. D. Jalas, A. Petrov, M. Eich, W. Freude, S. Fan, Z. Yu, R. Baets, M. Popović, A. Melloni, J. D. Joannopoulos, M. Vanwolleghem, C. R. Doerr, and H. Renner, "What is — and what is not — an optical isolator," Nat. Photonics **7** (8), 579-582 (2013).

3. A. A. Maznev, A. G. Every, and O. B. Wright, "Reciprocity in reflection and transmission: What is a 'phonon diode'?," Wave Motion **50** (4), 776-784 (2013).

4. R. Y. M. Wong, C. Y. Tso, C. Y. H. Chao, B. Huang, and M. P. Wan, "Ultra-broadband asymmetric transmission metallic gratings for subtropical passive daytime radiative cooling," Solar Energy Materials and Solar Cells **186**, 330-339 (2018).

5. X. Wu, and C. Wang, "The application of asymmetric transmission in daytime radiative cooling cannot increase the cooling power," Solar Energy Materials and Solar Cells **215** (2020).

6. J. C. Cuevas, and F. J. García-Vidal, "Radiative Heat Transfer," ACS Photonics **5** (10), 3896-3915 (2018).

7. D. Thompson, L. Zhu, R. Mittapally, S. Sadat, Z. Xing, P. McArdle, M. M. Qazilbash, P. Reddy, and E. Meyhofer, "Hundred-fold enhancement in far-field radiative heat transfer over the blackbody limit," Nature **561** (7722), 216-221 (2018).

8. G. Ulpiani, G. Ranzi, J. Feng, and M. Santamouris, "Expanding the applicability of daytime radiative cooling: Technological developments and limitations," Energy and Buildings **243** (110990), 110990 (2021).

Acknowledgement

I would like to thank all who have supported me in completing this dissertation.

First of all, I would like to express my great appreciation to my supervisor, Prof. Dr. Markus Retsch. On Christmas day 2018, I got an invitation from him for a Ph.D. position at his group. Ever since, he provided me with outstanding research projects, guided me in the right direction to complete my Ph.D. degree, and gave me much freedom to enjoy the science. In addition, I am grateful that he entrusted me to be the corresponding author for all my publications (and manuscripts that will hopefully be published!). The research experience with him was an invariable and life-changing experience, which will be a crucial milestone for my future career.

I also very much appreciate Prof. Dr. Ryushi Fujimura, who was my previous supervisor for my bachelor´s and master´s degrees. His supervision certainly developed essential skills and mindsets for researching and enabled me to do my Ph.D. research in Germany accordingly. He supported this dissertation as well to a significant extent. I always enjoyed discussions with him, providing me with deep insights and various ideas for my research.

I thank current and former colleagues at Physical Chemistry 1, including Tobias Lauster, Tanja Feller, Qimeng Song, Alexander Berger, Stefan Rettinger, Flora Lebeda, Ina Klein, Anna Lechner, Kai Herrmann, Marius Schöttle, Thomas Tran, Bernd A.F. Kopera, Argyrios Georgiadis, Daewoo Suh, and Nelson W. Pech-May. They made my Ph.D. journey special. It was a pleasure to work together with you and get to know you in the process.

My family, especially my parents, Satoshi and Rika, kept giving me tremendous support not only during my Ph.D. but also throughout my life. It is obvious that I would not be where I am without them.

Lastly, I owe the deepest gratitude to my girlfriend, Friederike Knoop. She has always been by my side, motivated me to work hard, and supported me throughout writing this dissertation.

Many thanks.

(Eidesstattliche) Versicherungen und Erklarungen

§8 Satz 2 Nr. 3 PromO Fakultät

Hiermit versichere ich eidesstattlich, dass ich die Arbeit selbstständig verfasst und keine anderen als die von mir angegebenen Quellen und Hilfsmittel benutzt habe

(vgl. Art. 64 Abs 1 Satz 6 BayHSchG).

§8 Satz 2 Nr. 3 PromO Fakultät

Hiermit erkläre ich, dass ich die Dissertation nicht bereits zur Erlangung eines akademischen Grades eingereicht habe und dass ich nicht bereits diese oder eine gleichartige Doktorprüfung endgültig nicht bestanden habe.

§8 Satz 2 Nr. 4 PromO Fakultät

Hiermit erkläre ich, dass ich Hilfe von gewerblichen Promotionsberatern bzw. –vermittlern oder ähnlichen Dienstleistern weder bisher in Anspruch genommen habe noch künftig in Anspruch nehmen werde.

§8 Satz 2 Nr. 7 PromO Fakultät

Hiermit erkläre ich mein Einverst¨andnis, dass die elektronische Fassung der Dissertation unter Wahrung meiner Urheberrechte und des Datenschutzes einer gesonderten Überprüfung unterzogen werden kann.

§8 Satz 2 Nr. 8 PromO Fakultät

Hiermit erkläre ich mein Einverständnis, dass bei Verdacht wissenschaftlichen Fehlverhaltens Ermittlungen durch universitätsinterne Organe der wissenschaftlichen Selbstkontrolle stattfinden können.

Ort, Datum, Unterschrift